The Mechanics of Continental Deformation in Asia and California

Philippa Louise Whitehouse

Wolfson College

Thesis submitted for the degree of D.Phil.

Faculty of Physical Sciences, University of Oxford

Trinity Term, 2004

Supervised by Prof. P.C. England

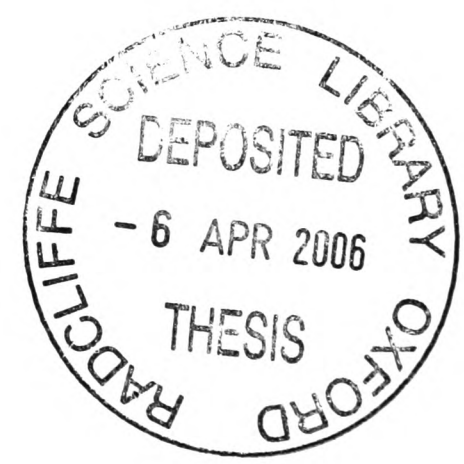

Extended Abstract

The Mechanics of Continental Deformation in Asia and California

Philippa Louise Whitehouse
Wolfson College, Oxford

D. Phil. Trinity 2004

The failure of plate tectonic theory to explain the deformation observed across continental plate boundary zones has led to the development of continuum models of lithospheric deformation in which the lithosphere is treated as a layer of viscous material governed by the equation for creeping viscous flow,

$$\frac{\partial \sigma_{ij}}{\partial x_j} = \rho g_i \tag{1}$$

where the left hand side represents spatial gradients of stress that are balanced by differences in gravitational potential energy on the right hand side.

Strain rates and an assumed power law rheology are used as a proxy for stress,

$$\tau_{ij} = B\dot{E}^{(1/n)-1}\dot{\varepsilon}_{ij} \tag{2}$$

where B is a strength parameter that represents the depth–averaged temperature dependence of the lithospheric rheology, $\dot{E}$ is the second invariant of the strain rate tensor, and n is the power law exponent in the stress–strain rate relationship. Finite element methods are used to solve the thin viscous sheet equations (England & McKenzie, 1982), yielding a velocity field that may be compared to observations from regions of continental deformation.

In this study I investigate the deformation of the lithosphere in two regions of active deformation: south–east Asia and the western North America plate boundary zone. Particular attention is paid to the degree to which the deformation fields reflect the driving forces, and the effect of lateral variations in effective viscosity and lithospheric strength upon the deformation field.

Asia

The collision of India with Asia is considered to be the driving force for deformation spanning a 2000 km by 3000 km area in south–east Asia. However strain rates do not decay monotonically with distance from the plate boundary as predicted for a homogeneous viscous fluid (England *et al.*, 1985). The distribution of deformation is dependent upon the distribution of driving forces, and the response of the lithosphere to these driving forces. The former must be constrained in order to gain insight into the latter.

Driving forces are classified in terms of boundary conditions or buoyancy forces. A velocity field for Asia, constrained by Quaternary slip rates and GPS data, defines boundary conditions for the region. Buoyancy forces arise from gradients of potential energy that result from crustal thickness variations.

A model for the potential energy distribution across south–east Asia has been developed. In this model I assume Airy isostasy, and consider two modes of lithospheric evolution for south–east Asia. In the first, lithospheric thickening is calculated assuming volume is conserved, while in the second, a constant lithospheric thickness is assumed to be maintained by small scale mantle convection. The possibility that overthickening of the lithosphere has led to the development of a gravitational instability, and the delamination of the lower lithosphere, is also considered.

Topographic heights are used to obtain estimates of present–day crustal thickness, given values for the thickness of the crust (S_0) and lithosphere (L) prior to collision. Assumptions about the vertical distribution of density permit the calculation of a potential energy distribution, from which geoid heights may be inferred. These models are tested against observed geoid data.

Gradients of potential energy drive lithospheric deformation, therefore I seek a model that can reproduce the observed geoid gradient, dN/de, where N is the height of the geoid and e is elevation above sea level. Below elevations of 4 km $dN/de \approx 4$ m km^{-1}. This relationship can be reproduced using a constant thickness model with an initial crustal thickness of $S_0 = 30$ km and a lithospheric thicknesses of $L = 200$ km. At elevations greater than 4km the gradient of the observed geoid abruptly steepens, and a different model of lithospheric evolution is required. It is assumed that a constant value of S_0 prevailed throughout south–east Asia prior to collision. Under this assumption, observed and calculated values of N are compared to determine a value of L that fits the data. Adopting the constant thickness model, predicted values of present–day crustal thickness are also calculated using

$S_0 = 30$ km, and compared to estimates from independent studies. These tests imply that $L = 110$ km for areas above 4 km, indicating that delamination of a significant proportion of the lithosphere has probably taken place beneath Tibet. The final geoid model is converted into a potential energy distribution that is used to constrain solutions to the thin viscous sheet equations.

A simple two–dimensional finite element approach is used to solve the thin viscous sheet equations according to the inputs of boundary and buoyancy forces. The accuracy of each solution is assessed by comparing calculated and observed values of the second invariant of the strain rate tensor within each element. A reasonable fit is obtained using a homogeneous viscous layer, but improvements are made by solving for the lateral variation in the strength parameter, B (equation 2). A relaxation method has been developed whereby the misfit in the second invariant of the strain rate tensor within each element of the finite mesh is used to iterate towards a solution that fits the data. Monte Carlo restart methods are used to vary the velocity data within error and the initial guess for the distribution of B.

Inversions for the strength parameter are first carried out using a value of $n = 1$ in the power–law equation for the rheology of the viscous layer. This yields a solution that is proportional to the effective viscosity distribution throughout south–east Asia. Values of 10^{21} to 10^{22} Pa s are calculated for the margins of the Tibetan plateau, 3×10^{22} to 10^{23} Pa s for Tibet, and 10^{23} to 10^{24} Pa s for the shield regions of India, Siberia and the Tarim Basin. The relationship between the distribution of B and the second invariant of the strain rate tensor allows bounds of $5 \leq n \leq 10$ to be placed upon the stress–strain rate exponent. Inversions are, therefore, also carried out using $n = 3$, 5 and 10 in the power–law relationship. In all cases, a poor fit to the data is found to the south–east of the Tibetan plateau, where the velocity field interpolated upon the finite element mesh is unable to resolve the rotation of lithospheric material. Otherwise, a good fit to the data is achieved in all cases, and I conclude that the deformation of the continental lithosphere in south–east Asia may be explained by the deformation of a power law fluid with a stress–strain rate exponent of $3 \leq n \leq 10$.

The distribution of the strength parameter for this region is found to vary within an order of magnitude for regions deforming at strain rates $\gtrsim 10^{-8}$ yr $^{-1}$. Adjacent to older, colder portions of the lithosphere, such as India, Siberia and the Tarim Basin, strain is concentrated and low effective viscosities are predicted. However, these values reflect the greater strength of the more rigid regions as well as the weakness of the deforming regions. Away from the rigid indenters the lithosphere

deforms in response to the distribution of driving forces, and there are few lithospheric strength heterogeneities to perturb the deformation field.

Western North America

Deformation in the western North America plate boundary zone is driven by motion along the Pacific–North America plate boundary. The equation for creeping viscous flow (equation 1) predicts steady decay of the along–strike component of velocity with distance from the driving boundary. However, velocity profiles taken perpendicular to the plate boundary reveal a step in velocities at distances between 100 km and 200 km from the plate boundary. The step is present throughout central California and corresponds with the location of the Sierra Nevada–Great Valley block (henceforth the Sierra block). This block undergoes negligible amounts of deformation and experiences weak seismic activity in relation to the rest of this plate boundary zone, therefore I treat it as a rigid body.

I investigate the effect of an elongate rigid block entrained within a non–Newtonian viscous fluid upon the surrounding deformation field. The velocity ratio V_1/V_0 is used to compare model results to observed data, where V_1 is the velocity of the block and V_0 is the constant velocity applied along a driving boundary parallel to the orientation of the block. Once again a power–law rheology is used, and I seek to constrain the value of the stress–strain rate exponent, n. This problem is investigated using both a numerical and an analytical approach.

In the first case a finite element method is used to solve the thin viscous sheet equations for the case where the deformation within a rectangular solution domain is defined by a driving velocity boundary condition applied along one boundary of this domain. Gradients of crustal thickness are small within the North America plate boundary zone, and the effect of buoyancy forces upon the deformation are neglected. The Sierra block is modelled as a high viscosity region within the fluid, and solutions are obtained for a suitable region of the parameter space. The length of the driving boundary condition, the dimensions of the block, the distance of the block from the driving boundary, and the value of the stress–strain rate exponent, n, are varied. The velocity ratio, V_1/V_0, is found to increase with the length of the driving boundary condition but decrease with n, and the presence of a rigid block within a distance $\sim D/(2\pi\sqrt{n})$ of the driving boundary, where D is the length of the driving boundary, acts to broaden the zone of deformation.

Experiments are also carried out using a more realistic geometry for the Pacific–North America plate boundary, and a realistic set of boundary conditions. The first–order dependence of V_1/V_0 upon the driving velocity boundary condition and n are unchanged, but differences are found in the distribution of deformation outside the higher viscosity region. When a bend is included in the boundary condition and the driving velocity is constrained using the relative Pacific–North America angular velocity, thickening of the viscous layer takes place between the bend in the boundary and the rigid block. Shear strain rates are concentrated along the driving boundary and either side of the higher viscosity block. These features are interpreted as representing crustal thickening to the south of the Sierra block, and dextral shear within the San Andreas fault zone, and are not realised in the simple model which uses a rectangular solution domain.

A force balance approach is also used to place bounds upon the motion of a rigid block entrained within a non–Newtonian viscous fluid undergoing simple shear flow. Shear stresses applied along the boundaries of the block are balanced to yield an expression for the motion of the block as a fraction of the driving velocity. Once again this ratio, V_1/V_0, is assumed to depend upon the geometry of the system and the stress–strain rate exponent, and the results of this study are in close agreement with the results of the numerical experiments.

The velocity of the Sierra block with respect to stable North America is ~ 12 mm yr^{-1} (Argus & Gordon, 2001) and the relative velocity across the Pacific–North America plate boundary is ~ 52 mm yr^{-1} (DeMets & Dixon, 1999), yielding an observed velocity ratio of $V_1/V_0 \approx 0.23$. This is compared to modelling estimates derived using suitable values for the dimensions of the rigid block, its distance from the driving boundary, and the length of the driving boundary. It is found that values of the stress–strain rate exponent in the range $2.5 \leq n \leq 4$ are required to reproduce the observed velocity ratio. The comparison of model velocity profiles with GPS data confirms this result.

Declaration

The contents of this thesis are all my own work, except where otherwise stated. The views and opinions expressed herein are mine and not necessarily those of any other person or body unless so attributed.

Acknowledgements

I would like to thank all those people who have guided, encouraged, and supported me throughout my time at Oxford. I thank my supervisor, Prof. Philip England, for his unerring ability to come up with new suggestions when I ran out of ideas, and for gently steering me in the right direction.

I thank all my contemporaries in the geodesy group, especially Tim, Gareth, Andy and Isabelle, for fielding my constant stream of geology-related questions, and broadening my knowledge of earth sciences; your advice has been invaluable. I also thank Steve Usher who has always been on hand to help with any technical problems.

I am also grateful to my examiners, Profs. Greg Houseman and Barry Parsons, for taking the time to review my work, and providing excellent discussion and insight during my viva.

I gratefully acknowledge funding from the Natural Environmental Research Council, Wolfson College (Oxford), and the Burdett-Coutts Fund (Earth Sciences, Oxford) for assistance with conference attendance and living expenses.

I would like to thank all those people, both inside and outside the department, who have kept me sane, and made my time at Oxford so enjoyable. Special mention goes to my brother, Robin, for his high–speed proof–reading abilities.

I thank Duncan for being there, for understanding, and for not complaining about the lack of climbing trips this summer.

Finally I thank my parents for tolerating my decision to remain a student for far too long, for their belief in me, and for their continual support in all that I choose to pursue.

Contents

Abstract i

Extended Abstract ii

Declaration vii

Acknowledgements vii

Table of Contents viii

List of Figures xiv

List of Tables xx

1 Introduction **1**

1.1 Plate tectonic theory 1

1.2 Block versus continuum behaviour 2

1.3 Modelling the deformation of south–east Asia 3

1.4 Modelling deformation in the western North America plate boundary zone 6

1.5 Lateral variations in the rheological properties of continental lithosphere 8

1.5.1 Rigid inclusions 9

1.6 Motivation 9

1.7 Objectives of this study 10

2 Mathematical methods: Forward and inverse calculations **12**

2.1 Introduction 12

2.2 Rheology 13

2.3 Governing Equations 17

2.3.1 Creeping viscous flow 17

2.3.2 Assumptions of the thin viscous sheet approximation 17

2.3.3 The thin viscous sheet equations 18

2.3.4 Non–dimensionalising the thin viscous sheet equations 20

2.3.5 Limitations of the thin viscous sheet approximation 21

2.3.6 Solutions to the thin viscous sheet equations 22

2.4 The application of finite element methods to the inversion of lithospheric effective viscosities 23

2.4.1 Interpolation of velocities 24

2.4.2 Solving the thin viscous sheet equations upon a finite element mesh 26

2.4.3 Boundary Conditions 28

2.4.4 Rheological specifications of the thin viscous sheet approximation 28

2.5 Application to determining effective viscosities 29

2.5.1 Relaxation of the viscosity distribution 30

2.5.2 Convergence Criteria 33

2.6 Two–dimensional experiments 34

2.6.1 Forward calculations 34

2.6.2 Viscosity inversions, Newtonian case : $n = 1$ 41

2.6.3 Viscosity inversions, non–Newtonian case : $n > 1$ 45

2.6.4 Solving for n 54

2.7 Monte Carlo restarts 59

2.7.1 Simulation of correlated noise 59

3 Distribution of Gravitational Potential Energy in Asia **65**

3.1 Introduction 65

3.2 Thermal evolution of thickened lithosphere 65

3.3 Topography 70

3.4 Density distribution 73

3.5 Gravitational potential energy of a lithospheric column 75

3.5.1 The calculation of model geoid distributions 80

3.6 Observed Geoid 80

3.7 Dependence of the geoid upon elevation 82

3.7.1 Dependence of the observed geoid upon elevation 82

3.7.2 Dependence of model geoid distributions upon elevation 84

3.8 Modelling the geoid anomaly in south–east Asia 85

3.9 Crustal thickness distribution in south–east Asia 91

3.10 Potential energy distribution 93

4 Viscosity Inversions for south–east Asia **96**

4.1 Introduction 96

4.2 Background 96

4.2.1 Uplift of the Tibetan plateau 98

4.2.2 Mechanisms of convergence 98

4.2.3 Present–day deformation 99

4.3 Use of the thin viscous sheet model to infer lateral variations in effective viscosity across the India–Asia convergence zone 104

4.3.1 The applicability of the thin viscous sheet model to south–east Asia 104

4.3.2 Details of numerical experiments 105

4.3.3 Velocity and Strain Rate Fields in Asia 107

4.3.4 Regionalisation 110

4.4 Results . . . 111

4.4.1 Velocity Fields . . . 111

4.4.2 Viscosity inversions: $n = 1$ . . . 114

4.4.3 Viscosity Inversions: $n > 1$ . . . 125

4.5 Discussion . . . 138

4.6 Conclusions . . . 139

5 Transcurrent Deformation of the western North America plate boundary zone 140

5.1 Introduction . . . 140

5.2 The Sierra Block . . . 142

5.2.1 Geological Setting . . . 144

5.2.2 Seismicity and Tectonics . . . 146

5.3 Numerical experiments to investigate deformation in the western North America plate boundary zone . . . 152

5.3.1 The thin viscous sheet approximation . . . 152

5.3.2 Finite element method . . . 153

5.3.3 Convergence Criteria . . . 153

5.3.4 Grid Accuracy : Comparison with Newtonian analytical solutions . . . 154

5.3.5 Model setup and boundary conditions . . . 155

5.4 Results of numerical experiments . . . 158

5.4.1 Dimensions of the solution domain: Rigid boundary effects . . . 158

5.4.2 Resolution of solutions . . . 160

5.4.3 Viscosity Contrasts . . . 161

5.4.4 Internal deformation of the block . . . 164

5.4.5 Dependence of block velocity upon n . . . 165

5.4.6 Location and shape of the block . . . 166

5.4.7 Length of the driving boundary 167
5.4.8 Strike–normal velocity 168
5.5 Force Balance Theory 170
5.5.1 Length scales of deformation 171
5.5.2 Estimation of tractions applied to the rigid block 172
5.6 Results 175
5.6.1 Agreement between numerical and analytical methods 175
5.6.2 Dependence of block velocity upon n 176
5.7 Preliminary conclusions 178
5.7.1 The estimation of n from simple models 178
5.7.2 Areas for further investigation 180
5.8 Fitting GPS data to simple rigid block models 181
5.8.1 GPS velocity field 181
5.8.2 Profiles of GPS velocities across the zone of deformation 184
5.8.3 Comparison between observed and calculated velocity profiles 188
5.8.4 Velocity normal to the plate boundary 195
5.9 Rotation of a rigid block embedded within viscous shear flow 201
5.9.1 Rotation due to extension in the Basin and Range Province 206
5.10 A more complex model for the western North America plate boundary zone 207
5.10.1 Boundary Conditions 209
5.10.2 Results of numerical experiments 214
5.10.3 Strain rates for modified geometry experiments 215
5.11 Lithospheric effective viscosity 220
5.11.1 Buoyancy forces in the western North America plate boundary zone 221
5.12 Conclusions 222

6 Conclusions **223**

6.1 Conclusions relating to this study 223

6.2 Limitations of this study and suggestions for future work 225

References **228**

Appendices **248**

A GPS data for south–east Asia **248**

B GPS data for the western United States **255**

List of Figures

1.1 Global seismicity 1901–2001 2

1.2 Topography and velocity field for south–east Asia 4

1.3 Topography and velocity field for the western North America plate boundary zone . . 7

2.1 Linear interpolation function 25

2.2 Flow diagram: inputs and outputs of the viscosity inversion calculations 29

2.3 Potential energy function for the two–dimensional finite element experiments 35

2.4 Analytical and numerical velocity solutions to the $n = 1$ forward calculation: $Ar = 1$ and 3 37

2.5 Analytical and numerical velocity solutions to the $n = 1$ forward calculation: $Ar = 3$ and 10 38

2.6 Analytical and numerical strain rate solutions to the $n = 1$ forward calculation 39

2.7 Viscosity inversions: solving for B in each element; no smoothing 42

2.8 Viscosity inversions: solving for B in each element with smoothing 43

2.9 Viscosity inversions: solving for B in 25 regions; no smoothing 44

2.10 Forward calculations of velocity fields: $n = 1$ and $n = 3$ 46

2.11 Forward calculation of effective viscosity for $B = 1$, $n = 3$ 46

2.12 Histograms of the distribution of B for the $n = 3$ inversion: regions 1 to 15 48

2.13 Histograms of the distribution of B for the $n = 3$ inversion: regions 16 to 25 49

2.14 Distribution of B and η_{eff} for 25 regions; $n = 3$ inversion 50

2.15 Histogram of the distribution of B for the sixth element; an example of a skewed distribution 51

2.16 Mean, median and modal distributions of B for the $n = 3$, 200 region inversion 52

2.17 Mean, median and modal effective viscosity distributions for the $n = 3$, 200 region inversion 53

2.18 Histograms for the distribution of B; $n = 1$ inversion of the $n = 3$ forward problem: regions 1 to 15 55

2.19 Histograms for the distribution of B; $n = 1$ inversion of the $n = 3$ forward problem: regions 16 to 25 56

2.20 Effective viscosity distributions for the $n = 1$ inversion of the $n = 3$ forward problem . 57

2.21 Plot of $\ln(B_{(n=1)})$ against $\ln(\dot{E})$: mean values for 25 regions 58

2.22 Plot of $\ln(B_{(n=1)}$ against $\ln(\dot{E})$: 200 region case 58

2.23 Definition of the terms used in calculating velocity perturbations 62

2.24 Normal Gaussian distribution; one and two sigma confidence intervals 63

2.25 Randomly generated correlated noise 63

3.1 Geotherms for thickened continental lithosphere 66

3.2 Dependence of potential energy upon lithospheric thickening 69

3.3 Topography of south–east Asia 71

3.4 Isostatic balance of lithospheric column with mid–ocean ridge column 72

3.5 The distribution of B_γ 77

3.6 Definition of terms used to calculate potential energy differences 78

3.7 Definition of terms used to calculate geoid anomalies 80

3.8 Observed geoid anomalies for south–east Asia 81

3.9 High–pass filtered geoid anomalies for south–east Asia 82

3.10 Dependence of observed geoid height upon elevation 83

3.11 Dependence of calculated geoid heights upon elevation 84

3.12 Geoid gradients, dN/dh, for the constant volume and constant thickness models 86

3.13 Dependence of geoid height upon lithospheric thickness and elevation when $S_0 = 30$ km 88

3.14 Geoid anomaly across south–east Asia, calculated using the constant thickness model . 89

3.15 Misfit to the observed geoid anomaly across south–east Asia 90

3.16 crustal thicknesses for south–east Asia calculated using the constant thickness model . 92

3.17 Potential energy distribution 94

4.1 Topographic relief and simplified tectonics of Tibet 97

4.2 Seismicity of Tibet 101

4.3 Finite element mesh for south–east Asia with node numbers 107

4.4 Campaign velocity and strain rate field 108

4.5 IGS velocity and strain rate field 109

4.6 Definition of tectonic regions within south–east Asia 110

4.7 Campaign velocity field compared to solution from $n = 1$ inversion 112

4.8 IGS velocity field compared to solution from $n = 1$ inversion 113

4.9 Distribution of B for $n = 1$ inversion, Experiment 1: regions 1 to 15 115

4.10 Distribution of B for $n = 1$ inversion, Experiment 1: regions 16 to 19 116

4.11 Distribution of B for $n = 1$ inversion, Experiment 2: regions 1 to 15 117

4.12 Distribution of B for $n = 1$ inversion, Experiment 2: regions 16 to 19 119

4.13 Results for $n = 1$ inversions: mean B distribution from Experiment 1 120

4.14 Results for $n = 1$ inversions: B–distribution for best solution of Experiment 1 121

4.15 Results for $n = 1$ inversions: mean B distribution from Experiment 2 123

4.16 Results for $n = 1$ inversions: B–distribution for best solution of Experiment 2 124

4.17 Plots of $\ln(B)$ against $\ln(\dot{E})$ for $n = 1$ 125

4.18 Mean effective viscosity distribution for $n = 3, 5, 10$, Experiment 1 128

4.19 Best–fitting effective viscosity distribution for $n = 3, 5, 10$, Experiment 1 129

4.20 Mean effective viscosity distribution for $n = 3, 5, 10$, Experiment 2 131

4.21 Best–fitting effective viscosity distribution for $n = 3, 5, 10$, Experiment 2 132

4.22 Mean distribution of B for $n = 3, 5, 10$, Experiment 1 134

4.23 Best–fitting distribution of B for $n = 3, 5, 10$, Experiment 1 135

4.24 Mean distribution of B for $n = 3, 5, 10$, Experiment 2 136

4.25 Best–fitting distribution of B for $n = 3, 5, 10$, Experiment 2 137

5.1 GPS velocity field for western North America 141

5.2 Topography of western North America 143

5.3 Crustal thickness map of California 146

5.4 Surface Heat Flow for North America 147

5.5 Seismicity of western North America 148

5.6 Fault map for California 149

5.7 Tectonics of the western North America plate boundary zone 150

5.8 Comparison of analytical and numerical solutions 155

5.9 Solution domain for the numerical method 156

5.10 Rigid boundary effects 159

5.11 Numerical resolution 160

5.12 Strength coefficient of the rigid block: velocity profiles 162

5.13 Strength coefficient of the rigid block: block velocity 163

5.14 Deformation of the fluid versus deformation of the block 165

5.15 Rotation of the rigid block 166

5.16 Effect of changing the length of the driving boundary 167

5.17 Effect of changing the model geometry 168

5.18 Two–dimensional y–velocity for different length driving boundaries 169

5.19 Two–dimensional x–velocity 169

5.20 The force balance model 170

5.21 Boundary condition approximations, and misfit to analytical solutions 173

5.22 Comparison of numerical and theoretical methods 176

5.23 Dependence of block velocity upon the stress–strain rate exponent 177

5.24 Dependence of block velocity upon W/D 179

5.25 GPS velocity field for western North America: USGS data 181

5.26 GPS velocity field for western North America: JPL data 182

5.27 Relative velocity between USGS and JPL GPS reference frames 183

5.28 Rotating the JPL GPS reference frame: Trade–off between Ω and Φ 185

5.29 Rotating the JPL GPS reference frame: Trade–off between Ω and Λ 185

5.30 Rotating the JPL GPS reference frame: Trade–off between Λ and Φ 185

5.31 Fitting the misfit between the USGS and JPL GPS reference frames 186

5.32 USGS and JPL GPS data in the same reference frame 187

5.33 The projection of GPS data 187

5.34 Along–strike velocity profiles: transects 1 to 4 189

5.35 Along–strike velocity profiles: transects 5 to 8 190

5.36 Along–strike velocity profiles: transects 9 to 12 191

5.37 Along–strike velocity profiles: transects 13 to 16 193

5.38 Along–strike velocity profiles: transects 17 to 20 194

5.39 Strike–normal velocity profiles: transects 1 to 4 196

5.40 Strike–normal velocity profiles: transects 5 to 8 197

5.41 Strike–normal velocity profiles: transects 9 to 12 198

5.42 Strike–normal velocity profiles: transects 13 to 16 199

5.43 Strike–normal velocity profiles: transects 17 to 20 200

5.44 Cartoon of flow around a rigid block 201

5.45 Definition of terms relating to the rotation of a rigid particle 202

5.46 Rate of rotation of an elliptical particle within viscous shear flow 205

5.47 Rotational forces acting upon the Sierra block 206

5.48 Cartoon to highlight the effect of a bend in the plate boundary 208

5.49 Geometry of the Pacific–North America plate boundary zone 209

5.50 Finite element mesh; altered to reflect plate boundary geometry 210

5.51 Boundary conditions for the new solution domain 211

5.52 GPS velocity field adjacent to the Pacific–North America plate boundary 212

5.53 Dependence of the block velocity upon boundary conditions 214

5.54 shear and vertical strain rates: $n = 1$ 216

5.55 shear and vertical strain rates: $n = 2$ 217

5.56 shear and vertical strain rates: $n = 3$ 218

5.57 shear and vertical strain rates: $n = 4$ 219

5.58 shear and vertical strain rates: $n = 5$ 220

List of Tables

2.1 Parameters used in rheology definitions, taken from Brace & Kohlstedt (1980) 15

2.2 Rms misfits to the analytical strain rate field 40

3.1 Definitions and values of physical constants referred to in the text 74

3.2 Values of ρ_{c0} (kg m^{-3}) 75

3.3 Values of B_γ 76

4.1 Strength parameters from viscosity inversions which use $n = 1$ 118

4.2 Mean strength parameters from non-linear viscosity inversions: $n = 3$, $n = 5$ and $n = 10126$

5.1 Model parameters for numerical experiments 157

5.2 Physical parameters for California 178

5.3 Rotation parameters for the Sierra block 205

5.4 Plate boundary velocities: Motion of the Pacific plate relative to the North America plate 213

A.1 Mesh information for the velocity field of south–east Asia: Campaign data 248

A.2 Mesh information for the velocity field of south–east Asia: IGS data 251

B.1 GPS data from JPL Time Series analysis 255

B.2 GPS data from USGS Time Series analysis 265

Chapter 1

Introduction

1.1 Plate tectonic theory

Plate tectonic theory describes the kinematics of motion at the surface of the Earth by the rigid body rotation of a small number of plates about axes passing through the centre of the Earth. Knowledge of the angular velocity of each plate allows the relative velocity of any two points to be determined. Geological evidence has been used to derive angular velocities for the major plates of the Earth (DeMets *et al.*, 1990, 1994), and these have been revised in the light of recent geodetic studies (Larson *et al.*, 1997; Sella *et al.*, 2002) to yield present–day plate motions. Aseismic regions, thousands of kilometres wide, are assumed to be rigid plates, and all plate relative motion is inferred to be accommodated across narrow bands of faulting at the boundaries of the plates. These assumptions are verified by observations of strain rates of $\sim 10^{-17}$ s^{-1} across regions several thousands of kilometres wide in the stable continental interiors of North America and Africa (Argus & Gordon, 1996), and by the lack of long–term strain accumulation across ocean–ocean plate boundaries.

However, the theory does not hold at continental plate boundary zones such as the western North America plate boundary zone, and along the Alpine–Himalayan belt (see Figure 1.1). Here, plate relative motion is accommodated across broad zones of deformation, up to several thousand kilometres wide (Molnar *et al.*, 1973; Molnar, 1988a; England & Jackson, 1989). The continental lithosphere in these regions is characterised by diffuse seismicity and faulting, and large–scale variations in crustal thickness. The discrepancy between rates of relative motion implied by the summation of seismic moment tensors and geodetically constrained rates indicates that a proportion of the deformation is accommodated aseismically. Such behaviour cannot be accounted for by a single plate rotation vector; it must be described in terms of strain rates and local rotations, not large–scale rigid body motions.

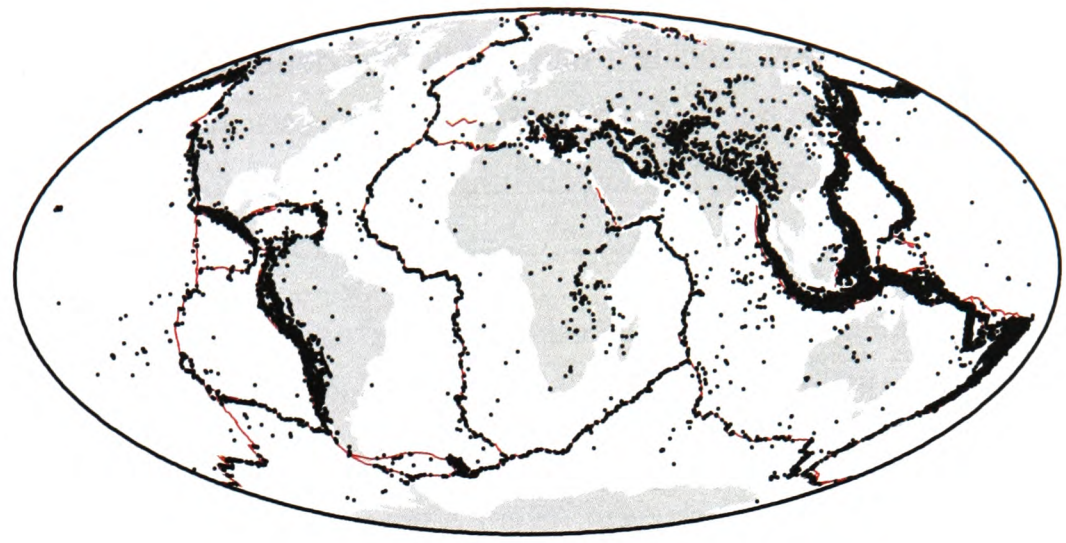

Figure 1.1: Global seismicity: all events of magnitude > 5.0 for 1901–2001. Taken from the EHB catalogue (Engdahl *et al.*, 1998).

1.2 Block versus continuum behaviour

Two principal explanations for the behaviour of continental lithosphere under stress have been put forward. In the first, it is proposed that the lithosphere consists of a large number of blocks that do not internally deform, and that large–scale deformation across the plate boundary zone is taken up along the numerous boundaries of these 'microplates', forming a kinematically consistent velocity field. Specific models for south–east Asia and the western North America plate boundary zone are discussed in sections 1.3 and 1.4.

In the second hypothesis the behaviour of the continental lithosphere under stress is approximated by the deformation of a continuous medium, where the pattern of faulting at the surface is assumed to be a reflection of diffuse ductile deformation at depth (Bourne *et al.*, 1998). Buoyancy forces have been shown to be as important as boundary forces in defining the distribution of continental deformation (Molnar *et al.*, 1973; Molnar & Tapponnier, 1978; Jones *et al.*, 1996), and both transcurrent and collisional plate boundary zones have been described in terms of the deformation of a viscous medium. Again, specific models relating to the distributed deformation of south–east Asia and the western North America plate boundary zone are discussed in sections 1.3 and 1.4.

The underlying principles of continuum models of continental deformation are set out in the thin viscous sheet model of England & McKenzie (1982), the details of which are discussed in chapter 2. In this model gradients of stress are balanced by gravitational body forces in an attempt to explain the long–term deformation of the lithosphere in the India–Asia collision zone. The time–dependent deformation of a viscous layer is defined to be dependent upon forces applied at its boundaries, and forces in its interior due to variations in crustal thickness. The viscous medium obeys either a

Newtonian or a power–law rheology, and the flow is dependent upon the stress–strain rate exponent of this power–law and the balance between driving stresses arising from variations in crustal thickness and the strength of the material, which inhibits deformation. A more detailed discussion into the rheology of continental lithosphere is presented in chapter 2.

The thin viscous sheet method neglects vertical gradients of horizontal velocities, and a vertically averaged value for the effective viscosity of the lithosphere is used. However, Bird (1991) predicts that vertical shear involving the lateral extrusion of the lower crust may be an important mechanism in regions of high topography. Several recent studies that permit the vertical variation of rheological parameters have found that a low viscosity lower crust is necessary to reproduce the observed features of deformation across the Tibetan plateau (Royden *et al.*, 1997; Clark & Royden, 2000; Shen *et al.*, 2001a). There is local geophysical evidence that the viscosity of the lower crust in southern Tibet is low (Nelson *et al.*, 1996; Zhao *et al.*, 2001; Rapine *et al.*, 2003), but there is no evidence for the widespread prevalence of such a layer.

1.3 Modelling the deformation of south–east Asia

Kinematic and geodynamical models for the deformation of the Tibetan plateau and surrounding regions (Figure 1.2) have been presented by many authors (England & McKenzie, 1982; England & Houseman, 1986, 1989; England & Molnar, 1990; Avouac & Tapponnier, 1993; Houseman & England, 1993; Peltzer & Saucier, 1996; England & Molnar, 1997b,a; Royden *et al.*, 1997; Flesch *et al.*, 2000; Holt *et al.*, 2000; Shen *et al.*, 2001a; Soofi & King, 2002a; Liu & Yang, 2003), with recent studies making use of the constantly–improving geodetic data for this region (Larson *et al.*, 1999; Calais *et al.*, 1998; Chen *et al.*, 2000; Shen *et al.*, 2000; Wang *et al.*, 2001; Zhang *et al.*, 2004). Recent kinematic descriptions combine information from seismology, geology and geodesy, all of which are flawed when used in isolation: many of the larger faults have been estimated to have a repeat time of > 1000 years, whereas the seismological record covers only 100 years. Rates determined from geological offsets cannot distinguish between present–day rates and the average for the whole for the Quaternary. While geodetic measurements give an accurate estimate for the present–day motion, they may be affected by postseismic and interseismic deformation on nearby faults. Problems also arise because the rheology of continental lithosphere permits deformation modes such as crustal thickening, decoupling of the crust and mantle, and the delamination of the lower lithosphere. These mechanisms cannot be uniquely determined from the surface velocity field, and the analysis of kinematic models of deformation in south–east Asia is therefore intrinsically linked to the dynamics controlling the deformation.

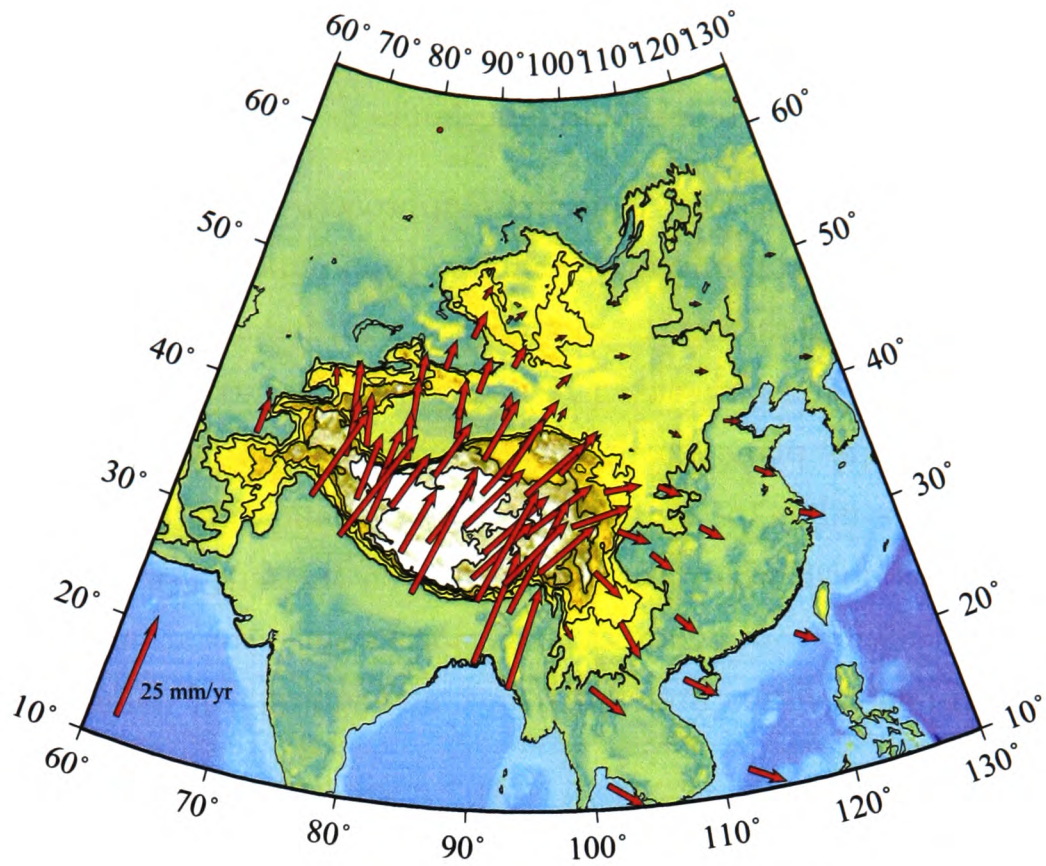

Figure 1.2: Topography and velocity field for south–east Asia. Velocity data taken from England & Molnar (2004).

Continuum deformation seems to be a good approximation for the deformation of the Tibetan plateau (England & Houseman, 1986), but away from the plateau block–like motion is observed in the Tarim Basin and within the Ordos and south China blocks (Wang *et al.*, 2001). Within the plateau there are strong velocity gradients, and more rapid contraction is found at the northern and southern margins of the plateau (Wang *et al.*, 2001). The different styles of deformation are an indication that the collision between India and Asia is not the sole driving force for deformation in south–east Asia; the distribution of gravitational potential energy, mantle dynamics, basal shear tractions, oceanic subduction and lithospheric strength heterogeneities all contribute to the regional pattern of deformation.

Models which attempt to explain the deformation throughout south–east Asia may be divided into two classes. In the first, it is assumed that all deformation is accommodated on faults which bound rigid lithospheric blocks, thus accounting for the fast slip rate estimates on the Karakoram, Kunlun and Altyn Tagh faults (Tapponnier *et al.*, 1982; Peltzer & Tapponnier, 1988; Peltzer & Saucier, 1996; Avouac & Tapponnier, 1993), and leading to the hypothesis that the convergence of India with Asia is accommodated by the extrusion of the Tibetan plateau to the east (Tapponnier *et al.*, 1986). Many of these models break down in the light of recent geodetic estimates which describe a diffuse surface velocity field throughout south–east Asia (Zhang *et al.*, 2004). Chen *et al.* (2004) attempt to reconcile

the idea of a block model with the new data, and present a deforming block model, in which motion is accommodated on major block–bounding faults as well as in the interior of the blocks.

The second class of models use a continuum approach. In the first attempt at describing continental deformation in terms of continuum mechanics, Tapponnier & Molnar (1976) investigate the deformation of a plastic medium due to the motion of a rigid indenter. They assume plane horizontal strain, and the resulting slip lines are taken to indicate the occurrence of large–scale strike–slip faulting in the collision zone. The plane strain approach is also used by Tapponnier *et al.* (1982), but in comparing both these studies to the full three–dimensional deformation field of Asia, the plane–strain assumption breaks down where the crust has been thickened or thinned. Vertical strains cannot be ignored in the study of continental deformation because variations in crustal thickness exert a force upon the deforming medium, and this refines any subsequent deformation.

The thin viscous sheet model (England & McKenzie, 1982) takes account of three–dimensional strain in a non–linear viscous layer, and forms the basis for several studies into the dynamics of the India–Asia collision and the evolution of the Tibetan plateau (England & Houseman, 1986, 1989). Both numerical (Houseman & England, 1993) and analogue (Davy & Cobbold, 1988) models have also successfully demonstrated that convergence between India and Asia may be accommodated by crustal thickening rather than extrusion if the plane strain limitation of earlier models is removed (Tapponnier & Molnar, 1976; Tapponnier *et al.*, 1982).

More recent models attempt to account for the three–dimensional nature of deformation in the India–Asia collision zone, and the effects of horizontal and vertical variations in the rheological parameters of the lithosphere are investigated:

Royden *et al.* (1997) and Shen *et al.* (2001a) implement a three–dimensional model with a depth–varying, but not laterally–varying, rheology. The models reproduce the observed patterns of east–west extension and north–south contraction within the plateau and clockwise rotation in south–east Tibet. Both studies find that a weak lower crust, which decouples upper crustal motions from the motion of the upper mantle, is required to reproduce such features.

Flesch *et al.* (2000) use estimates of gravitational potential energy and stress boundary conditions to determine the vertically–averaged deviatoric stress field for Asia, and hence place bounds upon the lateral variation of the rheology in this region. They calculate effective viscosity values of $0.5-5\times10^{22}$ Pa s for deforming Tibet, and $1-2.5\times10^{23}$ Pa s for the more rigid regions surrounding the plateau. Their results are also consistent with suggestions of a weak lower crust in southern Tibet (Nelson *et al.*, 1996; Rapine *et al.*, 2003), and they highlight the strong influence of gravitational potential energy differences upon the surface deformation field.

Soofi & King (2002a) introduce another level of complexity and investigate the effect of obliquely convergent boundary conditions upon the asymmetry of the deformation; a subject which is covered in theoretical detail by Ellis *et al.* (1995). Soofi & King (2002a) find that they can only reproduce the observed pattern of topography by including a high strength heterogeneity in the location of the Tarim Basin, reinforcing the conclusions of England & Houseman (1985) that strength heterogeneities play an important role in governing the distribution of deformation in the continental lithosphere. This point is covered in more detail in chapter 5. Soofi & King (2002a) also stress the importance of determining the correct direction and magnitude of the boundary conditions in continuum modelling. This observation is taken into consideration when implementing the two–dimensional finite element experiments of chapters 4 and 5.

Liu & Yang (2003) also use a three–dimensional approach to gain insight into the deformation of south–east Asia. They use a viscoelastic model, which permits lateral and vertical rheological variations, and are able to recover east–west extension across the central plateau, and north–south extension in the east. They calculate a long term crustal viscosity of $10^{21} - 10^{22}$ Pa s, but find that the crust behaves elastically over short time periods. An interesting result of their modelling is that they see no extension within the plateau if its mean elevation is below 75% of its current height. Below this height they predict strike–slip and reverse faulting, which may explain the discrepancy between geological and geodetic estimates for the slip rates of long, plateau–bounding strike–slip faults such as the Karakoram, Altyn Tagh and Kunlun faults.

1.4 Modelling deformation in the western North America plate boundary zone

Block models for the deformation of the western North America plate boundary zone (Luyendyk *et al.*, 1980; Bird & Rosenstock, 1984; King *et al.*, 1994; McClusky *et al.*, 2001) are derived from detailed observations of faulting along many well–defined faults. However, the discrepancy between geodetically–constrained slip rates and long–term rates estimated from Quaternary offsets for faults in the San Andreas fault zone, and the observation that earthquakes frequently rupture previously unfaulted lithosphere in this region, imply that continuum deformation provides a more accurate description for the deformation of this plate boundary zone (Figure 1.3).

Bird & Piper (1980) and Bird & Baumgardner (1984) use the thin sheet approximation to present a plane–stress finite element model for the deformation of southern California that seeks to explain the behaviour of the lithosphere over short timescales. This work is extended by Sonder *et al.* (1986), who investigate the dependence of length scales of the deformation upon the length of the driving

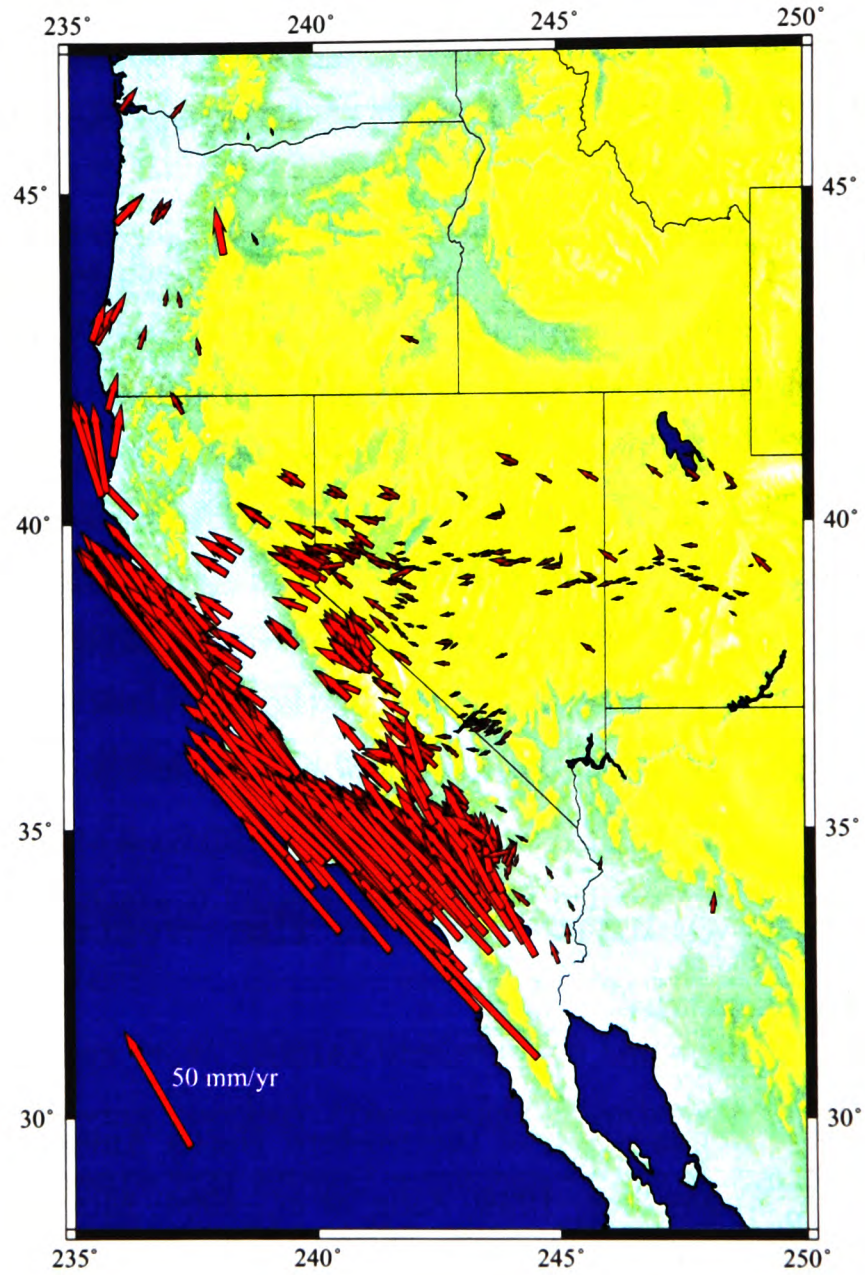

Figure 1.3: Topography and velocity field for the western North America plate boundary zone. Velocity data taken from USGS and JPL catalogues.

boundary condition and the power law exponent (n) in the constitutive equation. They compare their results with analytical solutions to the thin viscous sheet equations and conclude that a value of $n \geq 3$ is required to explain the observations of deformation in California, but do not consider any lateral variations in the rheology of the lithosphere.

Jones *et al.* (1996) and Flesch *et al.* (2000) both seek to understand the relative importance of boundary and buoyancy forces upon deformation in the western North America plate boundary zone. Jones *et al.* (1996) conclude that their estimates for the distribution of buoyancy forces across western North America sufficiently explain all of the observed deformation that is not related to motion on the transcurrent plate boundary. This result is confirmed by Flesch *et al.* (2000), who use topography, geoid, geodetic and Quaternary slip rate data to determine the vertically averaged deviatoric stress tensor field, and hence place constraints upon the vertically averaged effective viscosity of the lithosphere. They determine an effective viscosity of only 10^{21} Pa s for the San Andreas fault zone, and a higher value of 10^{22} Pa s for the Basin and Range Province.

Lateral variations in the viscosity of the lithosphere have also been considered by Choi & Gurnis (2003) and Zoback *et al.* (2002). Choi & Gurnis (2003) use a three–dimensional approach to demonstrate that strain will concentrate in weak, low–viscosity zones, while adjacent regions experience little deformation. They do not attempt to solve for lateral rheological variations in the western North America plate boundary zone, but note that heterogeneities within the lithosphere affect the width of deformation arising from motion on the transcurrent plate boundary. Zoback *et al.* (2002) claim that the main constraint upon the rate at which continental lithosphere may deform is crustal strength. They attribute lateral variations in strain rates across the Coast Ranges and Central Valley of California to differences in heat flux, and reinforce the inverse relationship between heat flux and effective viscosity for the ductile part of the lithosphere.

1.5 Lateral variations in the rheological properties of continental lithosphere

In order to determine the relative importance of plate boundary forces and buoyancy forces in driving the deformation of continental lithosphere, heterogeneities in lithospheric strength must be accounted for in deformation models. Lateral strength contrasts modify lithospheric deformation; stress concentrations at the boundaries of more rigid regions give rise to local crustal thickening. This in turn perturbs the distribution of buoyancy forces, thus further modifying the pattern of deformation.

Much research has been dedicated towards determining the three–dimensional properties of the continental lithosphere and upper mantle, including variations in P and S–wave velocities, and temperature

and gravity anomalies. Estimates for the strength of the lithosphere have been made in the light of these observations, where strength is defined to be the response of the lithosphere to a reference stress.

Many attempts have been made to explain the distribution of deformation in plate boundary zones in terms of the deformation of a laterally homogeneous deforming medium driven by plate boundary and buoyancy forces (see sections 1.3 and 1.4). More recently, several authors have studied the effect of lateral variations in rheology upon the deformation of the continental lithosphere (Burov *et al.*, 1998; Malservisi *et al.*, 2001; Zoback *et al.*, 2002; Choi & Gurnis, 2003; Liu & Yang, 2003), and conclude that rheological variations may be as important as the distribution of driving forces in determining the response of the lithosphere to these forces. However, few attempts have been made to invert for the lateral distribution of effective viscosity and lithospheric strength in the continental lithosphere using dynamical models of lithospheric deformation. Flesch *et al.* (2000) and Flesch *et al.* (2001) use similar methods to place constraints upon the vertically averaged effective viscosity for continental lithosphere in the western North America and south–Asian plate boundary zones. They determine values of 0.5×10^{21} and 2.5×10^{23} Pa s which are in good agreement with independent estimates from the geophysical observations.

1.5.1 Rigid inclusions

The Sierra block of western North America and the Tarim Basin of north–west China are topographically-flat, low–lying basins that do not seem to undergo significant deformation. That they are exposed to large stresses is apparent from the steep gradients of topography and strain rates, and high seismicity, that surround the blocks. But their lack of internal topography, and apparent aseismicity, imply rigid body behaviour, confirmed by recent geodetic measurements. These regions represent anomalously strong portions of the lithosphere, and the effect of the Tarim Basin upon the surrounding deformation field has been studied by several authors (Vilotte *et al.*, 1984; England & Houseman, 1985). A sharp lateral variation in lithospheric strength clearly dominates the distribution of deformation in the vicinity of such blocks, but by studying the response of the surrounding lithosphere, it should also be possible to place constraints on the rheology of this surrounding lithosphere.

1.6 Motivation

In order to test models of continental deformation, velocity and strain rate measurements throughout a deforming region are required to distinguish between different modes of strain accommodation. A classic example of the need for more data is found in eastern Tibet, where models of rigid body

extrusion, crustal thickening, block and continuum rotation have been proposed to explain the accommodation of strain along this boundary. This wide range of models all fit the data available at the time of their proposal: early attempts had to rely upon information from estimates of fault slip rates and seismic moment tensors to infer a crustal velocity field. Recent large–scale efforts to improve the coverage of data throughout south–east Asia (Larson *et al.*, 1999; Calais *et al.*, 1998; Chen *et al.*, 2000; Shen *et al.*, 2000; Wang *et al.*, 2001; Zhang *et al.*, 2004) means that models of deformation for this region may now be rigorously tested against observations, and conflicting hypotheses can be verified or rejected. The increased accuracy and resolution of the data also permits tighter constraints to be placed upon inversion calculations.

The western North America plate boundary zone is another region where the density and accuracy of surface velocity field data (Bennett *et al.*, 1999; Hammond & Thatcher, 2004; USGS, 2004) has reached a level where models of deformation may be critically compared using the data. There have been relatively few attempts to quantify the effect of the rigid Sierra block upon deformation in this region, but confirmation that it translates as a rigid body (Dixon *et al.*, 2000), and the availability of a vast array of high resolution data, lays the foundations for an elegant study.

1.7 Objectives of this study

In this study I investigate the dependence of continental deformation upon plate boundary forces, buoyancy forces, and lithospheric heterogeneities. I use the thin viscous sheet method, driven by velocity boundary conditions and gradients of gravitational potential energy derived from topography, to place bounds upon the vertically averaged effective viscosity, and relative strength, of the continental lithosphere of south–east Asia. I seek solutions to the instantaneous velocity field, but consider several models of lithospheric evolution for this region in order to determine the present–day distribution of buoyancy forces. Strain rates derived from Global Positioning System (GPS) and Quaternary fault slip rate data are used to constrain the relaxation of the effective viscosity field, and test the results of the modelling against observations. I investigate the relationship between effective viscosity and lithospheric strength with regard to the distribution of deformation in south–east Asia, and place constraints upon the stress-strain rate exponent of the governing viscous power–law equation.

In a complementary study of deformation in the western North America plate boundary zone, I treat the Sierra block as a highly viscous inclusion, and employ a finite element approach to solve the thin viscous sheet equations in the presence of such a heterogeneity. I investigate the dependence of the translational velocity of the inclusion upon variations in the stress–strain rate exponent, and test

the sensitivity of the solutions to changes in the aspect ratio of the inclusion, and the geometry and magnitude of the velocity boundary conditions. The Sierra block is also treated as a rigid block, and analytical expressions for forces acting upon the boundaries of a block entrained within a viscous layer undergoing simple shear are used to derive a force balance expression. This approach allows further constraints to be placed upon the motion of the heterogeneity for a suitable range of conditions. The results of both methods are compared with GPS estimates for the motion of the Sierra block relative to stable North America in order to place bounds upon the value of the stress–strain rate exponent that governs the behaviour of deforming lithosphere in the western North America plate boundary zone. Comparisons between observed and calculated styles of deformation outside the Sierra block, and profiles of the along–strike velocity component across the plate boundary zone, confirm the ability of these simple models to reproduce observed patterns of deformation.

Chapter 2

Mathematical methods: Forward and inverse calculations

2.1 Introduction

Many authors (Frank, 1972; Molnar *et al.*, 1973; Molnar & Tapponnier, 1978; Molnar *et al.*, 1993) have shown that continental deformation is driven by buoyancy forces arising from gradients of gravitational potential energy, and that such behaviour is not consistent with the theory of plate tectonics. In analysing this problem, simple models describing the deformation of a thin sheet of viscous material have been used to investigate the behaviour of the continental lithosphere under stress (Bird & Piper, 1980; England & McKenzie, 1982). Several authors have assumed that this sheet obeys a non–Newtonian rheology (England & Houseman, 1986, 1989; Flesch *et al.*, 2000), and find that lithosphere which deforms at $10^{-14} - 10^{-16}$ s^{-1} has an effective viscosity of $10^{22} - 10^{24}$ Pa s. In this study, I investigate the lateral variation of effective viscosity in south–east Asia, and the effect of lithospheric strength heterogeneities upon the surface deformation field.

The kinematics of deformation throughout the continental lithosphere are highly complex at length scales on the order of 10–100 km. However, at length scales several times the thickness of the lithosphere, regional patterns of deformation seem to be more simple, and offer an insight into the large scale dynamics which drive continental deformation. Estimates of instantaneous strain rates, from the measurement of baseline length changes and Quaternary fault slip rates, are used to generate a solution for the present–day velocity field defined on the scale of 100–300 km, across a deforming region several thousand kilometres in width.

Assumptions are made about the forces that drive the deformation, and I seek to place constraints

upon the spatial variation of lithospheric effective viscosities by comparing the results of my modelling to the observed, instantaneous velocity field. A continuum mechanics approach is used as the basis for the investigation; finite element methods are used to allow comparison between theoretical and observed deformation fields.

2.2 Rheology

The continental lithosphere is on average thicker and less dense than oceanic lithosphere. It has a different thermal and compositional structure, and its relatively low strength means that it deforms readily and cannot support large horizontal stresses. The vertically averaged rheology of the continental lithosphere may be approximated by a single power law for strains between $\sim 10^{-13}$ and $10^{-17}s^{-1}$ (Sonder & England, 1986). A constitutive equation for the relationship between stress and strain rates is assumed (England & McKenzie, 1982);

$$\tau_{ij} = B\dot{E}^{(1/n)-1}\dot{\varepsilon}_{ij} \tag{2.1}$$

where τ_{ij} is deviatoric stress, $\dot{E}$ is the second invariant of the strain rate tensor,

$$\dot{E} = \sqrt{\dot{\varepsilon}_{ij}\dot{\varepsilon}_{ij}}, \tag{2.2}$$

B is a strength parameter that represents the depth–averaged temperature dependence of the lithospheric rheology, and n is the power law exponent in the stress–strain rate relationship. For the case of a Newtonian fluid, when $n = 1$, this relationship reduces to

$$\tau_{ij} = 2\eta\dot{\varepsilon}_{ij} \tag{2.3}$$

where η is the viscosity of the fluid, and $B = 2\eta$. For a fluid with a generalised power law rheology ($n \geq 1$), the effective viscosity is defined;

$$\eta_{\text{eff}} = \frac{1}{2}B\dot{E}^{(1/n)-1} \tag{2.4}$$

The power law exponent and the strength of the lithosphere depend upon the depth of the transition from brittle to ductile deformation, the stress difference across this transition, the temperature at the Moho and the geothermal gradient. Previous studies estimate the magnitude of vertically averaged stress supported by the continental lithosphere to lie between 10^{12} and 10^{13} N m^{-1}, corresponding to a power law exponent of $5 \leq n \leq 10$ (equation 2.1) for strain rates of 10^{-13} to 10^{-17} s^{-1} (Sonder & England, 1986). I briefly outline the assumptions behind this result.

Separate expressions are used for the contribution of brittle deformation in the upper crust, and ductile deformation in the lower crust and upper mantle, to the vertically averaged strength of the lithosphere (Sonder & England, 1986):

$$F_L = \int_0^L (\sigma_1 - \sigma_3)\, dz \tag{2.5}$$

The strength, F_L, is defined to be the difference between the maximum and minimum principal stresses, σ_1 and σ_3, integrated over the thickness of the lithosphere, L. The distribution of strength with depth must be deduced for a given strain rate.

Brittle deformation in the upper crust is described by Byerlee's Law (Byerlee, 1978)

$$|\sigma_s| = c - \mu\overline{\sigma}_n \tag{2.6}$$

where σ_s is the shear stress at failure on a fault, $\overline{\sigma}_n$ is the effective normal stress, μ is the coefficient of friction, and c is a constant. This law is independent of both temperature and strain rate. Caution must be exercised in applying this law, because uncertainties are likely to be introduced by the extrapolation of laboratory flow laws to geological conditions.

No simple relationship exists between the proportion of vertically integrated strength due to brittle behaviour and the power law exponent, n, in equation 2.1. A recent re–assessment of earthquake depths and gravity anomalies has led to the suggestion that the seismogenic layer is the only strong part of the lithosphere (Jackson, 2002), although the thickness of this layer may vary between 10 km and $>$ 60 km. Even if there are significant contributions to the vertically averaged strength from other regions of the lithosphere, brittle deformation dominates if the brittle–ductile transition is very deep. Either way, the vertically averaged stress will be dominated by strain–independent friction supported upon faults, and a high power law exponent of $n > 10$ is required to describe the resulting deformation, which will closely approximate plastic behaviour. If brittle behaviour and creep processes are of equal importance, then power law behaviour, with $n \leq 10$, is a good approximation for the deformation. If there is no contribution from brittle deformation, the behaviour of the lithosphere will be governed by the deformation of olivine. A power law exponent of $n \approx 3$ describes such deformation.

Deformation in the lower crust follows a ductile law which is governed by the rheology of quartz,

$$\sigma_1 - \sigma_3 = \left(\frac{\dot{\varepsilon}}{A_c}\right)^{1/n_c} exp\left(\frac{Q_c}{n_c RT}\right) \tag{2.7}$$

where R is the gas constant, T is the absolute temperature, and A_c, Q_c and n_c are respectively the constant, activation energy and stress exponent for quartz flow, as given by Brace & Kohlstedt (1980) (see table 2.1). The creep strength of the lower crust may be reduced by the presence of small amounts of water (Jackson, 2002).

Table 2.1: Parameters used in rheology definitions, taken from Brace & Kohlstedt (1980)

A_c	constant for quartz flow law	5×10^{-6} s^{-1} MPa^{-3}
Q_c	activation energy for quartz flow law	1.9×10^5 J mol^{-1}
n_c	stress exponent for quartz flow law	3
A_p	constant for olivine power law creep	7×10^4 s^{-1} MPa^{-3}
Q_p	activation energy for olivine power law creep	5.2×10^5 J mol^{-1}
n_p	stress exponent for olivine power law creep	3
σ_D	threshold stress for olivine Dorn law creep	8500 MPa
$\dot{\varepsilon}_D$	threshold strain rate for olivine Dorn law creep	5.7×10^{11} s^{-1}
Q_D	activation energy for olivine Dorn law creep	5.4×10^5 J mol^{-1}
R	gas constant	8.314 J mol^{-1} K^{-1}

Uncertainties in the rheology of the crust are absorbed into an uncertainty in the depth of the brittle–ductile transition. Summing the contributions from the upper crust (brittle deformation) and the lower crust (ductile creep of quartz), the crustal contribution to the vertically integrated strength is;

$$F_C \cong z_{BD}(\sigma_1 - \sigma_3)_{BD}\left(\frac{1}{2} + \frac{n_c R T_{BD}}{Q_c}\right) \tag{2.8}$$

where z_{BD} is the depth of the brittle–ductile transition, $(\sigma_1 - \sigma_3)_{BD}$ is the stress difference at the brittle–ductile transition, and T_{BD} is the temperature at the brittle–ductile transition.

It is unlikely that brittle deformation is supported in the upper mantle (Maggi *et al.*, 2000; Jackson, 2002), and any contribution to lithospheric strength by this process will be negligible. The behaviour of the upper mantle is approximated by expressions for the creep of olivine, again given by Brace & Kohlstedt (1980):

$$(\sigma_1 - \sigma_3) = \left(\frac{\dot{\varepsilon}}{A_p}\right)^{1/n_p} exp\left(\frac{Q_p}{n_p R T}\right), |\sigma_1 - \sigma_3| < 200\text{MPa} \tag{2.9}$$

$$(\sigma_1 - \sigma_3) = \sigma_D\left(1 - \left[\frac{RT}{Q_D}\ln\left(\frac{\dot{\varepsilon}_D}{\dot{\varepsilon}}\right)\right]^{1/2}\right), |\sigma_1 - \sigma_3| > 200\text{MPa} \tag{2.10}$$

A_p, Q_p and n_p are respectively the constant, activation energy and stress exponent for olivine power law creep, while σ_D, Q_D and $\dot{\varepsilon}_D$ are the threshold stress, activation energy and threshold strain rate for olivine Dorn law creep (see table 2.1). Both this law, and the flow law for the lower crust, are extrapolated from laboratory experiments, and are sensitive to activation energies. Summing the upper mantle contribution (equation 2.9 or 2.10) and equation 2.8 gives the total vertically integrated strength of the lithosphere.

The strength supported in the upper mantle is strongly dependent upon Moho temperature and the thermal gradient within the upper mantle (see equations 2.9 and 2.10). A temperature structure of

$$T = T_M + \gamma(z - z_M) \tag{2.11}$$

is assumed within the mantle, where T_M is the Moho temperature, γ is the thermal gradient in the mantle, and z_M is the depth of the Moho. γ generally lies between 5–15 K km^{-1}, and Moho temperatures lie in the range 400–800° C. If the Moho temperature is high, the upper mantle will be weak, and brittle deformation in the upper crust will dominate the strength of the lithosphere.

The Argand number is defined to be the ratio of gravitationally induced stress, due to crustal thickness contrasts, to the vertically averaged stress difference required to deform the lithosphere at a reference strain rate of u_0/L (England & McKenzie, 1982):

$$Ar = \frac{g\rho_c(1 - \rho_c/\rho_m)L}{B(u_0/L)^{1/n}} \tag{2.12}$$

g is the acceleration due to gravity, ρ_c is the density of the crust, ρ_m is the density of the upper mantle, L is the thickness of the lithosphere, B is the strength coefficient for the viscous material, u_0 is a reference velocity and n is the stress–strain rate exponent. At high viscosities ($Ar \rightarrow 0$) crustal thickness variations have less effect upon the flow of the lithosphere, and there is effectively no limit to the maximum thickness which can be sustained. But as Ar increases, crustal thickness variations exert a greater influence upon the flow, and the maximum thickness which can be sustained is limited by the value of effective viscosity; for very large Ar no appreciable variations in thickness can be supported.

Once a threshold elevation is reached continued convergence will initially result in an increase in the area of the elevated region, but eventually forces arising from variations in crustal thickness will be large enough to produce extension of the lithosphere within the region of thickened crust. The Argand number is therefore not an intrinsic property of the lithosphere, and may change with the evolution of plate boundary zone deformation. The influence of gravitationally–induced buoyancy forces upon lithospheric deformation in south–east Asia is currently comparable to the influence of forces arising from the indentation of India into Asia, and an Argand number of $Ar \approx 1$ should adequately describe the behaviour at this plate boundary zone.

2.3 Governing Equations

2.3.1 Creeping viscous flow

The continental lithosphere is treated as a continuous viscous medium which deforms by creeping flow. The governing equation for creeping viscous flow is;

$$\frac{\partial \sigma_{ij}}{\partial x_j} = \rho g a_i \tag{2.13}$$

where ρ is the density of the fluid, g is gravity, and $a_i = (0, 0, 1)$. Gravity is assumed to act in the negative z direction. The justification for neglecting inertial terms in the force balance is found by considering the Reynolds number.

The Reynolds number is defined to be

$$Re = \frac{\text{inertial force}}{\text{viscous force}} = \frac{\mid \mathbf{u}.\nabla\mathbf{u} \mid}{\mid \nu\nabla^2\mathbf{u} \mid} \approx \frac{U^2}{D}\frac{D^2}{\nu U} = \frac{DU}{\nu} \ll 1 \tag{2.14}$$

where D is a typical length scale over which deformation takes place, and U is a typical value for the velocity field within the deforming region. Deformation of the continental lithosphere can take place over length scales of >1000 km, at velocities of 10–50 mm/yr. The depth–averaged viscosity of deforming continental lithosphere probably lies somewhere in the range 10^{19} Pa s to 10^{24} Pa s. These values imply Reynolds numbers on the order of 10^{-22} to 10^{-27}, thus defining continental deformation to be a very low Reynolds number flow, where viscous forces dominate over inertial forces. Therefore the momentum terms in the Navier-Stokes equation may be neglected.

The deviatoric stress tensor,τ_{ij}, is defined;

$$\sigma_{ij} = \tau_{ij} - \delta_{ij}p \tag{2.15}$$

where p is the isotropic pressure defined by

$$p = -\frac{1}{3}\sigma_{kk} \tag{2.16}$$

and the summation convention for repeated indices is assumed.

2.3.2 Assumptions of the thin viscous sheet approximation

The thin viscous sheet approximation is used to represent the continental lithosphere in this study. The main assumption of this approximation is that the horizontal extent of the deforming viscous layer under consideration is much greater than its thickness. This holds true for the regions in which

this model will be applied; continental lithosphere is ~100 km thick, but the horizontal scale of deformation in south–east Asia and the western United States is on the order of ~1000 km. The depth variation of velocity, stress and viscosity within this 'thin' layer may therefore be neglected, as long as gradients of crustal thickness are small, and horizontal components of velocity are assumed to be independent of depth;

$$\dot{\varepsilon}_{xz} = \dot{\varepsilon}_{zx} = \dot{\varepsilon}_{yz} = \dot{\varepsilon}_{zy} = 0 \tag{2.17}$$

The incompressibility condition ($\nabla.\mathbf{u} = 0$) is rearranged;

$$\dot{\varepsilon}_{zz} = -(\dot{\varepsilon}_{xx} + \dot{\varepsilon}_{yy}). \tag{2.18}$$

Equations 2.17 and 2.18 are substituted into equation 2.2 to yield an expression for the second invariant of the strain rate, $\dot{E}$, purely in terms of spatial derivatives of the horizontal components of velocity,

$$\dot{E} = \sqrt{2(\dot{\varepsilon}_{xx}^2 + \dot{\varepsilon}_{yy}^2 + \dot{\varepsilon}_{xy}^2 + \dot{\varepsilon}_{xx}\dot{\varepsilon}_{yy})}. \tag{2.19}$$

Another assumption of the thin viscous sheet approximation is that basal shear tractions may be neglected. While this assumption may not hold true at every point on the Earth's surface, it has been found to be a reasonable assumption in previous attempts at modelling deformation in regions of broad continental deformation. Jones *et al.* (1996) find that basal tractions are not required to reproduce the observed deformation field arising from buoyancy forces in the western United States, and England & Houseman (1989) and Flesch *et al.* (2001) have had much success in modelling the deformation that is observed throughout south–east Asia using thin sheet models with no basal tractions.

In the model, a free–slip boundary condition is assumed at the base of the thin viscous layer, therefore the deformation at any point within the model domain arises purely as a result of forces exerted by adjacent portions of the continental lithosphere. These forces may be due to motion of the adjacent lithosphere, or to horizontal density gradients which arise as a result of variations in crustal thickness across the model domain.

2.3.3 The thin viscous sheet equations

Gravity acts in the negative z direction, therefore the horizontal components of the right–hand side of the governing equation (equation 2.13) may be equated to zero. Using equation 2.15 to substitute for σ_{ij} in the governing equation (equation 2.13);

$$\begin{aligned} 0 &= \frac{\partial \sigma_{ij}}{\partial x_j} \\ &= \frac{\partial}{\partial x_j}(\tau_{ij} - \delta_{ij}p) \end{aligned} \tag{2.20}$$

where the subscripts i and j represent the two horizontal components x and y. Expanding equation 2.20, and integrating over the depth of the lithosphere, the force balance in the horizontal plane becomes;

$$\frac{1}{L}\int_0^L \left(\frac{\partial \tau_{xx}}{\partial x} + \frac{\partial \tau_{xy}}{\partial y} + \frac{\partial \tau_{xz}}{\partial z}\right) dz = \frac{1}{L}\int_0^L \frac{\partial p}{\partial x}\, dz \tag{2.21}$$

$$\frac{1}{L}\int_0^L \left(\frac{\partial \tau_{yx}}{\partial x} + \frac{\partial \tau_{yy}}{\partial y} + \frac{\partial \tau_{yz}}{\partial z}\right) dz = \frac{1}{L}\int_0^L \frac{\partial p}{\partial y}\, dz \tag{2.22}$$

I turn to isostasy to define the form of the pressure term in equations 2.21 and 2.22. Following England & McKenzie (1982), it is assumed that crustal thickness variations are in local isostatic equilibrium, and that there is no horizontal gradient of vertical stress below the depth of compensation, defined to be at $z = 0$. Γ is used to represent the gravitational potential energy of a lithospheric column.

The pressure term is defined from equation 2.15;

$$p = \tau_{zz} - \sigma_{zz} \tag{2.23}$$

Taking vertical averages of equation 2.23, and defining

$$\Gamma = -\int_0^L \sigma_{zz}\, dz \tag{2.24}$$

yields

$$\frac{1}{L}\int_0^L p\, dz = \bar{\tau}_{zz} + \frac{\Gamma}{L} \tag{2.25}$$

or

$$\bar{p} = \bar{\tau}_{zz} + \frac{\Gamma}{L} \tag{2.26}$$

where overbars indicate vertical averages over the thickness of the lithosphere. The form of the gravitational potential energy distribution which is used in viscosity inversions for south–east Asia is discussed further in chapter 3.

Differentiating the expression for the depth–averaged pressure field with respect to x and y yields

$$\frac{1}{L}\int_0^L \frac{\partial p}{\partial x}\, dz = \frac{\partial \bar{p}}{\partial x} = \frac{\partial \bar{\tau}_{zz}}{\partial x} + \frac{1}{L}\frac{\partial \Gamma}{\partial x} \tag{2.27}$$

$$\frac{1}{L}\int_0^L \frac{\partial p}{\partial y}\, dz = \frac{\partial \bar{p}}{\partial y} = \frac{\partial \bar{\tau}_{zz}}{\partial y} + \frac{1}{L}\frac{\partial \Gamma}{\partial y} \tag{2.28}$$

Vertical variations in stress are neglected for the reasons discussed in section 2.3.2, and therefore,

$$\frac{1}{L}\int_0^L \frac{\partial \tau_{xz}}{\partial z}\, dz = \frac{1}{L}\int_0^L \frac{\partial \tau_{yz}}{\partial z}\, dz = 0 \tag{2.29}$$

These assumptions, along with the expressions of equations 2.27 and 2.28 are substituted into equations 2.21 and 2.22 to yield the thin viscous sheet equations:

$$L\left(\frac{\partial\bar{\tau}_{xx}}{\partial x}+\frac{\partial\bar{\tau}_{xy}}{\partial y}-\frac{\partial\bar{\tau}_{zz}}{\partial x}\right)=\frac{\partial\Gamma}{\partial x} \tag{2.30}$$

$$L\left(\frac{\partial\bar{\tau}_{yx}}{\partial x}+\frac{\partial\bar{\tau}_{yy}}{\partial y}-\frac{\partial\bar{\tau}_{zz}}{\partial y}\right)=\frac{\partial\Gamma}{\partial y} \tag{2.31}$$

As before, overbars denote vertical averages over the thickness of the lithosphere.

2.3.4 Non–dimensionalising the thin viscous sheet equations

The thin viscous sheet equations are non–dimensionalised to allow analytical solutions to be found in section 2.6. Using the expressions $\bar{\tau}_{xx}=2\eta\frac{\partial\bar{u}}{\partial x}$, $\bar{\tau}_{yy}=2\eta\frac{\partial\bar{v}}{\partial y}$, $\bar{\tau}_{zz}=-2\eta\left(\frac{\partial\bar{u}}{\partial x}+\frac{\partial\bar{v}}{\partial y}\right)$ and $\bar{\tau}_{xy}=\eta\left(\frac{\partial\bar{u}}{\partial y}+\frac{\partial\bar{v}}{\partial x}\right)$, equations 2.30 and 2.31 may be rewritten:

$$4\frac{\partial^2\bar{u}}{\partial x^2}+3\frac{\partial^2\bar{v}}{\partial x\partial y}+\frac{\partial^2\bar{u}}{\partial y^2}=\frac{1}{\eta L}\frac{\partial\Gamma}{\partial x} \tag{2.32}$$

$$4\frac{\partial^2\bar{v}}{\partial y^2}+3\frac{\partial^2\bar{u}}{\partial x\partial y}+\frac{\partial^2\bar{v}}{\partial x^2}=\frac{1}{\eta L}\frac{\partial\Gamma}{\partial y} \tag{2.33}$$

Introducing the non–dimensional variables x', y', u', v' and Γ', the following expressions are defined

$$x = Lx' \tag{2.34}$$

$$y = Ly' \tag{2.35}$$

$$\bar{u} = U_0u' \tag{2.36}$$

$$\bar{v} = U_0v' \tag{2.37}$$

$$\Gamma = \rho gL^2\Gamma' \tag{2.38}$$

where L and U_0 are characteristic dimensional quantities representing the thickness of the lithosphere and the rate of deformation respectively, ρ is the density of the viscous material, and g is acceleration due to gravity. The viscosity, η, must also be rewritten in terms of its dimensional quantities. Equation 2.4 suggests

$$\eta\sim B\left(\frac{U_0}{L}\right)^{\frac{1}{n}-1} \tag{2.39}$$

where B is the strength coefficient of the viscous material and n is the power law exponent in the stress–strain rate relationship (see equation 2.1). Using the above expressions, equations 2.32 and 2.33 are non–dimensionalised:

$$4\frac{\partial^2u'}{\partial x'^2}+3\frac{\partial^2v'}{\partial x'\partial y'}+\frac{\partial^2u'}{\partial y'^2}=\frac{\rho gL}{B\left(\frac{U_0}{L}\right)^{\frac{1}{n}}}\frac{\partial\Gamma'}{\partial x'} \tag{2.40}$$

$$4\frac{\partial^2 v'}{\partial y'^2} + 3\frac{\partial^2 u'}{\partial x' \partial y'} + \frac{\partial^2 v'}{\partial x'^2} = \frac{\rho g L}{B\left(\frac{U_0}{L}\right)^{\frac{1}{n}}} \frac{\partial \Gamma'}{\partial y'} \tag{2.41}$$

The factor on the right–hand side of equations 2.40 and 2.41 is equivalent to the Argand number (equation 2.12). Finally, generalising the x and y components of the thin viscous sheet equations, and dropping the primes, yields

$$\frac{\partial^2 u_i}{\partial x_j^2} + 3\frac{\partial^2 u_j}{\partial x_i \partial x_j} = Ar\frac{\partial \Gamma}{\partial x_i} \tag{2.42}$$

The summation convention is assumed over repeated indices for $i, j = 1, 2$, where 1 and 2 refer to the horizontal components x and y, and velocities u and v.

2.3.5 Limitations of the thin viscous sheet approximation

The main drawback of using the thin viscous sheet approximation as a basis for studying the deformation of continental lithosphere lies in the assumption that rheological parameters, such as viscosity, do not vary with depth. There is widespread disagreement regarding the variation of strength with depth in the continental lithosphere, and the deformation mechanisms which operate at each depth. What is clear is that no single rheological profile can account for the behaviour of all continental lithosphere, and factors including the deformation history of the region, the state of the upper mantle, and the forces applied to the lithosphere will determine how it deforms, and by which mechanisms.

Many authors have put forward models that employ a number of distinct layers, or a depth–dependent viscosity or temperature profile, in order to more closely recreate the predicted conditions within the lithosphere, and to explain local phenomena (Medvedev & Podladchikov, 1999; Liu & Yang, 2003). Other authors include a low viscosity layer in the lower crust (Hopper & Buck, 1996; Royden *et al.*, 1997; Clark & Royden, 2000; Shen *et al.*, 2001a), across which a vertical velocity shear may develop, leading to the decoupling of motion between the upper mantle and the upper crust.

Another drawback of the thin viscous sheet method is its treatment of the lithosphere as a purely viscous layer. Many authors have investigated the range of deformation mechanisms which may accommodate strain; consequently the continental lithosphere has variously been modelled as brittle, elastic, viscous, viscoelastic and viscoplastic. While viscous flow has been shown to be a good approximation for the bulk surface velocity field in many regions, e.g. in Asia (England & Molnar, 1997b), the Aegean (Davies *et al.*, 1997) and western North America (Flesch *et al.*, 2000), the effect of placing a brittle layer, representive of the seismogenic potion of the upper crust, on top of the viscous layer is not negligible. Questions remain as to whether the cumulative strain in the brittle layer simply mirrors that in the underlying viscous medium (Bourne *et al.*, 1998), whether the presence of the brittle layer perturbs the velocity field throughout the lithosphere (Savage, 2000), or whether the two are completely decoupled.

Nevertheless, the thin viscous sheet approximation has the advantage of simplicity, and gives insight into the problem by allowing comparisons to be made with analytical solutions. Apart from a few accessible areas where the kinematics of continental deformation are well known (e.g. California, the Aegean), there do not exist data with a sufficiently dense spatial resolution to test more complex models. In the absence of a reliable, extensive data set for south–east Asia, the thin viscous sheet approximation is used to gain insight into the rheology of the lithosphere in this region.

2.3.6 Solutions to the thin viscous sheet equations

Analytical solutions to the thin viscous sheet equations for sinusoidal boundary conditions are presented by England *et al.* (1985). Solutions are given for two different sets of idealised boundary conditions, specified to permit the investigation of either the compression and extension, or the tangential shear, of continental lithosphere.

Solutions may also be sought for two distinct deformation regimes. In the first, vertical velocities are constrained to be zero throughout the thin layer, resulting in plane strain deformation, and in the second, the vertical stress at the surface of the layer is constrained to be zero.

Plane strain deformation has been investigated through the plasticine models of Tapponnier *et al.* (1982), and in the numerical experiments of Vilotte *et al.* (1982). Necessarily, any deformation which arises due to the motion of a rigid boundary of the thin sheet will be accommodated by the equal and opposite motion of material across a non–rigid boundary of the thin layer. The thickness of the layer is not permitted to change, therefore this model is of little use in providing insight into the kinematics or dynamics of continental deformation where crustal thickening or thinning (convergence or extension) is a major factor.

In the second case, the thickness of the viscous layer is permitted to vary, under the condition that the vertical stress, σ_{zz}, at the top of the layer is zero. The equations which govern the three–dimensional deformation of a thin viscous sheet were first presented and discussed by Bird & Piper (1980) and England & McKenzie (1982). Subsequent studies have used the method to investigate continental deformation throughout North America (Sonder *et al.*, 1986; Flesch *et al.*, 2000; Townsend & Sonder, 2001; Liu, 2001; Soofi & King, 2002b), Asia (England & Houseman, 1986, 1989; Holt *et al.*, 1995; England & Molnar, 1997a; Kong *et al.*, 1997; Flesch *et al.*, 2001; Soofi & King, 2002a), the Andes (Yanez & Cembrano, 2004), the Aegean (Davies *et al.*, 1997) and Iran (Sobouti, 1994; Jackson *et al.*, 1995; Sobouti & Arkani, 1996). The method has also provided the basis for more general theoretical studies of continental deformation (Vilotte *et al.*, 1982; Cohen & Morgan, 1986; Sun & Murrell, 1994; Ellis *et al.*, 1995; Medvedev & Podladchikov, 1999). The original theory has also been extended to include considerations of temperature–dependent rheology (Bird, 1989; Wdowinski

& Bock, 1994), and the role of strength heterogeneities within the lithosphere (Vilotte *et al.*, 1984; England & Houseman, 1985; Vilotte *et al.*, 1986).

Analytical solutions to the full thin viscous sheet equations, for the second case where the thickness of the layer is allowed to vary, have only been found for the Newtonian case where $n = 1$, and when $Ar = 0$. Many studies have shown that the continental lithosphere does not behave in a Newtonian fashion under stress, and therefore I seek solutions to the non–Newtonian ($n > 1$) form of the thin viscous sheet equations.

Setting $Ar = 0$ is equivalent to assuming a very high viscosity for the thin viscous layer, such that the forces required to deform the layer are much greater than the buoyancy forces which arise due to gradients of gravitational potential energy. Alternatively, $Ar = 0$ may represent the case where gradients of crustal thickness are negligible, for example in the early stages of deformation, or during shear–driven deformation. In all these scenarios, setting $Ar = 0$ limits solutions to the case where there is no contribution to deformation from forces in the interior of the viscous fluid. I wish to use the thin viscous sheet equations to investigate the viscosity distribution which is required to reproduce the observed velocity and strain rate fields in regions undergoing continent–continent collision, such as south–east Asia. The buoyancy forces which arise from gradients of potential energy in the region of the Tibetan plateau are on the same order of magnitude as the boundary forces applied by the collision of India with Eurasia. Therefore I require solutions to the thin viscous sheet equations where $Ar > 0$, and deformation is driven by forces distributed throughout the viscous layer.

Due to the requirements of this study, outlined above, and the complexity of determining analytical solutions to the full, non–linear thin viscous sheet equations, this subject is not discussed further in this chapter. Analytical solutions for the case $n = 1$, $Ar = 0$, are presented in chapter 5, along with approximate solutions for the case when $n > 1$, $Ar = 0$.

2.4 The application of finite element methods to the inversion of lithospheric effective viscosities

Finite element methods (Zienkiewicz & Taylor, 1989) are often used to solve the thin viscous sheet equations for a non–linear viscous fluid with a non–zero Argand number. To ensure continuity in the stress and strain rate fields, quadratic, or higher order, shape functions must be used. However, I use a triangular finite element mesh defined by a set of coplanar nodes where each element contains just three nodes; one at each corner of each element. This configuration only permits the use of linear shape functions, but is designed to give the greatest possible spatial resolution for the velocity field. The resulting solutions for the velocity field will be continuous, but solutions for the strain rate field

will not. An approximately regular spacing of nodes is preferable because solutions to the velocity and strain rate fields are more stable when interpolated upon a regular mesh.

An iterative method is used to determine the effective viscosity distribution throughout south–east Asia. Using a suitable initial distribution for the effective viscosity, forward calculations are carried out, and the input effective viscosity distribution is relaxed until the numerical and observed solutions converge.

2.4.1 Interpolation of velocities

I describe here the interpolation of velocities upon a finite element mesh where each node is defined by three nodes, and linear shape functions are used. The velocity of any node may be expressed as a vector

$$\mathbf{u_i} = \begin{pmatrix} u_i \\ v_i \end{pmatrix} \tag{2.43}$$

In the following analysis, u and v represent the x and y components of velocity respectively, and i, j and k refer to the three nodes of each triangular element, numbered in an anti–clockwise order. A column vector of nodal velocities for element **e** may be defined;

$$\mathbf{u^e} = \begin{pmatrix} \mathbf{u_i} \\ \mathbf{u_j} \\ \mathbf{u_k} \end{pmatrix} \tag{2.44}$$

In solving for the velocity field throughout the mesh, the velocity at any point within a given element is approximated by the expression

$$\mathbf{u} \approx \ \hat{\mathbf{u}} = (\hat{u}, \hat{v}) = \sum_{i=1}^{3} N_i \mathbf{u_i} \tag{2.45}$$

where the N_i are the interpolation functions;

$$N_i = (a_i + b_i x + c_i y) \tag{2.46}$$

The terms x and y in equation 2.46 represent the arbitrary location within the element at which the velocity is to be determined, while (x_i, y_i),(x_j, y_j) and (x_k, y_k) are the positions of the ith, jth and kth nodes respectively.

The interpolation functions, N_i, are defined to take the value 1 at the node they are related to (i.e. N_i=1 at node i), and 0 at the other two nodes (see Figure 2.1). The coefficients of the interpo-

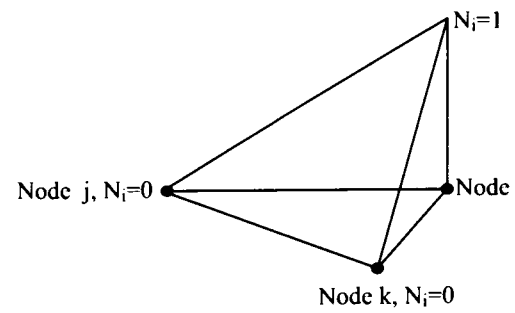

Figure 2.1: Interpolation function for node i; takes the value $N_i = 1$ at node i, and the value $N_i = 0$ at nodes j and k. The sloping plane represents the value of the interpolation function throughout the element.

lation functions are defined by the positions of the three nodes;

$$a_i = \frac{1}{2\Delta}(x_j y_k - x_k y_j) \tag{2.47}$$

$$b_i = \frac{1}{2\Delta}(y_j - y_k) \tag{2.48}$$

$$c_i = \frac{1}{2\Delta}(x_k - y_j) \tag{2.49}$$

with the other coefficients obtained by the cyclic permutation of subscripts in the order i, j, k. Δ is the area of the triangular element;

$$\Delta = \frac{1}{2}\begin{vmatrix} 1 & x_i & y_i \\ 1 & x_j & y_j \\ 1 & x_k & y_k \end{vmatrix} = \text{area of triangle } (ijk) \tag{2.50}$$

Strain rates within an element may be approximated by differentiating equation 2.45. The linearity of the interpolation functions allows the following expressions to be derived:

$$\frac{\partial \hat{u}}{\partial x} = \sum_{i=1}^{3} \frac{\partial N_i}{\partial x} u_i = \sum_{i=1}^{3} b_i u_i \tag{2.51}$$

$$\frac{\partial \hat{v}}{\partial x} = \sum_{i=1}^{3} \frac{\partial N_i}{\partial x} v_i = \sum_{i=1}^{3} b_i v_i \tag{2.52}$$

$$\frac{\partial \hat{u}}{\partial y} = \sum_{i=1}^{3} \frac{\partial N_i}{\partial y} u_i = \sum_{i=1}^{3} c_i u_i \tag{2.53}$$

$$\frac{\partial \hat{v}}{\partial y} = \sum_{i=1}^{3} \frac{\partial N_i}{\partial y} v_i = \sum_{i=1}^{3} c_i v_i \tag{2.54}$$

Components of deviatoric stress are defined using the above expressions for the strain rate within an

element. The effective viscosity for each element is defined to be η.

$$\bar{\tau}_{xx} = 2\eta\dot{\varepsilon}_{xx} = 2\eta\frac{\partial\hat{u}}{\partial x} \tag{2.55}$$

$$\bar{\tau}_{yy} = 2\eta\dot{\varepsilon}_{yy} = 2\eta\frac{\partial\hat{v}}{\partial y} \tag{2.56}$$

$$\bar{\tau}_{xy} = 2\eta\dot{\varepsilon}_{xy} = \eta\left(\frac{\partial\hat{u}}{\partial y} + \frac{\partial\hat{v}}{\partial x}\right) \tag{2.57}$$

$$\bar{\tau}_{zz} = 2\eta\dot{\varepsilon}_{zz} = -2\eta(\dot{\varepsilon}_{xx} + \dot{\varepsilon}_{yy}) = -2\eta\left(\frac{\partial\hat{u}}{\partial x} + \frac{\partial\hat{v}}{\partial y}\right) \tag{2.58}$$

For the moment it is assumed that η does not vary throughout the mesh: viscosity variations are discussed in section 2.5.

Under the assumptions of the thin viscous sheet approximation, the second invariant of the strain rate, $\dot{E}$, is defined in equation 2.19. In the finite element formulation described above, the linearity of the interpolation functions allows $\dot{E}$ to be evaluated by the expression

$$\dot{E} = \sqrt{2\left(\left(\sum_{i=1}^{3} b_i u_i\right)^2 + \left(\sum_{i=1}^{3} c_i v_i\right)^2 + \left(\sum_{i=1}^{3}\frac{1}{2}(c_i u_i + b_i v_i)\right)^2 + \sum_{i=1}^{3} b_i u_i \sum_{j=1}^{3} c_j v_j\right)}. \tag{2.59}$$

2.4.2 Solving the thin viscous sheet equations upon a finite element mesh

Applying Galerkin's method, which is based upon a weighted residual principle, similar to the variational principle, the dimensional thin viscous sheet equations (equations 2.30 and 2.31) are discretised, and integrated across each element of the mesh. The integral expression at each vertex of each element is weighted using the interpolation function N_i, where i continues to refer to a particular node within an element.

$$\int_\Omega N_i\left[\frac{\partial}{\partial x}\left\{2\eta\left(2\frac{\partial\hat{u}}{\partial x} + \frac{\partial\hat{v}}{\partial y}\right)\right\} + \frac{\partial}{\partial y}\left\{\eta\left(\frac{\partial\hat{u}}{\partial y} + \frac{\partial\hat{v}}{\partial x}\right)\right\} - \frac{\partial\Gamma}{\partial x}\right] d\Omega = 0 \tag{2.60}$$

$$\int_\Omega N_i\left[\frac{\partial}{\partial y}\left\{2\eta\left(2\frac{\partial\hat{v}}{\partial y} + \frac{\partial\hat{u}}{\partial x}\right)\right\} + \frac{\partial}{\partial x}\left\{\eta\left(\frac{\partial\hat{u}}{\partial y} + \frac{\partial\hat{v}}{\partial x}\right)\right\} - \frac{\partial\Gamma}{\partial y}\right] d\Omega = 0 \tag{2.61}$$

In equations 2.60 and 2.61, Ω represents the area of each triangular element in the (x, y) plane. The gravitational potential energy, Γ, is defined at each node. Integrating by parts yields the equations;

$$K^1_{ij}u_j + K^2_{ij}v_j = A_i \tag{2.62}$$

$$K^2_{ji}u_j + K^3_{ij}v_j = B_i \tag{2.63}$$

where the summation convention is assumed to hold, and the terms are defined as follows:

$$K_{ij}^1 = \int_\Omega \eta \left(4\frac{\partial N_i}{\partial x}\frac{\partial N_j}{\partial x} + \frac{\partial N_i}{\partial y}\frac{\partial N_j}{\partial y} \right) d\Omega \tag{2.64}$$

$$K_{ij}^2 = \int_\Omega \eta \left(2\frac{\partial N_i}{\partial x}\frac{\partial N_j}{\partial y} + \frac{\partial N_i}{\partial y}\frac{\partial N_j}{\partial x} \right) d\Omega \tag{2.65}$$

$$K_{ij}^3 = \int_\Omega \eta \left(\frac{\partial N_i}{\partial x}\frac{\partial N_j}{\partial x} + 4\frac{\partial N_i}{\partial y}\frac{\partial N_j}{\partial y} \right) d\Omega \tag{2.66}$$

Due to the linearity of the interpolation functions (equation 2.46), these matrix definitions may be reduced to

$$K_{ij}^1 = \eta(4b_ib_j + c_ic_j)\Omega \tag{2.67}$$

$$K_{ij}^2 = \eta(2b_ic_j + c_ib_j)\Omega \tag{2.68}$$

$$K_{ij}^3 = \eta(b_ib_j + 4c_ic_j)\Omega \tag{2.69}$$

The forcing terms in equations 2.62 and 2.63 are

$$A_i = -\int_\Omega N_i \frac{\partial \Gamma}{\partial x} d\Omega + \oint_c N_i[(2\bar{\tau}_{xx} + \bar{\tau}_{yy})n_x + \bar{\tau}_{xy}n_y]dl \tag{2.70}$$

$$B_i = -\int_\Omega N_i \frac{\partial \Gamma}{\partial y} d\Omega + \oint_c N_i[(2\bar{\tau}_{yy} + \bar{\tau}_{xx})n_y + \bar{\tau}_{xy}n_x]dl. \tag{2.71}$$

In the contour integrals of equations 2.70 and 2.71, n_x and n_y are the x and y components respectively of the normal to the boundary of the element containing node i. Note that the majority of nodes will lie on the boundary of more than one element. The contour integrals therefore do not need to be evaluated throughout the interior of the mesh because they are integrated in an anti–clockwise direction around each element, and therefore cancel out when the expressions are summed over all the triangles in the mesh.

Equations 2.62 and 2.63 may be combined to form a matrix equation which is used to determine the velocity components of every node throughout the mesh.

$$\begin{bmatrix} \mathbf{K^1} & \mathbf{K^2} \\ (\mathbf{K^2})^T & \mathbf{K^3} \end{bmatrix} \begin{bmatrix} \mathbf{u} \\ \mathbf{v} \end{bmatrix} = \begin{bmatrix} \mathbf{a} \\ \mathbf{b} \end{bmatrix} \tag{2.72}$$

Each $\mathbf{K}$–matrix has dimension $m \times m$, where m is the number of nodes in the finite element mesh. The number of variables to be solved for is $2m$, and sparse matrix methods (an LU–decomposition in this case) are used to determine the entries of the velocity component matrices, $\mathbf{u}$ and $\mathbf{v}$.

If the viscous layer is assumed to have a non-Newtonian rheology, then the velocity field must be determined iteratively. The method I use converges rapidly, generally requiring fewer than three iterations.

2.4.3 Boundary Conditions

Velocity boundary conditions are applied at all nodes that lie on the edge of the finite element mesh. Velocities at these nodes are fixed, and their values are constrained by geodetic observations.

A weighting method is used to fix the velocities at the chosen nodes during the thin viscous sheet finite element calculations. For a given node, i, where both the u and v components of velocity are to be fixed to the observed geodetic values, K^1_{ii} and K^3_{ii} are assigned large values (10^{40} is chosen here, this value is many orders of magnitude greater than the other stiffness coefficients, K_{ij}). The corresponding forcing term in the x component of the thin viscous sheet equation, a_i, is set to $u_i(in) \times 10^{40}$, where $u_i(in)$ is the observed u component of velocity for the ith node, and the forcing term in the y component of the thin viscous sheet equation, b_i, is set to $v_i(in) \times 10^{40}$, where $v_i(in)$ is the observed v component of velocity for the ith node. This replaces the governing equations for node i (equations 2.62 and 2.63) with the approximate equations

$$10^{40} \times u_i(out) \approx 10^{40} \times u_i(in) \tag{2.73}$$

$$10^{40} \times v_i(out) \approx 10^{40} \times v_i(in) \tag{2.74}$$

where $u_i(out)$ and $v_i(out)$ are the velocities to be solved for in equation 2.72. The weighting of the diagonal elements means that throughout the calculation of the new velocity field the velocities of the boundary nodes are essentially unchanged. In order to strictly apply the fixed velocity boundary conditions, once a new velocity field is calculated the u and v components of velocity are not updated at the fixed nodes: the original, input values are retained for use in the next iteration.

This scenario assumes both components of velocity are fixed. If it is required that the boundary velocity should only be fixed in one direction, then only K^1_{ii} and a_i, or K^3_{ii} and b_i should be altered in order to fix the u or v component respectively.

2.4.4 Rheological specifications of the thin viscous sheet approximation

The two-dimensional finite element method described in section 2.4.1 is used to solve for the two–dimensional velocity field of a thin layer of viscous material that is interpolated upon an irregular finite element mesh. The magnitude of the buoyancy force at every node in the interior of the mesh is defined using topography as a proxy for gravitational potential energy (see chapter 3). The depth–averaged effective viscosity of each element, η_{eff}, must be defined throughout the mesh, and the stress–strain rate exponent, n, must also be specified. The Argand number is defined upon the non–dimensionalisation of the thin viscous sheet equations.

The constitutive law that is used in determining the deformation of the viscous sheet under stress is

outlined in section 2.2. Equation 2.1 defines the relationship between deviatoric stress and the strain rate tensor. The power law exponent in this expression, n, defines the degree of non–linearity in the relationship, and the strength coefficient, B, is related to the effective viscosity, η_{eff}, of the material as defined in equation 2.4. n and B are poorly constrained with regard to the deforming continental lithosphere, and each influence the value of the Argand number.

As discussed in section 2.3.6, a non–zero Argand number permits the buoyancy forces arising from gradients of crustal thickness to contribute to the deformation of the thin viscous layer. The Argand number is defined in section 2.2 and represents the balance between the magnitude of the buoyancy forces arising from gradients of crustal thickness, and the forces required to deform the viscous medium at a given strain rate (u_0/L).

In this study I aim to place constraints upon the values of n and η_{eff} that best describe the behaviour of the vertically–averaged continental lithosphere under stress. This is achieved by determining which combinations of n and η_{eff} best reproduce the strain rate fields observed in regions of large scale continental deformation.

2.5 Application to determining effective viscosities

The flow diagram in Figure 2.2 outlines the steps that are carried out in order to determine the lateral variation of depth–averaged effective viscosity across a thin viscous layer, for a given stress–strain rate exponent, which is able to reproduce the observed strain rate field across the viscous layer as it deforms under the influence of boundary and internal forces. The inputs into the iterative process

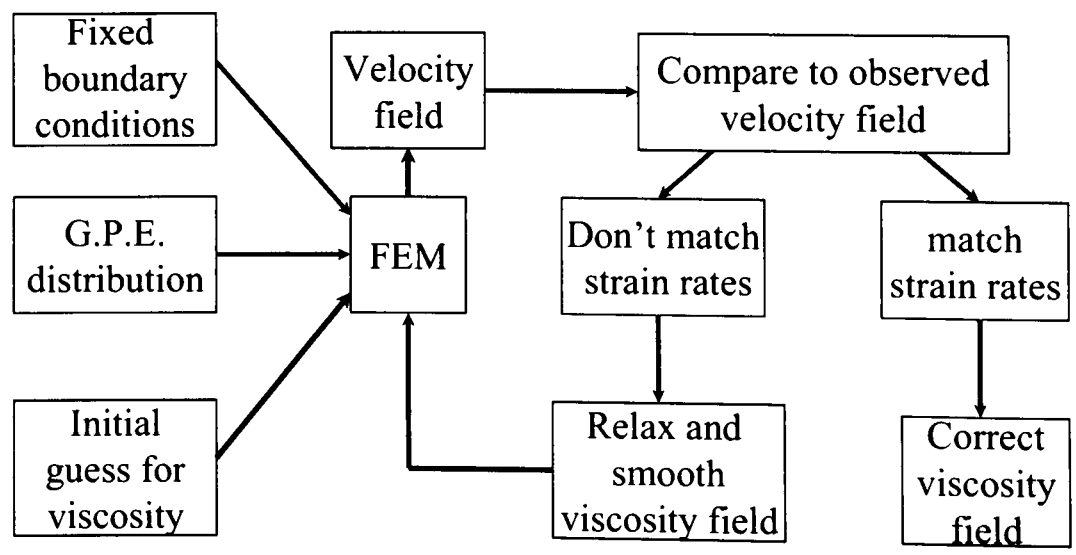

Figure 2.2: Flow diagram showing the inputs and outputs of the finite element calculations, and the iteration procedure used to determine the viscosity distribution

are a set of fixed velocity boundary conditions, a gravitational potential energy distribution which is defined over the whole region, and an initial guess at the viscosity distribution throughout the region. The parameter B is solved for in each iteration. The effective viscosity may be defined either in each individual element, or for a specified region (see section 2.5.1). The regions are defined according to styles of deformation; the details relating to specific cases are given in chapter 4.

Once the initial conditions have been specified, the finite element method described in section 2.4.1 is used to solve for the instantaneous velocity field throughout the mesh. This solution will be constrained by the input viscosity distribution, and therefore will not match the true velocity field throughout the deforming region. In order to match the observed strain rate and velocity fields, the viscosity in each element or region is relaxed in an attempt to find the best–fitting viscosity distribution; defined to be that which most closely allows the observed strain rate distribution to be recovered as a solution to the thin viscous sheet equations.

Once the best–fitting viscosity distribution is established, and the solution is deemed to have converged (see section 2.5.2), the final viscosity, velocity and strain rate fields are recorded, and the root mean squared (rms) misfit to the observed velocity field is calculated.

2.5.1 Relaxation of the viscosity distribution

The difference between the observed strain rate field, and the strain rate field of a solution calculated using the finite element method described in section 2.4.1 is used to determine how the viscosity distribution should be relaxed. Once a solution has been calculated using the finite element method, equation 2.59 is used to evaluate the second invariant of the strain rate ($\dot{E}$) for each element within the mesh. The value of $\dot{E}$ for the observed velocity field is also calculated for each element.

The central assumption of the relaxation method described here is that the scalar measure of the stress within each element should be invariant. The expression $B\,\dot{E}^{1/n}$ has the dimensions of stress, but is a scalar value, and therefore is independent of the directions of the principal stress and strain rate axes.

The stress scalar for the input velocity field and the stress scalar for the current solution are equated for each element;

$$B^i_{\text{in}}(\dot{E}^i_{\text{in}})^{1/n} = B^i_{\text{calc}}(\dot{E}^i_{\text{calc}})^{1/n} \tag{2.75}$$

The superscript, i, refers to the element under consideration, while $\dot{E}_{\text{in}}$ and $\dot{E}_{\text{calc}}$ refer to strain rates of the observed velocity field, and those calculated using the finite element method, respectively. B_{calc} is the value of the strength coefficient calculated during the previous viscosity relaxation iteration. In writing down this equation, B^i_{in} is the value of B that is required to give the correct value of the

stress scalar for element i when the correct (observed) strain rate field is used. If the ratio $\dot{E}^i_{\text{calc}}/\dot{E}^i_{\text{in}}$ is not equal to 1 for every element, then the correct viscosity distribution has not yet been determined, and the effective viscosity of each element must be relaxed, before being input back into the finite element calculations, and used to calculate a new velocity field.

Rearranging equation 2.75 yields,

$$B^i_{\text{in}} = B^i_{\text{calc}} \left(\frac{\dot{E}^i_{\text{calc}}}{\dot{E}^i_{\text{in}}} \right)^{1/n} \tag{2.76}$$

A proportion, $0 \leq \alpha \leq 1$, of this 'ideal' value for the strength coefficient is added onto the previous value for the strength coefficient in each element to give a new value for the strength coefficient in each element, B^i_{new}, which is then input into the next finite element calculation.

$$B^i_{\text{new}} = (1-\alpha)B^i_{\text{calc}} + \alpha B^i_{\text{in}} \tag{2.77}$$

A weighted arithmetic mean is used in this case. A multiplicative or logarithmic mean could equally be implemented; both these quantities would be smaller than the weighted arithmetic mean, and the use of these methods could be investigated to limit the increase in B for an unbounded problem, especially when differences between B^i_{calc} and B^i_{in} are large.

A value of $\alpha = 0.05$ has been used in the calculations. A larger value should allow the solution to converge more rapidly, since each new B^i_{new} would consist of a greater proportion of the 'ideal' strength coefficient, B^i_{in}. However, if the strength distribution is changed too much at each step, this may lead to an unstable, or oscillatory solution. A smaller value of α would ensure that the distribution evolved smoothly, but convergence would take longer.

If $\dot{E}^i_{\text{calc}} > \dot{E}^i_{\text{in}}$, this implies that the strain rate within element i, as calculated using the previous estimate for the strength distribution, was too large. The ratio $\dot{E}^i_{\text{calc}}/\dot{E}^i_{\text{in}}$ will be greater than 1, and since $n \geq 1$, equation 2.76 implies that B^i_{in} will be greater than B^i_{calc}, and the new strength coefficient, B^i_{new}, will be greater than the previous estimate (B^i_{calc}). An increase in the value of the strength coefficient means that the stress required to deform element i at a given strain rate will be increased. Since the driving forces that are input into the finite element calculation do not change with each iteration, the strain rates within this element should therefore decrease upon the calculation of a new velocity field. Similarly, if the strain rates within element i were too small in comparison to the observed velocity field ($\dot{E}^i_{\text{calc}} < \dot{E}^i_{\text{in}}$), equations 2.76 and 2.77 will act to decrease the strength coefficient within this element, thus decreasing the stress required to deform this element at a given strain rate, and increasing the second invariant of the strain rate following the calculation of a new velocity field.

Two methods of relaxing the viscosity distribution are used. In the first, the effective viscosity in each element is permitted to relax independently of the viscosity change in all the other elements.

This method can lead to steep gradients of effective viscosity across adjacent elements of the mesh. When this method is used, a smoothing algorithm is applied, to reduce the discontinuous nature of the resulting viscosity distribution.

Smoothing Algorithm

The smoothing algorithm is applied at every element in the finite element mesh by varying the value of the effective viscosity coefficient, B, within each element. A weighted sum of viscosity coefficients, containing contributions from every element in the mesh, is formed for each element. The weights are inversely proportional to the distance between the centroid of the contributing element and the centroid of the main element under consideration. This sum is divided by the sum of the weights, and divided by the second invariant of the strain rate for the element under consideration to yield an expression which has the dimensions of the effective viscosity coefficient, B. A small proportion, α_s, of this weighted, local, viscosity coefficient distribution is then added onto the value of B in the main element, to give a smoother effective viscosity distribution throughout the mesh after multiplying by $\dot{E}^{(1/n)-1}$.

$$B_s^i = (1 - \alpha_s)B_{\text{new}}^i + \alpha_s B_{\text{local}}^i \tag{2.78}$$

where B_s^i is the smoothed effective viscosity coefficient for element i, α_s is the smoothing factor, B_{new}^i is the effective viscosity coefficient for element i following the relaxation of the viscosity distribution, as described in section 2.5.1, and B_{local}^i is the locally weighted effective viscosity for element i:

$$B_{\text{local}}^i = \frac{\sum_j e^{-d_{ij}} B_{\text{new}}^j (\dot{E}_{\text{calc}}^j)^{(1/n)-1}}{\left(\sum_j e^{-d_{ij}}\right) (\dot{E}_{\text{calc}}^i)^{(1/n)-1}} \tag{2.79}$$

The summation convention is assumed, d_{ij} is a measure of the distance between the centroids of elements i and j, all other terms are defined above. A value of $\alpha_s = 0.05$ is found to be sufficient to enable the viscosity iterations to converge.

An averaging length scale is implicit in the definition of d_{ij}:

$$d_{ij} = \frac{1}{d_0}\sqrt{[(xcent_i - xcent_j)cos\theta]^2 + [ycent_i - ycent_j]^2} \tag{2.80}$$

where $xcent_i$ and $ycent_i$ are respectively the longitude and latitude of the centroid of element i in degrees, θ is the latitude of the centroid of element i in degrees, and d_0 is the characteristic length scale, chosen here to be 1.0 degrees, thus introducing an averaging length scale of ~100 km in the mid-latitudes, where the method will be applied. The dimensions of the triangular elements used in chapter 4 lie in the range 100 km to 1000 km, and the choice of d_0 ensures that only values of B in neighbouring elements influence the smoothing of the distribution of the effective viscosity coefficient.

The second method of relaxing the viscosity distribution involves grouping the elements of the finite element mesh into regions that display similar styles of deformation, or which define a specific topographic area. For example, in south–east Asia, all elements covering the Himalaya are grouped into one region, while all elements covering the Tarim Basin are grouped into another. In these two cases, the Himalaya is a region of steep topographic gradients, where rapid underthrusting takes place along the Main Boundary Thrust, while the Tarim Basin is a region of low elevation which does not support any appreciable gradients of topography, and whose internal strain rate is negligible. It is therefore reasonable to assume that the strength of the lithosphere may be very different in these two regions, but that it will not vary greatly within either.

Once all the elements have been grouped into regions, the average strain rate ratio is calculated for each region, and the ideal value of the effective viscosity coefficient for region I, B^I_{in}, is defined in the same manner as before:

$$B^I_{\text{in}} = B^I_{\text{calc}} \left(\frac{\sum_{i \in I} \dot{E}^i_{\text{calc}}}{\sum_{i \in I} \dot{E}^i_{\text{in}}} \right)^{1/n} \tag{2.81}$$

where I refers to a particular region, and B^I_{calc} is the previous value of the effective viscosity coefficient for region I. Equation 2.77 is then used to calculate the new effective viscosity coefficient for each region, which will be used in the finite element calculations to solve for a new velocity field. In this method a smoothing algorithm is not found to be necessary for convergence.

2.5.2 Convergence Criteria

Several iterations of the finite element calculation are required in order to determine the velocity field for a given field of effective viscosity. After each iteration, the updated velocity field, which is output in mm/yr (with all velocities defined relative to stable Eurasia), is compared with the previous solution. When the maximum absolute change of any velocity component, at any node, falls below 0.1 mm/yr, the velocity solution is deemed to have converged. In practice, fewer than 5 iterations are usually required before the solution converges.

Once the velocity field has converged, the effective viscosity distribution is relaxed, using the methods described in section 2.5.1. Following each viscosity relaxation, the velocity field is once again calculated, and this solution is compared with the observed strain rate field to ascertain whether the new viscosity field is able to reproduce the observed strain rates with sufficient accuracy.

In the case where the effective viscosity in each element is allowed to relax independently, the viscosity in element i is deemed to have converged when

$$\left| \frac{\dot{E}^i_{\text{calc}}}{\dot{E}^i_{\text{in}}} - 1 \right| < 0.01 \tag{2.82}$$

When the second invariant of the strain rate for the calculated solution lies within 1% of the input value in every element, the viscosity iterations are terminated, and the final velocity and strain rate fields are recorded.

For the method that solves for the effective viscosity within triangles grouped into a region, a slightly different convergence test is used. The effective viscosity of a whole region is deemed to have converged when

$$\left| \frac{\sum_{i \in I} \dot{E}^i_{\text{calc}}}{\sum_{i \in I} \dot{E}^i_{\text{in}}} - 1 \right| < 0.01 \tag{2.83}$$

where I represents a whole region. Equation 2.83 states that the average second invariant of the strain rate within a whole region must lie within 1% of the average input value of the second invariant of the strain rate for that region for convergence to be achieved. When the effective viscosity has converged within every region the viscosity iterations are terminated.

Holding the effective viscosity fixed in each element or region as soon as it converges would lead to an unphysical solution. Therefore, in both cases, the effective viscosity in every element or region continues to be allowed to relax at every iteration, until the viscosity has converged in every element or region. In practice, fewer than 100 iterations are usually required before convergence is achieved.

Accuracy of the solution

The rms misfit is calculated, following the convergence of the viscosity and velocity fields, in order to quantify the accuracy of each solution. The expression

$$\text{rms} = \sqrt{\frac{1}{N} \sum_{n=1}^{N} \left(\frac{(\Delta u^n)^2 + (\Delta v^n)^2}{\sqrt{((u^n_{\text{in}})^2 + (v^n_{\text{in}})^2)}} \right)} \tag{2.84}$$

is used, where N is the number of nodes, and $\Delta u^n = u^n_{\text{in}} - u^n$ and $\Delta v^n = v^n_{\text{in}} - v^n$ are the misfit between the calculated (u^n, v^n) and observed $(u^n_{\text{in}}, v^n_{\text{in}})$ velocity components at each node.

2.6 Two–dimensional experiments

2.6.1 Forward calculations

The ability of the methods described in sections 2.4.1 and 2.5 to recover the input viscosity distribution throughout a two–dimensional domain is tested using known analytical solutions, where the correct viscosity distribution is known. I solve the non–dimensional thin–sheet equations for a

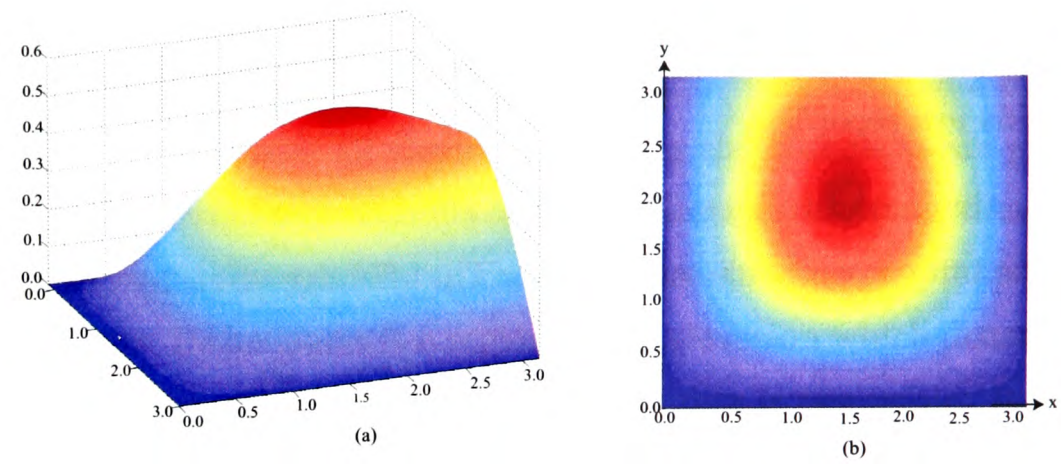

Figure 2.3: (a) 3D plot of the potential energy function (b) plan view

Newtonian ($n = 1$) fluid (see equation 2.42);

$$\frac{\partial^2 u_i}{\partial x_j^2} + 3\frac{\partial^2 u_j}{\partial x_i \partial x_j} = Ar\,\frac{\partial \Gamma}{\partial x_i} \tag{2.85}$$

where Γ is the potential energy throughout the viscous layer, and the summation convention is assumed over j. Specifying i to be 1 or 2 ($(x_1, x_2, x_3) \equiv (x, y, z)$ and $(u_1, u_2, u_3) \equiv (u, v, w)$) defines the x or y component of the thin sheet equation respectively. Solutions for the case $Ar > 0$, in the semi–infinite domain $y \geq 0$, $-\infty \leq x \leq \infty$, are presented in Bourne (1996).

Convergent boundary conditions are used to simulate the case of continent–continent collision, and u, v and Γ are non–dimensional variables.

$$\begin{aligned} u(x,0) &= 0 \\ u(x,\infty) &= 0 \\ v(x,0) &= V_0 \sin(kx) \\ v(x,\infty) &= 0 \\ \Gamma(x,0) &= 0 \\ \Gamma(x,\infty) &= 0 \end{aligned} \tag{2.86}$$

A potential energy distribution of the form $\Gamma(x, y) = y^2 e^{-ky}\sin(kx)$ is used. Plots of this function are shown in Figure 2.3. $k = 1$ is used throughout these forward calculations, and the effective viscosity of the layer is defined using an effective viscosity coefficient of $B = \frac{5}{3}$.

Taking the horizontal divergence of equation 2.85, and explicitly writing out all components yields:

$$\begin{aligned} 4\left(\frac{\partial^3 u}{\partial x^3}+\frac{\partial^3 v}{\partial y^3}+\frac{\partial^3 u}{\partial x \partial y^2}+\frac{\partial^3 v}{\partial y \partial x^2}\right) &= Ar\left(\frac{\partial^2 \Gamma}{\partial x^2}+\frac{\partial^2 \Gamma}{\partial y^2}\right) \\ \left(\frac{\partial^2}{\partial x^2}+\frac{\partial^2}{\partial y^2}\right)\left(\frac{\partial u}{\partial x}+\frac{\partial v}{\partial y}-\frac{1}{4}Ar\Gamma\right) &= 0 \\ \frac{\partial^2}{\partial x_{i_h}^2}\left(\frac{\partial u_{j_h}}{\partial x_{j_h}}-\frac{1}{4}Ar\Gamma\right) &= 0 \end{aligned} \tag{2.87}$$

where the subscript '$_h$' refers to horizontal derivatives in x and y only. Equation 2.87 is Laplace's equation, and the linearity of the problem implies that solutions of the form $\frac{\partial u_{j_h}}{\partial x_{j_h}} - \frac{1}{4}Ar\Gamma = Te^{-ky}\sin(kx)$ may be sought, where T is a constant determined by boundary conditions. Substituting this expression into equation 2.85 yields Poisson's equation for the two horizontal components of velocity;

$$\nabla^2 u = \left(3kT + \frac{1}{4}Ar\,ky^2\right)e^{-ky}\cos(kx) \tag{2.88}$$

$$\nabla^2 v = \left(-3kT - \frac{1}{4}Ar\,ky^2 + \frac{1}{2}Ar\,y\right)e^{-ky}\sin(kx) \tag{2.89}$$

Solutions to these equations are sought in the form $u(x,y) = (\gamma_u + \gamma_1 y + \gamma_2 y^2 + \gamma_3 y^3)e^{-ky}\cos(kx)$, and equivalently for the v–component, to give:

$$u = \left(-\frac{3}{5}kV_0 y - Ar\left(\frac{y}{16k^2}+\frac{y^2}{16k}+\frac{y^3}{24}\right)\right)e^{-ky}\cos(kx) \tag{2.90}$$

$$v = \left(V_0 + \frac{3}{5}kV_0 y - Ar\left(\frac{y}{16k^2}+\frac{y^2}{16k}-\frac{y^3}{24}\right)\right)e^{-ky}\sin(kx) \tag{2.91}$$

This two–dimensional velocity field is interpolated upon a regular finite element mesh covering the domain $0 \leq x,\, y \leq \pi$. The mesh contains 200 triangular elements, defined by the location of 121 equally–spaced nodes. The details of the triangulation are determined using the Delauney triangulation method (Wessel & Smith, 1998).

Results

For constant viscosity, an interpolation of the analytical solution to the velocity field for $Ar = 1$, 3, 5 and 10, is shown in red in Figures 2.4a, 2.4c, 2.5a and 2.5c respectively. Numerical solutions to the velocity field for each value of Ar are plotted in green (obscuring the red arrows of the analytical solution).

The numerical solutions are output from the finite element calculation, which solves the thin viscous sheet equations throughout the mesh, as described in section 2.4.1. Values of the analytical solutions along $y = 0$, $y = \pi$, $x = 0$, and $x = \pi$ are used as boundary conditions for the finite element calculations, and the potential energy function used in the analytical solutions is interpolated upon

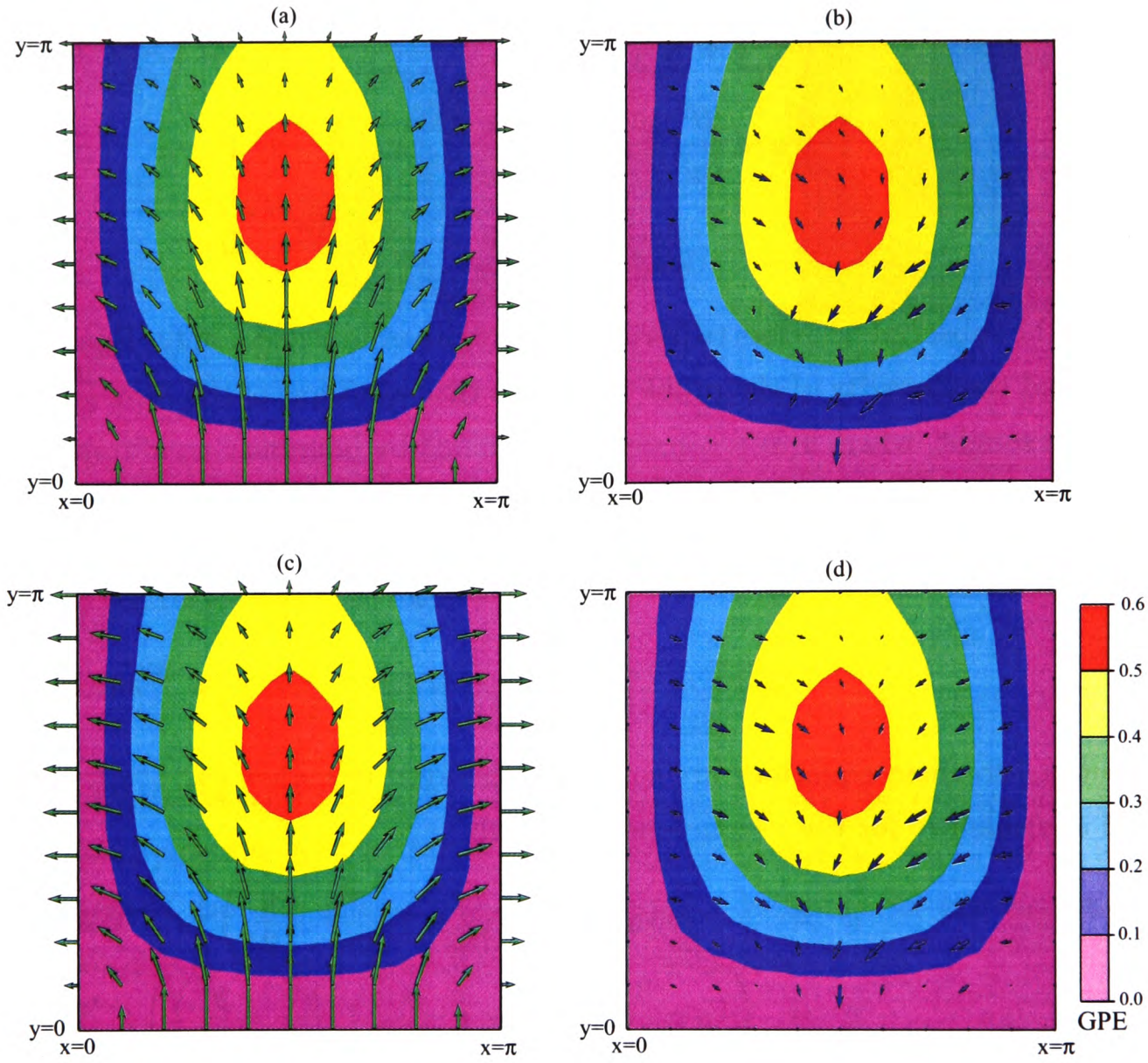

Figure 2.4: (a) and (c); Analytical and numerical solutions for the velocity field shown in red (obscured) and green respectively. (a) $Ar = 1$, (c) $Ar = 3$. (b) and (d); Misfit to the analytical velocity field. (b) $Ar = 1$, velocities multiplied by a factor of 20 with respect to plot (a). (d) $Ar = 3$, velocities multiplied by a factor of 10 with respect to plot (c). The colour scale used in these, and subsequent, figures represents the potential energy distribution throughout the solution domain.

the mesh. In this Newtonian case, the strength coefficient, B, is directly proportional to the effective viscosity since equation 2.4 reduces to $\eta_{\text{eff}} = \frac{1}{2}B$ when $n = 1$. A value of $B = \frac{5}{3}$ is used, equivalent to the value of η_{eff} used in obtaining the analytical solutions. The numerical solutions throughout the finite element mesh should therefore be identical to the interpolated analytical solutions.

The misfit between analytical and numerical solutions is used to test the accuracy of this finite element method when it is used to solve the thin viscous sheet equations. The misfit between the numerical and analytical velocity fields for each value of Ar are plotted in Figures 2.4b, 2.4d, 2.5b and 2.5d. Analytical and numerical strain rates for all four cases are shown in Figure 2.6.

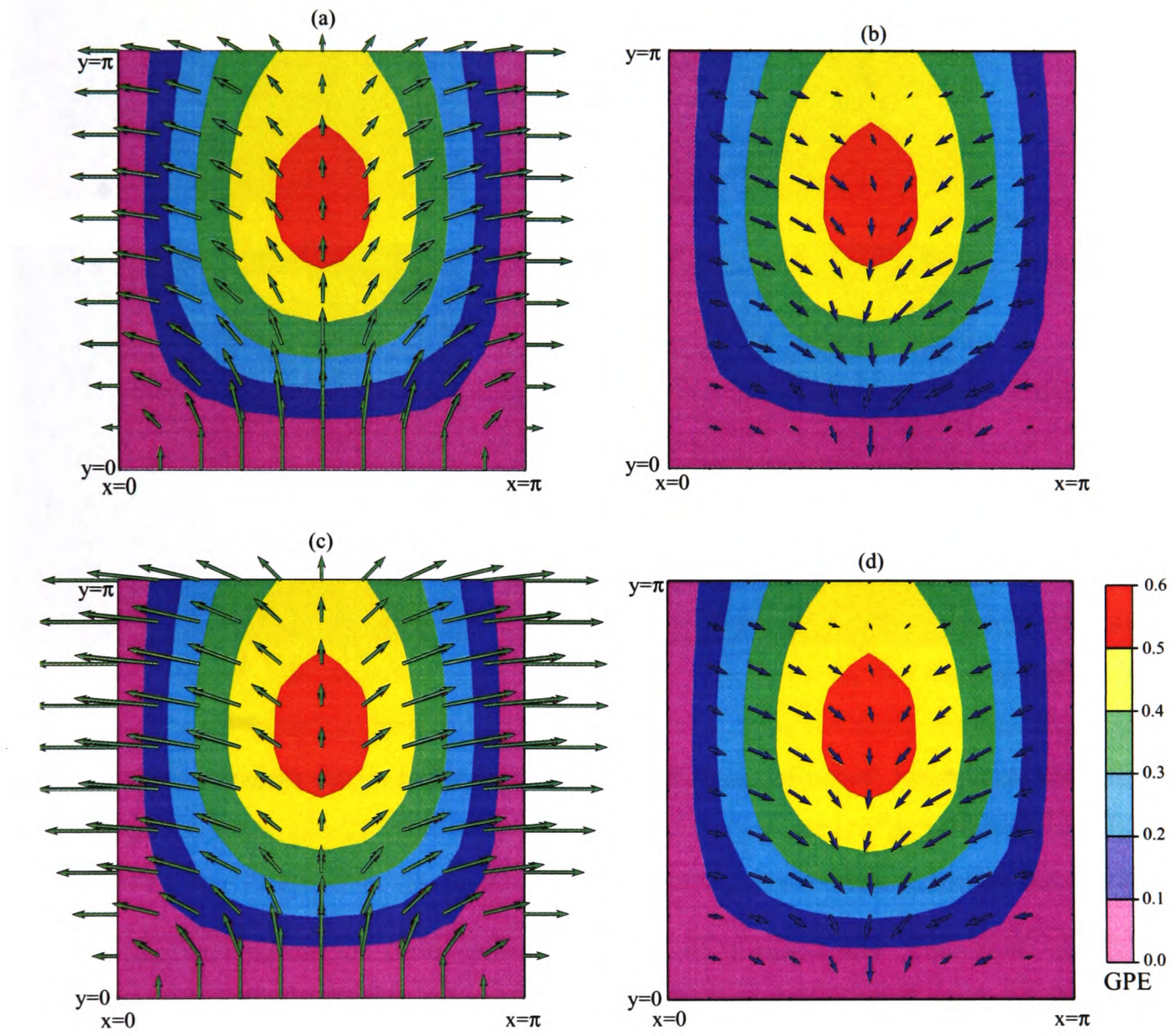

Figure 2.5: (a) and (c); Analytical and numerical solutions for the velocity field shown in red (obscured) and green respectively. (a) $Ar = 5$, (c) $Ar = 10$. (b) and (d); Misfit to the analytical velocity field. (b) $Ar = 5$, velocities multiplied by a factor of 10 with respect to plot (a). (d) $Ar = 10$, velocities multiplied by a factor of 5 with respect to plot (b).

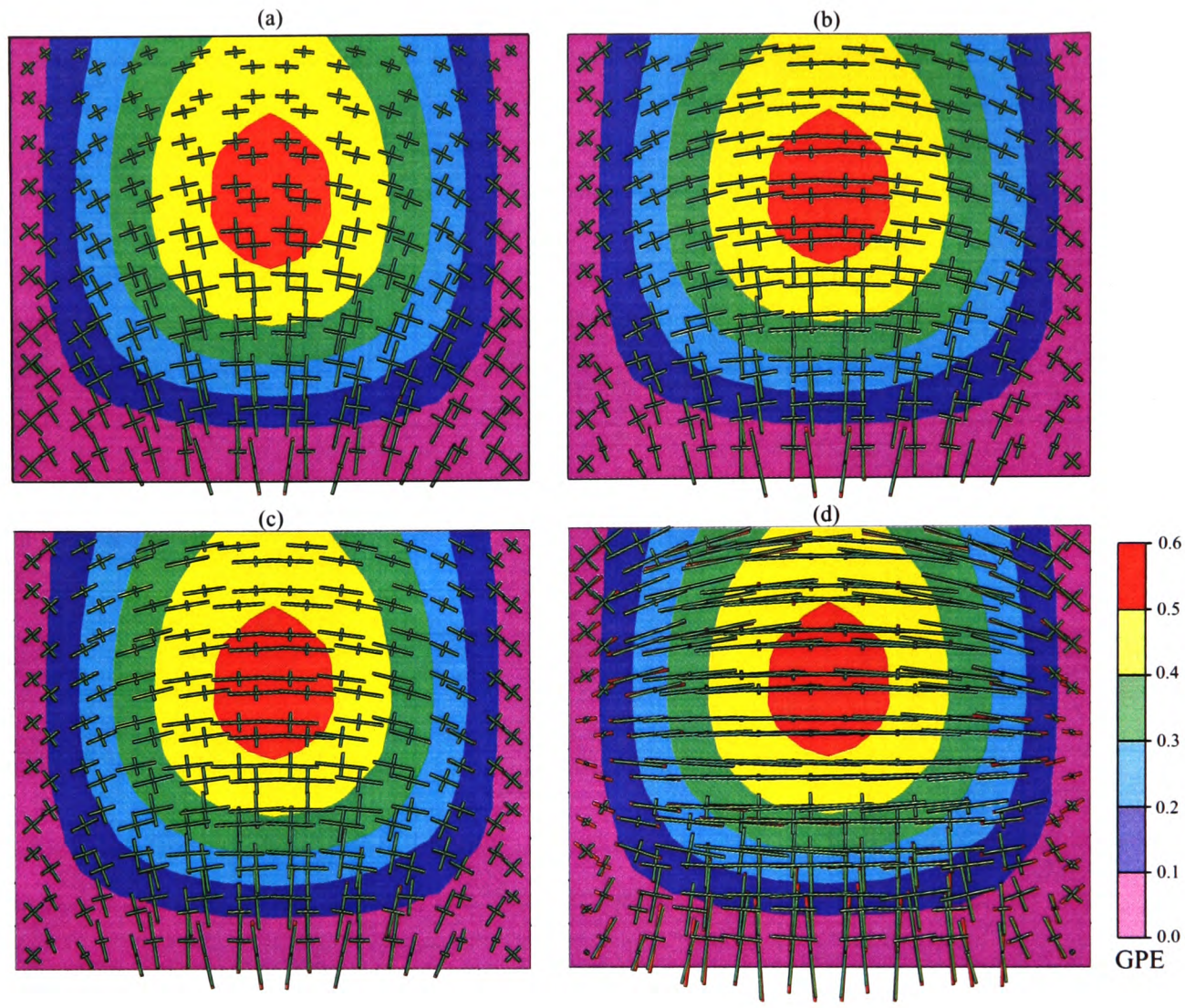

Figure 2.6: Analytical (red, obscured) and numerical (green) strain rates for the cases (a) $Ar = 1$ (b) $Ar = 3$ (c) $Ar = 5$ (d) $Ar = 10$.

As Ar is increased, the magnitude of the velocity field increases throughout the solution domain (compare Figures 2.4a and 2.5c). Extension becomes the dominant deformation mechanism across the region with the highest potential energy as Ar is increased (see Figure 2.6). The reason for this is that buoyancy forces are more dominant at large Ar, and the extensional regime represents an attempt to decrease gradients of potential energy across the centre of the solution domain. Extension is restricted to the 'east–west' direction because the indenting boundary condition along $y = 0$ prevents extension towards $y = 0$ at small y. The influence of this boundary condition decays with distance from the boundary, allowing buoyancy forces to take over at greater y.

The magnitude of the compressional component in the region $y \leq \frac{\pi}{5}$ increases as Ar is increased, as the stronger influence of potential energy gradients in this region force the y velocity to decay more rapidly with distance from the indenting boundary.

The rms misfit to the second invariant of the analytical strain rates throughout the solution domain,

Table 2.2: Rms misfits to the analytical strain rate field

Ar	rms (per unit time)
1	7.29×10^{-3}
3	1.66×10^{-2}
5	2.57×10^{-2}
10	4.73×10^{-2}

for the four values of Ar, are given in table 2.2 (all values are non–dimensional). The magnitude of the absolute misfit to the velocity increases as Ar increases, but the increase in the percentage misfit is negligible.

The misfit velocity field is approximately aligned with the true velocity field (see Figures 2.4b, 2.4d, 2.5b and 2.5d), implying that the directions of the strain rates for the two solutions are in good agreement, but the direction of the vectors is reversed, implying that the numerical solutions overestimate the magnitude of the velocity field in the interior of the mesh.

The misfit to the velocity field is influenced by the configuration of the finite element mesh; the misfit velocity field may mirror the structure of the mesh (see Figure 2.4b for an example). The potential energy distribution and velocity field are both interpolated upon a fairly coarse finite element mesh; the use of a finer mesh should yield a better fit to the interpolated analytical solution. This has not been investigated here, partly due to the increase in computation time which would be involved, and partly because the finite element mesh used to investigate deformation in south–east Asia (see chapter 4) is constrained by the location of strain rate measurements, and there is no option to use a finer mesh. The spacing of nodes with respect to the total area covered by the mesh in these test experiments is similar to the node density used in the mesh covering south–east Asia.

It has been demonstrated that the finite element method presented in section 2.4.1 can recover the analytical solution for the velocity field of a Newtonian viscous fluid by solving the thin viscous sheet equations, given the correct boundary conditions, potential energy distribution, and effective viscosity as inputs. I now demonstrate that the relaxation method presented in section 2.5.1 is capable of recovering the correct effective viscosity distribution, given a suitable initial guess. This method is then used to solve for the velocity and viscosity fields in the non–Newtonian case ($n > 1$).

2.6.2 Viscosity inversions, Newtonian case : $n = 1$

The method of section 2.6.1 is extended to allow a non–uniform distribution of the strength coefficient, B, to be input into the finite element calculations. The relaxation method is used to solve for the correct distribution of B, which is equivalent to solving for the effective viscosity distribution in this Newtonian case. The numerical solution for $n = 1$, $Ar = 1$, $B = 5/3$, output by the forward calculation of section 2.6.1, is used in the inversion to define the solution to which the strain rate field must converge as the viscosity distribution is relaxed. $Ar = 1$ is used in all the remaining calculations of this chapter.

A value of $\alpha = 0.05$ is used to update the distribution of B during each iteration of the relaxation method (see section 2.5.1, equation 2.77); larger values do not permit the viscosity distribution to converge. If smoothing is used, a smoothing parameter of $\alpha_s = 0.05$ (see equation 2.78) determines the weighting of B in neighbouring elements. In all cases a 1% convergence criterion (equation 2.82 or 2.83) is used to define when the second invariant of the strain rate in each element or region has converged.

Three experiments are carried out: in the first I solve for the value of B in each element separately, and no smoothing is used. In the second the same conditions apply, but smoothing is applied after each relaxation of the distribution of B. In the third the finite element mesh is divided into 25 regions, and a single value for B is solved for in each region. No smoothing is used in this third case. For all three experiments a number of different initial distributions of B are used to investigate the range of behaviour exhibited by the solutions. The initial values of B are taken from the uniform distribution $\mathrm{U}(e^{-2}, e^{2})$ using a numerical random number generator (Press *et al.*, 1992).

Results

Figure 2.7 displays a result from the first experiment. The second invariant of the strain rate field converged after 888 iterations. The strain rates are not plotted since the output solution is indistinguishable from the input solution by eye, but the fit to the velocity field is shown in Figure 2.7a. The green misfit arrows in this figure are plotted using a scale 50 times larger than the red arrows of the velocity field.

Despite the convergence of the strain rate field, the distribution of B does not converge towards the value used to calculate the analytical solution ($B = 5/3$) if no smoothing algorithm is employed. The range of B in the final solution is $0 < B < 5.7$, and the spatial distribution of B, shown in Figure 2.7b, bears no correlation to the velocity field or the potential energy distribution. Figure 2.7c reveals that the distribution of B exhibited a random spatial pattern throughout the experiment, and that the

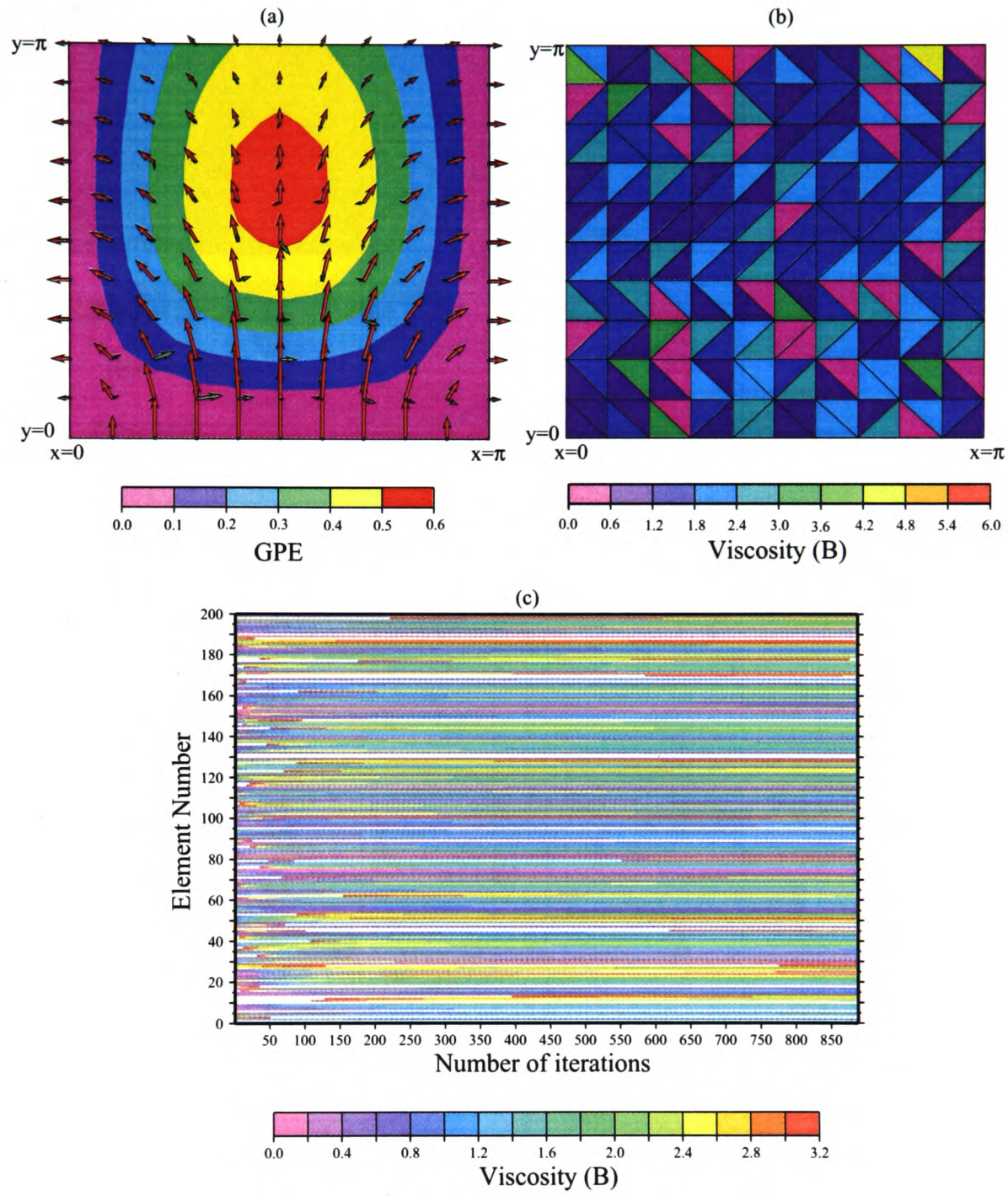

Figure 2.7: 200 viscosity regions. No smoothing. (a) Red arrows: numerical velocity field solution. Green arrows: misfit to the input velocity field solution, arrow scale magnified by 50. (b) Distribution of B for the final solution. (c) Evolution of B in each element. White indicates viscosity values > 3.2. Convergence occurred after 888 iterations.

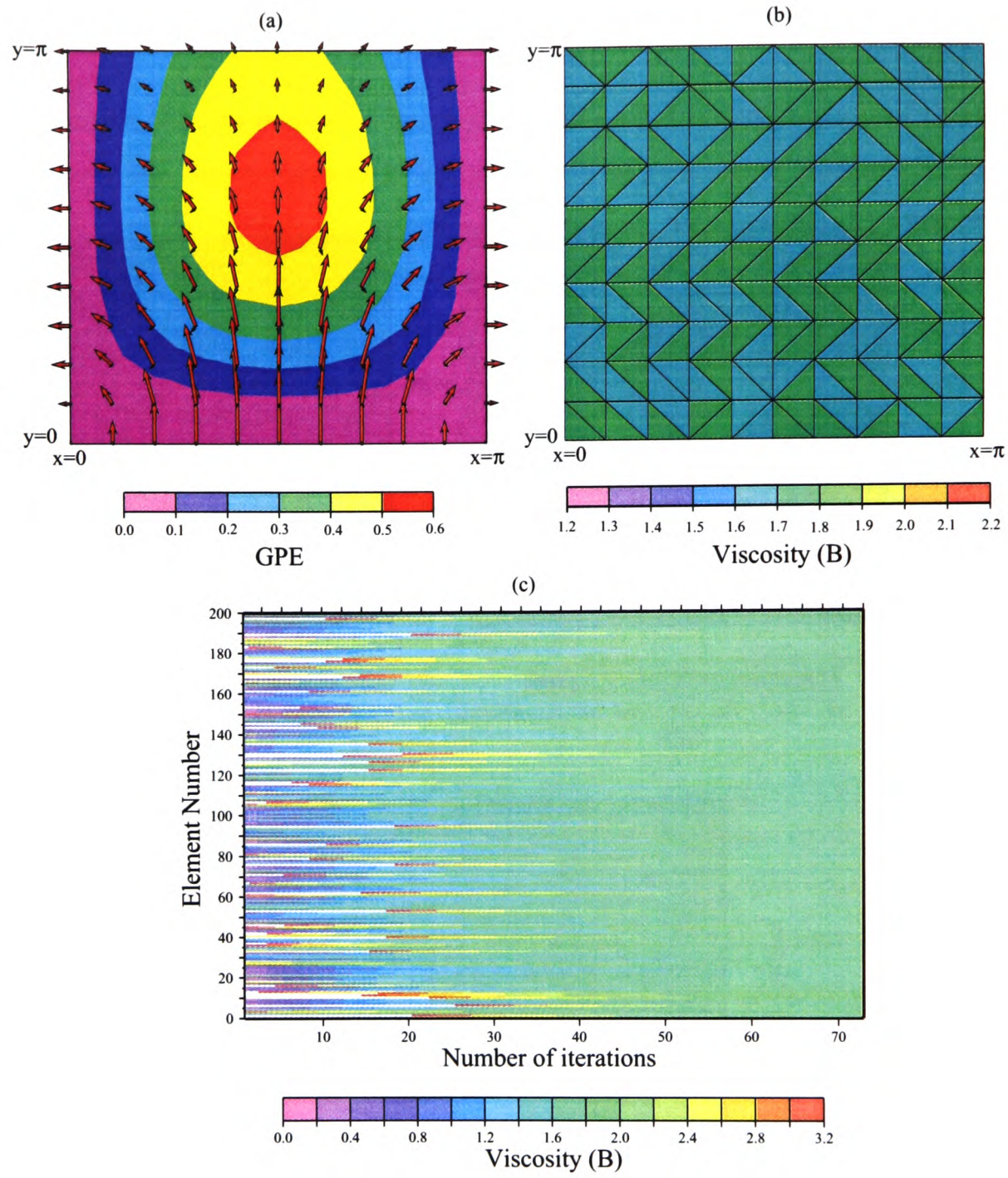

Figure 2.8: 200 viscosity regions. (a) Red arrows: numerical velocity field solution. Green arrows: misfit to the input velocity field solution, arrow scale magnified by 50. (b) Distribution of B for the final solution. (c) Evolution of B in each element. Convergence occurred after 73 iterations.

evolution of the solution slowed after the first ~100 iterations. The element–by–element convergence of the distribution of B, and equivalently η_{eff}, cannot be achieved if no smoothing is used.

Figure 2.8 displays a result from the second experiment, where the distribution of B is smoothed after each iteration. The second invariant of the strain rate field converged after 73 iterations, and Figures 2.8b and 2.8c demonstrate that the distribution of B, and hence η_{eff}, also converged. The rms misfit to the input solution is reduced from experiment 1, and the range of B following the final iteration is only $1.648 \leq B \leq 1.780$. Decreasing the value of the relaxation parameter, α, by an order

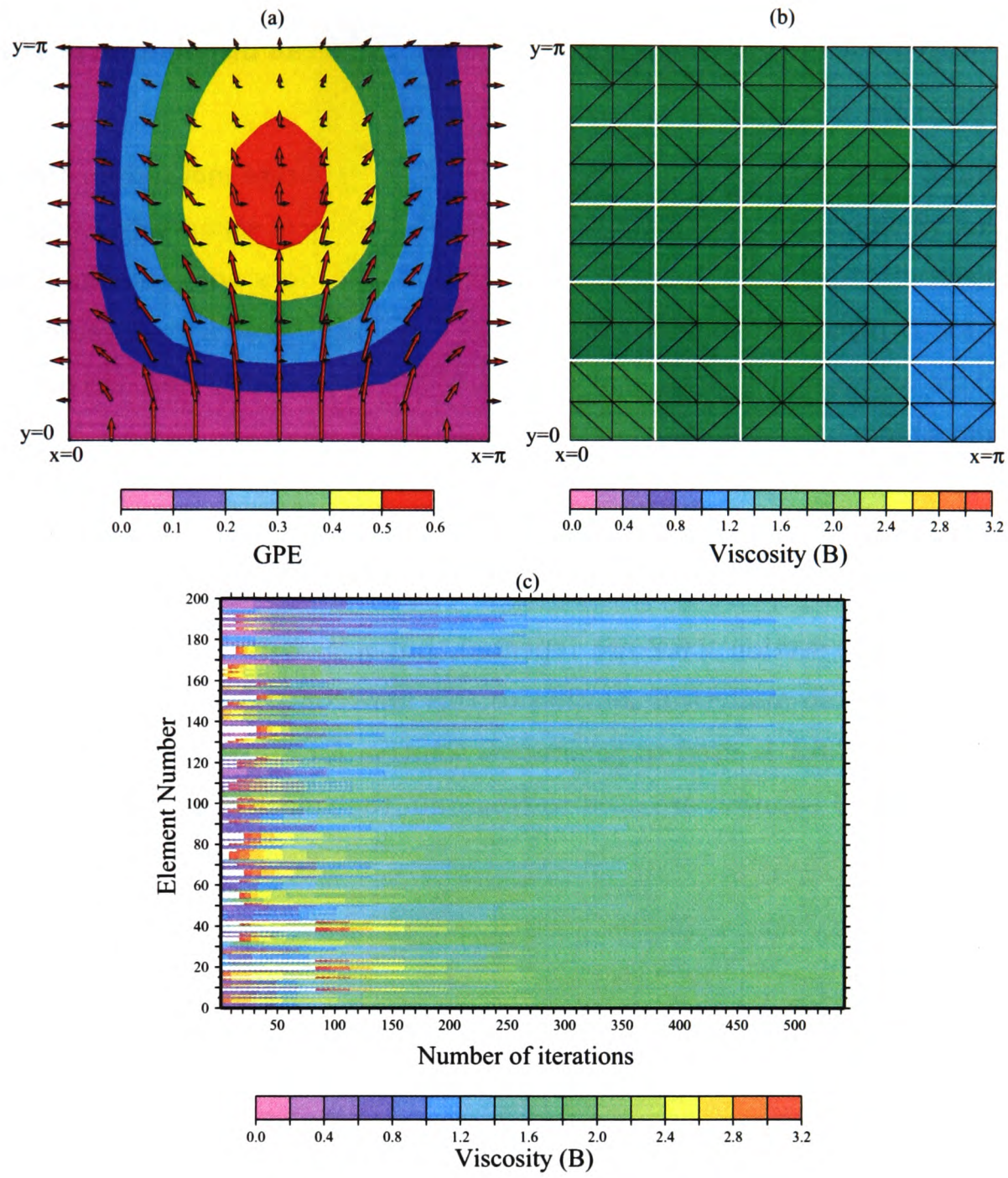

Figure 2.9: 25 viscosity regions, outlined in white, and numbered horizontally from top left to bottom right. (a) Red arrows: numerical velocity field solution. Green arrows: misfit to the input velocity field solution, arrow scale magnified by 50. (b) Distribution of B for the final solution. (c) Evolution of B in each element. Convergence occurred after 543 iterations.

of magnitude reduces this range, but increases the number of iterations required for convergence to >1000.

Figure 2.9 displays a result from the third experiment. The misfit to the analytical velocity field is still small, but there is greater variation in the final range for B; $1.238 \leq B \leq 1.862$. The range of this final distribution varies as the input distribution is varied. In order to better constrain the distribution of B output by the inversion calculations, many runs with different initial distributions

of B are carried out in the following experiments. The mean distribution of B is calculated using all the solutions that converge.

The results of these experiments imply that the most accurate method for inverting for the viscosity distribution when $n = 1$ involves solving for B in each element separately, using a smoothing algorithm between each viscosity relaxation. The distribution of B does not converge if smoothing is not used. Solutions for B obtained using the regional method are less well constrained, but this method still demonstrates a reasonable level of convergence for the velocity and viscosity fields, and does not require smoothing.

2.6.3 Viscosity inversions, non–Newtonian case : $n > 1$

The experiments of section 2.6.2 are repeated, but $n = 3$ is used in the forward and inverse calculations. There is no analytical solution to this non–Newtonian case, and the forward calculation method of section 2.6.1 is used to generate a solution for $Ar = 1$, $n = 3$, $B = 1$. Boundary conditions from the $n = 1$ solution are used to constrain the velocity field, and the same potential energy function is used.

The resulting velocity field is plotted in Figure 2.10, along with the $n = 1$ solution for comparison. There is little difference in the directions of the velocity vectors, as expected when using the same Argand number, but the magnitude of the velocity is smaller throughout the solution domain when $n = 3$. This $n = 3$ solution for the velocity field is used to define the convergence of the strain rate field in the following experiments.

In this non–linear case, solving for B is not equivalent to solving for the effective viscosity, and once the solution has converged, the effective viscosity throughout the solution domain is calculated using equation 2.4; $\eta_{\text{eff}} = \frac{1}{2} B \dot{E}^{(\frac{1}{n}-1)}$ with $n = 3$.

Two experiments are carried out: in the first the solution domain is divided into 25 regions, and a single value of B is solved for in each region. In this case no smoothing is used. In the second experiment I solve for B in each element separately. A smoothing algorithm, with $\alpha_s = 5.0 \times 10^{-6}$, is used. A value of $\alpha = 0.05$ is used to update the distribution of B in both experiments, and the mean values of B and η_{eff} are calculated from the results of 50 runs of each experiment.

Results: Forward calculations

In the $n = 3$ forward calculation a strength parameter of $B = 1$ is used, however, this does not define the effective viscosity throughout the solution domain, which is calculated using equation 2.4. The

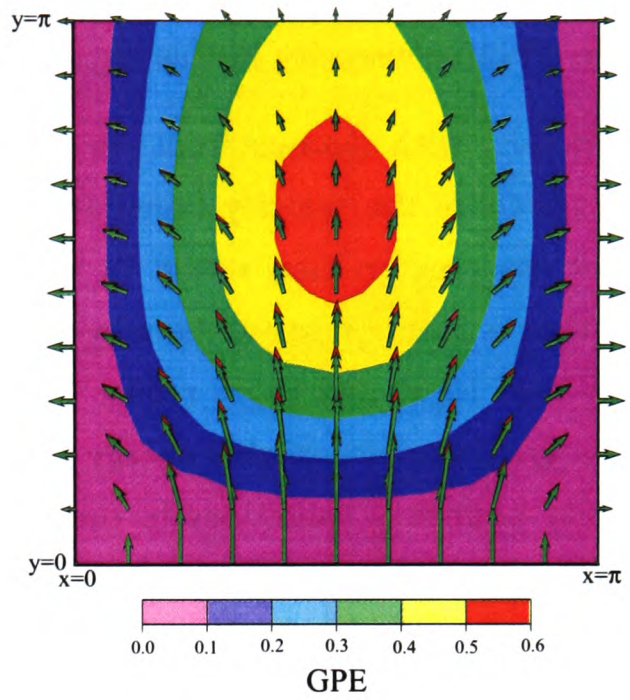

Figure 2.10: Numerical velocity fields input into the viscosity inversions. Red arrows; $n = 1$. Green arrows, $n = 3$.

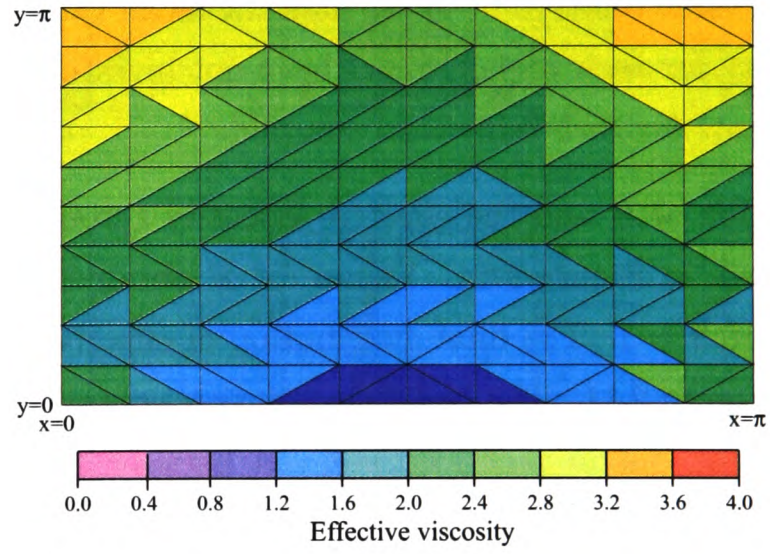

Figure 2.11: Effective viscosity calculated using $\eta_{\text{eff}} = B\dot{E}^{\frac{1}{n}-1}$, where $B = 1$, $n = 3$, and $\dot{E}$ is calculated using the input velocity field.

effective viscosity for the forwards solution is plotted in Figure 2.11. The lowest effective viscosity is found in the centre of the solution domain near $y = 0$, where there are large compressional strain rates despite low gradients of potential energy (see Figure 2.10). A decrease in the magnitude of the y component of velocity with distance from the driving boundary is expected due to the positive potential energy gradient at $y > 0$, but the rate of decrease is compounded by the decay of the y component of velocity with distance from the driving boundary when $n = 3$. These effects combine

to yield a low value for the effective viscosity in this region.

The increase in effective viscosity with distance from the x axis is a reflection of the greater influence of buoyancy forces as the effects of the velocity boundary condition decay with distance from $y = 0$. If solution strain rates are greater than would be expected given the local potential energy gradient, e.g. near $y = 0$, then a lower effective viscosity value will result, and vice versa. The high values of effective viscosity near $(0, \pi)$ and (π, π) reflect the low strain rates in these regions, which persist despite locally steep gradients of potential energy in the x direction. The low strain rates are constrained by fixed velocity boundary conditions in the corners of the solution domain, which do not reflect the effect of high potential energy gradients upon the velocity field.

Results: Inverse calculations

Figures 2.12 and 2.13 show histograms of the distribution of B obtained when the solution domain is divided into 25 regions, numbered horizontally from top left to bottom right (see Figure 2.9). There is generally a single modal value for B in each of the 25 regions. The data are positively skewed, therefore the modal value tends to be lower than the mean value. The mean value is used to calculate the effective viscosity for each region, and I have not investigated the correlation between values of B in different elements for each individual solution.

The mean distribution of B and the effective viscosity throughout the solution domain for the 25–region case are shown in Figure 2.14. Values for B obtained in the inversion calculation are close to the input value of $B = 1$. The final distribution of effective viscosity is compared with the input solution shown in Figure 2.11. The inversion solution contains higher values of η_{eff} in some regions of the solution domain, but in general agreement between the two solutions is good. The misfit is attributed to the use of mean values for B taken from a positively skewed set of data.

Figure 2.14c shows the distribution of effective viscosity calculated using the value of $\dot{E}$ in each element, instead of the average value for the region. The decrease in order between Figures 2.14b and 2.14c may partly be attributed to the geometry of the finite element mesh, which is not symmetric, and so cannot precisely recover the input effective viscosity solution. Such a mesh also cannot accurately interpolate velocity and strain rate fields without introducing singularities. Singularities in the strain rate field would render it impossible for the relaxation method to reach the correct effective viscosity solution; strain rates must therefore be reset to a small positive value in such locations, and convergence is consequently slow. Further investigation into relaxation techniques for finite element calculations is necessary to establish a robust method.

The distribution obtained by repeatedly solving for B in each element separately are more skewed,

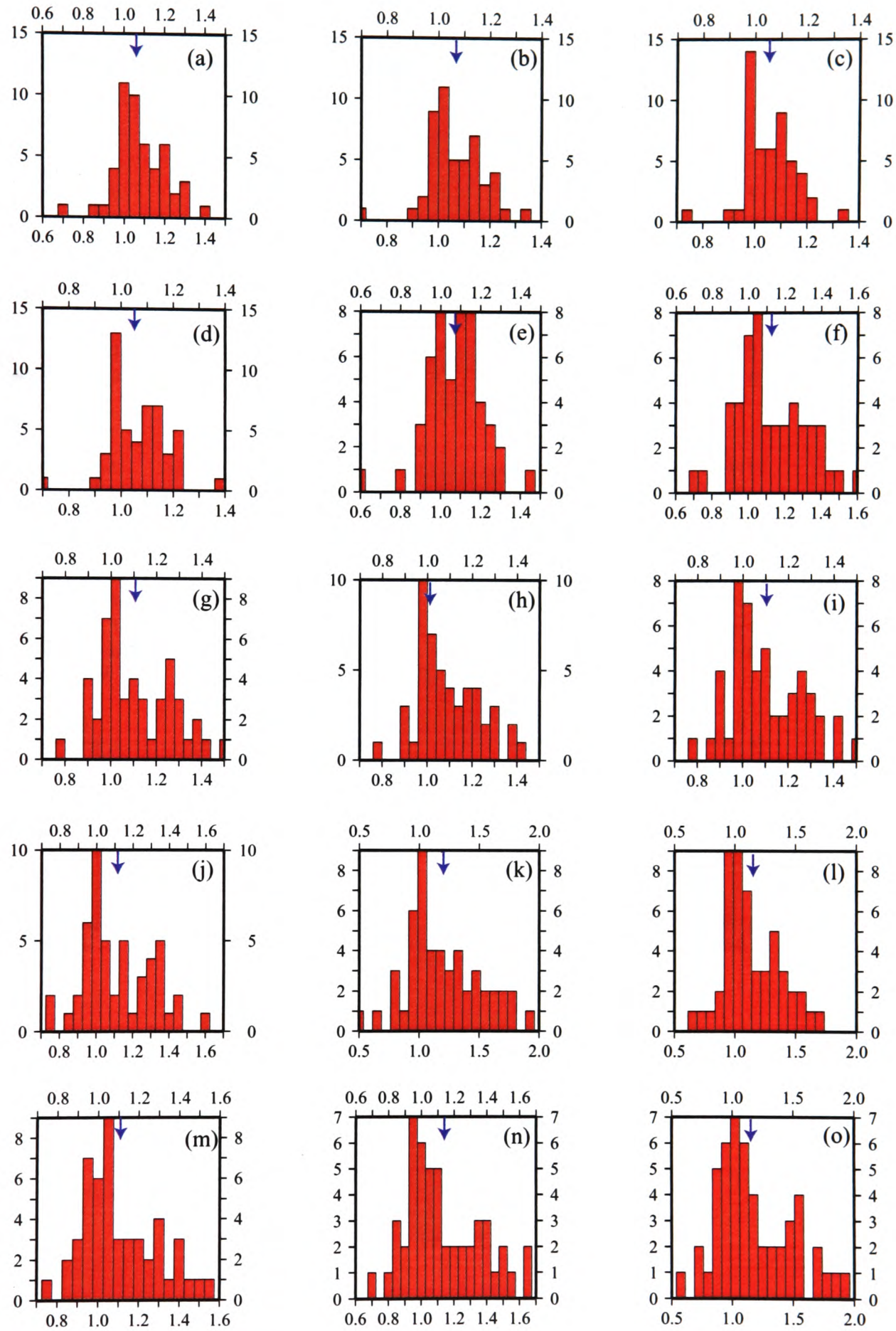

Figure 2.12: Histograms of the distribution of B obtained during 50 runs of the experiment described in section 2.6.3. The solution domain is divided into 25 regions. Plots (a) to (o) show results for regions 1 to 15 inclusive. The blue arrow marks the mean of each distribution.

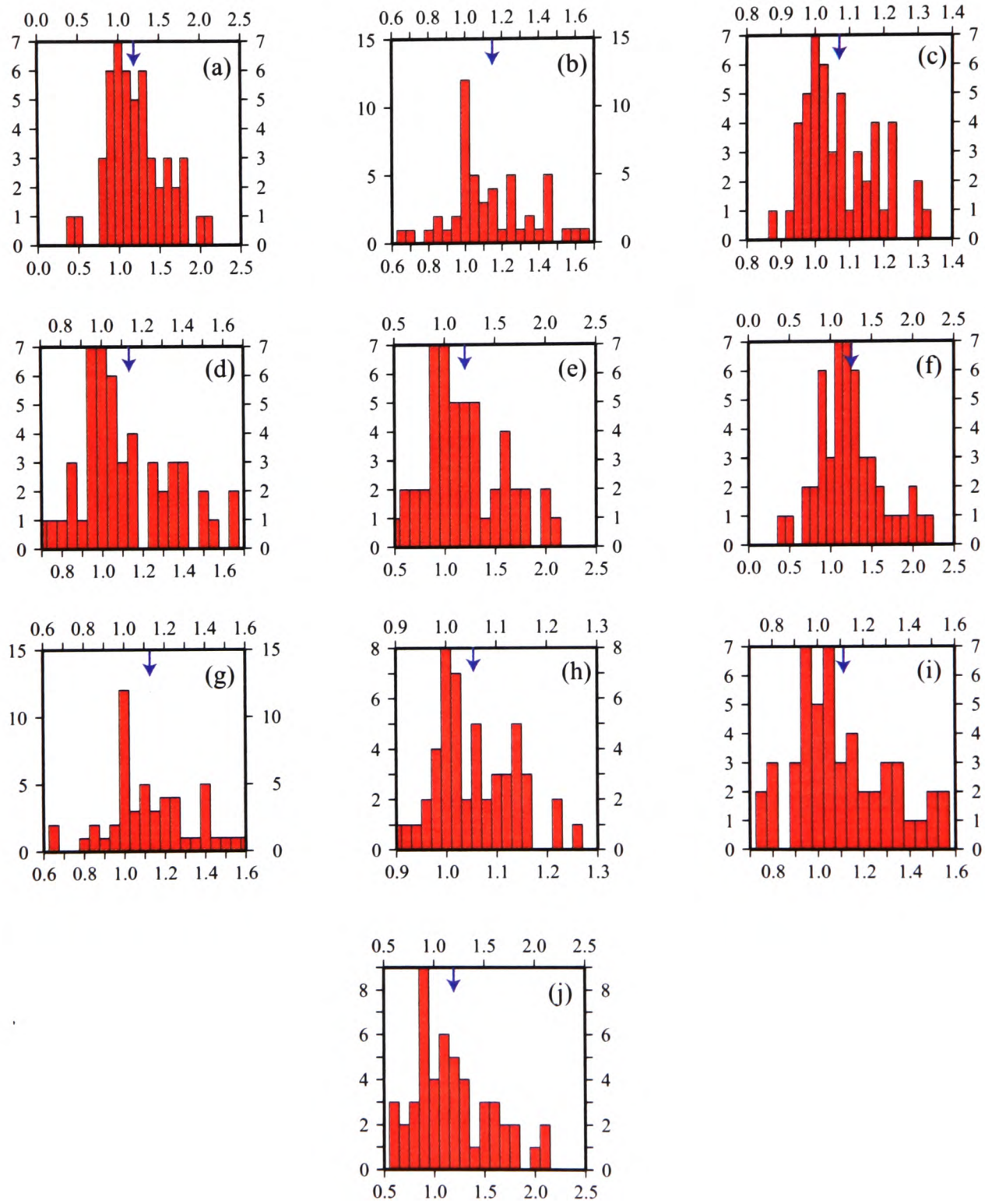

Figure 2.13: Details as for Figure 2.12. Plots (a) to (j) show results for regions 16 to 25 inclusive. The blue arrow marks the mean of each distribution.

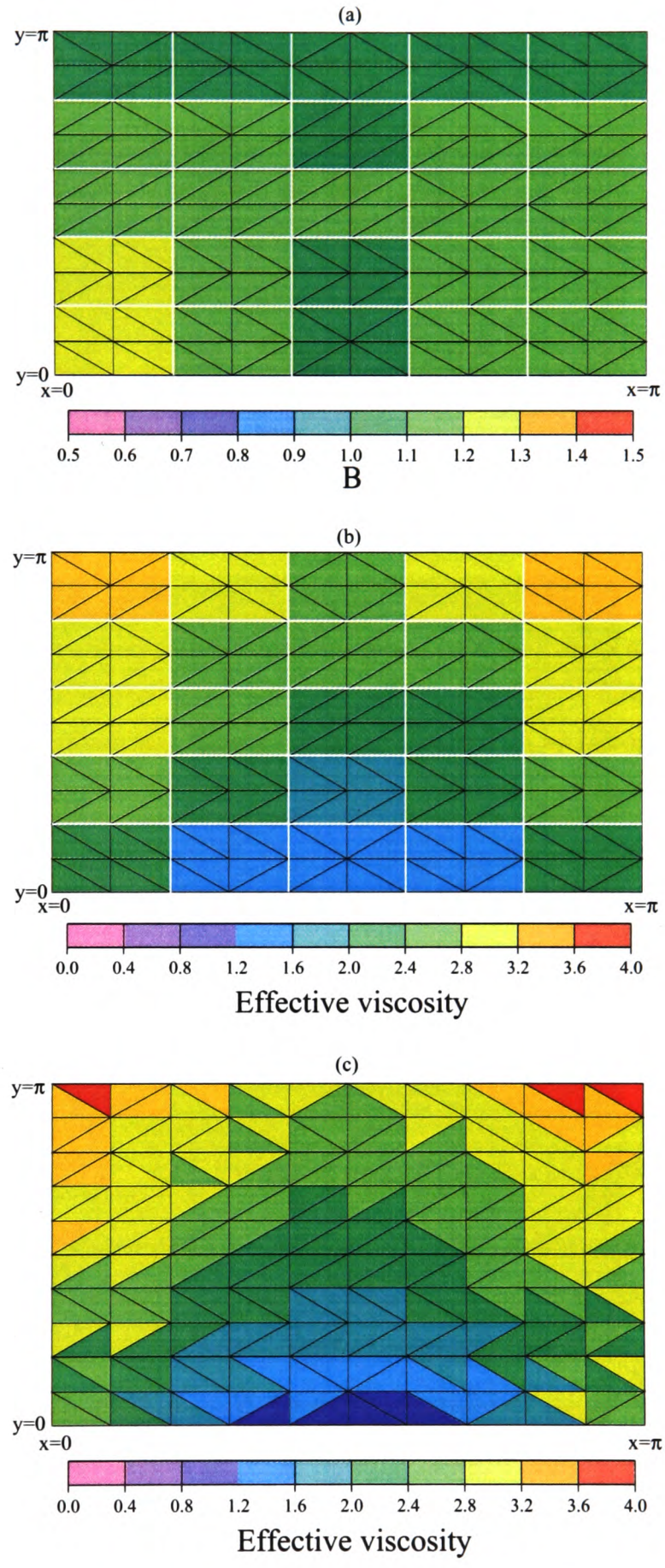

Figure 2.14: 25 viscosity regions, outlined in white. (a) Mean distribution of B, calculated from 50 runs of the first experiment of section 2.6.3. (b) Effective viscosity distribution for the distribution of B shown in (a), calculated using the mean value of $\dot{E}$ in each region, and $n = 3$. (c) As for (b), but η_{eff} is calculated using the individual value of $\dot{E}$ from each element.

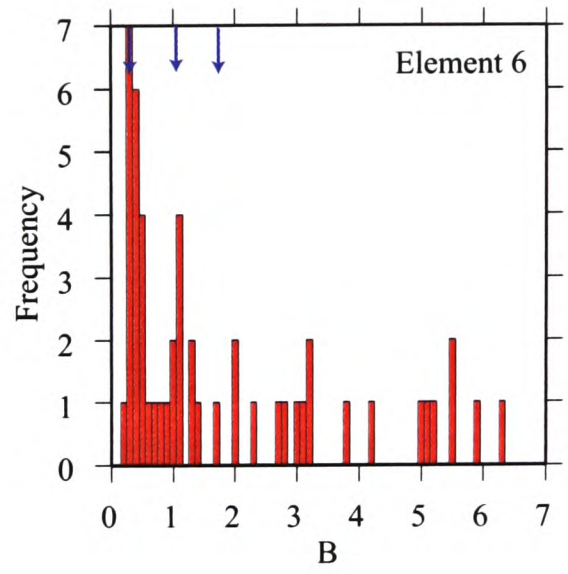

Figure 2.15: Histogram of values of B for the sixth element of the mesh (bottom left–hand corner), displayed in bins of width 0.1, from 50 runs of the second experiment of section 2.6.3. The arrow at $B = 0.25$ marks the mode of the distribution, the arrow at $B = 1.053$ marks the median, and the arrow at $B = 1.849$ marks the mean.

and have a greater range, than in the 25–region case (see Figure 2.15). In order to investigate the range of possible effective viscosity solutions, the mean, median, and modal distributions of B are all used to determine solutions for the effective viscosity. The modal value has been calculated by sorting the data into bins of width 0.1. The mid–value of the modal bin is then used to determine B and η_{eff}. The distribution of B for the three cases is plotted in Figure 2.16, and the corresponding effective viscosity solutions are plotted in Figure 2.17.

The modal distribution of B bears no correlation to the mean and median solutions, and I conclude that using modal values does not yield an accurate representation of the solution for B in this experiment. There is little difference between the mean and median distributions, although both give a slightly worse fit to the input value of $B = 1$ than the 25–region case. When the mean is used, higher values of B are found towards $y = \pi$, when the median is used, lower values of B are found towards $y = 0$. In general $B \geq 1$ for the mean and median of this solution. The effective viscosity distribution, calculated using the modal distribution of B, consists of a random distribution of values (Figure 2.17c). However, using either the mean or median values results in a reasonable fit to the input effective viscosity solution of Figure 2.11, with the the mean yielding a slightly smoother distribution.

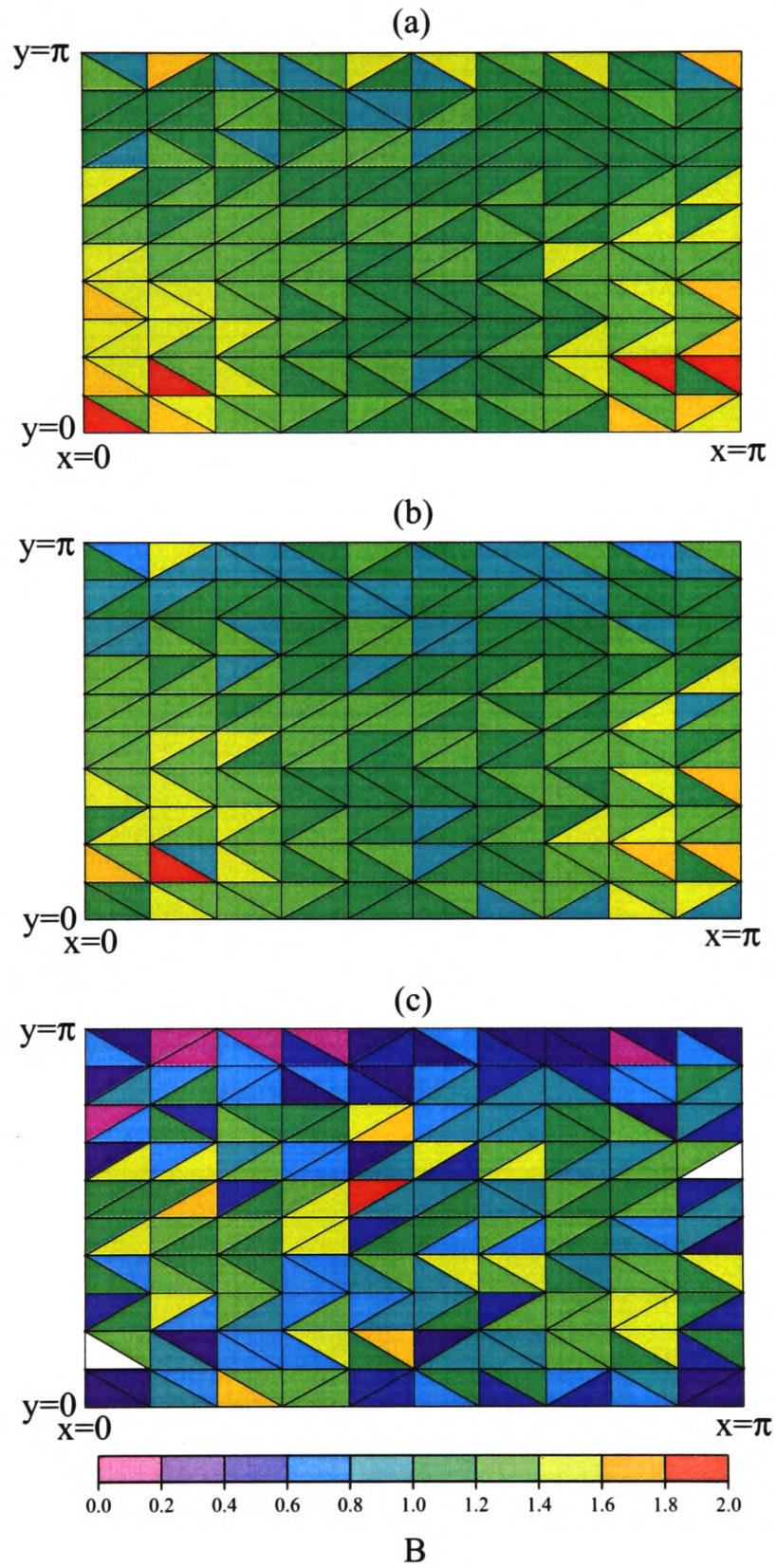

Figure 2.16: (a) Mean distribution of B in each element, calculated from 50 runs of the second experiment of section 2.6.3. (b) Median distribution of B in each element. (c) Modal distribution of B in each element. All solutions use the same colour scale, white indicates an element where $B > 2$.

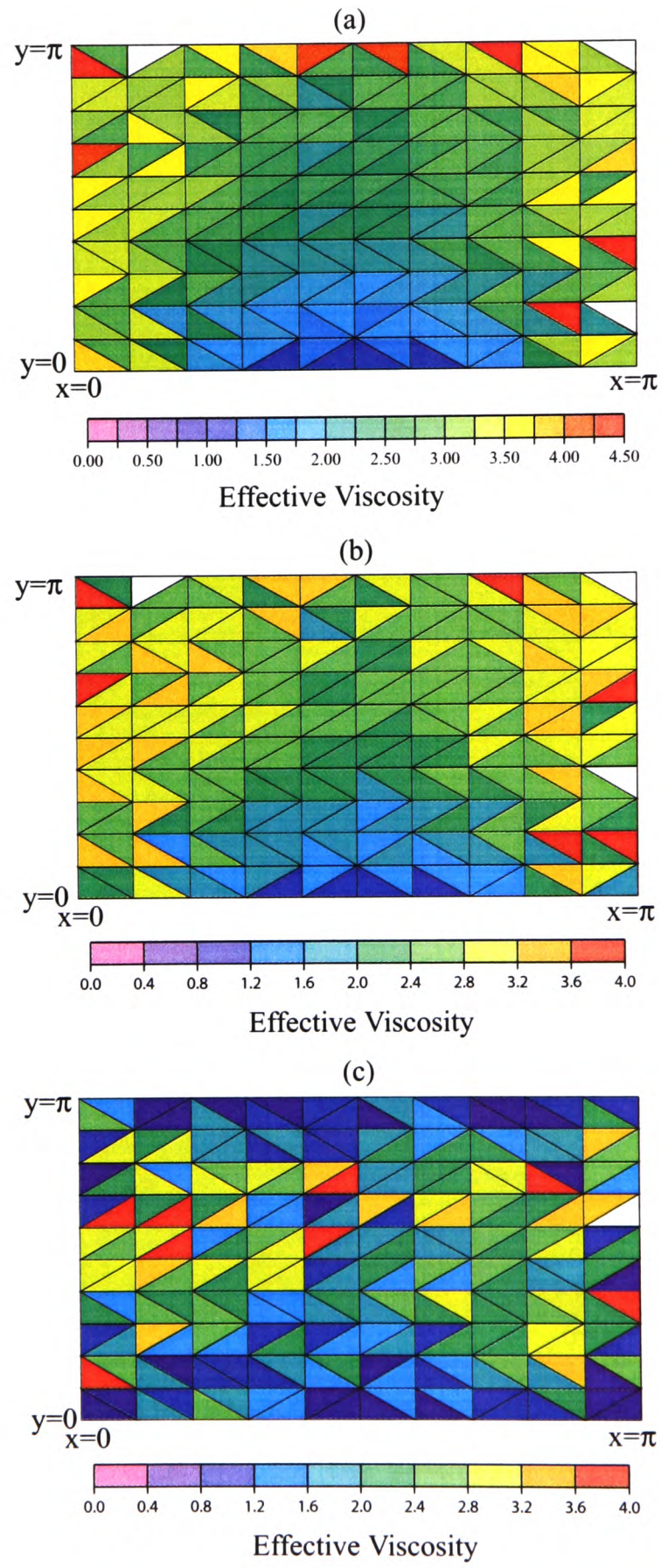

Figure 2.17: Effective viscosity solutions for the second experiment of section 2.6.3, calculated using (a) the mean, (b) the median, and (c) the mode of the distribution of B in each element.

2.6.4 Solving for n

In order to determine the value of the stress-strain rate exponent which governs the deformation of a viscous layer, viscosity inversions are carried out using $n = 1$. This yields a solution for B which is directly proportional to effective viscosity. Substituting $n = 1$ into the expression for effective viscosity derived from the constitutive equation (equation 2.4);

$$\eta_{\text{eff}} = B\dot{E}^{\frac{1}{n}-1} \Rightarrow \eta_{\text{eff}} = B_{(n=1)} \Rightarrow B_{(n=1)} = B_n\dot{E}^{\frac{1}{n}-1} \tag{2.92}$$

Taking the natural logarithm of equation 2.92 yields an equation whose gradient may be used to determine the value of the stress–strain rate exponent n;

$$\ln(B^i_{(n=1)}) = \left(\frac{1}{n} - 1\right)\ln(\dot{E}^i) + c \tag{2.93}$$

where the superscripts refer to each element or region, and c is the natural logarithm of the constant of proportionality in equation 2.92; $\ln(B_n)$. A straight line will result only if there is little variation in B_n across the solution domain.

The value of n implied by the gradient of the line is the true value of the stress-strain rate exponent which governs deformation in the viscous layer, and B_n is the spatially varying strength coefficient for the layer. The distribution of B_n is output from inversion calculations where the value of n is determined by equation 2.93. The values of $\dot{E}$ may be taken from any solution, or the input values, since the value of $\dot{E}$ within each element should lie within 1% of the value of the input value if convergence is attained.

The experiments of section 2.6.3 are repeated using $n = 1$ in inversions which attempt to recover velocity and strain rate fields originally calculated using $n = 3$. The input velocity field of section 2.6.3 was calculated using $n = 3$, and is used to define the convergence of the inversions which use $n = 1$. Once again $Ar = 1$ and $B = 1$ in the forward calculation, and $\alpha = 0.05$ in the inversions. A smoothing parameter of $\alpha_s = 5.0 \times 10^{-4}$ is used for the case with 200 regions. 50 runs of experiments using 200 regions (where each element is regarded as a region) and 25 regions are carried out, and the mean value of B in each region or element is calculated. Convergence took between 564 and 2595 iterations for this set of experiments, and all runs converged.

Results

Figures 2.18 and 2.19 show histograms of the distribution of B obtained when the solution space is divided into 25 regions. These distributions are not strongly skewed, and I do not investigate using the median or the mode of these distributions.

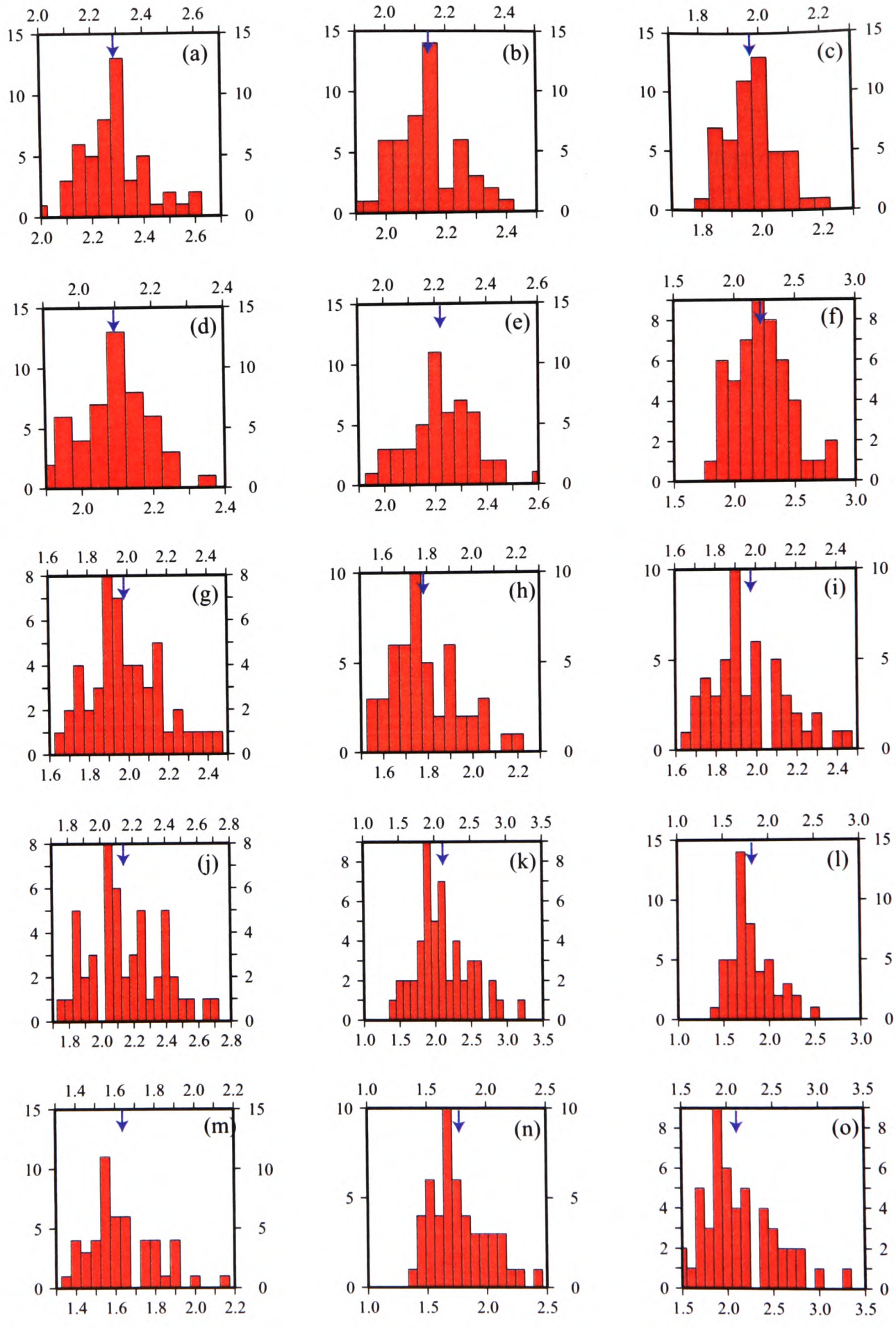

Figure 2.18: Histograms of the solutions to B obtained during 50 runs of the experiment described in section 2.6.4. Solution domain is divided into 25 regions. Plots (a) to (o) represent the first 15 regions, which are numbered horizontally from top left to bottom right (see Figure 2.9). The blue arrow marks the mean of each distribution.

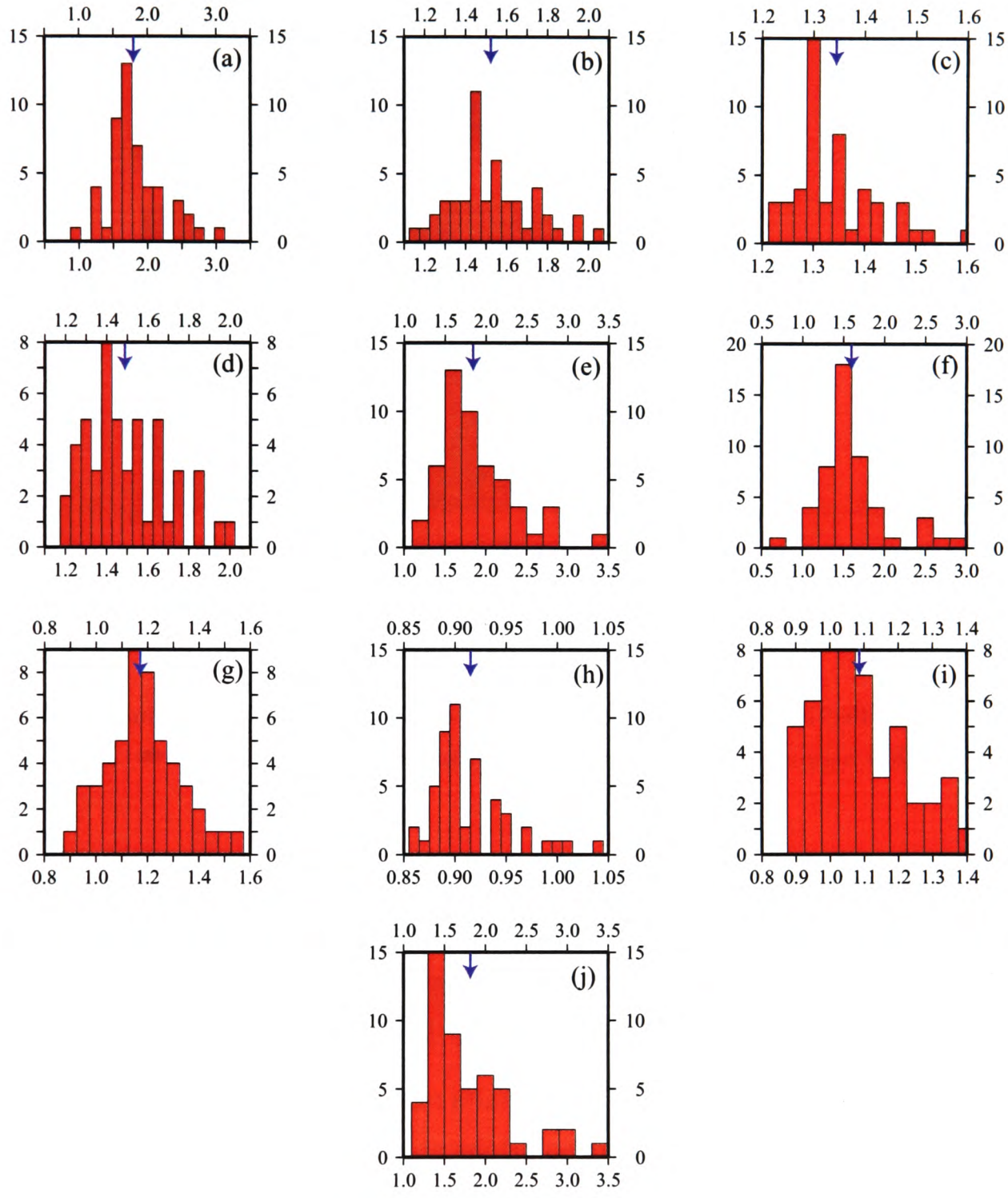

Figure 2.19: Details as for Figure 2.18. Plots (a) to (j) show results for regions 16 to 25 inclusive. The blue arrow marks the mean of each distribution.

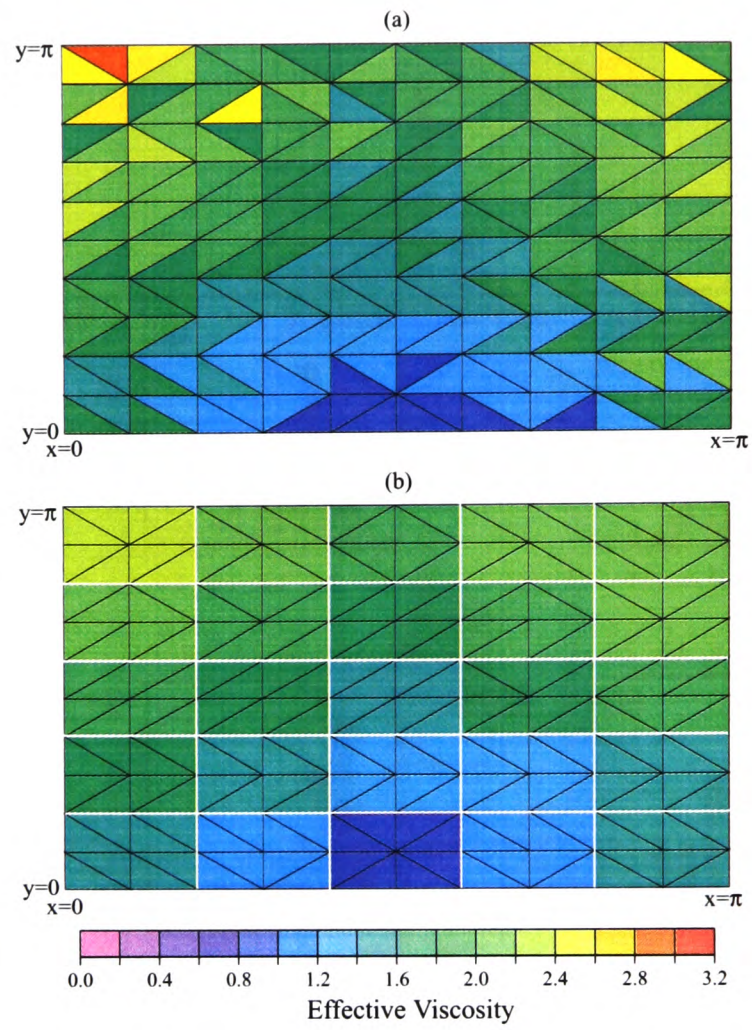

Figure 2.20: Effective viscosity solutions obtained by inverting for the values of B throughout the mesh using $n = 1$. (a) 200 regions. (b) 25 regions, outlined in white.

Figure 2.20 displays the mean values of B in each element or region calculated from the 50 runs of the two experiments. Since $n = 1$ is used in the inversion, but $n = 3$ was used in the forward calculation, the solutions for B are not expected to resemble the input value of $B = 1$ in this non–linear case. Instead, plotting B is equivalent to plotting the effective viscosity solution directly.

There is good agreement between the results obtained using 200 and 25 regions. The greatest misfits occur near $(0, \pi)$ and (π, π), where solutions are tightly constrained by the velocity boundary conditions. The values for B, and equivalently η_{eff}, obtained using $n = 1$ in the inversion calculations are slightly lower than the values calculated for the input solution (see Figure 2.11, and note the colour scale of Figure 2.20), but the first–order pattern of relative effective viscosity remains the same.

Graphs of $\ln(B_{(n=1)})$ against $\ln(\dot{E})$ are plotted for the 25–region and 200–region cases in Figures 2.21 and 2.22. In Figure 2.21 the average value of $\dot{E}$ for each region is used in conjunction with the mean value of B for that region to plot each point. The gradient of each graph is equated to the gradient of equation 2.93 in order to recover the value of n used to calculate the original deformation field.

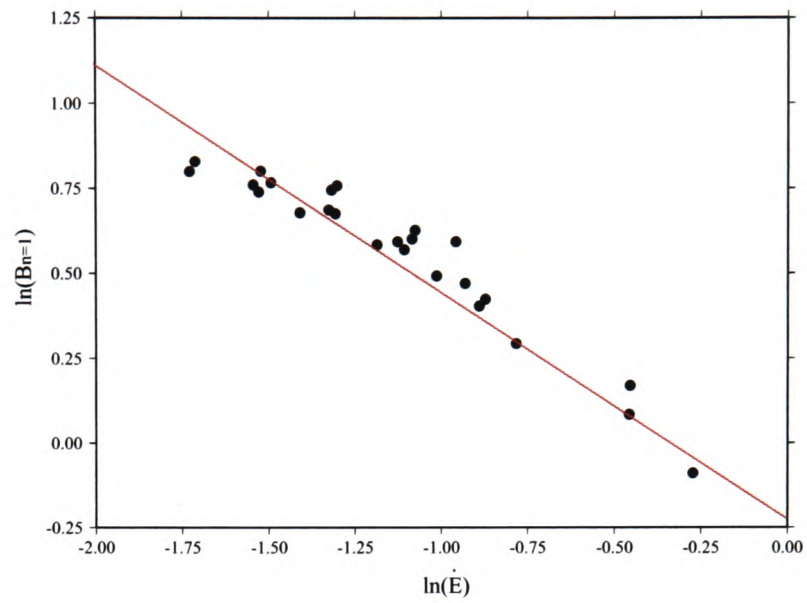

Figure 2.21: Plot of $\ln(B_{(n=1)})$ against $\ln(\dot{E})$ for the 25–region method. The red line has gradient $-2/3$.

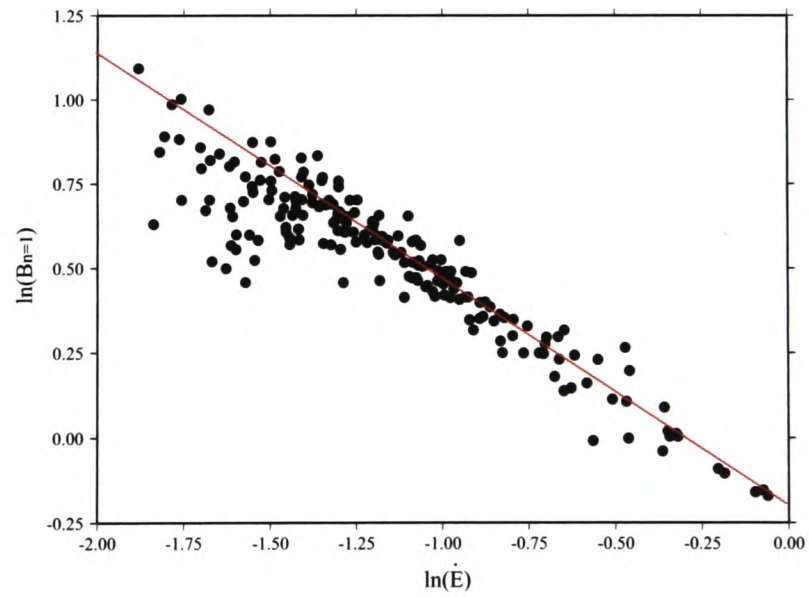

Figure 2.22: Plot of $\ln(B_{(n=1)}$ against $\ln(\dot{E})$ for the method which solves for B in each element independently. The red line has gradient $-2/3$.

In both figures, a line of gradient $-2/3$ has been drawn through the data. Referring to equation 2.93, it can be seen that this gradient corresponds to a stress–strain rate exponent for the viscous layer of $n = 3$. The data in both figures are fitted by this relationship, implying that the size of the region does not affect the value of n deduced by this method.

In chapter 4, inversions are first carried out using $n = 1$ in order to determine the potential range of the stress–strain rate exponent which governs deformation in south–east Asia. Inversions are then carried out using the deduced range of n to investigate the distribution of lithospheric strength in this region.

2.7 Monte Carlo restarts

In order to test the stability of viscosity distributions for south–east Asia obtained by the methods of section 2.6, a series of Monte Carlo restarts are carried out, and the velocity field data input into each experiment are perturbed.

As described in section 2.6.2, the initial viscosity distribution is defined by a set of values for the strength variable B, which is a random variable taken from the continuous uniform distribution $\mathrm{U}(e^{-2}, e^{2})$. Solutions for B approximately lie in the range 0–35 Pa $\mathrm{s}^{1/n}$. A series of experiments are carried out using the unperturbed velocity field data, where the initial input viscosity distribution is permitted to vary. The results of these experiments are used to assess the stability of the viscosity distribution, and draw conclusions about the value of n.

The input velocity data are then perturbed by adding correlated noise to each velocity vector of the observed velocity field such that the new vectors lie within the velocity error ellipse of each node. For each of these perturbed sets of velocity data, a number of different initial distributions for the viscosity data are used in the inversion calculations.The rms misfit of each solution is calculated to assess the accuracy of each result. The solutions are compared to the perturbed velocity field which is input into each experiment, to determine how well the method of relaxing the viscosity field permits the perturbed strain rate field to be recovered. The ability of the calculations to reproduce perturbed velocity fields also offers insight into the accuracy of the original velocity field data.

2.7.1 Simulation of correlated noise

The velocity at a point is input as a vector of easterly and northerly components of velocity, u and v, given in mm/yr. The standard deviations of the velocity components in the two directions, σ_u and σ_v, and the correlation coefficient, r_{uv}, are also given, where u and v refer to the east and north

directions respectively.

The covariance matrix may be constructed using the relationship

$$r_{ij} = \frac{cov(i,j)}{\sigma_i \sigma_j} \tag{2.94}$$

to yield

$$cov(u,v) = \begin{pmatrix} \sigma_u^2 & r\sigma_u\sigma_v \\ r\sigma_u\sigma_v & \sigma_v^2 \end{pmatrix} \tag{2.95}$$

where $r = r_{uv}$.

The eigenvectors of the covariance matrix define the principal axes of the error ellipse for this data point. The eigenvalue problem is solved;

$$0 = \begin{vmatrix} \sigma_u^2 - \lambda & r\sigma_u\sigma_v \\ r\sigma_u\sigma_v & \sigma_v^2 - \lambda \end{vmatrix} \tag{2.96}$$

$$\Rightarrow \lambda = \frac{1}{2}[(\sigma_u^2 + \sigma_v^2) \pm \sqrt{\sigma_u^4 + \sigma_v^4 + 2\sigma_u^2\sigma_v^2(2r^2 - 1)}] \tag{2.97}$$

The positive root, λ_1, determines the length of the major axis of the ellipse, and the negative root determines the minor axis. The angle between the major axis of the ellipse and the u–axis of the uv co–ordinate system is given by

$$\theta = tan^{-1}\left(\frac{\lambda_1 - \sigma_u^2}{r\sigma_u\sigma_v}\right) \tag{2.98}$$

A perturbation velocity must be defined within this error ellipse. The ellipse may be interpreted as the perpendicular superposition of two normal distributions, whose means coincide at the centre of the ellipse. The two distributions are defined by $\mathrm{N}(u, \sigma_u^2)$ and $\mathrm{N}(v, \sigma_v^2)$, and they lie along the two axes, λ_1 and λ_2 respectively, of the ellipse. In order to sample within the error ellipse, two random variables must be generated, one from each of these two normal distributions.

In order to generate two random variables from two correlated normal distributions, two independent values, x_1 and x_2, are chosen from the continuous uniform distribution U(0,1) using a random number generator. The Box–Muller transformation (Press *et al.*, 1992) is then used to transform these two independent data from a two–dimensional continuous uniform distribution to a two–dimensional bivariate normal distribution. This process yields two values, z_1 and z_2, which are defined to be from a normal distribution with mean $\mu = 0$ and variance $\sigma^2 = 1$.

$$z_1 = \sqrt{-2\ln(x_1)}\cos(2\pi x_2) \tag{2.99}$$

$$z_2 = \sqrt{-2\ln(x_1)}\sin(2\pi x_2) \tag{2.100}$$

The two values, z_1 and z_2, are then multiplied by the length of the major and minor axes of the ellipse respectively to yield a perturbation vector, $\Delta\mathbf{v} = (z_1\lambda_1, z_2\lambda_2)$ (see Figure 2.23), given in

the co–ordinate system defined by the axes of the ellipse. This vector is transformed back into the co–ordinate system defined by the east and north components of velocity to yield

$$u + \Delta u = u + z_1\lambda_1 \cos\theta - z_2\lambda_2 \sin\theta \tag{2.101}$$

$$v + \Delta v = v + z_1\lambda_1 \sin\theta + z_2\lambda_2 \cos\theta \tag{2.102}$$

This process is repeated at each node until a perturbed velocity field is defined across the whole mesh. The velocity at every node will lie within the error of the original data. This velocity field is then input into the viscosity inversion, where it is defined to be the solution which must be reproduced by the relaxation of the viscosity distribution.

The error ellipse which I describe defines the 1σ confidence interval for the two–dimensional bivariate normal distribution which governs the distribution of the two components of the velocity field. The equation that governs which points $(z_1\lambda_1, z_2\lambda_2)$ lie within the error ellipse, in the co–ordinate system aligned with the axes of the ellipse, is

$$\begin{aligned} \frac{z_1^2\lambda_1^2}{\lambda_1^2} + \frac{z_2^2\lambda_2^2}{\lambda_2^2} &\leq 1 \\ \Rightarrow z_1^2 + z_2^2 &\leq 1 \end{aligned} \tag{2.103}$$

where λ_1 and λ_2 are the major and minor axes of the ellipse, which correspond to the eigenvalues of the covariance matrix, and $z_1\lambda_1$ and $z_2\lambda_2$ are the components of the velocity perturbation in this co–ordinate system. The inequality is used to define points which lie within the 1σ confidence interval. The 2σ confidence interval for each velocity vector is defined by an ellipse whose major and minor axes are twice the length of those in the 1–σ ellipse:

$$\begin{aligned} \frac{z_1^2\lambda_1^2}{(2\lambda_1^2)} + \frac{z_2^2\lambda_2^2}{(2\lambda_2^2)} &\leq 1 \\ \Rightarrow z_1^2 + z_2^2 &\leq 4 \end{aligned} \tag{2.104}$$

A Gaussian distribution has a 1σ confidence interval of 68%, and a 2σ confidence interval 95% (see Figure 2.24). However, it is non–trivial to determine the confidence interval for two or more correlated sets of data; a volume must be defined, and the probability that the true means of the data lie within this volume computed. In order to determine the confidence interval defined by the 1σ and 2σ error ellipses described above, data points lying within 1000 such error distributions are generated using equations 2.101 and 2.102, where each distribution contains 10,000 data points. The original velocity components, u and v, are chosen to be zero, and the inputs which define the characteristics of each error distribution, σ_u, σ_v and r_{uv}, are chosen from uniform continuous distributions. The standard deviations are taken from the continuous uniform distribution U(-5,5) and the correlation coefficients are taken from the continuous uniform distribution U(-1,1). In each case, the 10,000

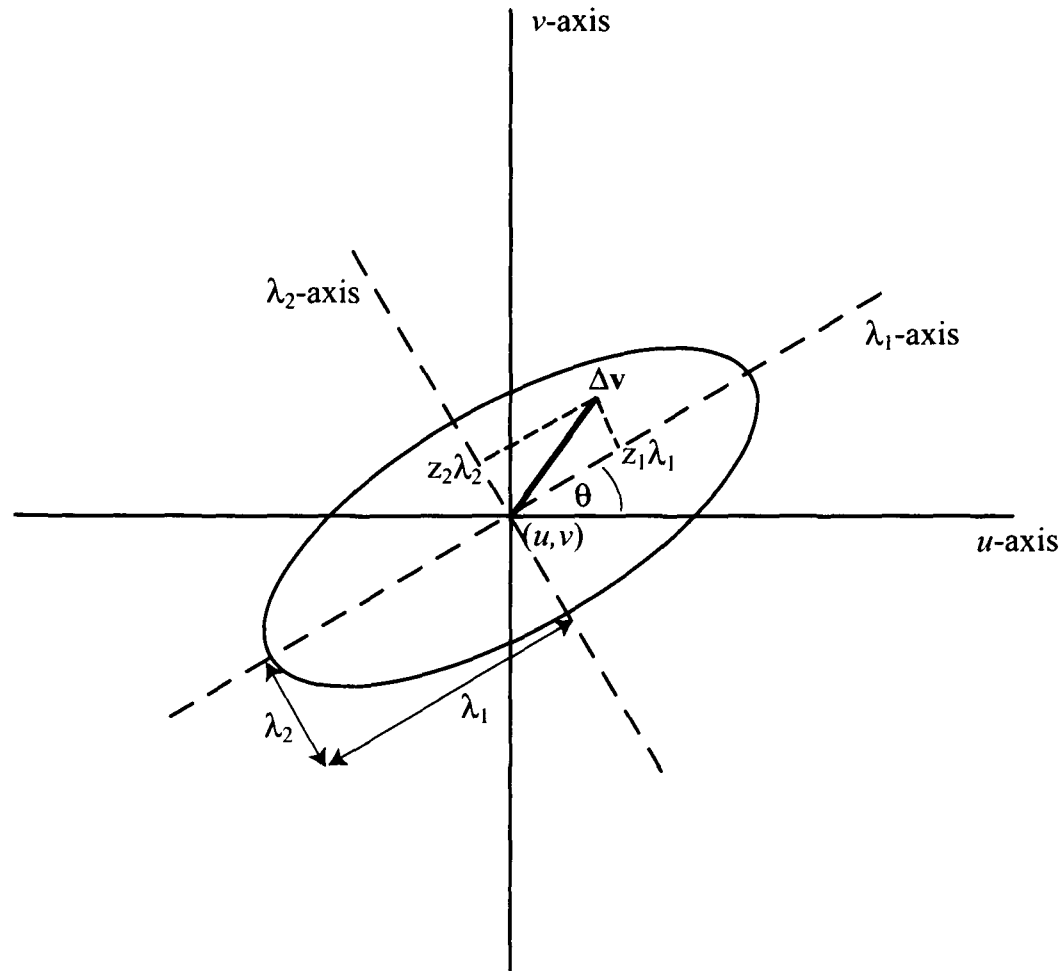

Figure 2.23: Diagram to define the terms used in calculating the velocity perturbation. Velocities are defined in the uv co–ordinate system, with the point (u, v) taken to lie at the origin of the axes. λ_1 and λ_2 define the lengths of the axes of the error ellipse, θ is the angle of rotation of the axes of the ellipse from the uv co–ordinate axes. Δv is the velocity perturbation, defined by the random variables z_1 and z_2, which are taken from a standard normal distribution.

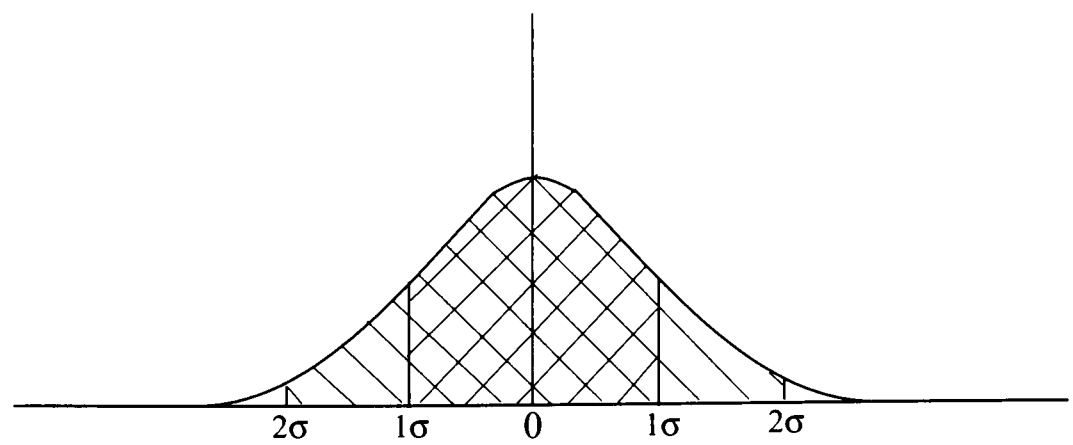

Figure 2.24: Standard normal N(0,1) Gaussian distribution. 68% of the distribution lies within 1σ of the mean (cross-hatched region), and 95% of the distribution lies with 2σ of the mean (hatched region)

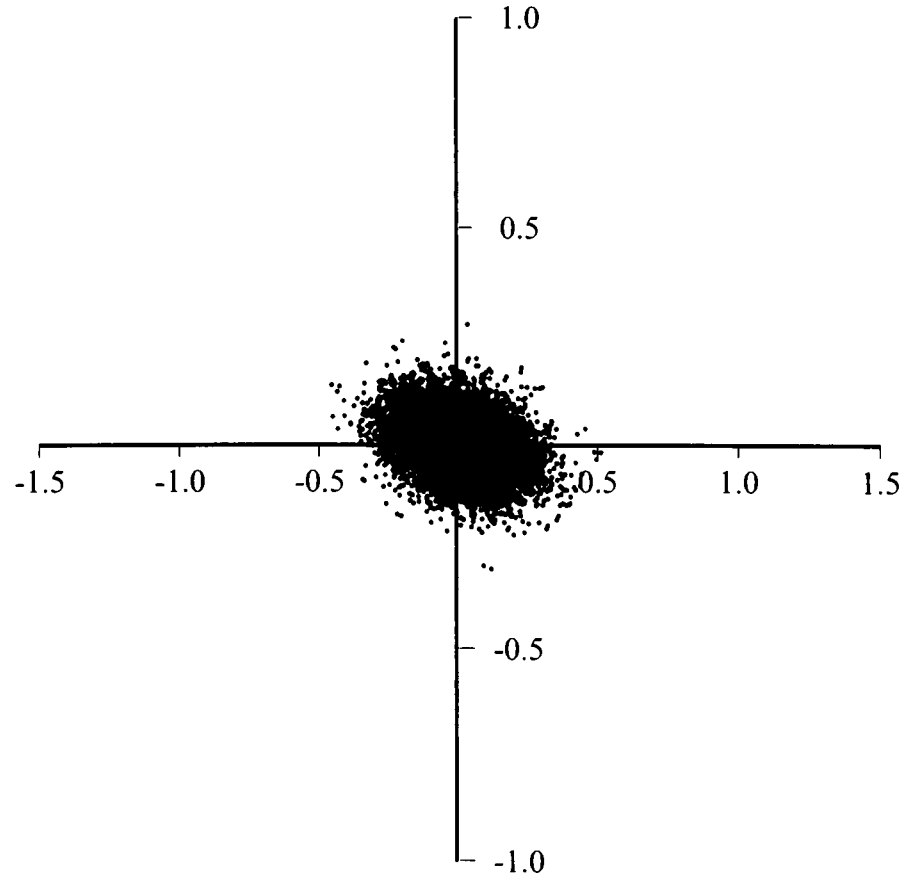

Figure 2.25: An example of a randomly–generated error distribution containing 10,000 points. In this case, $u = v = 0$, $\sigma_u = 0.25$, $\sigma_v = 0.35$ and $r_{uv} = -0.15$.

velocity perturbations are generated randomly by the methods outlined above. Figure 2.25 shows an example of the distribution of Δv for one set of $(\sigma_u, \sigma_v, r_{uv})$. The percentage of points lying inside the 1 and 2σ error ellipses is determined for each error distribution using equations 2.103 and 2.104. The mean percentage of points within each interval are calculated. This method yields a 1σ confidence interval of 39.36%, and a 2σ confidence interval of 99.97%, for a two–dimensional bivariate normal distribution.

Chapter 3

Distribution of Gravitational Potential Energy in Asia

3.1 Introduction

In order to solve the thin viscous sheet equations on a finite element mesh, the gravitational potential energy distribution must be known at all points throughout the mesh. In this chapter I present a method that approximates the potential energy distribution across a region using only topographic height, and a knowledge of the height of the geoid, in the chosen region.

Topographic heights are used to constrain the crustal structure, assuming Airy isostasy. Several models of lithospheric evolution following collision are considered. Knowledge of the local geoid height, and independent estimates of crustal thickness, are used to constrain the most suitable model. This density distribution is then used to generate an approximation to the geoid anomaly for south-east Asia, from which the gravitational potential energy field is calculated.

3.2 Thermal evolution of thickened lithosphere

Early calculations of the changes in potential energy in Tibet during lithospheric thickening (England & McKenzie, 1982; Houseman & England, 1986; England & Houseman, 1986; Vilotte *et al.*, 1986) used constant crust and mantle densities, and did not consider any density contrast between the lithosphere and the asthenosphere. Under these assumptions, changes in potential energy would arise purely from changes in crustal thickness. I follow the methods of England & Houseman (1989), and consider the thermal development of the continental lithosphere as it thickens. Internal heating

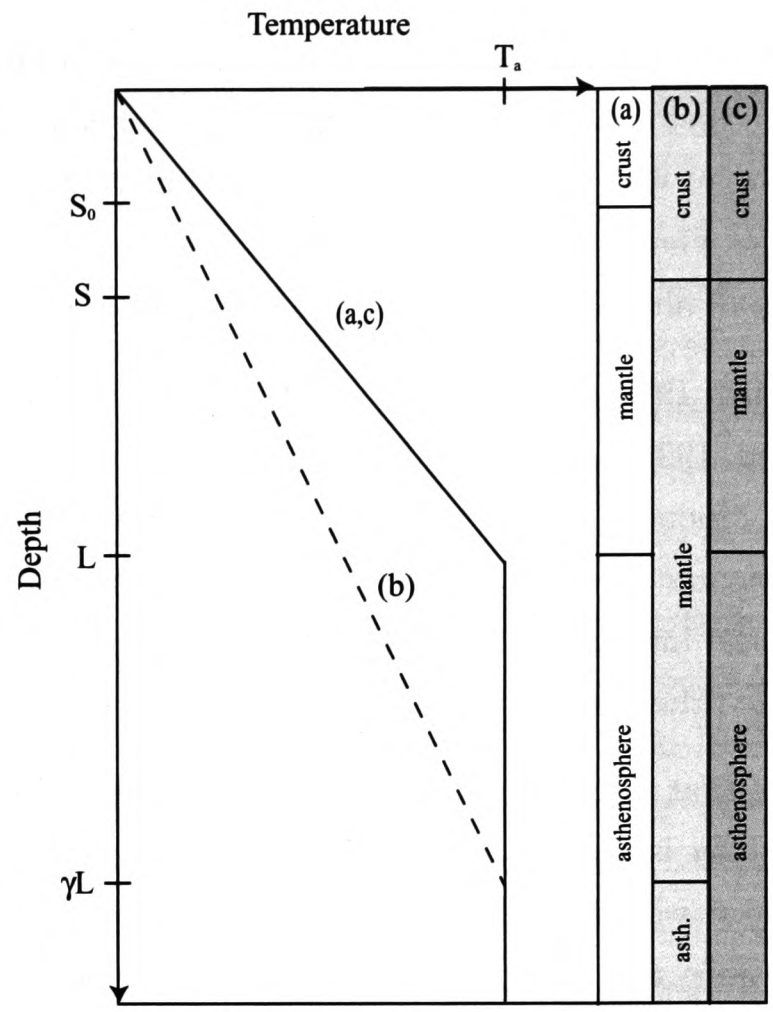

Figure 3.1: Proposed geotherms and lithospheric columns for continental lithosphere. T_a is the temperature of the asthenosphere, and γ is the thickening factor. Other terms are defined in the text. (a) reference lithospheric column, (b) rapidly thickened lithosphere assuming a constant volume model, (c) lithosphere which has been thickened by the same factor as (b) but which has undergone convective thinning, and a return to thermal equilibrium. (c) has the same geotherm as (a). Taken from England and Houseman, 1989.

is neglected, but the geotherm of the thickened lithosphere is assumed to be the result of both the downward advection of thickened lithosphere, and the heating of the lithosphere by conduction from below.

Figure 3.1 presents two models for lithospheric evolution following continental collision. In the first model it is assumed that the vertical strain rate in the lithospheric column is uniform, and sufficiently fast that strain occurs without any appreciable thermal diffusion. The resulting geotherm is given by curve (*b*) in Figure 3.1. In the following discussion, this model will be referred to as the constant volume model.

In continent–continent collision, the evolution of the resulting deformation may be characterised by three stages: (1) Tectonic forces cause crustal shortening, resulting in thickened continental crust and the growth of a plateau with high topography. (2) Thickened crust resists further shortening, and

the area, rather than the height, of the plateau continues to increase. (3) The plateau collapses due to the relaxation of tectonic forces. However, this model cannot account for the sudden rapid uplift of the Tibetan plateau which initiated between 14 and 11 Ma, and resulted in an absolute increase in the height of the whole plateau by 1–2.5 km over the relatively short period of 10 Ma (Molnar *et al.*, 1993). A set of alternative models have been proposed to explain this phenomenon.

Many authors (Bird, 1979; Houseman *et al.*, 1981; Zhao & Morgan, 1985, 1987; England & Houseman, 1989; England, 1993; Lenardic & Kaula, 1995; Houseman & Molnar, 1997; Schott & Schmeling, 1998; Meissner & Mooney, 1998; Pysklywec *et al.*, 2000; Morency *et al.*, 2002; Molnar & Houseman, 2004) have suggested that, as a result of lithospheric thickening, a convective instability may develop following the introduction of lithospheric material at depths normally associated with the asthenosphere. The lithospheric mantle is negatively buoyant with respect to the asthenosphere.

It should be noted that an increase in the thickness of a crustal root will act to increase the local topography if isostasy is maintained. This is because crustal material is more buoyant than the lithospheric mantle it would displace. However, the growth of a lithospheric root will decrease the local topography since the root will be negatively buoyant in relation to the hot asthenospheric material of the upper mantle.

The negative buoyancy of a lithospheric root contributes to the rate of shortening of the thickened lithosphere in a compressional regime. Eventually, buoyancy forces may lead to the detachment of the entire lithospheric mantle, which would be replaced by hot asthenospheric material, thus restoring the geothermal gradient of the lithospheric column to its pre–collisional value (see Figure 3.1). While the thickened mantle lithosphere provides a strong negative buoyancy force, its internal strength acts to inhibit deformation and delamination. One hypothesis to overcome this paradox invokes a weakening of the lithosphere, for example in the presence of water. Alternatively, the existence of a weak (low viscosity) lower crust could provide a detachment zone for the mantle lithosphere below. In this scenario, the lower crustal material may also be subducted into the upper mantle during delamination.

There is continued debate as to the processes which take place prior to delamination, the conditions required for delamination to take place, and the actual mechanisms involved in the removal of lithospheric material. I do not discuss these arguments here. However it is generally accepted that the delamination of cold, dense lithospheric material, combined with its replacement by hot, asthenospheric material, will generate a strong buoyancy force, which may result in the rapid uplift of the crust in this region. The process of delamination is likely to be delayed from the initial period of lithospheric thickening by a characteristic time, on the order of a few tens of millions of years (Houseman *et al.*, 1981; Lenardic & Kaula, 1995); the delay time is dependent upon the thickening factor and

material parameters which govern the thermal evolution of the lithosphere and upper mantle. Once initiated, lithospheric thinning should take place over much shorter timescales than thermal diffusion (Houseman *et al.*, 1981; Schott & Schmeling, 1998), although there will again be a delay of a few million years between delamination and the asthenospheric signatures which indicate the rise of more buoyant material. This process of the convective removal of lithospheric material results in a very different value for the potential energy of the lithospheric column to that which is predicted by simple thermal diffusion. After convective thinning has taken place, the restored geotherm is maintained by small scale mantle convection under the new regime as deformation continues (see Figure 3.2). In the following discussion, this model will be referred to as the constant thickness model.

The delamination model for Tibet is supported by a range of geophysical observations, including high heat flow in northern Tibet, and evidence for recent high–temperature, low–pressure metamorphism and mafic volcanic activity in southern Tibet (Meissner & Mooney, 1998). These observations can be associated with the replacement of a cold lithospheric root by hot asthenospheric material at shallow depths following the detachment and sinking of the lower lithosphere into the mantle. This re–organisation of subcrustal material inevitably leads to a change in the stress of the region; it has been suggested by Meissner & Mooney (1998) that the stress system of Tibet was rotated at about 14 to 11 Ma.

In a dominantly compressional setting, thick mantle lithosphere is expected to develop as a result of internal shortening, but the mantle lithosphere beneath the central Tibetan plateau is only ~90 km thick, in comparison with adjacent regions, where the mantle lithosphere is between 150 km and 200 km thick (Owens & Zandt, 1997). This suggests that a large proportion of the mantle lithosphere beneath the high Tibetan plateau has been removed. Present day convergence rates and paleomagnetic data imply that around 2000 km of convergence has taken place between India and Asia over the last 50 Ma, however gravity and seismic data indicate that the Indian lithosphere has only penetrated between 200 and 400 km north of the Main Boundary Thrust (Lyon-Caen & Molnar, 1985; Jin *et al.*, 1996), supporting the argument that a large amount of lithospheric material has been removed.

Low S_V velocities in southern Tibet imply an anomalously warm lithospheric mantle, and 'bright spots' in seismic reflection profiles (Brown *et al.*, 1996; Nelson *et al.*, 1996) have been interpreted to indicate the presence of partial melt at shallow depths, which can form following the decompression of rapidly upwelling asthenospheric material. A narrow, nearly vertical, high velocity zone extending 400 km beneath the southern Tibetan plateau has been detected using P–wave differential travel–time data (Zhou *et al.*, 1996). The body has been interpreted as a cold downwelling, possibly associated with the delamination process. Altogether, the amount of material which has been removed from beneath Tibet is estimated to be 50 to 500 km in horizontal extent, and between 50 and 200 km thick.

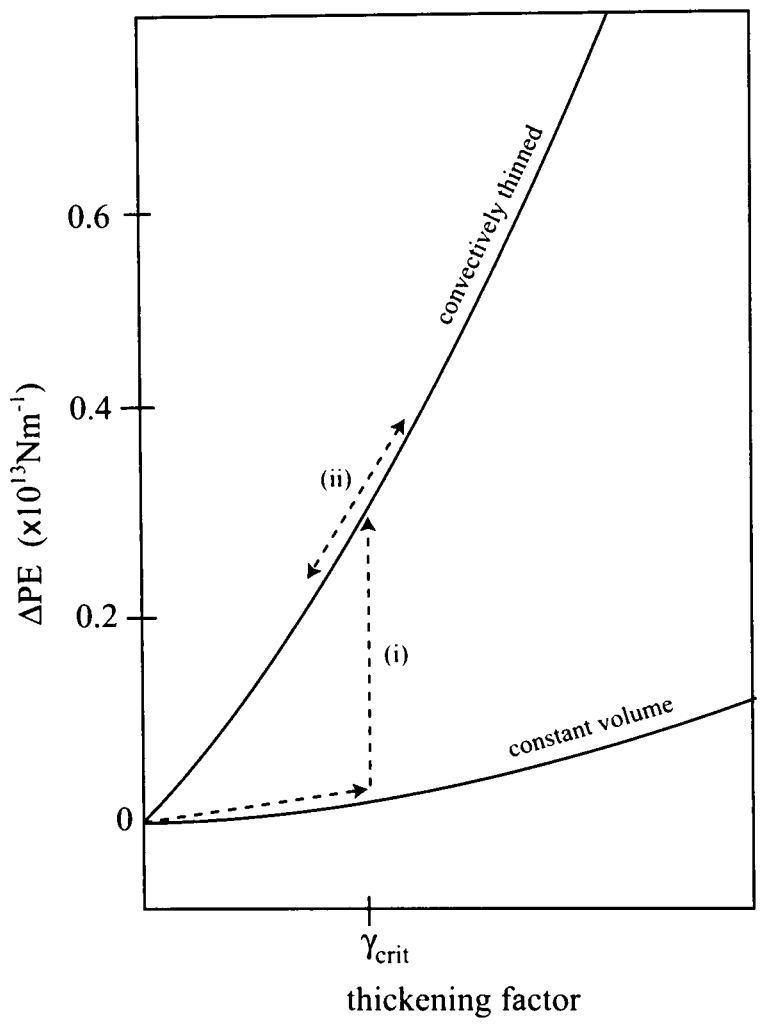

Figure 3.2: Dependence of potential energy upon lithospheric thickening. The lower curve represents the constant volume case, the higher curve represents the constant thickness case. In the sketch, convective thinning is assumed to take place when $L = \gamma_{\text{crit}} L$, leading to a rapid increase in the potential energy of the lithospheric column (i). Potential energy then increases or decreases (ii) according to the deformation of this thinned column. Adapted from England and Houseman, 1989.

Crustal thickening and small scale convection has also been inferred beneath the Tien Shan (Molnar, 1992), where it is thought that shortening of the warm, weak lithosphere has led to the development of gravitational instabilities on the margins of the convergent region, resulting in the thinning of the lithosphere beneath the central Tien Shan (Molnar & Houseman, 2004).

In the constant volume model, the potential energy of a lithospheric column will increase as a result of the formation of elevated, thickened crust. However, the displacement of asthenospheric material by cold, dense lithospheric material as the lithospheric part of the column thickens will act to decrease the potential energy of the column. Overall, the constant volume model may produce either an increase or a decrease in potential energy with respect to the reference column, and the sign of the change is dependent upon the initial thickness of the crust and lithosphere. For the case of the constant thickness model, if the cold lithospheric root has been removed, a higher value of potential energy will always result (see Figure 3.2).

Both models of deformation are considered in the following discussion. My line of investigation follows the argument that convective thinning takes place after a certain amount of thickening has occurred (when the lithospheric thickness, $L = \gamma_{\text{crit}} L$; see Figure 3.2). Following convective thinning, the geotherm, and hence the potential energy of the column, becomes dependent upon the deformation of the thinned lithospheric column. Two possibilities then exist; the lithosphere may thicken again as convergence continues to dominate, in which case the potential energy of the column will continue to increase. Alternatively, if the thinned lithosphere cannot support further thickening, extension may become the dominant mechanism of deformation in this region, leading to a decrease in the potential energy of the column. This is a highly simplified model, but one which is sufficient for the purposes of generating a potential energy distribution to be used in the thin viscous sheet calculations.

3.3 Topography

The topographic height above sea level, e, of each nodal point of the finite element mesh is determined using ETOPO5 (see Figure 3.3). The lithospheric column beneath each nodal point is then compared with a reference column of continental lithosphere. Assuming the two columns are in isostatic equilibrium, estimates for the crustal thickness at each nodal point, the amount of thickening the lithospheric column has undergone with respect to the reference column, and the resulting gravitational potential energy at each nodal point may be calculated.

The top of the reference column of continental lithosphere is specified to be at an elevation of 250 m above sea level (a.s.l.), and to be in isostatic balance with a mid–ocean ridge column consisting of 2.5 km of sea water of density ρ_w, 5 km of basalt of density ρ_{ba}, and an asthenosphere of density ρ_a.

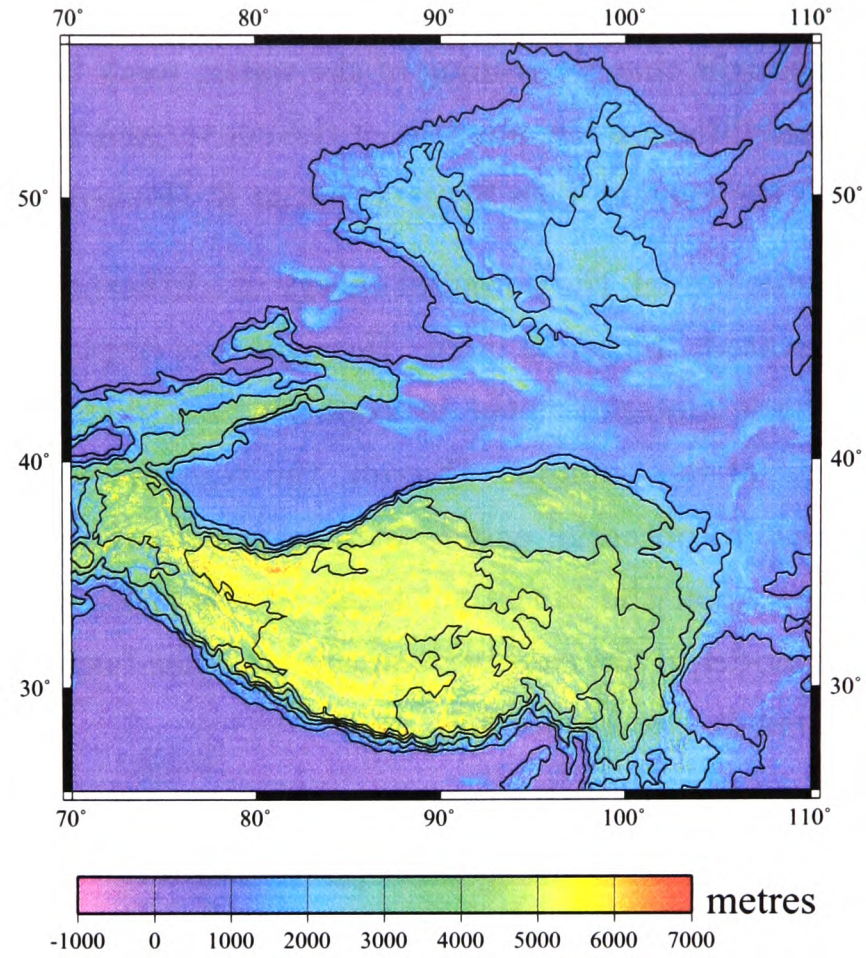

Figure 3.3: Topography of south–east Asia. Figure produced using Shuttle Radar Topography Mission (SRTM) data obtained from NASA-NGA, calculations carried out (prior to the release of SRTM data) using ETOPO5 data.

See table 3.1 for estimates of the physical parameters. The reference column has total lithospheric thickness L, and crustal thickness S_0 (see Figure 3.4). The lithospheric column beneath any point of interest is assumed to have the same crust and mantle densities as the reference column, and to have a crustal thickness of S, and a lithospheric thickness of γL, where γ is a thickening factor (see Figure 3.4). S and γ are to be calculated. In the following calculations, Δe refers to the difference in km between the height of the reference column above sea level and the height of a point of interest above sea level;

$$\Delta e = e - 0.25 \tag{3.1}$$

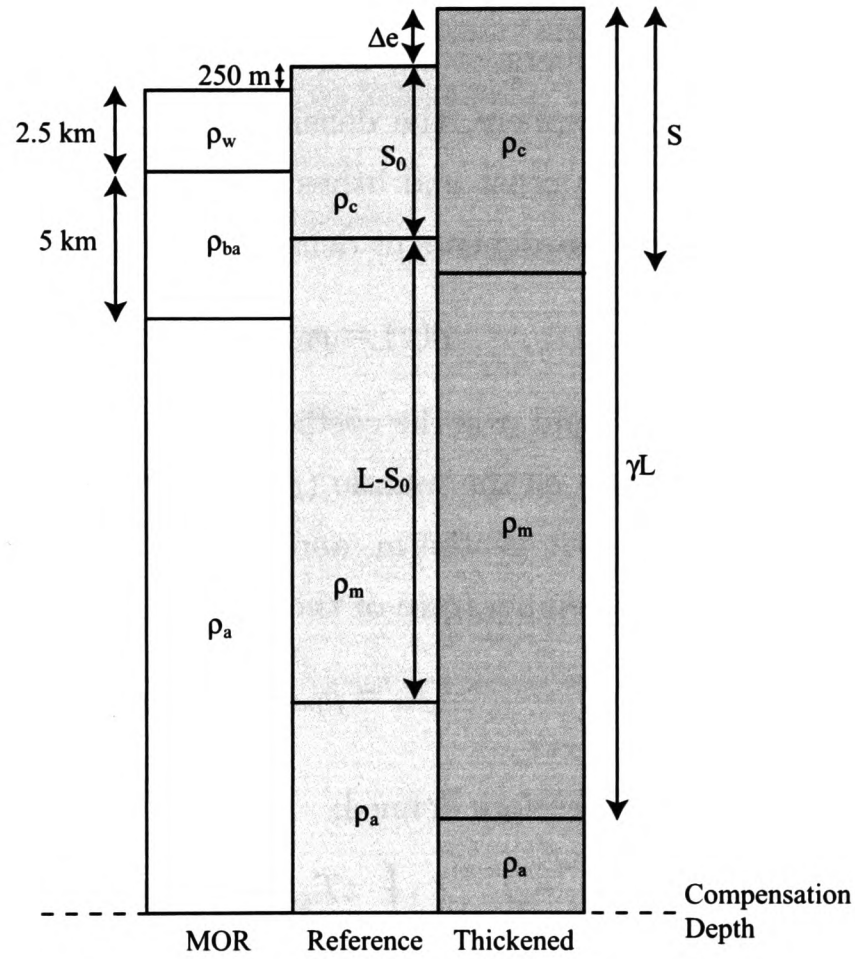

Figure 3.4: White represents a column of mid–ocean ridge lithosphere, light grey represents the reference lithospheric column, dark grey represents a lithospheric column at a point of interest within the continent. ρ_w; density of sea water, ρ_{ba}; density of basalt, ρ_c; density of the continental crust, ρ_m; density of the lithospheric upper mantle, ρ_a = density of the asthenosphere. Values are given in table 3.1. Depths are measured from the surface of each lithospheric column, and the location of the compensation depth is arbitrary. Thicknesses are defined in the text.

3.4 Density distribution

Airy isostasy is assumed throughout the calculations, i.e. the integral of density over the thickness of the lithosphere (L) at any point is constant;

$$\int_L \rho(z)\,dz = \text{const.} \tag{3.2}$$

This is a reasonable assumption across most of the Tibetan plateau and surrounding regions (Molnar, 1988b; Jin *et al.*, 1994; Braitenberg *et al.*, 2000). In order to compare the gravitational potential energy of two columns of lithosphere, the density distribution throughout both columns must be determined. The density of the crust and lithospheric upper mantle are assumed to be of uniform composition, with a temperature–dependent density profile;

$$\rho(z) = \rho_0(1 - \alpha T(z)) \tag{3.3}$$

where T is temperature in °C, and α is the coefficient of thermal expansion (see table 3.1). ρ_0 is the density of either the crust (ρ_{c0}) or the mantle (ρ_{m0}) at 0°C. The density of the asthenosphere, ρ_a, is used to specify the lithospheric geotherm, and is dependent upon the density of the lithospheric upper mantle at 0°C, and the temperature of the asthenosphere, T_a (see table 3.1);

$$\rho_a = \rho_{m0}(1 - \alpha T_a) \tag{3.4}$$

The lithospheric geotherm is therefore defined;

$$T(z) = \begin{cases} zT_a/\gamma L & z \leq \gamma L \\ T_a & z \geq \gamma L \end{cases} \tag{3.5}$$

where L is the thickness of the lithosphere before deformation, γ is a thickening factor, and z is depth, measured downwards from the surface of the lithospheric column. If lithospheric strain is assumed to obey a constant volume argument, then the crustal thickening factor is $\gamma = S/S_0$, where S_0 is the initial crustal thickness and S is the crustal thickness following deformation. If the convective instability of the thermal boundary layer acts to maintain a constant geotherm as the crust is thickened (see section 3.2), then $\gamma = 1$.

The density of the upper mantle at 0°C (ρ_{m0}) is taken to be 3330 kg m^{-3}, but the 0°C density of the continental crust must be determined by balancing the gravitational potential energy of the reference column with the gravitational potential energy of the mid–ocean ridge column (see Figure 3.4). Using the geotherm defined in equation 3.5, the average crustal density,

$$\begin{aligned} \bar{\rho}_c &= \frac{1}{S_0}\int_0^{S_0} \rho_{c0}(1 - \alpha T_a z/L)\,dz \\ &= \rho_{c0}(1 - \alpha T_a S_0/2L) \end{aligned} \tag{3.6}$$

Table 3.1: Definitions and values (where relevant) of physical constants referred to in the text

g	acceleration due to gravity	9.81 m s^{-2}
G	gravitational constant	6.67 $\times 10^{-11}$ m^3 kg^{-1} s^{-2}
L	initial thickness of the lithosphere	
S_0	initial thickness of the crust	
S	thickness of the crust following deformation	
Δe	corrected surface height for the column of interest	
γ	thickening factor for the whole lithosphere	
α	coefficient of thermal expansion	3.4×10^{-5} K^{-1}
T_a	temperature of the asthenosphere	1333°C
ρ_w	density of sea water	1030 kg m^{-3}
ρ_{ba}	density of basalt	2800 kg m^{-3}
$\bar{\rho}_c$	average crustal density	
ρ_{c0}	crustal density at 0°C	
$\bar{\rho}_m$	average upper mantle density	
ρ_{m0}	upper mantle density at 0°C	3330 kg m^{-3}
ρ_a	density of the asthenosphere	3180 kg m^{-3}

and the average upper mantle density,

$$\begin{aligned} \bar{\rho}_m &= \frac{1}{L - S_0} \int_{S_0}^{L} \rho_{m0}(1 - \alpha T_a z/L)\, dz \\ &= \rho_{m0}(1 - \alpha T_a (L + S_0)/2L) \end{aligned} \tag{3.7}$$

may be calculated. These expressions are substituted into the isostasy calculation (equation 3.2) and equated:

$$S_0\bar{\rho}_c + (L - S_0)\bar{\rho}_m = 2.5\rho_w + 5\rho_{ba} + (L - 7.75)\rho_a \tag{3.8}$$

As before, ρ_w is the density of sea water, and ρ_{ba} is the density of basalt. The density of the asthenosphere is calculated using equation 3.4 to give $\rho_a \approx 3180$ kg m^{-3}. Equations 3.8 and 3.6 are then rearranged to give an expression for the average crustal density,

$$\bar{\rho}_c = \frac{1}{S_0}(2.5\rho_w + 5\rho_{ba} + (L - 7.75)\rho_a - (L - S_0)\bar{\rho}_m) \tag{3.9}$$

and the crustal density at 0°C;

$$\rho_{c0} = \bar{\rho}_c/(1 - \alpha T_a S_0/2L). \tag{3.10}$$

Values of ρ_{c0} which are used to generate model geoid distributions are given in table 3.2 for a range of combinations of S_0 and L.

Table 3.2: Values of ρ_{c0} (kg m^{-3})

	L	80 km	100 km	120 km	140 km	200 km
S_0						
30 km		2855.98	2806.14	2756.14	2706.06	2555.53
35 km		2923.12	2880.46	2837.65	2794.76	2665.79
40 km		2973.47	2936.21	2898.79	2861.28	2748.49
45 km		3012.63	2979.56	2946.34	2913.02	2812.81

3.5 Gravitational potential energy of a lithospheric column

The difference between the elevation of a lithospheric column at a point of interest (with crustal thickness S) and the elevation of the reference column (with crustal thickness S_0) may be calculated using the argument of isostatic balance. The compensation depth is chosen to lie at the base of the mantle lithosphere of the column below the point of interest. Balancing the integral of the density distribution for the two columns, using expressions for the average crustal and upper mantle densities (equations 3.6 and 3.7), yields

$$\int_0^{S_0} \rho_{c0}(1-\alpha z T_a/L)\,dz + \int_{S_0}^{L} \rho_{m0}(1-\alpha z T_a/L)\,dz + \int_L^{\gamma L-\Delta e} \rho_a\,dz$$
$$= \int_0^{S} \rho_{c0}(1-\alpha z T_a/\gamma L)\,dz + \int_S^{\gamma L} \rho_{m0}(1-\alpha z T_a/\gamma L)\,dz \qquad (3.11)$$

This is rearranged to give an expression for the relative elevation;

$$\Delta e = (S-S_0)\left(\frac{\rho_{m0}-\rho_{c0}}{\rho_a}\right) - \frac{\alpha T_a}{2L}\left[\left(\frac{\rho_{m0}-\rho_{c0}}{\rho_a}\right)(S^2/\gamma - S_0^2) + \frac{\rho_{m0}}{\rho_a}(\gamma-1)L^2\right] \qquad (3.12)$$

Depth, z, is measured from the surface of each lithospheric column independently because temperature is depth–dependent. As a result of this, the integral of the two density profiles, on either side of equation 3.11, appear to be calculated to different compensation depths. By referring to Figure 3.4, this apparent discrepancy is explained; the integrals begin at different absolute heights (0 and Δe), but are evaluated to the same depth.

Equation 3.12 is quadratic in S, which I treat as an unknown. The numerical evaluation of equation 3.12 (England & Houseman, 1989) shows that the following relation holds to a good approximation;

$$\Delta e \simeq B_\gamma (S - S_0) \qquad (3.13)$$

Table 3.3: Values of B_γ

	Constant Volume $\gamma = S/S_0$				Constant Thickness $\gamma = 1$			
	L	80 km	100 km	120 km	140 km	80 km	100 km	120 km	140 km
S_0									
30 km		0.0845	0.0845	0.0845	0.0845	0.146	0.162	0.178	0.194
35 km		0.0725	0.0725	0.0725	0.0725	0.125	0.139	0.152	0.166
40 km		0.0634	0.0634	0.0634	0.0634	0.109	0.121	0.133	0.145
45 km		0.0564	0.0564	0.0564	0.0564	0.097	0.107	0.118	0.129

The values of B_γ for 80 km $\geq L \geq$ 140 km and 30 km $\geq S_0 \geq$ 45 km have been evaluated by England & Houseman (1989), and are given in table 3.3. Both the constant volume model ($\gamma = S/S_0$) and constant thickness model ($\gamma = 1$) are considered. B_γ is interpolated over 80 km $\geq L \geq$ 200 km and 30 km $\geq S_0 \geq$ 45 km at 1 km intervals using first and second order polynomials for the constant volume and constant thickness cases respectively (see Figure 3.5). These functions are used to determine values of L and S_0 for south–east Asia in section 3.8.

The gravitational potential energy of a column of lithosphere of thickness L, relative to the gravitational potential energy of the reference column, is

$$\Delta PE = -g \int_L z \Delta\rho(z)\, dz \tag{3.14}$$

where g is the acceleration due to gravity (see table 3.1) and $\Delta\rho(z)$ is the difference between the density at depth z in this column, and the density, at the same depth, in the reference column. Depth is measured from the surface of each column independently.

Equation 3.14 may be rewritten:

$$\Delta PE = g \int_{-\Delta e}^{\gamma L} \rho_{\text{def}}(\gamma L - z)\, dz - g \int_0^{\gamma L} \rho_{\text{ref}}(\gamma L - z)\, dz \tag{3.15}$$

where $\rho_{\text{def}}[z]$ is the density profile of the column of interest, and $\rho_{\text{ref}}[z]$ is the density profile of the reference column, both of which vary with depth. In equation 3.15, z is measured from the surface of the reference column, and down is positive, hence the terms in $\gamma L - z$ (see Figure 3.6).

In order to calculate the potential energy difference defined in equation 3.15, I need to evaluate three

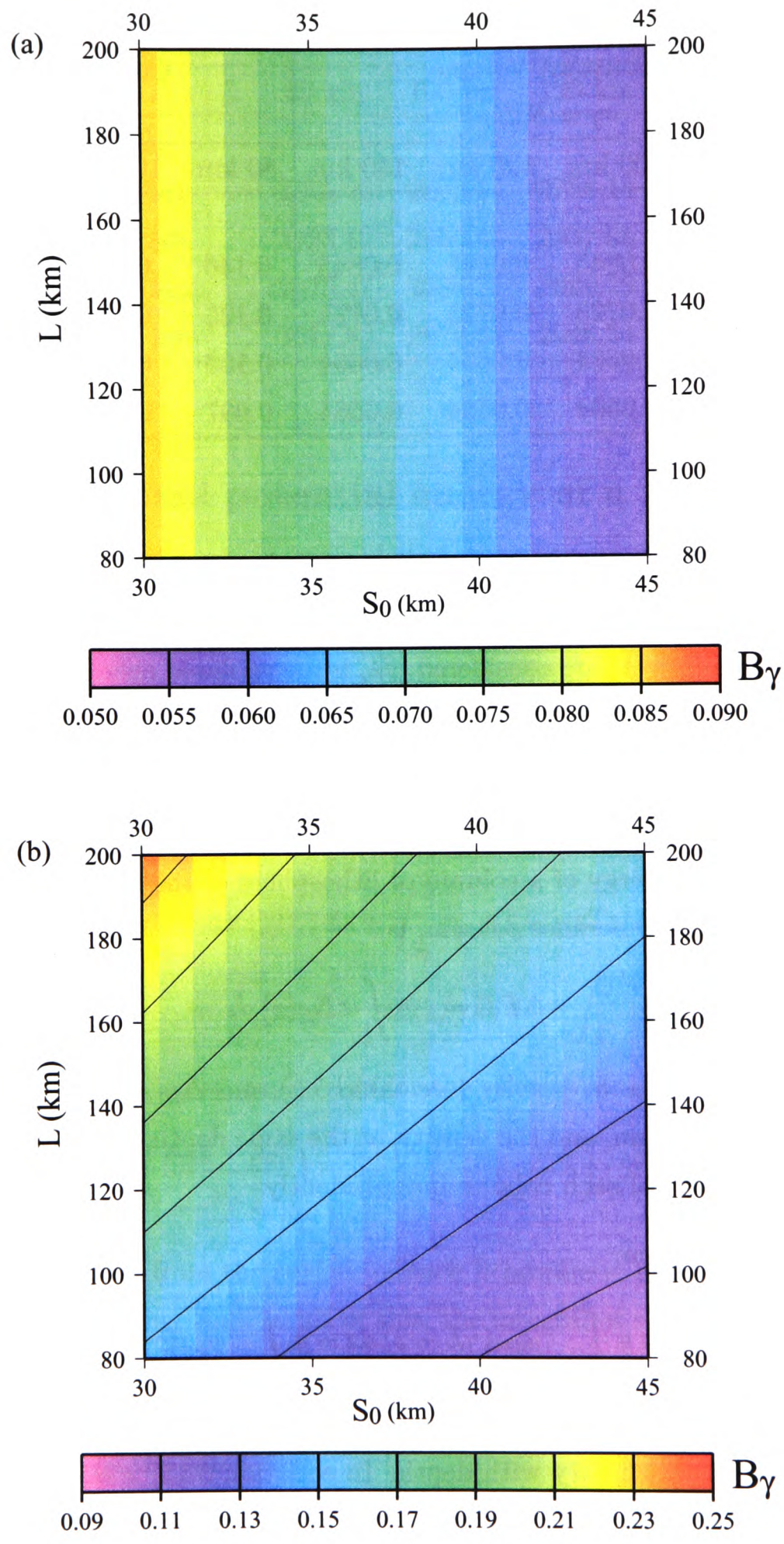

Figure 3.5: The distribution of B_γ for $30 \leq S_0 \leq 45$ km and $80 \leq L \leq 200$ km, for (a) the constant volume model, and (b) the constant thickness model.

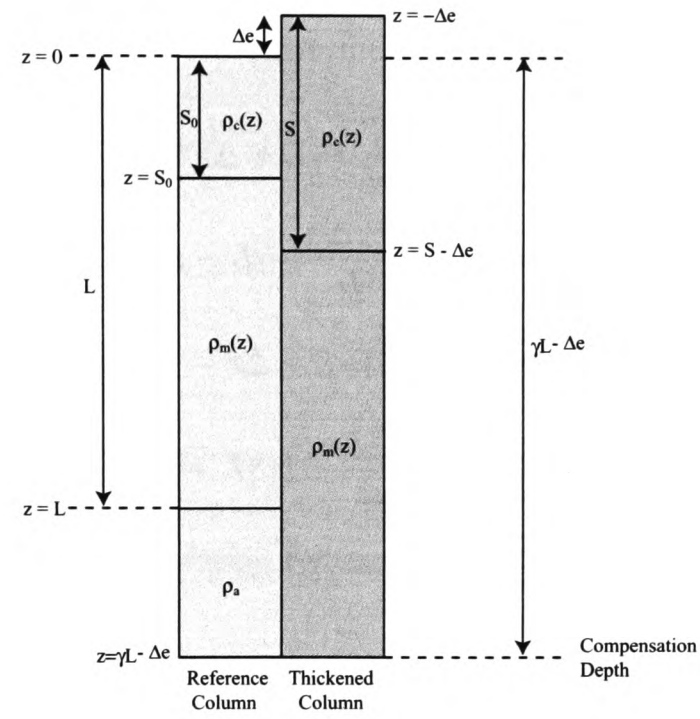

Figure 3.6: Terms used to calculate ΔPE. Light grey column represents the reference lithospheric column, dark grey column represents a lithospheric column which has been thickened by continental deformation. $\rho_c(z)$= density of continental crust, $\rho_m(z)$=density of upper mantle, ρ_a= density of asthenosphere. Depths are measured downwards from the surface of the undeformed column.

integrals across the reference column show in Figure 3.6,

$$
\begin{aligned}
I1 &= \int_0^{(\gamma-1)L-\Delta e} \rho_a \, z \, dz \\
&= \frac{1}{2}\rho_a(\gamma-1)^2L^2 \qquad (3.16)\\
I2 &= \int_{(\gamma-1)L-\Delta e}^{\gamma L-S_0-\Delta e} \bar{\rho}_m \, z \left(1 - \frac{\alpha T_a}{L}(\gamma L - z)\right) dz \\
&= \bar{\rho}_m \left[\frac{1}{2}(1-\alpha T_a\gamma)\left((\gamma L - S_0)^2 - (\gamma-1)^2L^2\right) + \frac{1}{3}\frac{\alpha T_a}{L}\left((\gamma L - S_0)^3 - (\gamma-1)^3L^3\right)\right] \qquad (3.17)\\
I3 &= \int_{\gamma L-S_0-\Delta e}^{\gamma L-\Delta e} \bar{\rho}_c \, z \left(1 - \frac{\alpha T_a}{L}(\gamma L - z)\right) dz \\
&= \bar{\rho}_c \left[\frac{1}{2}(1-\alpha T_a\gamma)\left(\gamma^2L^2 - (\gamma L - S_0)^2\right) + \frac{1}{3}\frac{\alpha T_a}{L}\left(\gamma^3L^3 - (\gamma L - S_0)^3\right)\right] \qquad (3.18)
\end{aligned}
$$

and two integrals across the column of interest,

$$I4 = \int_0^{\gamma L - S} \bar{\rho}_m \, z \left(1 - \frac{\alpha T_a}{\gamma L}(\gamma L + \Delta e - z)\right) dz$$
$$= \bar{\rho}_m \left[\frac{1}{2}(1 - \alpha T_a - \frac{\alpha T_a \Delta e}{\gamma L})(\gamma L - S + \Delta e)^2 + \frac{1}{3}\frac{\alpha T_a}{\gamma L}(\gamma L - S + \Delta e)^3\right] \quad (3.19)$$

$$I5 = \int_{\gamma L - S}^{\gamma L} \bar{\rho}_c \, z \left(1 - \frac{\alpha T_a}{\gamma L}(\gamma L + \Delta e - z)\right) dz$$
$$= \bar{\rho}_c \left[\frac{1}{2}(1 - \alpha T_a - \frac{\alpha T_a \Delta e}{\gamma L}) \left((\gamma L + \Delta e)^2 - (\gamma L - S + \Delta e)^2\right)\right.$$
$$\left. + \frac{1}{3}\frac{\alpha T_a}{\gamma L} \left((\gamma L + \Delta e)^3 - (\gamma L - S + \Delta e)^3\right)\right] \quad (3.20)$$

In equations 3.17–3.20 depths are measured upwards from the compensation depth. Expressions for the average crustal and mantle densities ($\bar{\rho}_c$ and $\bar{\rho}_m$ in equations 3.6 and 3.7) have been used in equations 3.17–3.20. The potential energy difference between the two columns, ΔPE, is therefore

$$\begin{aligned}
\Delta PE &= I5 + I4 - I3 - I2 - I1 \\
&= \bar{\rho}_c \left[\frac{1}{2}\left((1 - \alpha(\gamma L + \Delta e)\frac{T_a}{\gamma L})((\gamma L + \Delta e)^2 - (\gamma L - S + \Delta e)^2) - (1 - \alpha T_a \gamma)(\gamma^2 L^2 - (\gamma L - S_0)^2)\right)\right. \\
&\quad \left. + \frac{1}{3}\frac{\alpha T_a}{L}\left(\frac{1}{\gamma}((\gamma L + \Delta e)^3 - (\gamma L - S + \Delta e)^3) - (\gamma^3 L^3 - (\gamma L - S_0)^3)\right)\right] \\
&\quad + \bar{\rho}_m \left[\frac{1}{2}\left((1 - \alpha(\gamma L + \Delta e)\frac{T_a}{\gamma L})(\gamma L - S + \Delta e)^2 - (1 - \alpha T_a \gamma)((\gamma L - S_0)^2 - (\gamma - 1)^2 L^2)\right)\right. \\
&\quad \left. + \frac{1}{3}\frac{\alpha T_a}{L}\left(\frac{1}{\gamma}(\gamma L - S + \Delta e)^3 - ((\gamma L - S_0)^3 - (\gamma - 1)^3 L^3)\right)\right] \\
&\quad - \frac{1}{2}\rho_a(\gamma - 1)^2 L^2
\end{aligned} \quad (3.21)$$

The general form for the geoid anomaly due to the density distribution throughout the lithospheric column at a given point is derived by Haxby & Turcotte (1978);

$$N(x, y) = -\frac{2\pi G}{g} \int_0^f z \, \Delta\rho(x, y, z) \, dz \quad (3.22)$$

where $N(x, y)$ is the geoid anomaly, measured in metres, G is the gravitational constant (see table 3.1), $\Delta\rho$ is the density difference with respect to a reference column, and f is the topography at the base of the lithosphere (see Figure 3.7). This equation is only valid on length scales greater than the thickness of the lithosphere.

Assuming the form of ΔPE given in equation 3.21;

$$N = \frac{2\pi G}{g} \Delta PE. \quad (3.23)$$

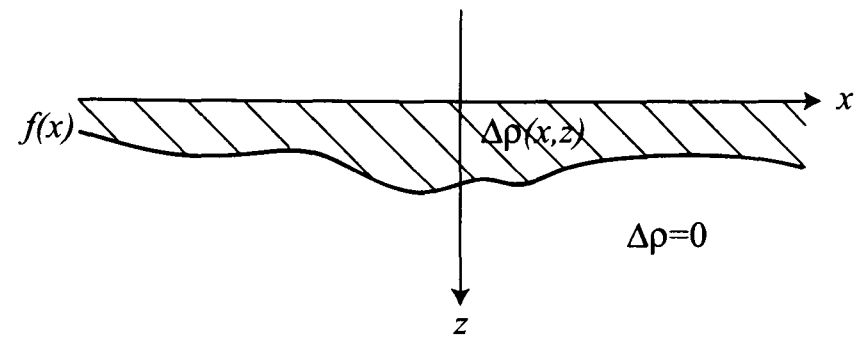

Figure 3.7: Diagram to illustrate the terms used in calculating the geoid anomaly at a point x. $\Delta\rho$ is the density difference with respect to a reference column of lithosphere, it is dependent upon horizontal location and depth. $f(x)$ is the local compensation depth. Below this depth the density profile is assumed to be laterally invariant.

3.5.1 The calculation of model geoid distributions

Equation 3.23 is used to generate a set of model geoid distributions for the region 70–110°E and 25–55°N, using the values of S_0, L and ρ_{c0} given in table 3.2. The coefficients B_γ are taken from the interpolation of values in table 3.3. In the first instance, a single set of parameters is used to calculate the geoid distribution for the whole region. However, I also consider the possibility that different regimes of lithospheric evolution, or different values of S_0 or L, may be relevant in different regions of south–east Asia.

The topography is not low–pass filtered prior to the construction of the model geoid distributions. If it were, this would eradicate some of the noise in Figure 3.10, thus clarifying the relationship between geoid height and elevation, and making it easier to identify model parameters that best reproduce the observed scenario.

3.6 Observed Geoid

The EGM96 geoid is used as an approximation for the true geoid anomaly at the surface of the Earth (Lemoine *et al.*, 1998), and Figure 3.8 shows the geoid anomaly for the region of interest; south–east Asia.

In addition to lithospheric structure, the geoid is affected by buoyancy differences in the convecting mantle. To remove the long wavelength components which may arise from convection in the lower mantle, a high pass filter is used to remove the long wavelength signal from the observed geoid; wavelengths less than 2500 km are passed, and wavelengths greater than 3000 km are removed (see

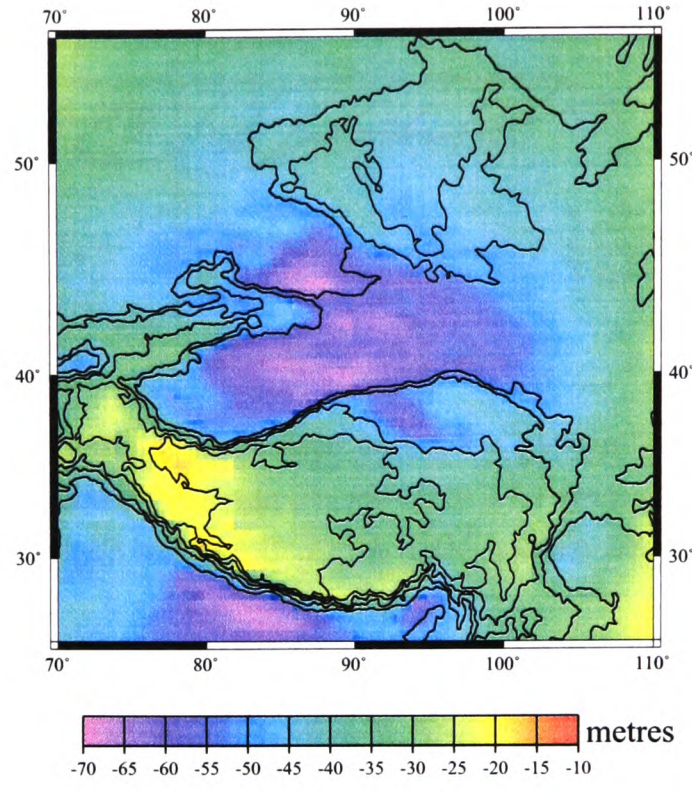

Figure 3.8: Geoid anomalies for south–east Asia from EGM96.

Figure 3.9).

In the thin viscous sheet approximation, the internal driving force of the system is dependent upon gradients of potential energy. The absolute value of the potential energy distribution is not important in these calculations, and since potential energy is pointwise linearly dependent upon the value of the geoid anomaly (equation 3.23), the absolute value of the geoid anomaly is also not important, and may be offset by an arbitrary constant without altering the driving forces of the system. The potential energy distribution which most closely replicates the observed geoid anomaly will be used. In the following sections, the term 'observed geoid' refers to the signal which remains after the high pass filter is applied.

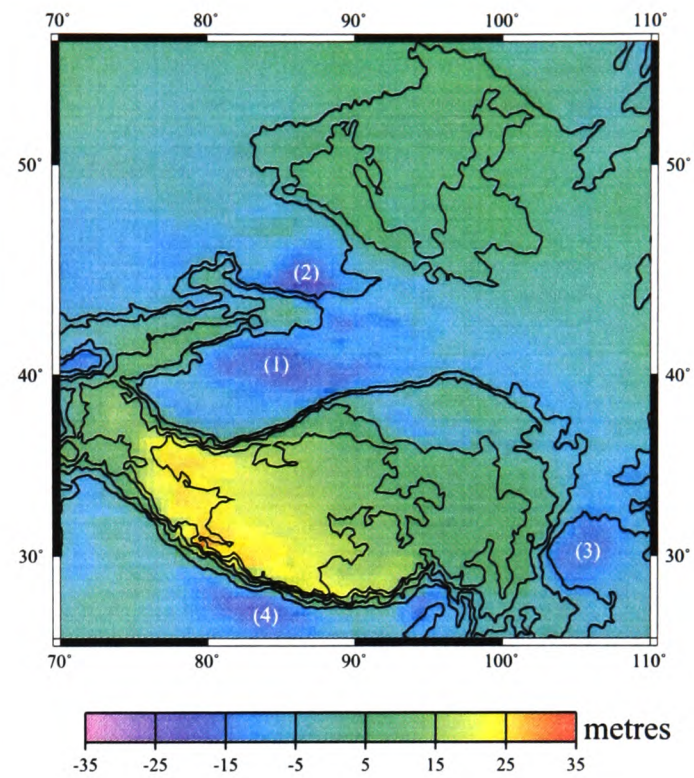

Figure 3.9: Geoid anomalies for south–east Asia, after using a high pass filter. Wavelengths $\lambda < 2500$ km are passed. Note the locations with a strong negative geoid anomaly in (1) the Tarim Basin, (2) the Junggar basin, (3) the Sichuan Basin and (4) the foreland basin south of the Himalayan arc.

3.7 Dependence of the geoid upon elevation

3.7.1 Dependence of the observed geoid upon elevation

The dependence of the height of the geoid anomaly upon topographic height is investigated for the region of interest, between 75°E and 105°E, and 25°N and 45°N. Figure 3.10 depicts the dependence of the height of the geoid anomaly (wavelengths λ >3000 km removed) upon height above sea level in south–east Asia.

Two modes of behaviour are evident in the scatter graph of Figure 3.10. Below ~2 km, there is a large amount of scatter in the data, which arises due to the presence of negative geoid anomalies (in the sedimentary basins surrounding the plateau) and positive geoid anomalies (away from these basins) at the same altitude. Figure 3.9 highlights the low–lying regions where an abnormally low geoid anomaly is measured. They correspond to the Tarim Basin, the Junggar Basin, the Sichuan Basin, and the foreland basin of the Himalayan arc. The first three basins contain between 5 km and 8 km of low–density, sedimentary deposits (Carroll *et al.*, 1995; Mooney & Coleman, 1999; Laske & Masters, 1997) to which the low geoid anomaly may be attributed. In the foreland basin in front of

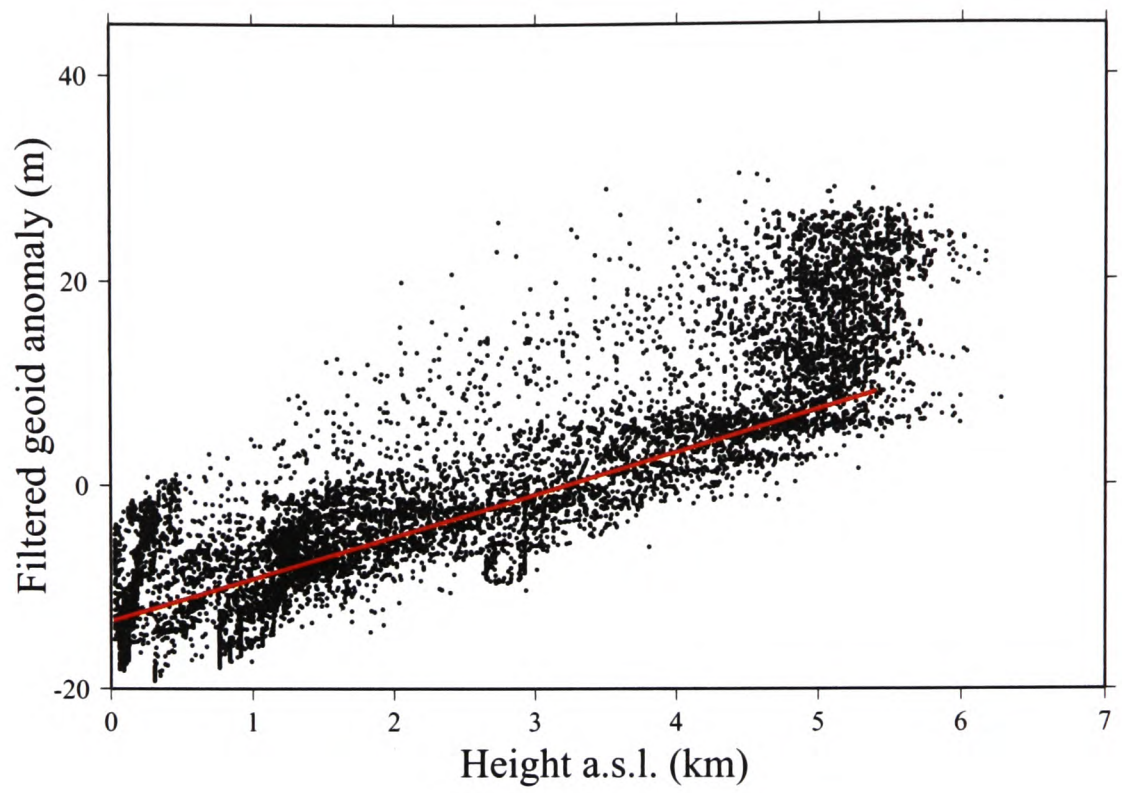

Figure 3.10: The dependence of the observed geoid upon elevation. The gradient of the red line is 3.9 m km^{-1}.

the Himalayan arc the signal is further complicated by the flexural bending of the underthrust Indian plate. This partially supports the high topography of the Himalaya, resulting in a departure from the assumption that high elevations are simply isostatically compensated. The mid–wavelength features of these basins are not removed by the high pass filtering of the geoid. They represent deviations from the standard model of a column of continental lithosphere in isostatic balance, and will not be accounted for in my models.

Between altitudes of 2 km and 4 km, there is a strong correlation between geoid height and altitude, which may be approximated by the linear function $N = 3.9e - 13$ (see Figure 3.10), where N is geoid height in metres and e is elevation in kilometres. The cloud of points which exhibit a higher geoid anomaly than that predicted by this simple linear relationship may be attributed to poor height resolution in the data along the steep topographic gradients of the Himalayan front. This results in a higher geoid anomaly being attributed to points which are deemed to be at lower altitudes. A second explanation is related to the high geoid anomaly which is observed in western Tibet (Figure 3.9). The increase in the height of the geoid anomaly across this whole region means that even points which lie 3–4 km above sea level will plot well above the line of best fit in Figure 3.10. The east–west gradient in the height of the geoid across the Tibetan plateau cannot be explained by a simple dependence of the geoid upon altitude, and the gradient may be attributed to poor gravity data, the remains of a

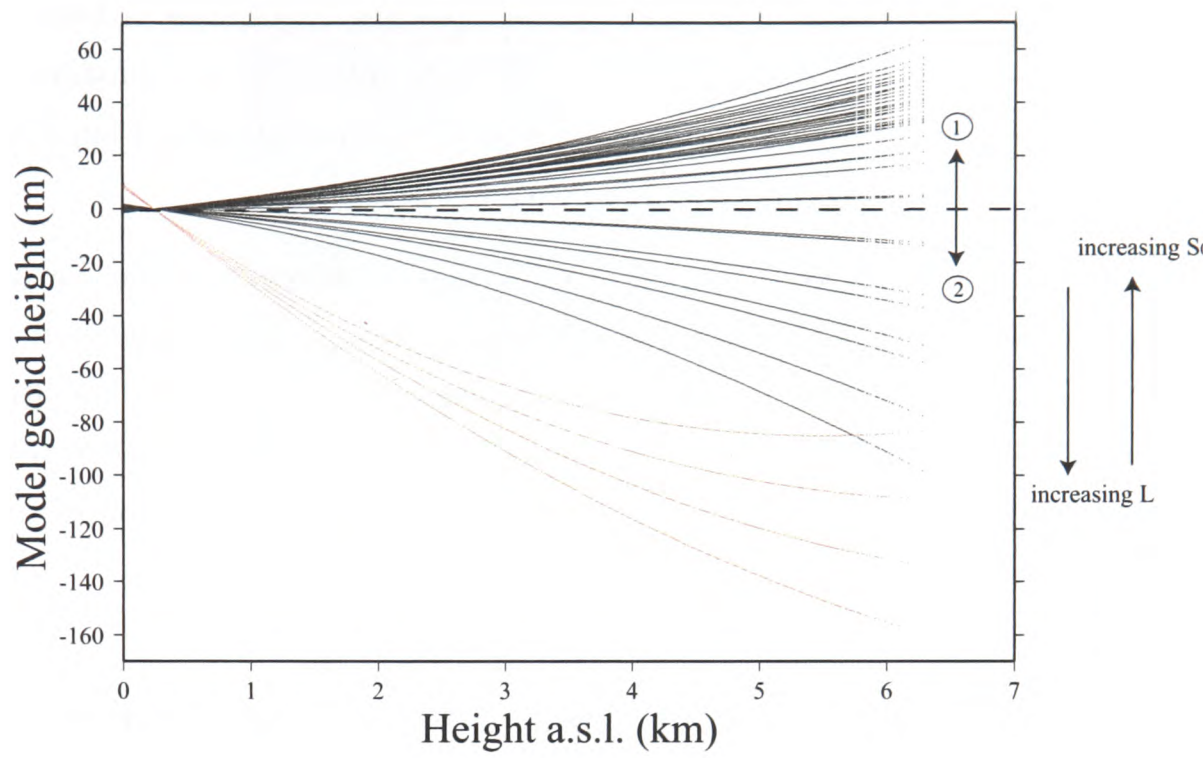

Figure 3.11: The dependence upon elevation of the 40 model geoid distributions described in section 3.5.1. The lines have not been individually labelled, for clarity, but the characteristics of the profiles are described in more detail in the text. Red lines: constant volume model, $L = 200$ km. (1) all constant thickness model profiles have a positive gradient. (2) only constant volume model profiles have a negative gradient.

long wavelength signal which was not removed by the high pass filter, or a distribution of lithospheric density which does not resemble anything accounted for in my model (e.g. a subducted slab).

Above 4 km, the gradient sharply increases. The high geoid anomaly in the west of the plateau contributes to the steepness of the gradient since the highest anomalies are not located in the highest part of the plateau. This should result in a negative gradient, but in fact just increases the amount of scatter in the geoid data at these altitudes.

3.7.2 Dependence of model geoid distributions upon elevation

Figure 3.11 demonstrates the dependence upon elevation of the model geoid distributions calculated in section 3.5.1. For all of the models, a value of $N = 0$ prevails at an elevation of 250 m, as prescribed by the definition of the reference lithospheric column. Above this elevation, the profiles exhibit a wide range of characteristics.

For the constant volume model (see section 3.2), the gradient of the profiles ranges between $\sim$-36 m km^{-1} and $\sim$+6 m km^{-1}. In general, the gradient decreases as L is increased, but the gradient

increases as S_0 is increased. The steep, convex profiles which form a lower bound to Figure 3.11 represent the cases $L = 200$ km, $S_0 = 30, 35, 40$ and 45 km, for the constant volume model. These, and all other models with a negative gradient may be rejected, since Figure 3.10 demonstrates that the observed geoid is positively correlated with height.

The gradients of profiles generated using the constant thickness model lie in the range; $\sim$+2.5 m km^{-1} to $\sim$+6.5 m km^{-1}. The gradient gradually increases as L is increased, but decreases as S_0 is increased. Once again profiles for the case $L = 200$ km are included, but here they do not demonstrate the extreme behaviour of the constant volume models. All the constant thickness profiles have a positive gradient, and therefore are potential models for the conversion of topographic height into potential energy in south–east Asia.

3.8 Modelling the geoid anomaly in south–east Asia

Figure 3.12 depicts the dependence of the calculated geoid distributions upon height. The geoid gradient for each combination of S_0 and L is determined by evaluating N for $0 \leq e \leq 4$ km, and calculating the gradient of the best fit line. The variation of the gradient of N with height for the profiles plotted in Figure 3.11 is small, therefore using the gradient of the best fit line to represent dN/de is a reasonable approximation. Both models of lithospheric evolution are considered.

An expression for dN/de can also been found by differentiating equation 3.23 with respect to height, and this yields an expression which is also dependent upon height. However there is an approximately linear relationship between observed geoid height and elevation between 0 km and 4 km throughout south–east Asia (Figure 3.10), and I therefore seek a combination of S_0 and L which yields a distribution of N whose gradient is not strongly dependent upon height, and matches that of the observed data. Calculating the gradient of the best fit line for each profile of N therefore provides a direct method for determining suitable values of S_0 and L.

In order to reproduce the observed gradient of $dN/de = 3.9$ using the constant volume model of lithospheric deformation, an unfeasibly high value of $S_0 > 45$ km must be assumed in order to yield acceptable values of $L \geq 120$ km for the initial thickness of the lithosphere (see Figure 3.12). Alternatively, unphysically low values of $L < 80$ km are required to yield a reasonable value for the initial thickness of the crust. There are no suitable combinations of S_0 and L which are able to reproduce the value of dN/de observed in the data.

When the constant thickness model of lithospheric deformation is assumed, high values of L and low values of S_0 are required to reproduce the observed gradient. From Figure 3.12 I deduce that a combination of $(S_0, L) = (30, 200)$ km is a suitable model for reproducing the geoid anomaly

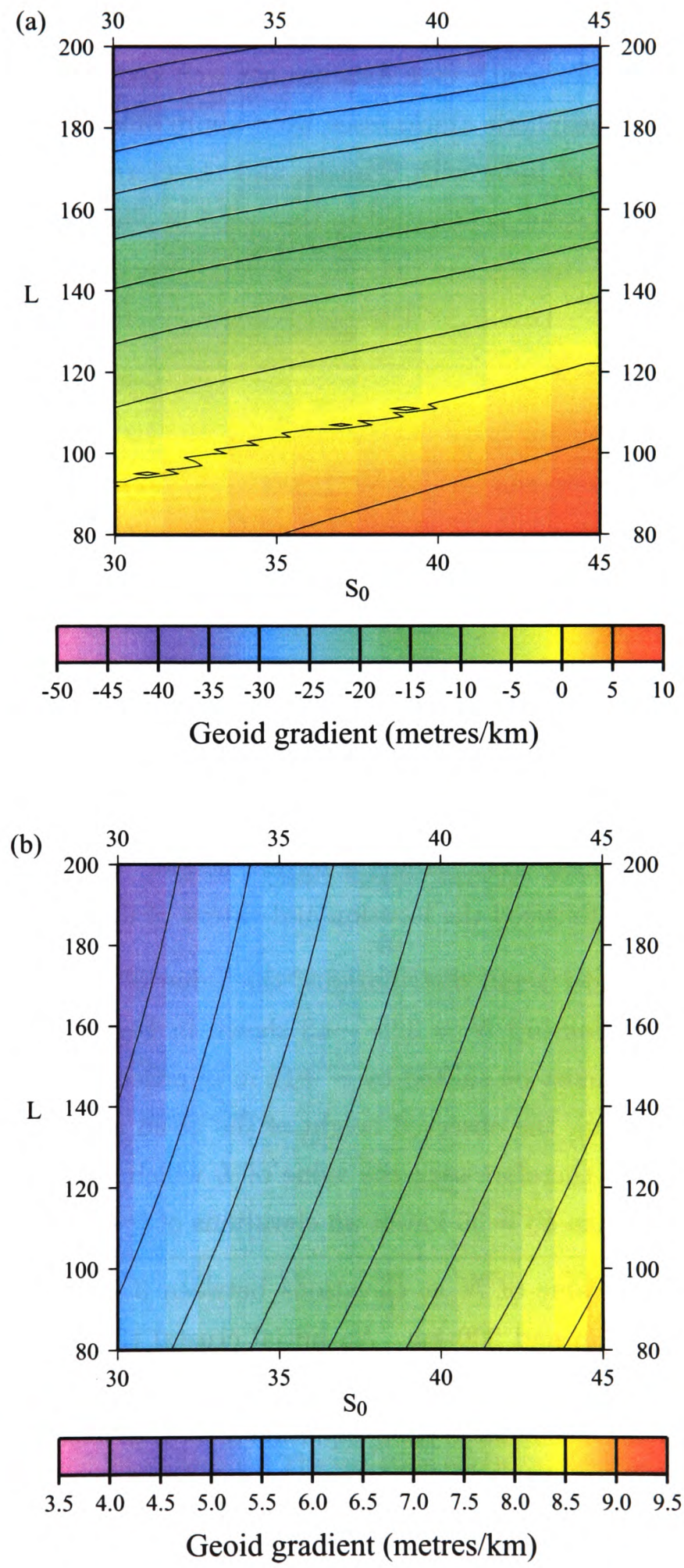

Figure 3.12: Geoid gradients, dN/dh, for (a) the constant volume model, and (b) the constant thickness model.

throughout south–east Asia at all points below 4 km in altitude.

Initial crustal thicknesses for south–east Asia are not well known (Zhang *et al.*, 1998), but I assume here that crustal and lithospheric thicknesses were approximately constant throughout south–east Asia prior to the collision of India with Eurasia, and therefore use $S_0 = 30$ km for points above, as well as below, 4 km. This value is identical to that used by Shen *et al.* (2001a) in their modelling of the crustal deformation of the Tibetan plateau. However, the dependence of the geoid anomaly upon elevation changes dramatically above 4 km, and I seek a different model of lithospheric evolution for the Tibetan plateau and other high–elevation regions.

There is extensive evidence for large–scale changes to the structure of the lithosphere beneath the present–day Tibetan plateau since $\sim$ 13 Ma (see section 3.2). Much of the evidence suggests that delamination of some portion of the mantle lithosphere beneath Tibet has taken place due to the gravitational instability of thickened lithosphere; the constant volume model is therefore unsuitable. In order to reproduce the present–day geoid anomaly at points above 4 km I adopt the constant thickness model, and seek the value of L which describes the thickness of the lithosphere beneath Tibet following delamination, and which is able to reproduce the observed step in the geoid anomaly when $S_0 = 30$ km. In adopting this approach I assume that the negative buoyancy associated with thickened lithosphere is great enough to initiate delamination once a certain crustal thickness is exceeded, i.e. once the topography attains a certain height. This is a simplification, and in reality many factors will have influenced the location and extent of delamination.

In the calculation of model geoid distributions, the value of N at $e = 0.25$ km is constrained to be zero. Using the relationship $N = 3.9e - 13$ shown in Figure 3.10, I deduce that the height of observed geoid anomaly must be shifted by $\sim +12$ m in order for calculated and observed values to be compared. Above 4 km, the observed height of the geoid anomaly lies in the range $8 \leq N \leq 27$ m. Applying the shift, I therefore seek the value of L which can reproduce geoid anomalies in the range $20 \leq N \leq 39$ m when $S_0 = 30$ km at an elevations of ≥ 4 km.

Figure 3.13a shows the value of N at elevations between 3 km and 6 km, for initial lithospheric thicknesses between 80 km and 200 km. An initial crustal thickness of $S_0 = 30$ km is used in the constant thickness model. The observed range of N above 4 km does not tightly constrain the value of L, therefore the value of S, calculated using equation 3.13, is plotted in Figure 3.13b for $80 \leq L \leq 200$ km. The constant thickness model is used, and an initial crustal thickness of $S_0 = 30$ km, and an elevation of 5 km, are assumed. Crustal thicknesses across the Tibetan plateau lie in the range 55 km to 85 km (Dricker & Roecker, 2002; Ritzwoller & Levshin, 1998; Owens & Zandt, 1997; Nelson *et al.*, 1996; Zhao *et al.*, 2001). Figure 3.13b therefore does not enable any tighter constraints to be placed upon L, but it does confirm that for $80 \leq L \leq 200$ km the model is consistent with observations of

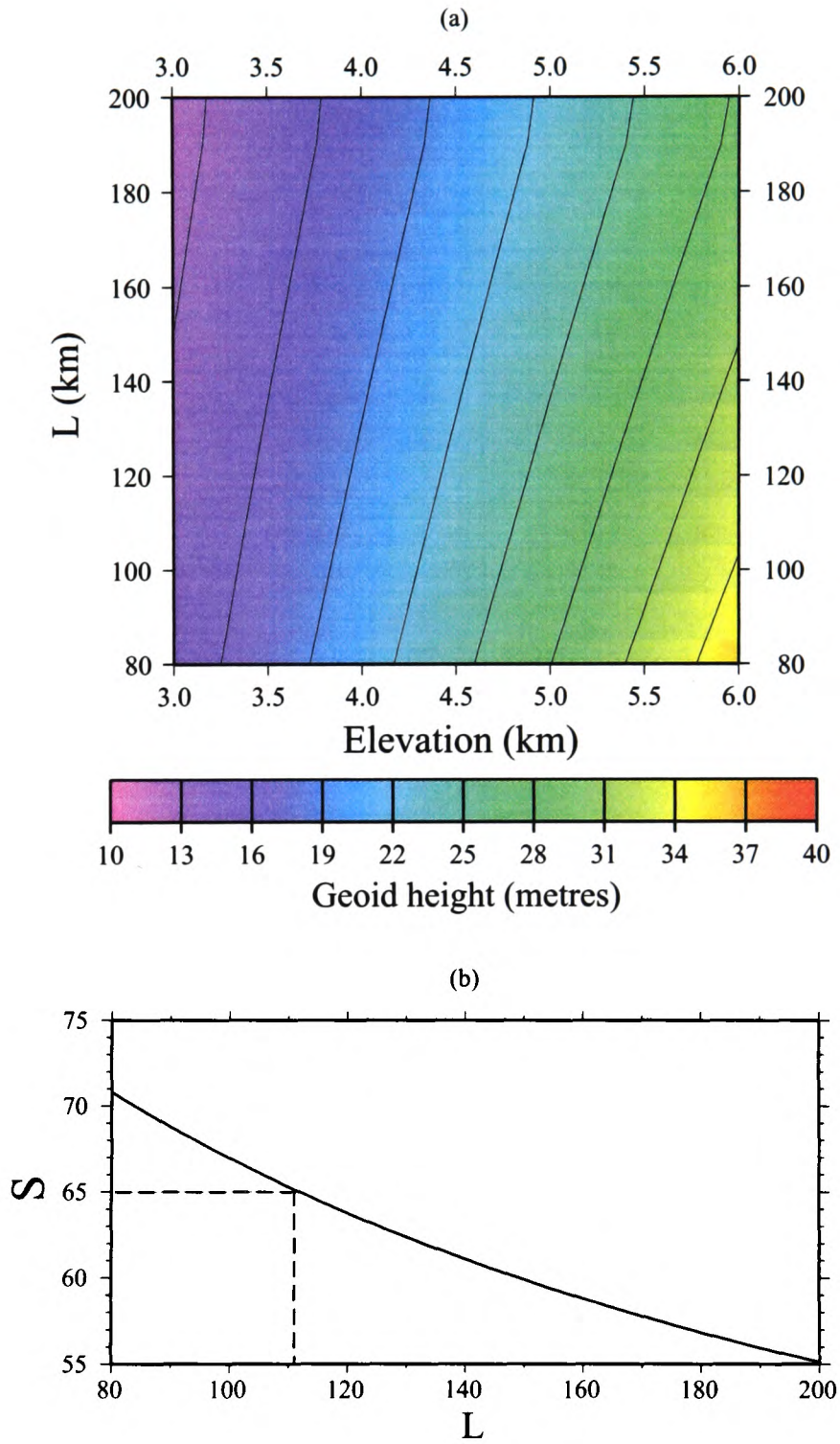

Figure 3.13: (a) Geoid anomaly for a range of lithospheric thicknesses and elevations, calculated using the constant thickness model and S0=30km. (b) The variation of crustal thickness with initial lithospheric thickness when $S_0 = 30$ km and $e = 5$ km, assuming the constant thickness model.

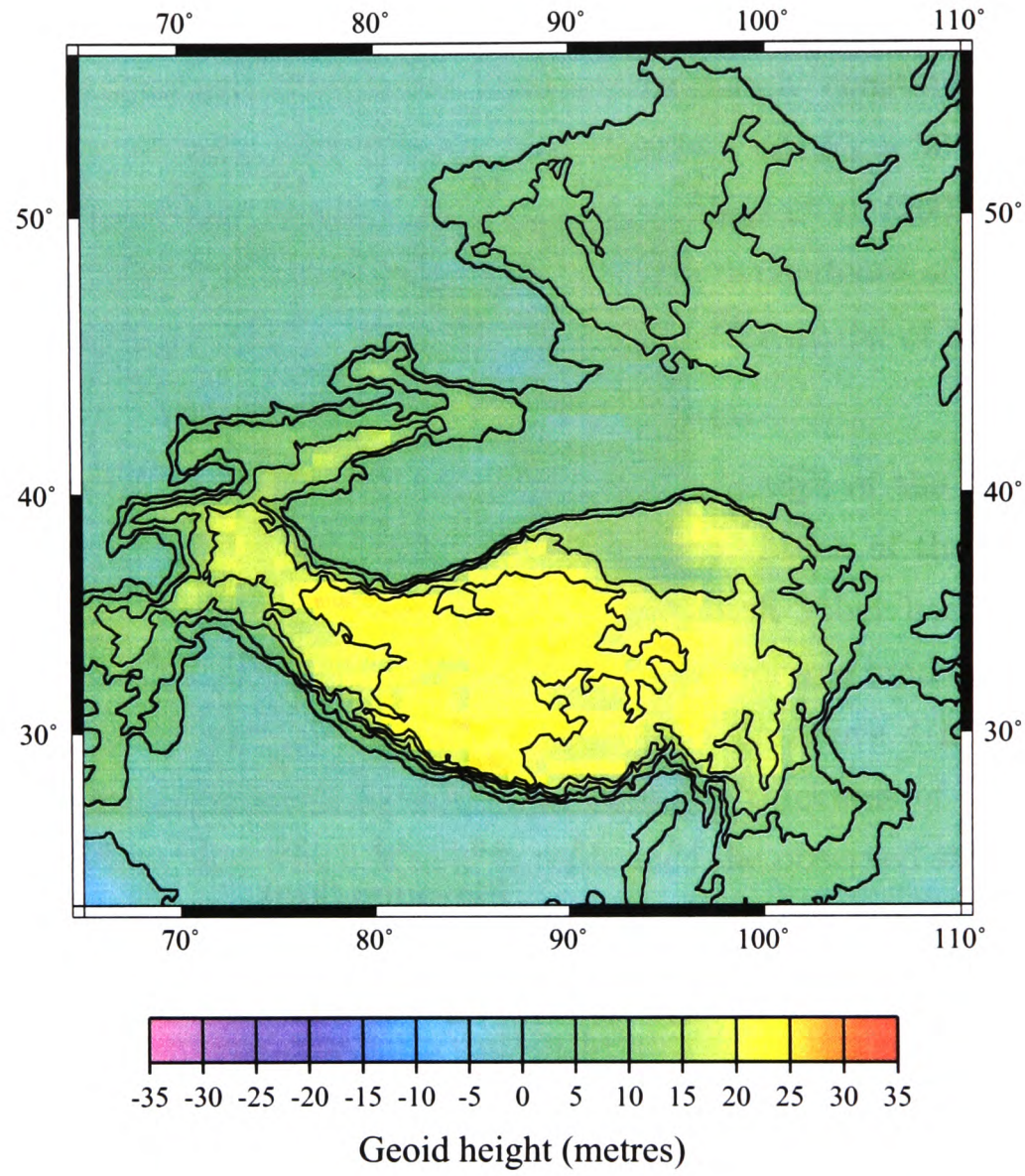

Figure 3.14: Geoid anomaly across south–east Asia, calculated using $L = 200$ km for points below 4 km, $L = 110$ km for points above 4 km, and $S_0 = 30$ km throughout the region. A constant thickness model is used.

both crustal thickness and geoid height. A value of $L = 110$ km is chosen to represent the thickness of the lithosphere at points above 4 km. Between 4 km and 6 km this yields geoid anomalies of 20 m to 33 m, in agreement with the data shown in Figure 3.10.

The geoid anomaly, calculated using $S_0 = 30$ km throughout south–east Asia, $L = 200$ km for points below 4 km, and $L = 110$ km for points above 4 km, is plotted in Figure 3.14. The misfit to the observed geoid (Figure 3.9) is plotted in Figure 3.15.

The main features of the observed geoid anomaly are reproduced in the model, but two fundamental differences may be identified. Firstly, the east–west gradient in the observed geoid anomaly across the Tibetan plateau is not reproduced in the model, resulting in the ~ 20 m misfit difference across the

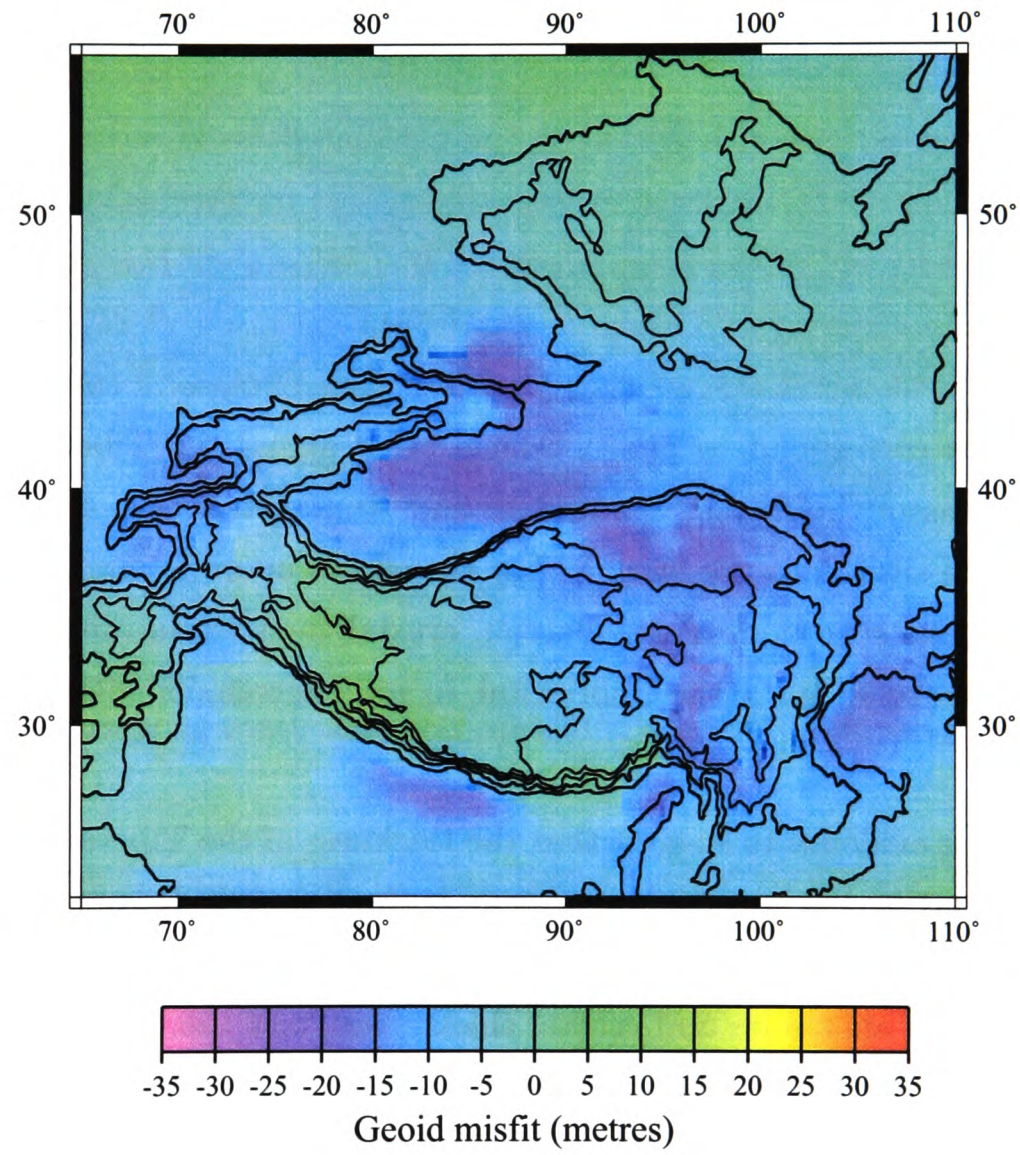

Figure 3.15: Misfit to the observed geoid anomaly across south–east Asia; observed minus calculated.

plateau in Figure 3.15. This gradient does not correspond to a topographic gradient, and therefore cannot be explained by this model. Secondly, the low negative geoid anomalies in the sedimentary basins which surround the plateau are also not reproduced, as highlighted by the negative misfits around the Tibetan plateau in Figure 3.15. The 5 to 10 km–thick layers of sediments have a lower density ($\sim$2100 kg m^{-3}) than the average density of the continental crust, therefore the calculations will overestimate the geoid height in these locations.

3.9 Crustal thickness distribution in south–east Asia

Crustal thicknesses for south–east Asia are calculated assuming Airy isostasy using the model described in section 3.8. Calculated crustal thicknesses for the Tibetan plateau lie in the range 47–60 km, at the bottom end of the range predicted by independent observations (Dricker & Roecker, 2002; Ritzwoller & Levshin, 1998; Owens & Zandt, 1997; Nelson *et al.*, 1996; Zhao *et al.*, 2001). These estimates could be increased by using a greater value of S_0, or a smaller value of L, in equation 3.13. Such scenarios correspond to pre–thickened crust across the Tibetan plateau, possibly due to the earlier collisions of the Lhasa, Qiangtang, and Kunlun terranes, or a greater amount of convective thinning. Both situations are feasible, but the effects upon S_0 and L are difficult to quantify. In the low–lying regions surrounding the plateau, crustal thicknesses range from 28 km in the Indian and Siberian shields to 40 km in the Gobi–Altai, in good agreement with geophysical observations (Wang, 2001).

There is strong evidence to suggest that the thickness of the Tibetan crust north of the Jinsha suture thins by around 15 km to $\sim$55 km (Owens & Zandt, 1997; Rodgers & Schwartz, 1997; Zhao *et al.*, 2001; Herquel *et al.*, 1995). This is not resolved in my model because elevation is used as a proxy for calculating geoid anomalies and crustal thicknesses, and there is no appreciable change in elevation from north to south across the plateau. The reason for the predicted variation in crustal thickness across the plateau is probably related to the underthrusting of Indian lithosphere beneath southern Tibet (Molnar *et al.*, 1973, 1993; Owens & Zandt, 1997).

It is unlikely that the entire 2000–2500 km of convergence which has taken place between Indian and Eurasia since collision (Achache *et al.*, 1984) has been accommodated by the subduction of Indian lithosphere beneath Tibet. Distributed shortening of Indian crustal material across the Himalaya, and as far north as the Indus–Tsangpo suture, has accommodated much of the convergence, whilst seismic studies (Zhou *et al.*, 1996; Owens & Zandt, 1997; Rodgers & Schwartz, 1997; Huack *et al.*, 1998), and studies of gravity anomalies in southern Tibet (Lyon-Caen & Molnar, 1984; Jin *et al.*, 1996), suggest that Indian crust is only underthrust beneath Tibet by around 350 km (Meissner

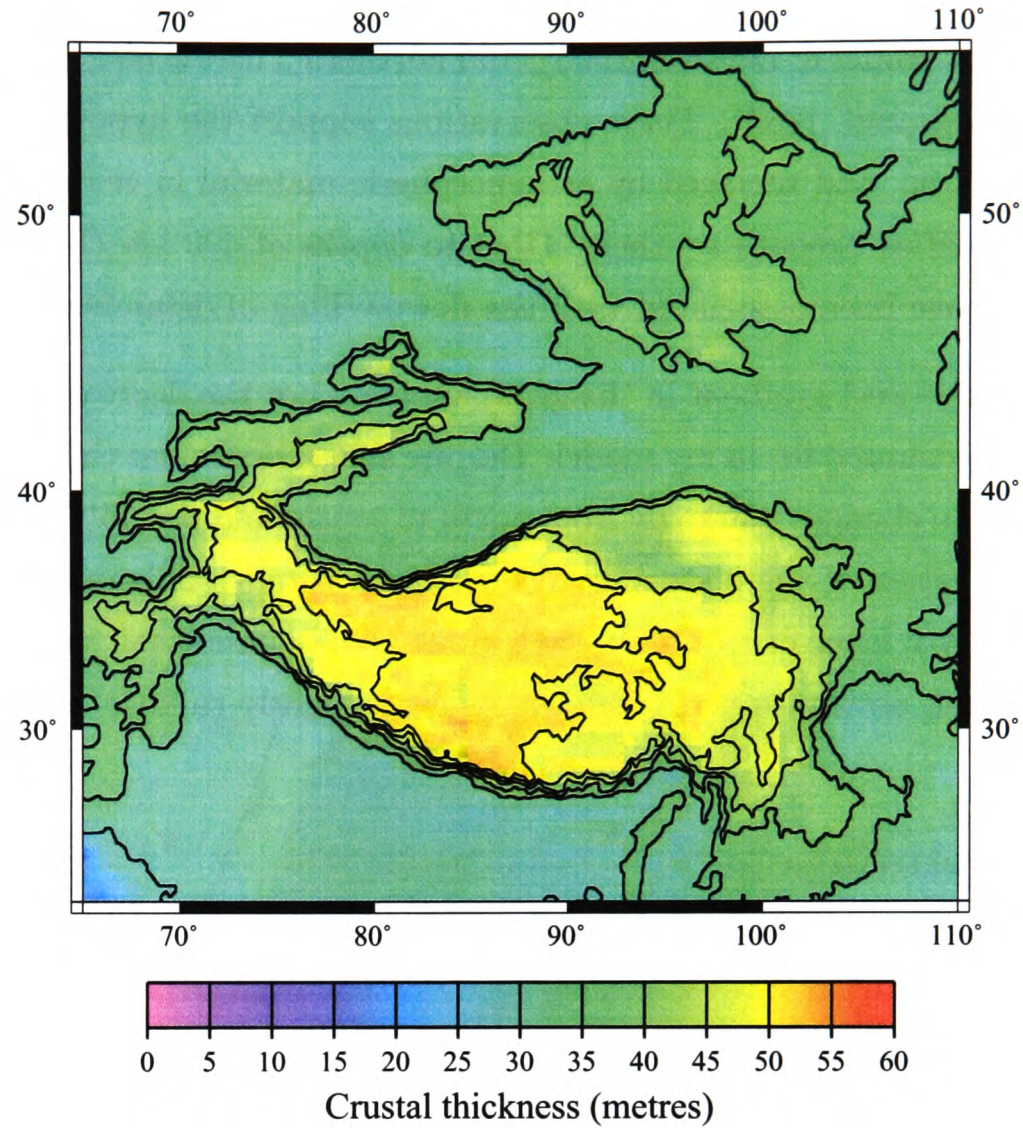

Figure 3.16: crustal thicknesses for south–east Asia calculated using the geoid model described in section 3.8.

& Mooney, 1998; Owens & Zandt, 1997). Distributed crustal shortening throughout the Tibetan plateau, thrusting at its northern margin, thickening in the Tien Shan, and the extrusion or rotation of material in the east also accommodate India–Asia convergence to varying degrees. The importance of each mechanism will vary over time as the morphology of the plateau changes.

If the current elevation of southern Tibet had been attained simply by lithospheric thickening, the increased volume of cold, high–density lower lithospheric material would result in a negative geoid anomaly beneath southern Tibet. However, average P–wave velocities in southern Tibet are low (Owens & Zandt, 1997), and this can be explained if Indian upper crustal material has been amalgamated with the Tibetan upper crust, thus creating a double–thickness, low–velocity, low–density felsic upper crust. The introduction of extra, low density, upper crustal material into the system more than counteracts negative buoyancy due to the thickening of the lithosphere, resulting in a positive geoid anomaly across southern Tibet.

Low shear velocities and Quaternary volcanism are found in central to northern Tibet (Villasenor

et al., 2001; Ritzwoller & Levshin, 1998), and northern Tibet is also a region of inefficient Sn propagation (Hi & Barazangi, 1983). These observations support the hypothesis that part of the lithosphere has been removed, and replaced by asthenospheric material in central and northern Tibet. Anomalous high velocities beneath southern Tibet to depths of 400 km (Ritzwoller & Levshin, 1998; Zhou *et al.*, 1996) have been associated with the downwelling of delaminated cold lithospheric material.

Neither the east–west gradient in the geoid anomaly nor the decrease in crustal thickness from south to north are accounted for in my model. Despite suggestions that the lithospheric structure across the Tibetan plateau changes markedly from north to south, and possibly east to west (Dricker & Roecker, 2002), the elevation of the plateau is remarkably constant. This may be explained if southern Tibet is supported by a layer of thick, buoyant, upper crustal material, while northern Tibet is supported by hot, buoyant, asthenospheric material below a slightly thinner crust.

3.10 Potential energy distribution

Once a model has been chosen, surface heights (Δe) are converted to yield a potential energy distribution. This is interpolated onto a finite element mesh and used in the finite element calculations described in chapter 2.

Equation 3.21 is used to convert surface heights into gravitational potential energy (relative to the reference column described in section 3.3). The interpolation of the potential energy distribution, which is defined upon a grid with data points located every 0.25° in both northerly and easterly directions, onto an irregular mesh is achieved using the following expression

$$PE(x,y) = \frac{\sum_{i,j} PE(i,j) e^{-\left(\frac{d}{2}\right)^2}}{\sum_{i,j} e^{-\left(\frac{d}{2}\right)^2}} \tag{3.24}$$

$PE(x,y)$ is the potential energy (to be calculated) at the node of the finite element mesh located at (x,y), and $PE(i,j)$ is the potential energy at position (i,j) in the regular grid. The sum over i and j represents a sum over two–dimensional space for the region of interest; between 70°E and 110°E, and 25°N and 55°N. $e^{-\left(\frac{d}{2}\right)^2}$ is the weighting factor for each point of the regular grid, and d is the distance between (x,y) and (i,j) in degrees; both points are assumed to lie on the surface of a sphere of radius 6378 km. The weights decay exponentially with distance, but the length scale of 2.0 degrees in the argument of $e^{-\left(\frac{d}{2}\right)^2}$ ensures that potential energy values within a distance of approximately twice the thickness of the lithosphere are considered during the interpolation.

The chosen potential energy distribution for south–east Asia is interpolated upon the finite element mesh described in chapter 4. A linear interpolation of the distribution across the elements of the mesh is shown in Figure 3.17.

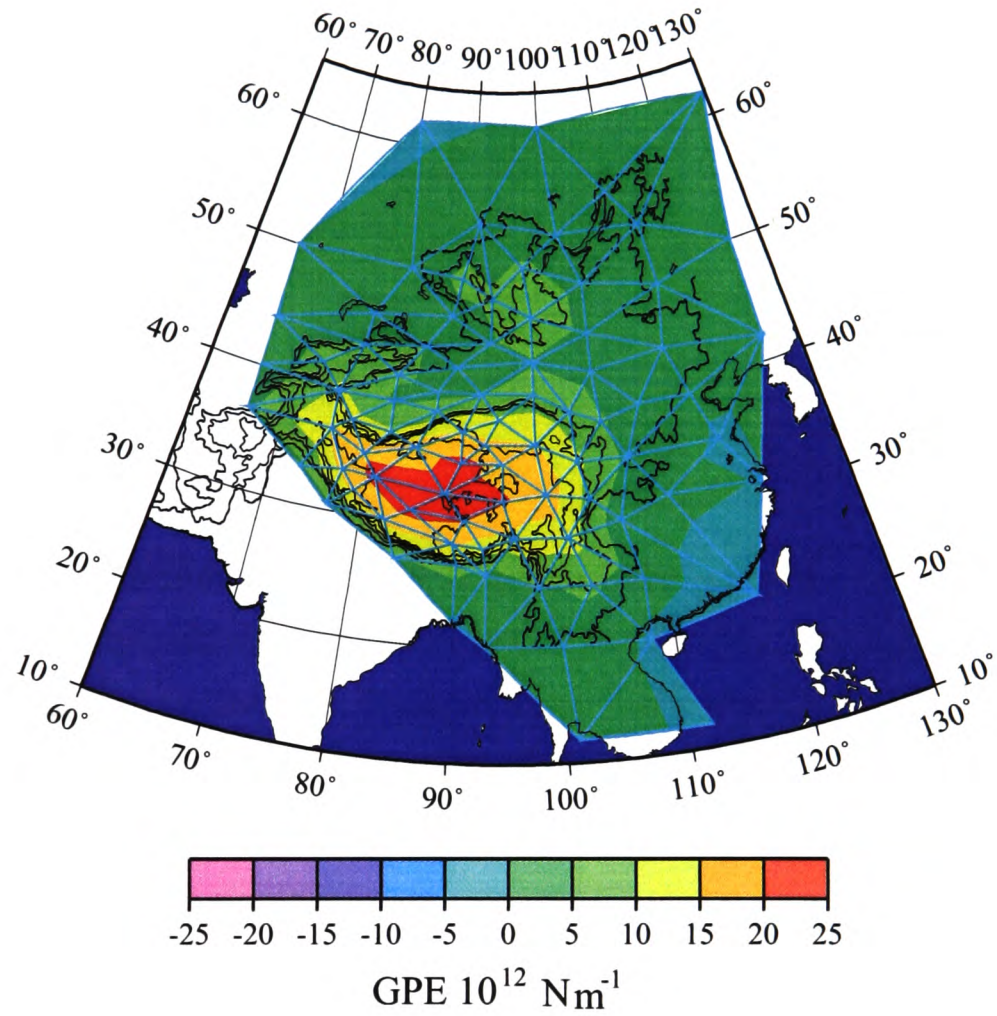

Figure 3.17: Potential energy distribution interpolated upon a finite element mesh covering south–east Asia. The solution is obtained from a model of the geoid which uses an initial crustal thickness of 30 km and an initial lithospheric thickness of 200 km for points below 4 km, and an initial crustal thickness of 30 km and an initial lithospheric thickness of 110 km for points above 4 km. The constant thickness model is used.

A potential energy model calculated directly from the geoid was also used in the inversion calculations of chapter 4, but was found to give poor results: Geoid height towards the south–east of the region under consideration is perturbed as a result of subduction processes. This long wavelength gradient in the signal assigns a potential energy distribution that is not representative of the buoyancy forces driving deformation throughout the study region. This method of obtaining a model potential energy distribution was therefore rejected.

Chapter 4

Viscosity Inversions for south–east Asia

4.1 Introduction

The ongoing convergence of India with Eurasia governs the present–day distribution of deformation throughout south–east Asia. Strain is accommodated at different rates, and by different mechanisms throughout the region. The methods of chapters 2 and 3 are employed to investigate the influence of variations in the strength and effective viscosity of the continental lithosphere upon the localisation of strain, in an attempt to constrain the power law exponent of the stress–strain rate relation which governs the deformation of the lithosphere in this region.

4.2 Background

The most striking topographical feature of south–east Asia is the Tibetan plateau. This elevated region extends >2000 km north–northeast from the northern edge of the Indian plate, and covers an area of $\sim$ 2 million km^2. Topography in the interior of the plateau is subdued, but it has a mean elevation of 5 km.

The lithosphere of the Tibetan plateau has been assembled by the accretion of continental and island arc material onto the southern edge of Eurasia throughout the Mesozoic (Zhang *et al.*, 1984; Dewey *et al.*, 1988). In the north, the Kunlun terrane (see Figure 4.1) was accreted to the southern margin of the Songban–Ganzi terrane in the Late Permian, forming the Kunlun–Qinling suture. The Qiangtang terrane was accreted in the Late Triassic or Early Jurassic, forming the Jinsha suture, and the Lhasa

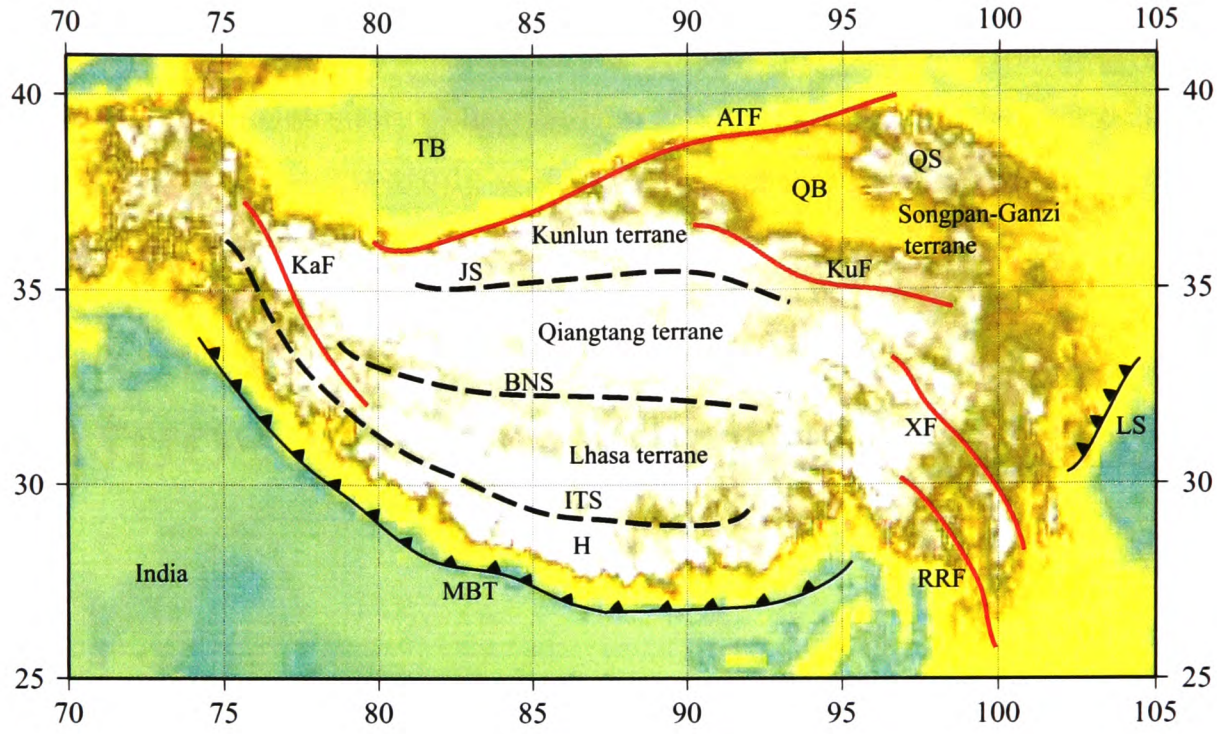

Figure 4.1: Topographic relief and simplified tectonics of Tibet. Red lines indicate strike slip faults: ATF: Altyn Tagh fault, KuF: Kunlun fault, KaF: Karakoram fault, XF: Xianshuihe fault, RR: Red River fault. Black lines with triangles indicate thrust faults: LS: Longmen Shan fault, MBT: Main Boundary Thrust. Dashed lines indicate sutures: JS: Jinsha suture, BNS: Banggong–Nujiang suture, ITS: Indus–Tsangpo suture. Other labels are TB: Tarim basin, QB: Qaidam basin, QS: Qilian Shan, H: Himalaya.

terrane was accreted in the Late Jurassic to early Cretaceous (Girardeau *et al.*, 1984), forming the Banggong–Nujiang suture. Most recently India was accreted onto the southern margin of Asia in the Middle Eocene following the closure of the Tethys, leading to the formation of the Indus–Tsangpo suture. The timing of collision is marked by a decrease in the rate of northwards motion of the Indian plate between 40 and 50 Ma, from ~ 100 mm yr^{-1} to ~ 50 mm yr^{-1} (Molnar & Tapponnier, 1975). The subsequent rise of the Tibetan plateau is a direct result of this collision, and the continued convergence between India and Asia over the past 40–50 Ma (Molnar & Tapponnier, 1975).

There is evidence that prior to the collision of India with Asia much of the region which now forms the Tibetan plateau was at or near sea level (Girardeau *et al.*, 1984; England & Searle, 1986; Norin, 1946). If this is true, the present elevation of the Tibetan plateau may be solely attributed to deformation of the lithosphere as a result of the collision of India with Asia.

4.2.1 Uplift of the Tibetan plateau

The timing and spatial distribution of uplift across the plateau is poorly constrained, but knowledge of the evolution of the plateau is crucial to determining the geodynamical processes that took place during the collision, and which drive the present–day deformation.

Climate changes between 6 Ma and 9 Ma, including the strengthening of the monsoon (Quade *et al.*, 1989), and increased weathering rates in eastern Tibet, were probably a result of a perturbation to the global circulation. These changes may have been caused by the uplift of the Tibetan plateau (Molnar *et al.*, 1993; Manabe & Broccoli, 1990). At the same time, the initiation of oceanic intraplate deformation in the Indian Ocean at 7.5–8 Ma (Curray & Munasinghe, 1989) implies a change in the regional stress field.

Prior to these events, normal faulting began in southern Tibet before $\sim$ 13.5 Ma (Coleman & Hodges, 1995; Blisniuk *et al.*, 2001), and there is evidence for basaltic volcanism in northern Tibet at around 13 Ma (Arnaud *et al.*, 1992; Turner *et al.*, 1993). Numerical experiments have shown that the initiation of normal faulting may be related to the gravitational collapse of a region of thickened lithosphere once a threshold thickness is reached (England & Houseman, 1989). The slightly potassic nature of the basaltic volcanism is indicative of lithospheric, rather than asthenospheric, melting (McKenzie, 1989). These observations led Molnar *et al.* (1993) to argue that rapid uplift of the Tibetan plateau took place following the convective removal of thickened mantle lithosphere in northern Tibet. Combined with geological evidence for uplift and erosion along the northern margin of the Tibetan plateau between the Miocene and Pliocene (Molnar *et al.*, 1987), these observations suggest that the uplift of the Tibetan plateau had begun by $\sim$ 15 Ma, and that the present elevation of the plateau was attained by 8 Ma (Harrison *et al.*, 1992).

4.2.2 Mechanisms of convergence

Paleomagnetic studies of the Gandese batholith, which lies immediately north of the Indus–Tsangpo suture, show that 2000–3000 km of north–south convergence has occurred between India and Asia since the Cretaceous (Achache *et al.*, 1984), but the mechanism by which this convergence has been accommodated is widely debated. Several authors have suggested that Indian lithosphere has been underthrust beneath the Tibetan plateau (Argand, 1924; Hi & Barazangi, 1983). Variations of this idea propose that Indian crust has been injected into the lower crust of Tibet (Zhao & Morgan, 1985), or that Indian lithosphere subducts steeply beneath southern Tibet (Owens & Zandt, 1997). Dewey & Burke (1973); Dewey *et al.* (1988) propose that indentation by the stronger Indian lithosphere has been accommodated by distributed thickening of the Asian lithosphere, while Willett

& Beaumont (1994) explain low velocities in the upper mantle of northern Tibet by the retreat of the Asian lithosphere. A modification of the Dewey *et al.* (1988) model involves the complete removal of thickened Asian lithosphere by convection (Houseman *et al.*, 1981; Molnar, 1988b; England & Houseman, 1988; Molnar *et al.*, 1993).

4.2.3 Present–day deformation

Estimates for the present–day rate of convergence between India and Asia lie between 36 ± 5 mm yr^{-1} and 47 mm yr^{-1} (DeMets *et al.*, 1990, 1994; Larson *et al.*, 1999; Holt *et al.*, 2000; Wang *et al.*, 2001), although recent GPS estimates (Paul *et al.*, 2001; Sella *et al.*, 2002) indicate that the current rate is 14% slower than the upper bound of this range predicted by the geologic NUVEL–1A plate motion model (DeMets *et al.*, 1994). Strain rates across India are only on the order of $\sim -2.6 \pm 0.9 \times 10^{-9}$ yr^{-1} (Paul *et al.*, 2001). In contrast, the rate of thrusting across the Himalaya is -4.5×10^{-8} yr^{-1} (Zhang *et al.*, 2004), corresponding to 16–18 mm yr^{-1} of convergence, (Molnar & Deng, 1984; Armijo *et al.*, 1986; Molnar & Lyon-Caen, 1989; Bilham *et al.*, 1997; Larson *et al.*, 1999; Wang *et al.*, 2001; Banerjee & Bürgmann, 2002), the majority of which is presently taken up along the Main Boundary Thrust (see Figure 4.1).

Deformation within the Tibetan plateau

Over 30% of the relative motion between India and Asia is taken up by internal shortening within the Tibetan plateau (Wang *et al.*, 2001; Zhang *et al.*, 2004), and up to 15% is accommodated north of the Tien Shan (Calais *et al.*, 2003). GPS studies show convergence rates of 9–12 mm yr^{-1} across the main Tibetan plateau (Wang *et al.*, 2001), corresponding to strain rates of $-1.3 \pm 0.4 \times 10^{-8}$ yr^{-1} to $-1.8 \pm 0.4 \times 10^{-8}$ yr^{-1}, with a further 10 mm yr^{-1} accommodated across the Qaidam basin and the Qilian Shan (Zhang *et al.*, 2004). GPS profiles reveal a linear velocity gradient from the Himalaya to the Qilian Shan (Wang *et al.*, 2001; Zhang *et al.*, 2004), implying that the lithosphere along this 1500 km transect deforms as a continuum.

The Tibetan plateau is characterised by diffuse seismicity on normal and strike–slip faults; thrusting is confined to the edges of the plateau (see Figure 4.2). In the high heat flux ($\sim$80 mW m^{-2}, (Wang, 2001)) region of southern and central Tibet, convergence is accommodated by east–west extension on north–striking normal faults (Molnar & Tapponnier, 1978; Molnar & Lyon-Caen, 1989; Harrison *et al.*, 1992; Blisniuk *et al.*, 2001) at rates of 11 ± 3 to 20 ± 3 mm yr^{-1} (Molnar & Deng, 1984; Larson *et al.*, 1999; Holt *et al.*, 2000; Wang *et al.*, 2001). In northern Tibet, east–west extension takes place at $\sim$ 10 mm yr^{-1} (Molnar & Lyon-Caen, 1989), corresponding to strain rates of $2.1 \pm 0.3 \times 10^{-8}$

yr^{-1} (Zhang *et al.*, 2004), on a combination of normal and strike–slip faults (Molnar & Lyon-Caen, 1989; Yin *et al.*, 1999). Deformation in the east is mainly accommodated on left–lateral strike–slip faults, striking between east–west and SSE–NNW, which are variously interpreted as accommodating approximately east–west left–lateral shear, or the 'extrusion' of Tibet (Molnar & Tapponnier, 1975; Tapponnier *et al.*, 1986), rotation of eastern Tibet about an axis in the north–east of India (Molnar & Lyon-Caen, 1989; Zhang *et al.*, 2004), or north–south dextral shear and clockwise rotation (England & Molnar, 1990). Most recent velocity fields incorporating Quaternary faults and GPS (England & Molnar, 2004), and dense GPS studies in eastern Tibet (Zhang *et al.*, 2004), favour a combination of the last two of these interpretations.

Much of the convergence between India and Asia has been accommodated by crustal thickening throughout the Tibetan plateau, although this mechanism now seems to be confined to the margins of the plateau. The Moho is at $\sim$ 35 km in India (Hirn *et al.*, 1984), similar to the global average of 39 km (Christensen & Mooney, 1995), but increases to 70–80 km beneath the Lhasa terrane (Nelson *et al.*, 1996; Owens & Zandt, 1997; Ritzwoller & Levshin, 1998; Zhao *et al.*, 2001; Dricker & Roecker, 2002). The crust then gradually thins towards the north of the plateau; it is 60–70 km thick beneath the Qiangtang terrane, and only $\sim$ 55 km thick at the northern boundary of the plateau (Owens & Zandt, 1997; Zhao *et al.*, 2001). This gradual thinning, combined with the observation of constant elevation throughout the Tibetan plateau, implies a change in the density structure across the plateau, as discussed in chapter 3.

Large–scale strike–slip faulting

The tectonic boundaries of the Tibetan plateau are characterised by long strike–slip faults, up to 2000 km in length. Slip rates on the main faults, including the right–lateral Karakoram fault and the left–lateral Kunlun and Altyn Tagh faults (see Figure 4.1), are a subject of active debate. The measurement of geological offsets suggests predominantly fast slip rates of 32–33 mm yr^{-1} for the Karakoram fault (Peltzer & Tapponnier, 1988; Liu, 1993) and 20–30 mm yr^{-1} for the Altyn Tagh fault (Peltzer *et al.*, 1989; Avouac & Tapponnier, 1993; Meriaux *et al.*, 2003), although some workers have suggested slower rates of 4–8 mm yr^{-1} for the slip rate of the Karakoram fault (Searle *et al.*, 1998; Brown *et al.*, 2002). Geodetic estimates for the slip rate on these faults are much lower; 1–11 mm yr^{-1} for the Karakoram fault (Banerjee & Bürgmann, 2002; Jade *et al.*, 2004; Wright *et al.*, 2004) and 5–10 mm yr^{-1} for the Altyn Tagh fault (Bendick *et al.*, 2000; Chen *et al.*, 2000; Shen *et al.*, 2001b; Wright *et al.*, 2004). A component of convergence is also detected across the Altyn Tagh fault (2.5 ± 2.5 mm yr^{-1}; Bendick *et al.* (2000), < 5 mm yr^{-1}; Chen *et al.* (2000), 2.9 ± 1.8 and 3.2 ± 1.5 mm yr^{-1}; Zhang *et al.* (2004)), and these findings are supported by observations of

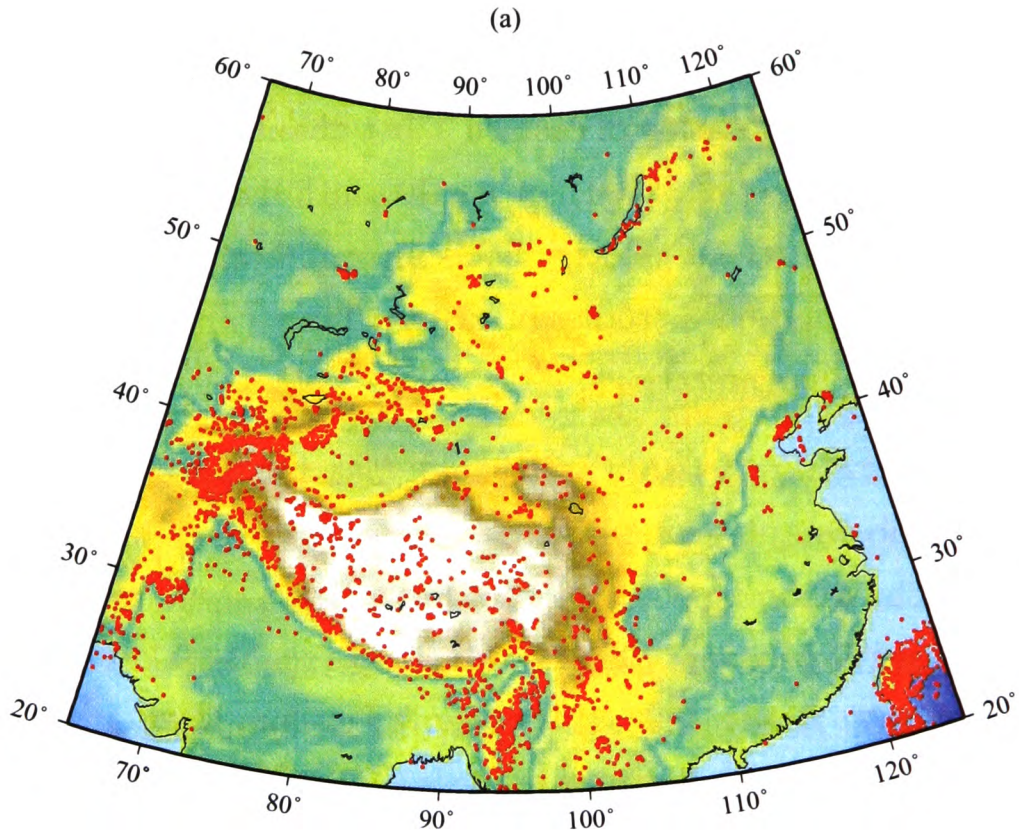

Figure 4.2: Seismicity of Tibet: (a) Epicentres of earthquakes of magnitude > 4.5, 1964–1984, taken from the International Seismological Centre (ISC) catalogue. (b) Focal mechanisms for selected events taken from Molnar & Deng (1984) and Molnar & Lyon-Caen (1989).

active thrust faulting on the northern margin of the plateau (Molnar *et al.*, 1987). The discrepancies between geological and geodetic slip rates arise due to the range in accuracy and the time span of the measurements, highlighting the fact that present–day rates do not necessarily represent average rates for the whole of the Quaternary. The wide range of data has led to two contrasting interpretations relating to the large–scale deformation of the Tibetan plateau.

The accommodation of convergence

Estimates of rapid slip rates on plateau–bounding faults have led to suggestions that the entire Tibetan plateau is being extruded to the east, with motion accommodated on a small number of long strike–slip faults, limited internal deformation away from these faults, and no large scale rotation (Molnar & Tapponnier, 1975; Tapponnier & Molnar, 1977, 1979; Armijo *et al.*, 1989). The lack of significant shortening in the Longmen Shan (see Figure 4.1, and King *et al.* (1997); Chen *et al.* (2000); Zhang *et al.* (2004)) has been interpreted to imply that up to 50% of the rate of convergence between India and Eurasia is accommodated by block displacement to the east (Avouac & Tapponnier, 1993). The implications of this block–extrusion model do not permit the treatment of the lithosphere as a continuum, however this hypothesis is not supported by the low geodetic slip rates for the Altyn Tagh and Karakoram faults (Bendick *et al.*, 2000; Chen *et al.*, 2000; Shen *et al.*, 2000; Wright *et al.*, 2004; Zhang *et al.*, 2004) or the observation of a steady northward increase in the eastward component of surface velocity from south to north across Tibet (Holt *et al.*, 2000; Zhang *et al.*, 2004).

South China is widely regarded to be a rigid block due to its lack of internal deformation (Molnar & Tapponnier, 1975; Holt *et al.*, 2000; Chen *et al.*, 2000; Shen *et al.*, 2000; Wang *et al.*, 2001). This inference is supported by measurements of low heat flux across the region (Wang, 2001). Despite the lack of crustal shortening on the eastern boundary of the Tibetan plateau, geodetic studies show that this region is translating at a rate of only 6–11 mm yr^{-1} to the east–southeast relative to stable Eurasia (Molnar & Gipson, 1996; Larson *et al.*, 1999; Holt *et al.*, 2000; Chen *et al.*, 2000; Wang *et al.*, 2001; Zhang *et al.*, 2004). This rate is much slower than that implied by the extrusion model of deformation.

An alternative hypothesis suggests that extrusion accounts for only $\sim$ 15% of the total rate of convergence between India and Eurasia, and that rotation, shear and crustal thickening absorb the majority of the eastward velocity component along the eastern margin of the plateau (England & Molnar, 1990; Molnar & Gipson, 1996; England & Molnar, 1997b). GPS data support the rotation of material around the Eastern Himalayan Syntaxis (King *et al.*, 1997; Holt *et al.*, 2000; Chen *et al.*, 2000; Wang *et al.*, 2001; Zhang *et al.*, 2004), and north–south dextral shear relating to the northwards progression of India is probably accommodated on a series of slowly–rotating left–lateral

faults (England & Molnar, 1990). The paradox of a 5–11 mm yr^{-1} velocity gradient across the Longmen Shan (Wang *et al.*, 2001) despite a lack of GPS evidence for shortening (King *et al.*, 1997; Chen *et al.*, 2000; Zhang *et al.*, 2004), is explained by the rotation model.

The Qaidam basin

The Qaidam basin is a prominent sedimentary basin lying at an elevation of $\sim$ 3 km in the north east of the Tibetan plateau (Figure 4.1). Unlike the Tarim and Junggar basins to the north, its sedimentary sequence is strongly folded (Wang *et al.*, 2003), but still underlain by strong crust (Zhu & Helmberger, 1998). The heat flux within the basin is 54 mW m^{-2} (Wang, 2001), while to the north east, the actively deforming Qilian Shan (see Figure 4.1) has a heat flux of 66 mW m^{-2}.

The Tarim basin

The Tarim basin delimits the northwestern boundary of the Tibetan plateau (Figure 4.1). Its basement consists of Ordovician or Cambrian lithosphere overlain by 6–10 km of sediments. It has a crustal thickness of 48 km (Wang, 2001), indicating that it has not undergone any appreciable compression or extension, and it appears to be anomalously strong (Neil & Houseman, 1997); a fact supported by the low regional heat flux of 44–45 mW m^{-2}. It undergoes little internal deformation, and its motion can be described by clockwise rotation relative to Eurasia, about a pole near the eastern end of the Tien Shan (Shen *et al.*, 2001b; Bendick *et al.*, 2000; Peltzer & Saucier, 1996). Its high strength allows stress from the convergence of India with Asia to be transmitted across the Tien Shan to the north (England & Houseman, 1985; Neil & Houseman, 1997).

The Tien Shan

The Tien Shan is an active fold and thrust belt with high seismicity that accommodates 16–20 mm yr^{-1} of shortening (Abdrakhmatov *et al.*, 1996; Holt *et al.*, 2000; Wang *et al.*, 2001) on Quaternary faults distributed throughout the centre of the range (Thompson *et al.*, 2002). Deformation was reactivated during the collision of the Qiangtang and Lhasa blocks (Hendrix *et al.*, 1992), and most recently following the collision of India with Asia (Avouac *et al.*, 1993; Hendrix *et al.*, 1994). The crust has a thickness of 50–55 km (Roecker *et al.*, 1993), and has probably been thickened during the current episode of tectonism due to the transfer of strain across the Tarim basin (Neil & Houseman, 1997). Several authors have suggested that the Tien Shan is a region of anomalously weak lithosphere (Neil & Houseman, 1997; Roecker *et al.*, 1993).

The Junggar Basin and Mongolian plateau

The Junggar basin is another large–scale, low–lying sedimentary basin that undergoes little internal deformation. It has a crustal thickness of 46 km (Wang *et al.*, 2003), and is thought to be underlain by Paleozoic oceanic crust (Coleman, 1989). To the north east again, the Gobi and Mongolian Altai form the boundary of the 2500 km high Mongolian plateau. Around 15% of the total convergence between India and Asia is accommodated across this plateau (Calais *et al.*, 2003), by a combination of north–south shortening and dextral shear. The region has an average crustal thickness of $\sim$ 50 km (Wang *et al.*, 2003; Calais *et al.*, 2003), and a relatively low heat flux of 47 mW m^{-2} (Wang, 2001) which increases to 50–70 mW m^{-2} towards Lake Baikal (Poort & Klerkx, 2004).

Baikal region

Far from the India–Asia collision zone, 4 mm yr^{-1} of extension takes place across the Lake Baikal rift zone (Calais *et al.*, 2003). It has been proposed that this motion is driven by an asthenospheric upwelling (Gao *et al.*, 1994), a hypothesis that is supported by evidence for low mantle P–wave velocities beneath the rift axis (Brazier & Nyblade, 2003; Gao *et al.*, 2003). However, this hypothesis is contradicted by recent gravity studies (Petit *et al.*, 1998) and the absence of a regional high heat flux (Lysack, 1992; Poort & Klerkx, 2004). Alternative hypotheses suggest that pre–existing heterogeneities in the lithosphere have allowed rifting to become localised in this region in response to the far–field boundary conditions (Tapponnier & Molnar, 1979; Petit *et al.*, 1996). To the north of the Mongolian plateau lies the stable Archaean Siberian platform, which is taken to be part of stable Eurasia.

4.3 Use of the thin viscous sheet model to infer lateral variations in effective viscosity across the India–Asia convergence zone

4.3.1 The applicability of the thin viscous sheet model to south–east Asia

The thin viscous sheet model is used to study the deformation of the continental lithosphere in eastern Asia. This model has previously been used to investigate the surface velocity field of the region (England & McKenzie, 1982; Houseman & England, 1986; England & Houseman, 1986), the role of crustal thickening in accommodating convergence in south–east Asia (Houseman & England, 1993), the influence of lithospheric heterogeneities upon deformation in south–east Asia (Vilotte *et al.*, 1984; England & Houseman, 1985), the growth of the Tibetan plateau (England & Houseman,

1986), and the distribution of strength throughout the region (Flesch *et al.*, 2000).

The assumptions of the model are outlined in chapter 2. In formulating the thin viscous sheet equations (equation 2.30 and 2.31), vertical gradients of velocity are neglected. This assumption is only applicable when the horizontal length scale of the deforming layer is an order of magnitude greater than the vertical length scale. In south–east Asia, collision takes place along a 2000 km–long boundary, and the resulting deformation extends >2000 km into the interior of the Asian lithosphere. These lengths are considerably greater than the average thickness of the lithosphere, which is taken to be $\sim 110 - -200$ km (see chapter 3).

In calculating the vertically averaged effective viscosity of the lithosphere I use the constitutive equation defined in equation 2.4 of chapter 2;

$$\eta_{\text{eff}} = \frac{1}{2} B \dot{E}^{(1/n)-1} \tag{4.1}$$

η_{eff} is the vertically averaged effective viscosity, B is the strength coefficient for the viscous layer, and $\dot{E} = \sqrt{\dot{\varepsilon}_{ij}\dot{\varepsilon}_{ij}}$ is the second invariant of the strain rate tensor, $\dot{varepsilon}_{ij}$. From equation 4.1 it can be seen that effective viscosity is dependent upon both the strength coefficient of the lithosphere and the local strain rate; it is therefore not an intrinsic property of the lithosphere. The strength coefficient, B, is intrinsic to the lithosphere and may be interpreted in terms of a temperature distribution and lithological differences (Sonder & England, 1986). I seek to explain variations in effective viscosity in terms of the distribution of strain throughout south–east Asia, and variations in the resistance of the lithosphere to stress.

4.3.2 Details of numerical experiments

The details of the numerical methods used to investigate the deformation and rheology of south–east Asia are set out in chapter 2. In order to carry out the inversion calculations, an observed solution for the velocity field (see section 4.3.3) is required to assign velocity boundary conditions at nodes on the edge of the mesh. In each element, strain rates calculated using the observed velocity field are used to constrain the relaxation of the viscosity distribution and define the convergence of the solution. A potential energy distribution is also put into the calculations (see chapter 3), and contributes to deformation in the interior of the mesh.

Preliminary inversions with $n = 1$, $n = 3$ and $n = 10$ are carried out using the two velocity fields described in section 4.3.3 in order to determine which gives the best fit between observed and calculated solutions. A regional method is used (see section 4.3.4), where a single value for the strength coefficient of the lithosphere, B, is solved for in each region (see chapter 2) . If the regional method is not used, and the strength coefficient is solved for in each element individually, solutions are found

to be highly sensitive to the input viscosity distribution. This line of investigation is not pursued further as it provides no more insight into the large–scale distribution of strength or effective viscosity in south–east Asia than the regional experiments.

The velocity field of England & Molnar (2004) (Figure 4.5) is used in a series of inverse calculations, where $n = 1$, to give an estimate for the effective viscosity distribution throughout the region. The Monte Carlo methods of chapter 2 are used. In the first case 1000 runs are carried out, each with a different B distribution. I refer to this as experiment 1. In the second case 10,000 runs are carried out. The mean distribution of B–values from experiment 1 is used as the starting condition for the second experiment, but a different perturbed velocity field is used to constrain each run. The velocity at each node of a perturbed velocity field is defined to lie within the GPS error ellipse for that node, and the resulting velocity field is used to define the relaxation of the viscosity field, and the convergence of the strain rate field for that run. I solve for the distribution of B–values that best fit each perturbed velocity field; this is referred to as experiment 2.

Each run outputs the rms misfit to the velocity field for that solution and a value for the strength coefficient in each region. Forward calculations are carried out using the mean value of B in each region from the two experiments, and also using the values of B from the solution with the smallest rms misfit, for each experiment. The forward calculations give the velocity, strain rate, and effective viscosity fields for the chosen distribution of B. A log–log plot of B against E is used to place constraints upon the value of the stress–strain rate exponent in the constitutive equation, as described in chapter 2.

Using $n = 1$ in the inverse calculations gives an estimate for the effective viscosity distribution throughout eastern Asia, but continental lithosphere does not deform according to a linear stress–strain rate relationship, and this calculation does not provide any insight into the fundamental variations in lithospheric strength throughout east Asia. Inversion calculations using $n = 3$, $n = 5$ and $n = 10$ are carried out in order to place constraints upon the underlying strength of the continental lithosphere throughout Asia. Monte Carlo methods are again employed in these inversion calculations: The two experiments described above are carried out for each value of n, and the results are again averaged to allow the forward calculation of the velocity, strain rate and effective viscosity fields for each output distribution of B. The effective viscosity and strength distributions for all values of n are compared, to determine the sensitivity of the solutions to the stress–strain rate exponent, and constrain the range of lithospheric strength throughout south–east Asia.

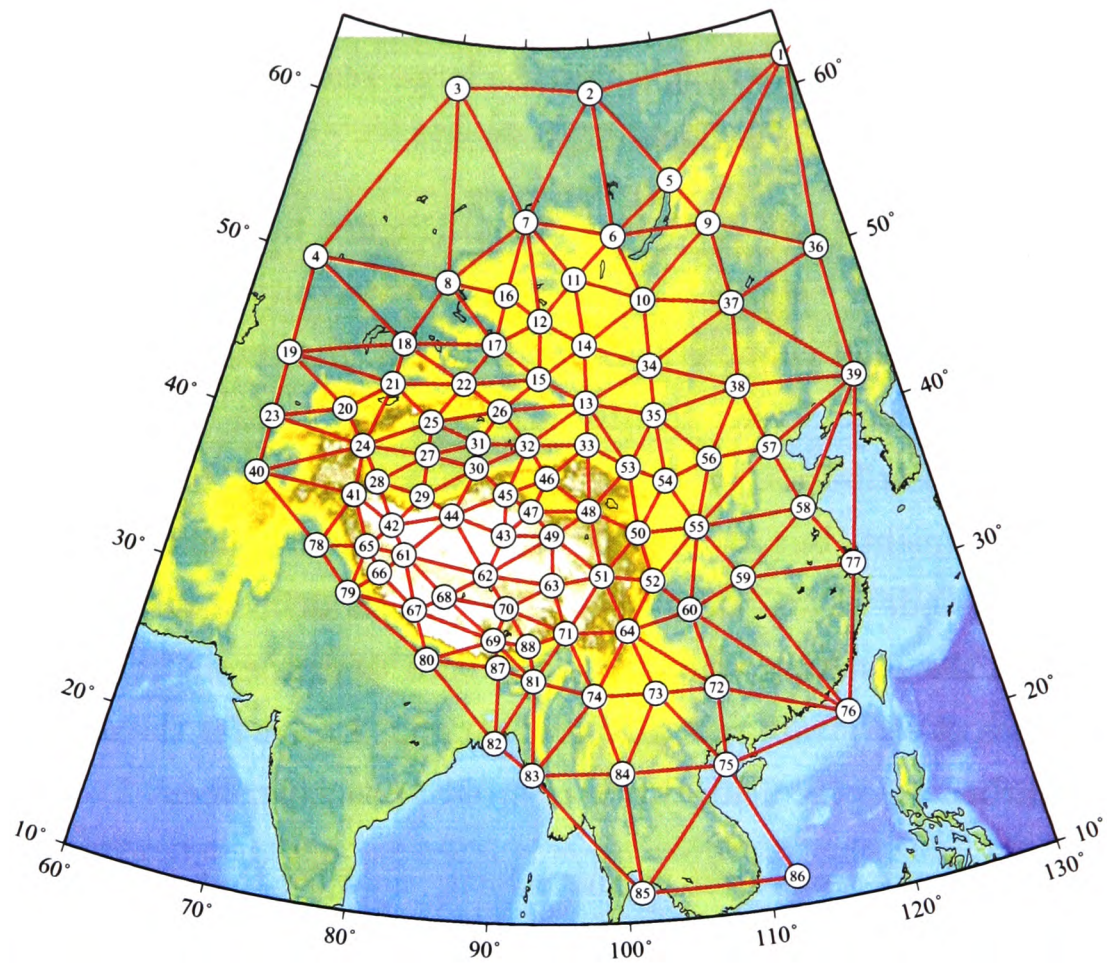

Figure 4.3: Finite element mesh for south–east Asia with node numbers

4.3.3 Velocity and Strain Rate Fields in Asia

A combination of GPS data, and information from Quaternary fault slip rates have been used to determine two internally consistent velocity fields for south–east Asia (England & Molnar, 2004). The GPS data are taken from the velocity estimates of Bendick *et al.* (2000); Calais *et al.* (2003); Chen *et al.* (2000); Shen *et al.* (2000, 2001b); Sella *et al.* (2002); Vigny *et al.* (2003); Wang *et al.* (2001); Zhang *et al.* (2004). Data from International GPS Service (IGS) sites are also used. The IGS sites are occupied continuously, whereas the other velocities are determined following the repeated reoccupation of GPS sites over a number of years.

Both velocity fields are interpolated by a coarse triangular mesh consisting of 155 elements defined by 88 nodes (see Figure 4.3). In determining the first velocity field, information from all the GPS data are interpolated onto the mesh. This is subsequently referred to as the campaign velocity field. In determining the second velocity field, information from the IGS sites only are used. This is subsequently referred to as the IGS velocity field. Each velocity field is also constrained by estimates of strain derived from the Quaternary slip rate estimates; the details of this method are given in England & Molnar (1997b).

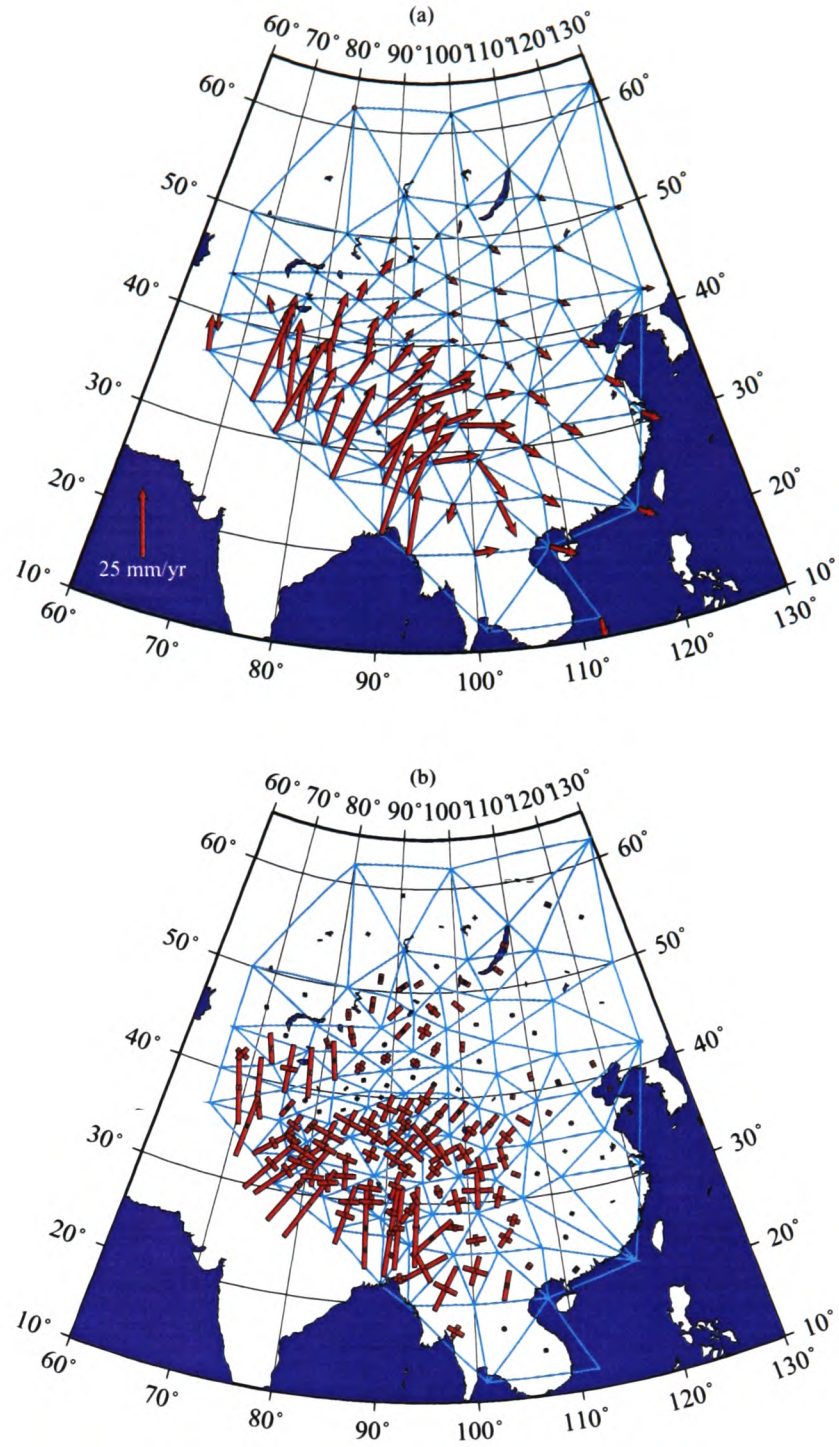

Figure 4.4: (a) Campaign velocity field (b) Campaign strain rate field

While data from the campaign GPS data set have greater errors than data from the continuous GPS stations, the density of the campaign coverage means that the velocity field constrained by these data gives a more detailed picture of the present–day surface deformation across south–east Asia. There are differences in the interpolated velocity fields (Figures 4.4 and 4.5). In particular, the campaign GPS data set provides dense coverage of the region south–east of the Tibetan plateau, where the IGS stations give poor resolution. The campaign velocity field resolves a more southerly component to the deformation field in this region.

Details of the two velocity fields, are given in Appendix A. East and north components are given

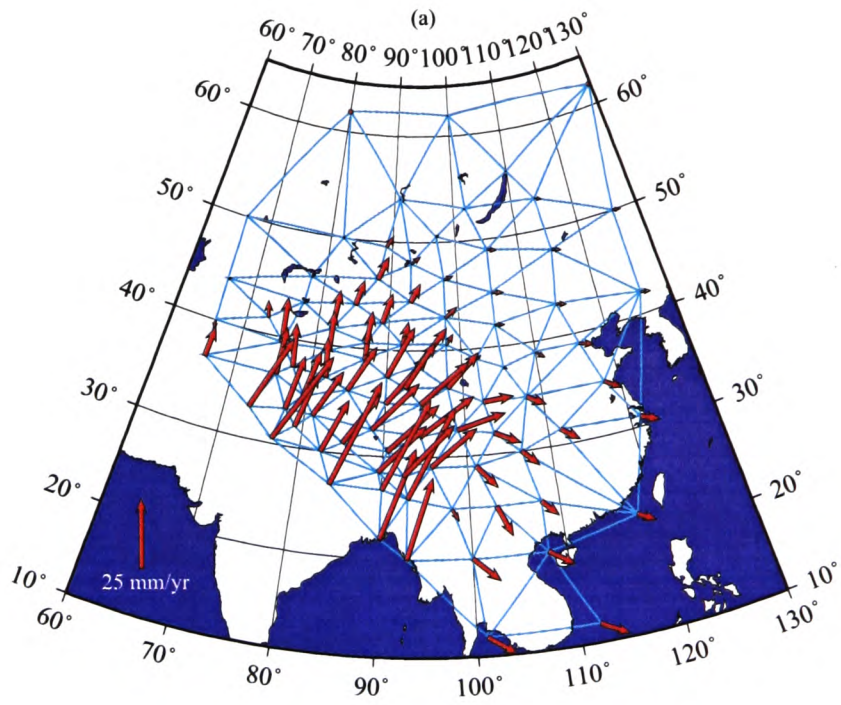

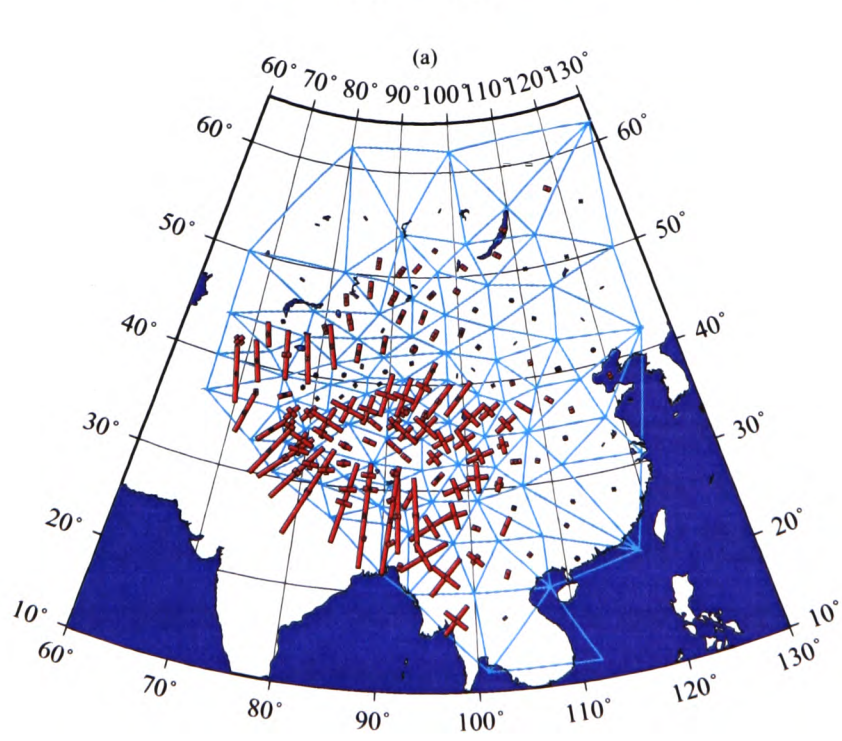

Figure 4.5: (a) IGS velocity field (b) IGS strain rate field

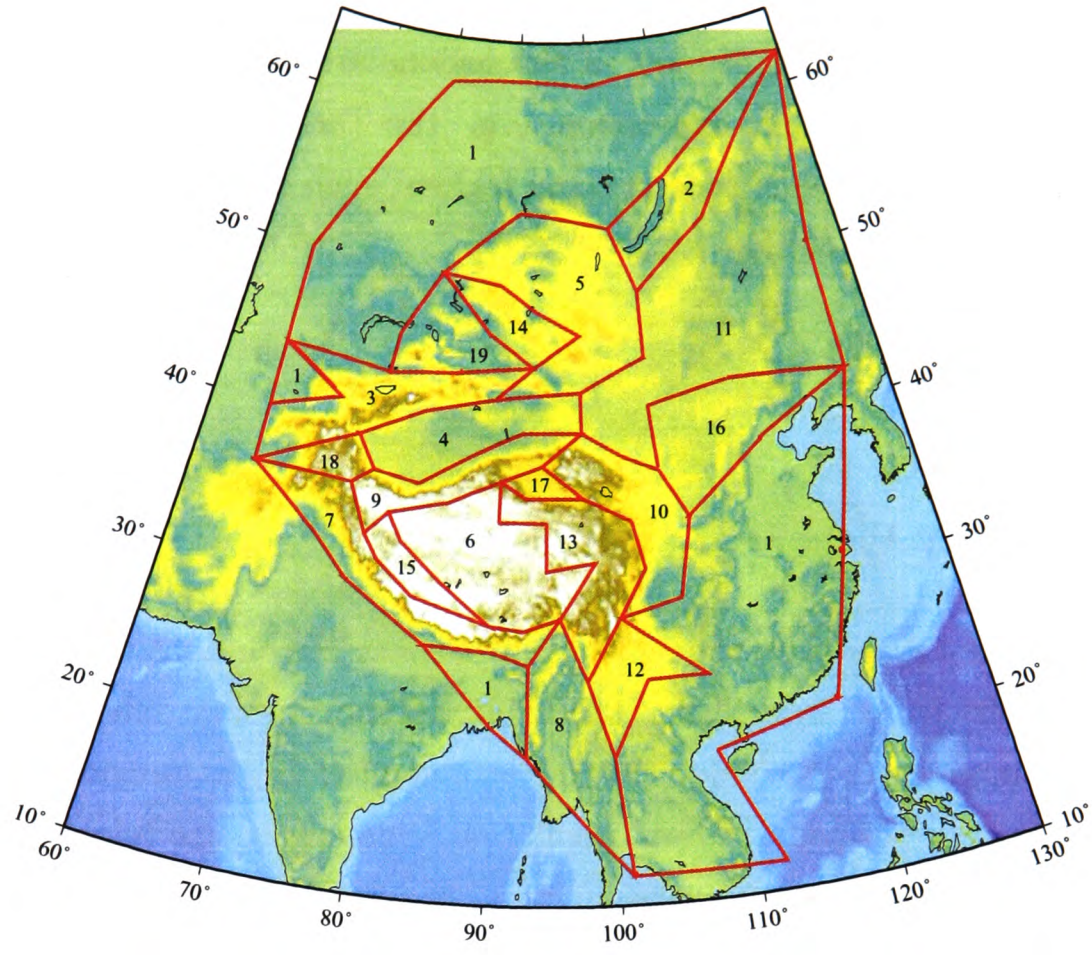

Figure 4.6: The regionalisation used in the viscosity inversion calculations. 1: very slowly deforming Asia, India, and the south China block. 2: Baikal. 3: Tien Shan. 4: Tarim basin. 5: Mongolian platform. 6: Tibet. 7: Himalaya. 8: Red River. 9: Altyn Tagh. 10: Qilian Shan and outer eastern margin. 11: Ordos block. 12: Yunnan. 13: eastern margin of Tibet. 14: Gobi–Altai and Mongolian–Altai. 15: southern Tibet. 16: region between south China and Ordos blocks. 17: Qaidam basin. 18: Pamirs. 19: Junggar basin. The jagged outlines to the regions are enforced by the geometry of the mesh.

with respect to a reference frame fixed relative to stable Eurasia. The standard deviation of each component is given, as is the correlation between the components. The correlation is used to perturb the velocity data within a 2σ confidence interval for input to the Monte Carlo experiments described in section 4.3.2.

4.3.4 Regionalisation

The finite element mesh (Figure 4.3) is divided into 19 regions according to styles of deformation. A single value of the strength coefficient, B, is solved for in each region. The shape of each region is constrained by the location of the nodes of the finite element mesh, therefore the regions defined in Figure 4.6 are an approximation to a regionalisation that would be defined solely by geological criteria.

The tectonic characteristics of most of the regions are described in section 4.2.3. Some regions are defined by their topographic expression, e. g. the Tarim basin, others by a change in the style of deformation, hence the separation of some regions, such as Baikal and the Yunnan, from the broader categories described in section 4.2.3.

4.4 Results

4.4.1 Velocity Fields

Figures 4.7 and 4.8 compare the results from inverse calculations using $n = 1$ to the input campaign and IGS velocity fields respectively. The numerical solutions are different because they are constrained by different input velocity fields. The mean value of B for each region from 1000 runs with different viscosity inputs is used in a forward calculation to determine the velocity and strain rate fields shown. The rms misfit between the numerical and observed velocity fields for the experiment constrained by the campaign data is 1.51 mm yr^{-1}, and for the IGS data it is 1.23 mm yr^{-1} .

The solution constrained by the campaign velocity field misfits the observed velocity by ~ 5 mm yr^{-1} in the south–east of the mesh, and it consistently overestimates the magnitude of the velocity field along the Altyn Tagh fault (Figure 4.7a). The strain rates for this solution highlight the poor fit in the south–east of the mesh and along the Altyn Tagh fault, but the solution also fails to recover the compressional component on the plateau which is evident in the campaign solution (Figure 4.8b). The data indicate higher rates of extension in the south–east Yunnan than are present in the numerical solution, but there is good alignment between the principal axes along the southern and northeastern margins of Tibet, and throughout the Tien Shan and Gobi–Altai. The low strain rates of the Tarim basin and the stable platforms are also accurately reproduced.

The solution constrained by the IGS data fits the data more closely in the south–east of the mesh than does the campaign solution. The numerical solution to the velocity field still underestimates the rotation in this region (Figure 4.8a), and there is misalignment between the observed and calculated velocity fields in the north–west of the plateau and the west of the Tarim basin, but the magnitude of the numerical solution is in good agreement with the observed data. The fit to the strain rates is good throughout the mesh, apart from a misalignment of observed and calculated principal axes around the Eastern Himalayan Syntaxis (Figure 4.8b). The observed data once again predict more extension in the Yunnan than is recovered by the numerical solution, but the prediction of pure extension across the Tibetan plateau is in good agreement with the numerical solution.

The campaign and IGS velocity fields have also been recovered using $n = 3$, $n = 5$ and $n = 10$. The

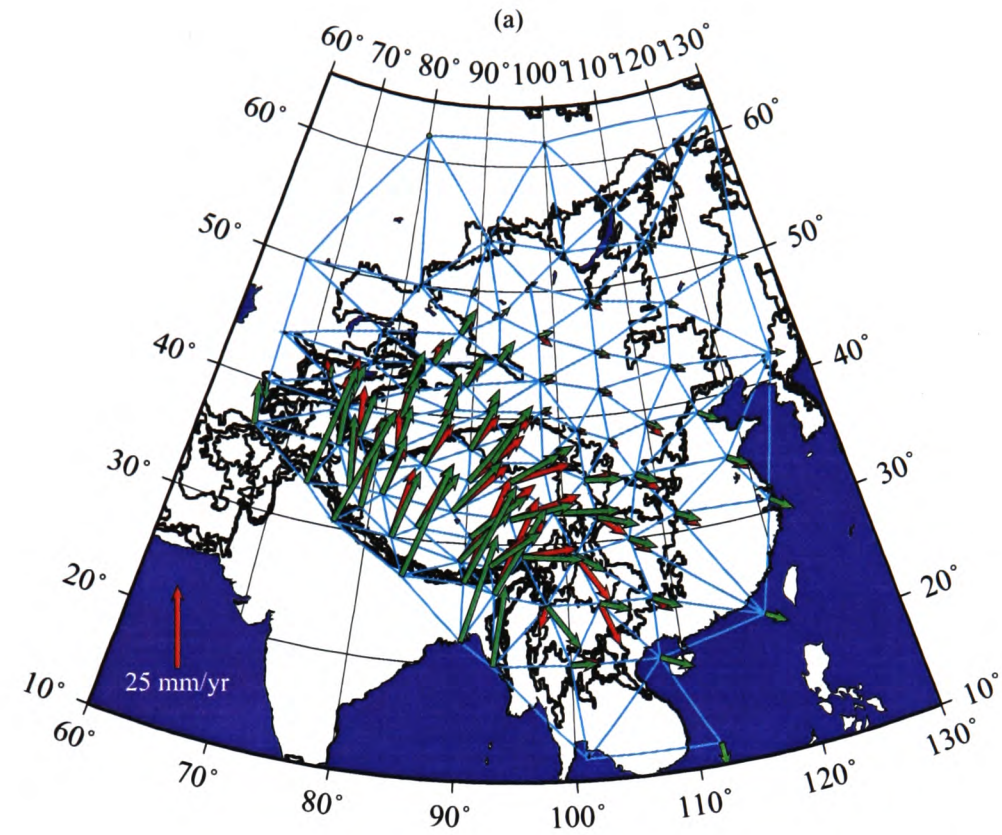

Figure 4.7: (a) Red arrows: campaign velocity field. Green arrows: velocity field obtained by inversion with $n = 1$, constrained by the campaign data. (b) Red crosses: strain rates for the campaign data. Green crosses: strain rates for the inversion of (a).

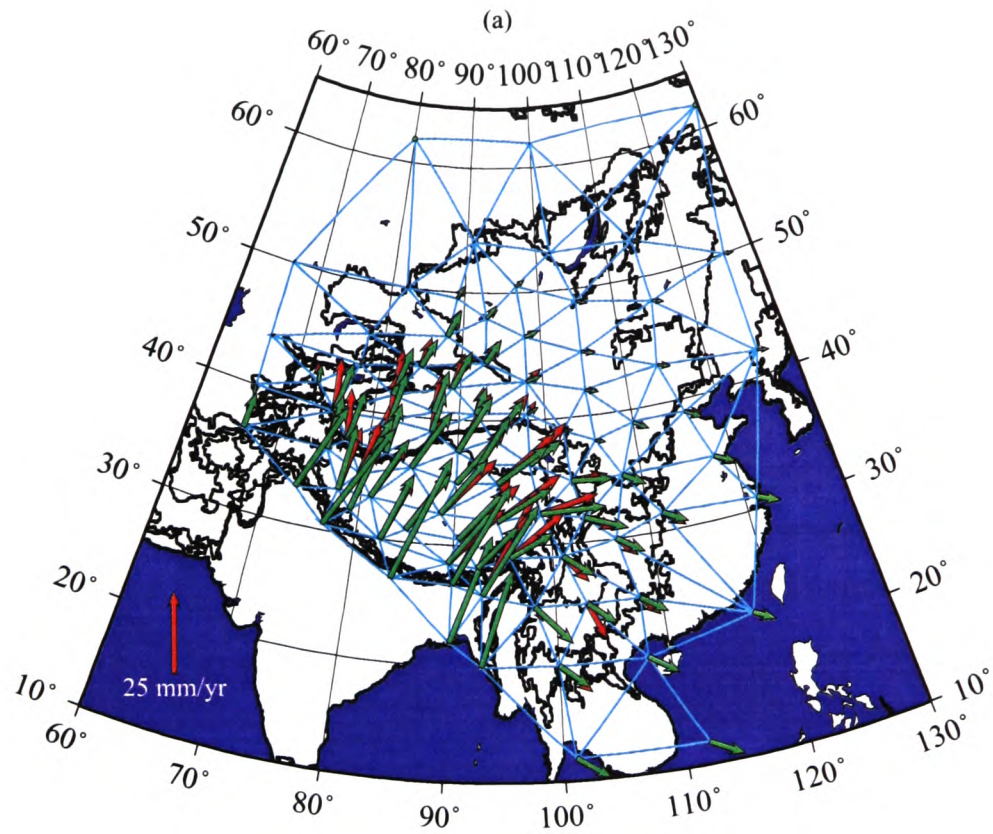

Figure 4.8: (a) Red arrows: IGS velocity field. Green arrows: velocity field obtained by inversion with $n = 1$, constrained by the IGS data. (b) Red crosses: strain rates for the IGS data. Green crosses: strain rates for the inversion of (a).

fit to the observed data is similar to the $n = 1$ cases.

I conclude that a physically self–consistent model that fits the observed velocity and potential energy fields cannot be found. Three possible explanations are offered: The velocity field may contain errors; this is least likely as the rms misfit of the velocity field to the GPS data is < 2 mm yr^{-1} (England & Molnar, 2004). Secondly the regionalisation may be inadequate. This is a reasonable possibility because the campaign data give much smaller–scale information (30–300 km) than the spacing of the IGS stations (500–1000 km) or the nodes of the finite element mesh ($\sim$ 500 km). Finally, the gravitational potential energy field may be wrong. Sensitivity tests could be carried out to determine the effect of small variations in the potential energy field upon the velocity field. Apart from the region around the Eastern Himalayan Syntaxis, the solution constrained by the IGS velocity field shows reasonable fit to the observed data, and is therefore used to constrain the distribution of strength and vertically averaged effective viscosity throughout east Asia on a scale of ≥ 300 km.

4.4.2 Viscosity inversions: $n = 1$

Figures 4.9–4.12 display the distributions of B calculated from the Monte Carlo experiments described in section 4.3.2. The blue arrow in each figure indicates the location of the mean for that distribution. Table 4.1 gives the mean value of B in each region for the two experiments, and the distribution of B for the solution with the lowest rms misfit from each experiment. The rms misfit to the velocity field for the best–fitting solutions from the two experiments are 1.2 mm yr^{-1} and 3.6 mm yr^{-1} respectively.

In Experiment 1, where the input distribution of B is varied, there is good agreement between the mean values for B and the values from the best–fitting solution, as demonstrated in Figures 4.13 and 4.14. The histograms are skewed for several of the regions, but the correspondence between the mean and the modal class is good, and the variance of the data are small. The ranges of B are small in comparison with the absolute values of B calculated for each region.

The difference between the mean and 'best' distributions for B when the velocity field is varied upon input is greater than in Experiment 1 (see table 4.1), and the variance of the distribution of B for each region is greater. The distributions are all positively skewed, and the mean is consequently greater than the modal class. The difference between the mean and mode for region 2 (Figure 4.11b) arises from a few large outliers not included in the histogram. An instability occasionally develops in the solutions, and the value of B in poorly constrained regions becomes exponentially large or small. The majority of these solutions have been omitted from the data set, but solutions where $B_2 \leq 5.0$ have been included.

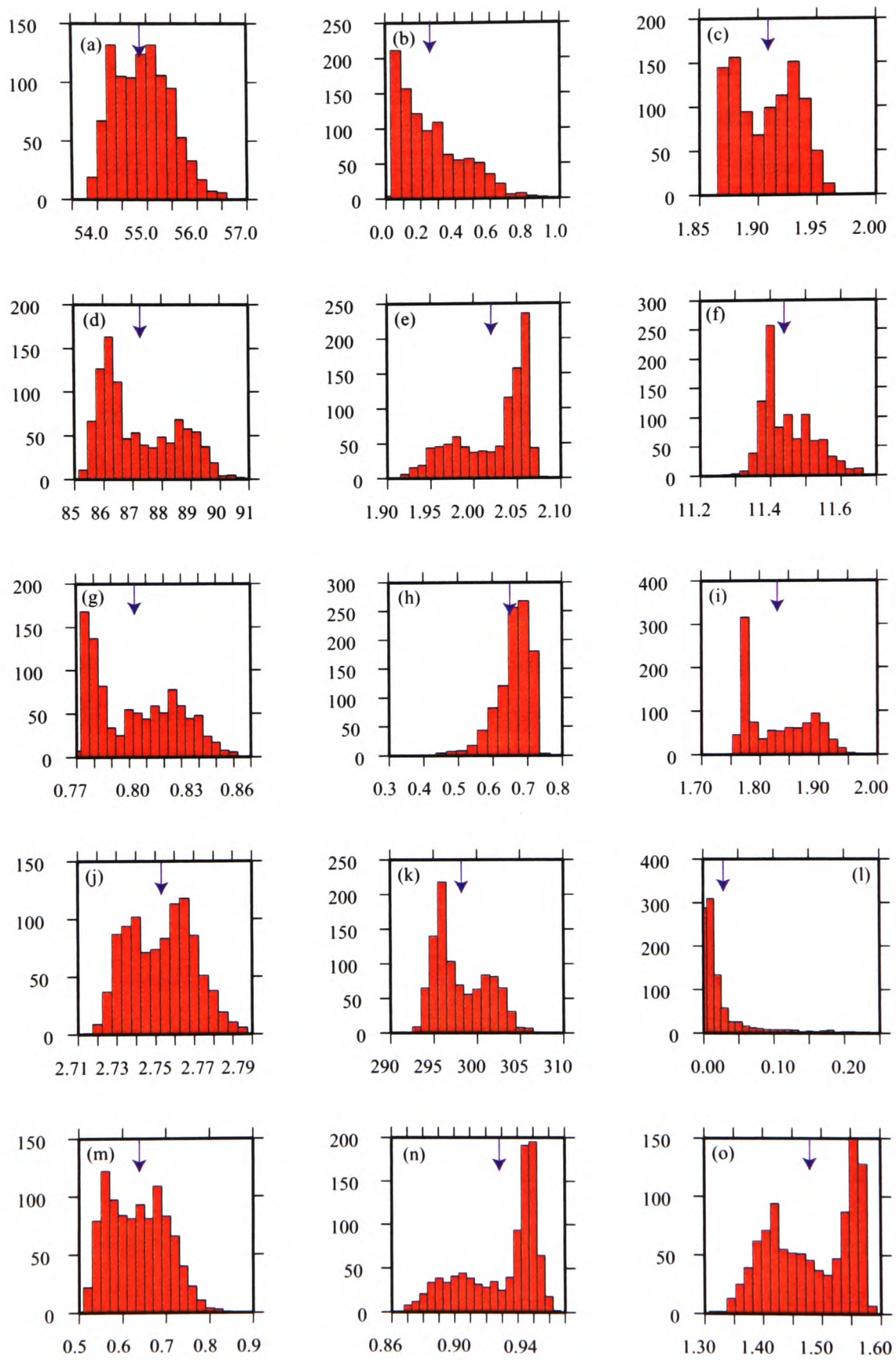

Figure 4.9: Histograms of the distribution of B in regions 1 to 15 (plots (a) to (o)) for 1000 runs of an $n = 1$ inversion calculation using the IGS velocity field. The input value of B is varied within the range (e^{-2}, e^{2}) in each region for each run.

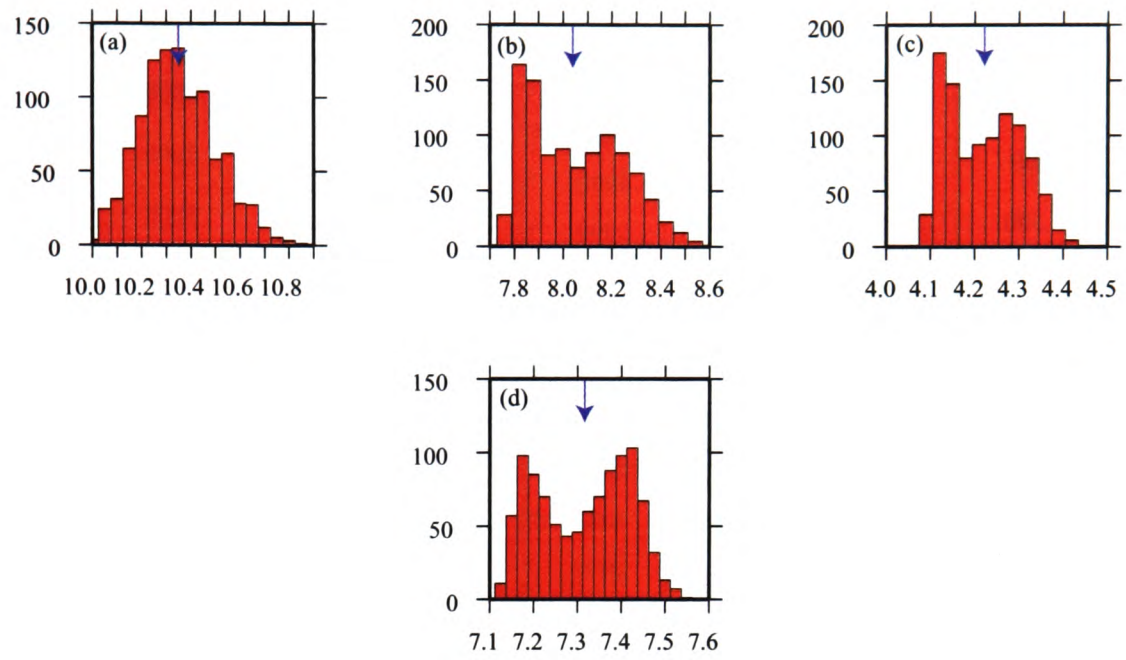

Figure 4.10: As for Figure 4.9. Histograms of the distribution of B in regions 16 to 19 (plots (a) to (d)).

Although the input velocity data are individually varied within error, each perturbed velocity field will not be internally consistent because the spatial correlation between sites has not been used to constrain the perturbations. This results in a decrease in order throughout the velocity field and the perturbed solutions used to constrain the inverse calculations of Experiment 2 exhibit greater internal deformation. In order to accommodate this deformation lower values of effective viscosity are implied, and this may explain the observation that the mean values of B obtained for each region during Experiment 2 are predominantly smaller than the mean values from Experiment 1. The rms misfits to the perturbed input velocity fields in Experiment 2 are greater than the rms misfits in Experiment 1, and varying the input velocity data results in an apparent decrease in the sensitivity of the solutions to variations in B, thus yielding a less tightly constrained mean effective viscosity distribution.

Considering both experiments, B is poorly constrained in regions with very high, or very low strength. For the regions that represent slowly deforming Asia, the Tarim basin and the Ordos block, values of B calculated in Experiment 1 are an order of magnitude greater than values from Experiment 2. The low values of B obtained for the Yunnan and Baikal regions also vary over several orders of magnitude.

If a region contains one element with a higher, or lower, strain rate than all other elements of that region, the numerical method has difficulty fitting a single value for B to all the data. If a single element deforms faster, the iterative viscosity relaxation method (chapter 2) decreases the value of

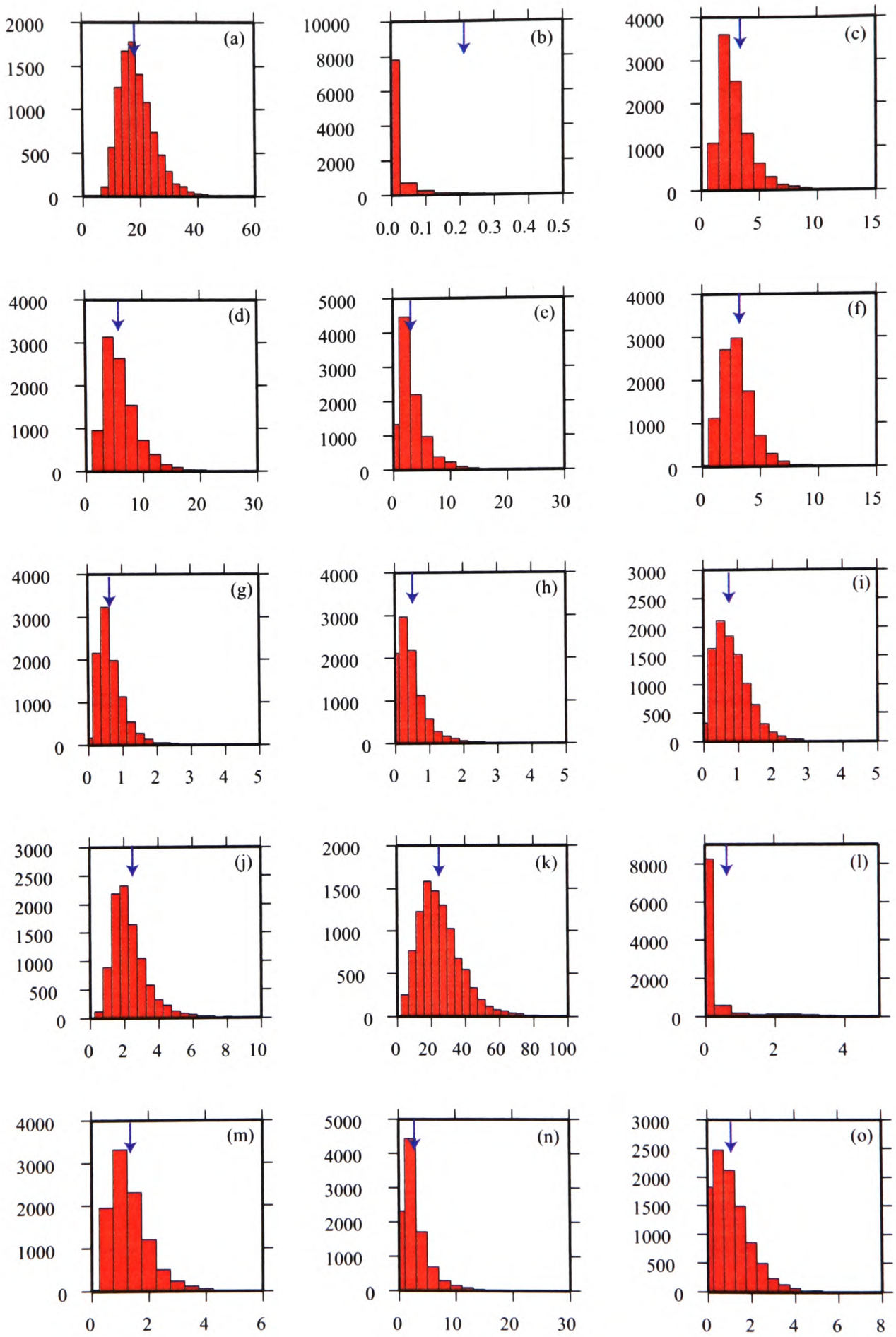

Figure 4.11: Histograms of the distribution of B in regions 1 to 15 (plots (a) to (o)) for 10,000 runs of an $n = 1$ inversion calculation using the IGS velocity field. The mean distribution of B from Experiment 1 is used as an initial solution for Experiment 2, and the input values of $\mathbf{u}$ are varied at each node for each run.

Table 4.1: Strength parameters from viscosity inversions which use $n = 1$

Region	Experiment 1 (varying B)		Experiment 2 (varying B and $\mathbf{u}$)	
	mean	best	mean	best
1	54.92	54.71	19.09	10.25
2	0.26	0.43	0.21	0.001443
3	1.91	1.88	3.05	1.88
4	87.24	85.86	6.31	5.27
5	2.02	1.94	3.35	0.87
6	11.45	11.25	3.00	4.84
7	0.80	0.78	0.68	0.30
8	0.66	0.76	0.52	0.57
9	1.83	1.75	0.84	0.23
10	2.75	2.76	2.42	4.32
11	298.08	295.60	25.73	37.20
12	0.04	0.11	0.32	0.39
13	0.63	0.62	1.37	0.75
14	0.93	0.88	2.86	1.18
15	1.48	1.55	1.10	2.14
16	10.35	10.19	2.47	0.46
17	8.05	7.99	2.59	6.01
18	4.22	4.16	3.78	1.88
19	7.31	7.17	8.34	2.56
rms velocity misfit (mm yr^{-1})	1.23	1.21	2.77	2.54

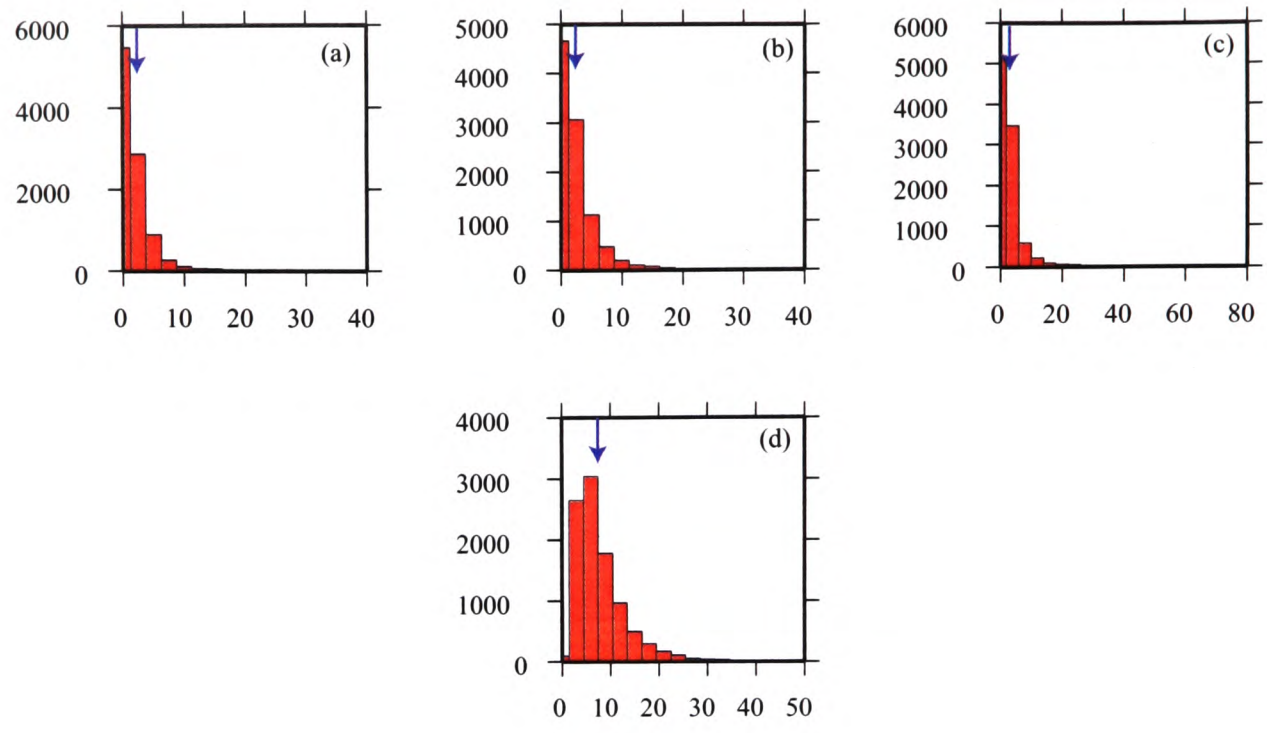

Figure 4.12: As for Figure 4.11. Histograms of the distribution of B in regions 16 to 19 (plots (a) to (d)).

B for that region beyond the value that fits the majority of the data. This problem is encountered with Yunnan, and could be rectified by using a different regionalisation.

For the high rigidity regions, the variation in solutions for B is a consequence of the iteration method. The calculation continues to solve for the value of B in every region until convergence is attained throughout the mesh. The more rigid regions are not the last to converge, and the strain rates throughout these regions are always slightly over–fit. Therefore, the value of B continues to be increased until convergence is reached throughout the solution domain. Increasing B in a more rigid region has little effect upon the resulting velocity and strain rate field, and there is no upper bound on values which fit the observed velocity field.

Using $n = 1$ in the inversion calculations yields a B–distribution that is proportional to the effective viscosity distribution because the exponent of the second invariant of the strain rate $(\frac{1}{n} - 1)$ reduces to zero, and thus there is no strain rate dependence in the expression for effective viscosity (see equation 4.1). The distributions of B and η_{eff}, shown in Figures 4.13 and 4.14, identify low strength, and low effective viscosity, in regions with high strain rates. Around the margins of the Tibetan plateau, these high strain rate regions correspond to regions with high topographic gradients, and hence high potential energy gradients.

Weak lithosphere is also identified along the Red River strike–slip fault system, between the south China and Ordos blocks, and in the Baikal region. These areas exhibit higher strain rates than

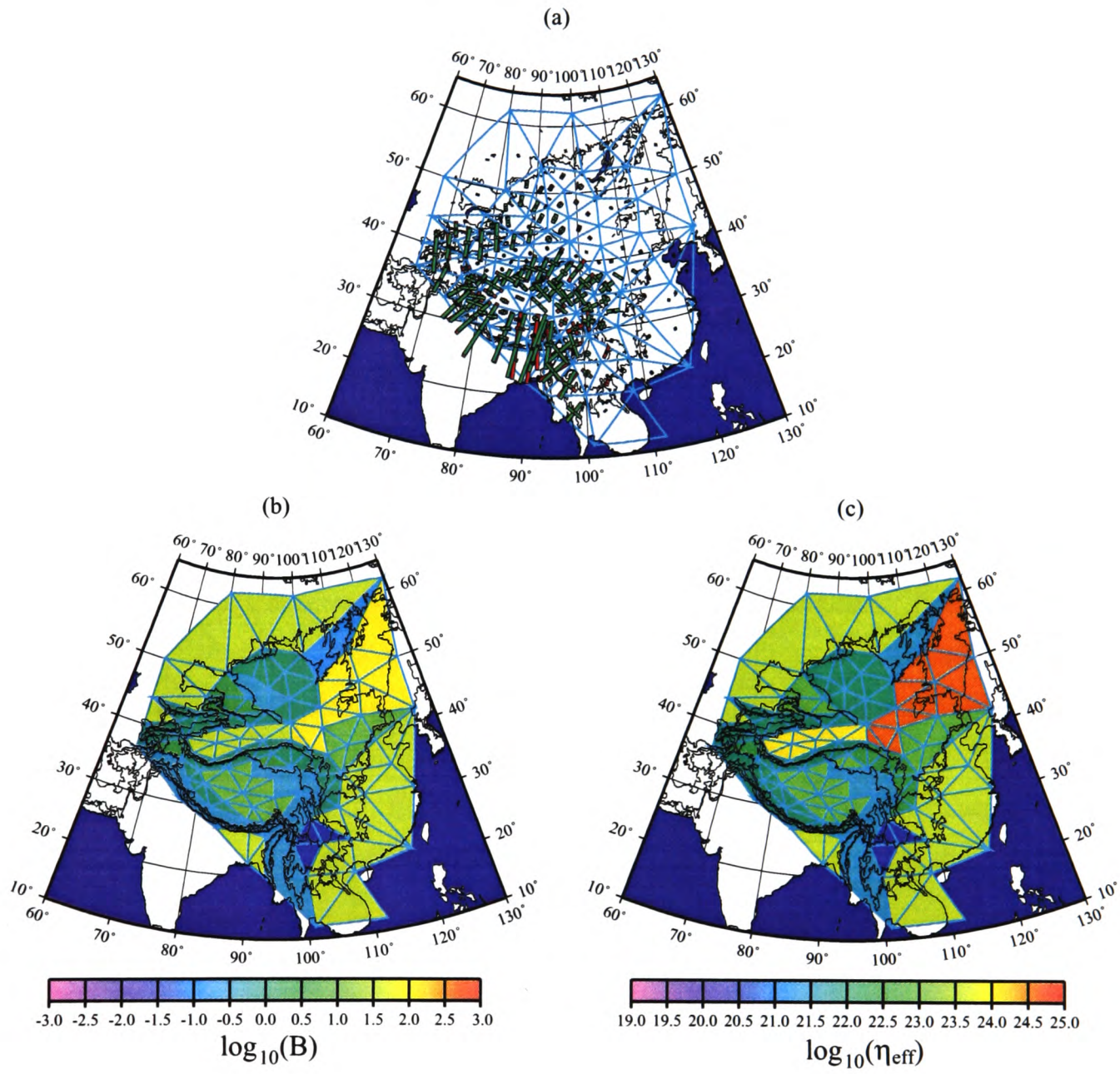

Figure 4.13: Results of forward calculation using $n = 1$, the IGS velocity field and the mean distribution of B from Experiment 1. (a) strain rates (b) $\log(B)$ (c) $\log(\eta_{\text{eff}})$.

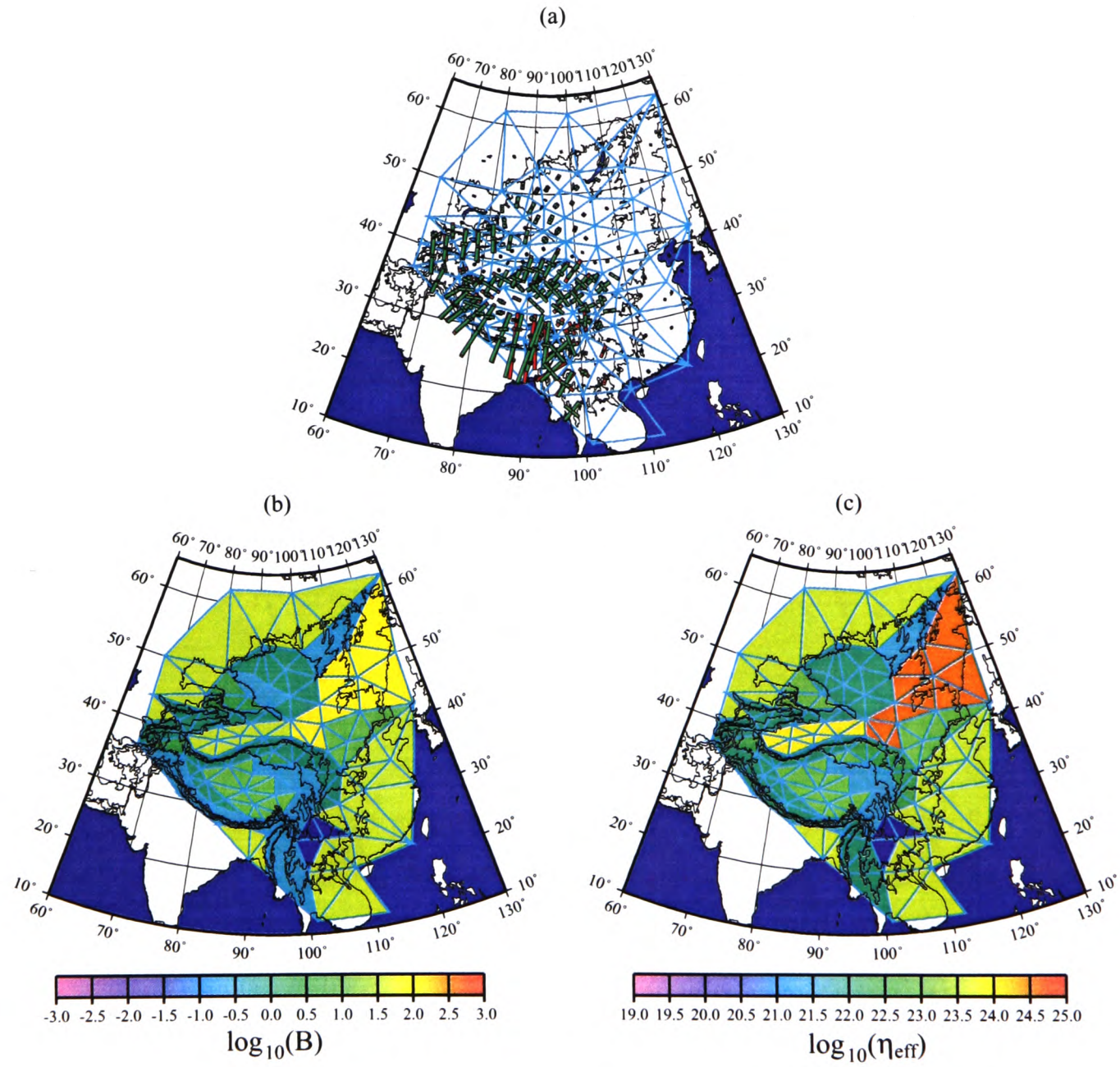

Figure 4.14: Results of forward calculation using $n = 1$, the IGS velocity field and the distribution of B from the solution with the smallest rms misfit from Experiment 1. (a) strain rates (b) $\log(B)$ (c) $\log(\eta_{\text{eff}})$.

predicted by the distributions of topography and potential energy. In the Red River fault system, the velocity gradient between northwards–translating India and the rigid south China block is accommodated on a narrow shear zone. A greater distribution of deformation is prevented by the stronger lithosphere to the east and west, and the low values of B in the Red River region reflect the difference in strength, rather than the absolute strength of the lithosphere. The same explanation may be applied to the zone accommodating relative motion between south and north China.

Topographic gradients are small in the Baikal region, and the region is far from both the India–Asia collision zone, and the subduction zones of the west Pacific. Reasons for the rapid strain in this region are discussed in section 4.2.3. Whether the deformation is due to a local mantle upwelling, or far–field boundary conditions, the low potential energy gradients in the model do not predict high strain rates, and the solution consequently assigns a low value of B.

The non–deforming regions of India, south China, and the Siberian craton are found to be stronger than actively deforming regions. Likely causes of the high values of B in the Ordos block and the Tarim basin are discussed in section 4.2.3.

Similar patterns of strength and effective viscosity are found in solutions of Experiment 2, but the absolute range of the distributions are smaller (see table 4.1), and lower effective viscosities are predicted for the slow–deforming regions surrounding the Tibetan plateau. The rate of convergence is underfit in the Tien Shan and, for the case of the mean solution, across the Himalaya (see Figures 4.15a and 4.16a). The model yields a greater SE–NW extensional component to the deformation in north–eastern Tibet than is observed, and the solution with the smallest rms misfit to the observed velocity field fails to reproduce components of strain pertaining to strike–slip deformation along the Altyn Tagh fault. The principal axes of strain rates south–east of the plateau are also poorly aligned with observed strain rates in the solution with the smallest rms misfit. The convergence criterion requires only that the mean value of $\dot{E}$ in each region lies within 1% of the observed value, and places no constraint upon the direction of the strain axes. The solutions to Experiment 2 consistently have a greater rms misfit to the velocity field; the poor alignment with observed strain rate axes arises from the perturbation of the velocity field as discussed above.

Figure 4.17 plots $\ln(B)$ against $\ln(\dot{E})$ for the four solutions of table 4.1. Data from the more rigid regions (Ordos block, Tarim basin, slowly deforming Asia) are highlighted in red, data from regions with anomalously low strength (Yunnan, Baikal) are highlighted in green. Deformation in the more rigid regions will not be governed by the same power law as deforming Asia, while the values of B obtained for the low strength regions may not be a true representation of the strength of these regions, as discussed previously. An approximate line of best fit has been drawn through the remaining data. In Figures 4.17a and 4.17b the gradient of the line is ~ -0.9, and in Figures 4.17c and 4.17d the

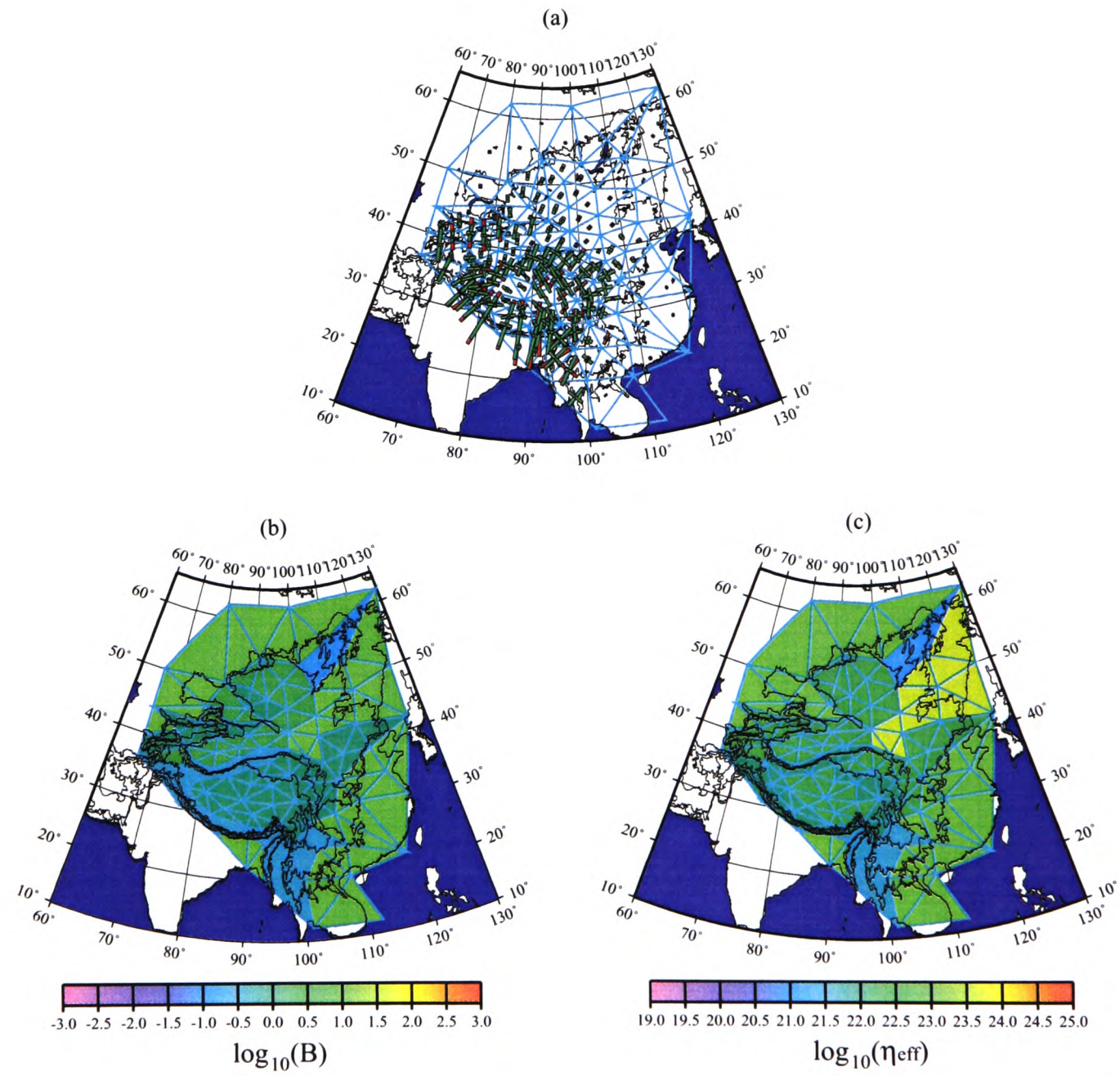

Figure 4.15: Results of forward calculation using $n = 1$, the IGS velocity field and the mean distribution of B from Experiment 2. (a) strain rates (b) $\log(B)$ (c) $\log(\eta_{\text{eff}})$.

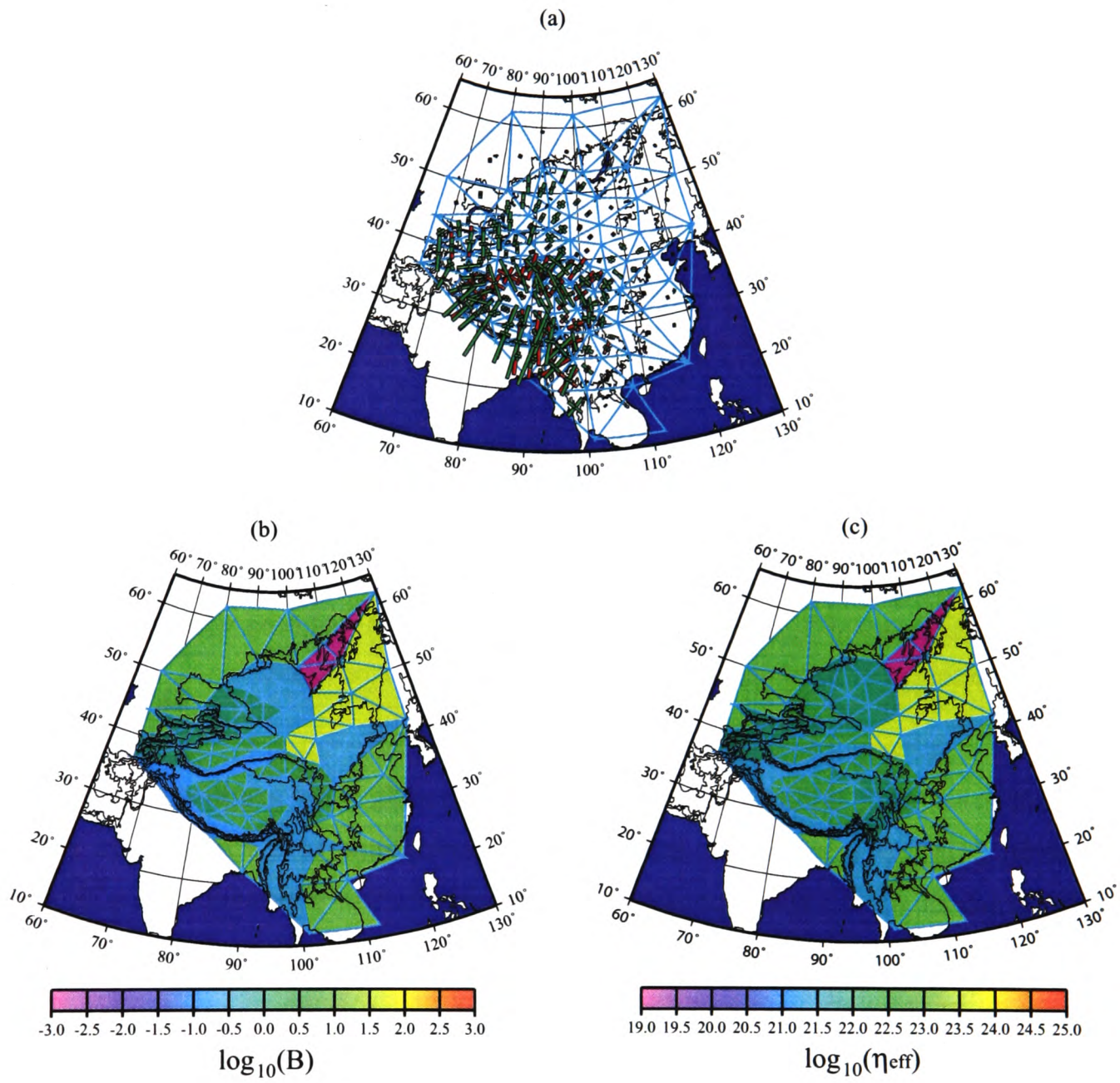

Figure 4.16: Results of forward calculation using $n = 1$, the IGS velocity field and the distribution of B from the solution with the smallest rms misfit from Experiment 2. (a) strain rates (b) $\log(B)$ (c) $\log(\eta_{\text{eff}})$.

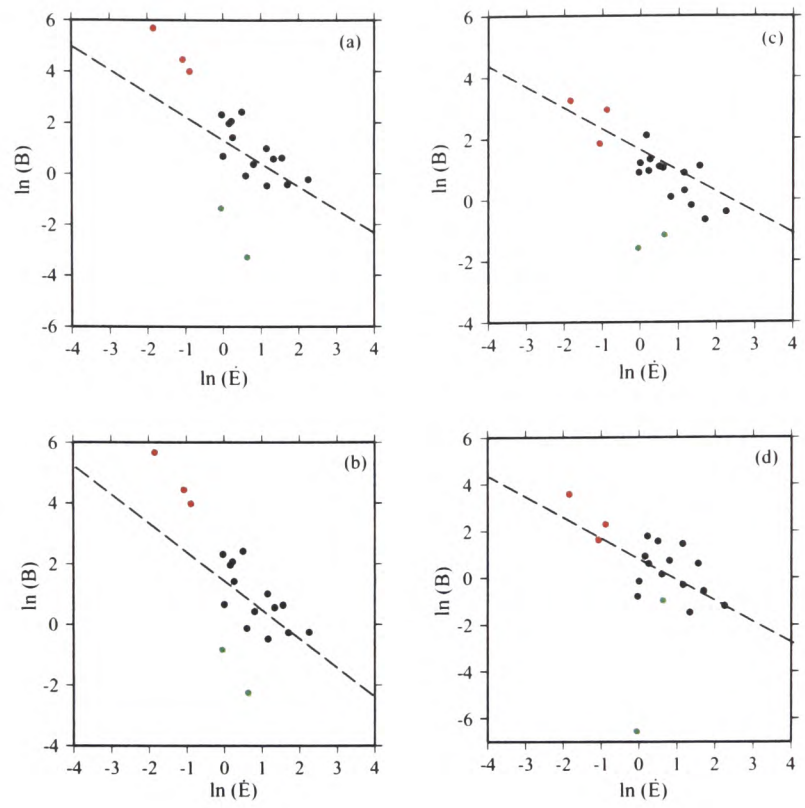

Figure 4.17: Plots of $\ln(B)$ against $\ln(\dot{E})$ for the four solutions of table 4.1. Red points represent data from the Ordos block, Tarim basin and slowly deforming Asia. Green points represent data from the Yunnan and Baikal regions. The dashed lines are an approximate line of best fit for the remaining data, represented by black points. (a) Experiment 1, mean solution. (b) Experiment 1, solution with lowest rms misfit. (c) Experiment 2, mean solution. (d) Experiment 2, solution with lowest rms misfit.

gradient is ~ -0.8. Following the analysis of chapter 2, these gradients may be equated to $(\frac{1}{n}-1)$ (see equation 2.93). A gradient of -0.9 therefore corresponds to a stress-strain rate exponent of $n = 10$, and a gradient of -0.8 corresponds to a stress–strain rate exponent of $n = 5$. The scatter of the data does not permit tight constraints to be placed upon the value of n by this method, and gradients corresponding to $n \approx 3$ up to $n \approx 16$ adequately fit the data.

4.4.3 Viscosity Inversions: $n > 1$

Experiments 1 and 2 are repeated using $n = 3$, $n = 5$ and $n = 10$ in the inversion calculations. The mean values of B for each experiment are given in table 4.2.

In the more rigid regions highlighted in section 4.4.2 values of B calculated in Experiment 1 decrease as n is increased. Throughout the rest of the solution domain, values of B either increase as n is increased, or remain roughly constant as n varies between 3, 5, and 10. The results of Experiment 1 therefore imply that the distribution of B is not strongly dependent upon n in the actively deforming regions of south–east Asia (compare Figures 4.22a–c and 4.23a–c).

Table 4.2: Mean strength parameters from non-linear viscosity inversions: $n = 3$, $n = 5$ and $n = 10$

Region	$n = 3$		$n = 5$		$n = 10$	
	Expt 1	Expt 2	Expt 1	Expt 2	Expt 1	Expt 2
1	28.27	15.16	21.25	11.47	21.21	19.23
2	1.00	0.88	2.03	0.52	4.25	0.71
3	7.64	8.14	7.90	6.95	9.50	10.97
4	40.03	9.17	27.08	7.91	24.29	12.94
5	4.51	5.04	4.14	4.68	4.53	6.63
6	15.61	10.23	13.25	10.25	13.74	10.44
7	4.20	2.45	4.62	2.54	5.88	5.81
8	2.70	1.10	2.75	1.50	3.27	2.45
9	4.67	2.75	4.38	2.63	4.89	4.65
10	6.79	5.32	6.46	6.09	7.31	7.67
11	91.83	16.11	58.61	13.79	49.89	22.45
12	0.41	1.10	0.68	1.09	0.95	1.34
13	2.29	5.71	2.63	5.95	3.43	5.30
14	3.60	5.10	3.66	4.30	4.36	5.66
15	3.68	5.16	3.80	5.38	4.61	5.06
16	11.42	3.33	9.88	2.86	11.08	4.93
17	10.463	5.61	9.16	4.48	9.83	5.08
18	6.73	5.51	5.98	3.78	6.47	5.80
19	12.67	10.98	11.16	10.24	11.83	13.61
rms velocity misfit (mm yr^{-1})	2.38	3.58	2.86	4.11	3.10	3.60

In solutions of Experiment 2, a smaller range of B describes the distribution of strength across south–east Asia (see Figures 4.24a–c). In particular, lower values of B are calculated for the more rigid regions surrounding the Tibetan plateau. The rms misfit to the velocity field for these solutions is again greater than for solutions to Experiment 1 (see table 4.2), due to the perturbation of the velocity data.

In both experiments extremely large values of B are obtained for several regions, including the Tarim basin, the Ordos block, Siberia and south China, where potential energy gradients imply that deformation should be taking place, but observed strain rates are negligible. According to the relaxation method of section 2.5.1, equation 2.76, the ratio $\dot{E}_{\text{calc}}/\dot{E}_{\text{in}}$ will always be greater than 1 in such a scenario, and therefore the updated value of B will always be greater than the previous estimate provided $n > 1$. The convergence criterion for the relaxation method specifies that model strain rates should lie within 1% of observed strain rates. In regions where the observed strain rates are infinitesimally small but potential energy gradients imply non–negligible model strain rates, the value of B may continue to increase virtually unbounded.

The coarsity of the finite element mesh also contributes to the lack of constraint upon B values, especially when vertices cross different tectonic regimes resulting in one node lying within a rapidly deforming region and one within a rigid region, e. g. around the edges of the Tarim basin. In such a situation it is difficult to classify the element into a single region, and the strain rates within the element will not accurately represent the situation in either region. It may not be possible to reproduce the strain rates for this element with the same value of B as for the other elements assigned to that region, resulting in 'runaway' solutions.

Effective viscosity distribution

Effective viscosity distributions for the six solutions of table 4.2 are plotted in Figures 4.18 and 4.20, and distributions for the solutions with the smallest rms misfit to the velocity field are plotted in Figures 4.19 and 4.21.

For Experiment 1 the distribution of effective viscosity is similar to that obtained in the $n = 1$ case; lower effective viscosities of 10^{21} to 10^{22} Pa s are found in regions with the greatest strain rates and steepest topographic gradients. Higher effective viscosities of $\sim 3 \times 10^{22}$ to 10^{23} Pa s are obtained for regions that deform at an intermediate rate, including the Tibetan plateau and Mongolian platform, and values of 10^{23} to 3×10^{24} Pa s are obtained for the Tarim basin and more rigid regions surrounding the Tibetan plateau.

The smaller Junggar and Qaidam sedimentary basins have an intermediate effective viscosity, sug-

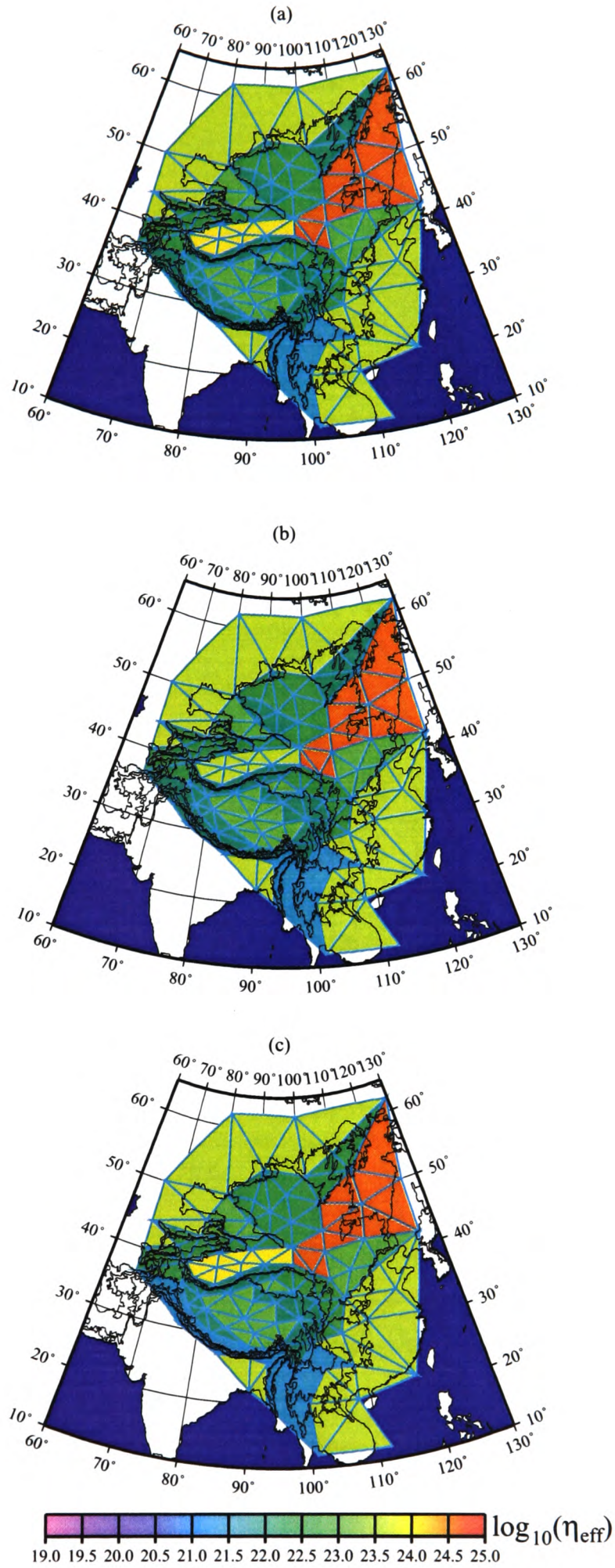

Figure 4.18: Log plot of the mean effective viscosity distribution; results from Experiment 1, using IGS velocity field. (a) $n = 3$ (b) $n = 5$ (c) $n = 10$

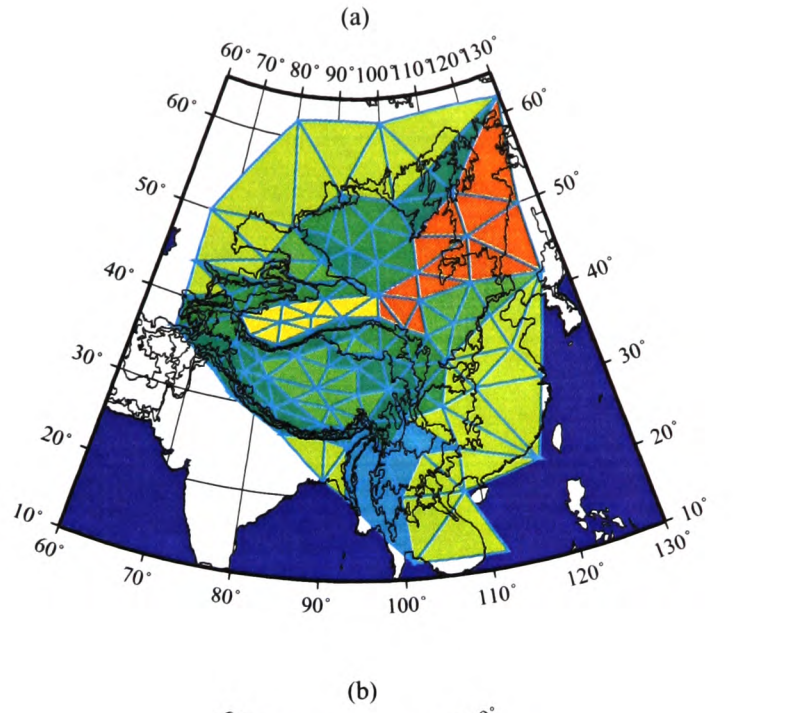

Figure 4.19: Log plot of the effective viscosity distribution for solutions with the smallest rms misfit; results from Experiment 1, using IGS velocity field. (a) $n = 3$ (b) $n = 5$ (c) $n = 10$

gesting that these basins are not underlain by such rigid lithosphere as the Tarim basin. However no data constrain deformation within these basins - there is no intermediate node in the centre of the basins, as there is in the Tarim basin - and the velocity field therefore reflects the total convergence across the whole basin. This convergence may be accommodated by thrusting at the edges of the basins, while the interior may be as resistant to internal deformation as the Tarim basin. Such details are not resolved in this study.

The value of effective viscosity across the Tibetan plateau is greater than values in neighbouring regions with steep topographic gradients. This reflects the contrast in strain rates and potential energy gradients between the plateau and its margins, rather than differences in absolute strength.

Anomalously high and low values of effective viscosity are found for the adjacent Ordos block and Baikal regions respectively; low values are also obtained for the region between the Ordos and South China blocks (region 16, Figure 4.6). These contrasts reflect the localisation of strain in areas of relatively weak lithosphere between older, more rigid blocks. The high strain rates in the bounding regions are not driven by gradients of potential energy, and the range of effective viscosity therefore indicates differences in the strength of the lithosphere. A similar interpretation may be applied to the range of effective viscosity determined for the Red River (region 8 in Figure 4.6), and surrounding regions.

In Experiment 2 values of effective viscosity calculated for deforming Asia (i.e. the Tibetan plateau and its margins, the Red River, Tien Shan, Gobi–Altai, Mongolian platform and Baikal regions) are in close agreement with values calculated in Experiment 1 (see table 4.2 and compare Figures 4.18–4.21). However, there is an order of magnitude difference between values obtained in Experiment 1 and Experiment 2 for the more rigid regions surrounding the Tibetan plateau, with lower values of 3×10^{22} to 3×10^{23} Pa s calculated for regions 1, 4, and 11 in Experiment 2. The vertically averaged effective viscosity is poorly constrained in these regions in both Experiment 1 and Experiment 2.

Solutions from Experiment 2 still demonstrate the first–order inverse relationship between strain rates and effective viscosity found in Experiment 1, but the greater rms misfit of the solutions indicates that they fail to accurately reproduce the observed deformation field. I therefore turn to the solutions of Experiment 1 to draw conclusions on the distribution of effective viscosity in south–east Asia. There is little variation in the vertically averaged effective viscosity distributions output by Experiment 1 (Figures 4.18 and 4.19), implying that this distribution is well constrained, and only weakly dependent upon n. I conclude that the deformation of south–east Asia may be approximated by the deformation of a thin viscous layer with a stress–strain rate exponent in the range $3 \leq n \leq 10$.

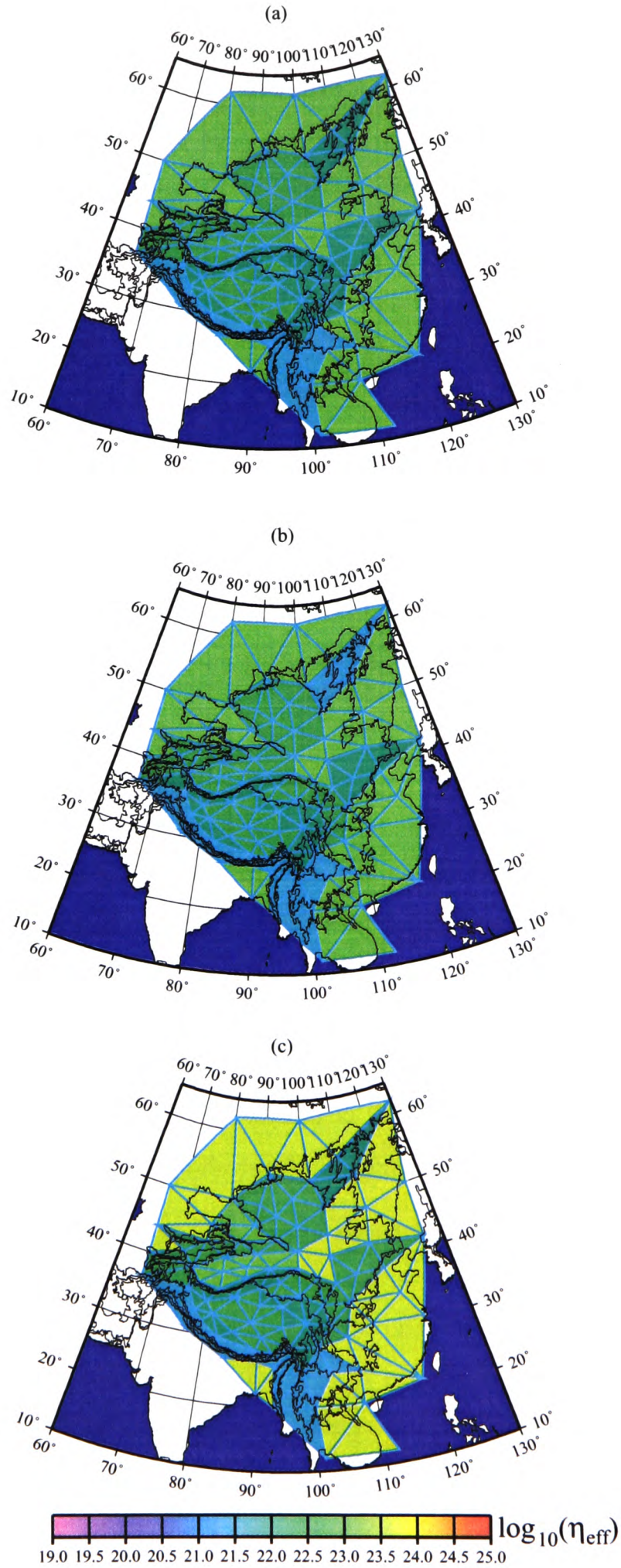

Figure 4.20: Log plot of the mean effective viscosity distribution; results from Experiment 2, using IGS velocity field. (a) $n = 3$ (b) $n = 5$ (c) $n = 10$

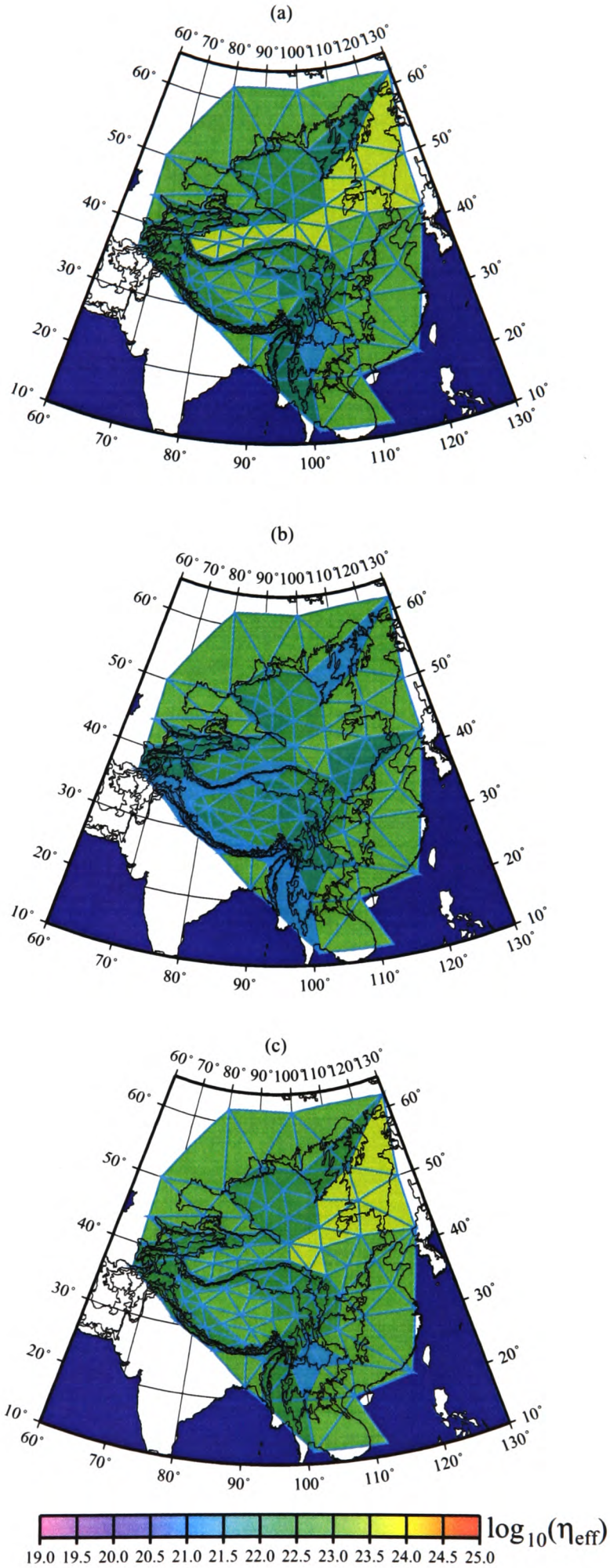

Figure 4.21: Log plot of the effective viscosity distribution for solutions with the smallest rms misfit; results from Experiment 2, using IGS velocity field. (a) $n = 3$ (b) $n = 5$ (c) $n = 10$

Strength distribution

For a value of n which is representative of the stress–strain rate exponent governing lithospheric deformation, the distribution of B represents lateral variations in the strength of the lithosphere. The distribution of B for the mean solution, and the solution with the smallest rms misfit, are plotted for each of the six cases outlined in table 4.2 in Figures 4.22–4.25. In all these solutions the strength parameter, B, approximately varies within one order of magnitude ($1 \lesssim B \lesssim 10$) across a large number of regions. A red boundary has been drawn around these regions on figures 4.22–4.25, and it is proposed that the regions contained within the boundary obey a power law rheology. This conjecture is supported by the good fit between observed strain rates and output from the numerical experiments throughout deforming Asia.

The values of B obtained for regions contained within the red boundary are similar for all solutions shown, implying that the large–scale distribution of lithospheric strength in deforming Asia is well constrained by these numerical experiments. The absolute value of B varies within an order of magnitude. Departures from this rule are discussed in section 4.5, and are found in regions with anomalously high strain rates in relation to the magnitude of the driving forces used in this study (e. g. regions 2 and 12 of Figure 4.6), and in regions which exhibit block–like behaviour (regions 1, 4 and 11 of Figure 4.6), as constrained by GPS studies (Holt *et al.*, 2000; Shen *et al.*, 2000; Wang *et al.*, 2001).

The approximately uniform strength of lithosphere which accommodates India–Asia convergence indicates that the spatial variation in strain rates, and hence vertically averaged effective viscosity, is a consequence of the distribution of potential energy gradients throughout the region. The distribution of buoyancy forces perturbs the velocity field principally constrained by velocity boundary conditions. Strain is currently localised in regions of high potential energy gradients. I postulate that the accommodation of strain has shifted with the evolution of the Tibetan plateau and its associated potential energy distribution, and that, with the exception of perturbations due to the presence of the Tarim basin, the growth of the plateau has not been influenced by small scale variations in the strength of the lithosphere.

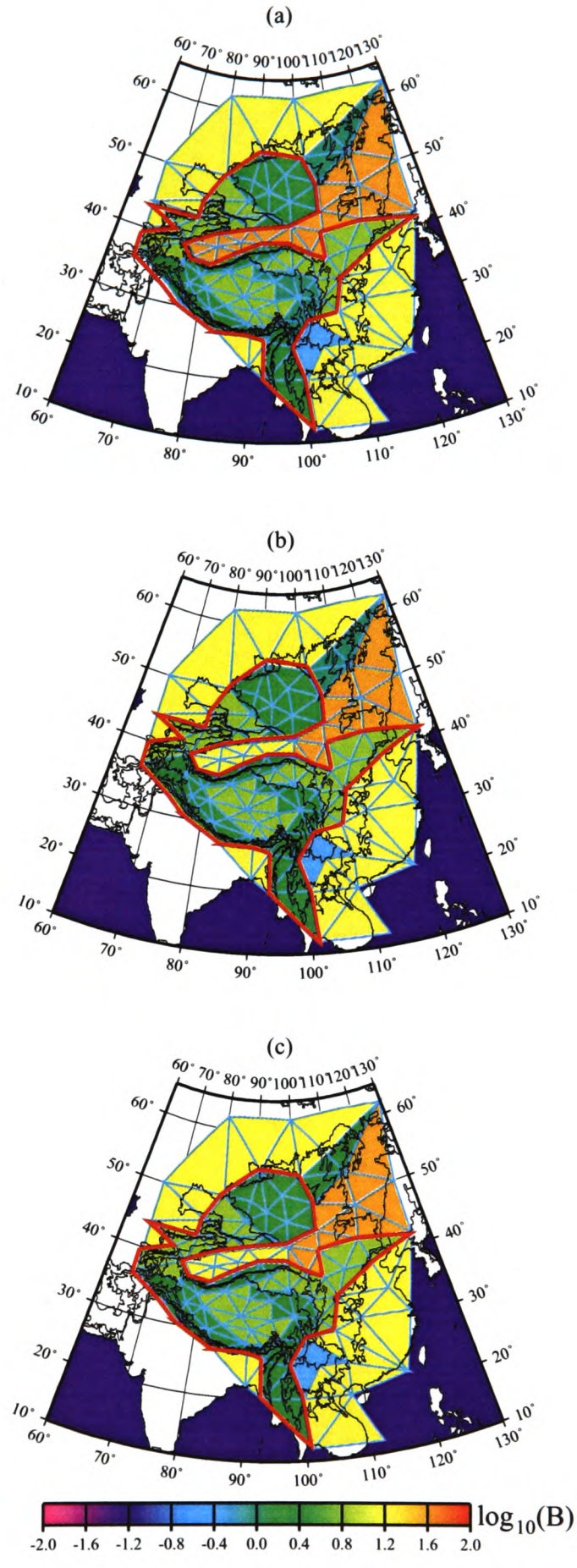

Figure 4.22: Log plot of the mean distribution of B; results from Experiment 1, using IGS velocity field. Red outline indicates regions considered to deform according to a power law rheology. (a) $n = 3$ (b) $n = 5$ (c) $n = 10$

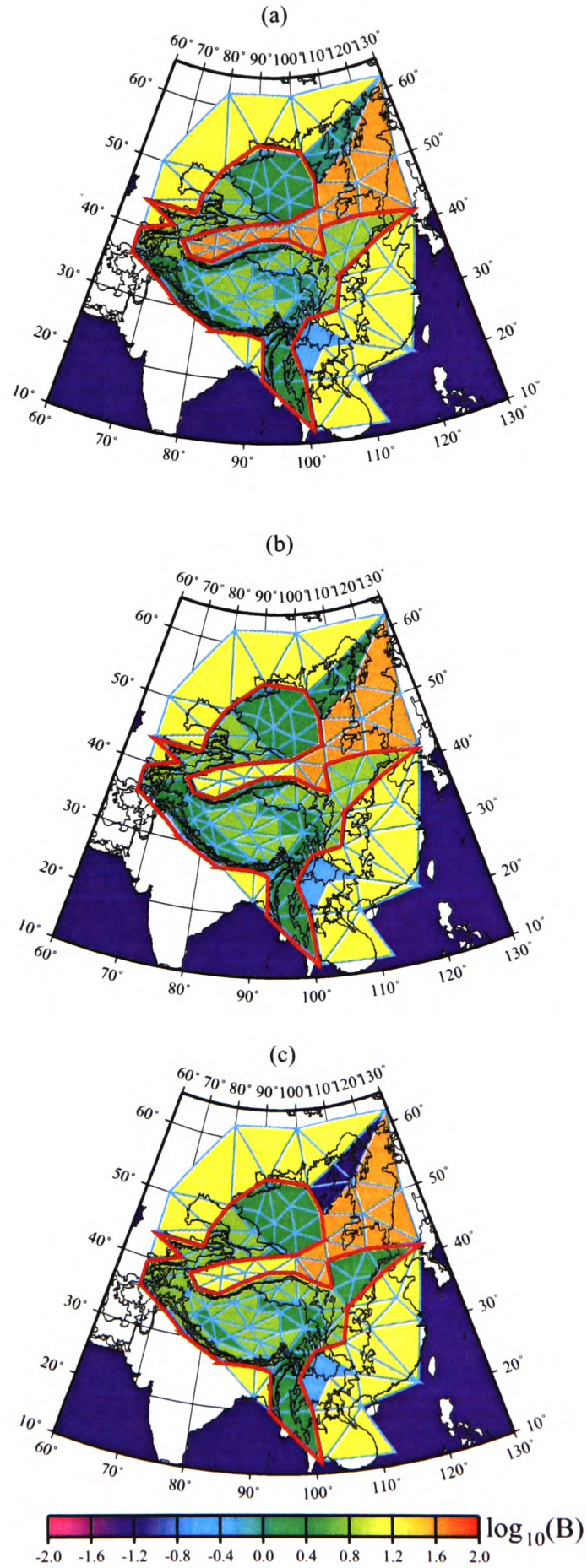

Figure 4.23: Log plot of the distribution of B for solutions with the smallest rms misfit; results from Experiment 1, using IGS velocity field. Red outline indicates regions considered to deform according to a power law rheology. (a) $n = 3$ (b) $n = 5$ (c) $n = 10$

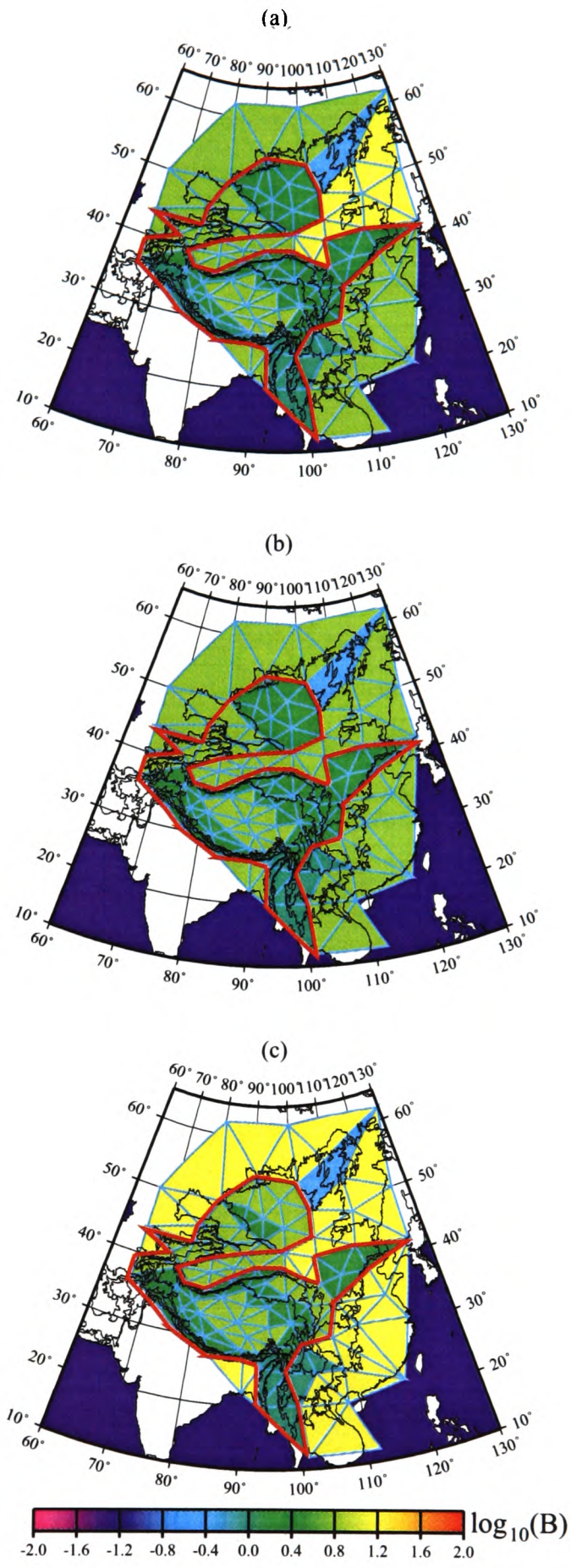

Figure 4.24: Log plot of the mean distribution of B; results from Experiment 2, using IGS velocity field. Red outline indicates regions considered to deform according to a power law rheology. (a) $n = 3$ (b) $n = 5$ (c) $n = 10$

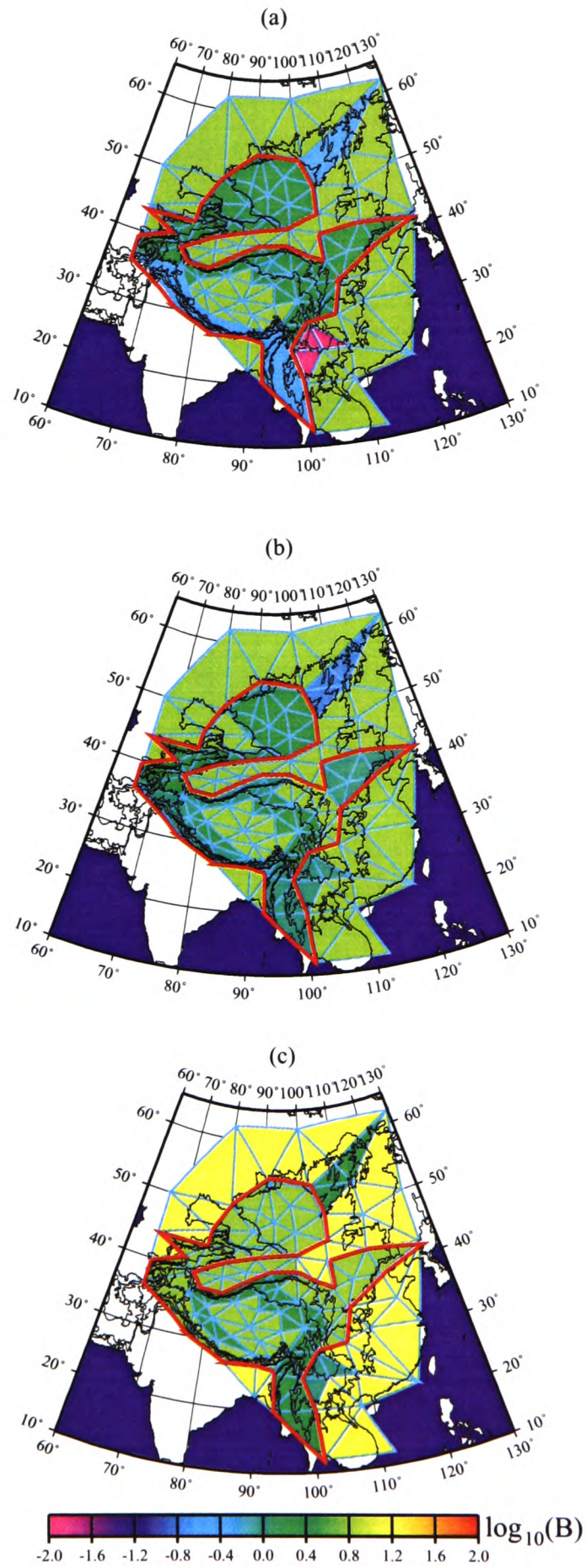

Figure 4.25: Log plot of the distribution of B for solutions with the smallest rms misfit; results from Experiment 2, using IGS velocity field. Red outline indicates regions considered to deform according to a power law rheology. (a) $n = 3$ (b) $n = 5$ (c) $n = 10$

4.5 Discussion

The lithosphere of south–east Asia may be broadly divided into regions which deform according to a viscous power law with a stress–strain rate exponent of $3 \leq n \leq 10$, and more rigid regions. Regions obeying the viscous power law seem to correspond to areas of actively deforming, younger, relatively hotter lithosphere. This trend is in agreement with the findings of Molnar & Tapponnier (1981), who correlate strength with low heat flux and the timing of the most recent orogenic activity.

Wang (2001) has shown that there is good correspondence between regions of high heat flux, and what are construed to be weak domains; i. e. regions undergoing rapid deformation. The relationship between high heat flux and fast strain rates may be attributed to the creep strength of olivine, which decreases as temperature is increased (Molnar & Tapponnier, 1981).

The age of the lithosphere becomes progressively older from south–west to north–east; from the Himalaya, across Tibet and the Tien Shan, to the Mongolian plateau. The magnitude of deformation within a non–linear viscous layer, arising from the motion of a rigid indenter (India), decreases with distance from the indenter (England *et al.*, 1985). This effect, combined with the increasing age and decreasing heat flux of the lithosphere, explains the general decrease in strain rates from south–west to north–east across south–east Asia.

The strength of the older, colder cratons of India, south and north China, the Tarim basin, and Siberia is confirmed by their lack of deformation, despite the stress applied at their boundaries. Relative motion between the south and north China blocks is preferentially taken up in a narrow zone between the older portions of lithosphere. The transition from strong to weak lithosphere adjacent to India and the Tarim basin is highlighted by steep topographic gradients and active thrusting at their boundaries. The Tarim basin is bounded by steep gradients to both the south and north. It acts as a stress guide, transferring stress from the India–Asia collision across to the Tien Shan, where the convergence continues to be accommodated by rapid shortening of the weaker lithosphere (Neil & Houseman, 1997).

High strain rates across the margins of the Tibetan plateau imply regions of low effective viscosity. The concentration of strain in these regions arises principally due to the presence of stronger lithospheric domains – the Indian plate and the Tarim basin – and not because this lithosphere is inherently weaker. The rigid domains limit the extent of deformation, causing lithospheric thickening and the development of potential energy gradients across the topographic boundaries. Larger buoyancy forces are therefore applied across these regions, and the lithosphere responds by deforming more rapidly.

Strain rates in the Baikal region are proportionally high considering the distance of this region from

the collision zone between India and Asia. The surface heat flux in this region is not anomalously high (Lysack, 1992; Poort & Klerkx, 2004), but high enough for the lithosphere to be slightly weakened. Deformation is localised here in preference to the surrounding stronger cratons, and this fact, combined with the lack of potential energy gradients due to variations in crustal thickness across this region, results in the low values of effective viscosity predicted by the numerical experiments.

Low strength is also predicted in the Yunnan. Recent high resolution GPS studies in this region (Wang *et al.*, 2001; Zhang *et al.*, 2004) reveal the rotation of lithospheric material around the Eastern Himalayan Syntaxis. The finite element mesh used in the numerical experiments of section 4.4 is unable to resolve this rotation, and instead attributes the different directions of nodal velocity vectors to high strain rates within the elements of this region. Strain in this region is not simply accommodated by convergence or extension of the lithosphere, but by deformation which may be approximated by the rotational flow of a viscous fluid. Such rotational deformation does not require the presence of very weak lithosphere, and the effective viscosity determined by the model is too low. A finer mesh is required to gain further insight into the dynamics of this region.

4.6 Conclusions

The velocity and strain rate fields of south–east Asia are successfully recovered by approximating the lithosphere to be a layer of non–Newtonian viscous material which deforms according to a viscous power law with a stress–strain rate exponent of $3 \leq n \leq 10$. Large values of n ($n \geq 5$) are implied following comparisons of the relative strength of the lithosphere with average strain rates in each tectonic region in section 4.4.2, but the distributions of data in figure 4.17 do not allow tight constraints to be placed upon the value of n, and further work is required to establish the relationship between lithospheric strength and observed strain rates.

A strong negative correlation between strain rates and vertically averaged effective viscosity is found throughout south–east Asia. The effective viscosity of the Precambrian shields is poorly constrained, and lies in the range $10^{23} - 3 \times 10^{24}$ Pa s. Rapidly deforming regions, with strain rates $>\sim 3 \times 10^{-8}$ yr^{-1}, are found to have a vertically averaged effective viscosity of $10^{21} - 10^{22}$ Pa s, and regions which deform at $\sim 1 - 3 \times 10^{-8}$ yr^{-1}, including the Tibetan plateau (Zhang *et al.*, 2004), have a vertically averaged effective viscosity of $3 \times 10^{22} - 10^{23}$ Pa s. The distribution of strength throughout deforming south–east Asia varies within one order of magnitude, implying that the distribution of deformation is constrained by gradients of potential energy, and not variations in lithospheric strength.

Chapter 5

Transcurrent Deformation of the western North America plate boundary zone

5.1 Introduction

Pacific–North America motion is accommodated by distributed deformation that extends across a region several hundred kilometres wide (Figure 5.1), demonstrating the inadequacy of plate tectonics for explaining the behaviour of the continental lithosphere under stress. Although modern geodetic techniques have increased the accuracy to which the kinematics of lithospheric deformation may be described, the dynamics of this motion are still far from understood.

The motion of the stable interior of North America may be described by a single vector, that describes the rotation of a rigid plate about an axis passing through the centre of the Earth (Dixon *et al.*, 1996; Argus & Gordon, 1996). Relative motion across the Pacific–North America plate boundary in the region of central California is 52 ± 2 mm yr^{-1} (DeMets & Dixon, 1999), along an azimuth of N36° $\pm$ 2°W (DeMets *et al.*, 1987, 1990). From the northern end of the Gulf of California to the Mendocino Triple Junction most of this plate boundary zone is characterised by transcurrent deformation stretching more than 100 km inland from the western edge of the continent, taken up at the surface by several faults (Lisowski *et al.*, 1991; Bennett *et al.*, 1996, 1999). Within central California, about 39 mm yr^{-1} of this motion is accommodated across a narrow zone containing the San Andreas fault system and the central California Coast Ranges (Argus & Gordon, 2001). Immediately to the east of this narrow zone of deformation lies the aseismic 100 km by 700 km Sierra block.

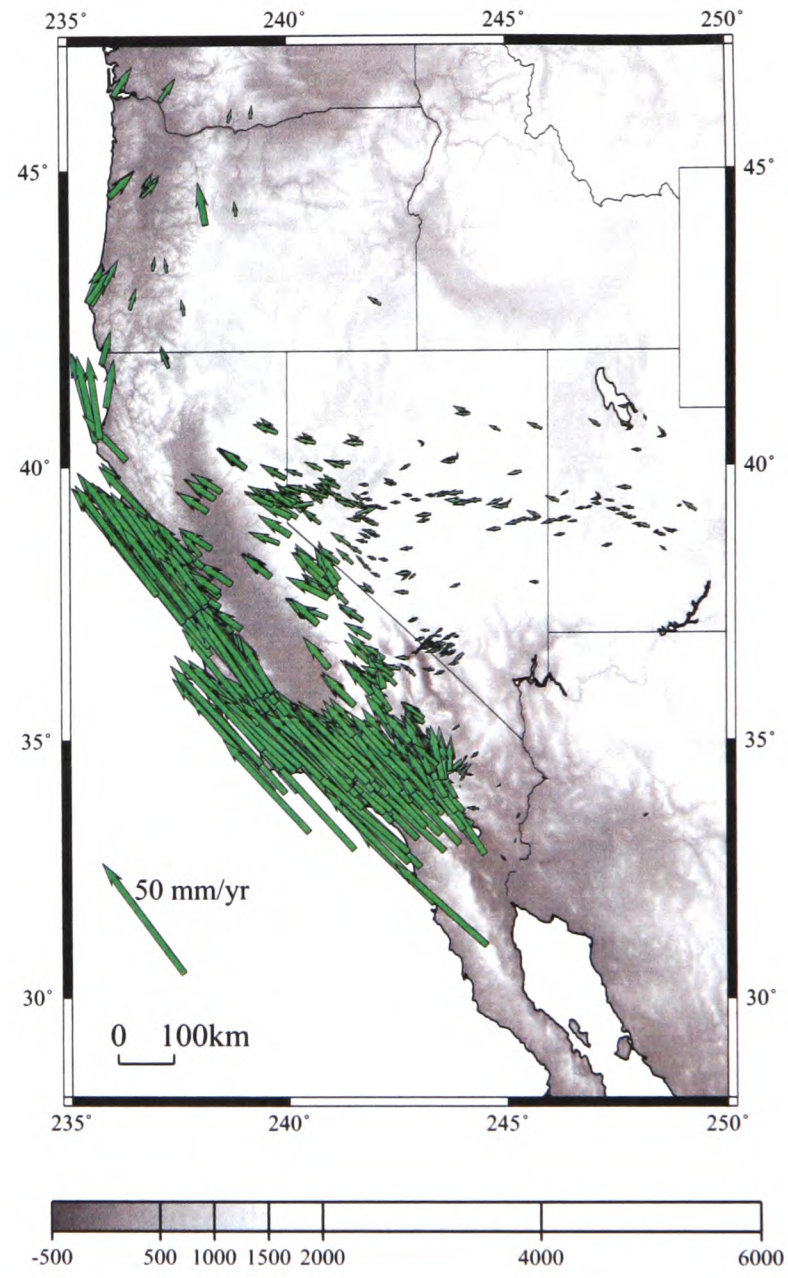

Figure 5.1: GPS velocities for the Pacific–North America plate boundary zone, velocities are relative to stable North America. (Data from United States Geological Survey (USGS) and Jet Propulsion Lab (JPL) websites: http://quake.wr.usgs.gov/research/deformation/gps/auto/CL.html and http://sideshow.jpl.nasa.gov/mbh/series.html)

Recent geodetic studies have established that the motion of the Sierra block may independently be described by rigid body rotation (Dixon *et al.*, 2000). Estimates for the velocity of this block relative to stable North America range between 10 mm yr^{-1} and 15 mm yr^{-1} (Argus & Gordon, 1991; Hearn & Humphreys, 1998; Argus & Gordon, 2001; Dixon *et al.*, 2000), in a direction that is nearly parallel to the relative motion of the Pacific plate (Dixon *et al.*, 2000; Argus & Gordon, 2001). There is no evidence of rapid rotation of this block about a proximal pole (Dixon *et al.*, 2000).

The stress state and distribution of deformation in California have been addressed by many authors, and there has been success in describing aspects of this deformation both using block models (e.g. Luyendyk *et al.* (1980); McClusky *et al.* (2001); Bird & Rosenstock (1984)), and models that regard the continental lithosphere as a continuously deforming medium (e.g. Bird & Piper (1980); Sonder *et al.* (1986); Jones *et al.* (1996); Flesch *et al.* (2000)). The thin viscous sheet model (England & McKenzie, 1982) has been successful in describing many first–order observations of continental deformation in a transcurrent environment (Sonder *et al.*, 1986), however questions still remain as to the relative importance of boundary forces and buoyancy forces in driving the deformation of the continental lithosphere (Jones *et al.*, 1996; Flesch *et al.*, 2000). Several studies have investigated the role of rheological contrasts within zones of continental deformation (e.g. Vilotte *et al.* (1984); England & Houseman (1985); Neil & Houseman (1997); Malservisi *et al.* (2001); Choi & Gurnis (2003); Dayem *et al.* (2003)), but none has produced a quantitative description of the relative motion of a strong plate–like region embedded within a tectonically active continuously deforming medium. In my work, I employ the thin viscous sheet model, and investigate the effect of placing a relatively rigid block within an otherwise homogeneous viscous fluid layer undergoing simple shear. I also aim to constrain lithospheric rheological parameters for this region of continental deformation. Results from numerical experiments are compared with analytical solutions for the motion of a rigid block within a simple shear flow, and also to velocity profiles of present–day motion in western North America.

5.2 The Sierra Block

In this investigation I treat the Sierra block (see Figure 5.2) as a rigid, or highly viscous, region within the deforming lithosphere of western North America. The justifications for this assumption are outlined within a brief review of the geological and tectonic setting of the western North America plate boundary zone below.

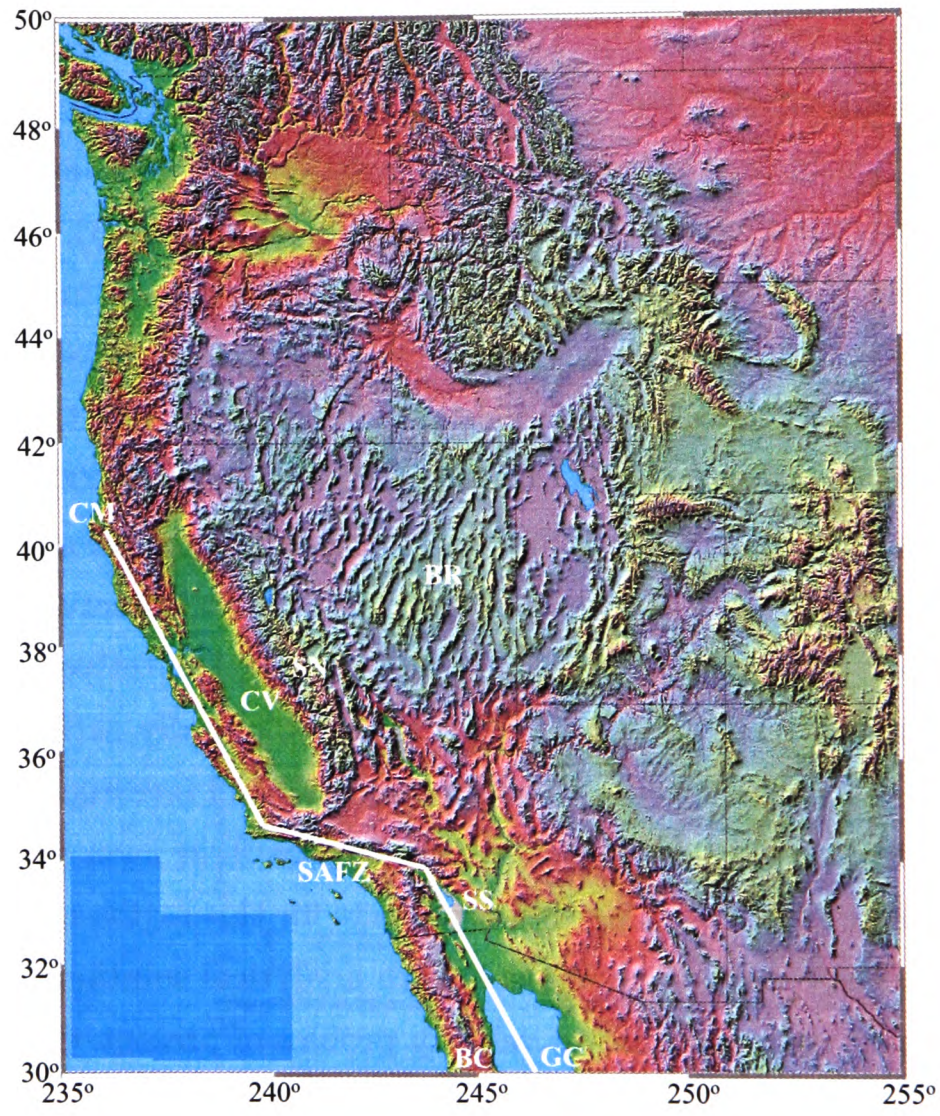

Figure 5.2: Shaded Relief for western North America, with lighting from the north–west. The Sierra block consists of the Central Valley (CV) and the Sierra Nevada (SN). Other regions referred to in the text are Cape Mendocino (CM), the San Andreas Fault Zone (SAFZ), the Basin and Range Province (BR), the Salton Sea (SS), Baja California (BC) and the Gulf of California (GC). (Andrew D. Birrell, copyright ©1994–2002)

5.2.1 Geological Setting

During the Mesozoic and Early Cenozoic, the coastal margin of western North America was an Andean–type continental margin. It has subsequently been modified by Late Cenozoic strike–slip faulting along the San Andreas fault zone, and by the uplift of the Sierra Nevada. Following little activity during the Late Paleozoic and Early Mesozoic, the main growth of the continent took place during the Mesozoic (248 to 65 Ma), during which time the margin grew by the accumulation of material from the south–west, transported towards North America mainly upon oceanic lithosphere, and emplaced during the subduction of this lithosphere. These terranes, which now form the west coast of North America, are of varying origin and were emplaced under a range of conditions.

During and following collision many of the terranes were deformed, so the present–day configuration of the terranes in North America, many of which have been elongated parallel to the plate boundary (Jones *et al.*, 1982), suggests oblique convergence dominated at this plate boundary.

The accreted material of North America consists mainly of oceanic lithosphere and island arc material which was not subducted during collision. This may have been due to the complex geometry of the terranes, an increased level of buoyancy due to great sedimentary thickness, or the age of the lithospheric material. Oceanic crust thickens and cools with age, and once emplaced would have resisted deformation more strongly than material of continental origin.

The currently non–deforming Sierra block consists of two major domains; the Central Valley of California, and the Sierra Nevada mountains (see Figure 5.2). The basement consists of a large region of competent Paleozoic and Mesozoic metamorphic and plutonic material which has undergone little deformation during the Cenozoic. This material consists mainly of dense mafic and ultramafic rocks which resemble oceanic crust (Wong *et al.*, 1988).

The Central Valley formed as a forearc basin around ~100 Ma, between a subduction zone to the west, and volcanic activity to the east. It has been topographically flat and low in altitude throughout its existence. To the west, between the Coast Ranges and the Sierra block, thick sediments cover the boundary between the rigid crystalline basement of the Sierra block and the comparatively ductile Franciscan complex of the Coast Ranges. Low seismic velocities of 1.6 km s^{-1} to 4.1 km s^{-1} indicate a sedimentary thickness of 12 km (Fliedner *et al.*, 2000), the crystalline basement layer below consists of several layers of increasing seismic velocity, and the Moho is well–constrained at 27 km (Fliedner *et al.*, 2000).

The sedimentary layers show strong lateral continuity, but the Quaternary alluvial deposits at the top of the Central Valley sequence have been deformed into a broad, asymmetric syncline, and the presence of lacustrine and alluvial (non–marine) deposits several hundreds of metres below sea level

suggests that sediment accumulation has been synchronous with basin subsidence. Some of this subsidence may be attributed to sediment loading and compaction. However, Dupre *et al.* (1991) suggest that the convergent component of the relative motion between the Pacific and North America plates has caused the tilting of the Sierra block to the west, along a hinge line lying approximately along the eastern margin of the Central Valley, resulting in a thickening of the Central Valley sequence to the west. This tilting has also been attributed to the convective removal of mantle lithosphere from beneath the Sierra Nevada since $\sim$ 10 Ma (Molnar & Jones, 2004). The axis of the syncline lies towards the western margin of the Central Valley, and may be the surface expression of the western boundary of the competent basement rock of the Sierra block.

The Sierra Nevada itself is a batholith of dominantly Cretaceous granitic rock, formed during the Mesozoic underthrusting of oceanic material at the plate margin to the west. This magmatic arc has subsequently been left behind during the general trend of northward shearing which has dominated since $\sim$15 Ma.

Seismic and gravity data have been used to constrain crustal thicknesses for western North America (Mooney & Weaver, 1989) (Figure 5.3). The crust is around 20–25 km thick throughout the Coast Ranges and the San Andreas Fault Zone, it then thickens from $\sim$20 km beneath the western Central Valley (Oppenheimer & Eaton, 1984) to 40–50 km beneath the Sierra Nevada (Hill *et al.*, 1991). There is continued debate as to the thickness of the crustal root beneath the Sierra Nevada, with some authors suggesting thicknesses of up to 55km. To the east, the crust thins again to $\sim$20 km beneath parts of the Great Basin, while to the north, in the region of the Mendocino Triple Junction, the crust thins to $\sim$10 km behind (south of) the subducting Gorda slab, before abruptly thickening to 30 km at the southern edge of the slab.

Crustal thickness does not closely correlate with surface topography across this region (Gilbert & Sheehan, 2004); for example, seismically constrained crustal thicknesses across the Great Basin are much smaller than values obtained by considering elevation as a proxy for crustal thickness, and assuming Airy isostasy (Humphreys & Dueker, 1994). Crustal density variations contribute to the departure from the crustal thicknesses predicted by isostatic arguments, but a mantle component is also required to support the high elevations across the western United States. The discrepancy between predicted and observed crustal thickness is attributed to a broad region of anomalously buoyant upper mantle lying beneath much of western North America, from the Great Basin to the Rocky Mountain Front.

Surface heat flow across the 250 km–wide plate boundary zone is generally lower than the North America average of $\sim$ 60 mW m^{-2} (see Figure 5.4). High heat flow is observed in the Coast Ranges, partly due to the batholithic origin of the crust in this region, but also due to ongoing deformation

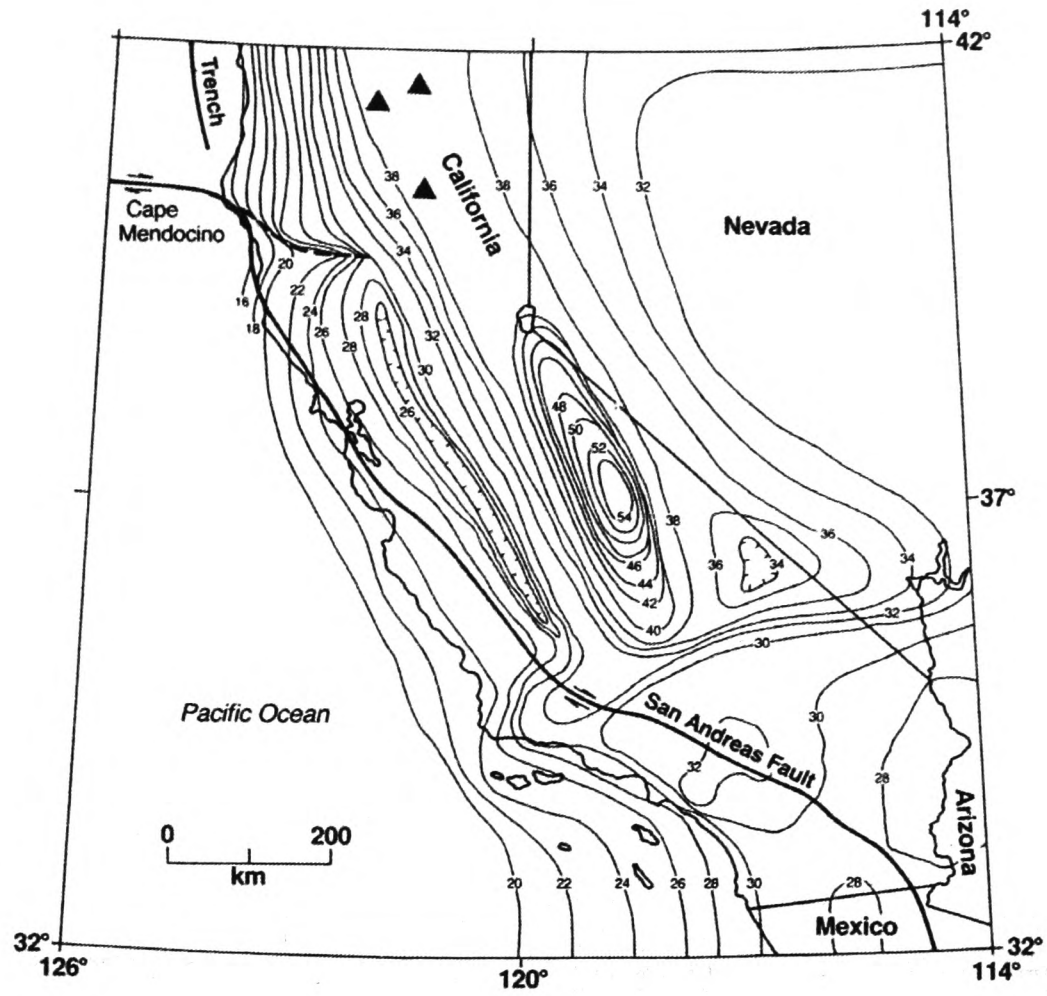

Figure 5.3: Contour map of crustal thickness for California derived from seismic refraction, seismic reflection and gravity data. Solid triangles are volcanos. Estimated error is 10%. Taken from Mooney and Weaver, 1989.

across the region. There is a narrow zone of low surface heat flow associated with the Transverse Ranges of California, and a region of very low heat flow, 31 mW m^{-2} (Humphreys & Dueker, 1994), coincides with the location of the Sierra block. Fast P–wave velocities are also found beneath this region (Humphreys & Dueker, 1994). To the east of the Sierra block there is a sharp rise in surface heat flow at the edge of the East California Shear Zone (ECSZ), which is maintained throughout the Basin and Range Province. I interpret the low temperature, high velocity anomaly beneath the Sierra block to imply that this region is stronger than the surrounding lithosphere.

5.2.2 Seismicity and Tectonics

Motion at the plate boundary in California shifted from oblique subduction to dextral shear around 15Ma, and much of the relative plate motion has since been accommodated along the San Andreas and parallel faults. Strike–slip faulting and related deformation extends across California and Nevada to the Basin and Range Province, 300 km inland.

The spatial distribution of seismicity in western North America is more diffuse than in the oceanic

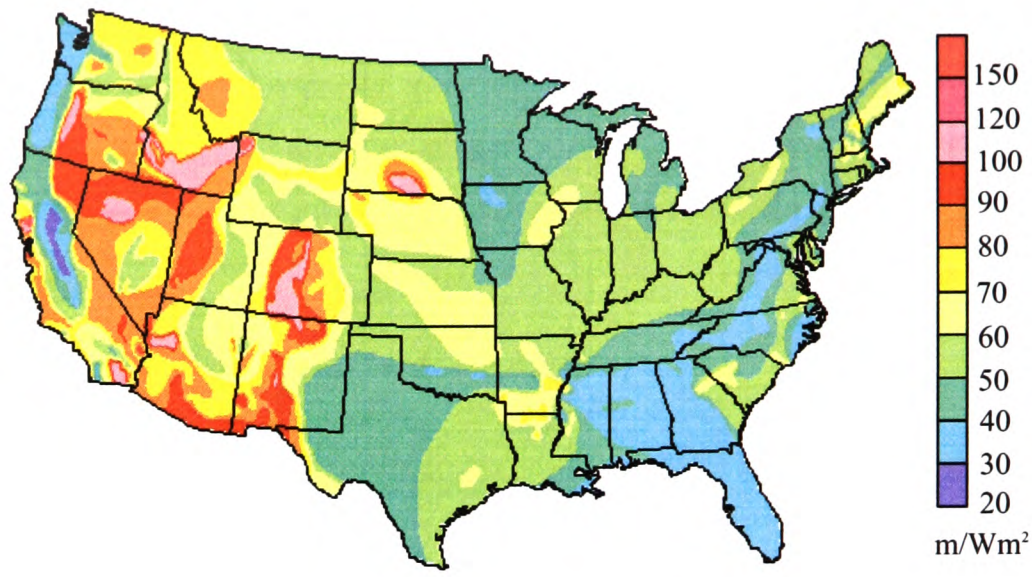

Figure 5.4: Surface Heat Flow for North America taken from http://www.smu.edu/geothermal/heatflow

crust, but distinct patterns can be detected throughout the region. In Figure 5.5 the location of all earthquakes of magnitude >3.0 since 1980 are plotted. Two bands of seismicity can be identified; one adjacent to the coast and one which branches off at (242°E, 35°N) to form a parallel band of seismicity to the west of the Sierra Nevada. The central, weakly seismic, region coincides with the location of the Sierra Block. Within the seismic bands, linear trends indicate activity along predominantly strike–slip faults, while clusters of microactivity are related to local geothermal fields or volcanic activity, the most active of these being the Long Valley caldera at ($\sim$ 241°E, 37.5°N) (Dreger *et al.*, 2000). To the south, seismicity continues along a clearly defined line within the Gulf of California, and almost no seismic activity is observed to the west of Baja California. To the north of the Mendocino Triple Junction, the subduction of the Gorda slab in a north–northeasterly direction is clearly outlined by seismicity within the downgoing slab and along the transform zone between the Gorda and Pacific plates.

The more westerly band of seismicity lies along the San Andreas fault zone. 34 ± 3 mm yr^{-1} of transcurrent plate boundary motion is taken up across this 50–150 km–wide region (Hill *et al.*, 1991). If all plate relative motion between the Pacific and North America had been taken up along the San Andreas fault since 15 Ma, this would amount to a total displacement of $\sim$500 km. Such displacements are not observed, and motion across the plate boundary zone is in fact accommodated on a large number of sub–parallel faults (see Figure 5.6).

Within the diffuse band of seismic activity there is quiescence along the rupture zones of great historic earthquakes, including the 1906 San Francisco earthquake and the 1857 event south of Parkfield. Dense clusters of epicentres in central California mark actively creeping sections of the San Andreas fault where the accumulation of interseismic strain is negligible, while sparse activity to the south and

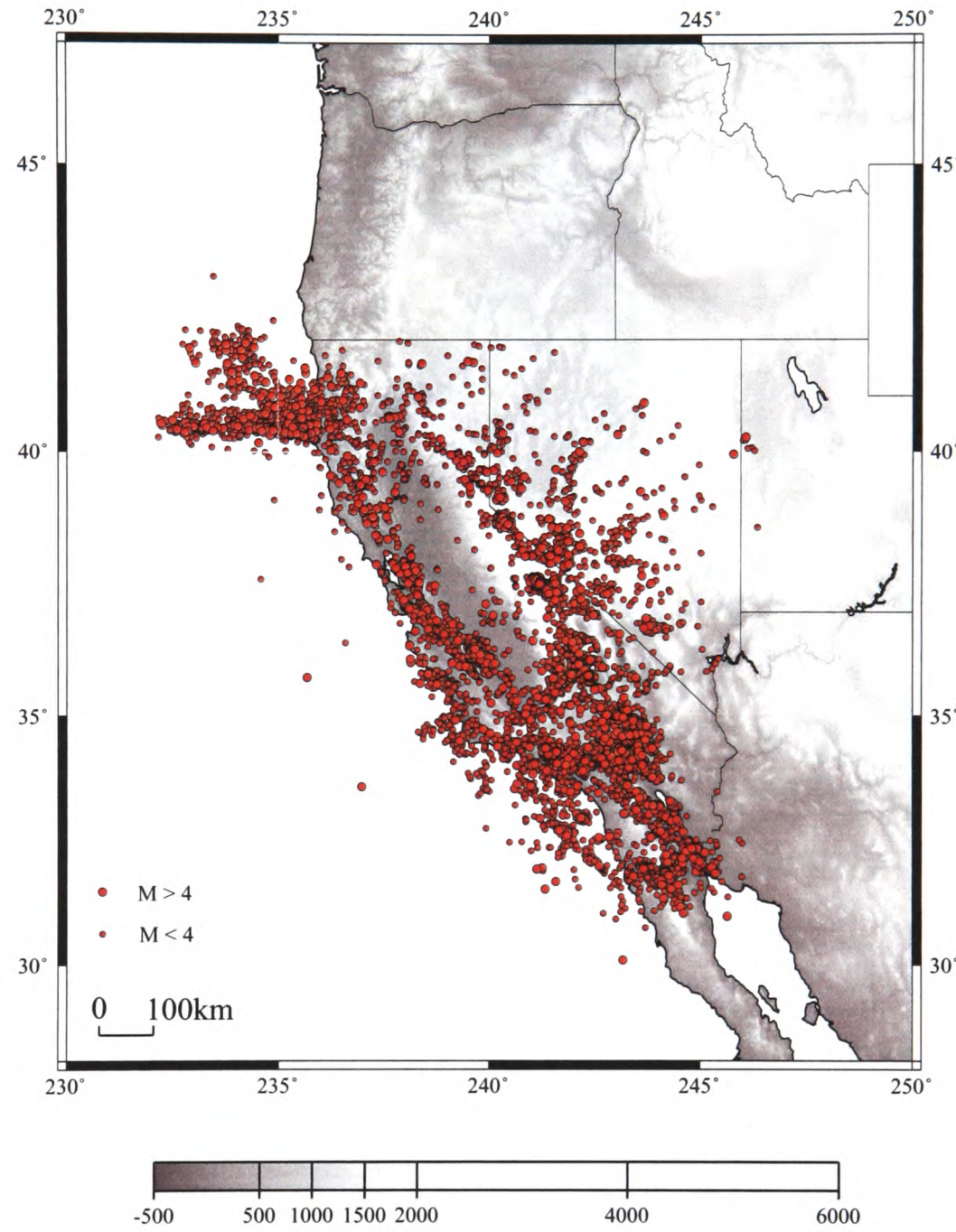

Figure 5.5: Seismicity of western North America: 1980–present, magnitude > 3.0 (Source: the Northern California Earthquake Data Center, including the Northern California Seismic Network (USGS) and Berkeley Seismological Laboratory, and the Southern California Earthquake Data Center, including the Southern California Seismic Network)

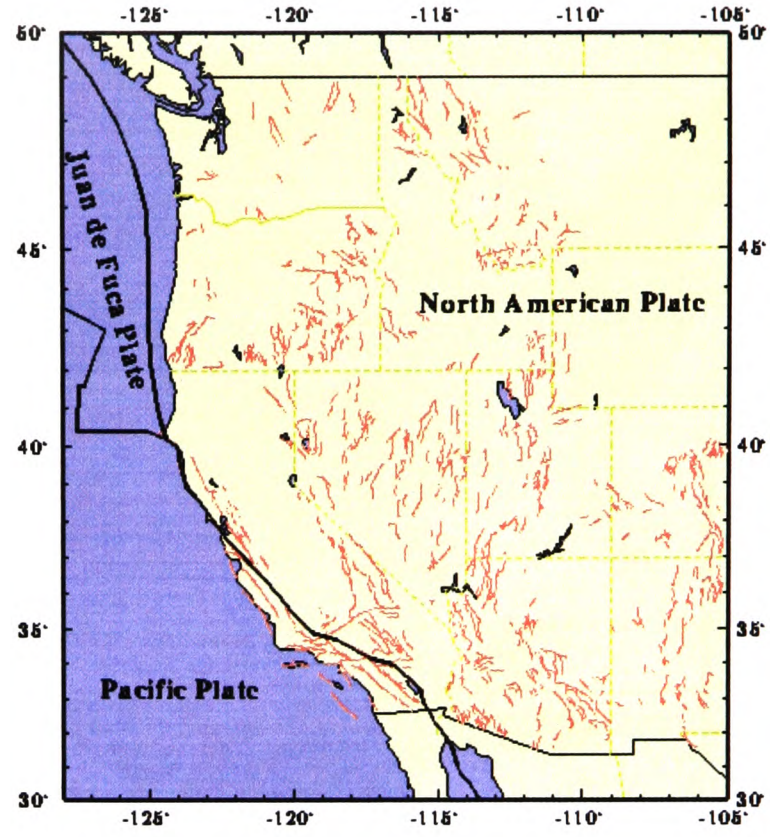

Figure 5.6: Fault map for the western United States

north indicates that the sections corresponding to the 1906 and 1857 earthquakes are currently locked, and accumulating shear strain at several tenths of microstrain per year. The vertical alignment of hypocentres throughout the region (Hill *et al.*, 1991) suggests dips of between 70° to the west and 80° to the east throughout the San Andreas fault zone.

East of the San Andreas fault, but west of the Central Valley, a small compressive component is observed in many earthquakes throughout the Coast Ranges. There is evidence for young folding throughout the Coast Ranges, and thrusting along both flanks at 4–13 mm $^{-1}$ (Wong *et al.*, 1988). These observations are explained by the misalignment of the San Andreas fault by 3 to 5° anti–clockwise with respect to the orientation of the Pacific–North America plate boundary (see Figure 5.6). There may also be a small compressional component applied by the ESE–WNW extension of the Basin and Range Province in the east, as stress is transferred across the rigid Sierra block.

It is difficult to determine precisely the compressional component of deformation at the plate boundary due to slip partitioning. The localisation of strain is affected by pre–existing crustal structures, which may result in the misalignment of principal stress and strain axes. The problem is further complicated by the presence of many sub–parallel, offset faults along the San Andreas fault zone, which accommodate a range of strike–slip and oblique convergent motion.

The motion of the Sierra block parallel to the plate boundary accounts for around 12 mm yr^{-1} of

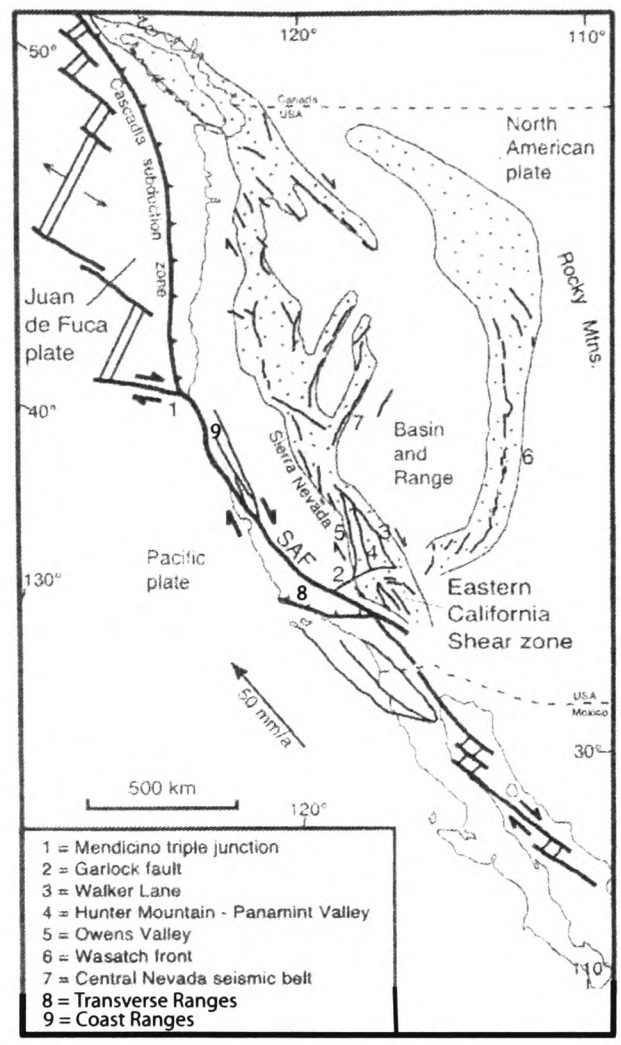

Figure 5.7: Tectonic details of the western United States. Figure modified from Miller *et al.*, 2001

dextral slip parallel to the plate boundary with respect to stable North America (Thatcher *et al.*, 1999; Dixon *et al.*, 1995; McClusky *et al.*, 2001; Argus & Gordon, 2001). This is taken up to the west of the block, along the sub–parallel faults of the ECSZ. This zone forms the second major band of seismicity, and is approximately 100 km–wide. The distributed deformation across the ECSZ is partitioned into strike–slip and extension, and is driven by shear stresses due to motion along the Pacific–North America plate boundary, and extensional forces which arise due to the high potential energy of the Basin and Range Province. Seismicity in the Basin and Range itself is unevenly distributed; deformation and seismicity are concentrated along its eastern and western boundaries.

The stable Sierra block, which extends from east of the Mendocino Triple Junction in the north to the Transverse Ranges in the south, and is bounded to the west by the Coast Ranges, and to the east by the Basin and Range Province, is characterised by very low levels of seismicity (Figure 5.5). The block is surrounded by tectonic activity, but seismicity within it is diffuse; a mixture of strike–slip, reverse, and normal faulting earthquakes, with focal depths between 12 km and 40 km, are scattered throughout the north and central section of the valley. The deep events are thought to be related to the subduction of the Gorda slab which underthrusts the valley in the north (Hill *et al.*, 1991).

There is no historical seismicity on the sinistral Garlock fault, which bounds the Sierra block to the south and runs between the Central Valley and the Transverse Ranges in southern California. Low slip rates on this fault, deduced from recent geodetic studies, strengthen the argument for only minimal rotation of the Sierra block relative to the background deformation field of western North America (see section 5.9).

These low levels of seismicity imply that the internal deformation of the Sierra block does not significantly contribute towards the accommodation of Pacific–North America relative motion. The lack of seismicity could be explained if the Sierra block consisted of hot, weak lithosphere undergoing aseismic deformation, or if strain were accumulating on a number of locked faults with very long repeat times. However, these hypotheses may be rejected in the light of recent geodetic studies (Dixon *et al.*, 2000) which confirm that motion of the Sierra block may be described by rigid body motion. Alternatively, the lack of seismicity may indicate that deformation has shifted away from this section of the plate boundary, but the high levels of seismicity which surround the Sierra block imply that the Sierra block is strong, and resists deformation despite the magnitude of the forces applied along its boundaries.

To the south, near the bend in the plate boundary, convergence across the Transverse Ranges is accommodated by thrusting. This drives the continued uplift of this range and the development of a crustal root (Kohler & Davis, 1997). A lithospheric downwelling beneath the Transverse Ranges, which extends to a depth of ~250km (Zhao *et al.*, 1996), further perturbs the upper mantle flow and crustal tectonics of this region away from a simple strike–slip regime.

Seismicity can account for the majority of relative motion at this plate boundary, but the summation of seismic moments gives lower slip rate estimate than the geodetic methods. If seismic moments are summed over a short time period, the data may not cover a whole seismic cycle, and a minimum estimate is obtained for the seismic energy released across a particular region for a given time period. The summation of seismic strain across the San Andreas fault zone yields a slip rate of 34 ± 3 mm yr^{-1} (Hill *et al.*, 1991) – approximately 65% of total relative motion between the Pacific and North America – which is accommodated on faults lying between the coast and the Central Valley. Geodetic techniques detect strain due to aseismic creep, postseismic relaxation and elastic strain accumulation upon locked faults, as well as seismic motion. These mechanisms account for some of the deficit in the seismic moment calculation of relative motion between the plates, but the majority of the deficit is taken up east of the Sierra block, in the ECSZ. The ~12 mm yr^{-1} total slip rate across this region (Hearn & Humphreys, 1998; Thatcher *et al.*, 1999) accounts for $\sim$ 25% of the total relative motion between the Pacific and stable North America.

The seismogenic layer in western California is approximately 12–15 km thick, below which deforma-

tion is taken up by dislocation creep. (Bird & Piper, 1980) interpreted the lack of mantle seismicity in this region as an indication of a weak upper mantle, and use this to justify their neglect of the effects of basal shear stress when considering the forces acting upon the deforming lithosphere. This argument is strengthened by observations of low seismic velocities in the upper mantle (Humphreys & Dueker, 1994), which imply a hot, weak mantle. I employ this same argument to justify using the thin viscous sheet equations, which assume no basal tractions at the base of the viscous layer.

5.3 Numerical experiments to investigate deformation in the western North America plate boundary zone

5.3.1 The thin viscous sheet approximation

I investigate an idealised model of the Pacific–North America plate boundary zone in which an elongate rigid body is embedded within a thin sheet of non–Newtonian viscous fluid. The long axis of that body is aligned with the boundary of the fluid, along which a uniform tangential velocity is applied for part of its length. This boundary condition drives deformation within the layer. The velocity component parallel to the long boundary decays to zero with distance from the boundary.

The horizontal extent of the western North America plate boundary zone is much greater than the thickness of the lithosphere, therefore, the thin viscous sheet model, outlined in chapter 2, is used to investigate this problem. The model does not allow for the inclusion of any faults within the region of deformation, and it is accepted that much of the deformation of the viscous fluid would in reality be equivalently accommodated by brittle deformation at the surface of the continental crust.

The rheology of the viscous layer is assumed to obey a power law rheology;

$$\overline{\tau}_{ij} = B\dot{E}^{(1/n)-1}\dot{\varepsilon}_{ij} \tag{5.1}$$

where B is a rheological coefficient which represents the vertically averaged strength of the lithosphere. Adopting this rheology, the governing equations for the deformation of a viscous layer (equations 2.30 and 2.31) become

$$L\left(\frac{\partial(B\dot{E}^{\frac{1}{n}-1}\dot{\varepsilon}_{xx})}{\partial x}+\frac{\partial(B\dot{E}^{\frac{1}{n}-1}\dot{\varepsilon}_{xy})}{\partial y}-\frac{\partial(B\dot{E}^{\frac{1}{n}-1}\dot{\varepsilon}_{zz})}{\partial x}\right)=\frac{\partial\Gamma}{\partial x} \tag{5.2}$$

$$L\left(\frac{\partial(B\dot{E}^{\frac{1}{n}-1}\dot{\varepsilon}_{yx})}{\partial x}+\frac{\partial(B\dot{E}^{\frac{1}{n}-1}\dot{\varepsilon}_{yy})}{\partial y}-\frac{\partial(B\dot{E}^{\frac{1}{n}-1}\dot{\varepsilon}_{zz})}{\partial y}\right)=\frac{\partial\Gamma}{\partial y} \tag{5.3}$$

where Γ is the gravitational potential energy of the viscous sheet. In the idealised model of the western North America plate boundary zone variations in the thickness of the lithosphere are negligible,

so a viscous layer of constant thickness is used and forces arising from internal gradients of gravitational potential energy of the lithosphere are small compared with the forces required to deform the lithosphere. The right–hand sides of equations 5.2 and 5.3 are therefore set to zero when seeking solutions to the governing equations.

In order to recover analytical solutions to the thin viscous sheet equations for a geometrically simple example with sinusoidal velocity boundary conditions (see section 5.3.4), equations 5.2 and 5.3 are non–dimensionalised using the methods of section 2.3.4.

5.3.2 Finite element method

Equations 5.2 and 5.3 are solved using the two–dimensional, thin viscous sheet code *basil*, which uses the method described by Houseman & England (1996). The solution domain is divided into triangular elements, each of which has six nodes, one at each vertex and one at the mid–point of each side.

A quadratic interpolation on the velocity field with the Galerkin finite element approximation (see Zienkiewicz & Taylor (1989)) is used to transform equations 5.2 and 5.3 into the matrix form of equation 2.72, chapter 2. Each of the four $\mathbf{K}$ matrices in equation 2.72 are $N \times N$ matrices, where N is the number of nodes. The matrix elements are calculated using a seven–point numerical integration scheme for triangles (see Huebner (1975)), which is accurate to sixth order.

For a Newtonian fluid, equation 2.72 is linear in u and v, however for a non–Newtonian material an iterative scheme is required to obtain a solution. In each iteration the matrix elements are recalculated using the velocity components from the previous iteration.

5.3.3 Convergence Criteria

The convergence of the solutions is controlled by a set of parameters, to be specified. These include the convergence criteria for the linear conjugate gradients iterations and for the non–linear iterations carried out when $n > 1$. Using a smaller convergence criterion increases the accuracy of the numerical solution, however, setting too small a value increases the computation time to inefficient levels and may render convergence impossible due to round–off errors in the solution. In all the numerical experiments carried out here, convergence criteria are used that maximise the accuracy of the solution, whilst ensuring convergence and efficiency.

5.3.4 Grid Accuracy : Comparison with Newtonian analytical solutions

Analytical solutions may be derived for an infinitely long thin viscous sheet of fixed width when $n = 1$ and $Ar = 0$, subject to sinusoidal tangential boundary conditions, and zero normal velocity on the boundary $x = 0$ (see Sonder *et al.* (1986)). For the case of an infinite Newtonian strip ($0 \leq x \leq D, -\infty \leq y \leq \infty$) with boundary conditions $u = 0, v = v_0 \sin(2\pi y/\lambda)$ on $x = 0$, and $u = v = 0$ on $x = D$,

$$u = v_0 \cos\left(\frac{2\pi y}{\lambda}\right)\left\{\left[-\frac{3}{5}\frac{2\pi}{\lambda}(A+1)x\right]\cosh\left(\frac{2\pi x}{\lambda}\right) + \left[A - \frac{3}{5}\frac{2\pi}{\lambda}Cx\right]\sinh\left(\frac{2\pi x}{\lambda}\right)\right\} \tag{5.4}$$

$$v = v_0 \sin\left(\frac{2\pi y}{\lambda}\right)\left\{\left[1+\frac{3}{5}\frac{2\pi}{\lambda}Cx\right]\cosh\left(\frac{2\pi x}{\lambda}\right) + \left[C + \frac{3}{5}\frac{2\pi}{\lambda}(A+1)x\right]\sinh\left(\frac{2\pi x}{\lambda}\right)\right\} \tag{5.5}$$

$$\overline{p} = -\frac{4}{5}\frac{2\pi}{\lambda}\eta v_0 \cos\left(\frac{2\pi y}{\lambda}\right)\left\{[A+1]\cosh\left(\frac{2\pi x}{\lambda}\right) + C\sinh\left(\frac{2\pi x}{\lambda}\right)\right\} + p_0 \tag{5.6}$$

where λ is the wavelength of the sinusoidal tangential boundary condition, $\bar{p}$ is the vertically averaged pressure, p_0 is the background lithospheric pressure, η is the viscosity of the layer, and

$$A = -\frac{1}{1 - \frac{25}{9}\left(\frac{\lambda}{2\pi D}\right)^2 \sinh^2\left(\frac{2\pi D}{\lambda}\right)} \tag{5.7}$$

$$C = \frac{\frac{25}{9}\left(\frac{\lambda}{2\pi D}\right)^2 \sinh\left(\frac{2\pi D}{\lambda}\right)\cosh\left(\frac{2\pi D}{\lambda}\right) - \frac{5}{3}\left(\frac{\lambda}{2\pi D}\right)}{1 - \frac{25}{9}\left(\frac{\lambda}{2\pi D}\right)^2 \sinh^2\left(\frac{2\pi D}{\lambda}\right)} \tag{5.8}$$

These solutions are periodic in the y direction, and are compared with numerical solutions obtained using a finite element mesh with an aspect ratio of 1:2 (width:length) where the width is equivalent to the width, D, used in the numerical solutions, and the length of the solution domain is $L = 2D$. A resolution test has been carried out, and a value of $nx = 32$, where nx is the number of triangles across the width of the mesh, is found to give a sufficient level of accuracy. In calculating the numerical solutions, rigid boundary conditions ($u = v = 0$) are defined along $x = D$, and the same sinusoidal boundary condition is used along $x = 0$; $u = 0$ and $v = \sin\frac{\pi y}{L}$. Along $y = 0$ and $y = L$ analytical solutions for u and v are evaluated every 0.1 non–dimensional units using equations 5.4 and 5.5, and a linear interpolation is used between these points to assign the boundary conditions for the numerical experiment. Due to the nature of the numerical code it is not possible to assign the exact analytical expressions as continuous boundary conditions along the $y = 0$ and $y = L$ boundaries.

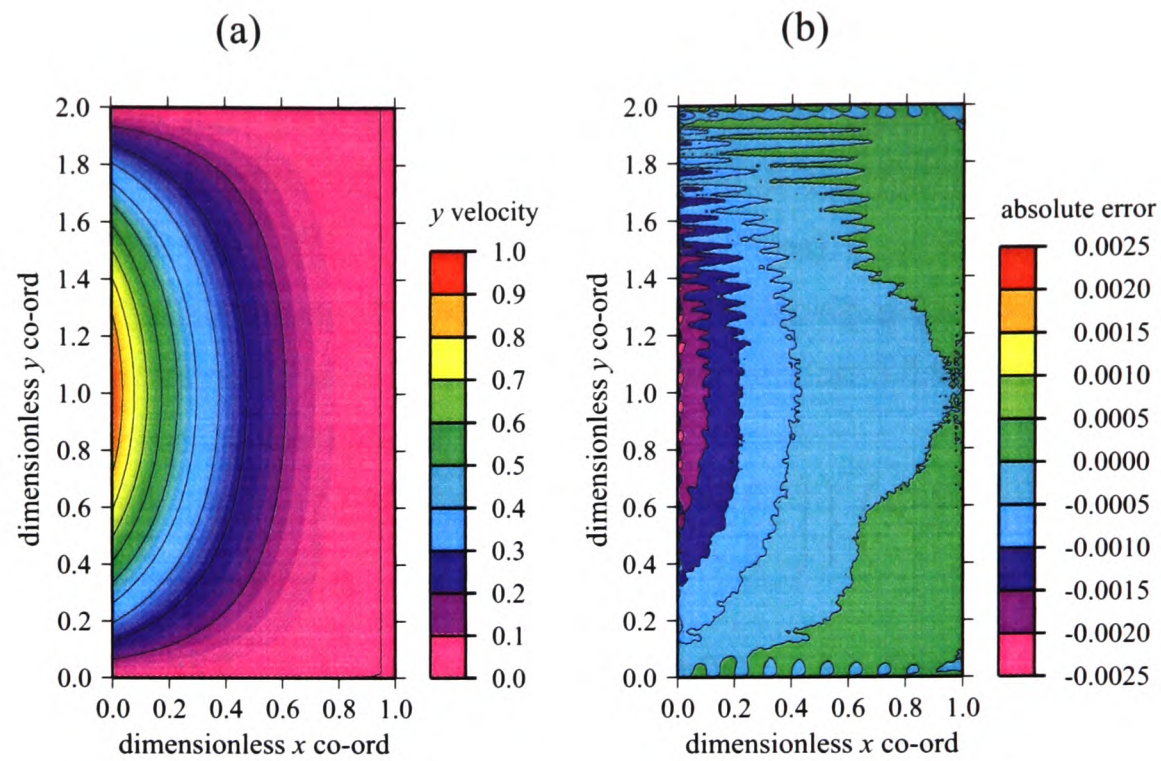

Figure 5.8: (a) Analytical solution for v, (b) Absolute error between numerical and analytical solutions for v

The analytical and numerical solutions for u and v are identical along $x = 0$, $x = D$, $y = 0$ and $y = L$ when $\lambda = 2L$ and $v_0 = 1$ are used in the analytical solutions. I am principally interested in the y component of velocity, and a two dimensional contour plot of the analytical solution for v is shown in Figure 5.8a for the domain $0 \leq x \leq D$, $0 \leq y \leq L$, where $D = 1$ and $L = 2$. The absolute difference between the numerical and analytical solutions for v in this domain is shown in Figure 5.8b.

The maximum absolute error between the analytical and numerical solutions for v is $\sim$0.002, which is small in comparison to the maximum magnitude of v. The region of greatest interest is located within a non–dimensional distance of 0.5 from the driving boundary ($x = 0$), between $y = 0.6$ and $y = 1.4$, since this corresponds to the location of the Sierra block in later experiments. The maximum percentage error throughout this region is $\sim 0.25\%$.

5.3.5 Model setup and boundary conditions

Two–dimensional finite deformation calculations are carried out in order to quantify the motion of the rigid block described in section 5.2[1]. Figure 5.9a shows the solution domain, which consists of a triangular finite element mesh (Figure 5.9b), and covers the region $0 \leq x \leq 2.5$ and $0 \leq y \leq 5$, in dimensionless co–ordinates. A higher viscosity region is specified within the flow, and its length,

[1]This work, and the theoretical modelling of section 5.5, is an extension of the work presented in Whitehouse *et al.* (2004).

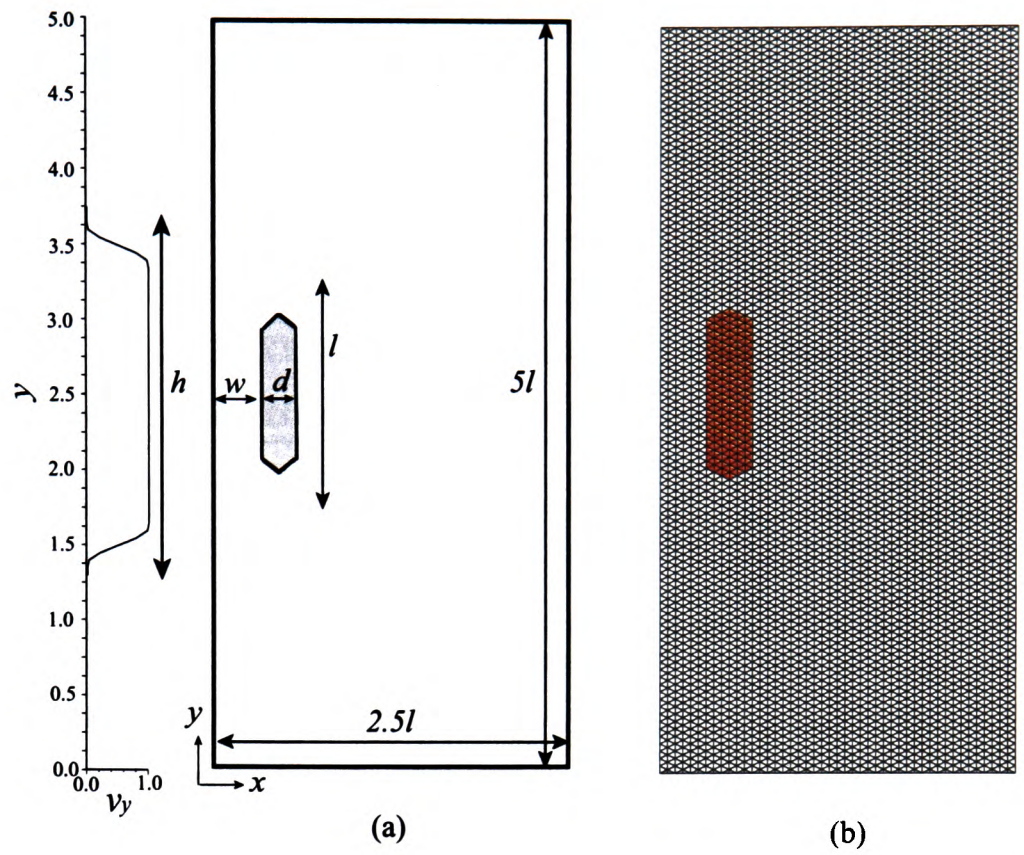

Figure 5.9: (a) Solution domain used in the numerical method (not to scale). The shaded area is defined to have a strength coefficient ten times greater than the rest of the box. Length scales are non–dimensionalised using the length, l, of the shaded area (see text).The velocity boundary condition, v_y, for $x = 0$ is plotted alongside the solution domain. (b) Triangular finite element mesh. Red area represents the high–viscosity region.

l, is used to non–dimensionalise the problem: Any length x becomes $x' = x/l$. The width (d) and distance of the higher viscosity region from the driving boundary (w) are varied to produce four different possible geometries for the higher viscosity block (table 5.1).

In the numerical experiments, a simply–connected region may be specified in which the dimensionless rheological coefficient, B, is different from the background value in the viscous layer. I wish to study the motion of a rigid elongate block aligned with the simple shear velocity field. In order to distinguish the block from the surrounding fluid, a region with a large aspect ratio (length:width) is allotted a value of B which is sufficiently high that its strain rate is negligible with respect to that in the surrounding fluid, for equivalent deviatoric stress; because buoyancy forces are neglected ($Ar = 0$), only relative magnitudes of B influence the solution. Setting the ratio of B values to be 10 is found to be sufficiently large to produce rigid behaviour. This is in agreement with the findings of England & Houseman (1985), who employ the thin viscous sheet approximation to investigate the influence of a rigid block in a compressional environment, and find that for $n = 3$, increasing the strength

Table 5.1: Model parameters for numerical experiments

Experiment	Length l^1	Width d^1	Distance from driving boundary, w^1	Aspect Ratio l/d	w/d
A	1	0.26088	0.17392	3.8332	0.6667
B	1	0.26088	0.2174	3.8332	0.8333
C	1	0.17392	0.17392	5.7498	1.0
D	1	0.34784	0.17392	2.8749	0.5

[1]all length scales have been non–dimensionalised using the length of the higher viscosity region, l.

of the block by one order of magnitude compared with that of the surrounding lithosphere creates a contrast in deformation rates of order 10^3, similar to the observed contrast in deformation rates in western North America. For larger values of n, a smaller contrast in B would be sufficient to represent the behaviour of a rigid inclusion. The size and location of the higher viscosity block may be varied in order to carry out experiments using different geometries.

Rigid boundary conditions ($\boldsymbol{v}$= 0) are specified along the $x = 2.5l$, $y = 0$ and $y = 5l$ boundaries, and a constant tangential velocity is specified along a length h of the $x = 0$ boundary. The boundary condition is centred upon the position of the higher viscosity region, and the velocity is tapered to zero at either end using a $\cos^2$ taper (see velocity profile in Figure 5.9a) to ensure that the derivative of the velocity boundary condition is continuous along the whole $x = 0$ boundary. This prevents the calculation of solutions with discontinuous velocity gradients, and increases the numerical stability of the solutions near the boundaries. The length, h, of the driving boundary is measured as the length of the portion to which a constant velocity is applied. Outside the region of non–zero tangential velocity boundary conditions a zero traction boundary condition is used.

Relative motion between the North America and Pacific plates is approximately parallel to the plate boundary at the latitude of the Sierra block, and values of h are used that are representative of the geometry of the plate boundary. The predominantly strike–slip motion is replaced by subduction (of the Gorda and Juan de Fuca slabs) north of the Mendocino Triple Junction. Very low levels of stress are supported along this subduction zone (Wang & Jiangheng, 1999), and there is only a small strike–slip component to the relative motion (Miller *et al.*, 2001a), therefore zero–traction boundary conditions are used along the corresponding region of the model, $x = 0$, $y > 3.75$, and this section of the plate boundary is treated as a free boundary.

South of the Sierra block the plate boundary passes through the Salton Sea and enters the Gulf of California. Relative motion between the North America and Pacific plates in the Gulf of California

is taken up along a series of rift zones connected by transform faults, similar to a mid–ocean ridge. I assume that the plate relative motion is taken up entirely along this ridge–transform zone, with no internal deformation of North America, and therefore use zero–traction boundary conditions applied along $x = 0$, $y < 1.25$ of the solution domain, which corresponds to the plate boundary south of the Salton Sea.

For values of $h < 2.5l$, the presence of rigid boundaries at $x = 2.5l$, $y = 0$ and $y = 5l$ have little influence upon the solution in the region of interest; near the driving boundary. This has been established by considering velocity profiles along the length and width of different size solution domains (see results of section 5.4.1).

In the finite element mesh, the number of elements in the x direction (nx) is 100. This gives a sufficient level of resolution for the solutions, and no significant difference is observed when a finer mesh is used (see results of section 5.4.2).

Because the results from the numerical experiments will be compared with GPS data, which give an instantaneous representation of the present–day surface velocity field, only instantaneous numerical solutions are calculated for these experiments, and no time–stepping is carried out. Stress–strain rate exponent values of $n = 1$ to $n = 5$ are used in the experiments.

5.4 Results of numerical experiments

Experiments are carried out to investigate what governs the motion of a higher viscosity block embedded within a viscous layer undergoing simple shear flow. Solutions for the translational velocity of the block are found for a range of n, d, w and h. Calculating the average y component of velocity for elements within the higher viscosity region yields a good approximation for the bulk motion of the higher viscosity block with respect to the background fluid, and with respect to the velocity applied at the driving boundary. The ratio between the average velocity of the block, V_1, and the velocity applied at the driving boundary, V_0, is used to compare the results of different experiments. Note that $V_0 = 1$ is used in all experiments.

5.4.1 Dimensions of the solution domain: Rigid boundary effects

Experiments are carried out to determine the effect of changing the dimensions of the solution domain, and in particular to study how the location of the rigid boundaries along $x = D$, $y = 0$ and $y = L$ affect the solution for the velocity field.

Figure 5.10a is a plot of profiles taken across the midpoint of the solution domain ($y = 2.5$, see inset)

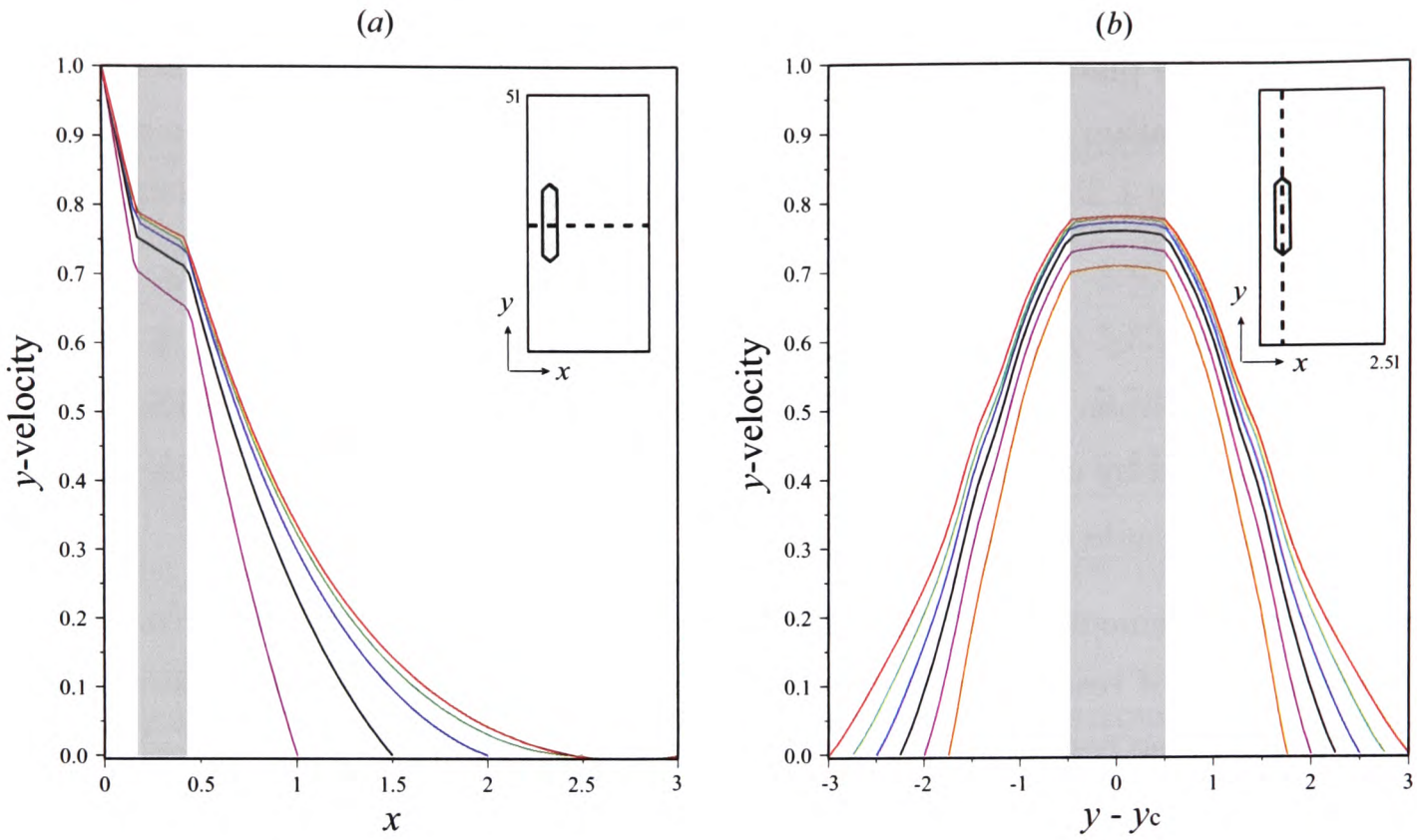

Figure 5.10: y–velocity profiles taken through the centre of the higher viscosity block (see insets). The location of the rigid block is indicated by the shaded columns. Stress–strain rate exponent, $n = 1$, length of driving boundary, $h = 2.5l$, length of higher viscosity block $= l$, width of block $= 0.26l$, distance of block from driving boundary $= 0.17l$. (a) Total length of the solution domain $= 5l$. Purple: width of solution domain $= 1.0l$. Black: width $= 1.5l$. Blue: width $= 2.0l$. Green: width $= 2.5l$. Red: width $= 3.0l$. (b) Width of solution domain $= 2.5l$. Orange: length of solution domain $= 3.5l$. Purple: length $= 4.0l$. Black: length $= 4.5l$. Blue: length $= 5.0l$. Green: length $= 5.5l$. Red: length $= 6.0l$. Profiles are centred to aid comparison.

for experiments whose domain width ranges between $1.0l$ and $2.5l$. A stress–strain rate exponent of $n = 1$ is used in all cases because the linear solution has the broadest velocity field, and thus any misfit is maximised. An identical higher viscosity region, and a driving boundary condition of length $h = 2.5l$, are used in all cases. This is the longest driving boundary condition used in any experiment, and hence will generate deformation over the widest area, again maximising any discrepancies between the solutions. The velocity parallel to the driving boundary is plotted on the y axis in Figures 5.10a and 5.10b; the levelling–off of the profiles is due to the presence of the higher viscosity block. Figure 5.10a demonstrates that there is very little difference between solutions obtained using domain widths of $2.5l$ and $3.0l$. For narrower solution domains, the y component of velocity decays more rapidly than is expected if the rigid boundaries have no influence upon the decay of velocity with distance from the driving boundary. A width of $2.5l$ is used in the following experiments to maximise accuracy and minimise computation time.

Figure 5.10b plots y–velocity profiles taken along the length of the solution domain, through the

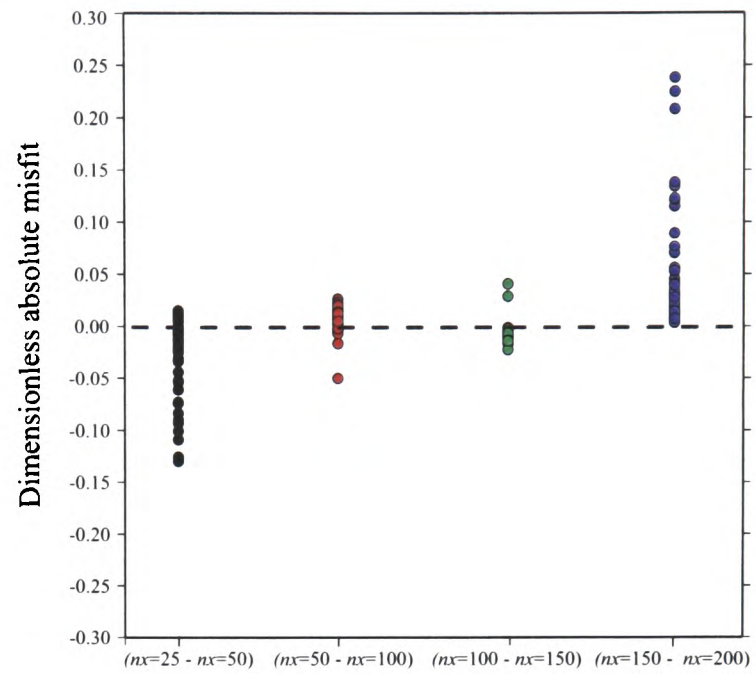

Figure 5.11: Misfit between solutions for V_1/V_0 using nx=25, 50, 100, 150, and 200. In each case the solution with a greater density of elements along the x axis is subtracted from the solution with a lower density of elements along the x axis. The misfit is non–dimensionalised by dividing all velocities by the uniform velocity of the driving boundary, V_0.

middle of the higher region (see inset). $n = 1$ is used to give linear solutions, and a driving boundary condition of length $h = 2.5l$ is centred upon the location of the higher viscosity block. Solution domain lengths of $3.5l$ to $6l$ are used. The velocity profiles do not match towards the ends of the solution domain (at large or small y) because the zero traction boundary condition applied along these sections forces a continuous velocity gradient between the end of the constant velocity boundary condition and the edge of the domain. For domain lengths $\geq 5l$ there is little variation between the y–velocity profiles in the region of the higher viscosity block, and a length of $5l$ is used in all subsequent experiments.

5.4.2 Resolution of solutions

Experiments are carried out in order to determine the optimum density of mesh which should be used in the investigation. Figure 5.11 demonstrates the stability of the ratio V_1/V_0 as the mesh density is altered. The absolute size of the solution domain is not altered during the following experiments. For values of $nx = 25, 50, 100, 150$ and 200 a series of experiments with identical initial and boundary conditions are carried out. The four geometries outlined in table 5.1 are used; n is allowed to vary between 1 and 5; and the length of the driving boundary condition is varied between $h = 1.0l$, $h = 1.5l$ and $h = 2.5l$: A total of 60 experiments are carried out for each mesh. The velocity ratio,

V_1/V_0, obtained using the finer mesh is subtracted from the ratio obtained using the coarser mesh for each set of initial and boundary conditions, to enable a comparison to be made between experiments.

For any given set of boundary conditions, the absolute misfit between values of V_1/V_0, calculated using two different meshes decreases as nx is increased from $nx = 25$ through to $nx = 150$, with very little misfit observed between solutions calculated using $nx = 50$ and $nx = 100$, and $nx = 100$ and $nx = 150$. The variation in the misfit between solutions obtained using $nx = 25$ and $nx = 50$ may be attributed to the interpolation of the velocity field upon different densities of mesh. At different resolutions, the details of which elements are defined to lie within the higher viscosity region will vary, leading to small differences in the geometry of the experiment. The parametrisation of the driving velocity boundary condition will also vary because velocities are assigned to specific nodes. The length of the driving boundary has a strong influence upon the width of the resulting velocity field, and hence the motion of the block.

When the mesh density is increased to $nx = 200$ the absolute misfit between solutions obtained using $nx = 150$ and $nx = 200$ increases again. This divergence of solutions for the finest mesh may be attributed to a rounding error within the numerical method, or poor accuracy. In order for solutions to be obtained for the finest mesh, the non–linear convergence criterion has to be increased, which in turn decreases the accuracy of the solution. The misfit is more pronounced in the case of strongly non–linear flow ($n = 4, 5$). A mesh of density $nx = 100$ is used in the following experiments. This choice optimises the trade–off between increasing the numerical accuracy whilst decreasing computation times.

5.4.3 Viscosity Contrasts

I wish to determine what value of B, the strength coefficient for the higher viscosity region within the mesh, is optimal for the experiments I wish to carry out. Figure 5.12 shows y–velocity profiles, taken from numerical solutions calculated using values of B which range between 2 and 100. The profiles are taken across the centre of the solution domain, perpendicular to the long side of the higher viscosity region. The location of the higher viscosity region is highlighted in grey in Figure 5.12. Solutions obtained using $n = 1$ correspond to the fastest profiles, while solutions obtained using $n = 5$ correspond to the slowest.

When the strength within the stronger region is double that of the background fluid ($B = 2$), there is little discernible decrease in the velocity gradient in the region of the block, and for small n, there is little departure from the smooth velocity profile obtained in the case when no heterogeneity is present (dashed lines in Figure 5.12). Doubling the strength coefficient is therefore insufficient to produce the block–like behaviour required. Increasing B to values of $B = 5$ and $B = 10$ yields profiles which

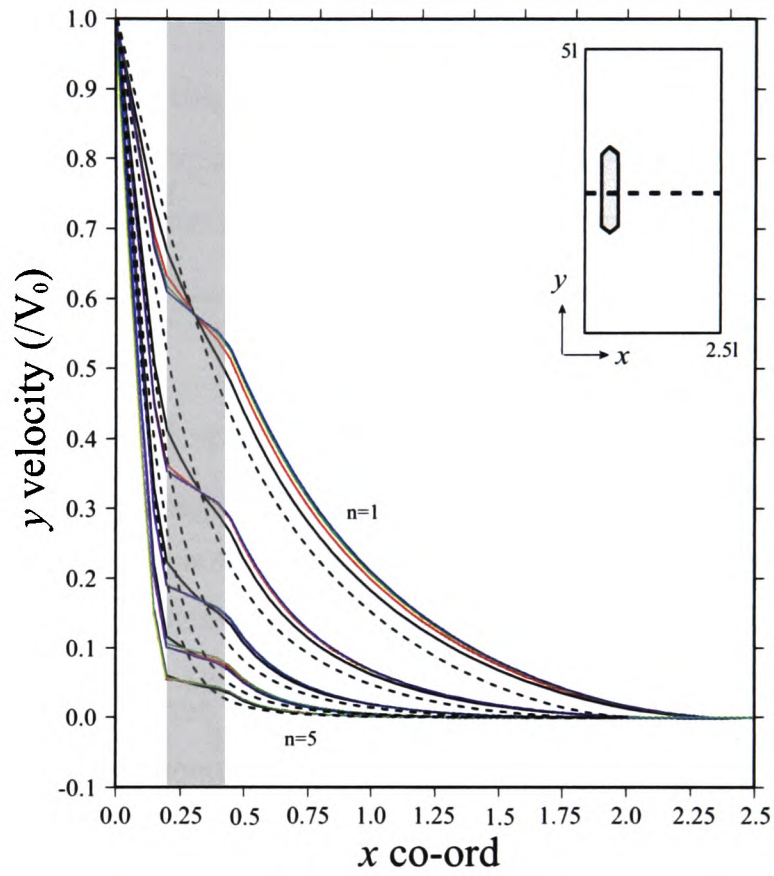

Figure 5.12: Profiles of V_1/V_0 taken across the centre of the solution domain ($y = 2.5$) for case A, table 5.1. A driving boundary of length $h = 1.5l$ is used. Values of $n = 1, 2, 3, 4$ and 5 are used, and the strength coefficient, B, is varied over several orders of magnitude. Black: $B = 2$. Red: $B = 5$. Green: $B = 10$. Blue: $B = 20$. $B = 100$ is indistinguishable from $B = 20$ for $n = 1$ and $n = 2$, and has not been plotted for clarity. Experiments where $B = 100$ experienced convergence problems for $n \geq 3$. The grey column indicates the approximate location of the higher viscosity block, and the dashed lines are numerical solutions for the case with no heterogeneity.

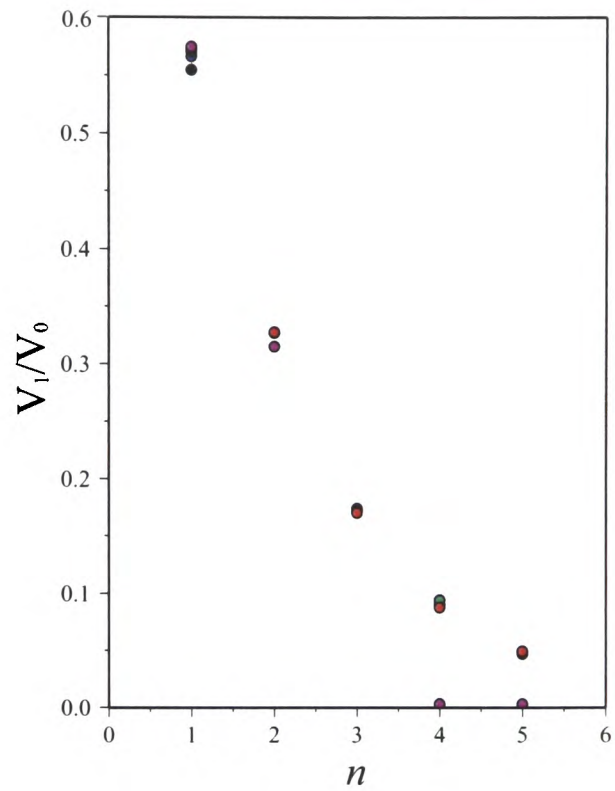

Figure 5.13: Average velocity of the block (V_1/V_0) plotted against n for a range of values of B. Other parameters as for Figure 5.12. Black: $B = 2$. Blue: $B = 5$. Green: $B = 10$. Red: $B = 20$. Purple: $B = 100$.

display a sharper decrease in the y–velocity gradient across the location of the block. This behaviour is more pronounced for greater values of n, and is closer to the block–like behaviour which I wish to reproduce. The prevalence of a slight velocity gradient across the block, even when $B = 100$, may be attributed to the deformation of the fluid within the higher viscosity region, or to the rotation of the entire region. These possibilities are discussed in section 5.4.4.

The average y–velocity for the fluid within the higher viscosity region is calculated for each of the 25 experiments described above, and plotted in Figure 5.13. Many of the points are obscured, implying that the value of V_1/V_0 output from the numerical method is only very weakly dependent upon the value of B used to define the strength of the higher viscosity region. The method used to calculate V_1/V_0 acts to average out the velocity gradient across the block, resulting in the small range of values plotted for each n in Figure 5.13.

There is no value plotted for $n = 3$, $B = 100$ because this solution failed to converge. To aid the convergence of the solutions, and increase the efficiency of the calculations, the solution from the previous experiment, which had the same boundary conditions, but which used a value of $n - 1$, is used as a starting solution for all experiments when $n > 1$. Since the solution using $n = 3$, $B = 100$ failed to converge, it is likely that the solutions obtained for $n = 4$ and $n = 5$, with $B = 100$, did not properly converge. The values of V_1/V_0 calculated from the results of these experiments are

much smaller than values obtained when a smaller strength contrast is used. The solutions have been plotted in Figure 5.13, only to highlight their probable inaccuracy.

In order to strike a balance between ensuring the accuracy and convergence of solutions, and using a value of B which produces rigid behaviour, a strength difference which represents a contrast of one order of magnitude in viscosity ($B = 10$) is used in the following calculations.

5.4.4 Internal deformation of the block

The higher viscosity region within the shear zone undergoes a small amount of internal deformation and rotation, as predicted by the equations which govern the deformation of a highly viscous fluid. From the definition of the strength coefficient, B, in equation 5.1, it may be shown that the strain rate is related to B by the equation

$$\dot{\varepsilon} \sim \left(\frac{\overline{\tau}}{B}\right)^n \tag{5.9}$$

Figure 5.14 compares the averaged strain rate for the viscous fluid which lies between the driving boundary and the higher viscosity region, with the averaged strain rate for the fluid of higher viscosity inside the heterogeneous region. The mean strain rate in each of these two regions is calculated using the values of $\dot{\varepsilon}_{xy}$ at points along a line passing through the centre of the block. Equation 5.9 implies that the strain rate for the fluid in the higher viscosity region should be B^n times smaller than the strain rate in the background fluid. The strain rate at points which lie within the higher viscosity region is multiplied by B^n to enable comparisons to be made between theory and the numerical solutions.

The data for Figure 5.14 are taken from twelve numerical experiments. In all cases the length of the driving boundary is $h = 1.5l$. Four shapes for the higher viscosity region have been used (see table 5.1), and values of $n = 1, 2$ and 3 are used in each case. $B = 10$ defines the viscosity contrast between the block and the background fluid.

The numerical calculations give results which are close to those predicted by the first–order theory of equation 5.9; second–order corrections should explain some of the remaining discrepancies. However, closer inspection is required to determine the degree to which the velocity gradient across the block is due to internal deformation, and the degree to which it is due to the rotation of the block.

In Figure 5.15 the gradient in x and y–velocities across the block is evident for the cases $n = 1$ to 3 (case A, table 5.1). Calculation of the velocity gradients, $\partial u/\partial y$ and $\partial v/\partial x$, at the centre of the block allows $\dot{\varepsilon}_{xy}$ to be determined for each of $n = 1$ to $n = 3$. This value is compared with the total strain rate at the centre of the block, as calculated by the numerical method, and reveals that in all three cases, over 95% of the velocity gradient across the higher viscosity block is due to the rotation

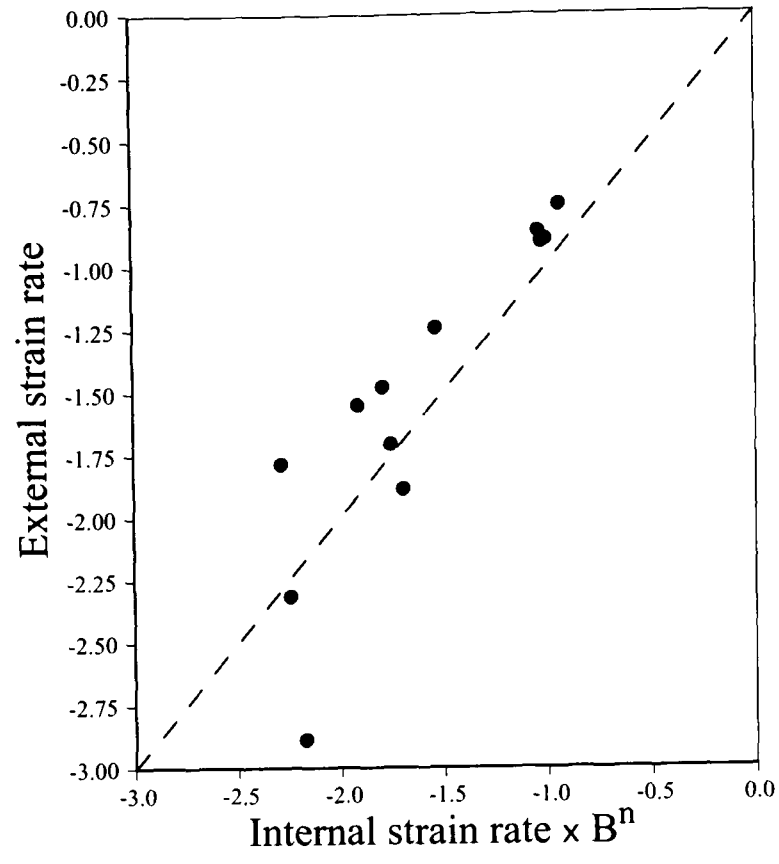

Figure 5.14: Strain rate for fluid between the driving boundary and the block plotted against strain rate within the block multiplied by B^n. Data taken from experiments which use four different model geometries; $n = 1, 2$ and 3 in the constitutive equation.

of the block.

Since the majority of the velocity gradient across the block arises from its rotation, y–velocities greater than and less than the average over the whole block cancel out. The mean therefore gives a good approximation for the bulk velocity of the block parallel to the $x = 0$ boundary.

5.4.5 Dependence of block velocity upon n

Figures 5.16 and 5.17 contain the same data. For each of the four cases outlined in table 5.1, an instantaneous solution for the velocity field is found for $n = 1$ to $n = 5$, using velocity boundary conditions of lengths $h = 1.0l$, $1.5l$ and $2.5l$. Figure 5.16 highlights the effect of changing the dimensions of the block, and its location, whilst Figure 5.17 highlights the effect of changing the length of the velocity boundary condition.

In all cases, the translational velocity of the higher viscosity region decreases as n is increased. The width of the deformation field due to a transcurrent boundary condition decreases as the non–linearity of the viscous fluid is increased (England *et al.*, 1985), and therefore the background velocity at a given distance from the driving boundary decreases as n is increased. This results in a smaller shear

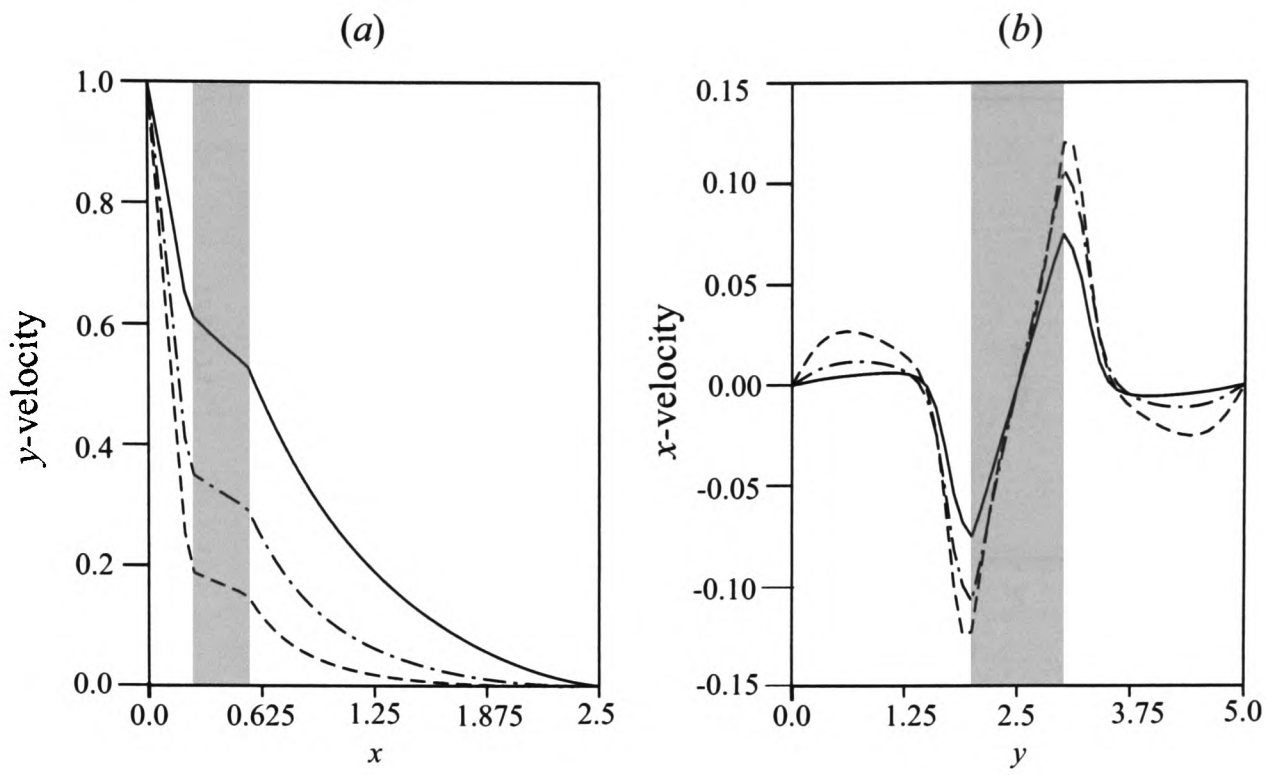

Figure 5.15: (a) y–velocity profiles taken through the centre of the block (along $y = 2.5$). Case A (see table 5.1) is used, with a driving boundary of length $h = 1.5l$. The block is located between $x = 0.17l$ and $x = 0.43l$, as indicated by the grey column. Solid line: $n = 1$. Dot–dashed line: $n = 2$. Dashed line: $n = 3$. (b) x–velocity profiles taken along the centre of the block (along $x = 0.304l$). Again case A is used, with a driving boundary of length $h = 1.5l$. The block is located between $y = 2.0l$ and $y = 3.0l$, as indicated by the grey column. Solid line: $n = 1$. Dot–dashed line: $n = 2$. Dashed line: $n = 3$.

force being applied along the left–hand boundary of the higher viscosity region, and a smaller normal force being applied along its $y = 2l$ boundary. With a smaller driving force, the block therefore translates more slowly for greater n.

5.4.6 Location and shape of the block

For cases A and B of table 5.1, the higher viscosity region is the same size, but in case B it is located further from the driving boundary. A comparison of the red (case A) and green (case B) points in Figure 5.16 indicates that if the block is located further from the driving boundary it will translate at a slower rate due to the lower shear stress applied to the long side closest to the driving boundary.

In cases A, C and D, the left–hand side of the higher viscosity region is located at the same distance from the driving boundary, but the width of the heterogeneous regions vary. A comparison of the blue (case C, narrowest), red (case A) and black (case D, widest) points in Figure 5.16 indicates that a narrower block will translate at a greater velocity relative to the velocity applied along the driving boundary.

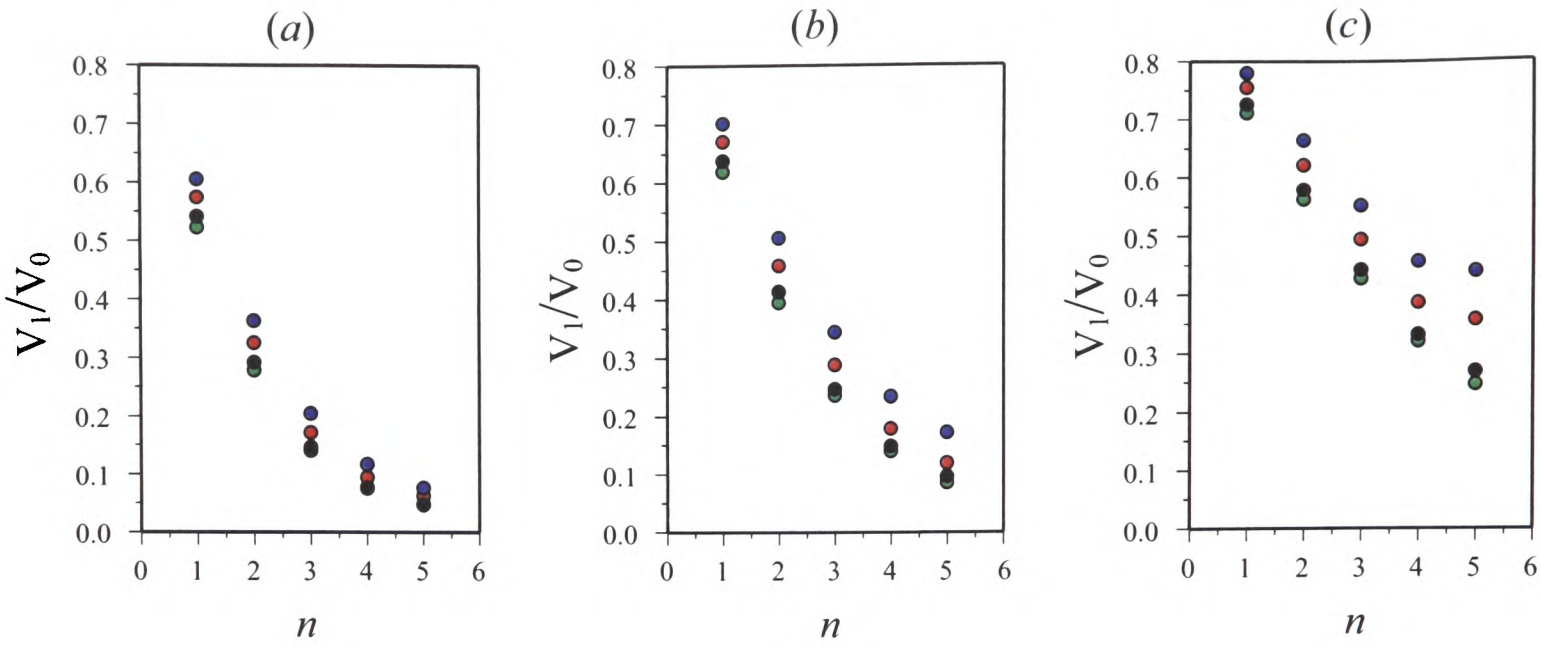

Figure 5.16: V_1/V_0 plotted against n. Colours represent the following: red: case A, green: case B, blue: case C, black: case D. (a) short driving boundary condition ($h = 1.0l$) (b) medium driving boundary condition ($h = 1.5l$) (c) long driving boundary condition ($h = 2.5l$).

A block of negligible width, and hence negligible resistance, located at some distance from the driving boundary should translate at the same velocity as the background fluid located the same distance from the driving boundary. I postulate that the velocity of a block is related to its width via the force applied along its short boundaries parallel to the x axis. Calculating the average y–velocity of the background fluid adjacent to the $y = 2l$ boundary of the block yields a greater value for a narrower block since its centre is closer to the driving boundary. It will therefore experience a greater driving force along this boundary, and similarly a smaller resistive force along the $y = 3l$ boundary, than for a wider block. The average velocity across the ends of a wider block located at the same distance from the driving boundary will be smaller, and hence it will translate more slowly. A wider block also experiences a greater velocity gradient, $\partial v/\partial x$, across its end boundaries, and hence a greater turning moment.

5.4.7 Length of the driving boundary

Figure 5.17 demonstrates that the higher viscosity region will translate at a greater velocity if the length of the velocity boundary condition is increased. England *et al.* (1985) note that in a transcurrent regime, along–strike velocity decays with distance from the driving boundary, and that the characteristic length scale for this decay is dependent upon the length of the driving boundary (see section 5.5.1). Therefore, for a longer driving boundary condition, the block will be entrained within faster moving fluid, and hence will translate at a greater velocity. This is demonstrated in Figure 5.18;

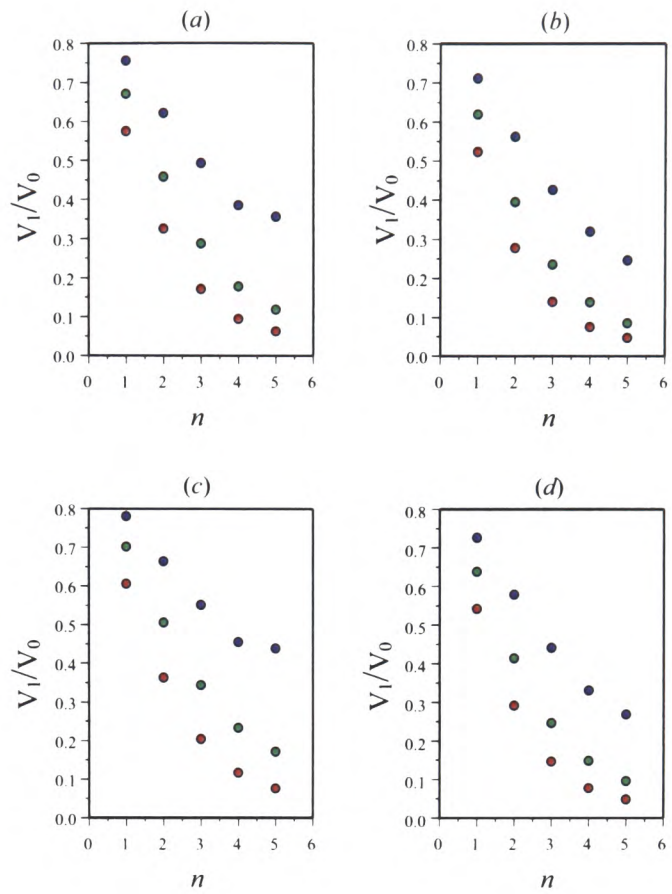

Figure 5.17: V_1/V_0 plotted against n. Colours represent different lengths of boundary conditions: red: short, green: medium, blue: long. (a) case A (b) case B (c) case C (d) case D.

driving boundaries of lengths $h = 1.0l$ and $h = 2.5l$ are used in Figures 5.18a and 5.18b respectively for the $n = 1$, geometry A experiment. In the first case, the region containing the block has an average translational velocity of $\sim 0.5V_0$, whilst in the second, this region translates at $\sim 0.7V_0$. V_0 is used to scale the velocity throughout the solution domain.

5.4.8 Strike–normal velocity

Figure 5.19 displays an example of the x component of velocity output by the experiments of section 5.4.5. The velocity gradient, $\partial u/\partial y$, evident along the central section of the solution domain, is focussed by the presence of the higher viscosity region, and arises as a result of the slow rotation of the block. The expected rate of rotation of a rigid ellipsoid entrained within a viscous fluid is discussed in section 5.9, but in the following analysis (section 5.5), forces due to this rotation are neglected.

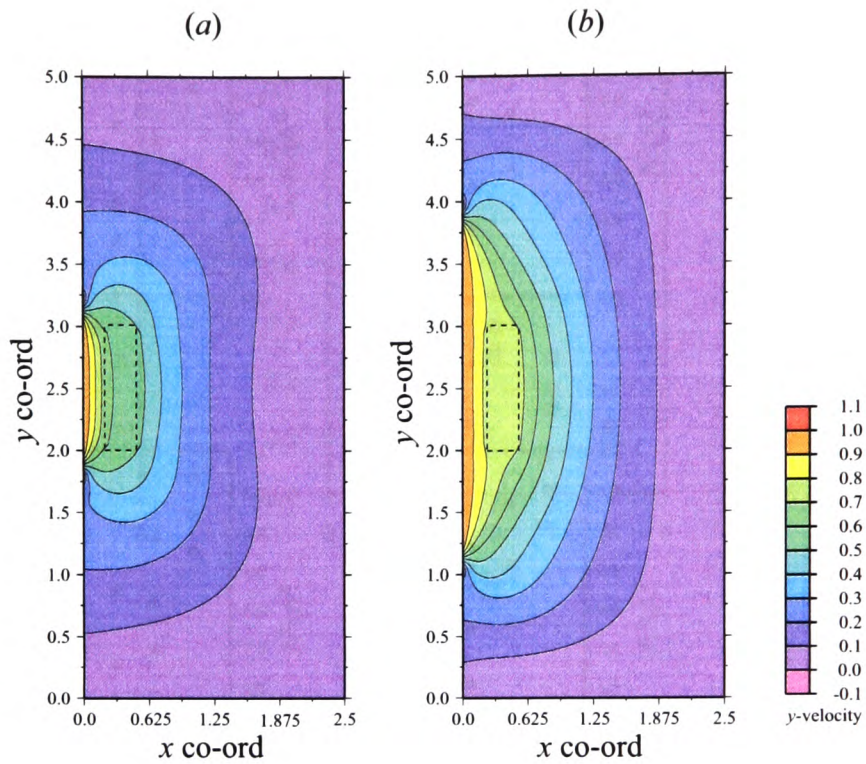

Figure 5.18: y–velocity field scaled using V_0. Solutions obtained using case A from table 5.1 and $n = 1$. The dashed line marks the approximate location of the higher viscosity block. (a) driving boundary of length $h = 1.0l$ (b) driving boundary of length $h = 2.5l$.

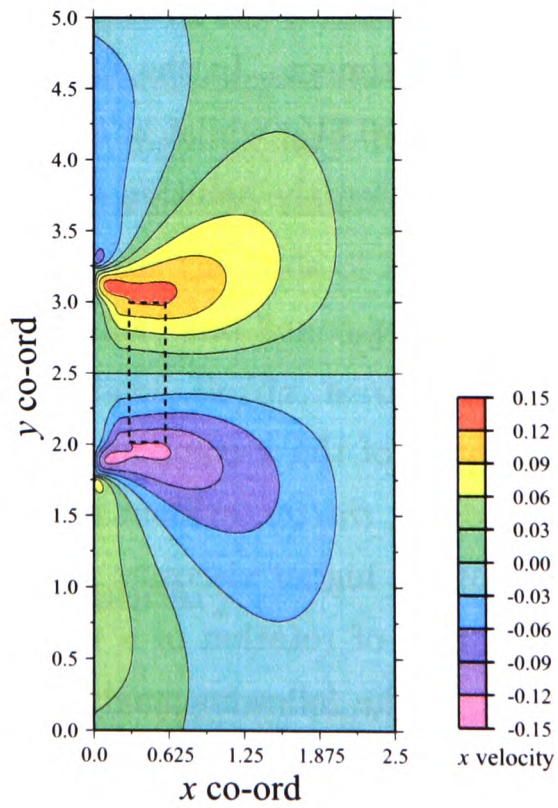

Figure 5.19: x–velocity field. Solution obtained using case A from table 5.1 and $n = 1$. The dashed line marks the approximate location of the higher viscosity block. Driving boundary has length $h = 1.5l$.

5.5 Force Balance Theory

The motion of a rigid block entrained within a viscous fluid is also investigated by considering the forces applied along its boundaries. The high viscosity of the fluid surrounding the block means that accelerations may be neglected in the stress balance, and the sum of the forces acting on the block must vanish. The boundaries and interior of the block are assumed not to deform, and as before, vertical averages of stress are used, and the thickness of the block is treated as uniform.

Approximate expressions for the forces on the four vertical boundaries of the block are derived using the expressions of England *et al.* (1985) for the velocity field in a non–Newtonian thin viscous sheet driven by velocities applied along one edge. The geometry of the problem is set out in Figure 5.20, and the constitutive law given in equation 5.1 is used for all calculations. The heterogeneous block is taken to be rigid with respect to the surrounding viscous fluid, and strain rates in the fluid are approximated using the relationship $\dot{\varepsilon}_{ij} \sim (\Delta V/2L)$, where ΔV is the velocity difference between two points, and L is a characteristic length scale.

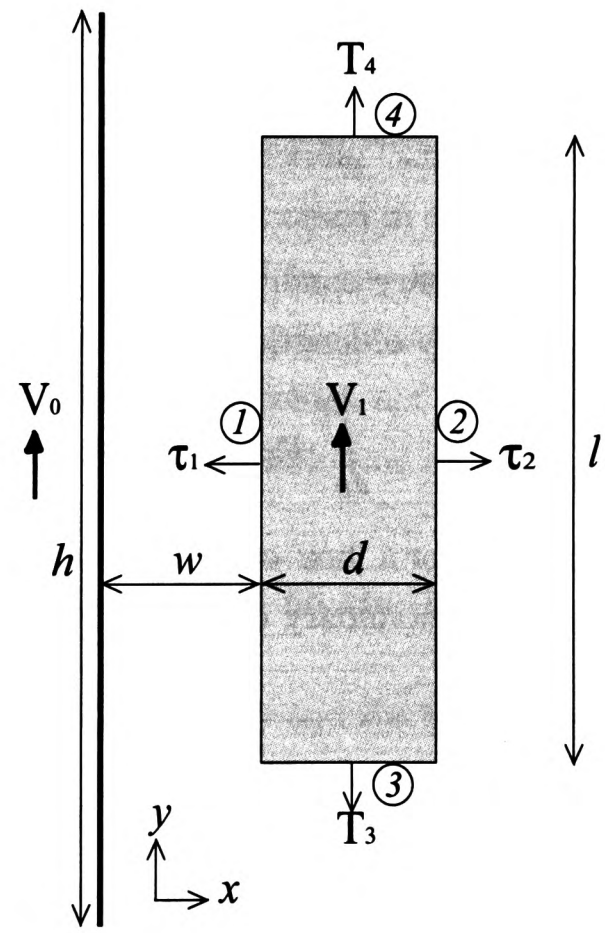

Figure 5.20: Definition of the terms used in the force balance approach. The shaded block represents the rigid inclusion, and the thicker line represents a boundary of specified length translating at a constant velocity of V_0. Far–field boundary conditions are zero velocity as $x \rightarrow \infty$, and simple shear in the y direction as $y \rightarrow \pm\infty$. Numbers in circles define the four boundaries of the rigid block.

5.5.1 Length scales of deformation

England *et al.* (1985) found that, for a driving velocity of amplitude V_0, applied parallel to the boundary and varying sinusoidally along the boundary, the velocity in the interior is nearly parallel to the boundary, and has amplitude approximately

$$V_y \simeq V_0 e^{-x/\lambda} \tag{5.10}$$

where x is distance from the driving boundary. For a driving velocity with wavelength $2L$,

$$\lambda \sim L/(2\pi\sqrt{n}) \tag{5.11}$$

If the driving velocity is applied normal to the y axis, the velocity in the interior is almost perpendicular to the boundary, and

$$\lambda \sim 2L/(\pi\sqrt{n}) \tag{5.12}$$

These expressions must be modified for the problem considered here, to take account of the 'box–car' profile of the velocity boundary condition (Figure 5.20). It is assumed that two sets of velocity boundary conditions will generate deformation that decays away from the boundary with the same length scale, λ, if the integral of the driving velocity along the length of the boundary in the two cases is the same.

For a sinusoidally varying boundary condition, of wavelength $2L$, amplitude V_0, the integral of the driving velocity along a boundary of length L is

$$\int_0^L V_0 \sin\left(\frac{\pi x}{L}\right) dx = \frac{2LV_0}{\pi} \tag{5.13}$$

Equating this to the integral under a 'box–car' boundary condition of length L', amplitude V_0, reveals that the length of the 'box–car' boundary condition required to give the same velocity integral is

$$L' = \frac{2L}{\pi} \tag{5.14}$$

Taking $V_0 = 1$, and substituting for L in equations 5.11 and 5.12, yields

$$\lambda_{\parallel} \cong L'/4\sqrt{n} \tag{5.15}$$

$$\lambda_{\perp} \cong L'/\sqrt{n} \tag{5.16}$$

for tangential and normal boundary conditions respectively.

This length scale approximation was validated by comparing profiles calculated using the analytical expression of equation 5.10, where $\lambda = L'/4\sqrt{n}$, with profiles of along–strike velocity from the

numerical method generated using 'box–car' and sinusoidal boundary conditions, with lengths L' and L respectively (see Figure 5.21). There is some misfit between solutions calculated for a Newtonian ($n = 1$) viscous fluid (Figure 5.21a), but for the non–linear cases (Figures 5.21b–e) the decay of the along–strike velocity with distance from the driving boundary is comparable for all three profiles.

It should be noted that a 'box–car' boundary condition is assumed in the analysis, whilst a tapered 'box–car' function (see Figure 5.9) has been used in the numerical experiments to prevent the growth of singularities in the solutions. The tapered 'box–car' function uses a $\cos^2$ taper over a short distance at both ends of the velocity boundary condition. This difference is taken into account in comparing results from the numerical and theoretical methods, and calculations are scaled to ensure that the integral of the velocity along the length of the driving boundary is the same in both cases.

It should also be noted that the velocity in the interior of a semi–infinite viscous sheet will be approximately aligned with the velocity applied along its boundary; this result is demonstrated in earlier thin sheet calculations (Houseman & England, 1986; England *et al.*, 1985; England & Jackson, 1989) and is confirmed by the results of numerical experiments presented in section 5.4. These results also suggest that for this configuration of the block the velocity component normal to the driving boundary is anti–symmetric about an axis passing through the centre of the block (see Figure 5.19). Any motion of the block in the normal direction therefore cancels out, and there is no overall translation of the block in this direction. The velocity gradient, $\partial u/\partial y$, of Figure 5.19 indicates that the rigid inclusion rotates, as discussed in section 5.4.4. The magnitude of the velocity gradient is small, and this effect is neglected in the following analysis. The rotation of a rigid inclusion embedded within viscous shear flow is discussed further in section 5.9. In the light of these observations, only driving or retarding forces which act parallel to the driving boundary (in the y direction of Figure 5.20) are considered in the following analysis.

5.5.2 Estimation of tractions applied to the rigid block

The velocity field between the driving boundary and the block is approximated using a linear velocity gradient from the boundary velocity, V_0, to the block velocity, V_1, over the distance, w, which separates the block from the boundary. Shear strain rates just outside the block, and the vertically averaged shear stress, $\overline{\tau}_1$, which acts on the left–hand (1) boundary of the block (see Figure 5.20) are given by

$$\dot{\varepsilon}_{xy_1} \sim -\frac{1}{2}\left(\frac{V_0 - V_1}{w}\right) \tag{5.17}$$

$$\overline{\tau}_1 \sim -\frac{B}{\sqrt{2}^{(1+(1/n))}}\left(\frac{V_0 - V_1}{w}\right)^{1/n} \tag{5.18}$$

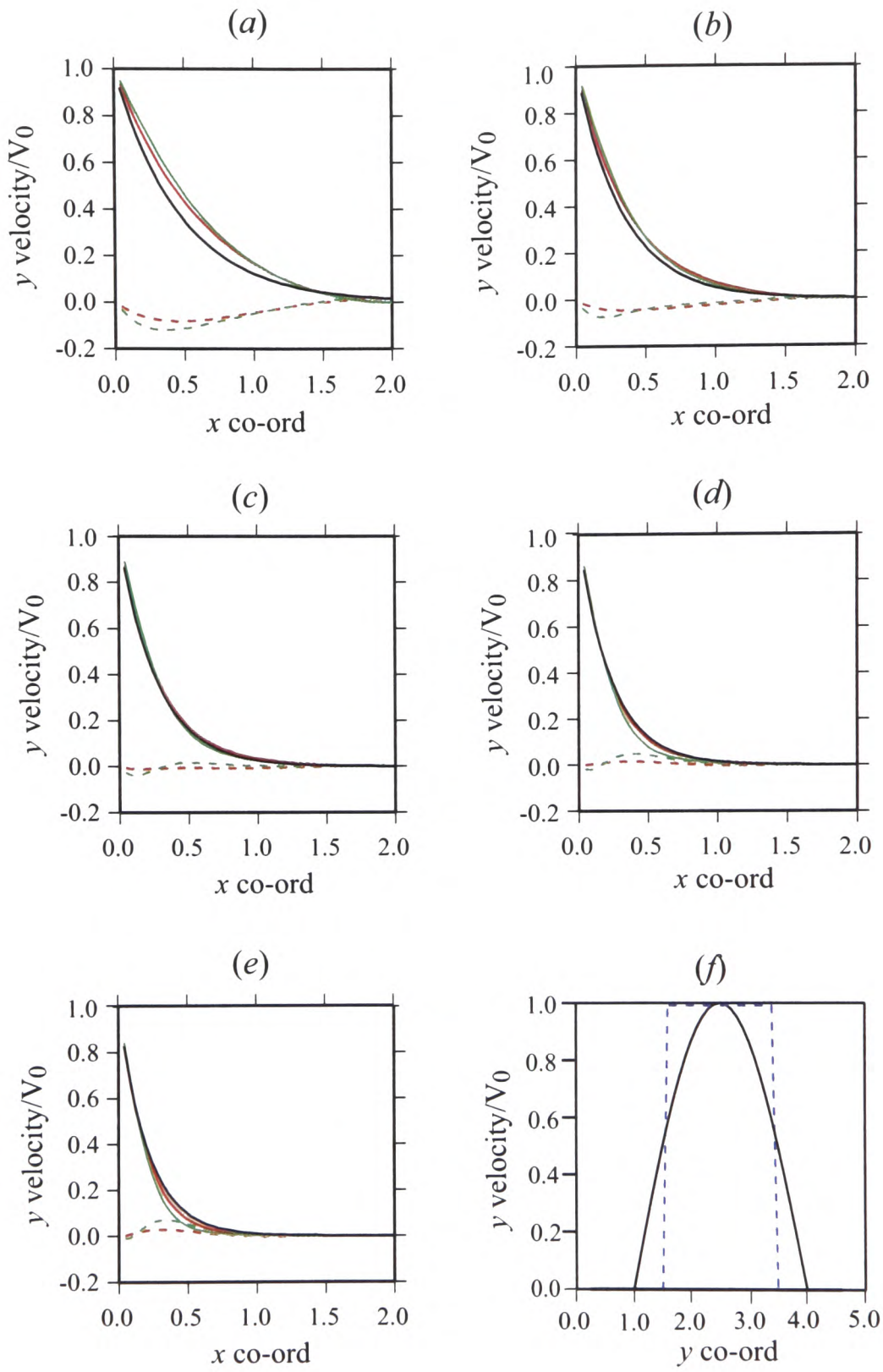

Figure 5.21: Figures (a)–(e); profiles of the y–velocity across a homogeneous solution domain (no rigid block) along $y = 2.5$, for $n = 1$ to $n = 5$ respectively. $V_0 = 1$. Black line: analytical solutions calculated using equation 5.10 with $\lambda = L'/4\sqrt{n}$, $L' = 6/\pi$. Solid red line: numerical solutions obtained using a sinusoidal boundary condition of length $L = 3$, centred upon $y = 2.5$. Solid green line: numerical solutions calculated using a 'box–car' boundary condition of length $L = 6/\pi$, centred upon $y = 2.5$. Dashed red line: misfit between the analytical solution and the solution with sinusoidal boundary condition. Dashed green line: misfit between the analytical solution and the solution with a 'box–car' boundary condition. (f) velocity boundary conditions used in the sinusoidal (solid black line) and 'box–car' (blue dashed line) cases in the numerical method. Profile taken along $x = 0$, maximum velocity is $V_0 = 1$.

The velocity field adjacent to the right–hand (2) boundary of the block (see Figure 5.20) is approximated using a linear velocity gradient from the block velocity V_1 to the background velocity V_b, over the distance $\lambda_{\|} = l/4\sqrt{n}$, where l is the length of the block. The background velocity, V_b, arises due to the motion of the long driving boundary at velocity V_0, and is given by equation 5.10 with $x = (w+d+l/4\sqrt{n})$ and $\lambda_{\|} = h/4\sqrt{n}$, where h is the length of the boundary over which the tangential velocity condition is applied. Shear strain rates just outside boundary 2, and shear stress, $\overline{\tau}_2$, are therefore given by

$$\dot{\varepsilon}_{xy_2} \sim -\frac{1}{2}\left(\frac{V_1 - V_b}{\lambda_{\|}}\right) \sim -\frac{1}{2}\left(\frac{4\sqrt{n}(V_1 - V_b)}{l}\right) \tag{5.19}$$

$$\overline{\tau}_2 \sim -\frac{B}{\sqrt{2}^{(1+(1/n))}}\left(\frac{4\sqrt{n}(V_1 - V_0 e^{-(4\sqrt{n}(w+d)+l)/h})}{l}\right)^{1/n} \tag{5.20}$$

where $V_b = V_0 e^{-(4\sqrt{n}(w+d)+l)/h}$.

The y component tractions which act on the ends of the rigid block are estimated by assuming that the dominant forces on boundaries 3 and 4 (the faces of the block whose normals point in the $\pm y$ direction) arise from normal tractions generated by the difference between the y–velocity of the block and the velocity in the background fluid (the reference velocity) that would be expected at the same range of x coordinates. It is assumed that the velocity difference decays with distance from the block in the y direction according to equation 5.10; $\lambda_{\perp} = d/\sqrt{n}$ is used, where d is the width of the block in the x direction.

The reference velocity at the ends of the block may be calculated using equation 5.10, with $\lambda_{\|} = h/4\sqrt{n}$. The reference velocity field is integrated across the width of the block to yield its average value,

$$V_{\text{av}} = \frac{V_0 h}{4d\sqrt{n}} e^{-4\sqrt{n}w/h}\left(1 - e^{-4\sqrt{n}d/h}\right), \tag{5.21}$$

which is used to estimate the velocity gradient in the viscous fluid at the ends of the block:

$$\dot{\varepsilon}_{yy} \sim \pm\left(\frac{(V_1 - V_{\text{av}})\sqrt{n}}{d}\right) \tag{5.22}$$

The normal tractions, $\overline{\text{T}}_3$ and $\overline{\text{T}}_4$, which act along the two boundaries parallel to the x axis may now be approximated, noting that the pressure term must be included when considering normal tractions in the y direction. Recall that

$$\overline{\tau}_{xx} + \overline{\tau}_{yy} + \overline{\tau}_{zz} = 0 \tag{5.23}$$

$$\Rightarrow \overline{\tau}_{zz} = -\overline{\tau}_{yy}, \tag{5.24}$$

since $\dot{\varepsilon}_{xx} = 0$. Therefore,

$$\overline{\sigma}_{yy} = \overline{p} + \overline{\tau}_{yy} = -\overline{\tau}_{zz} + \overline{\tau}_{yy} = 2\overline{\tau}_{yy} \tag{5.25}$$

Using $\dot{E} = \sqrt{2}\|\dot{\varepsilon}_{yy}\|$, and $-\overline{\mathrm{T}}_3 = \overline{\mathrm{T}}_4 = -2\overline{\tau}_{yy}$, expressions for the tractions at the ends of the block are

$$-\overline{\mathrm{T}}_3 = \overline{\mathrm{T}}_4 \sim -B\sqrt{2}^{((1/n)+1)}\left(\frac{V_1\sqrt{n}}{d} - \frac{V_0 h}{4d^2}e^{-4\sqrt{n}w/h}(1-e^{-4\sqrt{n}d/h})\right)^{1/n} \tag{5.26}$$

The tractions on all the boundaries are resolved into the y direction. Integrating these tractions over the entire boundary of the strong region, and setting the result to zero, gives

$$\begin{aligned} 0 &= \oint_{\text{boundary}} \tau.\mathbf{n}\, ds = l\left(-\overline{\tau}_1 + \overline{\tau}_2\right) + d\left(-\overline{\mathrm{T}}_3 + \overline{\mathrm{T}}_4\right) \\ \Rightarrow 0 &= \left(\frac{1-V}{W}\right)^{1/n} - (4\sqrt{n}(V - e^{-\delta_3}))^{1/n} - 4D\left(\frac{2V\sqrt{n}}{D} - \frac{H}{2D^2}e^{-\delta_1}(1-e^{-\delta_2})\right)^{1/n} \end{aligned} \tag{5.27}$$

where $V = V_1/V_0$, $W = w/l$, $D = d/l$, $H = h/l$, $\delta_1 = 4\sqrt{n}W/H$, $\delta_2 = 4\sqrt{n}D/H$ and $\delta_3 = (4\sqrt{n}(W+D)+1)/H$. This equation gives an expression for the velocity of the block relative to that of the boundary in closed form.

5.6 Results

5.6.1 Agreement between numerical and analytical methods

Figure 5.22 compares the numerical and theoretical estimates for the velocity of the rigid block. Results are shown for the four configurations given in table 5.1, where block aspect ratios range from $1/D = 2.87$ to $1/D = 5.75$. Driving boundary conditions of lengths $H = 1.0$, 1.5 and 2.5 are used, and the stress–strain rate exponent is varied between $n = 1$ and $n = 5$. The distribution of values for V_1/V_0 indicates that the motion of a rigid block within a simple shear flow depends upon a combination of the aspect ratio of the block, the degree of non–linearity of the viscous fluid, and the length of the driving boundary, as implied by equation 5.27.

When $V_1/V_0 \lesssim 0.4$, corresponding to solutions which use $n \geq 3$, the approximate expressions agree with the numerical solutions to within $\sim 10\%$ (Figure 5.22). At higher values of V_1/V_0 (generally corresponding to $n = 1$ or $n = 2$) the analytical expression underestimates V_1/V_0 probably because the retarding force on boundary 2 of the rigid block is overestimated. The shear stress on this boundary arises from the velocity gradient between the block and the background velocity field. Using equation 5.20 the background velocity field is estimated from the decay (equation 5.10) of the velocity which arises as a result of the motion of a boundary of length H. However, the presence of a rigid block within the flow will act to broaden this background velocity field, thus V_b in equation 5.20 is underestimated. The agreement between simple analytical and full numerical solutions is good

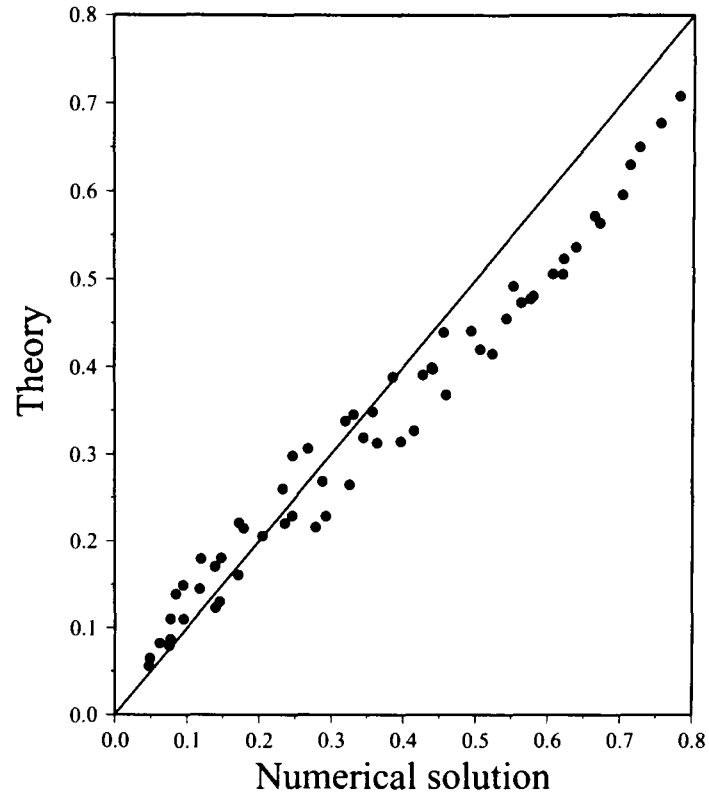

Figure 5.22: Solutions for V_1/V_0 calculated using equation 5.27, plotted against values obtained using the numerical method outlined in section 5.3.5. Solutions are calculated for integer values of n in the range $n = 1$ to $n = 5$, using driving boundaries which vary between 1.0 times the length of the rigid inclusion and 2.5 the length of the rigid inclusion (see text). Results are shown for four different shapes of rigid blocks with aspect ratios ranging from $1/D = 2.87$ to $1/D = 5.75$.

in the range of V_1/V_0 exhibited by the Sierra block (see section 5.7.1), and even outside this range, agreement is adequate. Therefore more complicated analytical models are not considered.

5.6.2 Dependence of block velocity upon n

Figure 5.23 demonstrates the relationship between the value of V_1/V_0, calculated using equation 5.27, and n, over a range of values for W/D. For each value of n, H is varied between 1.0, 1.5 and 2.5, and W/D takes the values 2 (case D, table 5.1, black circles), 1.5 (case A, red), 1.2 (case B, green), and 1.0 (case C, blue). At each n, the smallest calculated value for V_1/V_0 corresponds to the case H=1.0, and the largest value corresponds to the case H=2.5.

Reasons for the variation of V_1/V_0 within the parameter space have been discussed previously with regard to the numerical experiments of section 5.4. I simply note that the analytical model implies that the relative velocity of the rigid block decreases as n is increased, for a fixed set of boundary conditions. This is in agreement with the numerical experiments presented in section 5.4 and thin viscous sheet models, where the characteristic length scale for the decay of velocity decreases as the

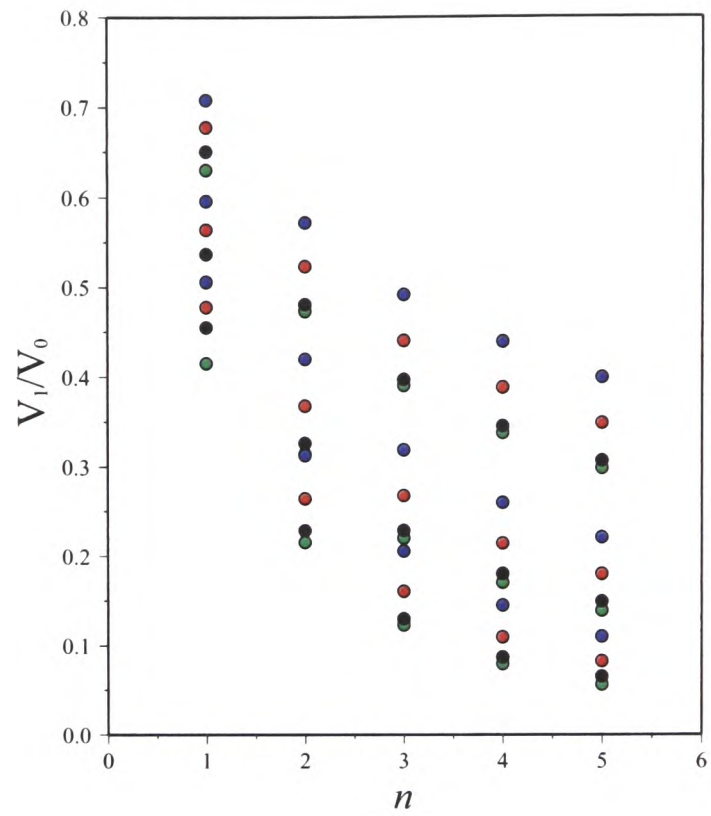

Figure 5.23: The relationship between the relative velocity of the rigid block (V_1/V_0), calculated using equation 5.27, and the stress versus strain–rate exponent, n. Results are shown for four blocks of varying aspect ratio, as specified in table 5.1; shape A (red), shape B (green), shape C (blue) and shape D (black). Three different lengths of driving boundary have been used; $H = 1.0$, 1.5 and 2.5.

non–linearity of the fluid increases (England *et al.*, 1985; Sonder *et al.*, 1986).

5.7 Preliminary conclusions

5.7.1 The estimation of n from simple models

The Sierra block may be considered to be a rigid block translating within a simple shear velocity field driven by motion along the Pacific–North America plate boundary. The physical quantities which define this plate boundary zone are non–dimensionalised, and this defines its location in the parameter space of both the approximate and numerical models. Constraints may then be placed upon the value of the stress–strain rate exponent, n, which governs the non–linear behaviour of the continental lithosphere in the western North America plate boundary zone.

Values of l, d, w, h, V_0 and V_1, which approximate the dimensions, location, and motion of the Sierra block in California, are given in table 5.2. The non–dimensional length scale parameters W, D and H are defined as in section 5.5.2, and take the values $W = 0.18, D = 0.26$ and $H = 1.5$ for this study. The length of the Sierra block has been used to non–dimensionalise all length scales.

It has been demonstrated in section 5.6.1 that there is good agreement between the approximate solutions and the results generated by the numerical method. Approximate solutions are therefore used to calculate an expected velocity ratio (V_1/V_0) using the parameters which describe the Sierra block within western North America. Substituting values for the non–dimensional length scales W, D and H into the force balance equation, equation 5.27, I solve for $V = V_1/V_0$ and plot V against W/D (see Figure 5.24) for a range of values of n.

If a rate of 52 mm yr^{-1} (DeMets & Dixon, 1999) is used as an estimate for motion along the plate boundary (V_0), and 12 mm yr^{-1} (Argus & Gordon, 2001) for motion of the Sierra block relative to North America (V_1), this yields an observed velocity ratio of $V_1/V_0 = 0.23$ at this plate boundary. However, estimates for the relative velocity of the Sierra block to stable North America are currently

Table 5.2: Physical parameters for California

Length, l	715 km
Width, d	185 km
Distance from plate boundary, w	130 km
Length of driving boundary, h	1100 km
Velocity across plate boundary[1], V_0	52 mm yr^{-1}
Velocity of rigid Sierra block[1], V_1	12 mm yr^{-1}

[1]Velocities relative to stable North America

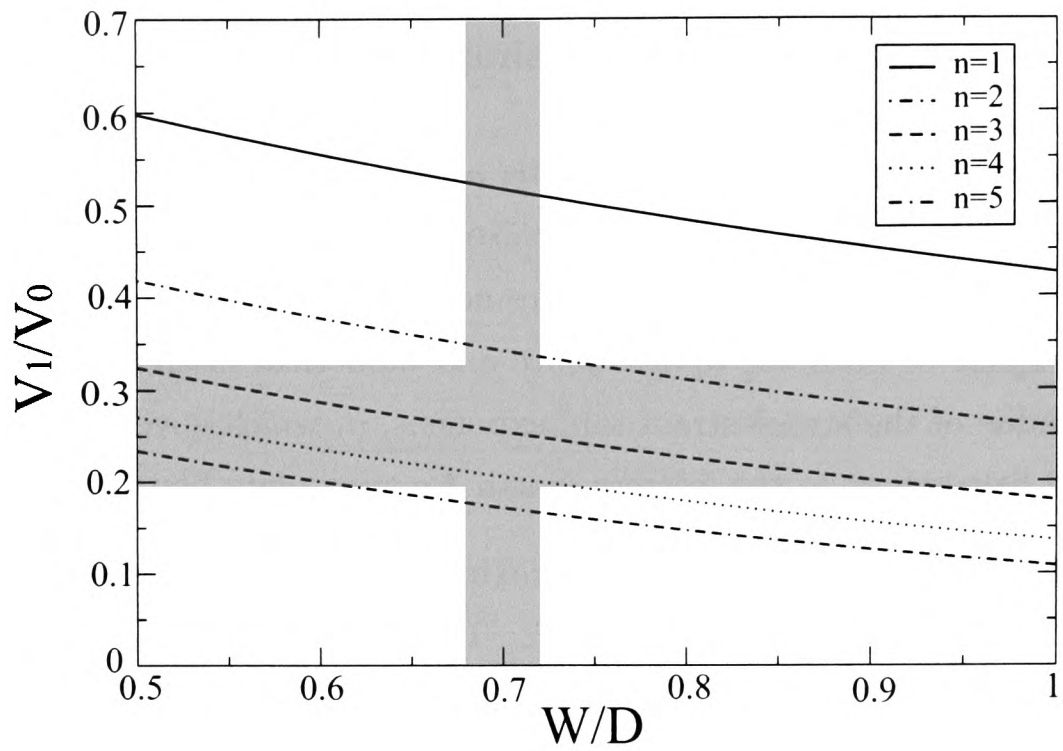

Figure 5.24: The ratio between velocity of the rigid block (V_1) and the driving velocity (V_0) plotted against the non–dimensional ratio W/D, for values of n in the range $n = 1$ to $n = 5$, $H = 1.5$. The shaded regions correspond to the parameter space covered by estimates for the velocity ratio and length scales observed in North America (see text).

poorly constrained, and lie in the range 10 mm yr^{-1} to 15 mm yr^{-1} (Minster & Jordan, 1987; Wernicke & Snow, 1998; Hearn & Humphreys, 1998; Thatcher *et al.*, 1999; Dixon *et al.*, 2000; Argus & Gordon, 2001). Similarly, studies of plate boundary motion across the Pacific–North America plate boundary yield values for the plate relative velocity which lie between 46 mm yr^{-1} and 52 mm yr^{-1} (Larson *et al.*, 1997; Bennett *et al.*, 1999; DeMets & Dixon, 1999; Argus & Gordon, 2001). These ranges of values give maximum and minimum estimates for V_1/V_0 of 0.326 and 0.192 respectively. The shaded regions in Figure 5.24 represent these uncertainties in the measurements of V_1 and V_0, as well as in the estimation of the length, width and distance of the Sierra block from the plate boundary, for a driving boundary condition of fixed length H. There are uncertainties associated with estimating H, but varying H within error has little effect upon the results plotted in Figure 5.24. The error in estimating W/D is compounded by the variation in the width of the Sierra block, and its distance from the plate boundary, along strike. The bounds of Figure 5.24 constrain the value of the stress–strain rate exponent, required to reproduce the observed ratio of velocities, to lie in the range $n = 3$ to $n = 4$.

5.7.2 Areas for further investigation

The results of the simple models are tested against observations in section 5.8. Profiles of velocity parallel to the plate boundary are constructed using GPS estimates of the surface velocity field in the western North America plate boundary zone. These profiles are compared to y–velocity profiles obtained using a range of values of n in the numerical experiments of section 5.4. The fit of the observed and calculated velocities is used to further constrain the value of n which governs deformation in this plate boundary zone. GPS profiles which cross the plate boundary at a range of latitudes are compared to determine the effect of the Sierra block upon the surface velocity field in western North America.

Forces associated with the rotation of a rigid block embedded within a viscous layer undergoing simple shear flow are neglected in the force balance analysis of section 5.5. If the Sierra block is rotating it will become misaligned with the direction of shear. The forces along the boundaries of the block would therefore need to be resolved into components normal and parallel to the boundaries. The expected and observed rate of rotation of the Sierra block is studied in section 5.9 in order to ascertain whether this complication should be taken into account when balancing the forces applied to the boundaries of the Sierra block.

A 550 km-long section of the Pacific–North America plate boundary in southern California is misaligned by $\sim 35^{o}$ anti–clockwise. Relative motion along this section of the plate boundary is accommodated by a combination of strike–slip and thrust faulting. Evidence for thrusting at the southern margin of the Sierra block implies that it does not translate completely passively within the lithosphere, and far field estimates for the forces applied to the boundaries of the block will be modified as a result of deformation of the lithosphere in the near field.

In section 5.10 numerical experiments are carried out using a solution domain which more closely represents the geometry of the Pacific–North America plate boundary. The effect of a bend in the plate boundary upon the motion of a higher viscosity region, and the resulting deformation in the adjacent viscous fluid, are investigated for a range of boundary conditions. It is postulated that for suitable boundary conditions a greater normal force will be applied across the inclined boundary to the 'southern' edge of the higher viscosity region than in the original experiments of section 5.4. Strain rates for the new numerical solutions are studied to ascertain whether this force is accommodated by thickening of the viscous layer, or by an increase in the velocity of the higher viscosity region. The distribution of shear strain in the numerical solutions is used to evaluate the effect of varying the orientation of the plate boundary and the velocity boundary conditions. The ability of the model to reproduce the main features of the plate boundary zone when realistic boundary conditions are applied is used to assess the suitability of using the thin viscous sheet model to investigate the

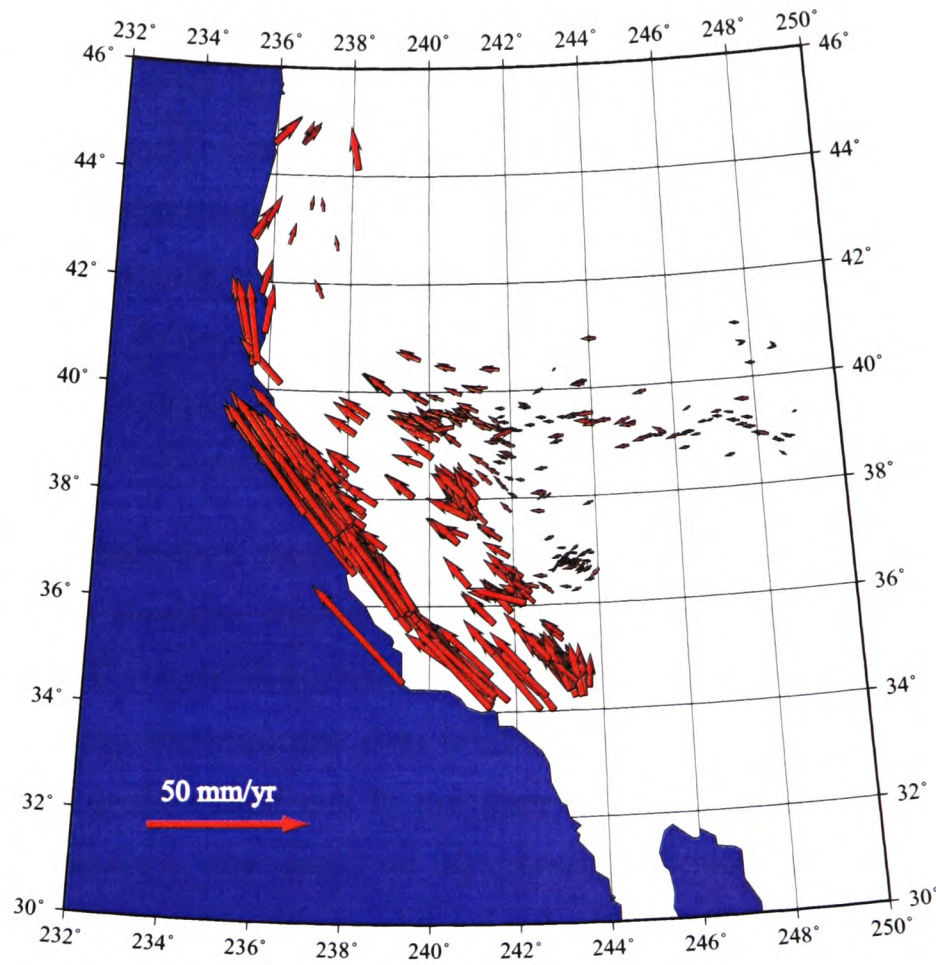

Figure 5.25: GPS velocity field compiled from USGS data. Velocities are in a North–America–Fixed reference frame.

rheological parameters governing continental deformation in westernmost North America

5.8 Fitting GPS data to simple rigid block models

5.8.1 GPS velocity field

GPS velocity data, acquired from publicly available data sets published on the USGS and JPL websites (http://quake.wr.usgs.gov/research/deformation/gps/auto/CL.html for the USGS and http://sideshow.jpl.nasa.gov/mbh/series.html for JPL), are used to test the conclusions of the simple modelling. Data between 30°N and 45°N, and −110°E and −125°E,s are considered. USGS data are discarded if they do not span a period of ≥two years, if the site has been reoccupied fewer than ten times, or if the time series is obviously disrupted. The USGS data are given in a North–America–fixed reference frame (Figure 5.25).

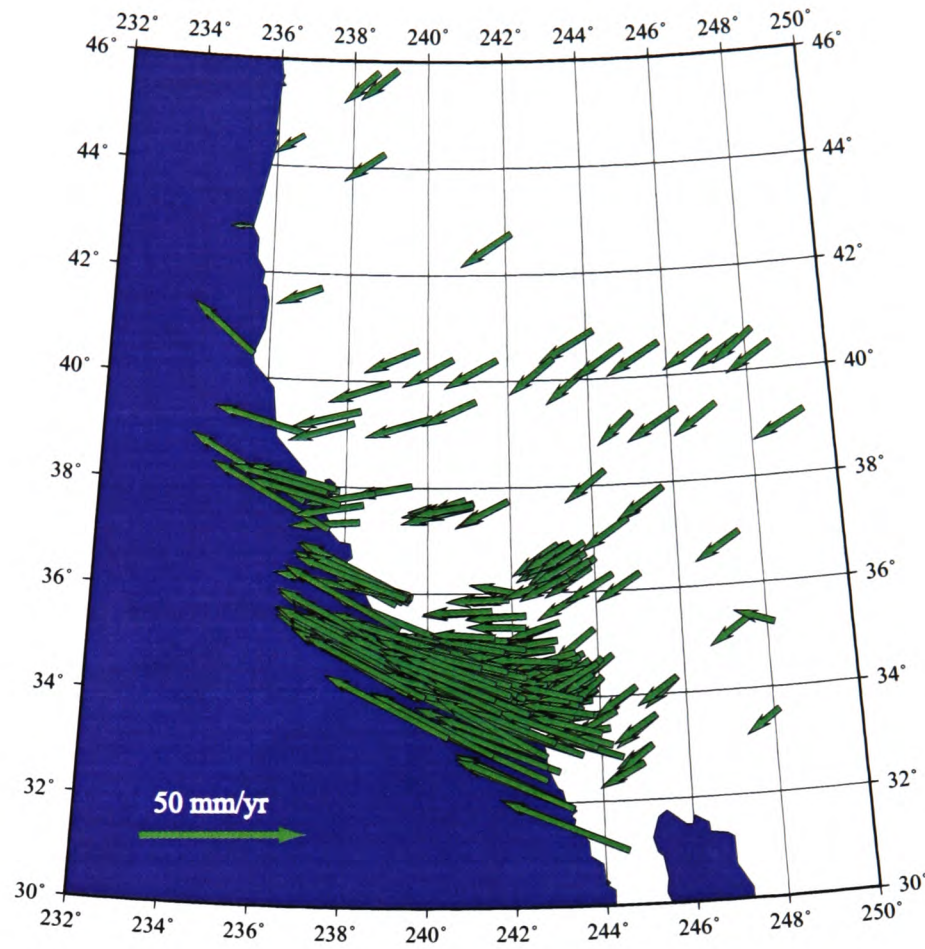

Figure 5.26: GPS velocity field compiled from JPL data. Velocities are in an ITRF 2000 reference frame.

The JPL data are given in an ITRF 2000 reference frame (Figure 5.26). Several sites are common to both data sets, and this fact is used to determine the rigid body rotation that transforms the JPL data into the same reference frame as the USGS data. Relative velocities ($\mathbf{u}$) between common JPL and USGS sites are plotted in Figure 5.27. The splay of arrows at (-119°E, 37.5^{o}N) is centred upon the Long Valley caldera. This region has been the site of several recent GPS campaigns by the USGS, carried out to study the recent rapid deformation of the caldera. The radial vectors are an artifact of the inflation of the caldera; they are present in the USGS data, but not the JPL data, and therefore prevail in the relative velocity field. These data will be discarded from the final data set of GPS velocities, and no attempt is made to fit them as part of a rigid body rotation.

The motion of a rigid body upon the surface of a sphere of radius R may be described by a rotation, at a rate Ω, about an axis passing through a point with longitude Λ and latitude Φ. The velocity of a point (λ, ϕ), where λ represents longitude, and ϕ represents latitude, due to this rotation is given by

$$\frac{d\lambda}{dt} = R\Omega(\sin(\Phi) - \cos(\lambda - \Lambda)\tan(\phi)\cos(\Phi)) \tag{5.28}$$

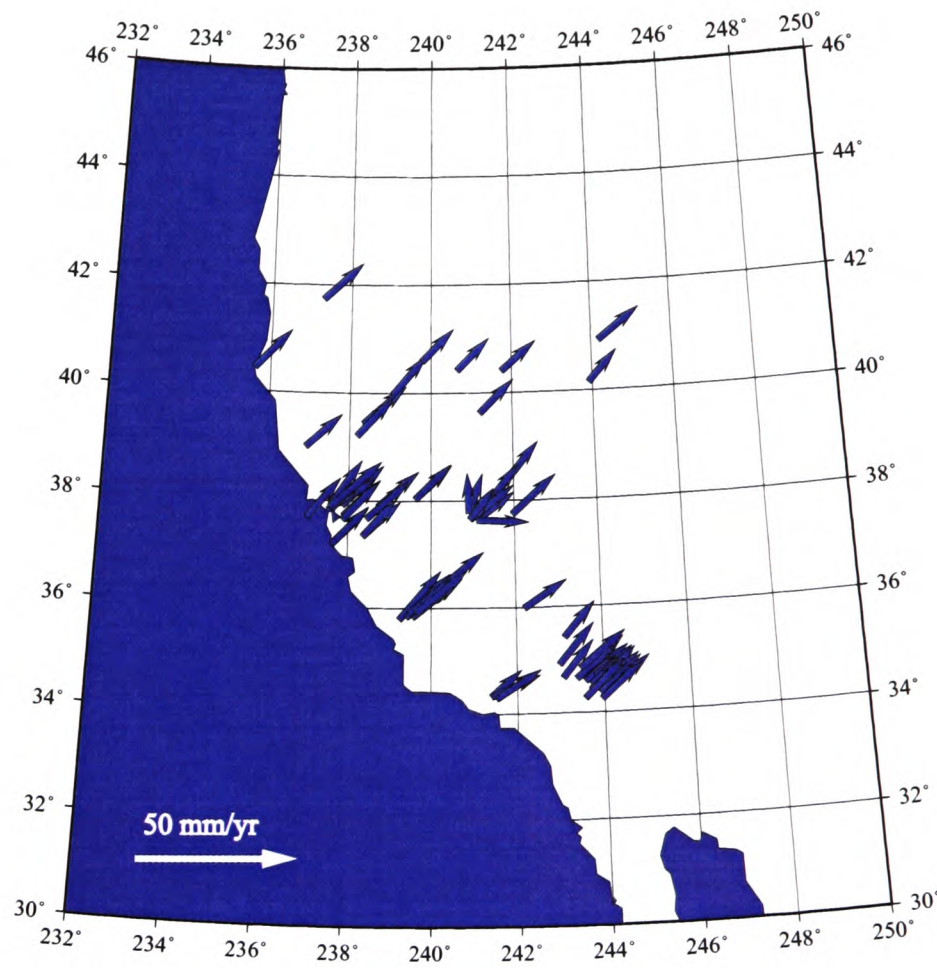

Figure 5.27: Relative velocity between USGS and JPL (USGS minus JPL) data for sites common to both data sets.

$$\frac{d\phi}{dt} = R\Omega\cos(\Phi)\sin(\lambda - \Lambda) \tag{5.29}$$

In order to determine the rigid body rotation which transforms the JPL data into the same reference frame as the USGS data, I minimise the function

$$\sum_i \left[(u_i - \frac{d\lambda_i}{dt})^2 + (v_i - \frac{d\phi_i}{dt})^2 \right]^{1/2} \tag{5.30}$$

where the sum is taken over every point common to the USGS and JPL data sets. u_i and v_i are determined from the GPS data, and are the east and north components respectively of the ith relative velocity vector ($\mathbf{u}_i$), located at $\mathbf{r_i} = \phi_i, \lambda_i$. For a given rotation, (Λ, Φ, Ω), the predicted velocity at $\mathbf{r_i}$ is calculated using equations 5.28 and 5.29.

A least squares approach is used to determine the rotation vector, ω, that describes the relative velocity field, $\mathbf{u}$. For a sphere of radius R, the velocity of a point, $\mathbf{r}$, on the surface of the sphere is given by $\mathbf{u} = \omega \wedge \mathbf{r}$, ω describes a rotation about an axis passing through the centre of the sphere. $R = 6378$ km is used for the radius of the Earth, and the rotation vector which minimises the function

in equation 5.30 is determined by solving the matrix equation;

$$\begin{pmatrix} u_x^{(1)} \\ u_y^{(1)} \\ u_z^{(1)} \\ u_x^{(2)} \\ u_y^{(2)} \\ . \\ . \end{pmatrix} = \begin{pmatrix} 0 & r_z^{(1)} & -r_y^{(1)} \\ -r_z^{(1)} & 0 & r_x^{(1)} \\ r_y^{(1)} & -r_x^{(1)} & 0 \\ 0 & r_z^{(2)} & -r_y^{(2)} \\ -r_z^{(2)} & 0 & r_x^{(2)} \\ . & . & . \\ . & . & . \end{pmatrix} \begin{pmatrix} \omega_x \\ \omega_y \\ \omega_z \end{pmatrix} \tag{5.31}$$

Positions and velocities have been converted from spherical co–ordinates (r, θ, ϕ) into Cartesian co–ordinates (x, y, z). Superscripts are used to index each of the GPS sites, and u_α^j and r_α^j are known, where $\alpha = x$, y or z. For a relative velocity field defined at m points, where $m > 1$, equation 5.31 defines an overdetermined problem. It is solved using the least squares method to yield the rotation vector $\omega = (\omega_x, \omega_y, \omega_z)$.

Converting back into spherical co–ordinates, $\omega = (\Lambda, \Phi, \Omega)$, where Ω defines the rate of rotation of the rigid body and (Λ, Φ) are the longitude and latitude of the intersection of the rotation axis with the surface of the Earth. The transformation that best fits the USGS–JPL relative velocity field is $(-20.86°\text{E}, -50.08°\text{N}, 0.1707°\ \text{Ma}^{-1})$. The value of the misfit function (equation 5.30) for this solution is ~ 0.11 mm yr^{-1}.

This minimum is confirmed in Figures 5.28, 5.29, and 5.30, where the misfit function is plotted for $(0° \leq \Lambda \leq 360°, -90° \leq \Phi \leq 90°, -0.5 \leq \Omega \leq 0.5)$. In each figure, one of Λ, Φ or Ω are held fixed at the solution from the least squares calculation. The minimum in all three figures coincides with the solution from the least squares calculation, and takes the value ~ 0.11 mm yr^{-1}.

The relative velocity field and the velocity due to the rigid body rotation are plotted in Figure 5.31 for points common to both data sets. Apart from the region surrounding the Long Valley caldera, there is good agreement between the calculated rotation in yellow and the relative velocity field in blue. This rotation is therefore applied to the whole JPL data set via equations 5.28 and 5.29. The rotated JPL velocity data are plotted with the USGS data in Figure 5.32. The light green arrow in the south–east of the figure is discarded at this point; comparison with the background velocity field indicates that there are clearly large errors associated with this measurement.

5.8.2 Profiles of GPS velocities across the zone of deformation

The GPS velocity data are projected onto twenty transects positioned 0.5° apart between 30°N and 39.5°N. Each transect is defined to be perpendicular to an estimation of the local strike of the plate

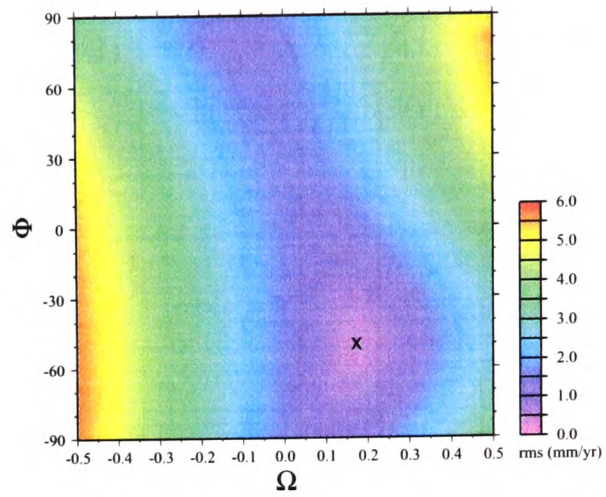

Figure 5.28: The misfit function of equation 5.30 is plotted as Ω and Φ are varied, and $\Lambda = -20.86°$E is held constant. x marks the approximate location of the minimum for this plot.

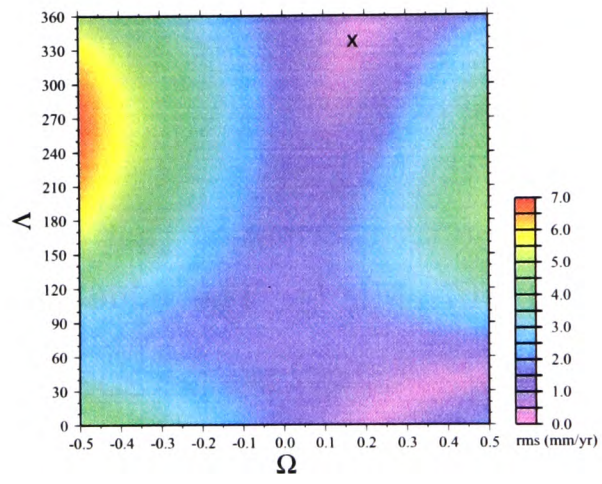

Figure 5.29: as for Figure 5.28. The misfit is plotted as Ω and Λ are varied, and $\Phi = -50.08°$N is held constant. x marks the approximate location of the minimum for this plot.

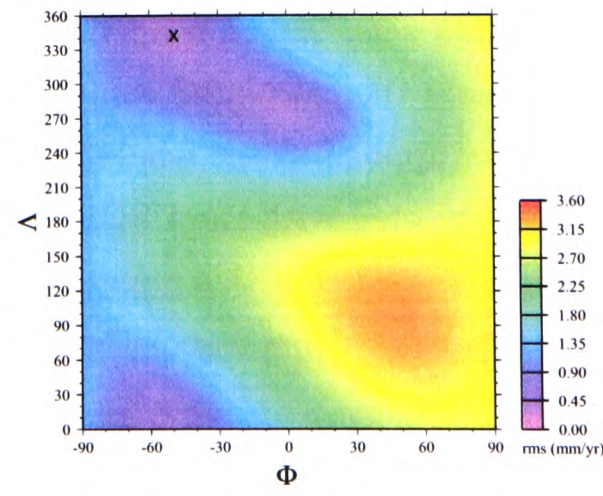

Figure 5.30: as for Figure 5.28. The misfit is plotted as Φ and Λ are varied, $\Omega = 0.1707$ Ma^{-1} is held constant. x marks the approximate location of the minimum for this plot.

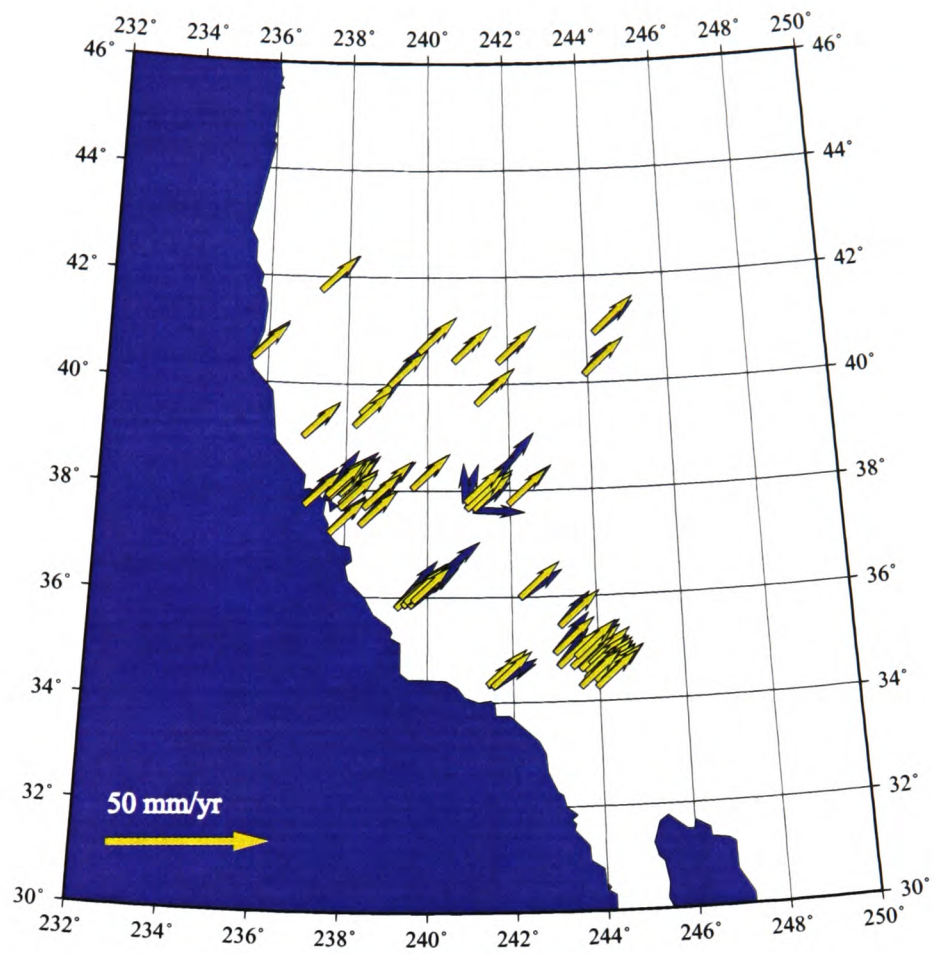

Figure 5.31: Rigid body rotation shown in yellow, calculated at points common to both GPS data sets. Relative velocity between USGS and JPL (USGS minus JPL) data shown in blue (as in Figure 5.27).

boundary, as defined by a small circle, and the velocity data are resolved into strike–normal and strike–parallel components.

The projection of the velocity data defines a series of velocity profiles normal to the idealised plate boundary. The position of the plate boundary in each profile will vary because the Pacific–North America plate boundary does not describe a perfect small circle. When presenting the data, the profiles are shifted accordingly in Figures 5.34–5.38 to allow comparison to model velocity profiles.

The projection of GPS data onto velocity transects

Co–ordinate axes are defined such that the origin lies at the centre of the Earth, which is approximated to be spherical with radius R. The GPS data are projected onto transects that are perpendicular to a small circle (the plate boundary). Let $\mathbf{A}$ represent the position vector of the intersection between a transect and the plate boundary. This transect therefore passes through the centre of the small circle (the axis of rotation for Pacific–North America relative motion; position vector $\mathbf{P}$), and hence

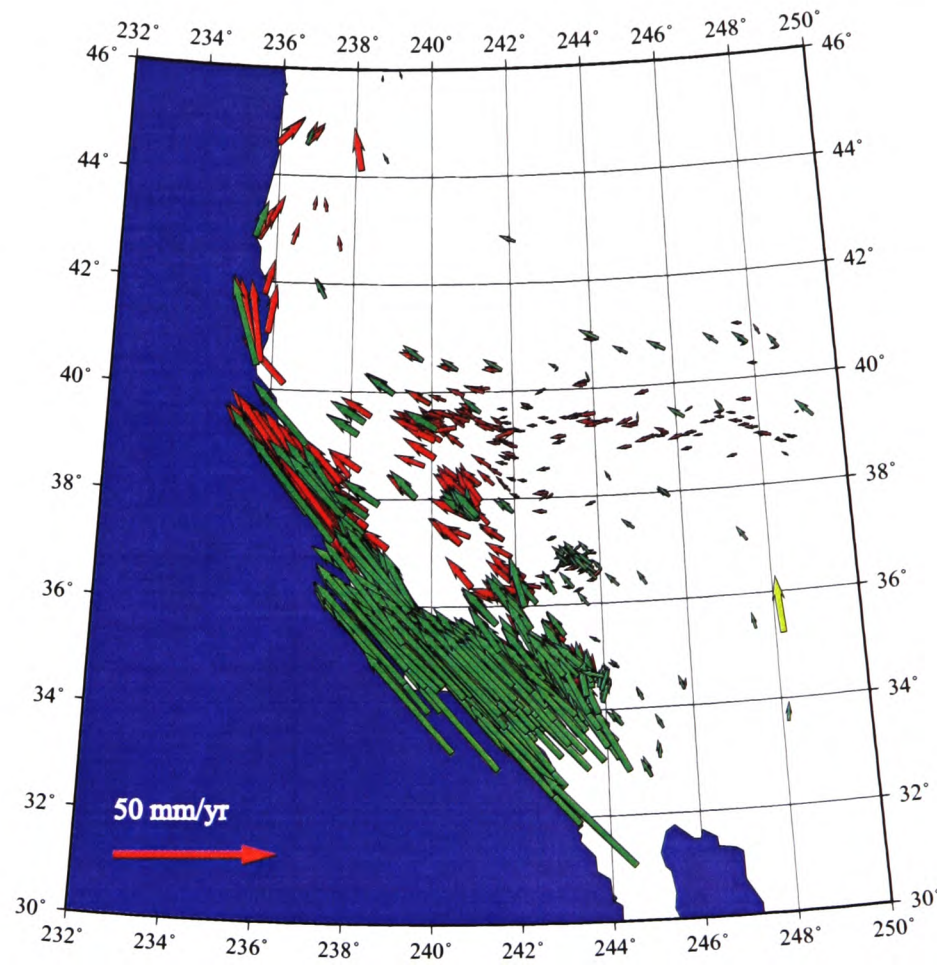

Figure 5.32: USGS GPS velocity data shown in red. JPL GPS velocity data, following the application of a rigid body rotation, shown in green. The JPL GPS velocity datum shown in light green clearly contains errors, and is neglected in the following analysis.

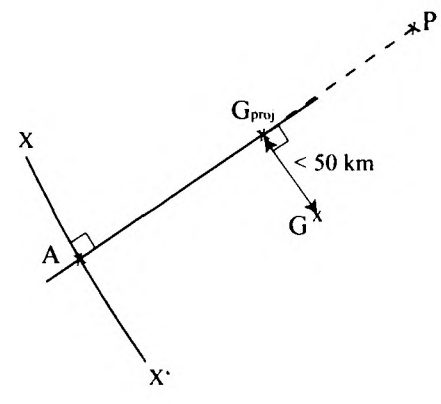

Figure 5.33: Geometry for the projection of GPS data onto transects perpendicular to the plate boundary (XX'). P is the axis of rotation, A is the intersection of the transect with the plate boundary, and G_{proj} is the projection of the position of the GPS site onto the transect.

defines a great circle. A great circle defines a plane, and the normal to this plane is

$$\mathbf{n_1} = \frac{\mathbf{A} \wedge \mathbf{P}}{|\mathbf{A}||\mathbf{P}|}. \tag{5.32}$$

A second plane may be defined, one which contains the normal to the first plane and the position vector of a GPS site, $\mathbf{G}$. The normal to this second plane is

$$\mathbf{n_2} = \mathbf{n_1} \wedge \frac{\mathbf{G}}{|\mathbf{G}|}. \tag{5.33}$$

The intersection of the two planes defines a line; the intersection of this line with the surface of the sphere defines the projection of the GPS datum onto the transect $\overrightarrow{\mathbf{AP}}$: $\mathbf{G_{proj}} = R\,\mathbf{n_1} \wedge \mathbf{n_2}$.

The velocity data are resolved into components parallel and perpendicular to the plate boundary. They are then projected onto a given transect if the perpendicular distance of the GPS site from the transect is $\leq$50 km. .

5.8.3 Comparison between observed and calculated velocity profiles

The along–strike component of the projected GPS data and a profile from the numerical experiments are plotted for the 20 transects in Figures 5.34–5.38. The profiles are taken perpendicular to the driving boundary ($x = 0$) across $y = 2.5l$ (see Figure 5.9). Where suitable, the numerical experiment contains a higher viscosity region; if the GPS profile does not cross the Sierra block the numerical profile is taken from an experiment with no heterogeneity. Values of d and w (see Figure 5.9) are chosen to reflect the geometry of the plate boundary zone.

The horizontal distance represented by the profiles from the numerical model is determined by the length, l, of the higher viscosity region. The Sierra block is approximately 715 km long, and the width of the solution domain in the numerical method is $2.5l$, therefore the horizontal distance represented by each numerical profile is $\sim$1800 km. The position of the x–axis with respect to the GPS profiles is fit by eye. Velocities are scaled using a Pacific–North America plate boundary velocity of 52 mm yr^{-1} (DeMets & Dixon, 1999), which is assumed to correspond to the maximum y–velocity of each model profile.

GPS velocity errors are propagated in the calculation of velocity components parallel and perpendicular to the strike of the plate boundary. The maximum error for the along–strike velocity components of transects 1 to 20 is $\pm$2.9 mm yr^{-1}; the average is $\pm$0.83 mm yr^{-1}. Error bars for the GPS data are not shown for clarity, but are small in comparison to the magnitude of the velocity signal.

The shapes of the GPS profiles depend upon the strike of the transects onto which they are projected. The strike of the true plate boundary varies along its length, but the transects are defined

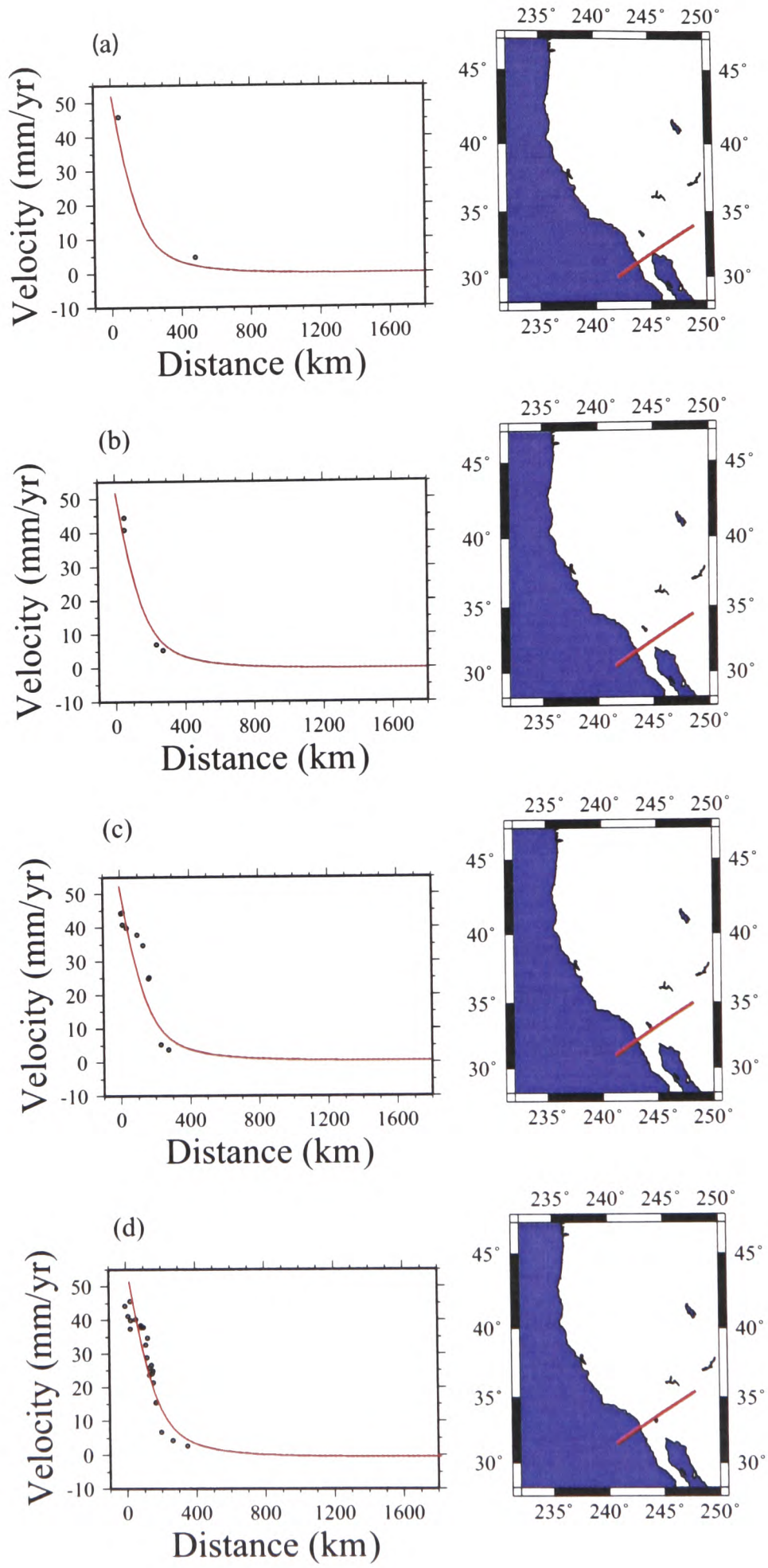

Figure 5.34: Velocities parallel to the plate boundary. $n = 3$ is used in the numerical profiles. (a) transect 1: no rigid inclusion. (b) transect 2: no rigid inclusion. (c) transect 3: no rigid inclusion. (d) transect 4: no rigid inclusion.

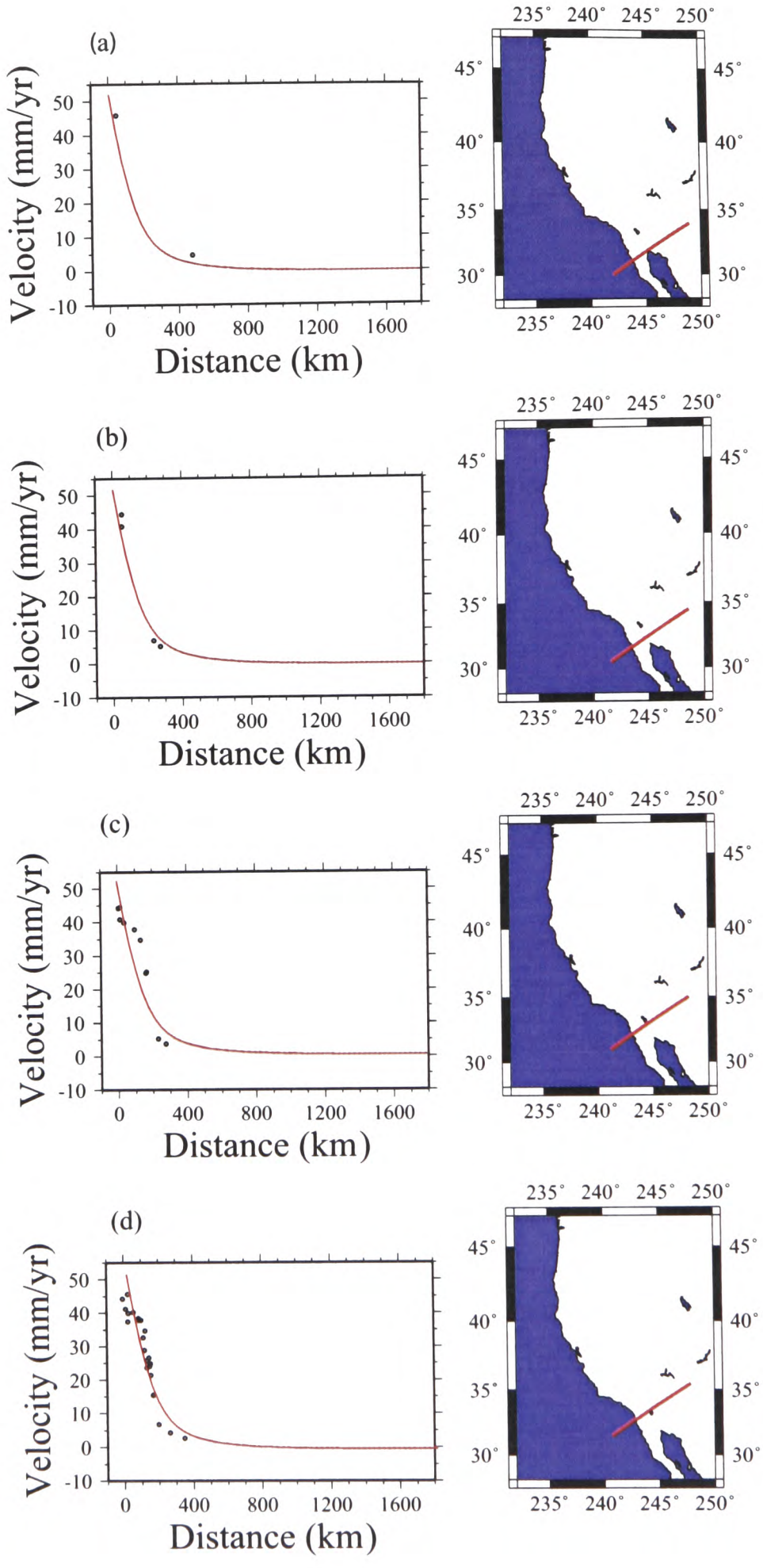

Figure 5.35: Velocities parallel to the plate boundary. $n = 3$ is used in the numerical profiles. (a) transect 5: no rigid inclusion. (b) transect 6: no rigid inclusion. (c) transect 7: no rigid inclusion. (d) transect 8: no rigid inclusion.

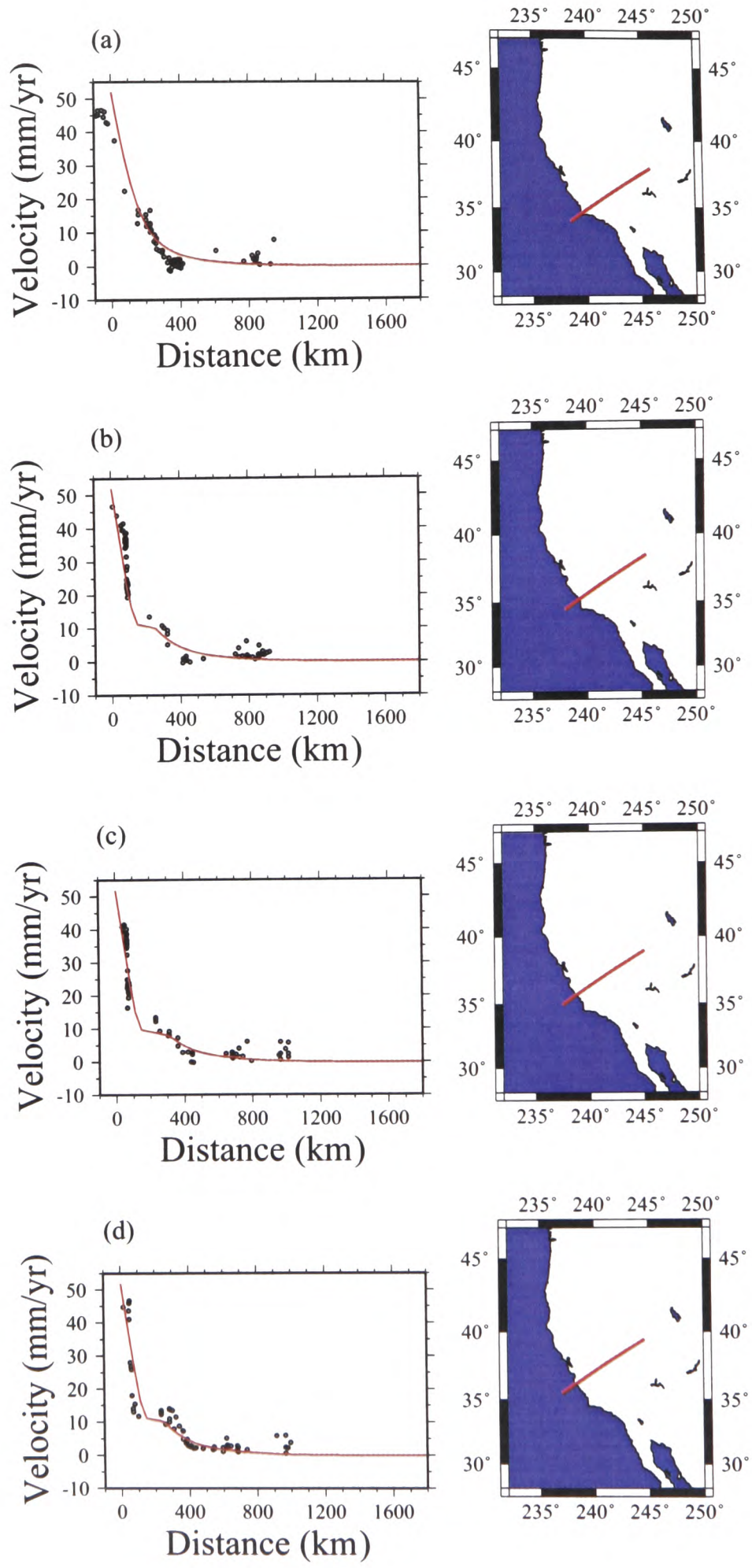

Figure 5.36: Velocities parallel to the plate boundary. $n = 3$ is used in the numerical profiles. (a) transect 9: no rigid inclusion. (b) transect 10: contains rigid inclusion. (c) transect 11: contains rigid inclusion. (d) transect 12: contains rigid inclusion.

to be perpendicular to an idealised plate boundary defined by a small circle, and are therefore not necessarily perpendicular to the local strike of the actual plate boundary. Since the GPS data are projected from up to 50 km away, this introduces another level of inaccuracy into the shape of the velocity profiles. I do not increase the complexity of the problem by attempting to account for local variations in the strike of the plate boundary.

Profiles to the north and south of the studied region contain few data, and little is learnt by attempting to fit model profiles for these transects. To the north of the Sierra block (transects 17 and 18) profiles with and without a rigid inclusion are equally viable.

For the majority of the profiles across the Sierra block, the best–fitting model is one that contains a rigid region in the location approximately corresponding to the Sierra block. The shape of the observed velocity profiles and the observed velocity ratio ($V_1/V_0 \simeq 0.23$) are best reproduced when a power law exponent of $n = 3$ is used to generate the model profiles. A smaller power law exponent yields a shallower velocity curve and a greater velocity ratio, implying a block velocity of >18 mm yr^{-1}. A greater power law exponent yields a steeper velocity curve and a smaller velocity ratio, implying block velocities of <10 mm yr^{-1}.

In many of the GPS profiles, the along–strike velocity does not decrease monotonically at distances > 700 km from the plate boundary. The length scale analysis of section 5.5.1 implies that the strike–slip motion of a 1100 km–long driving boundary will have little effect upon the surface velocity field 700 km inland. Even allowing for the broadening of the velocity field due to the presence of a rigid inclusion, it is unlikely that these data reflect a response to plate boundary motion. Data from GPS sites more than ~1000 km from the plate boundary are not included in this study, and it is impossible to tell whether the signal is due to local deformation, or whether it is part of a background signal which extends into the interior of the continent. The signal is small, and may reflect a change in the orientation of velocity vectors as well as their magnitude.

There is a small increase in the magnitude and range of the along–strike velocity along the eastern boundary of the Sierra block (transects 12–15). This corresponds to the location of the East California Shear Zone, where slip is partitioned between strike–slip and normal motion. This is a tectonically active region, and the range of observed velocities may be attributed to a combination of elastic strain accumulation and postseismic relaxation associated with the active faulting, as well as the misalignment of velocity vectors due to the partitioning of strain along pre–existing zones of weakness.

GPS profiles south of the Sierra block are fit to $n = 3$ and $n = 4$ model profiles which do not contain a rigid inclusion. $n = 4$ is required to fit the steeper GPS profiles (transects 3–6) taken across the 'Big Bend' section of the plate boundary. This 300 km–long segment of the San Andreas fault in southern California strikes roughly 25° counter–clockwise from the main strike of the plate boundary.

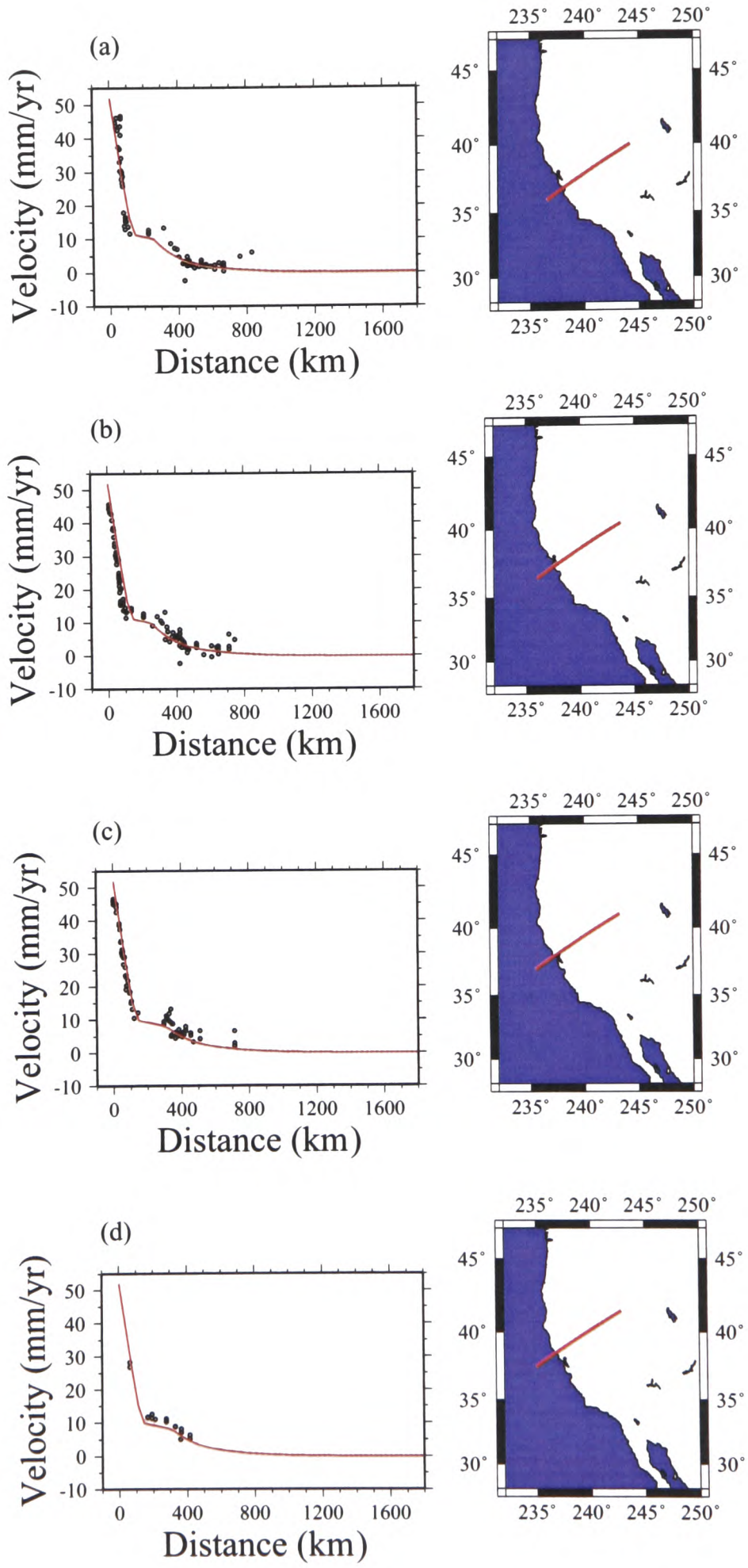

Figure 5.37: Velocities parallel to the plate boundary. $n = 3$ is used in the numerical profiles. (a) transect 13: contains rigid inclusion. (b) transect 14: contains rigid inclusion. (c) transect 15: contains rigid inclusion. (d) transect 16: contains rigid inclusion.

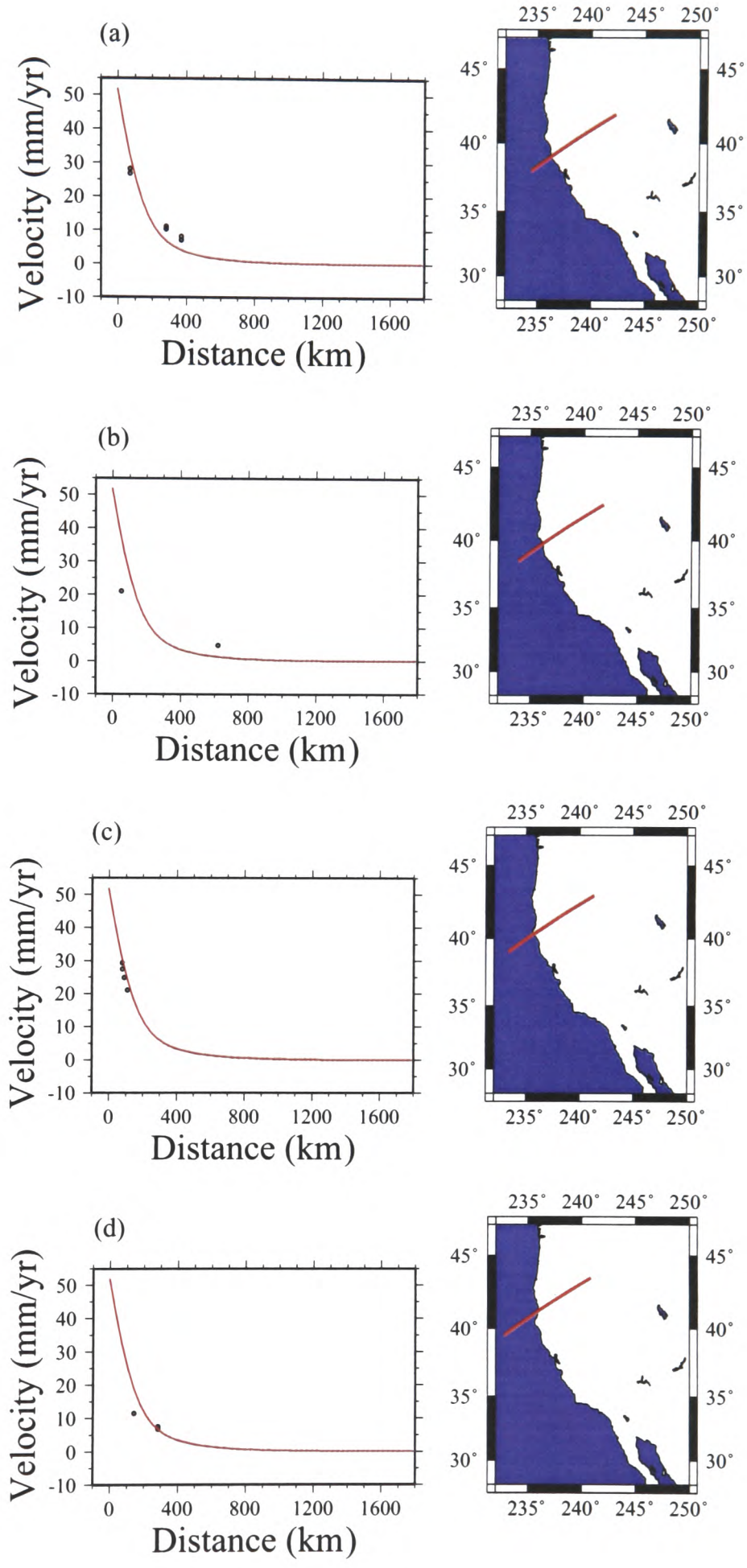

Figure 5.38: Velocities parallel to the plate boundary. $n = 3$ is used in the numerical profiles. (a) transect 17: no rigid inclusion. (b) transect 18: no rigid inclusion. (c) transect 19: no rigid inclusion. (d) transect 20: no rigid inclusion.

The prevalence of offshore seismicity in this region indicates that the plate boundary is probably straighter than suggested by the topography onshore, but seismicity is scattered (Figure 5.5), and does not clearly define the location of the plate boundary. The steep, almost convex, GPS profiles across the plate boundary here are probably the result of projecting the data onto transects which are oblique to the local plate boundary.

5.8.4 Velocity normal to the plate boundary

Profiles of the across–strike velocity are plotted in Figures 5.39–5.43. A negative velocity indicates a component of motion to the west of the estimated strike of the plate boundary, away from the pole of rotation, but in most cases this simply reflects the mix of strike–parallel and strike–normal components in the projected velocities.

In general, the magnitude of the across–strike component of velocity is an order of magnitude smaller than the along–strike component, and second order effects which are not correlated to motion at the plate boundary, such as the relaxation of buoyancy forces, add to the noise of the signal. The exception to this is found in the profiles across the 'Big Bend' (transects 4–8), where large negative values highlight the change in the orientation, but not necessarily the magnitude, of velocities in this region. The data in these profiles have a steep positive gradient, which may indicate a rotation of the velocity field to the east inland, towards the strike of the main plate boundary. In transects 5 and 6 a large positive velocity component is evident between 100 km and 200 km from the plate boundary, indicating that the velocities may continue to rotate inland, until they strike east of the plate boundary. This pattern could be interpreted as the flow of lithospheric material around the rigid Sierra block as shown in Figure 5.44.

The across–strike data in transects 10–18 are scattered over a range of $\sim$6 mm yr^{-1}, which decreases slightly inland. The data are approximately centred on a normal velocity of 3 mm yr^{-1} in a roughly south–westerly direction. This may be due to a misalignment of the estimated strike of the plate boundary, or it may imply that there is a component of compression between the Pacific and North America along this section of the plate boundary. The strong signal in the region of the Coast Ranges (transects 10–14), supports the findings of Argus & Gordon (2001), who deduce that fault normal rates are small, vary with along–strike position, and have a maximum of 3.3 ± 1.0 mm yr^{-1} south–east of Point Arena. Some of this compression is due to the misalignment of the plate boundary with relative motion between the Pacific and North America plates.

Unlike the profiles of along–strike velocity, there is no discernible change in the gradient of the velocity profiles across the Sierra block, implying that its presence does not perturb the normal component of the velocity field.

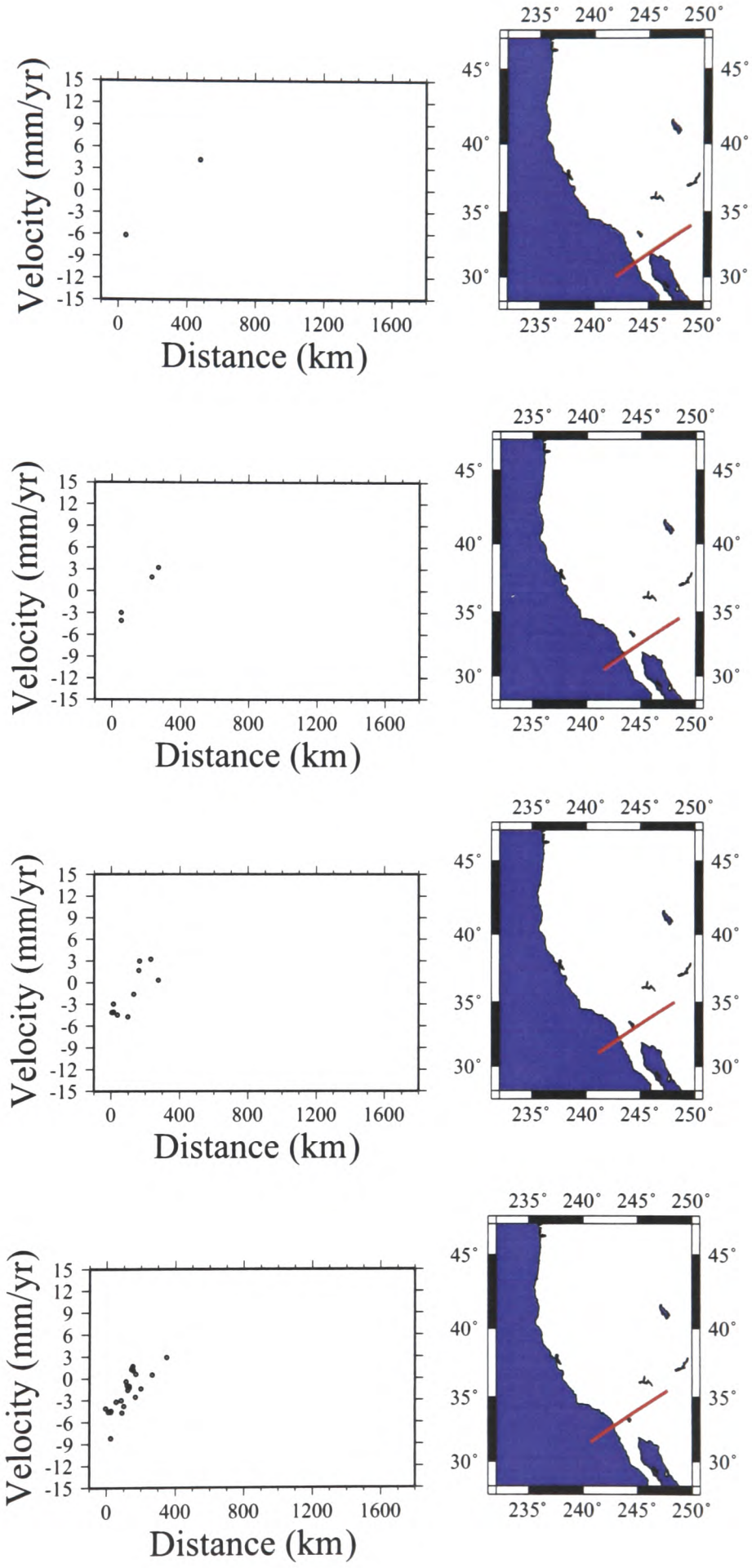

Figure 5.39: Velocities normal to the plate boundary. (a) transect 1 (b) transect 2 (c) transect 3 (d) transect 4

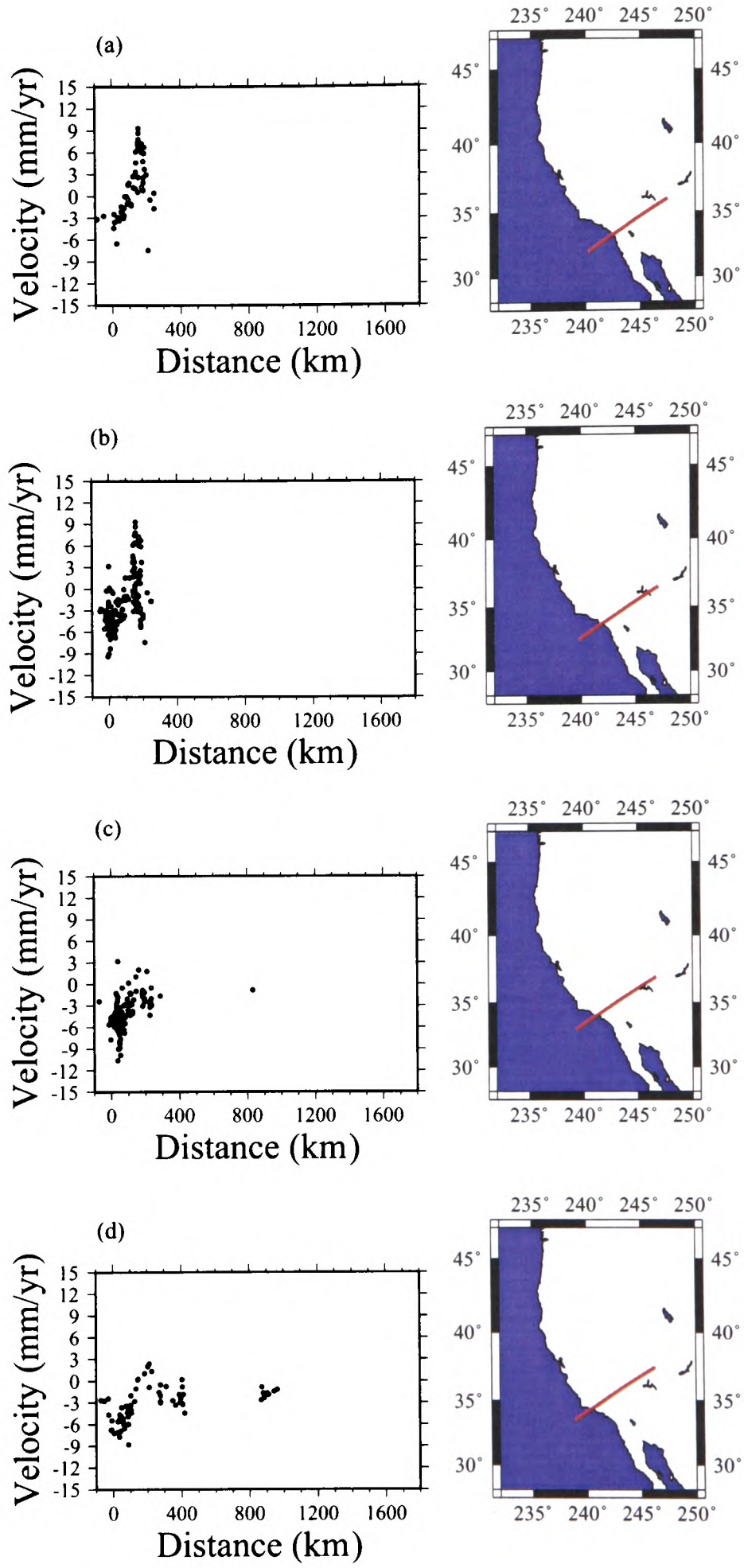

Figure 5.40: Velocities normal to the plate boundary. (a) transect 5 (b) transect 6 (c) transect 7 (d) transect 8

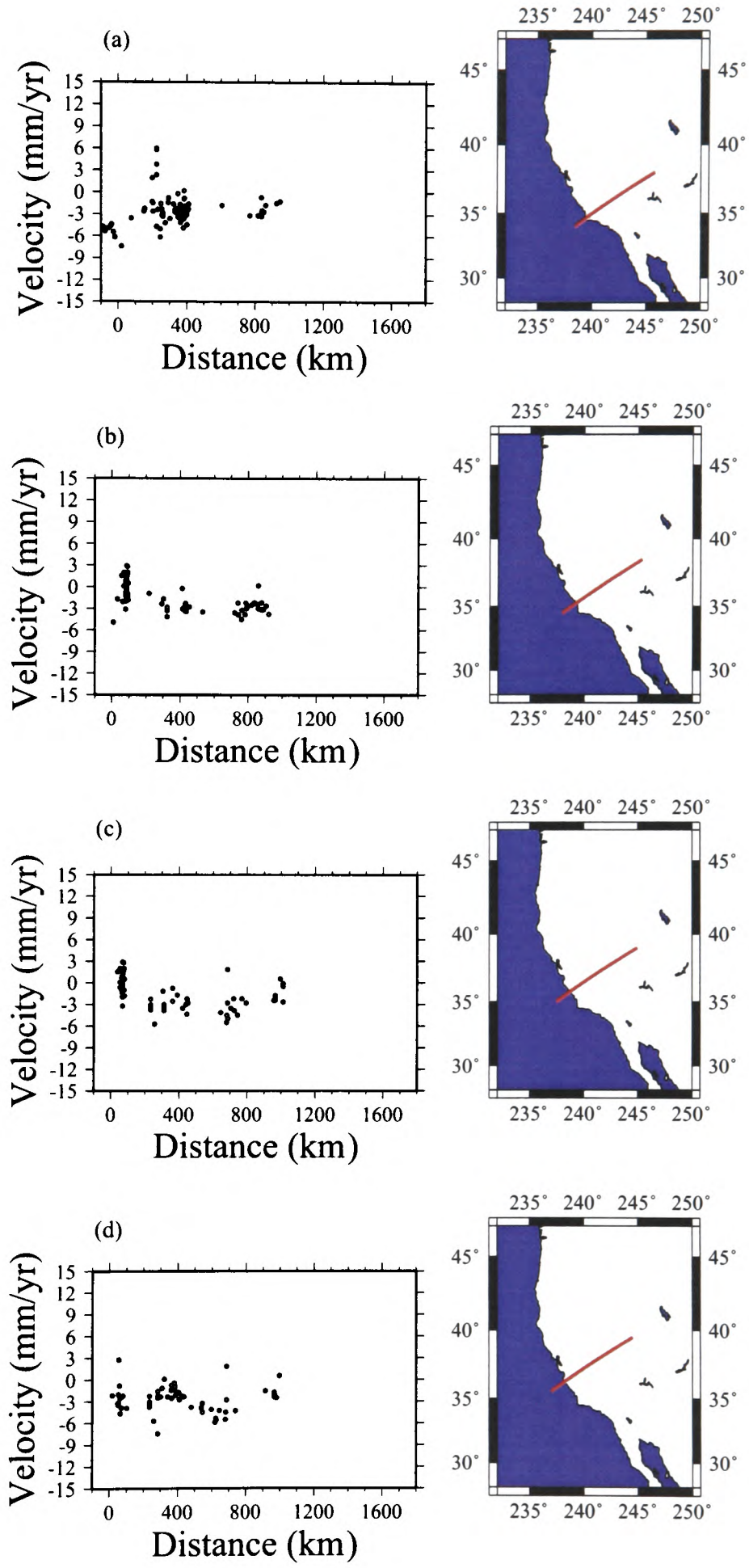

Figure 5.41: Velocities normal to the plate boundary. (a) transect 9 (b) transect 10 (c) transect 11 (d) transect 12

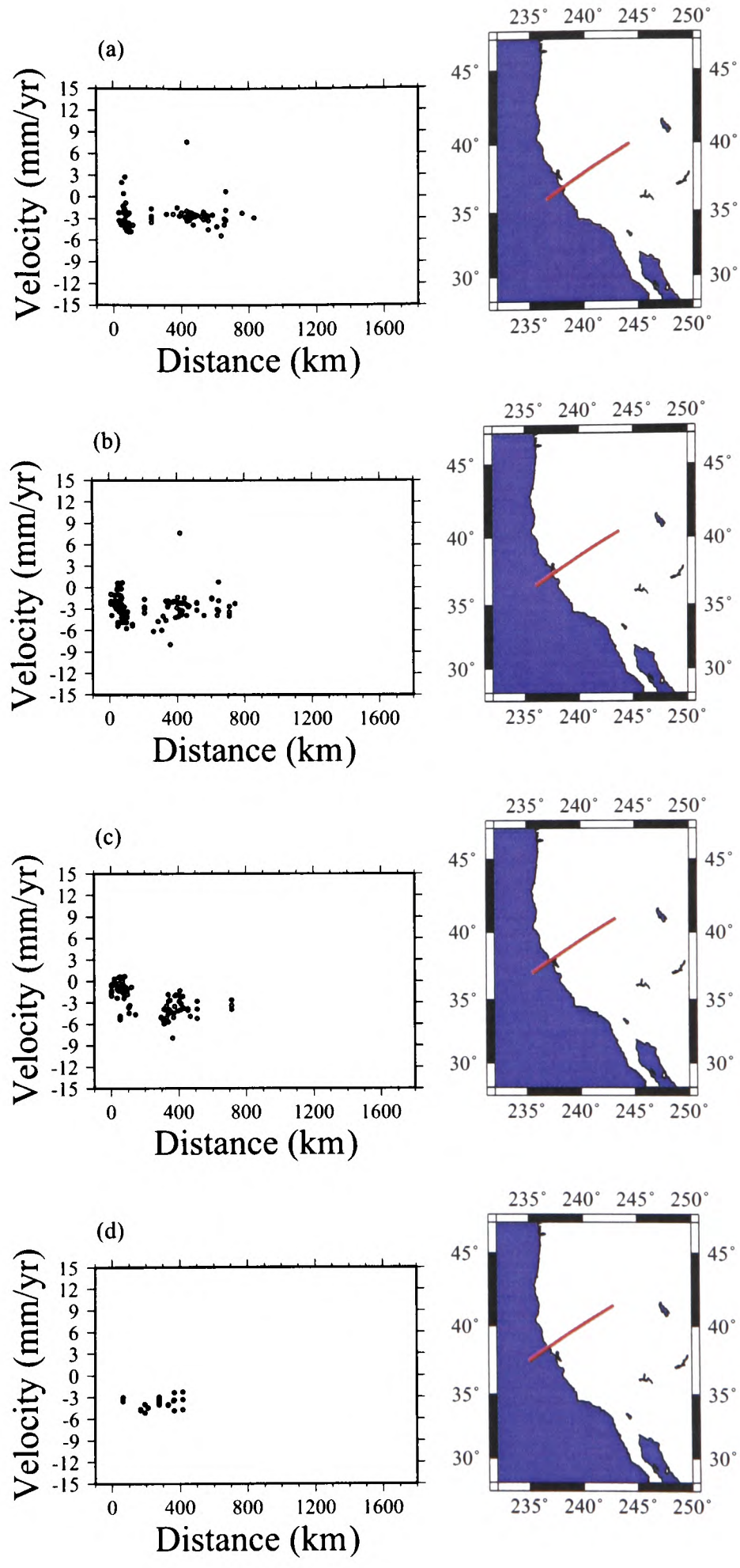

Figure 5.42: Velocities normal to the plate boundary. (a) transect 13 (b) transect 14 (c) transect 15 (d) transect 16

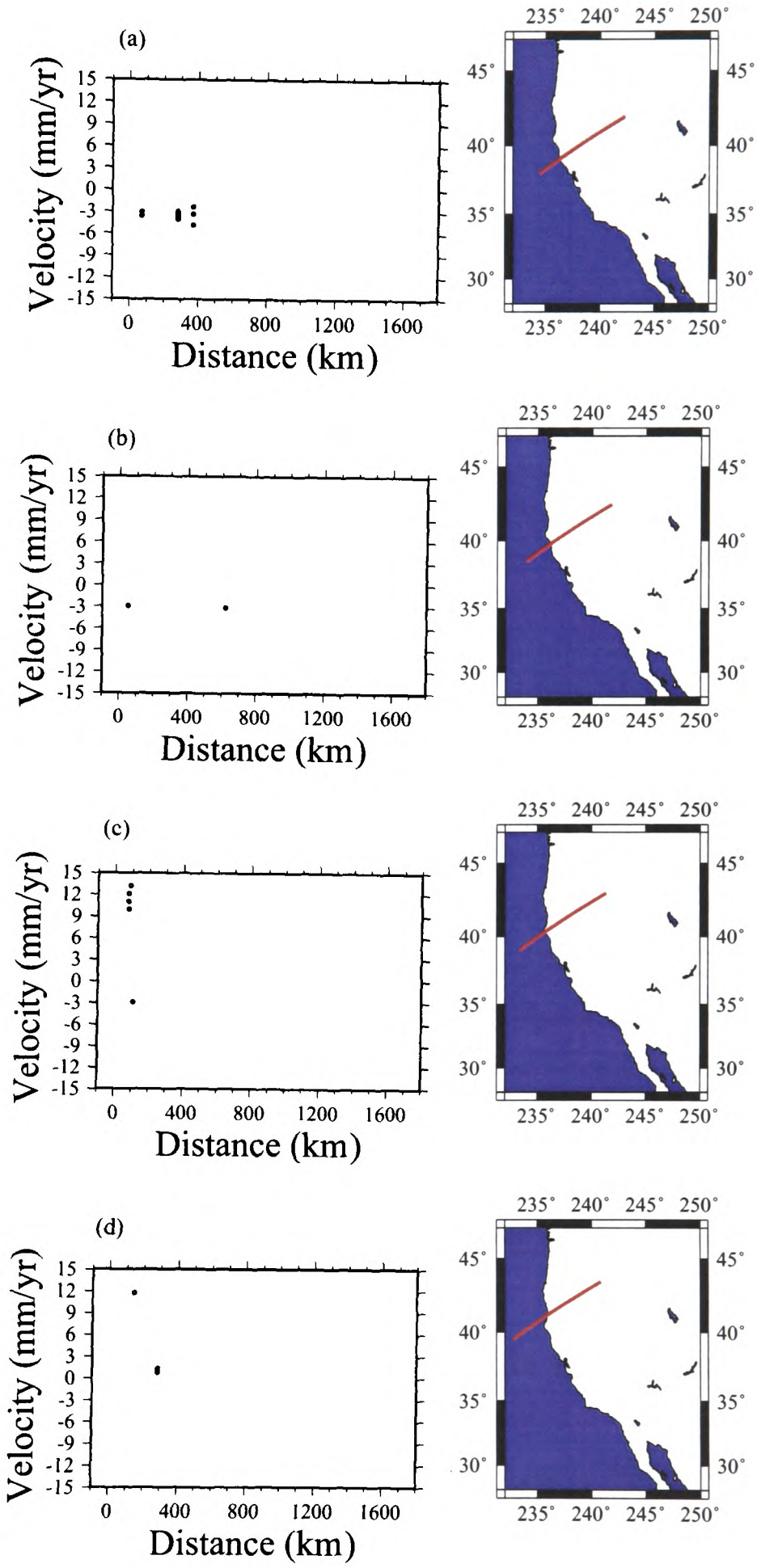

Figure 5.43: Velocities normal to the plate boundary. (a) transect 17 (b) transect 18 (c) transect 19 (d) transect 20

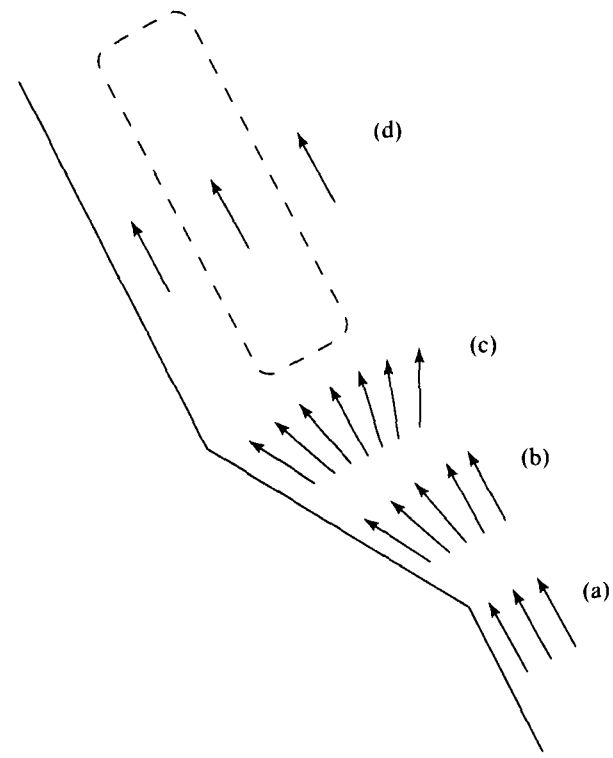

Figure 5.44: Cartoon of possible flow profiles in the plate boundary zone. Constant magnitude velocity arrows highlight the pattern of the flow. Dashed rectangle marks the approximate location of the Sierra block. (a) Flow parallel to the plate boundary. (b) Flow aligned with the local plate boundary at the coast rotates to become aligned with the dominant plate boundary inland. (c) Flow around a rigid inclusion. (d) Flow parallel to the plate boundary.

Further inland, at distances between ~400 km and ~1000 km from the plate boundary, the data contain a signal from the extension of the Basin and Range Province, which manifests itself as a westerly (negative) component of velocity with respect to stable North America.

In the last two profiles (transects 19 and 20), high positive (easterly) velocities are associated with the velocity field north of the Mendocino Triple Junction where the surface velocity is aligned with the subduction of the Gorda slab in a north–easterly direction.

5.9 Rotation of a rigid block embedded within viscous shear flow

In balancing the forces that act upon a rigid inclusion embedded within simple shear flow (section 5.5), the component of velocity normal to the shear direction is assumed to be negligible. A contour plot of this component of velocity, generated using the numerical method (see section 5.4.8, Figure 5.19), confirms that it is an order of magnitude smaller than the along–strike velocity (which takes a maximum non–dimemsional value of 1). To the degree that they are antisymmetrical, these perpendicular components represent the rotation of the Sierra block.

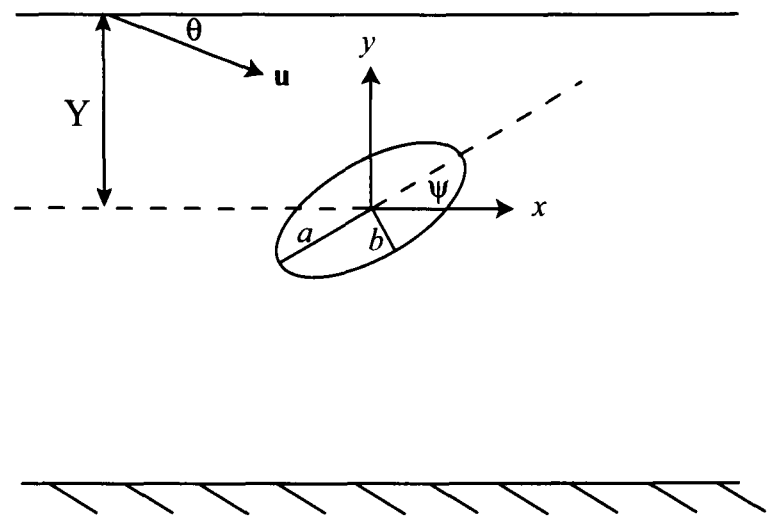

Figure 5.45: Diagram illustrating the terms used to analyse the rotation of an ellipsoidal rigid inclusion embedded within highly viscous simple shear flow. a and b are the long and short axes of the ellipse respectively. x and y define the co–ordinate system, which is fixed with reference to the boundaries, but not the orientation of the ellipse. ψ is the orientation of the long axis of the ellipse with respect to the x axis, θ indicates the direction of the relative velocity, $\mathbf{u}$, between the two boundaries, and Y is the distance of the centre of the ellipse from the near boundary.

The rotation of a rigid particle within a highly viscous fluid has been addressed by Jeffery (1922), and more recently by Lamb (1987). Lamb (1987) presents analytical solutions for the motion of a rigid inclusion with an elliptical cross–section within a highly viscous fluid. Principal axes of the ellipsoid are taken to have lengths a and b, with $a > b$, and these axes are assumed to always lie in the xy–plane (see Figure 5.45). The velocity field for the fluid surrounding the ellipsoid is defined relative to the xy–axes, and z is taken to point out of the page. The axes of the ellipsoid rotate relative to the fixed axes.

Various components of the two–dimensional background velocity field, $\mathbf{u} = (u, v, w)$ are defined;

$$\frac{\partial u}{\partial x} - \frac{\partial v}{\partial y} = \dot{\gamma}_1 \tag{5.34}$$

$$\frac{\partial u}{\partial y} + \frac{\partial v}{\partial x} = \dot{\gamma}_2 \tag{5.35}$$

$$\frac{\partial u}{\partial y} - \frac{\partial v}{\partial x} = W \tag{5.36}$$

$$-\frac{1}{2}\left(\frac{\partial u}{\partial x} + \frac{\partial v}{\partial y}\right) = T \tag{5.37}$$

$\dot{\gamma}_1$ is a measure of the rate of pure shear, while $\dot{\gamma}_2$ is a measure of the rate of simple shear. W is twice the rate of rigid body rotation within the fluid, and T is the divergence of the flow.

Figure 5.45 illustrates the geometry for the case of a particle with an elliptical cross-section. ψ is defined to be the angle between the long axis of the ellipsoid and the x axis. The rate of change

of ψ gives the rate of rotation of the ellipsoid. θ defines the direction of the relative velocity of the two planes. In this analysis I neglect the small component of compression across the Pacific–North America plate boundary, and use $\theta = 0$. The instantaneous rotation rate of the inclusion about the z axis when $\theta = 0$ is given by

$$\frac{d\psi}{dt} = \frac{1}{2}\left(\frac{1-k^2}{1+k^2}\right)(\dot{\gamma}_2 \cos 2\psi - \dot{\gamma}_1 \sin 2\psi) - \frac{1}{2}W \tag{5.38}$$

where $k = b/a$ is the aspect ratio of the ellipse, and a positive rate indicates anti–clockwise rotation. For the case of simple shear parallel to the x axis; $\theta = 0$, $\mathbf{u} = (u(y), 0, 0)$ and the only non–zero component of the strain rate is $\partial u/\partial y$. Equation 5.38 simplifies;

$$\frac{d\psi}{dt} = \frac{1}{2}\frac{\partial u}{\partial y}\left(\frac{1-k^2}{1+k^2}\cos 2\psi - 1\right) \tag{5.39}$$

The only stationary state ($d\psi/dt = 0$) for $\theta = 0^\circ$ occurs when $k = 0$, and $\psi = 0^\circ$ (or 180°); this defines a line of zero width aligned with the x axis. An ellipsoid of finite width has no stationary state if it is embedded within simple shear flow; its rate of rotation varies with time and is dependent upon its orientation. If there is a component of compression in the background velocity field ($\theta > 0^\circ$) there are two stationary states when

$$k < k_{crit} = \left(\frac{1-\cos\theta}{1+\theta}\right)^{1/2}, \tag{5.40}$$

but this case is not investigated further.

Approximate values for the velocity of the driving boundary, and the dimensions and orientation of the Sierra block may be used to determine an order of magnitude estimate for the instantaneous rate of rotation of the Sierra block, which is approximated to have an elliptical cross-section for the purposes of this analysis. Taking the origin of the co–ordinate axes to be fixed to the centre of the ellipsoid, a driving boundary is defined parallel to the x axis, a distance Y from the centre of the ellipsoid. A constant velocity boundary condition of magnitude V_0 is applied along a length, H, of this boundary, and is centred upon the location of the rigid inclusion. The second, fixed, boundary (see Figure 5.45) is assumed to be far from the ellipsoid, such that its presence does not influence the simple shear velocity field generated by the motion of the driving boundary: $u \to 0$ as $y \to -\infty$. Following the length scaling arguments of England *et al.* (1985), and using the results of section 5.5.1 for a 'box–car' velocity boundary condition, the velocity field in the background fluid is

$$u = V_0 e^{4\sqrt{n}(y-Y)/H} \tag{5.41}$$

This expression is substituted into equation 5.39 to yield

$$\frac{d\psi}{dt} = \frac{2\sqrt{n}V_0}{H} e^{4\sqrt{n}(y-Y)/H}\left(\left(\frac{1-k^2}{1+k^2}\right)\cos 2\psi - 1\right) \tag{5.42}$$

Approximations can be made using the assumptions $k, \psi << 1$. For the Sierra block, $k = b/a \simeq 185/715 \simeq 0.26$ (see table 5.3), and $\psi \simeq 0^{\circ}$ because the long axis of the Sierra block is approximately aligned with Pacific–North America relative motion. Rewriting equation 5.42 using Taylor series expansions about zero yields;

$$\frac{d\psi}{dt} = -\frac{4\sqrt{n}V_0}{H} e^{4\sqrt{n}(y-Y)/H}(\psi^2 + k^2 + O(\psi^2 k^2)) \tag{5.43}$$

The minus sign indicates clockwise rotation. Table 5.3 gives predicted values for the terms of equation 5.43, which yield an instantaneous rotation rate of $d\psi/dt \simeq 5.5 \times 10^{-9}$ degrees yr^{-1}, or 5.5×10^{-3} degrees Ma^{-1}. This low rate is in agreement with geodetic estimates of negligible slip on the left–lateral Garlock fault (Miller *et al.*, 2001b), which would accommodate any rotation of the Sierra block at its southern margin. However, the rate is smaller than that observed by recent geodetic studies, and in the opposite sense. Argus & Gordon (1991) use Very Long Baseline Interferometry (VLBI) to determine an anti–clockwise rate of $0.61 \pm 0.15^{\circ}$ Ma^{-1} for the rotation of the Sierra block about 32°N 128°W. This Euler pole lies only 10° south–west of the Sierra block, and they conclude that this implies a rotation rate of $\sim 0.5^{\circ}$ Ma^{-1} anti–clockwise about a local vertical axis. This estimate is supported by the GPS/VLBI study of Bennett *et al.* (1999), but is contradicted by the GPS study of Dixon *et al.* (2000), who find the motion of the Sierra block to be defined by rigid body rotation about a more distant axis. Dixon *et al.* (2000) predict that the block translates almost parallel to the local plate motion direction; this is in agreement with the kinematic modelling results of Hearn & Humphreys (1998) who predict a small rate of anti–clockwise rotation for the Sierra block. These observations, combined with the results of my calculations, indicate that stresses arising from the rotation of the Sierra block due to motion along the plate boundary are likely to be small.

The orientation at time t of an ellipsoid embedded within simple shear may be found by integrating equation 5.39. Lamb (1987) presents solutions for the relationship between the angular position of the ellipse (ψ) and time (t) for the case when $\partial u/\partial x = \partial v/\partial y = 0$. Assuming that the long axis of the inclusion is perpendicular to the driving boundary at $t = 0$:

$$\frac{\left(1 - \frac{1}{C^2}\sec^2\theta\right)^{1/2}}{\left(\frac{C+1}{C}\right)\tan\psi - \frac{\tan\theta}{C}} = \tan\left[\frac{W}{2}\left(1 - \frac{\sec^2\theta}{C^2}\right)^{1/2} t\right] \tag{5.44}$$

where $C = (1+k^2)/(1-k^2)$. For the case of simple shear, $\theta = 0^{\circ}$ and $W = \partial u/\partial y$. Using the velocity field given in equation 5.41, equation 5.44 is rearranged to give an expression for the orientation of the ellipse at time t;

$$\psi = \tan^{-1}\left[\sqrt{\frac{C-1}{C+1}}\left(\tan\left(\frac{1}{2C}\frac{4\sqrt{n}V_0}{H} e^{4\sqrt{n}(y-Y)/H}\sqrt{C^2-1}\, t\right)\right)^{-1}\right] \tag{5.45}$$

Using values of V_0, H, n, k, y and Y given in table 5.3, the orientation of an ellipse which approximates the shape of the Sierra block is plotted against time in Figure 5.46. The function is periodic, in

Table 5.3: Rotation parameters for the Sierra block

Long axis of ellipse, a	715 km
Short axis of ellipse, b	185 km
Aspect ratio, $k = b/a$	0.26
Distance of the centre of the ellipse from the driving boundary, Y	220 km
Reference distance from the centre of the ellipsoid, y	0 km
Length of the driving boundary, H	1100 km
Velocity at the driving boundary[1], V_0	52 mm yr^{-1}
Stress–strain rate power law exponent, n	3
Orientation of Sierra block with respect to the driving boundary, ψ	$\sim 0^o$
Orientation of the plate relative motion vector with the plate boundary, θ	$\sim 0^o$

[1]Velocity relative to stable North America

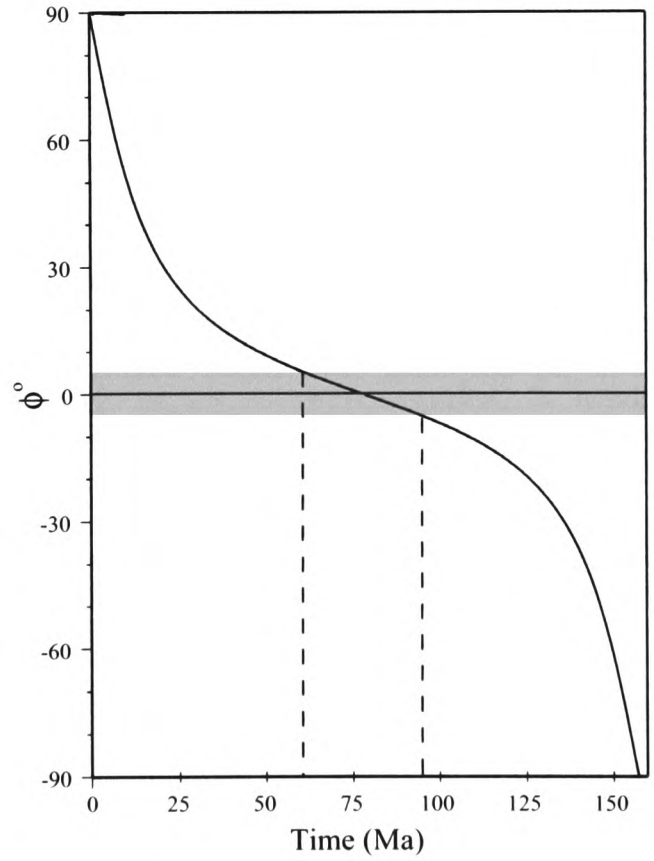

Figure 5.46: Orientation of the long axis of an elliptical disc over time. Geometry is defined in Figure 5.45; the long axis of the elliptical disc is initially assumed to be perpendicular to the orientation of the driving boundary. The shaded region highlights $\pm 5^o$, and the dashed lines indicate the length of time which the disc will spend between these orientations.

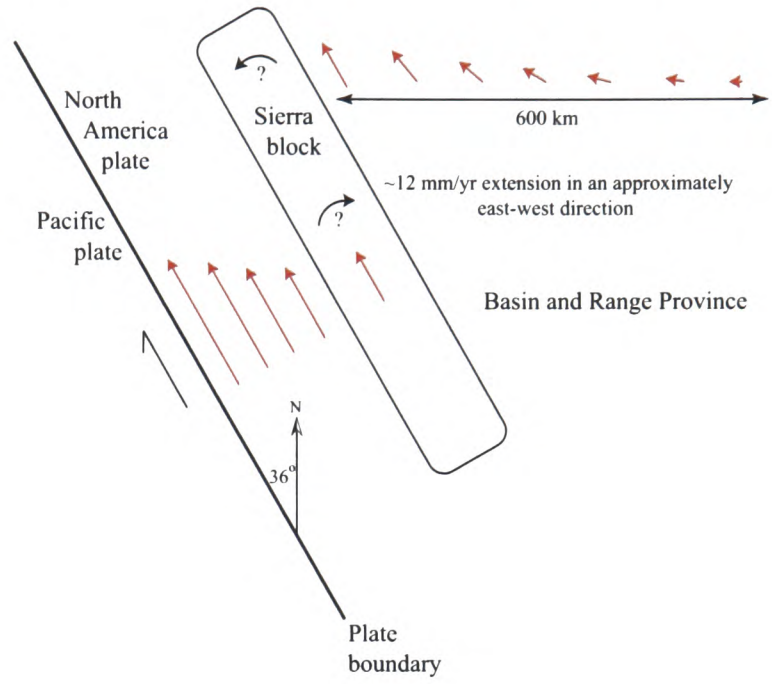

Figure 5.47: Cartoon to show the turning forces acting upon the Sierra block. Motion along the plate boundary provides a clockwise turning force, whilst extension in the northern Basin and Range exerts an anti–clockwise turning force upon the block. Red arrows represent the simplified velocity field.

this case over a period of ~160Ma. The ellipsoid is predicted to spend ~35 Ma with its long axis orientated less than 5° from the direction of flow in the background fluid. The Sierra block is orientated approximately parallel to Pacific–North America relative motion, and there is no evidence to suggest that it has been orientated at any other angle since its emplacement around 100 Ma, or since the initiation of strike–slip motion along this plate boundary at around 29 Ma (Atwater, 1970). These observations concur with the analysis presented above, which predicts a negligible rate of rotation for an inclusion which is already approximately aligned with the direction of shear flow.

5.9.1 Rotation due to extension in the Basin and Range Province

The principal component of extension across the Basin and Range Province is roughly aligned east–west, at an oblique angle to the long axis of the Sierra block (see Figure 5.47). This observation is borne out by GPS data (Bennett *et al.*, 1998), and results in the partitioning of slip on strike–slip and normal faults along the length of the eastern boundary of the Sierra block.

The magnitude of GPS velocity vectors, relative to stable North America, increases from east to west (Bennett *et al.*, 1998) as the Sierra block is approached (see Figure 5.1), and their azimuth swings round to a more northerly direction until the velocity field is approximately aligned with the motion of the Sierra block (see Figure 5.47).

Any extension immediately east of the Sierra block will apply a normal force to its eastern boundary.

If the rate of extension is constant along the length of the boundary, no torque is applied to the block. However, if there is a velocity gradient, this will act to rotate the block, with the direction being dependent upon the direction of the velocity gradient.

In the Basin and Range Province, the component of east–west extension is greater in the north (A. Sorby, pers. comm.), where ~12 mm yr^{-1} of extension is accommodated across ~600 km, giving a strain rate of $\sim 20 \times 10^{-9}$ yr^{-1}. This result implies that a greater normal force is probably applied to the northern half of the Sierra block: In the absence of other forces, this will result in the anti–clockwise rotation of the block. However, due to the superposition of deformation due to motion of the plate boundary upon the predominantly extensional velocity field of the Basin and Range Province, any component of rotation due to extension within the Basin and Range is difficult to quantify.

The two mechanisms discussed in this section predict rotation of the Sierra block in opposite directions. The anti–clockwise rotation determined by recent geodetic measurements may be an indication that extension across the Basin and Range Province is currently the dominant mechanism. However, I seek to explain the instantaneous deformation of the North America plate boundary zone, and the rate of rotation predicted by both mechanisms is small enough that any resulting rotation will be negligible over short geological time periods, and may therefore be neglected when considering the forces acting upon the Sierra block. This conclusion justifies the assumptions of the force balance model of section 5.5.2.

5.10 A more complex model for the western North America plate boundary zone

The geometry of the Pacific–North America plate boundary is more complex than the geometry of the models outlined in sections 5.3 and 5.5, therefore experiments are also carried out using a modified geometry for the solution domain. Boundary conditions that more closely resemble the strike and magnitude of relative Pacific–North America motion are also investigated.

The 'Big Bend' in the San Andreas fault is located in southern California (Figure 5.7), and the left step in the right–lateral fault creates a region of compression along the section of the fault immediately north of the bend (see Figure 5.48). This zone of compression corresponds with the location of the Transverse Ranges, which accommodate between 10 and 14 mm yr^{-1} of thrusting (Huftile & Yeats, 1995). If a proportion of this normal motion is transferred across the Transverse Ranges to the southern edge of the Sierra block this will increase the driving force applied to the southern edge of the block, potentially increasing its velocity relative to stable North America. However, there is

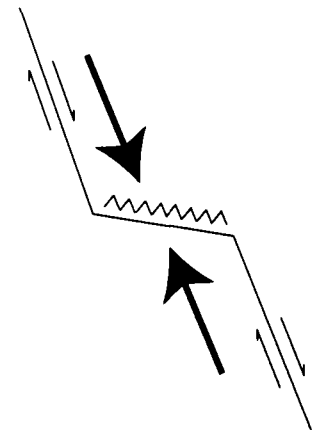

Figure 5.48: Cartoon to highlight the compressional component which arises when a dextral shear zone steps to the left. Zigzags indicate the region which corresponds to the location of the Transverse Ranges. If the dextral shear zone stepped to the right, extension would be expected in this region.

strong seismic evidence (Hadley & Kanamori, 1977; Zhao *et al.*, 1996; Kohler & Davis, 1997; Fuis, 1998) for a cold lithospheric downwelling beneath the Transverse Ranges. While such downwelling will act to increase the rate of convergence across the Transverse Ranges it might also act to decrease the velocity of the Sierra block with respect to stable North America, because the negative buoyancy of the downwelling could draw the Sierra block back towards the location of the downwelling (Zhao *et al.*, 1996). This force has not been included in the modelling presented here, but should be taken into account when interpreting both the results of the modelling and the observed surface velocity field in this region.

Assuming the Sierra block to be approximately rectangular, the geometry of the plate boundary is set out as follows: The points A, B, C and D represent Cape Mendocino, the bend in the coast northwest of the Los Angeles basin, the northern tip of the Salton Sea, and a point in the Gulf of California respectively. The geometry and spacing of the points is given in Figure 5.49. Plane geometry is used to determine the angles defined in the figure rather than spherical geometry, because the region under consideration is small enough for the curvature of the Earth to be neglected.

The geometry of the solution domain used in the numerical experiments is altered to reflect the geometry of Figure 5.49. The middle portion of the $x = 0$ boundary is inclined at an angle of 35° to the y axis, and the two remaining segments of this boundary are parallel (see Figure 5.50).The number of nodes and elements in the altered solution domain is maintained from the original finite element mesh of Figure 5.9b, and the major dimensions of the solution domain are unchanged; the mesh has length $5l$ and width $2.5l$ at its wider end. The y axis also remains fixed (see Figure 5.50). A region of higher viscosity is again specified within the mesh, and the length, l, of this region is used to non–dimensionalise all other length scales. Its dimensions and location within the mesh are chosen to closely reflect the geometry observed at the plate boundary.

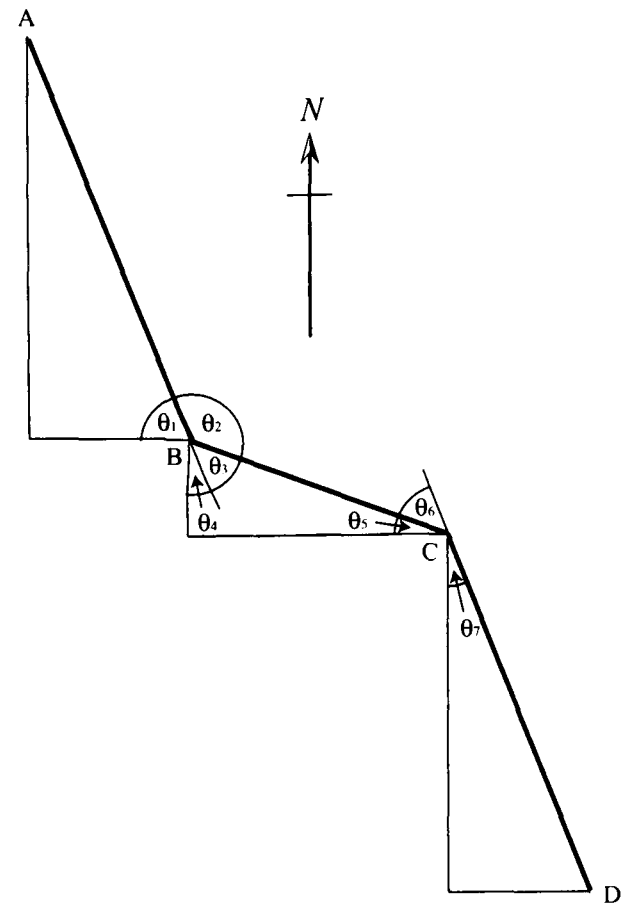

Figure 5.49: Geometry of the Pacific–North America plate boundary, with an approximation to the geometry of the plate boundary indicated by the heavier line. Points A to D specify the simplified geometry of the plate boundary. A: Cape Mendocino, B: coastal point, north–west of Los Angeles, C: Northern tip of the Salton Sea, D: Gulf of California. $\vec{AB} = 715$ km, $\vec{BC} = 550$ km, $\theta_1 = 56.3°$, $\theta_2 = 144.5°$, $\theta_3 = 35.5°$, $\theta_4 = 33.7°$, $\theta_5 = 20.9°$, $\theta_6 = 33.7°$, $\theta_7 = 35.5°$.

5.10.1 Boundary Conditions

Four different sets of boundary conditions are used in the modified model in an attempt to account for the additional normal force arising from the oblique convergent motion of stronger oceanic lithosphere towards the rotated section of the plate boundary. Varying velocity boundary conditions are specified along the left–hand boundary of the solution domain, and the other boundaries are held fixed.

Each of the four sets of boundary conditions consists of a set of vectors of unit magnitude that are applied at a specified angle along a specified section of the boundary. The magnitudes of the velocity vectors are again tapered to zero towards the ends of each boundary segment using a $\cos^2$ taper. In the first set of boundary conditions the driving velocity is aligned with the y axis of the solution domain (Figure 5.51a), and applied between $y = l$ and $y = 3.5l$. The second set of boundary conditions are also applied between $y = l$ and $y = 3.5l$, but the driving velocity is defined to be parallel to the mesh boundary at all points (Figure 5.51b). The third and fourth sets of boundary conditions (Figures 5.51c,d) aim to reflect more accurately the motion of the Pacific plate with respect to North

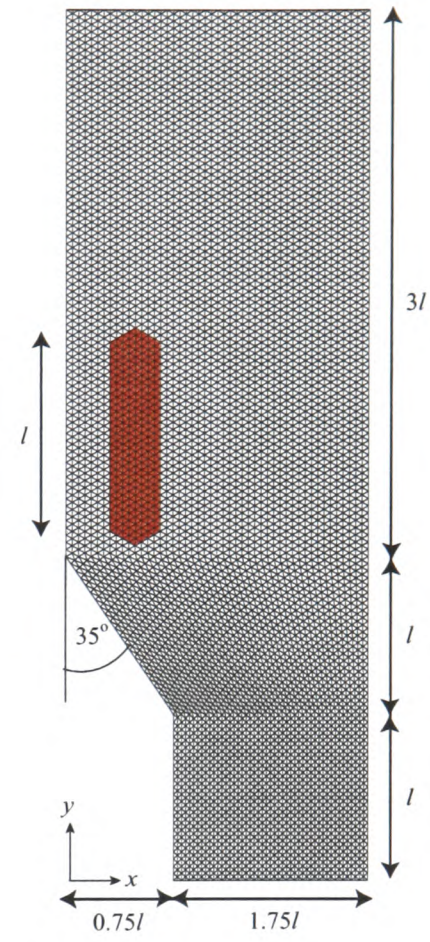

Figure 5.50: Diagram to show the modified geometry of the finite element mesh described in section 5.10. Dimensions of the indentation are scaled to represent the geometry of the Pacific–North America plate boundary. The red region indicates the location of the rigid block within the mesh. Length of the block=l, total length of solution domain=$5l$. (Not to scale)

America, and relative velocity vectors are calculated using the Pacific–North America angular velocity (see below). In the third case, the average direction of the relative velocity vectors for the north and middle segments of the plate boundary are applied along the vertical and rotated sections of the mesh boundary respectively. In the fourth case, the direction of the relative velocity vector is calculated every 50km along the plate boundary, and the direction of each vector is used to assign a boundary condition to the corresponding section of the mesh boundary.

The Pacific–Plate–Fixed NUVEL–1A Euler pole for North America (DeMets *et al.*, 1994), (-78.167°E, 48.709°N,0.7486° Ma^{-1}) is used to calculate the motion of the Pacific plate relative to North America at 50 km intervals along an approximation of the location of the plate boundary (see Figure 5.52b and table 5.4). In order to determine the boundary conditions of the numerical model, the velocities of table 5.4 are normalised, and their directions specify the direction of the velocity boundary condition along the corresponding section of the model. The distance of each point from the Euler pole, and therefore the magnitude of the velocity calculated at each point, varies, but a constant, normalised boundary condition is used in the numerical model for consistency. The variation in the Euler–pole–

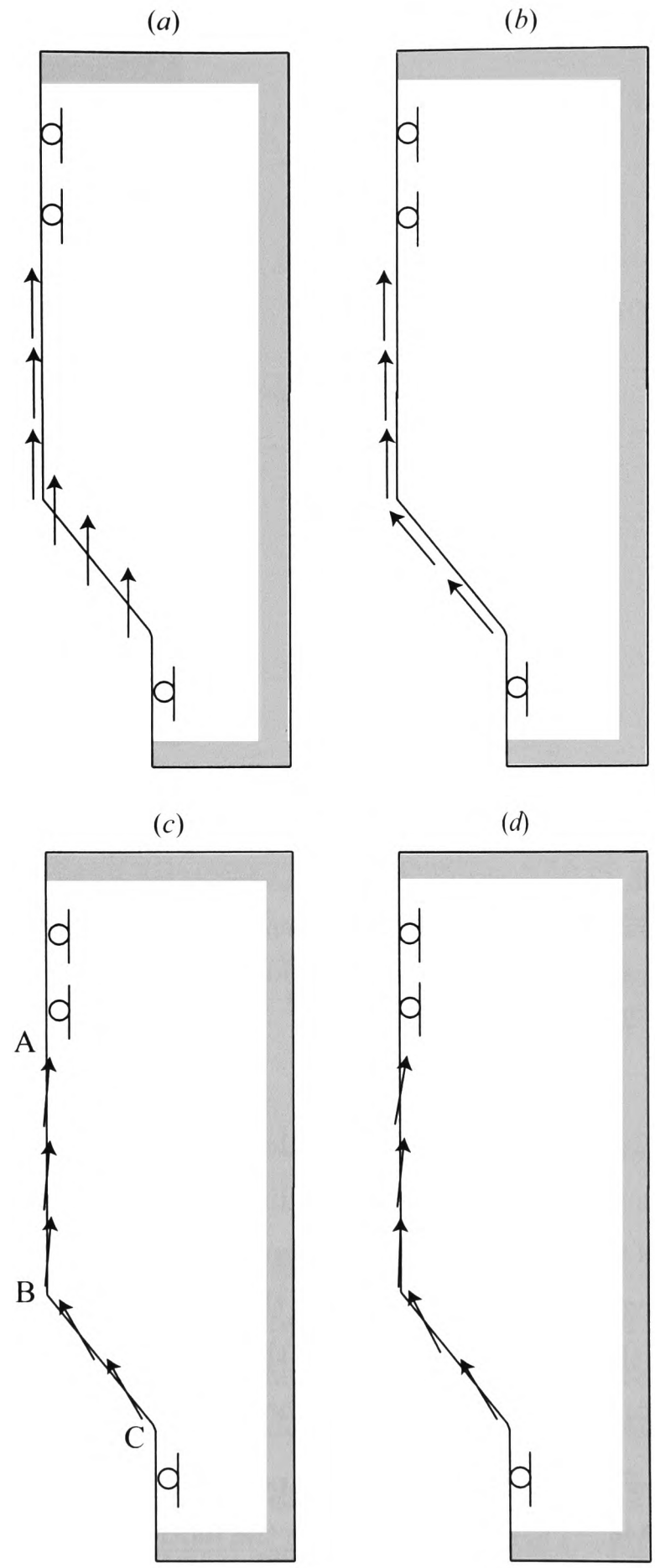

Figure 5.51: Boundary conditions for the four cases outlined in section 5.10.1. Arrows represent directions of the unit magnitude velocity boundary conditions, rollers indicate boundaries with zero traction, and grey strips indicate rigid boundaries. (a) velocity aligned with the y axis (b) velocity aligned with the boundary of the solution domain (c) average Euler pole velocity direction for each of the two segments is applied along AB and BC respectively (d) calculated Euler pole velocity applied along the whole driving boundary, direction varies with position.

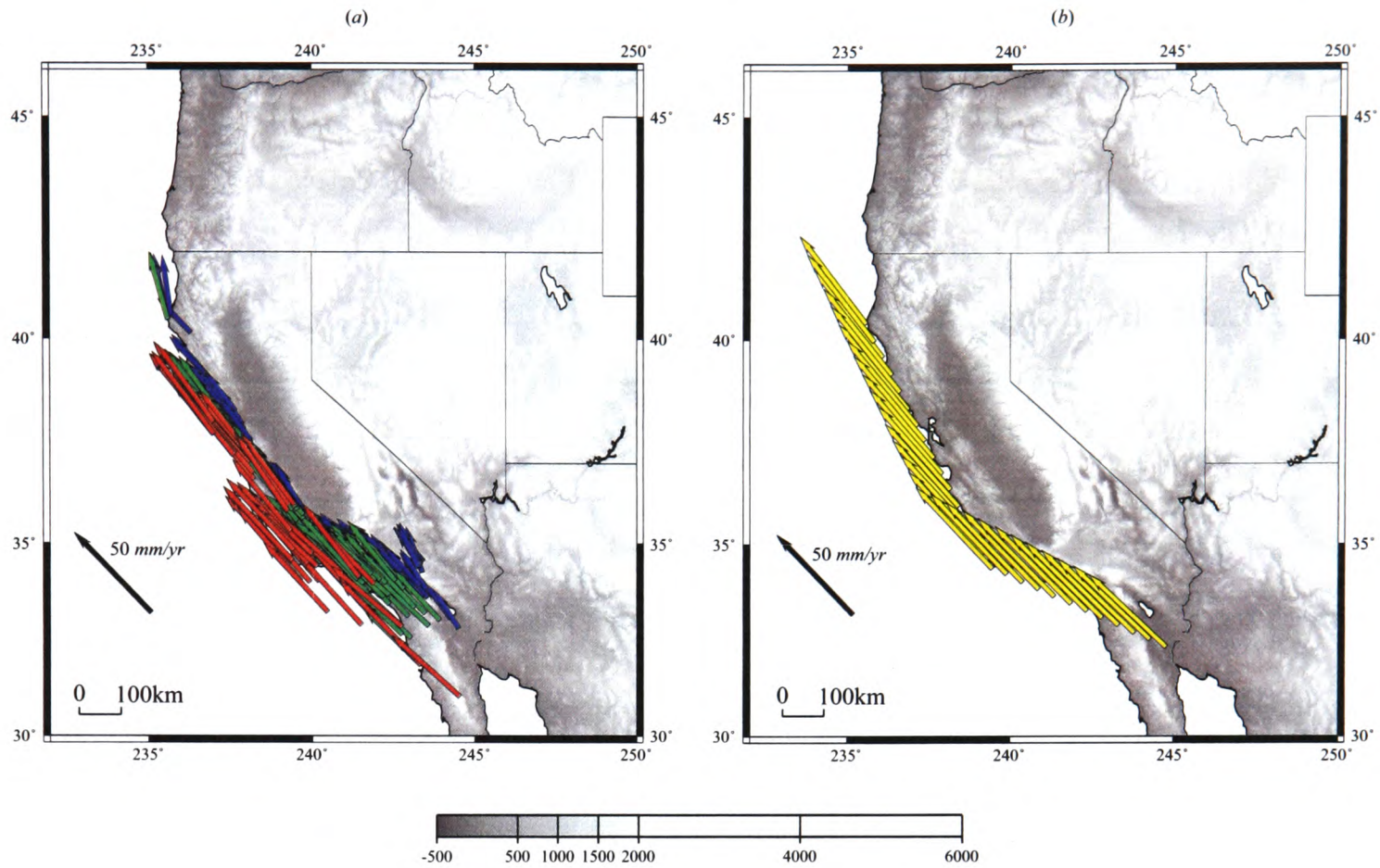

Figure 5.52: (a) GPS velocities near the plate boundary. Blue:magnitude>20 mm yr^{-1}. Green:magnitude>30 mm yr^{-1}. Red:magnitude>40mm yr^{-1}. (Source: USGS, JPL) (b) Velocities along the plate boundary calculated using the Euler pole and rotation rate of NUVEL–1A. The directions of these vectors are used to determine the boundary conditions for the modified numerical model.

calculated velocities is only 2 mm yr^{-1} out of $\sim$ 50 mm yr^{-1}, and the location of the plate boundary, as defined by the points in table 5.4, is only approximate, therefore a higher level of accuracy is unnecessary. The velocity boundary conditions reproduce the shear force applied to North America by the motion of the Pacific plate.

Figure 5.52a plots GPS velocity vectors for sites located close to the edge of the plate boundary zone. The velocity data are taken from the combined USGS and JPL data sets described in section 5.8. Velocities greater than 20 mm yr^{-1}, 30 mm yr^{-1} and 40 mm yr^{-1} are represented by blue, green and red arrows respectively in Figure 5.52a. In general, the magnitude of the surface velocity relative to stable North America, measured by GPS, increases as the plate boundary is approached.

For the modified solution domain, experiments are carried out using values of the stress–strain rate exponent in the range $n = 1$ to $n = 5$. The effect of altering the length of the driving boundary or the dimensions of the higher viscosity block are not investigated for this more complex model.

Table 5.4: Plate boundary velocities: Motion of the Pacific plate relative to North America, calculated using NUVEL–1A

Latitude °N	Longitude °E	V_{north} (mm yr^{-1})	V_{east} (mm yr^{-1})	Strike °W of N	Magnitude (mm yr^{-1})	Distance from Euler pole (km)
40.37	-124.42	39.68	-30.25	37.32	49.89	3724.14
39.95	-124.17	39.51	-30.58	37.74	49.96	3729.47
39.58	-123.91	39.34	-30.85	38.10	49.99	3731.55
39.16	-123.63	39.15	-31.16	38.52	50.04	3735.36
38.75	-123.38	38.98	-31.48	38.92	50.11	3741.14
38.33	-123.12	38.80	-31.81	39.34	50.18	3747.15
37.94	-122.84	38.61	-32.09	39.72	50.21	3750.22
37.57	-122.61	38.46	-32.37	40.09	50.27	3756.05
37.15	-122.33	38.26	-32.68	40.50	50.33	3761.64
36.76	-122.08	38.09	-32.98	40.88	50.39	3767.90
36.37	-121.82	37.91	-33.27	41.26	50.44	3773.76
35.95	-121.57	37.74	-33.60	41.67	50.53	3782.63
35.54	-121.31	37.56	-33.91	42.07	50.60	3790.49
35.17	-121.04	37.37	-34.17	42.44	50.64	3795.32
34.77	-120.78	37.18	-34.47	42.83	50.71	3803.21
34.38	-120.53	37.01	-34.77	43.21	50.78	3811.49
34.24	-120.09	36.69	-34.72	43.41	50.52	3789.15
34.03	-119.60	36.34	-34.73	43.69	50.27	3768.13
33.85	-119.11	35.99	-34.71	43.96	50.00	3745.21
33.66	-118.63	35.64	-34.71	44.24	49.75	3723.89
33.48	-118.12	35.27	-34.69	44.52	49.47	3699.90
33.29	-117.63	34.91	-34.69	44.82	49.22	3678.24
33.11	-117.17	34.57	-34.70	45.11	48.98	3658.21
32.92	-116.68	34.20	-34.71	45.42	48.73	3636.97
32.72	-116.19	33.83	-34.74	45.75	48.49	3616.67
32.55	-115.71	33.47	-34.74	46.06	48.24	3595.13
32.35	-115.22	33.09	-34.77	46.41	48.00	3575.32

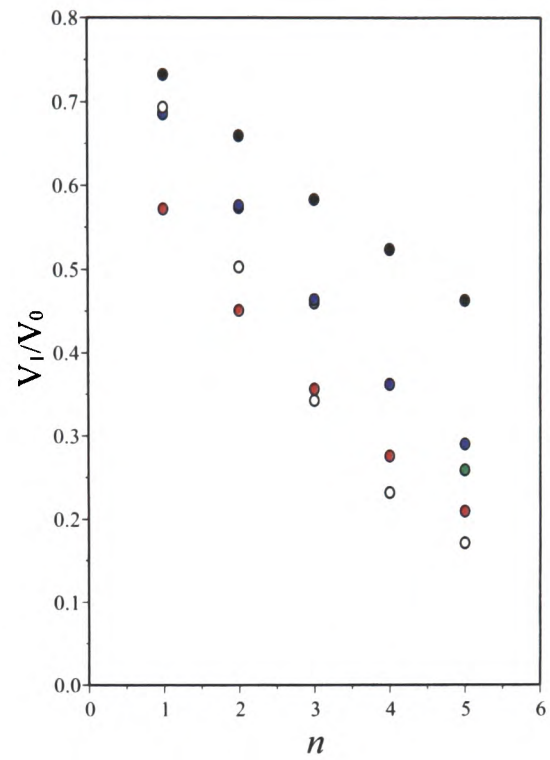

Figure 5.53: V_1/V_0, calculated using the modified solution domain, plotted against n, for four different sets of boundary conditions (see Figure 5.51). Black: driving velocity aligned with the y axis. Red: driving velocity aligned with the boundary of the solution domain. Green (largely obscured by blue): average NUVEL–1A velocity applied to the two segments of the solution domain. Blue: NUVEL–1A velocity calculated at $0.065l$ increments along the boundary. White: case C (table 5.1), with a driving boundary of length $h = 2l$.

5.10.2 Results of numerical experiments

For experiments carried out using the modified solution domain, the velocity of the block is again determined by calculating the average velocity of the fluid within the region defined to be of a higher viscosity. Figure 5.53 compares the ratio V_1/V_0 for solutions obtained using the modified solution domain, using the four different sets of boundary conditions outlined in section 5.10.1. The results from the corresponding experiment (same location and dimensions of block, same length of driving boundary) with a straight driving boundary are also plotted for comparison.

The reason for the decrease in the velocity ratio as n is increased is discussed in section 5.4.5. The greatest values of V_1/V_0 are obtained when the velocity boundary condition is aligned with the y axis of the modified solution domain (see Figure 5.51a). This geometry exerts the greatest normal force upon the $y = 2l$ end of the higher viscosity block (see Figures 5.54d to 5.58d). The smallest values of V_1/V_0 are obtained when the velocity boundary condition is aligned with the boundary of the solution domain (see Figure 5.51b). This geometry transmits the smallest normal force across the inclined boundary of the mesh to the higher viscosity region (see Figures 5.54e to 5.58e). The results from the

two sets of boundary conditions calculated using the Pacific–Plate–Fixed NUVEL–1A Euler pole for North America plot between the two extreme cases (see Figures 5.54f to 5.58f), and the discrepancy between them at $n = 5$ probably arises from the poor convergence of the numerical method in this strongly non–linear case. The values of V_1/V_0 from the corresponding experiments with a straight driving boundary are similar at $n = 1$, but decrease more rapidly as n is increased. This divergence in the results is due to the complex interaction between the viscous fluid and the irregular boundaries of the modified solution domain in the non–linear cases.

A driving boundary of length $2l$ has been used in the experiments presented here. This is longer than the observed length of $\sim 1.5l$ (scaled by the length of the Sierra block; see table 5.2), and the resulting values of V_1/V_0 are greater than the observed ratio of ~ 0.23. Quantitive conclusions about the value of n which governs deformation in the western North America plate boundary should therefore not be drawn form these results. Further refinement of the geometry of the modified solution domain is required; this experiment seeks only to investigate the first–order effects of the bend in the plate boundary.

5.10.3 Strain rates for modified geometry experiments

Figures 5.54 to 5.58 highlight the different strain rate regimes that arise in the neighbourhood of the higher viscosity block for the different sets of boundary conditions described in section 5.10.1. Strain rates are calculated from an instantaneous solution to the viscosity field.

$\dot{\varepsilon}_{xy}$ is shown in plots a–c of each figure; this component of the strain rate is representative of shear deformation. $\dot{\varepsilon}_{zz}$ is shown in d–f of each figure; this component of the strain rate represents the thickening or thinning of the lithosphere which takes place during deformation.

Maximum thickening at the ends of the block occurs when the velocity boundary condition is aligned with the y axis, as discussed previously. Minimum thickening at the ends of the higher viscosity region takes place when the velocity boundary condition is aligned with the boundary of the mesh. Intermediate amounts of thickening are found when the velocity boundary condition is calculated using the plate relative motion model.

The results of the numerical experiments show thickening of the viscous layer at both ends of the higher viscosity region. The thickening at $y = 2l$ coincides with the location of the Transverse Ranges in southern California. This seems to lead to the conclusion that the thrusting in this region may be attributed to the bend in the plate boundary, since such thickening is not found in the original experiments of section 5.4. However, other factors, including the geological history of the region, and forces due to the lithospheric downwelling beneath the Transverse Ranges, are not accounted

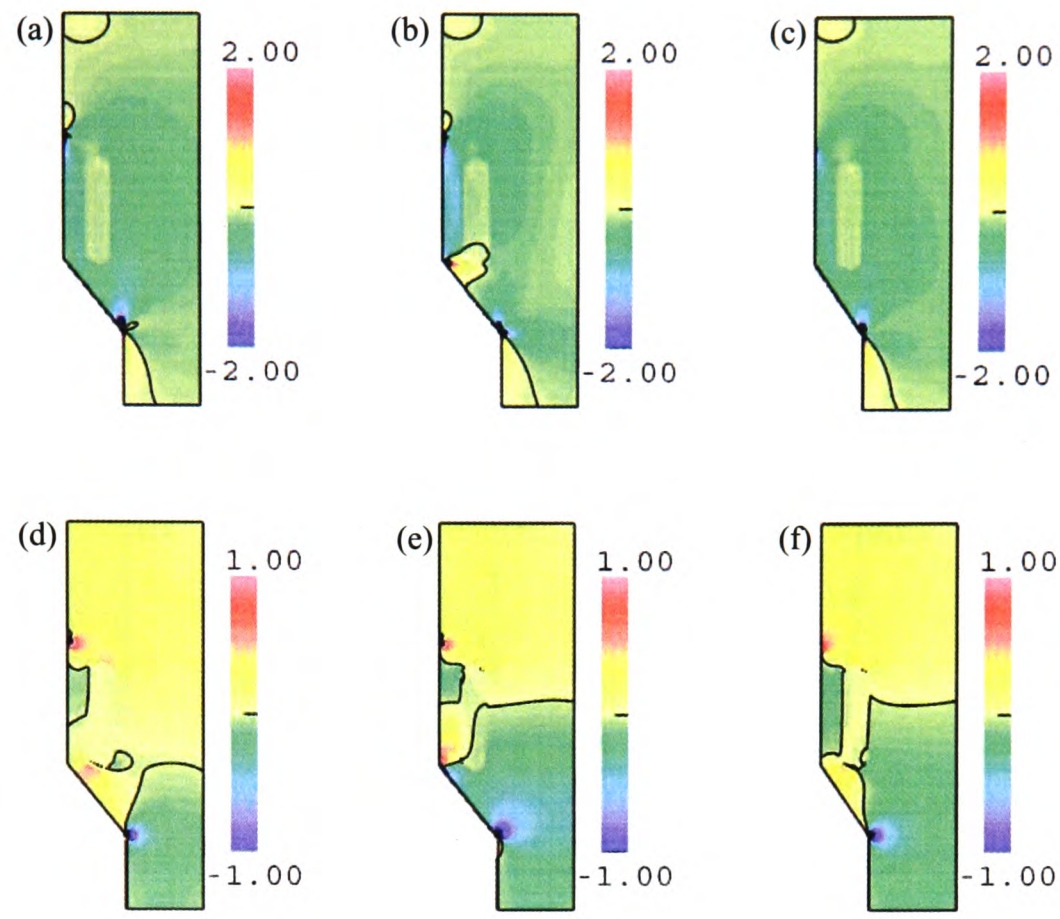

Figure 5.54: (a)–(c) component of the strain rate representative of shear deformation; $\dot{\varepsilon}_{xy}$. (d)–(f) vertical component of the strain rate; $\dot{\varepsilon}_{zz}$. $n = 1$ in all cases. The position of the higher viscosity region has not been indicated, but its location is apparent from the strain rate patterns, and the strain rate contours plotted in the figures. Plots (a,d): velocity boundary condition aligned with the y axis. Plots (b,e): velocity boundary condition aligned with the mesh boundary. Plots (c,f): velocity boundary condition deduced from Pacific–North America rotation vector.

for in the viscous sheet modelling. The observed pattern of strain in this region will be due to a combination of these factors.

The thickening of the viscous layer at $y = 3l$ is not observed in the real world. The complex dynamics of the plate interactions in the region of the Mendocino Triple Junction are not accounted for in these finite element experiments, and comparisons between model and observed strain rates in this region cannot be made.

For all four sets of boundary conditions, thinning of the viscous layer (indicated by negative $\dot{\varepsilon}_{zz}$) occurs at the $y = l$ bend in the boundary of the solution domain. The location of this thinning coincides with the location of the pull–apart basin which contains the Salton Sea, where lithospheric thinning is actively taking place (Lewis *et al.*, 2001); in the calculations, the concentration of thinning results from the change in the boundary conditions. The high values of $\dot{\varepsilon}_{zz}$ on the boundary of the mesh, at the northern limit of the driving velocity boundary condition, are an artifact of the change

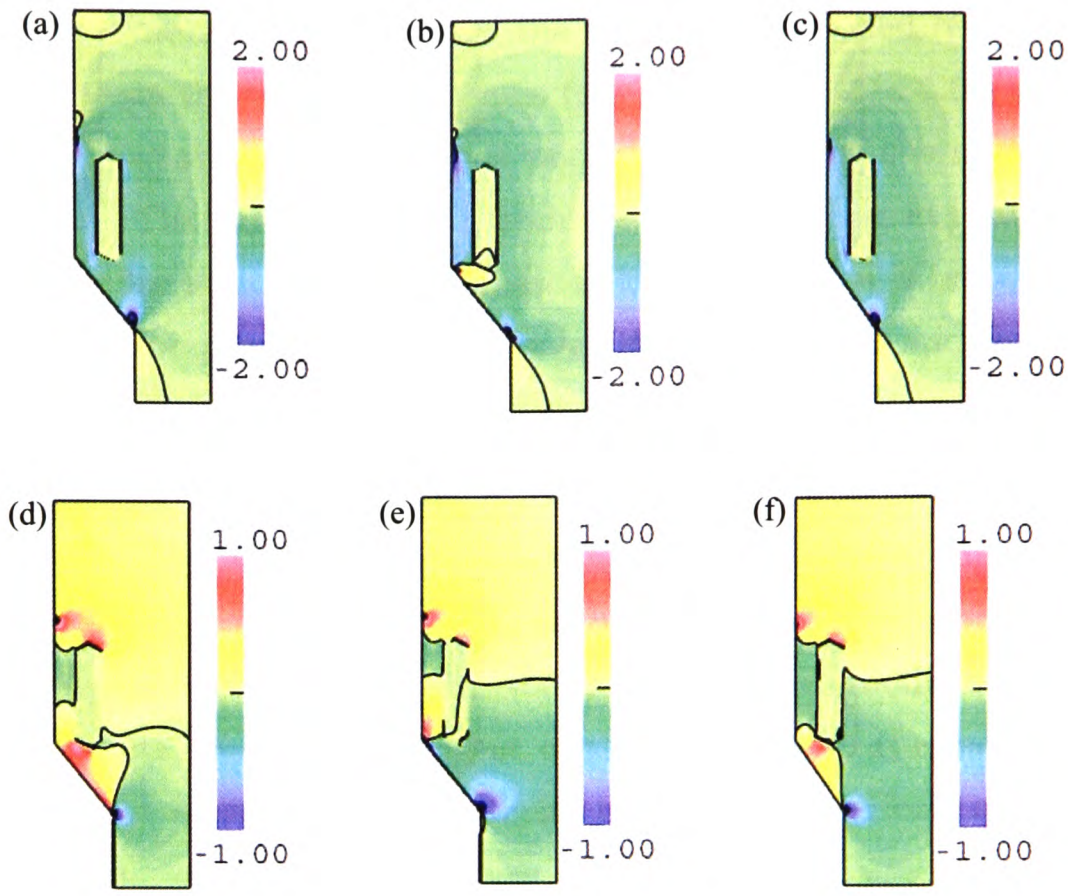

Figure 5.55: as for Figure 5.54, but $n = 2$ in all cases.

in the boundary conditions at this point.

The magnitudes of shear strain rates, $\dot{\varepsilon}_{xy}$ vary with n, and with the different boundary conditions. The width of the deformation zone is greater for small n (compare Figures 5.54 and 5.58), while the magnitude of $\dot{\varepsilon}_{xy}$ increases as n is increased. When the velocity boundary condition is aligned with the y axis of the solution domain, large negative values of $\dot{\varepsilon}_{xy}$ are found on both sides of the higher viscosity region, indicating a pattern of right–lateral shear. This pattern of deformation is similar to that observed in southern California, where deformation jumps from the San Andreas fault system to the East California Shear Zone across the southern portion of the Sierra block. However, the East California Shear Zone only accommodates 8–12 mm yr^{-1} of right–lateral shear (Hearn & Humphreys, 1998; Thatcher *et al.*, 1999), whereas the San Andreas fault zone accommodates 34 ± 3 mm yr^{-1} (Hill *et al.*, 1991); this ratio is more closely reproduced by the third and fourth sets of boundary conditions. Between the driving boundary and the higher viscosity region, the strongest shear arises when the velocity boundary condition is aligned with the boundary of the mesh.

Left–lateral shear is not found in the majority of the solution domain. Localised positive values of $\dot{\varepsilon}_{xy}$ are found in the vicinity of discontinuities of the velocity boundary conditions, but are predominantly numerical artifacts. Right–lateral shear is predicted along the inclined section of the mesh boundary when the velocity boundary condition is either aligned with the y axis of the solution domain, or the

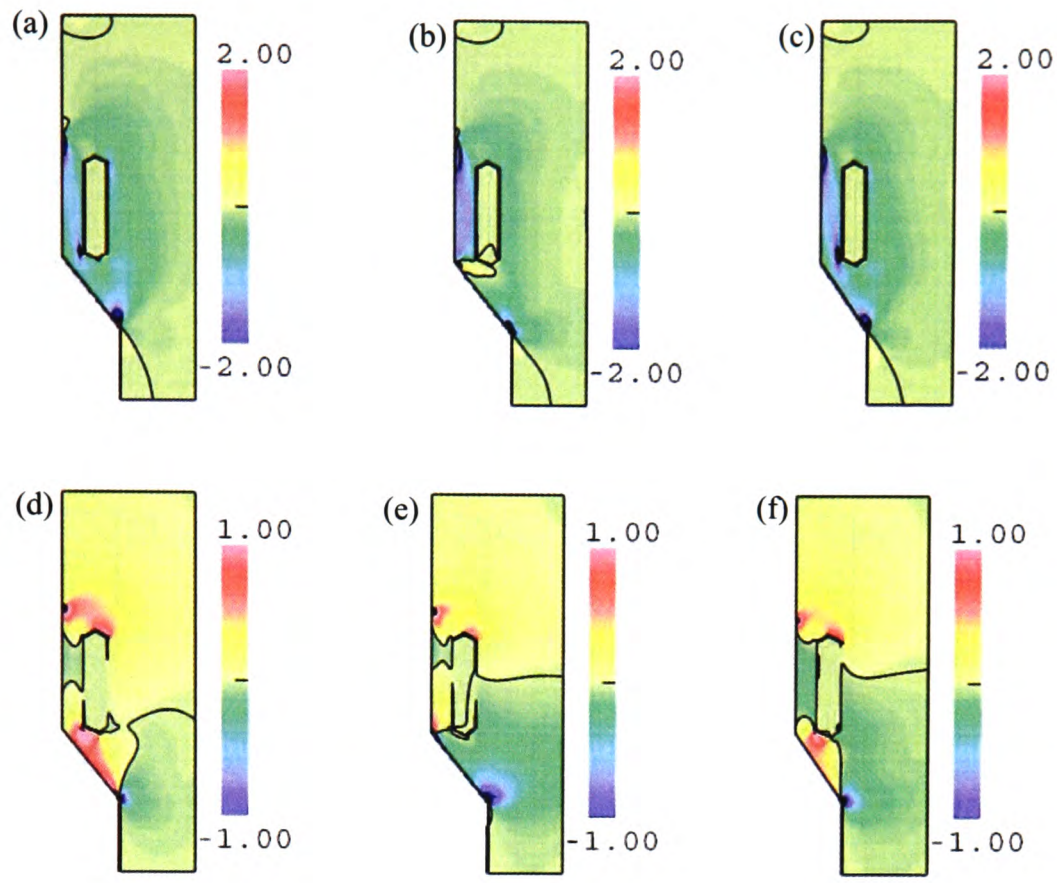

Figure 5.56: as for Figure 5.54, but $n = 3$ in all cases.

plate relative motion model is used. This last set of boundary conditions, which most closely represent motion along the Pacific–North America plate boundary, give rise to the most continuous pattern of right–lateral deformation along the boundary of the mesh. This pattern reflects the strike–slip deformation which prevails throughout California along the edge of the plate boundary.

The amount of rotation exhibited by the higher viscosity region cannot be determined from these plots of $\dot{\varepsilon}_{xy}$. A small amount of deformation in the interior of the higher viscosity region occurs when $n = 1$, but this decreases rapidly as n is increased. These observations concur with analysis of the constitutive equation (equation 5.1), which predicts that for any value of n, strain rates within a region whose viscosity is k times greater than the background viscosity will be k^n times smaller than the strain rates in the background fluid. For the case when $B = 10$, this implies that strain rates within the higher viscosity region will be reduced by an order of magnitude each time n is increased by one.

The magnitude of the strain rates outside the higher viscosity region increases as the non–linearity of the viscous layer increases (Compare Figures 5.54 and 5.58). I do not attempt to estimate the value of n which best describes the behaviour of the lithosphere in western North America from these contour plots because the magnitudes of the strain rates are strongly dependent upon the degree of non–linearity of the fluid and the geometry of the boundary conditions. The lack of shear strain

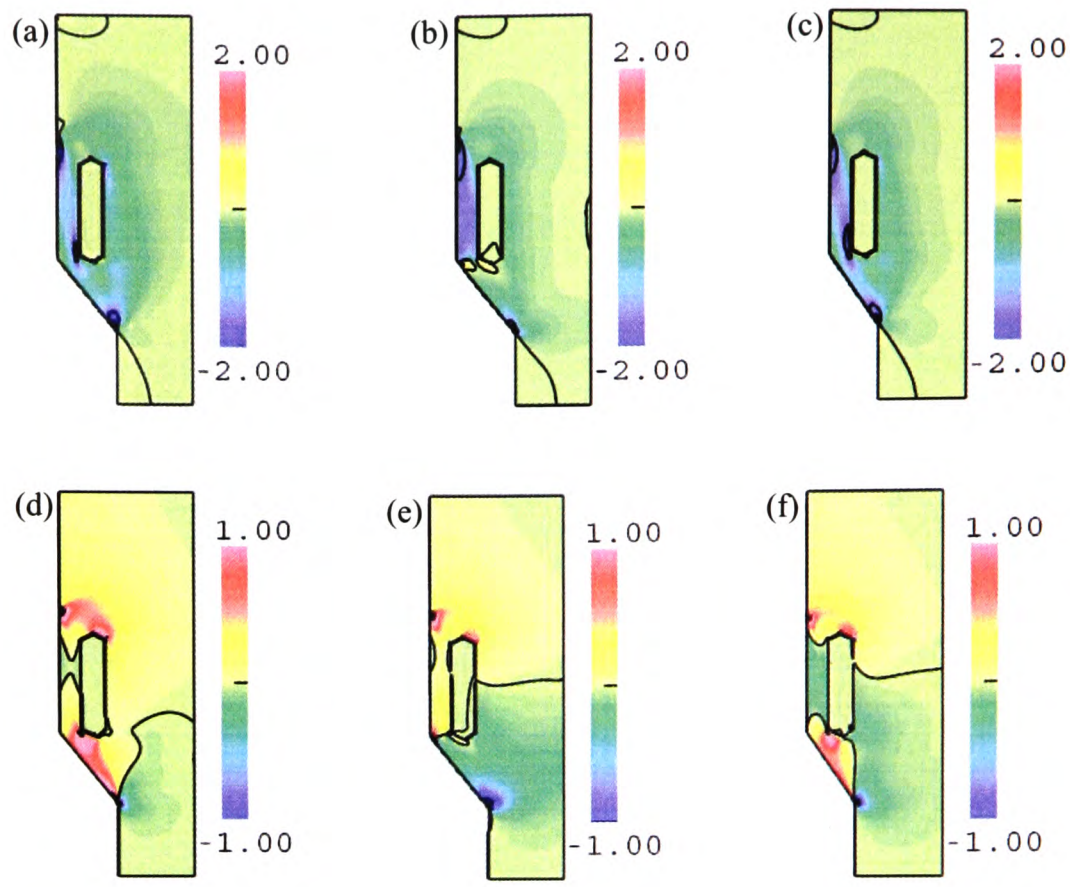

Figure 5.57: as for Figure 5.54, but $n = 4$ in all cases.

when $n = 1$ (Figure 5.54) implies that this solution is not applicable to the lithosphere of westernmost North America, but since the exact geometry of the boundary condition applied to North America by motion along the plate boundary is poorly constrained, tighter constraints cannot be placed upon n.

From the observations discussed above, I conclude that the boundary conditions calculated using the Pacific–Plate–Fixed NUVEL–1A Euler pole for North America are able to reproduce a pattern of deformation which closely resembles that observed throughout western North America when $n \geq 2$. However, the deformation of a viscous layer is strongly dependent upon the direction and magnitude of the velocity boundary conditions, and caution must be exercised when drawing quantitative conclusions from these experiments.

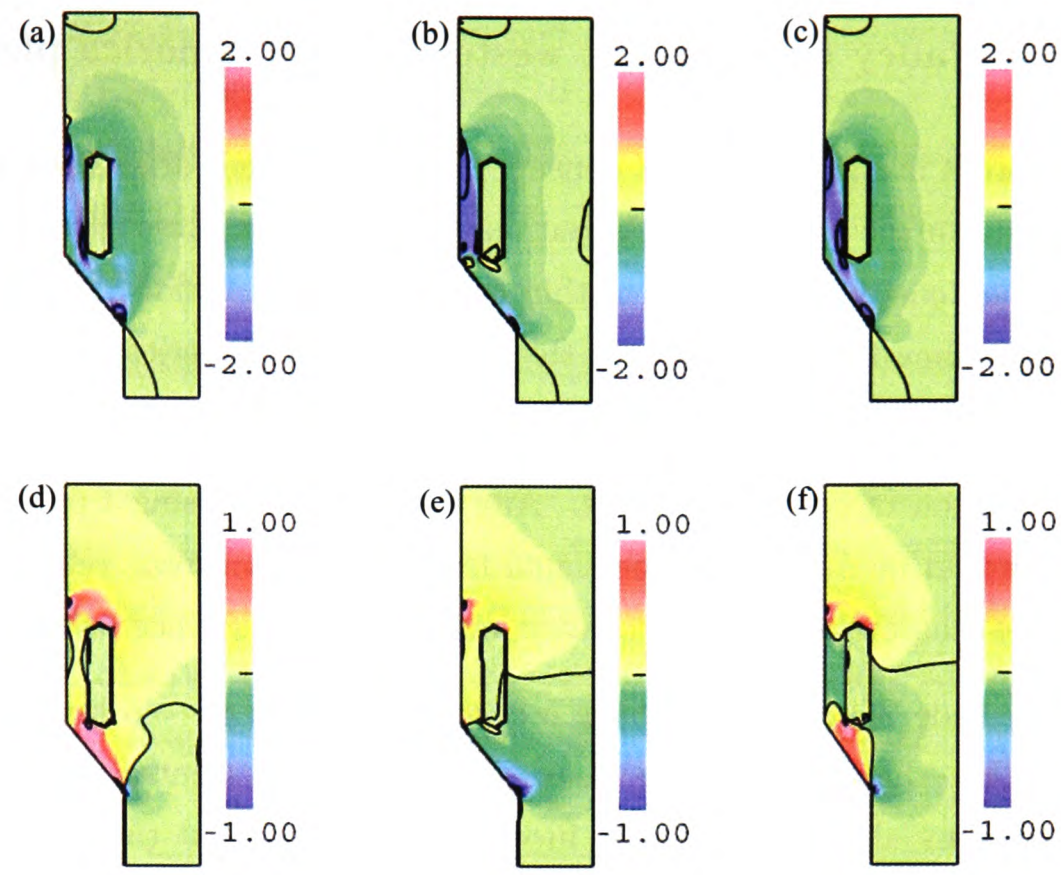

Figure 5.58: as for Figure 5.54, but $n = 5$ in all cases.

5.11 Lithospheric effective viscosity

In order to constrain the vertically averaged effective viscosity of the continental lithosphere it is necessary to determine the buoyancy forces, as well as the plate boundary forces, which drive the deformation. As discussed in chapter 2, gradients of crustal thickness give rise to buoyancy forces which in turn drive horizontal deformation.

In my analysis of plate boundary zone deformation in western North America, the component of the surface velocity field parallel to the plate boundary is used to study the effect of the rigid Sierra block upon the surface velocity field. The strike–normal component of velocity throughout the deforming plate boundary zone is of a smaller magnitude, but is not negligible (see section 5.8.4). The full surface velocity field reflects horizontal motion due to the relaxation of buoyancy forces. As discussed in chapter 3, topography may be used as a proxy for gradients of potential energy, but other factors perturb this signal.

5.11.1 Buoyancy forces in the western North America plate boundary zone

Buoyancy forces are generated by density gradients, which arise from compositional and thermal differences within the lithosphere. Variations in crustal thickness and perturbations to the geotherm both alter the density distribution within the lithosphere. Below, I attempt to constrain the distribution of buoyancy forces throughout the western North America plate boundary zone.

Crustal thickness variations in the Coast Ranges are probably too small to generate deformation via the relaxation of buoyancy forces. Any deformation arising from the relaxation of stresses in this region would be masked by the signal from the transcurrent velocity field, and it is difficult to constrain the magnitude of any buoyancy forces from the surface velocity field.

The 100 km–wide Sierra Nevada have a crustal thickness of ~45 km, which is significantly greater than the 30 km–thick crust of the Coast Ranges and the Central Valley. This difference would be sufficient to bring about deformation in weak lithosphere, but the lithosphere of the Sierra block is strong, and such buoyancy forces are insufficient to bring about any appreciable deformation on the western flank of the Sierra Nevada..

On the eastern flank, the crust thins to ~25 km beneath the Basin and Range Province. Any study of the deformation arising from the resulting buoyancy forces is complicated by the extension across the Basin and Range Province. This broad region of deformation, situated on average at an altitude >1 km, is not supported by a crustal root, but instead seems to be supported by hot, low density mantle material. The interaction of forces due to gravitational spreading and buoyant upper mantle material is beyond the scope of this work, and it is left to other authors (e.g. Jones *et al.* (1996)) to postulate on the magnitude of the resulting buoyancy forces.

In northern California crustal thickness variations, and hence buoyancy forces, predicted from the surface topography are small. However, the northward translation of the subducted Gorda slab has left a void into which hot asthenospheric material may flow (Guzofski & Furlong, 2002; Goes *et al.*, 1997), thus perturbing the thermal structure beneath this portion of the lithosphere, and hence the distribution of buoyancy forces.

The subducted slab has a cooling effect upon the thermal structure of the slab window; this effect is dependent upon the age of the slab. The motion of the slab will also draw material into the window by viscous drag; the source of this material influences the resulting thermal structure, which may be modified by convection.

Maximum surface heat flow associated with the passage of the Mendocino Triple Junction is observed 200 km south of its present position (Lachenbruch & Sass, 1980), and is probably associated with asthenospheric upwelling into the slab window beneath the northern Coast Ranges. It has been

postulated that hot material is prevented from upwelling into the slab window immediately south of the Gorda slab by the underthrust Pacific plate, or due to thickening of the crust by the accretion of cooled asthenospheric material (Goes *et al.*, 1997). A mantle upwelling to shallow depths could therefore only take place further south, but the distribution of buoyancy forces due to such an upwelling is poorly constrained.

There are many uncertainties in the thermal and density structure of this region of the plate boundary, making it very difficult to predict the contribution to buoyancy forces from the various effects. As noted above, there is also no simple relationship between topography and crustal thickness in western North America, making it difficult to predict the distribution of buoyancy forces which arise from crustal thickness variations across this region. Flesch *et al.* (2000) use a combination of topographic data, geoid data, GPS observations, strain rate magnitudes and Quaternary faulting observations to determine the vertically averaged deviatoric stress tensor field in western North America, and from this draw conclusions about the vertically averaged viscosity of the lithosphere. They conclude that the California shear zone has a low vertically averaged viscosity of $\sim 10^{21}$ Pa s, while the Basin and Range has a higher vertically averaged viscosity of $\sim 10^{22}$ Pa s. Without considering the dynamic forces acting in the Basin and Range region the buoyancy forces governing deformation across the western North America plate boundary zone cannot be completely defined, I therefore do not attempt to quantify regional strength variations using the methods of chapter 2.

5.12 Conclusions

I have demonstrated that the observed relative motion of the Sierra block in western North America may be reproduced by considering a thin viscous sheet model of the lithosphere driven by strike–parallel motion on one boundary. The lithosphere behaves as a non–Newtonian viscous fluid, and contains a rigid block that translates within the flow and acts to broaden the zone of deformation. I have demonstrated that once it is aligned with the shear direction, the rotation of such a narrow block will be negligible. There is no evidence for the rotation of the Sierra block, and I conclude that the rigid–body translation of the block may be explained by a force balance in the direction parallel to the Pacific–North America plate boundary. Using a realistic plate boundary geometry in the thin viscous sheet model allows second–order details of the strain rate field in the western North America plate boundary zone to be recovered, but such complications do not alter the conclusions of the simple modelling. The comparison of model velocity profiles with GPS data confirms that the stress–strain rate exponent required to reproduce the observed relative motion of the block is $n = 3$ $(-\frac{1}{2}, +1)$. Lateral variations in the effective viscosity of the lithosphere cannot be recovered without more detailed knowledge of the distribution of potential energy throughout this plate boundary zone.

Chapter 6

Conclusions

6.1 Conclusions relating to this study

The lithosphere of south–east Asia is treated as a thin layer of viscous material, and the first order characteristics of the observed velocity and strain rate fields are reproduced by considering the response of this viscous layer to boundary and buoyancy forces. Regions of high strain rates in the observed deformation field may be attributed to lateral strength heterogeneities in the lithosphere, or variations in the magnitude of the driving forces applied to this region. In order to distinguish between these two scenarios a realistic potential energy distribution is used to constrain the distribution of buoyancy forces throughout south–east Asia. The distribution of a strength parameter is then solved for, using the assumption that any strain which cannot be reproduced by the deformation of a homogeneous power law fluid can be explained by a perturbation to the strength of the lithosphere in that region.

GPS and Quaternary fault slip rate data have been used to constrain a surface velocity field interpolated upon a two–dimensional finite element mesh. The fit of numerical solutions, obtained by the method described above, to the principal strain axes of this velocity field is good throughout the compressional regions of the Himalaya and the Tien Shan, across the Tibetan plateau, and in the shield areas surrounding the plateau. A poor fit is achieved to the south–east of the plateau. It has been proposed that the convergence of India with Asia is partly accommodated by the motion of lithospheric material across the eastern margin of the Tibetan plateau. The slow velocity of south China away from stable Eurasia, and the lack of shortening across this margin of the plateau implies that much of the convergence may be accommodated by the rotation of lithospheric material. This process is poorly resolved by the data interpolated upon the finite element mesh, and velocity differences in this region are interpreted to represent high rates of strain, with the result that low effective

viscosities are predicted, and the direction of the velocity vectors do not fit the observed data.

Around the margins of the Tibetan plateau, in regions of steep topographic and potential energy gradients, low effective viscosities of 10^{21} to 10^{22} Pa s are predicted. Across the Tibetan plateau, the Mongolian platform and other deforming regions effective viscosities of $\sim 3 \times 10^{22}$ to 10^{23} Pa s are calculated, while values of 10^{23} to 3×10^{24} Pa s are obtained for the more rigid regions of India, South and North China, the Tarim Basin and Siberia. Apart from these Precambrian shield areas, the behaviour of the lithosphere of south–east Asia is found to be governed by a power law rheology. Suitable values for the stress–strain exponent lie in the range $3 \leq n \leq 10$. The strength parameter for this deforming region varies within one order of magnitude, implying that the variation in effective viscosity is an artifact of the strain rate distribution which in turn is completely determined by the distribution of potential energy gradients throughout this plate boundary zone.

In a study of lithospheric deformation in the western North America plate boundary zone, the thin viscous sheet approximation is used to investigate the motion of the Sierra block, which is approximated to be a high viscosity block embedded within viscous shear flow, and the behaviour of the surrounding fluid. Numerical solutions highlight the sensitivity of the motion of the block to the length of the driving boundary, the aspect ratio of the block, its position in relation to the driving boundary, and the stress–strain rate exponent of the viscous fluid, n. A strength difference of one order of magnitude between the block and the surrounding fluid is found to be sufficient to reproduce rigid behaviour within the block; strain rates within the high viscous region are found to be a factor of 10^n smaller than rates in the rest of the fluid. The block does undergo a small amount of clockwise rotation, but this motion is negligible in relation to the translational velocity of the block.

When a realistic geometry for the plate boundary is used in conjunction with the numerical model, and realistic boundary conditions are imposed, thickening of the viscous layer between the inclined boundary and the block takes place, and shear strain rates are concentrated along the boundary of the solution domain and the long sides of the high viscosity block. These features have been interpreted to represent the crustal thickening of lithosphere to the south of the Sierra block, and the concentration of right–lateral shear in the San Andreas fault zone. The numerical experiments also demonstrate that the width of the deformation zone relating to transcurrent motion along the boundary of the solution domain is widened in the presence of a rigid block. This effect is probably reproduced in the Pacific–North America plate boundary zone.

Analytical expressions for the deformation of a viscous fluid due to the motion of a rigid boundary are used to determine expressions for the vertically averaged stress applied along each boundary of a rigid block embedded within a viscous layer undergoing simple shear flow. The forces acting upon the block are balanced to yield an expression for the translational velocity of the block that is dependent

upon the geometry of the system and the stress–strain rate of the viscous fluid. Ratios of the velocity of the rigid block to the velocity of the driving boundary are in good agreement with values obtained using the numerical method. These results are therefore compared with estimates for the velocity ratio of the Sierra block–North America plate boundary system; a value of $n = 3$ (with upper and lower limits of 2.5 and 4 respectively) is required to reproduce the observed ratio of $V_1/V_0 \approx 0.23$. This result is confirmed by the agreement between along–strike velocity profiles constructed using GPS data, and profiles generated using $n = 3$ in the numerical method, both with and without the inclusion of a higher viscosity block.

6.2 Limitations of this study and suggestions for future work

Improvements in both forward and inverse modelling techniques are required in order to gain further insight into the dynamics of continental deformation. A better spatial and temporal resolution of the three–dimensional deformation field, and more accurate constraints for the rheological properties of the lithosphere, will allow more rigorous testing of forward models and enable tighter constraints to be placed upon inverse calculations.

I use the thin viscous sheet approximation in forward calculations, and as a basis for an iterative inverse method. The main limiting factor of the approximation is the assumption that velocity gradients, stress, and effective viscosity do not vary with depth. Vertical variations in viscosity have implications for the level of coupling between the crust and mantle, and hence the driving stress applied at the base of the lithosphere. The thin viscous sheet approximation assumes no basal tractions, and this seems to yield close agreement between predicted and observed deformation. However the presence of a low viscosity layer within the crust would permit vertical gradients of horizontal velocity, potentially leading to large discrepancies between long–term predictions of lithospheric deformation and the physical evolution of a continental plate boundary zone. The effect of the transition from brittle to ductile deformation with depth is contained within the power–law exponent of the constitutive equation, and the use of a bulk rheology to describe the properties of the lithosphere provides little insight into the distribution of strength with depth in the continental lithosphere. At present estimates for this distribution are derived from observations of the seismic properties of the lithosphere, surface heat flux, gravity anomalies and the distribution of seismicity. The development of models that solve the full three–dimensional force balance equation, and allow for vertical and lateral variations in lithospheric properties, would provide a much–needed test of these hypotheses.

Several attempts have been made to model the continental lithosphere as a layered continuum (Royden, 1996; Liu & Yang, 2003; Shen *et al.*, 2001a), and Medvedev & Podladchikov (1999) present an

extension of the thin sheet approximation that uses asymptotic approximations of three–dimensional force balance and rheological relations in order to construct depth distributions of stress and velocity fields. Further work in this area is ongoing, however there have still been relatively few attempts at constraining lateral variations in lithospheric rheology using continuum models. The response of the lithosphere to stress is modified by both vertical and horizontal heterogeneities on a range of scales. It is important to quantify the sensitivity of the deformation to these effects independently before attempting to constrain the three–dimensional distribution of lithospheric strength using continuum models.

So far, length scale assumptions of the thin viscous sheet approximation have meant that it has only been applied to deforming regions whose lateral extent is on the order of 1000 km or more. It is not known to what degree this constraint may be relaxed, although a lower bound will be ~100 km, or the thickness of the lithosphere. Large–scale deformation is controlled by the average mechanical properties of the lithosphere, but on the order of the thickness of the lithosphere the brittle layer dominates, giving rise to local complexities. At this scale fault strength determines the localisation of strain, and hence the surface velocity field. It seems likely that the thin viscous sheet method may be used to investigate continental deformation on a smaller scale, but caution must be exercised in the implementation of the method, the application of boundary conditions, and the interpretation of results.

Recent improvements in the spatial coverage of surface velocity data will be used to constrain future deformation models, but at present the data must be extrapolated to determine the full three-dimensional deformation of the lithosphere. As yet we do not have a comprehensive understanding of the kinematics of three–dimensional deformation; the complexity of the problem is enhanced by the fact that the rheology of the continental lithosphere permits such mechanisms as crustal thickening, crust-mantle decoupling, and the delamination of thickened lithosphere. We must also extrapolate from observations of deformation in the brittle upper crust to continuous deformation at depth (Lamb, 1994). The extent to which the surface velocity field represents ductile deformation at depth is poorly known; the degree of coupling will vary with space, and maybe even time.

Continental deformation is driven by boundary forces applied by plate motions and buoyancy forces arising from density gradients within the lithosphere. Plate motions are relatively well constrained by geodetic observations, but the distribution of density gradients must be inferred from gravity anomalies, geoid height, topography, or even the inversion of strain rates. Improvements in the data and methods for determining gradients of gravitational potential energy are needed to define realistic boundary conditions for models of continental deformation. Basal tractions are generally regarded to be negligible with regard to the driving forces of the system, but this is still a subject of debate (Bokelmann, 2002). The degree of coupling at the base of the lithosphere is poorly known,

and a better knowledge of the structure and flow of the upper mantle would be useful in assessing the importance of basal tractions upon continental deformation.

The thin viscous sheet model calculates the long term, viscous, response of the lithosphere to driving forces, and assumes that the response of the system to these driving forces is instantaneous. Viscoelastic relaxation of the lithosphere, in response to the earthquake cycle, takes place on much shorter time scales, but it is assumed that the effect of such processes averages out over many earthquake cycles, and such complications are neglected in this study. However, it is important to ascertain to what extent present–day surface velocities represent the long term average. Comparisons between Quaternary slip rate data and GPS data collected over a maximum of 10 years reveal differences that may be attributed to the migration of deformation, changes in the geometry of the system or the distribution of driving forces, or different mechanisms of strain accommodation. It is important to distinguish between a change in the style or rate of deformation, and the case where a proportion of the deformation is accommodated aseismically, and therefore will not be recorded in terms of fault slip. In general, the errors involved with GPS data are much smaller than errors attached to strain rates derived from geological estimates, however care must be taken when using GPS data to constrain long–term surface velocity fields because the data will also contain information relating to the short–term, elastic response of the lithosphere to driving forces and loads. As longer GPS time series become available, the acceleration, as well as the rate, of baseline changes must be considered, in order to distinguish between long and short term deformation.

The introduction of continuous GPS monitoring has proved to be a valuable tool for detecting signals with a period of several tens or hundreds of days, such as postseismic relaxation and slow earthquakes. The deployment of such instruments on a regular spatial scale in regions of diffuse deformation like the Basin and Range Province of North America will allow short–period and long–period signals relating to the local accommodation of strain by the earthquake cycle, and the permanent aseismic accommodation of strain on a regional scale, to be separated. The first generation of continuum models have successfully demonstrated the inadequacy of plate tectonic theory in explaining the behaviour of continental lithosphere under stress. Eventually we must attempt to resolve the discrepancy in the time–dependent response of the continental lithosphere, but the next generation of continuum models should first look to develop three–dimensional models that accurately represent the behaviour of the continental lithosphere in a range of tectonic settings without *a priori* assumptions. Improvements in the resolution of data should permit three–dimensional inversions for the rheological properties of the lithosphere to be carried out, thus providing an invaluable tool for future generations of earth scientists.

Bibliography

ABDRAKHMATOV, K. YE., ALDAZHANOV, S. A., HAGER, B. H., HAMBURGER, M. W., HERRING, T. A., KALABAEV, K. B., MAKAROV, MOLNAR, P., PANASYUK, S. V., PRILEPIN, M. T., REILINGER, R. E., SADYBAKASOV, I. S., SOUTER, B. J., TRAPEZNIKOV, YU. A., TSURKOV, V. YE., & ZUBOVICH, A. V. 1996. Relatively recent construction of the Tien Shan inferred from GPS measurements of present-day crustal deformation rates. *Nature*, **384**, 450–453.

ACHACHE, J., COURTILLOT, V., & ZHOU, Y.X. 1984. Paleogeographic and tectonic evolution of southern Tibet since middle Cretaceous time: New paleomagnetic data and synthesis. *J. Geophys. Res.*, **89**, 10,311–10,340.

ARGAND, E. 1924. La tectonique de l'Asie. *Proc. 13th Int. Geol. Congr.*, **7**, 171–372.

ARGUS, D. F., & GORDON, R. G. 1991. Current Sierra Nevada-North America motion from very long baseline interferometry; implications for the kinematics of the Western United States. *Geology (Boulder)*, **19**(11), 1085–1088.

ARGUS, D. F., & GORDON, R. G. 1996. Test of the rigid-plate hypothesis and bounds on intraplate deformation using geodetic data from very long baseline interferometry. *Journal of Geophysical Research, B, Solid Earth and Planets*, **101**(6), 13,555–13,572.

ARGUS, D. F., & GORDON, R. G. 2001. Present tectonic motion across the Coast Ranges and San Andreas fault system in Central California. *Geological Society of America Bulletin*, **113**(12), 1580–1592.

ARMIJO, R., TAPPONNIER, P., MERCIER, J., & HAN, TONGLIN. 1986. Quaternary extension in southern Tibet: Field observations and tectonic implications. *J. Geophys. Res.*, **91**, 13,803–13,872.

ARMIJO, R., TAPPONNIER, P., & HAN, TONGLIN. 1989. Late Cenozoic right-lateral strike-slip faulting in southern Tibet. *J. Geophys. Res.*, **94**, 2787–2838.

ARNAUD, N.O., VIDAL, P., TAPPONNIER, P., MATTE, P., & DENG, W.M. 1992. The high K20 volcanism of northwestern Tibet–geochemistry and tectonic implications. *Earth Planet. Sci. Lett.*, **111**(2–4), 351–367.

ATWATER, T. 1970. Implications of Plate Tectonics for the Cenozoic Tectonic Evolution of Western North America. *Geol. Soc. Am. Bull.*, **81**, 3513–3536.

AVOUAC, J.-P., & TAPPONNIER, P. 1993. Kinematic model of active deformation in Asia. *Geophys. Res. Let.*, **20**, 895–898.

AVOUAC, J.-P., TAPPONNIER, P., BAI, M., YOU, H., & WANG, G. 1993. Active thrusting along the northern Tien Shan and late Cenozoic rotation of the Tarim relative to Dzungaria and Kazakhstan. *J. Geophys. Res.*, **98**, 6755–6804.

BANERJEE, P., & BÜRGMANN, R. 2002. Convergence across the northwest Himalaya from GPS measurements. *Geophys. Res. Lett.*, **29**(13), 30, doi:10.1029/2002GL015184.

BENDICK, R., BILHAM, R., FREYMUELLER, J. T., LARSON, K., & YIN, G. 2000. Geodetic evidence for a low slip rate in the Altyn Tagh fault system. *Nature (London)*, **404**(6773), 69–72.

BENNETT, R. A., DAVIS, J. L., & WERNICKE, B. P. 1999. Present-day pattern of Cordilleran deformation in the Western United States. *Geology (Boulder)*, **27**(4), 371–374.

BENNETT, R.A., RODI, W., & REILINGER, R.E. 1996. Global Positioning System constraints on fault slip rates in southern California and north Baja, Mexico. *J. Geophys. Res..*, **101**, 21,943–21,960.

BENNETT, R.A., WERNICKE, B.P., & DAVIS, J.L. 1998. Continuous GPS measurements of contemporary deformation across the northern Basin and Range Province. *Geophys. Res. Lett.*, **25**(4), 563–566.

BILHAM, R., LARSON, K. M., FREYMUELLER, J. T., JOUANNE, F., LE, F. P., LETURMY, P., MUGNIER, J. L., GAMOND, J. F., GLOT, J. P., MARTINOD, J., CHAUDURY, N. L., CHITRAKAR, G. R., GAUTAM, U. P., KOIRALA, B. P., PANDEY, M. R., RANABHAT, R., SAPKOTA, S. N., SHRESTHA, P. L., THAKURI, M. C., TIMILSINA, U. R., *et al.* 1997. GPS measurements of present-day convergence across the Nepal Himalaya. *Nature*, **386**, 61–64.

BIRD, P. 1979. Continental delamination and the Colorado Plateau. *J. Geophys. Res.*, **84**, 7,561–7,571.

BIRD, P. 1989. New finite element techniques for modeling deformation histories of continents with stratified temperature-dependent rheology. *Journal of Geophysical Research, B, Solid Earth and Planets*, **94**(4), 3967–3990.

BIRD, P. 1991. Lateral Extrusion of Lower Crust from under High Topography, in the Isostatic Limit. *J. Geophys. Res.*, **96**, 10,275–10,286.

BIRD, P., & BAUMGARDNER, J. 1984. Fault friction, regional stress, and crust–mantle coupling in southern California from finite element models. *J. Geophys. Res.*, **89**, 1932–1944.

BIRD, P., & PIPER, K. 1980. Plane-stress finite-element models of tectonic flow in southern California. *Phys. Earth Planet Inter.*, **21**, 158–175.

BIRD, P., & ROSENSTOCK, R. W. 1984. Kinematics of present crust and mantle flow in southern California. *Geol. Soc. Am. Bull.*, **95**, 946–957.

BLISNIUK, P. M., HACKER, B. R., GLODNY, J., RATSCHBACHER, L., BI, S., WU, Z., MCWILLIAMS, M. O., & CALVERT, A. 2001. Normal faulting in central Tibet since at least 13.5 Myr ago. *Nature (London)*, **412**(6847), 628–632.

BOKELMANN, G. H. R. 2002. Which forces drive North America? *Geology (Boulder)*, **30**(11), 1027–1030.

BOURNE, S., ENGLAND, P., & PARSONS, B. 1998. The motion of crustal blocks driven by flow of the lower lithosphere and implications for slip rates of continental strike-slip faults. *Nature*, **391**, 655–659.

BOURNE, S.J. 1996. *Distributed Deformation of the South Island of New Zealand.* D.Phil. dissertation, University of Oxford, Oxford, UK.

BRACE, W.F., & KOHLSTEDT, D.L. 1980. Limits on lithostatic Stress Imposed by Laboratory Experiments. *J. Geophys. Res.*, **85**, 6,248–6,252.

BRAITENBERG, C., ZADRO, M., FANG, J., WANG, Y., & HSU, H. T. 2000. The gravity and isostatic Moho undulations in Qinghai-Tibet plateau. *Journal of Geodynamics*, **30**(5), 489–505.

BRAZIER, R.A., & NYBLADE, A.A. 2003. Upper mantle P velocity structure beneath the Baikal Rift from modelling regional seismic data. *Geophys. Res. Let.*, **30**(4), 1153, doi:10.1029/2002GL016115.

BROWN, E. T., BENDICK, R., BOURLÈS, D., GAUR, V., MOLNAR, P., & RAISBECK, G. 2002. Slip rates of the Karakorum fault, Ladakh, India, determined using cosimic ray exposure dating of debris flows and moraines. *J. Geophys. Res.*, **107**(B9), 2192, doi:10.1029/2000JB000100.

BROWN, L.D., ZHAO, W.J., NELSON, D.K., HAUCK, M., ALSDORF, D., ROSS, A., COGAN, M., CLARK, M., LIU, X.W., & CHE, J.K. 1996. Bright spots, structure, and magmatism in southern Tibet from INDEPTH seismic reflection profiling. *Science*, **274**(5293), 1688–1690.

BUROV, E., JAUPART, C., & MARESCHAL, J.C. 1998. Large–scale crustal heterogeneities and lithospheric strength in cratons. *Earth Planet. Sci. Lett.*, **164**(1–2), 205–219.

BYERLEE, J. 1978. Friction of Rocks. *Pure. Appl. Geophys.*, **116**, 615–626.

CALAIS, E., LESNE, O., DÉVERCHÈRE, J., K. V. SAN, LUKHNEV, A., MIROSHNITCHENKO, A., BUDDO, V., LEVI, K., ZALUTZKY, V., & BASHKUEV, Y. 1998. Crustal deformation in the Baikal Rift from GPS measurements. *Geophys. Res. Let.*, **25**, 4003–4006.

CALAIS, E., VERGNOLLE, M., SAN'KOV, V., LUKHNEV, A., MIROSHNITCHENKO, A., AMARJARGAL, S., & DÉVERCHÈRE, J. 2003. GPS measurements of crustal deformation in the Baikal–Mongolia area (1994–2002):Implications for current kinematics of Asia. *J. Geophys. Res.*, **108**(10), 2501, doi:10.1029/2002JB002373.

CARROLL, A.R., GRAHAM, S.A., HENDRIX, M.S., YING, D., & ZHOU, D. 1995. Late Paleozoic tectonic amalgamation of northwestern China; sedimentary record of the northern Tarim, northwestern Turpan, and southern Junggar basins. *Geol. Soc. Am. Bull.*, **107**(5), 571–594.

CHEN, Q., FREYMUELLER, J. T., WANG, Q., YANG, Z., & XU, C. 2004. A deforming block model for the present-day tectonics of Tibet. *Journal of Geophysical Research, B, Solid Earth and Planets*, **109**. B01403,doi:10.1029/2002JB002151.

CHEN, Z., BURCHFIEL, B. C., LIU, Y., KING, R. W., ROYDEN, L. H., TANG, W., WANG, E., ZHAO, J., & ZHANG, X. 2000. Global Positioning System measurements from eastern Tibet and their implications for India/Eurasia inter-continental deformation. *J. Geophys. Res.*, **105**, 16,215–16227.

CHOI, E.-S., & GURNIS, M. 2003. Deformation in transcurrent and extensional environments with widely spaced weak zones. *Geophysical Research Letters*, **30**(2). 1076,doi:10.1029/2002GL016129.

CHRISTENSEN, M.I., & MOONEY, W.D. 1995. Seismic velocity structure and composition of the continental crust – A global view. *J. Geophys. Res.*, **100**(6), 9761–9788.

CLARK, M. K., & ROYDEN, L. H. 2000. Topographic ooze; building the eastern margin of Tibet by lower crustal flow. *Geology (Boulder)*, **28**(8), 703–706.

COHEN, S.C., & MORGAN, R.C. 1986. Intraplate deformation due to continental collision; a numerical study of deformation in a thin viscous sheet. *Tectonophysics*, **132**(1–3), 247–259.

COLEMAN, M., & HODGES, K. 1995. Evidence for Tibetan plateau uplift before 14–Myr ago from a new minimum age for east–west extension. *Nature*, **374**(6517), 49–52.

COLEMAN, R.G. 1989. Continental growth of Northwest China. *Tectonics*, **8**(3), 621–635.

CURRAY, J.R., & MUNASINGHE, T. 1989. Timing of intraplate deformation, northeastern Indian Ocean. *Earth Planet. Sci. Lett.*, **94**, 71–77.

DAVIES, R., ENGLAND, P., PARSONS, B., BILLIRIS, H., PARADISSIS, D., & VEIS, G. 1997. Geodetic strain of Greece in the interval 1892-1992. *Journal of Geophysical Research, B, Solid Earth and Planets*, **102**(11), 24,571–24,588.

DAVY, P., & COBBOLD, P. 1988. Indentation tectonics in nature and experiment. 1. Experiments scaled for gravity. *Bull. Geol. Inst. Uppsala, N.S.*, **14**, 129–141.

DAYEM, K. E., HOUSEMAN, G. A., & MOLNAR, P. 2003. Localization of Shear along a Strong Inclusion in a Continuous Deformation Model: An Application to the Altyn Tagh Fault. *Eos Trans. AGU*, **84**(46). Fall Meet. Suppl., Abstract T21D-0486.

DEMETS, C., & DIXON, T. H. 1999. New kinematic models for Pacific-North America motion from 3 Ma to present; I, Evidence for steady motion and biases in the NUVEL-1A model. *Geophysical Research Letters*, **26**(13), 1921–1924.

DEMETS, C., GORDON, R. G., STEIN, S., & ARGUS, D. F. 1987. A revised estimate of Pacific-North America motion and implications for western North America plate boundary zone tectonics. *Geophysical Research Letters*, **14**(9), 911–914.

DEMETS, C., GORDON, R. G., ARGUS, D. F., & STEIN, S. 1990. Current plate motions. *Geophysical Journal International*, **101**(2), 425–478.

DEMETS, C., GORDON, R. G., ARGUS, D. F., & STEIN, S. 1994. Effect of recent revisions to the geomagnetic reversal time scale on estimates of current plate motions. *Geophysical Research Letters*, **21**(20), 2191–2194.

DEWEY, J. F., & BURKE, K. C. A. 1973. Tibetan, Variscan and Precambrian basement reactivation: products of a continental collision. *Journal of Geology*, **81**, 683.

DEWEY, J. F., SHAKLETON, R. M., CHANG, CHENGFA, & SUN, YIYIN. 1988. The tectonic evolution of the Tibetan Plateau. *Philos. Trans. R. Soc. London.*, **327**(Series A), 379–413.

DIXON, T. H., MAO, A., & STEIN, S. 1996. How rigid is the stable interior of the North American Plate? *Geophysical Research Letters*, **23**(21), 3035–3038.

DIXON, T. H., MILLER, M., FARINA, F., WANG, H., & JOHNSON, D. 2000. Present-day motion of the Sierra Nevada block and some tectonic implications for the Basin and Range Province, North American Cordillera. *Tectonics*, **19**(1), 1–24.

DIXON, T.H., ROBAUDO, S., LEE, J., & REHEIS, M.C. 1995. Constraints on present–day Basin and Range deformation from space geodesy. *Tectonics*, **14**(4), 755–772.

DREGER, D.S., TKALČIĆ, H., & JOHNSTON, M. 2000. Dilational Processes Accompanying Earthquakes in the Long Valley Caldera. *Science*, **288**, 122–125.

DRICKER, I.G., & ROECKER, S.W. 2002. Lateral heterogeneity in the upper mantle beneath the Tibetan plateau and its surroundings from SS–S travel time residuals. *J. Geophys. Res.*, **107**(11).

DUPRE, W. R., MORRISON, R. B., CLIFTON, H. E., LAJOIE, K. R., PONTI, D. J., POWELL, C. L., II, MATHIESON, S. A., SARNA, W. A. M., LEITHOLD, E. L., LETTIS, W. R., MCDOWELL, P. F., ROCKWELL, T. K., UNRUH, J. R., & YEATS, R. S. 1991. Quaternary geology of the Pacific margin. *In: Quaternary nonglacial geology; conterminous U S.* Am.: Geol Soc.

ELLIS, S., FULLSACK, P., & BEAUMONT, C. 1995. Oblique convergence of crust driven by basal forcing; implication for lengthscales of deformation and strain partitioning in orogens. *Geophys. J. Int.*, **120**, 24–44.

ENGDAHL, E.R., VAN DER HILST, R., & BULAND, R. 1998. Global Teleseismic Earthquake Relocation with Improved Travel Times and Procedures for Depth Determination. *Bull. Seismol. Soc. Amer.*, **88**, 722–743.

ENGLAND, P. 1993. Convective removal of thermal boundary layer of thickened continental lithosphere: a brief summary of causes and consequences with special reference to the Cenozoic tectonics of the Tibetan Plateau and surrounding regions. *Tectonophysics*, **223**, 67–73.

ENGLAND, P., & HOUSEMAN, G. 1985. Role of lithospheric strength heterogeneities on the tectonics of Tibet and surrounding regions. *Nature*, **315**, 297–301.

ENGLAND, P., & HOUSEMAN, G. 1986. Finite strain calculations of continental deformation 2. Comparison with the India–Asia collision zone. *J. Geophys. Res.*, **91**, 3,664–3,676.

ENGLAND, P., & HOUSEMAN, G. 1988. The mechanics of the Tibetan Plateau. *Philos. Trans. R. Soc. London.*, **326**, 301–320.

ENGLAND, P., & HOUSEMAN, G. 1989. Extension During Continental Convergence, with application to the Tibetan Plateau. *J. Geophys. Res.*, **94**, 17561–17579.

ENGLAND, P., & JACKSON, J. 1989. Active deformation of the continents. *Annu. Rev. Earth Planet. Sci.*, **17**, 197–226.

ENGLAND, P., & MCKENZIE, D. 1982. A thin viscous sheet model for continental deformation. *Geophys. J. R. Astron. Soc.*, **70**, 295–321.

ENGLAND, P., & MOLNAR, P. 1990. Right–lateral shear and rotation as the explanation for strike–slip faulting in eastern Tibet. *Nature*, **344**, 140–142.

ENGLAND, P., & MOLNAR, P. 1997a. Active Deformation of Asia: From Kinematics to Dynamics. *Science*, **278**, 647–650.

ENGLAND, P., & MOLNAR, P. 1997b. The Field of Crustal Velocity in Asia Calculated from Quaternary Rates of Slip on Faults. *Geophys. J. Int.*, **131**, 551–582.

ENGLAND, P., & MOLNAR, P. 2004. The velocity field in Asia derived from slip rates on Quaternary faults and GPS observations. *Geophys. J. Int.*, **in prep.**

ENGLAND, P., & SEARLE, M. 1986. The Cretaceous–Tertiary deformation of the Lhasa Block and its implications for crustal thickening in Tibet. *Tectonophysics*, **5**, 1–14.

ENGLAND, P., HOUSEMAN, G., & SONDER, L. 1985. Length scales for continental deformation in convergent, divergent and strike-slip environments: analytical and approximate solutions for a thin viscous sheet model. *J. Geophys. Res.*, **90**, 3,551–3,557.

FLESCH, L. M., HOLT, W. E., HAINES, A. J., & SHEN, T. B. 2000. Dynamics of the Pacific-North American plate boundary in the Western United States. *Science*, **287**(5454), 834–836.

FLESCH, L.M., HAINES, A.J., & HOLT, W.E. 2001. Dynamics of the India-Eurasia collision zone. *J. Geophys. Res.*, **106**(B8), 16,435–16,460.

FLIEDNER, M.M., KLEMPERER, S.L., & CHRISTENSEN, N.I. 2000. Three–dimensional seismic model of the Sierra Nevada arc, California, and its implications for crustal and upper mantle composition. *J. Geophys. Res.*, **105**(5), 10,899–10,921.

FRANK, F.C. 1972. Plate tectonics, the analogy with glacier flow, and isostasy. *Pages 285–292 of:* HEARD, H. C. (ed), *Flow and Fracture of Rocks, The Griggs Volume, Geophysical Monograph Series.* AGU, Washington D.C.

FUIS, G. S. 1998. West margin of North America; a synthesis of recent seismic transects. *Tectonophys.*, **288; 1-4**, 265–292.

GAO, S., DAVIS, P.M., LIU, H., SLACK, P.D., ZORIN, Y.A., MORDVINOVA, V.V., KOZHEVNIKOV, V.M., & MEYER, R.P. 1994. Seismic anisotropy and mantle flow beneath the Baikal rift–zone. *Nature*, **371**(6493), 149–151.

GAO, S.S., LIU, K.H., DAVIS, P.M., SLACK, P.D., ZORIN, Y.A., MORDVINOVA, V.V., & KOZHEVNIKOV, V.M. 2003. Evidence for small–scale mantle convection in the upper mantle beneath the Baikal rift zone. *J. Geophys. Res.*, **108**(4). 2194,doi:10.1029/2002JB002039.

GILBERT, H.J., & SHEEHAN, A.F. 2004. Images of crustal variations in the intermountain west. *J. Geophys. Res.*, **109**. B03306,doi:10.1029/2003JB002730.

GIRARDEAU, J., MARCOUX, J., ALLEGRE, C.J., BASSOULET, J.P., TANG, Y., XIAO, X., ZAO, Y., & WANG, X. 1984. Tectonic environment and geodynamic significance of the Neo–Cimmerian Dongqiao ophiolite, Banggong–Nujiang suture zone, Tibet. *Nature*, **307**, 27–31.

GOES, S., GOVERS, R., SCHWARTZ, S., & FURLONG, K. 1997. Three dimensional thermal modeling for the Mendocino Triple Junction area. *Earth Planet. Sci. Lett.*, **148**, 45–57.

GUZOFSKI, C. A., & FURLONG, K. P. 2002. Migration of the Mendocino triple junction and ephemeral crustal deformation; implications for California Coast Range heat flow. *Geophysical Research Letters*, **29**. doi:10.1029/2001GL013614.

HADLEY, D., & KANAMORI, H. 1977. Seismic structure of the Transverse Ranges, California. *Geological Society of America Bulletin*, **88**(10), 1469–1478.

HAMMOND, W.C., & THATCHER, W. 2004. Contemporary tectonic deformation of the Basin and Range province, western United States: 10 years of observation with the Global Positioning System. *J. Geophys. Res.*, **109**. B08403,doi:10.1029/2003JB002746.

HARRISON, T.M., COPELAND, P., KIDD, W.S.F., & YIN, A. 1992. Raising Tibet. *Science*, **255**(5052), 1663–1670.

HAXBY, W. F., & TURCOTTE, D. L. 1978. On isostatic geoid anomalies. *Journal of Geophysical Research, A, Space Physics*, **83**(B11), 5473–5478.

HEARN, E. H., & HUMPHREYS, E. D. 1998. Kinematics of the southern Walker Lane Belt and motion of the Sierra Nevada block, California. *Journal of Geophysical Research, B, Solid Earth and Planets*, **103**(11), 27,033–27,049.

HENDRIX, M.S., GRAHAM, S.A., CARROLL, A.R., SOBEL, E.R., MCKNIGHT, C.L., SCHULEIN, B.J., & Z., WANG. 1992. Sedimentary record and climatic implications of recurrent deformation in the Tien Shan; evidence from Mesozoic strata of the north Tarim, south Junggar, and Turpan basins, Northwest China. *Geol. Soc. Am. Bull.*, **104**(1), 53–79.

HENDRIX, M.S., DUMITRU, T.A., & GRAHAM, S.A. 1994. Late Oligocene–early Miocene unroofing in the Chinese Tien Shan; an early effect of the India–Asia collision. *Geology*, **22**(6), 487–490.

HERQUEL, G., WITTLINGER, G., & GUILBERT, J. 1995. Anisotropy and crustal thickness of northern Tibet: New constraints for tectonic modelling. *Geophys. Res. Let.*, **22**(14), 1925–1928.

HI, J., & BARAZANGI, M. 1983. High–frequency seismic–wave propogation beneath the Indian shield, Himalayan arc and Tibetan plateau: High uppermost mantle velocities and efficient Sn propogation beneath Tibet. *Geophys. J. R. Astron. Soc.*, **72**(3), 665–689.

HILL, D. P., EATON, J. P., ELLSWORTH, W. L., COCKERHAM, R. S., LESTER, F. W., & CORBETT, E. J. 1991. The seismotectonic fabric of Central California. *In: Neotectonics of North America.* Geol. Soc. Am.

HIRN, A., LEPINE, J.-C., JOBERT, G., SAPIN, M., WITTLINGER, G., XIN, X.Z., GAO, E.-Y., JING, W.X., WEN, T.J., BAI, X.S., PANDEY, M.R., & TATER, J.M. 1984. Crustal structure and variability of the Himalayan border of Tibet. *Nature*, **307**, 23–25.

HOLT, W. E., LI, MING, & HAINES, A. J. 1995. Earthquake strain rates and instantaneous relative motions within central and eastern Asia. *Geophys. J. Int.*, **122**, 569–593.

HOLT, W. E., CHAMOT-ROOKE, N., LE PICHON, X., HAINES, A. J., SHEN-TU, B., & REN, J. 2000. Velocity field in Asia inferred from Quaternary fault slip rates and Global Positioning System observations. *J. Geophys. Res.*, **105**, 19,185–19,209.

HOPPER, J.R., & BUCK, W.R. 1996. The effect of lower crustal flow on continental extension and passive margin formation. *J. Geophys. Res.*, **101**(9), 20,175–20,194.

HOUSEMAN, G., & ENGLAND, P. 1986. Finite strain calculations of continental deformation 1. Method and general results for convergent zones. *J. Geophys. Res.*, **91**, 3,651–3,663.

HOUSEMAN, G., & ENGLAND, P. 1993. Crustal Thickening versus Lateral Expulsion in the Indian–Asian Continental Collision. *J. Geophys. Res.*, **98**, 12,233–12,249.

HOUSEMAN, G., & ENGLAND, P. 1996. A lithospheric-thickening model for the India-Asia collision zone. *Pages 1–17 of:* YIN, A., & HARRISON, M. (eds), *The Tectonic Evolution of Asia.* New York: Cambridge University Press.

HOUSEMAN, G.A., & MOLNAR, P. 1997. Gravitational (Rayleigh–Taylor) instability of a layer with non–linear viscosity and convective thinning of continental lithosphere. *Geophys. J. Int.*, **128**(1), 125–150.

HOUSEMAN, G.A., M^{c}KENZIE, D.P., & MOLNAR, P. 1981. Convective instability of a thickened boundary layer and its relevance for the thermal evolution of continental convergent belts. *J. Geophys. Res.*, **86**(7), 6115–6132.

HUACK, M.L., NELSON, K.D., BROWN, L.D., ZHAO, W.J., & ROSS, A.R. 1998. Crustal structure of the Himalayan orogen at similar to 90 degrees east longitude from Project INDEPTH deep reflection profiles. *Tectonics*, **17**(4), 481–500.

HUEBNER, K.H. 1975. *The Finite Element Method for Engineers.* New York: Wiley.

HUFTILE, G.J., & YEATS, R.S. 1995. Convergence rates across a displacement transfer zone in the western Transverse Ranges, Ventura basin, California. *J. Geophys. Res.*, **100**(2), 2043–2067.

HUMPHREYS, E. D., & DUEKER, K. G. 1994. Physical state of the Western U.S. upper mantle. *Journal of Geophysical Research, B, Solid Earth and Planets*, **99**(5), 9635–9650.

JACKSON, J. 2002. Strength of the continental lithosphere; time to abandon the jelly sandwich? *GSA Today*, **12**(9), 4–10.

JACKSON, J., HAINES, A.J., & HOLT, W.E. 1995. The accommodation of Arabia-Eurasia plate convergence in Iran. *J. Geophys. Res.*, **100**, 15,205–15,220.

JADE, S., BHATT, B., BENDICK, R., GAUR, V., MOLNAR, P., ANAND, M., & KUMAR, D. 2004. GPS measurements from the Ladakh Himalaya, India: preliminary tests of plate-like or continuous deformation in Tibet. *J. Geophys. Res.*, **In Press**.

JEFFERY, G.B. 1922. The Motion of Ellipsoidal Particles Immersed in a Viscous Fluid. *Proc. R. Soc. Lond. A*, **102**, 161–179.

JIN, Y., MCNUTT, M.K., & ZHU, Y.S. 1994. Evidence from gravity and topography data for folding of Tibet. *Nature*, **371**(6499), 669–674.

JIN, Y., MCNUTT, M.K., & ZHU, Y.S. 1996. Mapping the descent of Indian and Eurasian plates beneath the Tibetan Plateau from gravity anomalies. *J. Geophys. Res.*, **101**(5), 11,275–11,290.

JONES, C.H., UNRUH, J.R., & SONDER, L.J. 1996. The role of gravitational potential energy in active deformation in the southwestern United States. *Nature*, **381**, 37–41.

JONES, D. L., COX, A., CONEY, P., & BECK, M. 1982. The growth of western North America. *Scientific American*, **247**(5), 70–84.

KING, G. C., OPPENHEIMER, D. H., & AMELUNG, F. 1994. Block versus continuum deformation in the Western United States. *Earth and Planetary Science Letters*, **128**(3-4), 55–64.

KING, R. W., SHEN, F., BURCHFIEL, B. C., ROYDEN, L. H., WANG, E., CHEN, Z., LIU, Y., ZHANG, X.-Z., & LI, Y. 1997. Geodetic measurement of crustal motion in southwest China. *Geology*, **25**, 179–182.

KOHLER, M. D., & DAVIS, P. M. 1997. Crustal thickness variations in Southern California from Los Angeles Region Seismic Experiment passive phase teleseismic travel times. *Bulletin of the Seismological Society of America*, **87**(5), 1330–1344.

KONG, X., YIN, A., & HARRISON, T.M. 1997. Evaluating the role of preexisting weaknesses and topographic distributions in the Indo–Asian collision by use of a thin–shell numerical model. *Geology*, **25**(6), 527–530.

LACHENBRUCH, A.H., & SASS, J.H. 1980. Heat flow and energetics of the San Andreas Fault zone. *jgr*, **85**, 6185–6222.

LAMB, S. H. 1987. A model for tectonic rotations about a vertical axis. *Earth and Planetary Science Letters*, **84**(1), 75–86.

LAMB, S.H. 1994. Behaviour of the brittle crust in wide plate boundary zones. *J. Geophys. Res.*, **99**, 4,457–4,483.

LARSON, K. M., BUERGMANN, R., BILHAM, R., & FREYMUELLER, J. T. 1999. Kinematics of the India-Eurasia collision zone from GPS measurements. *J. Geophys. Res.*, **104**, 1077–1093.

LARSON, K.M., FREYMUELLER, J., & PHILLIPSEN, S. 1997. Global plate velocities from the Global Positioning System. *J. Geophys. Res.*, **102**, 9,961–9,981.

LASKE, G., & MASTERS, G. 1997. A Global Digital Map of Sediment Thickness. *Eos Trans. AGU*, **78**(F483).

LEMOINE, F.G., KENYON, S.C., FACTOR, J.K., TRIMMER, R.G., PAVLIS, N.K., CHINN, D.S., COX, S.M., KLOSKO, S.M., LUTHCKE, S.B., TORRENCE, M.H., WANG, Y.M., WILLIAMSON, R.G., PAVLIS, E.C., RAPP, R.H., & OLSON, T.R. 1998. The development of the NASA GSFC and the NIMA Joint Geopotential Model. *Gravity, Geoid and Marine Geodesy*, **117**, 461–469.

LENARDIC, A., & KAULA, W.M. 1995. More thoughts on convergent crustal plateau formation and mantle dynamics in Tibet. *J. Geophys. Res.*, **100**(8), 15,193–15,203.

LEWIS, J.L., DAY, S.M., MAGISTRALE, H., CASTRO, R.R., ASTIZ, L., REBOLLAR, C., EAKINS, J., VERNON, F.L., & BRUNE, J.N. 2001. Crustal thickness of the peninsular ranges and gulf extensional province in the Californias. *J. Geophys. Res.*, **106**(7), 13,599–13,611.

LISOWSKI, M., SAVAGE, J.C., & PRESCOTT, W.H. 1991. The velocity field along the San Andreas fault in central and southern California. *J. Geophys. Res.*, **96**, 8,369–8,389.

LIU, M. 2001. Cenozoic extension and magmatism in the North American Cordillera; the role of gravitational collapse. *Tectonophysics*, **342**(3-4), 407–433.

LIU, M., & YANG, Y. 2003. Extensional collapse of the Tibetan Plateau: Results of the three-dimensional finite element modeling. *Journal of Geophysical Research, B, Solid Earth and Planets*, **108**(8). 2361,doi:10.1029/2002JB002248.

LIU, Q. 1993. *Paléoclimat et contraintes chronologiques sur les mouvements récent dans l'Ouest du Tibet: Failles du Karakorum et de Longmu Co-Gozha Co, lacs en pull-apart de Longmu Co et de Sumxi Co.* Ph.D. thesis, Thèse de Doctorat de l'Université Paris VII. 358pp.

LUYENDYK, B. P., KAMERLING, M. J., & TERRES, R. 1980. Geometric model for Neogene crustal rotations in southern California. *Geological Society of America Bulletin*, **91**(4), I 211–I 217.

LYON-CAEN, H., & MOLNAR, P. 1984. Gravity anomalies and the structure of western Tibet and the southern Tarim Basin. *Geophys. Res. Let.*, **11**, 1251–1254.

LYON-CAEN, H., & MOLNAR, P. 1985. Gravity anomalies, flexure of the Indian plate, and the structure, support and evolution of the Himalaya and Ganga Basin. *Tectonics*, **4**, 513–538.

LYSACK, S. 1992. Heat flow variations in continental rifts. *Tectonophysics*, **208**, 309–323.

MAGGI, A., JACKSON, J. A., MCKENZIE, D., & PRIESTLEY, K. 2000. Earthquake focal depths, effective elastic thickness, and the strength of the continental lithosphere. *Geology (Boulder)*, **28**(6), 495–498.

MALSERVISI, R., FURLONG, K. P., & DIXON, T. H. 2001. Influence of the earthquake cycle and lithospheric rheology on the dynamics of the eastern California shear zone. *Geophysical Research Letters*, **28**(14), 2731–2734.

MANABE, S., & BROCCOLI, A.J. 1990. Mountains and arid climates of middle latitudes. *Science*, **247**(4939), 192–194.

MCCLUSKY, S. C., BJORNSTAD, S. C., HAGER, B. H., KING, R. W., MEADE, B. J., MILLER, M. M., MONASTERO, F. C., & SOUTER, B. J. 2001. Present day kinematics of the eastern California shear zone from a geodetically constrained block model. *Geophysical Research Letters*, **28**(17), 3369–3372.

MᶜKENZIE, D. 1989. Some remarks on the movement of small melt fractions in the mantle. *Earth Planet. Sci. Lett.*, **95**(1–2), 53–72.

MEDVEDEV, S. E., & PODLADCHIKOV, Y. Y. 1999. New extended thin-sheet approximation for geodynamic applications; I, Model formulation. *Geophysical Journal International*, **136**(3), 567–585.

MEISSNER, R., & MOONEY, W. 1998. Weakness of the lower continental crust: a condition for delamination, uplift and escape. *Tectonophysics*, **296**(1–2), 47–60.

MERIAUX, A-S., TAPPONNIER, P., RYERSON, F., XIWEI, X., DER WOERD, J. VAN, KING, G., FINKEL, R., HAIBING, L., CAFFEE, M., & ZHIQIN, X. 2003. Post-glacial slip-rate on the Aksay Segment of the northern Altyn Tagh Fault, derived from cosmogenic radionuclide dating of morphological offset features. *Geophysical Research Abstracts*, **5**, 08062.

MILLER, M. M., JOHNSON, D. J., RUBIN, C.M., DRAGERT, H., WANG, K., QAMAR, A., & GOLDFINGER, C. 2001a. GPS–determination of along–strike variation in Cascadia margin kinematics: Implications for relative plate motion, subduction zone coupling, and permanent deformation. *Tectonics*, **20**(2), 161–176.

MILLER, M. M., JOHNSON, D. J., DIXON, T. H., & DOKKA, R. K. 2001b. Refined kinematics of the Eastern California shear zone from GPS observations, 1993-1998. *Journal of Geophysical Research, B, Solid Earth and Planets*, **106**(2), 2245–2263.

MINSTER, J. B., & JORDAN, T. H. 1987. Vector constraints on Western U.S. deformation from space geodesy, neotectonics, and plate motions. *Journal of Geophysical Research, B, Solid Earth and Planets*, **92**(6), 4798–4804.

MOLNAR, P. 1988a. Continental tectonics in the aftermath of plate tectonics. *Nature*, **335**, 131–137.

MOLNAR, P. 1988b. A review of geophysical constraints on the deep structure of the Tibetan Plateau, the Himalaya, and the Karakorum, and their tectonic implications. *Philos. Trans. R. Soc. London.*, **326**, 33–88.

MOLNAR, P. 1992. Crust in mantle overdrive. *Nature (London)*, **358**, 144–147.

MOLNAR, P., & DENG, Q. 1984. Faulting associated with large earthquakes and the average rate of deformation in central and eastern Asia. *J. Geophys. Res.*, **89**, 6203–6227.

MOLNAR, P., & GIPSON, J.M. 1996. A bound on the rheology of continental lithosphere using very long baseline interferometry: The velocity of south China with respect to Eurasia. *J. Geophys. Res.*, **101**(1), 545–553.

MOLNAR, P., & HOUSEMAN, G.A. 2004. The effects of buoyant crust on the gravitational instability of thickened mantle lithosphere at zones of intracontinental convergence. *Geophys. J. Int.*, **158**, 1134–1150.

MOLNAR, P., & JONES, C.H. 2004. A test of laboratory based rheological parameters of olivine from an analysis of late Cenozoic convective removal of mantle lithosphere beneath the Sierra Nevada, California, USA. *Geophys. J. Int.*, **156**, 555–564.

MOLNAR, P., & LYON-CAEN, H. 1989. Fault plane solutions of earthquakes and active tectonics of the Tibetan Plateau and its margins. *Geophys. J. Int.*, **99**, 123–153.

MOLNAR, P., & TAPPONNIER, P. 1975. Cenozoic tectonics of Asia: effects of a continental collision. *Science*, **189**, 419–426.

MOLNAR, P., & TAPPONNIER, P. 1978. Active Tectonics of Tibet. *J. Geophys. Res.*, **83**, 2648–2682.

MOLNAR, P., & TAPPONNIER, P. 1981. A possible dependence of tectonic strength on the age of the crust in Asia. *Earth Planet. Sci. Lett.*, **52**, 107–114.

MOLNAR, P., FITCH, T.J., & WU, F.T. 1973. Fault plane solutions of shallow earthquakes in Asia. *Earth Planet. Sci. Lett.*, **19**, 101–112.

MOLNAR, P., BURCHFIEL, B. C., ZHAO, Z., LIANG, K. U., WANG, S., & HUANG, M. 1987. Geologic evolution of northern Tibet; results of an expedition to Ulugh Muztagh. *Science*, **235**(4786), 299–305.

MOLNAR, P., ENGLAND, P., & MARTINOD, J. 1993. Mantle dynamics, Uplift of the Tibetan Plateau, and the Indian monsoon. *Reviews of Geophysics*, **31**, 357–396.

MOONEY, W.D., & COLEMAN, R.G. 1999. The crustal structure in northwest China. *Pages 182–189 of: 21st Seismic Research Symposium.*

MOONEY, W.D., & WEAVER, C.S. 1989. Regional crustal structure and tectonics of the Pacific coastal states; California, Oregon and Washington. *Pages 129–161 of:* PAKISER, L.C., & MOONEY, W.D. (eds), *Geophysical framework of the continental United States.* Boulder: Geological Society of America.

MORENCY, C., DOIN, M.P., & DUMOULIN, C. 2002. Convective destabilization of a thickened continental lithosphere. *Earth Planet. Sci. Lett.*, **202**(2), 303–320.

NEIL, E. A., & HOUSEMAN, G. A. 1997. Geodynamics of the Tarim Basin and the Tian Shan in Central Asia. *Tectonics*, **16**(4), 571–584.

NELSON, K. D., ZHAO, W., BROWN, L. D., KUO, J., CHE, J., LIU, X., KLEMPERER, S. L., MAKOVSKY, Y., MEISSNER, R., MECHIE, J., KIND, R., WENZEL, F., NI, J., NABELEK, J., CHEN, L., TAN, H., WEI, W., JONES, A. G., BOOKER, J., UNSWORTH, M., KIDD, W. S. F., HAUCK, M., ALSDORF, D., ROSS, A., COGAN, M., WU, C., SANDVOL, E. A., & EDWARDS, M. 1996. Partially molten middle crust beneath southern Tibet; synthesis of Project INDEPTH results. *Science*, **274**(5293), 1684–1688.

NORIN, E. 1946. Geological explorations in western Tibet. *In: Reports from the Scientific Expedition to the Northwestern Provinces under the leadership of Dr Sven Hedin.*

OPPENHEIMER, D.H., & EATON, J.P. 1984. Moho orientation beneath Central California from regional earthquake travel times. *J. Geophys. Res.*, **89**, 10,267–10,282.

OWENS, T.J., & ZANDT, G. 1997. Implications of crustal property variations for models of Tibetan plateau evolution. *Nature*, **387**(6628), 37–43.

PAUL, J., BÜRGMANN, R., GAUR, V.K., BILHAM, R., LARSON, K., ANANDA, M.B., JADE, S., MUKUL, M., ANUPAMA, T.S., SATYAL, G., & KUMAR, D. 2001. The motion and active deformation of India. *Geophys. Res. Let.*, **28**, 647–651.

PELTZER, G., & SAUCIER, F. 1996. Present-day kinematics of Asia derived from geologic fault rates. *J. Geophys. Res.*, 27,943–27,956.

PELTZER, G., & TAPPONNIER, P. 1988. Formation and evolution of strike-slip faults, rifts, and basins during the India-Asia collision: An experimental approach. *J. Geophys. Res.*, **93**, 15,085–15,117.

PELTZER, G., TAPPONNIER, P., & ARMIJO, R. 1989. Magnitude of Late Quaternary left-lateral displacements along the north edge of Tibet. *Science*, **246**, 1285–1289.

PETIT, C., DÉVERCHÈRE, J., HOUDRY, F., SANKOV, V., & MELNIKOVA, V. 1996. Present–day stress field changes along the Baikal rift and tectonic implications. *Tectonophysics*, **15**, 1171–1191.

PETIT, C., KOULAKOV, I., & DÉVERCHÈRE, J. 1998. Velocity structure around the Baikal rift zone from teleseismic and local earthquake traveltimes and geodynamic implications. *Tectonophysics*, **296**(1–2), 125–144.

POORT, J., & KLERKX, J. 2004. Absence of a regional surface thermal high in the Baikal rift; new insights from detailed contouring of heat flow anomalies. *Tectonophysics*, **383**(3–4), 217–241.

PRESS, W.H., TEUKOLSKY, S.A., VETTERLING, W.T., & FLANNERY, B.P. 1992. *Numerical Recipes: The Art of Scientific Computing.* Second edn. Cambridge: Cambridge University Press.

PYSKLYWEC, R.N., BEAUMONT, C., & FULLSACK, P. 2000. Modeling the behaviour of the continental mantle lithosphere during plate convergence. *Geology*, **28**(7), 655–658.

QUADE, J., CERLING, T.E., & BOWMAN, J.R. 1989. Development of Asian monsoon revealed by marked ecological shift during the latest Miocene in northern Pakistan. *Nature*, **342**(6246), 163–166.

RAPINE, R., TILMAN, F., WEST, M., NI, J., & RODGERS, A. 2003. Crustal structure of northern and southern Tibet from surface wave dispersion analysis. *J. Geophys. Res.*, **108**(2). 2120,doi:10.1029/2001JB000445.

RITZWOLLER, M.H., & LEVSHIN, A.L. 1998. Eurasian surface wave tomography: Group velocities. *J. Geophys. Res.*, **103**, 4839–4878.

RODGERS, A.T.J., & SCHWARTZ, S.Y. 1997. Low crustal velocities and mantle lithospheric variations in southern Tibet from regional Pn1 waveforms. *Geophys. Res. Lett.*, **24**(1), 9–12.

ROECKER, S.W., SABITOVA, T.M., VINNIK, L.P., BURMAKOV, Y.A., GOLVANOV, M.I., MAMATKANOVA, R., & MUNIROVA, L. 1993. 3–dimensional elastic–wave velocity structure of the western and central Tien–Shan. *J. Geophys. Res.*, **98**(9), 15,779–15,795.

ROYDEN, L. H. 1996. Coupling and decoupling of crust and mantle in convergent orogens: Implications for strain partitioning in the crust. *Journal of Geophysical Research, B, Solid Earth and Planets*, **101**(8), 17,679–17,705.

ROYDEN, L. H., BURCHFIEL, B. C., KING, R. W., WANG, E., CHEN, Z., SHEN, F., & LIU, Y. 1997. Surface Deformation and Lower Crustal flow in Eastern Tibet. *Science*, **276**.

SAVAGE, J. C. 2000. Viscoelastic-coupling model for the earthquake cycle driven from below. *Journal of Geophysical Research, B, Solid Earth and Planets*, **105**(11), 25,525–25,532.

SCHOTT, B., & SCHMELING, H. 1998. Delamination and detachment of a lithospheric root. *Tectonophysics*, **296**(3–4), 225–247.

SEARLE, M.P., WEINBERG, R. F., & DUNLAP, W. J. 1998. Transpressional tectonics along the Karakoram fault zone, northern Ladakh: constraints on Tibetan extrusion. *Pages 307–326 of:* HOLDSWORTH, R.E., STRACHAN, R.A>, & DEWEY, J. F. (eds), *Continental Transpressional and Transtensional Tectonics.* Geol. Soc. Spec. Pub., vol. 135.

SELLA, G. F., DIXON, T. H., & MAO, A. 2002. REVEL: A model for Recent plate velocities from space geodesy. *J. Geophys. Res.*, **107**, ETG 11–1–11–32.

SHEN, F., ROYDEN, L. H., & BURCHFIEL, B. C. 2001a. Large-scale crustal deformation of the Tibetan Plateau. *Journal of Geophysical Research, B, Solid Earth and Planets*, **106**(4), 6793–6816.

SHEN, Z.-K., ZHAO, C., YIN, A., LI, Y., JACKSON, D. D., FANG, P., & DONG, D. 2000. Contemporary crustal deformation in east Asia constrained by Global Positioning System measurements. *J. Geophys. Res.*, **105**, 5721–5734.

SHEN, Z. K., WANG, M., LI, Y., JACKSON, D. D., YIN, A., DONG, D., & FANG, P. 2001b. Crustal deformation along the Altyn Tagh Fault system, western China, from GPS. *J. Geophys. Res.*, **106**, 30,607–30,621.

SOBOUTI, F. 1994. *A numerical study of deformation of the Iranian Plateau.* Diploma thesis, McGill University, Montreal, Canada.

SOBOUTI, F., & ARKANI, H. J. 1996. Numerical modelling of the deformation of the Iranian Plateau. *Geophysical Journal International*, **126**(3), 805–818.

SONDER, L.J., & ENGLAND, P.C. 1986. Vertical Averages of Rheology of the Continental Lithosphere: Relation to Thin Sheet Parameters. *Earth Planet. Sci. Lett.*, **77**, 81–90.

SONDER, L.J., ENGLAND, P.C., & HOUSEMAN, G.A. 1986. Continuum Calculations of Continental Deformation in Transcurrent Environments. *J. Geophys. Res.*, **91**, 4,797–4,810.

SOOFI, M. A., & KING, S. D. 2002a. Oblique convergence between India and Eurasia. *Journal of Geophysical Research*, **107**(B5). 2101,doi:10.1029/2001JB000636.

SOOFI, M. A., & KING, S. D. 2002b. Post–rift deformation of the Midcontinent Rift under Grenville tectonism. *Tectonophysics*, **359**(3–4), 209–223.

SUN, J., & MURRELL, S. A. F. 1994. On the growth and collapse of wide orogenic belts. *Geophysical Journal International*, **118**(1), 255–268.

TAPPONNIER, P., & MOLNAR, P. 1976. Slip-line field theory and large-scale continental tectonics. *Nature*, **264**, 319.

TAPPONNIER, P., & MOLNAR, P. 1977. Active Faulting and Tectonics of China. *J. Geophys. Res.*, **82**, 2905–2928.

TAPPONNIER, P., & MOLNAR, P. 1979. Active Faulting and Cenozoic Tectonics of the Tien San, Mongolia, and Baykal regions. *J. Geophys. Res.*, **84**, 3425–3459.

TAPPONNIER, P., PELTZER, G., LE DAIN, A. Y., ARMIJO, R., & COBBOLD, P. 1982. Propagating extrusion tectonics in Asia: new insights from simple experiments with plasticene. *Geology*, **10**, 611–616.

TAPPONNIER, P., PELTZER, G., & ARMIJO, R. 1986. On the mechanics of the collision between India and Asia. *Pages 115–157 of:* COWARD, M.P., & RIES, A.C. (eds), *Collision Tectonics, Spec. Publ. 19.* Geological Society London, Special Publication No. 19.

THATCHER, W., FOULGER, G. R., JULIAN, B. R., SVARC, J. L., QUILTY, E., & BAWDEN, G. W. 1999. Present-day deformation across the Basin and Range Province, Western United States. *Science*, **283**(5408), 1714–1718.

THOMPSON, S.C., WELDON, R.J., RUBIN, C.M., ABDRAKHMATOV, K., MOLNAR, P., & BERGER, G.W. 2002. Late Quaternary slip rates across the central Tien Shan, Kyrgyzstan, central Asia. *J. Geophys. Res.*, **107**(9), 2203, doi:10.1029/2001JB000596.

TOWNSEND, D. A., & SONDER, L. J. 2001. Rheologic control of buoyancy-driven extension of the Rio Grande Rift. *Journal of Geophysical Research, B, Solid Earth and Planets*, **106**(8), 16,515–16,523.

TURNER, S., HAWKESWORTH, C., LIU, J.Q., ROGERS, N., KELLEY, S., & VANCALSTEREN, P. 1993. Timing of Tibetan uplift constrained by analysis of volcanic–rocks. *Nature*, **364**(6432), 50–54.

USGS, EARTHQUAKE HAZARDS PROGRAM. 2004.

VIGNY, C., SOCQUET, A., RANGIN, C., CHAMOT-ROOKE, N., PUBELLIER, M., BOUIN, M.N., BERTRAND, G., & BECKER, M. 2003. Present–day crustal deformation around Sagaing fault, Myanmar. *J. Geophys. Res.*, **108**(B11), 2533, doi:10.1029/2002JB001999.

VILLASENOR, A., RITZWOLLER, M. H., LEVSHIN, A. L., BARMIN, M. P., ENGDAHL, E. R., SPAKMAN, W., & TRAMPERT, J. 2001. Shear velocity structure of central Eurasia from inversion of surface wave velocities. *Physics of the Earth and Planetary Interiors*, **123; 2-4**, 169–184.

VILOTTE, J.P., DAIGNIÈRES, M., & MADARIAGA, R. 1982. Numerical modeling of intraplate deformation: Simple mechanical models of continental collision. *J. Geophys. Res.*, **87**, 10709–10728.

VILOTTE, J.P., DAIGNIÈRES, M., MADARIAGA, R., & ZIENKIEWICZ, O. 1984. The role of a heterogeneous inclusion during continental collision. *Physics of the Earth and Planetary Interiors*, **36**, 236–259.

VILOTTE, J.P., MADARIAGA, R., DAIGNIÈRES, M., & ZIENKIEWICZ, O. 1986. Numerical studies of continental collision: Influence of buoyancy forces and a stiff inclusion. *Geophys. J. R. Astron. Soc.*, **84**, 279–310.

WANG, K., & JIANGHENG, H. 1999. Mechanics of low–stress forearcs, Nankai and Cascadia. *J. Geophys. Res.*, **7**, 15,191–15,205.

WANG, Q., ZHANG, P., FREYMUELLER, J. T., BILHAM, R., LARSON, K. M., LAI, X., YOU, X., NIU, Z., WU, J., LI, Y., LIU, J., YANG, Z., & CHEN, Q. 2001. Present-day crustal deformation in China constrained by Global Positioning System measurements. *Science*, **294**(5542), 574–577.

WANG, Y. 2001. Heat flow pattern and lateral variations of lithosphere strength in China mainland: constraints on active deformation. *Physics of the Earth and Planetary Interiors*, **126**(3–4), 121–146.

WANG, Y.X., MOONEY, W.D., YUAN, X.C., & COLEMAN, R.G. 2003. The crustal structure from the Altai mountains to the Altyn Tagh fault, northwest China. *J. Geophys. Res.*, **108**(6), 2322, doi:10.1029/2001JB000552.

WDOWINSKI, S., & BOCK, Y. 1994. The evolution of deformation and topography of high elevated plateaus 1. Model, numerical analysis, and general results. *J. Geophys. Res.*, **99**, 7,103–7,119.

WERNICKE, B., & SNOW, J. K. 1998. Cenozoic tectonism in the central Basin and Range; motion of the Sierran-Great Valley Block. *International Geology Review*, **40**(5), 403–410.

WESSEL, P., & SMITH, W. H. F. 1998. New, improved version of Generic Mapping Tools released. *Eos Trans. AGU*, **79**, 579.

WHITEHOUSE, P.L., ENGLAND, P.C., & HOUSEMAN, G.A. 2004. A physical model for the motion of the Sierra block. *Earth Planet. Sci. Lett.*.

WILLETT, S.D., & BEAUMONT, C. 1994. Subduction of Asian lithopsheric mantle beneath Tibet inferred from models of continental collision. *Nature*, **369**, 642–645.

WONG, I. G., ELY, R. W., & KOLLMANN, A. C. 1988. Contemporary seismicity and tectonics of the northern and central Coast Ranges-Sierran Block boundary zone, California. *Journal of Geophysical Research, B, Solid Earth and Planets*, **93**(7), 7813–7833.

WRIGHT, T. J., PARSONS, B., ENGLAND, P.C., & FIELDING, E.J. 2004. InSAR observations of low slip rates on the major faults of western Tibet. *Science*, **305**(5681), 236–239.

YANEZ, G., & CEMBRANO, J. 2004. Role of viscous plate coupling in the late Tertiary Andean tectonics. *J. Geophys. Res.*, **109**(2).

YIN, A., HARRISON, T. M., MURPHY, M. A., GROVE, M., NIE, S., RYERSON, F. J., WANG, X., & CHEN, Z. 1999. Tertiary deformation history of southeastern and southwestern Tibet during the Indo-Asian collision. *Geol. Soc. Am. Bull.*, **111**, 1644–1664.

ZHANG, K.J., ZHANG, Y.J., & XIA, B.D. 1998. Did the Indo–Asian collision alone create the Tibetan plateau?: Comment. *Geology*, **10**, 958–959.

ZHANG, P.-Z., SHEN, Z., WANG, M., GAN, W., BÜRGMANN, R., MOLNAR, P., WANG, Q., NIU, Z., SUN, J., WU, J., & HANRONG, S. XINZHAO, Y. 2004. Continuous deformation of the Tibetan Plateau from global positioning system data. *Geology*, **32**(9), 809–812.

ZHANG, Z.M., LIOU, J.G., & COLEMAN, R.G. 1984. An outline of the plate–tectonics of China. *Geol. Soc. Am. Bull.*, **95**(3), 295–312.

ZHAO, D., KANAMORI, H., & HUMPHREYS, E. 1996. Simultaneous inversion of local and teleseismic data for the crust and mantle structure of Southern California. *Physics of the Earth and Planetary Interiors*, **93**(3-4), 191–214.

ZHAO, W., MECHIE, J., BROWN, L. D., GUO, J., HAINES, S., HEARN, T., KLEMPERER, S. L., MA, Y. S., MEISSNER, R., NELSON, K. D., NI, J. F., PANANONT, P., RAPINE, R., ROSS, A., & SAUL, J. 2001. Crustal structure of central Tibet as derived from project INDEPTH wide-angle seismic data. *Geophysical Journal International*, **145**(2), 486–498.

ZHAO, W.L., & MORGAN, W.J. 1985. Uplift of the Tibetan Plateau. *Tectonics*, **4**(4), 359–369.

ZHAO, W.L., & MORGAN, W.J. 1987. Injection of Indian crust into Tibetan lower crust. *Tectonics*, **6**(4), 489–504.

ZHOU, R., GRAND, S.P., TAJIMA, F., & DING, X.Y. 1996. High velocity zone beneath the southern Tibetan plateau from P–wave differential travel–time data. *Geophys. Res. Let.*, **23**(1), 25–28.

ZHU, L., & HELMBERGER, D V. 1998. Moho offset across the northern margin of the Tibetan Plateau. *Science*, **281**(5380), 1170–1172.

ZIENKIEWICZ, O.C., & TAYLOR, R.L. 1989. *The Finite Element Method.* Fourth edn. Vol. 1. Maidenhead UK: McGraw-Hill.

ZOBACK, M.D., TOWNEND, J., & GROLLIMUND, B. 2002. Steady–state failure equilibrium and deformation of intraplate lithosphere. *International Geology Review*, **44**(5), 383–401.

Appendix A

GPS data for south–east Asia

Table A.1: Mesh information for the velocity field of south–east Asia: Campaign data from Bendick *et al.* (2000); Calais *et al.* (2003); Chen *et al.* (2000); Shen *et al.* (2000, 2001b); Sella *et al.* (2002); Vigny *et al.* (2003); Wang *et al.* (2001); Zhang *et al.* (2004)

Longitude	Latitude	V_{east}	V_{north}	$Error_{east}$	$Error_{north}$	Correlation
°E	°N	mm/yr	mm/yr	mm/yr	mm/yr	
129.68	62.03	0.0000	0.0000	0.0000	0.0000	0.0000
100.00	62.00	0.1022	-1.9148	0.7313	0.7376	-0.2140
80.00	62.00	0.0000	0.0000	0.0000	0.0000	0.0000
66.00	50.00	0.6511	-0.3897	1.0862	1.1587	-0.2691
110.00	56.00	0.1180	-1.9929	0.6938	0.6825	-0.2599
102.00	53.00	-0.3544	-1.3013	0.6556	0.5449	-0.4979
91.00	54.00	-0.2478	-0.9138	0.6839	0.5933	-0.3125
82.00	50.00	0.3872	-0.6588	0.9416	0.6435	-0.3793
114.00	53.00	2.8866	-2.5936	0.7902	0.6264	-0.4311
105.00	49.00	3.6250	-3.3955	0.8427	0.5653	-0.4438
97.00	50.50	-1.3752	-1.5306	0.8970	0.6913	-0.3488
93.00	48.00	0.8502	0.2426	0.9794	0.8362	-0.4085
98.00	43.00	4.6081	-0.2975	0.9517	0.6188	-0.4816
98.00	46.50	4.0473	-3.4371	0.9643	0.7071	-0.3504
93.00	44.50	3.4716	3.6929	1.0066	1.0056	-0.3187
89.00	49.50	2.2447	2.2933	1.0491	0.7370	-0.3877
88.00	46.50	4.0553	6.3137	1.0600	0.6788	-0.4854

continued on next page

Table A.1: *continued*

Longitude °E	Latitude °N	V_{east} mm/yr	V_{north} mm/yr	$Error_{east}$ mm/yr	$Error_{north}$ mm/yr	Correlation
78.00	46.00	1.2321	-0.2344	1.0058	0.7195	-0.5519
66.00	44.00	1.5064	0.1647	1.2522	1.1337	-0.5386
73.00	41.50	-2.7446	5.8988	1.2290	0.9067	-0.6136
77.50	43.50	1.9342	-0.1027	1.0593	0.7428	-0.5966
85.00	44.00	2.1355	7.8538	0.9816	0.7444	-0.5477
66.00	40.00	1.1224	-5.8397	1.4771	1.2394	-0.5455
75.50	39.50	0.9248	16.2556	1.1772	0.8693	-0.5718
82.00	41.50	3.0839	12.1191	1.0834	0.7535	-0.5743
89.00	42.50	4.6612	6.9035	1.0278	0.7059	-0.5352
82.00	39.50	1.3447	12.3147	1.1211	0.7505	-0.6029
77.50	37.50	-0.9752	15.7595	1.2309	0.8132	-0.6326
82.00	37.00	-0.9931	12.4262	1.2234	0.7604	-0.5757
87.00	39.00	1.0971	8.3848	1.1139	0.7052	-0.5668
87.00	40.50	2.6028	8.4211	1.0650	0.7004	-0.5787
92.00	40.50	2.8204	4.4581	1.0466	0.6705	-0.5446
98.00	40.50	3.3617	-0.2093	1.0097	0.6125	-0.5264
105.00	45.00	4.3275	-2.3799	0.8908	0.5557	-0.4457
105.00	42.00	4.0060	-2.4038	0.9515	0.5660	-0.4375
126.00	50.00	3.1601	-1.1562	0.8812	0.7801	-0.1759
115.00	48.00	3.3790	-2.5287	0.8049	0.5480	-0.4538
114.00	43.00	4.0652	-2.5851	0.9639	0.6202	-0.3115
126.00	42.00	4.4790	-1.1705	1.0914	0.8654	0.0032
66.00	36.50	-2.3653	13.1125	2.6846	2.4208	-0.3177
75.50	36.50	-1.4513	22.0768	1.4174	1.0282	-0.4644
79.50	35.00	0.6238	16.7361	1.4370	0.9708	-0.4540
90.00	35.00	14.3378	12.3364	1.5743	1.0406	-0.2729
85.00	36.00	8.1848	13.6963	1.5869	1.1234	-0.2416
90.00	37.50	8.5055	11.1925	1.3756	0.9425	-0.2076
94.00	38.50	8.0452	6.3484	1.2782	0.8614	-0.2994
92.50	36.50	9.7427	8.7902	1.3658	0.8677	-0.3498
98.00	36.50	9.3931	4.2687	1.3541	0.8203	-0.3201

continued on next page

Table A.1: *continued*

Longitude °E	Latitude °N	V_{east} mm/yr	V_{north} mm/yr	$Error_{east}$ mm/yr	$Error_{north}$ mm/yr	Correlation
94.50	35.00	19.0700	5.9757	1.4652	0.8955	-0.2988
102.50	35.00	10.6892	1.1193	1.4838	0.9619	-0.1818
99.00	32.50	20.4213	-0.9270	1.5158	0.9235	-0.1709
103.50	32.00	8.6808	-6.3897	1.6169	1.0662	-0.0961
102.00	39.00	2.8871	-1.5270	1.0730	0.5921	-0.4496
105.50	38.00	2.6019	-2.9756	1.1622	0.6714	-0.1986
108.00	35.00	7.0488	-5.9199	1.1474	0.5581	-0.2902
110.00	39.00	4.4608	-5.2221	1.3506	0.9302	-0.0633
116.00	39.00	5.8451	-4.3221	1.0719	0.5534	-0.1454
118.00	35.00	6.0739	-5.1072	1.1856	0.6746	-0.0094
111.50	31.50	6.9818	-5.2484	1.2727	0.6320	-0.1927
106.50	30.00	6.3584	-5.0845	1.3780	0.7760	-0.2247
81.00	33.30	5.3277	16.5908	1.5844	0.9954	-0.3910
88.50	32.50	16.7832	15.7757	1.5158	0.8815	-0.3692
94.50	32.00	21.8723	7.9625	1.4185	0.8299	-0.3891
101.00	29.00	10.1676	-14.9178	1.6929	0.9466	-0.1492
77.50	33.50	-1.2379	20.8061	1.4747	1.0858	-0.4554
79.00	32.00	0.4867	19.6600	1.6361	1.0466	-0.3761
82.50	30.00	4.6411	22.1191	1.5452	0.8820	-0.4685
85.00	31.00	9.4479	20.9397	1.6574	0.9835	-0.3956
89.50	28.50	15.4948	21.0986	1.4901	0.9307	-0.4905
90.50	30.50	19.6033	17.5989	1.3878	0.7694	-0.4765
95.71	29.01	17.3191	2.5971	1.6300	1.1736	-0.1548
108.00	25.00	5.8152	-4.8795	1.4930	0.6852	-0.2502
103.00	25.00	5.5073	-13.8887	1.4579	0.5870	-0.4018
98.00	25.00	-2.5117	-7.2180	1.7324	1.0226	-0.0840
108.00	20.00	10.4227	-4.4878	1.7099	0.7164	-0.1792
118.00	22.00	6.7169	-3.9610	1.6997	0.9014	0.0914
121.21	31.00	6.7079	-4.9898	1.2807	0.6793	0.1234
73.00	33.00	7.3984	39.0893	2.4211	2.2472	0.0033
76.50	30.50	12.9058	37.6652	2.2096	1.3898	-0.0258

continued on next page

Table A.1: *continued*

Longitude °E	Latitude °N	V_{east} mm/yr	V_{north} mm/yr	$Error_{east}$ mm/yr	$Error_{north}$ mm/yr	Correlation
84.00	27.00	12.0900	36.2673	1.6046	1.1003	-0.3962
93.00	26.00	13.3065	30.5736	1.9292	1.8782	-0.1320
90.00	22.00	9.9074	33.8960	2.1621	1.3153	0.0263
93.00	20.00	3.5430	25.7378	2.0596	1.0927	0.0173
100.00	20.00	9.1677	1.1404	1.9533	1.1257	-0.2404
101.00	12.00	0.6942	0.9802	2.5913	1.2891	-0.3999
112.00	12.00	0.7545	-8.4857	2.7108	1.5814	0.3884
90.00	26.80	13.1235	33.7291	1.6120	1.2395	-0.3201
92.50	28.20	17.5447	14.8402	1.5969	1.0581	-0.3110

Table A.2: Mesh information for the velocity field of south–east Asia: IGS data (source: http://igscb.jpl.nasa.gov/)

Longitude °E	Latitude °N	V_{east} mm/yr	V_{north} mm/yr	$Error_{east}$ mm/yr	$Error_{north}$ mm/yr	Correlation
129.68	62.03	0.0000	0.0000	0.0000	0.0000	0.0000
100.00	62.00	-0.3060	0.0082	0.7973	0.9066	0.0443
80.00	62.00	0.0000	0.0000	0.0000	0.0000	0.0000
66.00	50.00	0.3313	0.8503	1.4890	1.3697	-0.1479
110.00	56.00	-0.4090	0.0916	0.9321	0.8458	0.1861
102.00	53.00	-0.5362	0.1396	1.0159	0.8101	0.2463
91.00	54.00	-0.2210	-0.1202	0.9760	0.6839	0.0872
82.00	50.00	0.3300	1.0283	1.3694	0.7977	-0.1818
114.00	53.00	2.5897	-0.9025	1.2307	1.0229	0.3316
105.00	49.00	3.2172	-0.6655	1.2396	0.9112	0.4490
97.00	50.50	0.8305	0.7341	1.8055	1.4996	0.0223
93.00	48.00	3.3647	2.6831	1.8329	1.5146	-0.0051
98.00	43.00	4.4390	3.7428	1.5130	0.9723	0.1972
98.00	46.50	3.4877	1.3485	1.9403	1.5176	0.0756
93.00	44.50	3.5963	6.8288	1.4594	1.2399	0.0681
89.00	49.50	2.3869	3.9753	1.7903	1.3423	-0.0406

continued on next page

Table A.2: *continued*

Longitude °E	Latitude °N	V_{east} mm/yr	V_{north} mm/yr	$Error_{east}$ mm/yr	$Error_{north}$ mm/yr	Correlation
88.00	46.50	3.5209	8.2566	1.4947	0.7798	0.0018
78.00	46.00	1.0823	1.5898	1.4416	0.8085	-0.3102
66.00	44.00	1.1562	0.6957	1.6546	1.4020	-0.3948
73.00	41.50	-1.3668	6.0577	1.6617	1.1532	-0.3807
77.50	43.50	1.7695	1.7632	1.4680	0.7996	-0.3667
85.00	44.00	2.4966	9.1459	1.4393	0.9282	-0.0877
66.00	40.00	0.2278	-3.1412	1.9360	1.6902	-0.4081
75.50	39.50	-0.7523	16.7130	1.7709	1.4608	-0.2822
82.00	41.50	1.4739	14.4766	1.6297	1.0858	-0.1607
89.00	42.50	3.3994	10.8215	1.5570	0.9404	-0.0180
82.00	39.50	0.3424	14.4499	1.7213	1.0815	-0.2116
77.50	37.50	-1.2986	16.0147	1.8934	1.3014	-0.3565
82.00	37.00	-0.8641	14.4537	1.9104	1.0908	-0.2400
87.00	39.00	0.6171	11.9377	1.7413	0.9515	-0.0829
87.00	40.50	1.6364	11.9355	1.6487	0.9453	-0.0779
92.00	40.50	2.0444	8.5783	1.6430	0.9174	0.0485
98.00	40.50	2.5724	3.7839	1.6411	0.9628	0.1780
105.00	45.00	4.2981	-0.3435	1.4170	0.9172	0.3961
105.00	42.00	3.6832	-0.2537	1.5740	0.9336	0.3933
126.00	50.00	2.9979	-0.4922	1.4379	1.1255	0.3999
115.00	48.00	3.3338	-0.8183	1.3348	1.0125	0.4550
114.00	43.00	3.7851	-0.8525	1.5799	1.0321	0.4860
126.00	42.00	3.5582	-0.9177	1.8379	1.3074	0.5119
66.00	36.50	0.8598	11.3442	3.2181	3.8356	-0.2564
75.50	36.50	0.9973	17.6981	2.2646	1.7765	-0.2193
79.50	35.00	4.1151	16.9797	2.3690	1.5125	-0.1870
90.00	35.00	14.9261	17.9946	2.3173	1.3049	0.0250
85.00	36.00	9.4490	16.7424	2.2381	1.3466	-0.0516
90.00	37.50	9.6040	18.5986	2.1562	1.3846	0.0273
94.00	38.50	10.8087	14.2431	2.1309	1.4054	0.0830
92.50	36.50	10.8628	16.9132	2.2258	1.3214	0.0632

continued on next page

Table A.2: *continued*

Longitude °E	Latitude °N	V_{east} mm/yr	V_{north} mm/yr	$Error_{east}$ mm/yr	$Error_{north}$ mm/yr	Correlation
98.00	36.50	11.6909	12.5089	2.3135	1.6107	0.1207
94.50	35.00	17.9522	15.4577	2.3841	1.4044	0.0947
102.50	35.00	11.2007	1.1933	2.3770	1.5788	0.1874
99.00	32.50	18.0375	5.3625	2.5140	1.7280	0.1291
103.50	32.00	9.4946	-4.4638	2.4774	1.5696	0.2438
102.00	39.00	1.7416	1.3862	1.7620	0.9277	0.3147
105.50	38.00	1.2409	-0.5469	1.8858	1.0301	0.4508
108.00	35.00	6.9162	-3.8669	1.9690	0.9745	0.5879
110.00	39.00	3.1705	-2.4163	2.1442	1.5569	0.2904
116.00	39.00	5.2745	-1.4435	1.8170	1.1467	0.6652
118.00	35.00	5.8262	-3.7912	2.0204	1.1569	0.6781
111.50	31.50	6.5833	-4.9387	2.1470	0.9901	0.6662
106.50	30.00	6.1074	-5.9646	2.2424	1.0780	0.4704
81.00	33.30	9.3323	17.4613	2.5624	1.6042	-0.1075
88.50	32.50	16.6290	17.8563	2.4426	1.2233	0.0149
94.50	32.00	19.7678	14.7243	2.4862	1.4610	0.0511
101.00	29.00	7.6716	-8.4382	2.7151	1.6044	0.1856
77.50	33.50	4.0695	20.1712	2.5669	1.8198	-0.1600
79.00	32.00	5.6769	20.5510	2.6765	1.7369	-0.1371
82.50	30.00	8.2934	19.9197	2.7470	1.7943	-0.0535
85.00	31.00	12.3793	18.9283	2.5712	1.4542	-0.0348
89.50	28.50	17.2410	17.8234	2.4858	1.2491	-0.0480
90.50	30.50	18.5738	17.8526	2.2062	0.8303	0.0680
95.71	29.01	17.1958	14.2258	2.5628	1.7309	0.1012
108.00	25.00	5.7549	-6.0296	2.4965	1.0461	0.5079
103.00	25.00	5.0664	-11.4598	2.4516	0.8103	0.5172
98.00	25.00	2.4477	-4.4686	2.9869	2.2064	0.0775
108.00	20.00	9.2869	-6.1188	2.8560	1.1057	0.4876
118.00	22.00	6.5902	-3.9101	2.7852	1.3278	0.6547
121.21	31.00	6.9974	-3.2191	2.2312	1.2111	0.7548
73.00	33.00	11.0908	27.9408	3.3124	3.3159	-0.0023

continued on next page

Table A.2: *continued*

Longitude °E	Latitude °N	V_{east} mm/yr	V_{north} mm/yr	$Error_{east}$ mm/yr	$Error_{north}$ mm/yr	Correlation
76.50	30.50	17.2748	33.6227	3.6846	3.0511	0.1641
84.00	27.00	15.4839	39.5373	2.7700	2.9063	-0.0214
93.00	26.00	17.3057	34.1918	2.9259	2.5583	0.0596
90.00	22.00	12.2029	33.9933	3.5778	2.1960	0.0742
93.00	20.00	9.3308	30.5236	4.1020	3.1311	0.1293
100.00	20.00	10.0567	-8.7757	3.7206	2.5263	0.0118
101.00	12.00	10.7179	-6.9544	5.8602	3.9253	-0.6813
112.00	12.00	10.4360	-5.6776	5.8776	2.9026	0.8007
90.00	26.80	16.7889	33.8353	2.7261	2.1461	-0.0394
92.50	28.20	18.6194	19.0830	2.4580	1.1929	0.0994

Appendix B

GPS data for the western United States

Table B.1: GPS data from JPL Time Series analysis (source: http://sideshow.jpl.nasa.gov/mbh/series.html)

Longitude	Latitude	V_{east}	V_{north}	$Error_{east}$	$Error_{north}$	Station Name
°E	°N	mm/yr	mm/yr	mm/yr	mm/yr	
-116.429378	34.594282	-8.42	13.50	0.23	0.13	AGMT
-118.694798	34.824490	-16.71	19.61	0.86	0.47	ALPP
-118.830315	34.157443	-28.27	31.32	0.05	0.02	AOA1
-117.153971	34.468301	-12.59	15.03	0.20	0.11	AVRY
-116.629696	33.540072	-19.51	26.16	0.20	0.11	AZRY
-117.896485	34.126018	-26.48	24.95	0.16	0.08	AZU1
-119.981511	34.582197	-29.68	31.60	0.36	0.20	BBDM
-116.884241	34.264278	-12.21	19.54	0.21	0.12	BBRY
-118.074091	35.878388	-7.51	13.68	0.58	0.32	BEPK
-118.159695	33.967117	-27.29	31.24	0.44	0.25	BGIS
-117.064598	33.578242	-23.70	28.47	0.34	0.19	BILL
-116.080424	35.287048	-3.36	1.83	0.45	0.25	BKAP
-118.094696	33.962257	-28.90	33.02	0.19	0.11	BKMS
-114.714850	33.610415	-1.92	3.27	0.10	0.05	BLYT
-116.052977	34.251445	1.03	6.82	0.24	0.14	BMHL
-116.984701	33.962682	-15.10	23.53	0.19	0.11	BMRY

continued on next page

Table B.1: *continued*

Longitude °E	Latitude °N	V_{east} mm/yr	V_{north} mm/yr	$Error_{east}$ mm/yr	$Error_{north}$ mm/yr	Station Name
-118.277048	34.184894	-25.10	26.10	0.11	0.05	BRAN
-122.152552	37.919404	-13.96	15.18	0.10	0.05	BRIB
-118.576805	34.682283	-20.09	20.82	0.42	0.23	BRPK
-117.011992	34.918612	-10.56	10.87	0.20	0.12	BSRY
-118.188224	34.292805	-24.65	25.79	0.71	0.40	BTDM
-117.843529	42.779502	-5.37	2.14	0.22	0.13	BURN
-124.563345	42.836099	4.10	11.96	0.22	0.13	CABL
-115.989948	33.655135	-8.68	12.95	0.65	0.35	CACT
-120.433696	35.939353	-11.95	19.64	0.43	0.24	CAND
-120.430819	35.888383	-24.49	30.21	0.83	0.47	CARH
-118.896663	37.644636	-11.99	7.98	0.15	0.09	CASA
-110.677313	39.191022	-5.58	5.60	0.20	0.11	CAST
-118.483006	33.445771	-28.54	34.12	0.05	0.03	CAT1
-118.333814	33.311615	-27.95	33.88	0.47	0.26	CAT2
-118.629803	34.138560	-28.03	30.91	0.16	0.09	CBHS
-117.671171	35.565312	-7.98	13.25	0.58	0.32	CCCC
-118.211195	33.876259	-25.32	31.88	0.15	0.09	CCCO
-117.864940	33.862742	-26.22	30.16	0.14	0.08	CCCS
-116.335930	34.829468	-7.52	4.42	0.57	0.30	CDMT
-112.860481	40.680696	-4.74	3.85	0.20	0.11	CEDA
-117.964944	34.243992	-20.24	19.99	1.51	0.86	CGDM
-122.119309	37.724115	-16.29	18.23	0.08	0.04	CHAB
-118.025997	34.333422	-22.89	22.27	0.10	0.05	CHIL
-117.827700	34.640462	-14.99	18.32	0.20	0.12	CHMS
-121.664962	39.432639	-11.61	7.25	0.21	0.13	CHO1
-116.665760	31.870678	-28.51	34.23	0.19	0.10	CIC1
-116.667382	31.871264	-27.31	30.74	0.14	0.07	CICE
-118.937293	34.109552	-28.55	31.06	0.39	0.21	CIRX
-118.127283	34.136708	-23.56	24.48	0.08	0.04	CIT1
-117.479382	34.313799	-18.11	20.18	0.34	0.19	CJMS
-117.708808	34.109928	-23.74	24.98	0.19	0.10	CLAR

continued on next page

Table B.1: *continued*

Longitude °E	Latitude °N	V_{east} mm/yr	V_{north} mm/yr	$Error_{east}$ mm/yr	$Error_{north}$ mm/yr	Station Name
-120.386039	38.034176	-8.87	9.45	0.19	0.09	CMBB
-124.396334	40.441773	-9.16	29.56	0.11	0.07	CME1
-118.411423	34.353179	-24.14	23.89	0.11	0.06	CMP9
-121.278495	37.896405	-12.67	8.75	0.29	0.17	CNDR
-117.608918	33.857631	-22.88	28.64	0.54	0.30	CNPP
-112.121011	40.652592	-4.97	3.88	0.30	0.19	COON
-119.879523	34.414906	-29.65	29.36	0.87	0.48	COPR
-123.304604	44.585535	2.15	5.84	0.27	0.18	CORV
-117.248181	32.415372	-29.36	33.41	0.48	0.28	CORX
-111.882160	33.568721	0.62	6.36	0.42	0.24	COSA
-117.808889	35.982343	-5.19	16.97	0.09	0.04	COSO
-116.386888	33.732486	-14.63	22.25	0.27	0.16	COTD
-117.573022	35.071734	-8.22	14.73	0.48	0.26	CPBN
-120.750751	35.791611	-23.51	31.54	1.29	0.72	CRBT
-117.099681	34.039051	-16.19	20.61	0.10	0.05	CRFP
-118.272764	33.823503	-26.28	30.93	0.19	0.11	CRHS
-115.735040	33.069807	-13.26	21.17	0.20	0.11	CRRS
-119.784809	34.029259	-28.52	35.19	0.29	0.17	CRU1
-119.038978	34.168402	-29.07	30.91	0.43	0.24	CSCI
-118.256715	33.861477	-28.64	30.76	0.11	0.06	CSDH
-118.523810	34.253549	-27.30	27.44	0.07	0.03	CSN1
-119.371247	34.408089	-28.32	26.93	0.43	0.24	CSST
-118.613209	34.516549	-24.55	23.65	0.79	0.44	CTDM
-116.370425	34.124101	-3.48	16.97	0.20	0.11	CTMS
-119.673946	34.942646	-28.05	26.01	0.30	0.18	CUHS
-117.901715	34.082010	-26.72	26.01	0.20	0.11	CVHS
-118.397360	34.333995	-26.09	22.99	0.14	0.07	DAM1
-118.396862	34.334835	-26.12	24.61	0.15	0.08	DAM2
-115.788027	33.389806	-11.17	11.01	0.13	0.07	DHLG
-118.348540	34.023931	-24.96	30.43	0.16	0.09	DSHS
-116.712088	33.733331	-15.80	24.87	0.21	0.11	DSSC

continued on next page

Table B.1: *continued*

Longitude °E	Latitude °N	V_{east} mm/yr	V_{north} mm/yr	$Error_{east}$ mm/yr	$Error_{north}$ mm/yr	Station Name
-117.860126	34.413412	-20.61	22.26	0.29	0.17	DVPB
-118.039336	37.742804	-6.34	4.40	0.49	0.26	DYER
-118.125980	33.937988	-30.97	28.55	0.12	0.07	DYHS
-118.329024	33.886752	-27.01	31.63	0.17	0.10	ECCO
-117.411692	33.647683	-25.62	29.58	0.88	0.48	ECFS
-114.264247	37.915534	-4.12	2.70	0.48	0.26	ECHO
-118.830407	34.946194	-16.23	16.60	1.01	0.62	EDPP
-114.938854	39.345244	0.01	3.10	0.23	0.13	EGAN
-115.817197	40.914691	-6.58	3.31	0.20	0.12	ELKO
-118.208431	34.029733	-27.07	25.42	0.18	0.10	ELSC
-116.991006	33.672830	-21.15	29.10	0.50	0.28	ESRE
-117.066950	33.681779	-22.68	26.81	0.42	0.24	ESRW
-117.525583	34.104198	-22.62	25.14	0.21	0.12	EWPP
-123.000766	37.697207	-27.54	35.59	0.21	0.10	FARB
-120.009379	34.733008	-30.06	30.93	0.38	0.21	FGST
-118.609702	34.514655	-25.95	20.73	0.56	0.33	FHFF
-118.894141	34.409863	-26.10	25.82	0.54	0.30	FMTP
-118.884029	34.356335	-28.22	29.06	0.44	0.24	FMVT
-113.805372	39.369397	-5.41	3.68	0.20	0.12	FOOT
-123.956095	46.204888	5.29	7.05	0.24	0.16	FTS1
-117.935712	33.662326	-25.33	35.17	0.13	0.07	FVPK
-118.359476	34.080604	-30.46	26.65	0.19	0.11	FXHS
-118.893379	34.800193	-20.97	20.52	0.19	0.11	FZHS
-119.355456	40.416527	-5.57	3.81	0.20	0.12	GARL
-117.397893	34.203889	-17.89	19.96	0.39	0.23	GHRP
-114.827345	33.051085	-0.46	6.14	0.69	0.36	GMPK
-115.660229	34.783998	-3.36	1.80	0.30	0.18	GMRC
-114.189449	34.308557	0.77	3.84	0.32	0.18	GNPS
-120.814676	45.838819	-0.70	2.25	0.22	0.14	GOBS
-116.889250	35.425156	-5.88	7.20	0.09	0.04	GOL2
-116.889250	35.425156	-5.69	7.30	0.06	0.04	GOLD

continued on next page

Table B.1: *continued*

Longitude °E	Latitude °N	V_{east} mm/yr	V_{north} mm/yr	$Error_{east}$ mm/yr	$Error_{north}$ mm/yr	Station Name
-114.179697	40.640169	-5.94	3.33	0.20	0.11	GOSH
-118.289681	28.884058	-28.95	29.08	1.78	0.86	GUAX
-118.112892	34.047446	-25.74	26.57	0.36	0.20	GVRS
-121.327562	45.782633	0.02	2.02	0.23	0.15	GWEN
-120.682065	34.469400	-30.28	33.60	0.12	0.06	HARV
-118.285793	33.783645	-23.20	31.56	0.55	0.30	HBCO
-116.430074	34.754774	-10.46	6.08	0.31	0.18	HCMN
-111.372717	40.514099	-3.49	4.65	0.23	0.13	HEBE
-117.799453	34.759919	-16.99	17.01	0.34	0.20	HIVI
-115.635335	33.705006	-5.14	4.68	0.28	0.16	HNPS
-120.479494	35.866713	-23.60	30.61	0.87	0.48	HOGS
-117.845125	34.458155	-18.22	20.56	0.76	0.42	HOL3
-117.845160	34.458186	-17.48	19.18	0.11	0.05	HOLC
-118.168169	33.924539	-22.61	21.91	0.15	0.07	HOLP
-123.074726	38.995184	-19.03	21.05	0.09	0.05	HOPB
-120.402382	35.880812	-15.22	23.22	0.84	0.47	HUNT
-119.187539	34.441230	-27.28	25.77	0.40	0.22	HVYS
-115.911448	34.727325	-1.96	1.92	0.50	0.27	I40A
-115.031802	32.706169	-2.57	6.85	0.64	0.34	IID2
-115.145099	34.157564	-2.08	3.74	0.27	0.16	IMPS
-118.474300	35.662271	-11.79	12.23	0.21	0.12	ISLK
-115.506789	32.829381	-12.40	22.18	0.39	0.21	IVCO
-119.084735	37.771744	-1.17	8.83	3.14	2.01	JNPR
-118.177842	34.201790	-24.01	25.28	0.88	0.50	JPLF
-118.173225	34.204820	-24.28	24.44	0.08	0.04	JPLM
-119.008196	34.398527	-26.31	27.42	0.48	0.27	KBRC
-122.896069	46.118178	4.18	5.04	0.29	0.16	KELS
-118.881141	37.713128	-6.75	7.25	0.56	0.32	KRAK
-116.173394	33.925369	-6.67	13.72	0.71	0.39	KYVW
-120.473281	35.899789	-23.01	29.39	0.38	0.22	LAND
-118.574649	34.181921	-27.18	30.20	0.28	0.16	LAPC

continued on next page

Table B.1: *continued*

Longitude °E	Latitude °N	V_{east} mm/yr	V_{north} mm/yr	$Error_{east}$ mm/yr	$Error_{north}$ mm/yr	Station Name
-118.306503	33.927941	-28.14	29.67	0.14	0.08	LASC
-118.137181	33.832069	-27.12	31.61	0.19	0.10	LBC1
-118.173240	33.791608	-29.27	29.50	0.15	0.09	LBC2
-118.203341	33.787769	-31.61	27.57	0.16	0.09	LBCH
-116.432803	34.267340	-2.78	18.61	0.20	0.11	LDES
-116.209141	34.699427	-5.11	0.25	0.37	0.21	LDSW
-118.321753	34.134600	-27.11	27.72	0.06	0.03	LEEP
-116.861872	40.403513	-3.12	1.64	0.28	0.19	LEWI
-120.430838	35.888351	-21.86	29.88	0.05	0.02	LEXI
-118.412823	34.095070	-27.10	28.44	0.16	0.09	LFRS
-118.139199	34.662021	-17.34	20.34	0.19	0.10	LINJ
-118.867740	34.807523	-20.93	21.89	0.44	0.27	LJRN
-117.834954	34.485457	-18.09	19.83	0.42	0.24	LL01
-117.837930	34.585975	-14.96	18.53	0.20	0.11	LLAS
-116.939651	35.090202	-6.63	12.16	0.75	0.41	LNMT
-118.003408	34.111899	-25.86	26.54	0.17	0.09	LONG
-117.754068	34.133326	-24.32	25.18	0.19	0.11	LORS
-120.594282	35.828708	-24.36	33.68	0.81	0.46	LOWS
-117.956718	34.026769	-28.29	29.21	0.21	0.12	LPHS
-119.103684	34.733605	-24.46	22.54	0.20	0.12	LVMS
-120.443057	35.832596	-23.66	30.82	0.82	0.46	MASW
-117.436697	33.856760	-21.83	27.63	0.57	0.31	MAT2
-117.436814	33.856685	-21.63	26.21	0.10	0.04	MATH
-121.642577	37.341533	-12.66	11.30	0.19	0.12	MHCB
-118.244130	33.939054	-15.83	27.19	0.69	0.33	MHMS
-120.458829	35.921913	-13.90	20.79	0.50	0.25	MIDA
-120.351389	34.038257	-29.78	36.45	0.32	0.18	MIG1
-116.095511	40.148366	-1.12	2.88	0.25	0.14	MINE
-119.060899	37.653764	-10.16	9.77	0.14	0.08	MINS
-117.550468	33.714481	-25.39	30.05	0.77	0.42	MJPK
-117.317956	33.918403	-21.96	27.52	0.20	0.11	MLFP

continued on next page

Table B.1: *continued*

Longitude °E	Latitude °N	V_{east} mm/yr	V_{north} mm/yr	$Error_{east}$ mm/yr	$Error_{north}$ mm/yr	Station Name
-120.434051	35.969472	-12.57	20.38	0.80	0.45	MNMC
-122.419923	37.946575	-16.61	21.09	0.32	0.15	MOLA
-116.422347	32.891939	-26.07	27.91	0.10	0.05	MONP
-118.878014	34.295510	-28.54	30.24	0.20	0.12	MPWD
-117.210124	34.230844	-16.22	19.78	0.21	0.12	MSOB
-118.245499	34.055218	-23.35	26.59	0.55	0.32	MTA1
-119.096049	34.261603	-32.39	31.45	0.13	0.07	MUSD
-116.525311	33.210872	-25.31	28.40	0.20	0.11	MVFD
-116.148172	34.508622	2.07	3.57	0.32	0.18	NBPS
-114.618629	34.767688	11.53	-14.85	1.18	0.65	NDAP
-119.141257	34.498657	-22.76	25.08	0.39	0.22	NHRG
-117.569579	33.919708	-22.34	27.82	0.63	0.34	NOCO
-118.348010	33.979735	-27.05	29.80	0.18	0.10	NOPK
-116.972680	32.579314	-27.04	29.68	0.37	0.20	NSSS
-122.246297	37.963121	-13.09	19.02	0.36	0.16	NUNE
-116.067736	34.141005	-0.82	3.36	0.25	0.14	OAES
-118.601378	34.329891	-26.96	26.11	0.07	0.04	OAT2
-118.601210	34.330075	-33.16	27.95	1.49	0.53	OATT
-117.744133	33.765857	-27.84	28.75	0.83	0.46	OEOC
-117.041766	33.130606	-26.25	30.69	0.23	0.13	OGHS
-115.918056	34.369883	1.08	3.62	0.24	0.14	OPBL
-116.305456	34.427716	-1.28	13.31	0.23	0.13	OPCL
-116.083372	34.367130	3.09	7.34	0.23	0.13	OPCP
-116.149483	34.430082	2.72	6.42	0.23	0.13	OPCX
-116.292278	34.533032	-4.96	10.03	0.26	0.15	OPRD
-120.278556	34.739059	-30.77	34.83	0.20	0.12	ORES
-116.815091	34.674904	-12.06	13.23	0.44	0.24	ORMT
-119.141945	34.327359	-28.45	31.24	0.19	0.11	OVLS
-118.207313	34.128811	-26.03	25.49	0.24	0.14	OXYC
-122.418946	37.853054	-22.43	22.49	0.14	0.08	PBL1
-117.694478	34.925423	-10.17	15.82	0.31	0.18	PHLB

continued on next page

Table B.1: *continued*

Longitude °E	Latitude °N	V_{east} mm/yr	V_{north} mm/yr	$Error_{east}$ mm/yr	$Error_{north}$ mm/yr	Station Name
-116.457617	33.612148	-15.99	20.26	0.25	0.14	PIN2
-116.458159	33.612156	-14.92	18.42	0.11	0.05	PINY
-118.232902	34.071559	-25.93	25.28	0.57	0.30	PKRD
-117.243027	32.665420	-27.92	30.64	0.33	0.19	PLO3
-118.153684	33.902633	-27.86	28.27	0.19	0.11	PMHS
-116.859544	33.357239	-25.02	29.34	0.20	0.11	PMOB
-120.478433	35.919910	-22.65	27.83	0.38	0.21	POMM
-117.182087	33.835726	-21.09	26.31	0.20	0.11	PPBF
-122.389951	37.187085	-28.71	35.73	0.13	0.08	PPT1
-116.493991	33.819237	-12.84	22.37	0.19	0.11	PSAP
-117.807089	34.091764	-24.74	25.74	0.28	0.16	PSDM
-118.404253	33.743295	-21.81	20.67	0.37	0.20	PVE3
-118.404246	33.743289	-27.17	32.34	0.12	0.05	PVEP
-118.372162	33.779453	-28.30	31.76	0.19	0.11	PVHS
-118.320586	33.773862	-28.82	32.24	0.16	0.09	PVRS
-118.244812	34.628680	-17.96	19.92	0.38	0.21	QHTP
-120.944427	39.974554	-9.13	6.24	0.08	0.04	QUIN
-117.683349	35.338714	-7.57	14.44	0.45	0.25	RAMT
-111.808760	40.781063	-1.82	3.43	0.33	0.19	RBUT
-119.719994	34.499980	-29.56	28.40	0.36	0.20	RCA2
-116.624686	34.643941	-12.83	12.51	0.24	0.14	RDMT
-121.147881	44.259767	-1.81	3.31	0.22	0.14	REDM
-118.026168	34.019050	-25.90	28.42	0.15	0.09	RHCL
-120.524824	35.899993	-33.54	22.50	1.34	0.76	RNCH
-116.609770	33.611024	-17.79	22.85	0.17	0.09	ROCH
-118.676429	34.235674	-27.65	30.04	0.06	0.03	ROCK
-118.192924	34.875080	-12.32	17.28	0.30	0.18	RSTP
-117.353332	34.089150	-22.02	24.23	0.20	0.11	RTHS
-115.122834	40.617210	-4.70	2.73	0.25	0.15	RUBY
-121.558267	37.666507	-12.51	8.96	0.37	0.20	S300
-117.895576	33.743244	-23.66	28.53	0.18	0.10	SACY

continued on next page

Table B.1: *continued*

Longitude °E	Latitude °N	V_{east} mm/yr	V_{north} mm/yr	$Error_{east}$ mm/yr	$Error_{north}$ mm/yr	Station Name
-117.661484	33.552999	-26.64	30.60	0.30	0.18	SBCC
-117.388300	34.607446	-14.09	17.76	0.20	0.12	SCIA
-118.487936	32.914426	-30.18	36.17	0.12	0.07	SCIP
-117.634561	33.444139	-25.61	31.12	0.30	0.15	SCMS
-118.754504	34.459805	-24.31	27.55	0.61	0.33	SFDM
-118.108975	34.088625	-23.33	25.32	0.24	0.14	SGHS
-116.695684	33.912535	-17.07	21.38	0.37	0.22	SGPS
-120.225043	40.591679	-6.71	5.24	0.20	0.12	SHIN
-116.015582	34.624259	-7.84	-1.76	0.25	0.15	SIBE
-118.263869	34.102861	-26.91	26.19	0.45	0.25	SILK
-117.250407	32.864702	-25.75	27.58	0.11	0.05	SIO3
-117.252467	32.867458	-33.48	32.09	2.84	1.57	SIO4
-118.478627	34.438623	-21.85	13.29	1.09	0.66	SKYB
-119.884287	39.314278	-11.11	6.61	0.23	0.13	SLID
-115.977840	33.292227	-12.98	20.39	0.21	0.12	SLMS
-112.844927	39.425644	-2.68	4.03	0.21	0.12	SMEL
-117.928626	33.927336	-25.52	29.52	0.17	0.10	SNHS
-119.524363	33.247874	-30.15	35.07	0.12	0.05	SNI1
-119.064331	34.319938	-27.67	29.97	0.43	0.24	SOMT
-118.646159	34.059342	-27.95	30.76	0.06	0.03	SPK1
-117.848773	33.992653	-25.58	29.31	0.13	0.07	SPMS
-115.465859	31.045044	-31.96	33.49	0.16	0.09	SPMX
-120.065219	34.004334	-29.67	36.20	0.63	0.35	SRS1
-121.820598	39.205836	-10.73	6.61	0.20	0.13	SUTB
-117.678281	34.381848	-19.80	19.92	0.13	0.07	TABL
-120.360336	35.917411	-14.92	18.87	1.09	0.59	TBLP
-118.414570	35.158182	-10.23	14.60	0.46	0.26	THCP
-122.447601	37.890874	-21.79	21.73	0.30	0.17	TIBB
-120.132561	34.483473	-29.94	33.32	0.39	0.22	TJRN
-116.160459	33.641245	-11.67	17.93	0.52	0.28	TMAP
-118.330601	33.797797	-27.85	32.01	0.09	0.04	TORP

continued on next page

Table B.1: *continued*

Longitude °E	Latitude °N	V_{east} mm/yr	V_{north} mm/yr	$Error_{east}$ mm/yr	$Error_{north}$ mm/yr	Station Name
-118.836662	34.247955	-29.04	30.39	0.37	0.21	TOST
-117.803433	33.617934	-26.36	28.91	0.11	0.05	TRAK
-116.530544	34.838597	-10.76	7.48	0.24	0.14	TROY
-118.257504	40.403201	-6.20	3.74	0.20	0.12	TUNG
-117.725519	33.972454	-26.31	26.63	0.86	0.46	TWMS
-118.441908	34.069120	-26.64	28.70	0.05	0.02	UCLP
-119.843812	34.413305	-30.32	30.35	0.15	0.09	UCSB
-118.802279	39.627112	-6.40	5.24	0.20	0.12	UPSA
-118.285113	34.023950	-26.42	29.73	0.05	0.02	USC1
-116.085332	33.030063	-21.75	27.19	0.47	0.25	USGC
-120.661091	35.311803	-27.22	34.60	0.39	0.22	USLO
-120.563506	34.826613	-31.38	34.87	0.29	0.17	VAN1
-118.219998	34.178565	-24.23	25.44	0.55	0.29	VDCY
-118.514411	34.126447	-27.39	28.77	0.41	0.23	VIMT
-119.237667	34.275764	-28.95	30.36	0.43	0.25	VNCO
-118.484538	34.293192	-27.02	26.75	0.86	0.47	VNCX
-120.616449	34.556310	-31.42	34.72	0.06	0.03	VNDP
-118.121156	34.501480	-21.52	22.22	0.21	0.12	VNPS
-118.293821	33.712639	-27.77	32.60	0.17	0.10	VTIS
-117.992048	34.030915	-22.48	30.08	0.12	0.07	VYAS
-117.911109	34.061897	-26.56	27.52	0.21	0.12	WCHS
-118.983687	35.010848	-16.07	16.11	1.28	0.75	WGPP
-118.031167	33.979884	-26.93	27.26	0.05	0.02	WHC1
-118.034467	33.973806	-20.67	28.05	0.33	0.13	WHI1
-117.643455	33.674490	-27.91	27.39	1.30	0.68	WHYT
-116.391781	33.934757	-9.98	19.41	0.19	0.11	WIDC
-122.140567	37.652643	-19.43	21.34	0.15	0.07	WINT
-118.741516	34.568498	-22.68	23.81	0.63	0.35	WKPK
-118.055910	34.226121	-21.53	24.58	0.15	0.07	WLSN
-118.414290	34.259423	-31.08	29.18	0.35	0.21	WMAP
-118.059256	34.043237	-25.03	27.98	0.36	0.20	WNRA

continued on next page

Table B.1: *continued*

Longitude °E	Latitude °N	V_{east} mm/yr	V_{north} mm/yr	$Error_{east}$ mm/yr	$Error_{north}$ mm/yr	Station Name
-116.931664	34.669014	-11.91	14.95	0.51	0.27	WOMT
-118.427605	33.958151	-27.44	30.22	0.22	0.13	WRHS
-122.710735	41.731656	-3.76	6.57	0.25	0.14	YBHB

Table B.2: GPS data from USGS Time Series analysis (source: http://quake.wr.usgs.gov/research/deformation/gps/auto/CL.html)

Longitude °E	Latitude °N	V_{east} mm/yr	V_{north} mm/yr	$Error_{east}$ mm/yr	$Error_{north}$ mm/yr	Station Name
-122.152551	37.919405	-13.15	15.68	0.61	0.59	BRIB
-120.430836	35.888350	-22.85	28.22	0.34	0.34	CARR
-122.119308	37.724115	-15.74	17.68	0.38	0.38	CHAB
-121.664961	39.432639	-9.88	6.92	0.54	0.53	CHO1
-120.386038	38.034177	-9.44	8.02	0.58	0.57	CMBB
-124.396332	40.441773	-8.42	30.27	0.38	0.38	CME1
-121.278494	37.896406	-12.39	8.01	0.52	0.51	CNDR
-121.915626	37.878576	-11.32	11.07	0.46	0.45	DIAB
-123.000764	37.697207	-28.11	36.16	0.33	0.33	FARB
-123.074725	38.995184	-18.66	19.67	0.36	0.36	HOPB
-121.865223	37.286851	-19.04	23.00	0.40	0.39	LUTZ
-121.642576	37.341533	-12.14	10.34	0.38	0.38	MHCB
-122.419922	37.946574	-18.32	22.96	0.38	0.38	MOLA
-121.866863	37.485326	-15.57	16.27	0.47	0.46	MONB
-119.309348	37.169941	-10.12	8.75	0.47	0.45	MUSB
-122.246295	37.963121	-12.67	14.61	0.48	0.47	NUNE
-121.500289	39.554628	-10.14	6.39	0.40	0.39	ORVB
-122.418945	37.853054	-22.24	21.77	0.36	0.36	PBL1
-120.541554	35.945237	-23.59	30.72	0.40	0.39	PKDB
-121.935385	38.202626	-10.52	8.82	0.49	0.48	POTB
-122.389949	37.187084	-28.32	35.26	0.37	0.37	PPT1
-123.018716	37.996174	-26.03	35.73	0.47	0.46	PTRB

continued on next page

Table B.2: *continued*

Longitude °E	Latitude °N	V_{east} mm/yr	V_{north} mm/yr	$Error_{east}$ mm/yr	$Error_{north}$ mm/yr	Station Name
-124.255198	41.782742	3.11	11.43	0.58	0.55	PTSG
-120.944426	39.974555	-9.90	6.73	0.31	0.31	QUIN
-121.558266	37.666508	-10.82	8.94	0.52	0.51	S300
-121.447182	36.765303	-29.97	35.89	0.42	0.41	SAOB
-121.925517	37.166404	-21.17	25.54	0.52	0.51	SODB
-122.173286	37.426905	-22.31	25.73	0.36	0.35	SUAA
-121.820597	39.205837	-10.72	6.82	0.41	0.41	SUTB
-122.447599	37.890874	-16.82	24.28	0.34	0.34	TIBB
-124.150866	41.053886	2.69	16.29	0.60	0.56	TRND
-121.751229	38.536240	-10.92	7.15	0.39	0.38	UCD1
-122.140565	37.652643	-19.17	21.53	0.38	0.38	WINT
-122.710734	41.731656	-2.90	6.26	0.40	0.39	YBHB
-117.139206	34.013787	-15.77	21.67	1.33	0.81	BRIN
-117.451092	34.347207	-18.09	17.98	1.14	0.70	CAJO
-117.442770	34.032352	-21.69	27.17	1.90	1.17	JURU
-117.292040	34.281449	-17.08	17.31	1.29	0.82	MLUN
-123.304603	44.585536	5.92	7.22	0.72	0.71	CORV
-121.849360	44.119527	-2.61	14.39	0.73	0.72	HUSB
-124.061886	44.585025	8.52	9.08	0.72	0.71	NEWP
-122.069239	37.732369	-15.75	16.55	0.84	0.58	CAS2
-122.119307	37.724115	-17.18	18.60	0.62	0.52	CHAB
-121.914753	37.881853	-12.77	11.05	1.23	0.74	DBLO
-121.915626	37.878576	-13.23	11.74	1.14	0.82	DIAB
-123.000763	37.697206	-28.94	36.42	0.48	0.41	FARB
-121.792459	37.921529	-12.62	7.68	0.99	0.63	JOBE
-122.456167	37.526825	-26.01	31.76	0.74	0.55	PALO
-122.382154	37.592236	-23.33	27.41	0.92	0.70	PEEE
-122.061478	37.815016	-14.61	14.42	1.36	1.01	ROC2
-122.183706	37.690824	-18.91	21.75	0.92	0.67	SLBB
-122.458057	37.609442	-24.64	29.96	0.86	0.65	SWEE
-122.503901	37.509119	-26.84	33.47	0.92	0.70	WHAL

continued on next page

Table B.2: *continued*

Longitude °E	Latitude °N	V_{east} mm/yr	V_{north} mm/yr	$Error_{east}$ mm/yr	$Error_{north}$ mm/yr	Station Name
-122.140565	37.652643	-20.21	22.24	0.59	0.50	WINT
-116.889249	35.425156	-7.60	5.39	0.57	0.39	GOL2
-122.140565	37.652643	-19.33	21.29	0.40	0.39	WINT
-122.221992	37.883569	-14.68	18.31	0.67	0.52	BAPK
-123.000763	37.697206	-27.57	37.08	0.45	0.38	FARB
-122.128232	37.936898	-11.43	16.94	0.90	0.62	HILL
-122.366155	37.809960	-18.90	24.42	0.63	0.54	NAVY
-122.418944	37.853054	-22.65	22.05	0.53	0.44	PBL1
-122.455071	37.805303	-18.06	24.43	1.13	0.78	PRSD
-122.598525	37.923231	-20.82	26.46	0.65	0.48	T3R2
-122.265151	37.871788	-17.09	23.60	0.89	0.70	UCBK
-117.011991	34.918612	-10.98	10.97	0.67	0.62	BSRY
-116.931663	34.669014	-13.83	13.83	0.70	0.64	WOMT
-116.430073	34.754774	-9.67	4.28	0.82	0.73	HCMN
-116.624685	34.643941	-10.54	10.75	0.76	0.69	RDMT
-116.429377	34.594282	-5.95	11.78	0.78	0.71	AGMT
-116.292277	34.533032	-3.14	8.74	1.00	0.89	OPRD
-116.305455	34.427717	0.57	11.62	0.78	0.71	OPCL
-116.432802	34.267340	-1.61	18.11	0.67	0.62	LDES
-116.530543	34.838597	-7.72	6.10	0.80	0.72	TROY
-116.557068	34.574404	-12.10	13.32	0.71	0.65	LAE1
-116.486830	34.617943	-10.82	11.43	0.78	0.71	LAE3
-116.588158	34.542358	-13.58	15.03	0.78	0.71	LAW1
-116.623692	34.526691	-11.70	17.19	1.57	1.26	LAW2
-116.669005	34.501503	-12.03	16.36	1.22	1.06	LAW3
-116.665206	34.453826	-10.27	18.15	1.30	1.10	LAW4
-116.617423	34.257910	-7.41	20.65	1.07	0.91	MEEK
-116.697946	34.390504	-10.31	17.18	1.07	0.91	OLDD
-116.751874	34.388664	-11.11	14.97	1.05	0.90	OLDW
-116.468878	34.264113	-4.84	17.61	1.09	0.92	RICH
-117.011991	34.918612	-8.80	10.16	0.97	0.87	BSRY

continued on next page

Table B.2: *continued*

Longitude °E	Latitude °N	V_{east} mm/yr	V_{north} mm/yr	$Error_{east}$ mm/yr	$Error_{north}$ mm/yr	Station Name
-116.931663	34.669014	-11.50	12.82	1.12	0.98	WOMT
-116.624685	34.643941	-9.58	10.16	0.98	0.88	RDMT
-116.429377	34.594282	-5.90	10.68	0.96	0.86	AGMT
-116.292277	34.533032	-3.46	6.20	1.50	1.30	OPRD
-116.305455	34.427717	0.11	10.24	0.99	0.88	OPCL
-116.432802	34.267340	-1.01	14.77	0.96	0.86	LDES
-116.530543	34.838597	-7.65	5.10	0.97	0.87	TROY
-116.557068	34.574404	-9.86	12.36	1.08	0.95	LAE1
-116.486830	34.617943	-8.86	10.61	1.11	0.98	LAE3
-116.588158	34.542358	-7.69	12.03	1.25	1.07	LAW1
-116.669005	34.501503	-9.73	14.24	1.96	1.59	LAW3
-116.665206	34.453826	-7.97	17.44	1.96	1.56	LAW4
-116.617424	34.257910	-6.39	16.74	1.56	1.33	MEEK
-116.697946	34.390504	-7.98	15.49	1.57	1.30	OLDD
-116.751874	34.388664	-8.66	16.30	1.51	1.29	OLDW
-116.468878	34.264113	-3.99	18.22	1.58	1.34	RICH
-123.304603	44.585536	3.29	7.68	0.71	0.58	CORV
-116.588156	34.542357	-8.97	9.56	0.91	0.68	LAW1
-116.623691	34.526689	-11.63	13.77	1.10	0.86	LAW2
-116.665205	34.453825	-8.95	17.41	1.21	0.96	LAW4
-116.697945	34.390502	-9.32	20.27	1.05	0.85	OLDD
-116.751873	34.388663	-8.67	18.35	1.20	0.96	OLDW
-116.588156	34.542357	-8.58	7.57	1.47	0.99	LAW1
-121.782635	37.186382	-21.17	21.78	0.92	0.65	CAAA
-122.051598	36.949754	-28.47	33.62	0.94	0.63	CLIF
-121.737952	37.219232	-20.17	21.08	0.83	0.58	COYY
-121.937757	37.046945	-20.41	31.54	0.80	0.63	FIRE
-121.923648	36.982268	-28.13	32.16	0.94	0.64	GREG
-121.643023	37.341736	-13.65	10.65	0.90	0.61	HAML
-121.844636	37.109594	-17.53	25.01	0.60	0.46	LP1X
-121.838799	37.050062	-22.74	29.20	0.97	0.63	LP4X

continued on next page

Table B.2: *continued*

Longitude °E	Latitude °N	V_{east} mm/yr	V_{north} mm/yr	$Error_{east}$ mm/yr	$Error_{north}$ mm/yr	Station Name
-121.787506	37.137143	-20.81	22.78	0.79	0.60	MAZZ
-121.642576	37.341533	-12.90	10.60	0.68	0.53	MHCB
-121.555937	37.477330	-11.99	8.33	0.70	0.52	MOCH
-122.389949	37.187084	-26.83	35.43	0.72	0.55	PPT1
-120.386038	38.034177	-9.08	7.98	0.54	0.54	CMBB
-119.060897	37.653764	-7.76	7.96	0.37	0.37	MINS
-119.309348	37.169941	-10.27	8.63	0.44	0.44	MUSB
-118.901305	37.783938	-7.09	14.95	0.53	0.45	BAMT
-119.044512	37.916915	-11.55	10.43	0.82	0.66	CART
-118.890363	37.746171	-5.75	17.28	0.78	0.64	G916
-118.893966	37.875232	-7.21	12.69	0.81	0.66	K204
-118.947463	37.728739	-12.85	16.84	0.74	0.61	LKMT
-119.055331	37.856370	-12.59	11.65	0.58	0.51	M903
-119.060897	37.653764	-7.76	6.75	0.58	0.50	MINS
-118.283573	37.231991	-8.18	5.48	0.49	0.41	OVRO
-119.060510	37.656031	-14.31	6.98	0.79	0.65	RETT
-118.632850	37.544509	-5.61	5.79	0.61	0.49	WINN
-123.304603	44.585536	4.08	6.07	1.37	1.10	CORV
-124.061886	44.585025	8.36	8.67	1.39	1.13	NEWP
-124.396332	40.441773	-6.36	29.30	1.36	1.09	CME1
-123.693173	40.120288	-14.73	15.38	0.59	0.51	ALDE
-124.294484	40.497700	-3.94	27.85	0.55	0.48	BEAR
-119.696937	39.284720	-6.66	1.45	1.65	1.38	10BB
-117.424247	36.339574	-6.17	1.37	1.97	1.54	13DD
-116.163181	36.690264	-2.55	-2.02	0.87	0.67	1PDI
-118.143349	39.540231	-2.53	-0.59	1.65	1.16	3756
-119.658370	39.847909	-5.80	2.07	1.67	1.49	43JD
-116.396250	36.813224	-5.15	-1.28	1.11	0.86	67TJ
-117.675245	36.150394	-9.36	2.39	1.56	1.21	6813
-120.142190	39.357727	-11.10	5.83	1.42	1.29	A210
-120.032564	39.238418	-9.62	6.64	1.29	1.11	A220

continued on next page

Table B.2: *continued*

Longitude °E	Latitude °N	V_{east} mm/yr	V_{north} mm/yr	$Error_{east}$ mm/yr	$Error_{north}$ mm/yr	Station Name
-119.774216	39.101455	-9.14	5.83	0.89	0.80	A250
-119.647044	39.219974	-9.30	9.67	1.98	1.84	A255
-119.550279	39.282213	-7.37	5.61	0.93	0.88	A270
-119.405468	39.349848	-9.01	-1.15	0.71	0.71	A280
-119.193491	39.429087	-5.76	4.67	0.85	0.77	A290
-119.075846	39.464541	-6.72	2.22	1.97	1.89	A295
-119.924057	38.777250	-10.86	6.95	0.61	0.54	A300
-118.938781	39.513071	-5.18	3.62	0.69	0.64	B200
-118.867447	39.493354	-6.92	2.74	1.00	0.88	B210
-118.646426	39.397623	-6.00	2.97	0.92	0.80	B220
-118.472030	39.298852	-6.19	2.11	0.87	0.77	B230
-118.172783	39.286142	-3.93	1.77	0.85	0.76	B270
-118.016582	39.274792	-4.65	-0.15	1.46	1.22	B280
-117.859206	39.283814	-3.63	0.53	0.97	0.85	B290
-119.244112	38.988116	-6.29	4.64	0.47	0.41	B300
-118.143534	39.674020	-3.24	0.19	1.96	1.15	B387
-117.220800	38.060563	-2.40	-1.80	1.29	0.87	B410
-116.674569	36.842977	-2.46	0.61	1.11	0.84	BARE
-116.574801	36.808813	-3.70	-0.49	1.25	1.00	BL91
-119.057808	39.579263	-5.11	2.25	1.28	1.14	BLAB
-116.977577	36.723537	-1.30	-2.25	1.83	1.46	BM80
-117.699267	38.328148	-3.09	0.42	1.41	0.83	BRAN
-116.635154	36.958952	-3.04	-1.61	1.07	0.84	BRIC
-118.310687	39.273810	-4.69	2.76	0.78	0.65	BX46
-117.508868	39.685748	-4.03	0.31	0.59	0.50	C100
-117.711690	39.263716	-2.99	-0.16	0.70	0.63	C200
-117.411510	39.357644	-3.35	0.03	0.99	0.88	C220
-117.142320	39.486615	-3.27	0.22	0.81	0.72	C240
-116.941704	39.402194	-3.46	0.24	1.02	0.88	C260
-116.621333	39.476787	-3.17	0.22	0.89	0.77	C280
-117.883924	38.759922	-3.24	0.45	0.61	0.51	C300

continued on next page

Table B.2: *continued*

Longitude °E	Latitude °N	V_{east} mm/yr	V_{north} mm/yr	$Error_{east}$ mm/yr	$Error_{north}$ mm/yr	Station Name
-116.177604	36.776114	-2.67	0.56	1.14	0.79	CAN5
-118.103353	38.150104	-3.18	2.80	0.81	0.48	CAND
-117.786760	36.537694	-5.33	2.56	1.95	1.41	CERR
-119.202780	39.358173	-5.03	3.51	1.39	1.20	CHIL
-119.875750	39.513470	-5.36	2.71	1.50	1.24	CHLK
-117.885549	38.030915	-3.09	1.36	1.64	0.97	CLDL
-120.386038	38.034177	-9.90	7.71	0.98	0.78	CMBB
-117.238398	37.743471	-4.67	0.36	0.96	0.69	COLU
-112.121009	40.652592	-2.29	-0.91	1.08	0.71	COON
-117.808888	35.982343	-4.48	12.60	0.41	0.39	COSO
-116.160861	40.083625	-4.03	0.42	0.63	0.55	D100
-116.306331	39.533710	-4.70	-0.49	0.76	0.67	D200
-115.976060	39.543158	-6.19	-0.62	0.99	0.85	D220
-115.873945	39.368485	-7.81	0.72	0.50	0.50	D235
-115.799061	39.380553	-5.92	-1.30	1.02	0.84	D240
-115.555752	39.402146	-5.07	-0.29	0.89	0.81	D260
-115.081555	39.415199	-5.30	-2.08	1.37	1.15	D280
-116.745652	39.056159	-4.17	-0.89	0.67	0.54	D300
-116.058202	37.893835	-3.36	-1.26	1.38	0.76	DRYY
-118.039335	37.742804	-3.48	3.50	0.88	0.72	DER
-114.651958	39.901669	-4.48	-1.11	0.71	0.56	E100
-114.953473	39.289685	-5.36	-0.30	0.74	0.62	E200
-114.657896	39.032973	-5.17	-1.28	1.17	0.92	E220
-114.453462	39.068685	-4.22	-0.27	1.18	0.85	E240
-114.238907	39.097771	-4.23	2.04	0.50	0.50	E259
-114.204243	39.096840	-3.92	-1.18	1.19	0.95	E260
-113.886925	39.044537	-4.57	-1.40	1.10	0.82	E280
-115.130191	38.889882	-4.77	-0.49	0.61	0.50	E300
-119.482475	39.552108	-7.81	2.14	0.84	0.76	EARN
-114.938853	39.345244	-2.86	-0.82	0.72	0.64	EGAN
-115.817196	40.914691	-3.26	0.08	0.70	0.60	ELKO

continued on next page

Table B.2: *continued*

Longitude °E	Latitude °N	V_{east} mm/yr	V_{north} mm/yr	$Error_{east}$ mm/yr	$Error_{north}$ mm/yr	Station Name
-118.501742	38.267866	-5.53	5.14	1.42	0.82	EXCE
-113.584818	39.548487	-2.46	-1.36	0.62	0.49	F100
-113.629681	39.081268	-3.85	-1.16	0.89	0.74	F200
-113.530383	39.086399	-3.55	-0.15	1.53	1.17	F210
-113.384783	39.023790	-3.05	-0.33	1.00	0.87	F220
-113.223598	39.253836	-2.73	-0.40	0.98	0.86	F230
-116.861964	36.857568	-0.02	-0.28	1.81	1.46	F23X
-113.045836	39.282944	-2.14	-0.70	0.93	0.80	F250
-112.837191	39.316593	-3.20	0.33	0.93	0.82	F270
-112.545609	39.366996	-3.01	0.47	1.21	1.13	F280
-112.411595	39.206440	-4.39	0.66	1.97	1.84	F291
-113.666752	38.794744	-3.51	-0.58	0.65	0.51	F300
-118.161167	38.657266	-3.94	0.72	1.14	0.66	FERG
-119.202690	39.943713	-5.81	2.61	0.95	0.81	FLRN
-117.884327	36.062468	-9.85	5.59	1.75	1.17	FORK
-118.103896	38.730655	-3.60	1.69	1.46	0.85	FT73
-112.151046	39.601646	-4.75	0.18	1.18	1.04	G101
-117.211798	36.542522	-4.63	0.25	1.96	1.50	G165
-112.242087	39.139917	-3.69	-0.16	0.88	0.74	G200
-112.098325	39.241044	-3.64	0.55	1.06	0.83	G210
-112.041549	39.078436	-4.07	0.05	1.22	1.05	G220
-111.914549	38.961320	-3.03	0.01	1.26	1.08	G230
-111.941055	38.901532	-1.25	0.64	0.50	0.50	G235
-111.738330	38.904363	-4.34	1.46	1.33	1.03	G250
-111.536769	38.839153	-1.61	-0.71	1.16	0.84	G270
-111.381029	38.754919	-3.48	0.78	1.21	0.95	G280
-111.205558	38.807617	-3.19	1.54	1.22	0.97	G290
-112.593681	38.602335	-3.34	-0.77	0.70	0.54	G300
-117.916390	38.970333	-4.36	1.16	0.63	0.59	GABB
-119.355455	40.416527	-5.70	2.22	0.45	0.43	GARL
-111.020379	39.293266	-1.45	-0.49	0.77	0.60	H100

continued on next page

Table B.2: *continued*

Longitude °E	Latitude °N	V_{east} mm/yr	V_{north} mm/yr	$Error_{east}$ mm/yr	$Error_{north}$ mm/yr	Station Name
-120.176700	38.633391	-10.32	3.86	1.58	1.28	H112
-111.111439	38.832623	-2.47	0.18	1.05	0.86	H200
-111.359003	38.482802	-2.17	1.52	0.81	0.60	H300
-117.074439	38.075378	-2.21	-1.73	1.62	0.94	HAYE
-111.372716	40.514100	-2.93	-0.49	0.83	0.61	HEBE
-118.817762	38.279858	-7.09	5.78	1.48	0.84	HICK
-117.027300	36.637880	-1.98	0.02	1.75	1.32	HOLD
-118.809124	37.979130	-6.72	9.40	0.87	0.53	HORU
-116.416475	36.304432	-3.29	-1.18	1.32	0.94	JCTN
-116.861871	40.403513	-0.96	-1.03	1.11	0.86	LUIE
-118.560745	40.071604	-5.88	-0.22	1.77	0.90	LOLA
-118.308352	38.456423	-4.59	2.66	0.84	0.52	MABL
-119.790070	39.367267	-10.06	4.11	1.06	0.90	MAGU
-117.133181	38.552475	-4.27	-0.58	0.79	0.69	MAHH
-116.469283	36.837658	-3.66	-1.15	0.84	0.67	MILE
-116.095511	40.148366	-1.85	-0.55	1.02	0.82	MINE
-116.148871	36.993988	-2.33	-0.74	1.18	0.81	MN71
-116.929248	36.792192	-1.03	-2.38	1.93	1.54	MO93
-118.259667	38.279634	-2.49	2.65	1.56	0.90	MOHO
-118.282948	39.395901	-3.65	2.65	1.03	0.79	MOND
-116.715570	39.147710	-3.74	-0.35	1.13	0.96	MONI
-119.309348	37.169941	-10.98	8.76	0.54	0.49	MUSB
-117.985674	38.820214	-4.35	1.05	1.42	0.79	N295
-117.508934	39.685617	-3.55	1.27	1.33	1.03	NPAS
-119.088050	37.291154	-10.11	4.24	1.87	1.38	OBSE
-118.283573	37.231991	-7.96	4.39	0.61	0.51	OVRO
-116.745998	36.828158	-2.87	-0.41	1.11	0.79	P16X
-119.922698	39.110823	-11.09	5.18	1.17	0.93	P208
-116.080918	36.941327	-1.78	-0.30	1.13	0.80	PASS
-117.974070	38.342958	-2.94	1.06	1.49	0.93	PIPK
-118.035597	39.035919	-4.03	0.72	1.31	0.87	POST

continued on next page

Table B.2: *continued*

Longitude °E	Latitude °N	V_{east} mm/yr	V_{north} mm/yr	$Error_{east}$ mm/yr	$Error_{north}$ mm/yr	Station Name
-120.944426	39.974554	-9.34	6.23	0.35	0.33	QUIN
-118.703180	39.995377	-6.83	2.48	0.78	0.64	RATT
-116.262905	36.722860	0.05	0.29	1.15	0.86	RK59
-116.538742	36.696916	-4.47	-0.93	1.26	0.94	ROSS
-120.038837	39.790918	-8.59	4.89	0.54	0.46	SAGE
-117.027592	37.274286	-3.22	-1.06	1.09	0.74	SARC
-118.324484	39.043190	-4.55	0.64	1.69	1.12	SHEL
-120.225042	40.591679	-6.90	3.79	0.45	0.43	SHIN
-117.192310	40.034177	-3.36	-1.93	1.25	0.81	SHON
-116.261124	36.943377	-2.96	-1.24	0.85	0.65	SHOS
-119.884286	39.314278	-8.50	5.80	1.92	1.60	SLID
-118.206086	39.109174	-4.14	0.26	1.63	1.07	SLR1
-112.844926	39.425644	-3.32	-0.53	0.60	0.51	SMEL
-118.422468	39.147509	7.50	2.72	0.40	0.40	SNDS
-116.180613	36.655463	-1.18	0.28	1.23	0.84	SPEC
-116.753271	37.047943	-2.80	0.06	1.00	0.77	SPRI
-116.402550	36.641423	-1.91	-0.48	1.59	1.16	T15S
-116.461005	37.087670	-2.24	-1.63	1.75	1.36	TIMB
-117.184039	38.097195	-3.09	0.54	0.79	0.67	TONO
-118.257503	40.403202	-5.67	1.16	0.45	0.42	TUNG
-118.802278	39.627113	-6.96	3.26	0.51	0.49	UPSA
-120.324940	39.317951	-9.67	4.78	0.91	0.78	UU83
-119.698011	39.532995	-6.92	2.25	1.26	1.02	VSTA
-118.576946	38.606088	-6.27	4.24	1.62	0.86	W078
-119.160385	38.045247	-9.87	9.56	1.42	1.03	W916
-116.329524	36.667191	-2.06	-1.17	1.38	1.09	WELL
-116.323376	36.781377	-0.67	-0.65	1.25	0.91	WHME
-118.056820	39.409275	-3.28	0.46	1.66	1.22	WOND
-116.485021	36.940214	-2.84	0.38	1.06	0.81	YUCC
-117.174343	36.294054	-3.62	2.60	0.79	0.67	3059
-118.135659	36.023252	-8.25	8.86	0.67	0.59	3187

continued on next page

Table B.2: *continued*

Longitude °E	Latitude °N	V_{east} mm/yr	V_{north} mm/yr	$Error_{east}$ mm/yr	$Error_{north}$ mm/yr	Station Name
-118.132162	36.466093	-8.29	7.44	0.69	0.60	3188
-118.119482	36.602558	-7.37	7.35	0.85	0.71	3190
-118.101031	36.914136	-8.94	5.21	0.67	0.59	3191
-118.507753	35.085757	-10.09	12.08	0.81	0.67	DEER
-118.587731	35.745012	-9.67	8.91	0.68	0.59	H614
-117.692063	35.337016	-8.14	9.77	0.83	0.69	JBRG
-117.705896	34.742960	-12.84	13.99	0.83	0.70	MNDY
-116.891522	35.331235	-6.98	5.63	0.66	0.57	MOJ7
-117.207503	34.974841	-9.26	10.44	0.77	0.65	RAIN
-116.889248	35.425156	-6.44	5.49	0.52	0.48	GOLD
-117.808888	35.982343	-5.53	11.64	0.72	0.66	COSO
-118.173223	34.204819	-22.94	21.46	0.48	0.45	JPLM
-120.944426	39.974554	-8.98	6.45	0.59	0.50	QUIN
-120.616446	34.556309	-30.96	33.48	0.50	0.47	VNDP
-121.568333	36.873389	-21.51	26.80	0.87	0.67	77RT
-121.772810	36.589777	-28.08	35.03	0.71	0.55	BRU2
-121.518441	36.822664	-29.63	35.35	0.80	0.62	CROS
-121.563517	36.860960	-26.95	31.26	0.85	0.66	DGA3
-121.357162	36.925804	-11.37	9.12	0.79	0.62	FV30
-121.559972	36.820395	-28.36	33.51	0.90	0.68	HIWA
-121.401789	36.893280	-14.36	11.86	1.02	0.84	HOLL
-121.453349	36.872237	-16.43	21.25	0.64	0.52	KNOB
-121.494155	36.841053	-14.24	24.33	1.05	0.85	MORS
-121.798972	36.749054	-30.08	35.34	1.33	0.88	MULL
-121.059958	37.079811	-10.06	7.18	0.81	0.62	ONIE
-121.287803	37.007749	-10.88	11.23	0.76	0.56	PACH
-121.462366	36.908765	-17.32	19.49	1.40	1.06	RAIL
-121.447181	36.765302	-29.07	36.65	0.66	0.52	SAOB
-121.299342	36.899981	-9.59	9.20	0.89	0.67	TURK
-122.812643	38.087308	-22.67	29.78	0.99	0.80	1395
-122.527467	38.236422	-15.59	20.80	0.83	0.64	ADOO

continued on next page

Table B.2: *continued*

Longitude °E	Latitude °N	V_{east} mm/yr	V_{north} mm/yr	$Error_{east}$ mm/yr	$Error_{north}$ mm/yr	Station Name
-122.455672	38.223185	-14.80	18.40	0.68	0.53	AIRR
-121.994708	38.416680	-6.90	8.12	0.92	0.68	CAML
-122.595284	38.185992	-17.71	22.86	0.62	0.47	CORD
-122.337976	38.257812	-13.60	17.32	1.36	1.01	DEAL
-123.000764	37.697207	-27.52	36.87	0.43	0.37	FARB
-122.175244	38.350685	-11.85	10.12	0.75	0.58	GAME
-122.114605	38.331179	-12.86	10.10	0.88	0.74	GORR
-122.259201	38.323878	-11.64	14.11	0.84	0.65	HAGG
-122.203191	38.312607	-12.42	14.01	1.04	0.80	MADI
-122.736541	38.092654	-19.47	27.80	1.07	0.83	NICC
-122.868727	38.079711	-23.93	31.17	0.85	0.67	PRH2
-123.014904	37.996405	-26.85	36.27	0.69	0.51	PRH3
-123.018716	37.996174	-24.78	34.72	0.70	0.59	PTRB
-118.640854	34.256931	-25.35	28.53	0.67	0.49	CH33
-118.511083	34.257580	-22.20	24.45	0.93	0.72	DELO
-118.540112	34.407133	-24.43	18.50	0.67	0.52	HP74
-118.542611	34.202054	-23.87	30.15	0.77	0.58	MCDS
-118.559861	34.130137	-25.46	32.93	1.32	0.96	MULH
-118.555205	34.232840	-25.79	28.47	0.68	0.53	NRID
-118.562227	34.179283	-25.25	30.06	0.76	0.59	OXCO
-118.601270	34.330627	-28.79	21.61	0.52	0.43	PICO
-118.488244	34.291684	-23.93	22.93	0.53	0.44	RESV
-118.561456	34.693141	-18.45	17.93	0.73	0.54	SAEC
-118.595516	34.063038	-26.02	29.11	0.76	0.59	TUNA
-124.485732	42.801104	6.36	11.08	1.38	1.17	BLCO
-124.565311	42.836635	8.78	12.17	1.26	1.08	CAPE
-124.175170	43.123631	4.57	8.75	1.10	0.97	P750
-123.597091	42.718775	2.15	7.10	1.03	0.83	REUB
-122.348051	42.619259	-0.95	5.19	1.06	0.82	RUST
-123.064892	43.372264	0.77	4.76	0.89	0.73	SCOT
-122.738278	43.343542	-0.77	4.71	1.16	1.04	STEA

continued on next page

Table B.2: *continued*

Longitude °E	Latitude °N	V_{east} mm/yr	V_{north} mm/yr	$Error_{east}$ mm/yr	$Error_{north}$ mm/yr	Station Name
-120.464677	35.942852	-12.72	18.50	0.60	0.46	33JD
-120.453095	35.551773	-24.99	30.87	0.49	0.39	ALMO
-120.351311	35.745649	-21.34	27.17	0.50	0.39	BENC
-120.462478	35.887746	-20.99	29.25	0.53	0.41	BREK
-120.430837	35.888351	-23.17	31.12	0.37	0.33	CARR
-120.430576	35.888126	-22.41	27.78	0.54	0.42	CARX
-120.222461	35.787754	-15.10	17.74	0.58	0.46	CTWD
-120.540378	35.956597	-24.10	32.20	0.57	0.45	JD84
-120.435213	35.909442	-13.50	19.25	0.55	0.45	JOAQ
-120.442985	35.832594	-22.41	29.61	0.47	0.38	MASO
-120.498285	35.949646	-21.63	24.35	0.44	0.38	MIDE
-120.596006	36.078888	-9.29	13.61	0.50	0.38	MITH
-120.434890	35.969394	-9.96	16.76	0.46	0.37	MNMT
-120.707567	35.948937	-24.73	32.94	0.47	0.38	MONT
-120.442162	35.885044	-23.35	28.84	0.59	0.46	OQUI
-120.306065	35.895551	-11.62	16.86	0.46	0.38	PK59
-120.541555	35.945238	-23.30	31.50	0.56	0.49	PKDB
-120.260597	35.604955	-22.65	25.94	0.56	0.44	RH32
-120.018146	35.487704	-18.16	22.38	0.51	0.40	TWR2
-120.273324	35.708269	-19.57	25.03	0.54	0.41	WATH
-120.433695	35.939353	-11.56	18.76	0.51	0.51	CANP
-120.430818	35.888384	-20.87	28.05	0.75	0.74	CARH
-120.430837	35.888351	-21.86	28.23	0.53	0.53	CARR
-120.750751	35.791611	-22.89	34.10	0.78	0.76	CRBT
-120.479493	35.866714	-21.19	30.45	0.74	0.72	HOGS
-120.402381	35.880812	-12.98	21.16	0.75	0.74	HUNT
-120.473280	35.899789	-21.43	29.30	0.51	0.51	LAND
-120.594281	35.828709	-21.58	33.14	0.75	0.73	LOWS
-120.443056	35.832596	-20.49	29.68	0.75	0.74	MASW
-120.458828	35.921913	-10.91	19.91	0.52	0.51	MIDA
-120.434050	35.969472	-10.18	18.74	0.75	0.73	MNMC

continued on next page

Table B.2: *continued*

Longitude °E	Latitude °N	V_{east} mm/yr	V_{north} mm/yr	$Error_{east}$ mm/yr	$Error_{north}$ mm/yr	Station Name
-119.309348	37.169941	-9.05	8.63	0.55	0.54	MUSB
-120.541555	35.945238	-22.12	30.81	0.52	0.51	PKDB
-120.478432	35.919910	-21.44	27.70	0.51	0.51	POMM
-120.524823	35.899994	-22.30	29.27	0.75	0.74	RNCH
-120.360335	35.917411	-10.88	18.42	0.79	0.77	TBLP
-120.944426	39.974555	-9.18	7.07	0.43	0.41	QUIN
-116.889249	35.425156	-7.59	5.34	0.43	0.41	GOL2
-123.304603	44.585536	5.66	5.61	0.94	0.85	CORV
-124.061886	44.585025	8.68	8.72	0.94	0.84	NEWP
-121.871312	37.498920	-14.42	15.74	0.96	0.63	ALLI
-122.034858	37.426340	-16.23	22.49	1.82	1.04	BEND
-122.123286	37.362687	-21.97	26.17	1.19	0.83	FOOT
-122.359466	37.228388	-28.61	32.85	1.44	0.98	HALM
-121.566307	37.755305	-10.12	6.98	1.18	0.69	MEDA
-121.866863	37.485326	-16.07	16.90	0.89	0.71	MONB
-122.167159	37.324488	-23.79	29.67	0.97	0.61	PAWT
-122.394532	37.183024	-28.32	35.77	1.14	0.75	PIGE
-122.389949	37.187084	-28.48	35.76	0.58	0.48	PPT1
-121.809951	37.593997	-11.98	10.92	0.95	0.63	SARE
-121.869851	37.541314	-13.59	18.42	0.87	0.55	SHER
-122.216321	37.312267	-23.29	30.28	0.85	0.55	TRUE
-123.000764	37.697207	-27.80	37.47	0.95	0.73	FARB
-116.095510	40.148366	-3.77	-0.28	0.82	0.63	MINE
-115.817196	40.914691	-4.93	0.03	0.83	0.63	ELKO
-117.184039	38.097195	-5.15	-0.32	1.21	0.94	TONO
-116.715570	39.147710	-5.15	-0.53	1.24	0.98	MONI
-116.160861	40.083625	-4.64	-0.17	0.68	0.54	D100
-116.306331	39.533710	-4.02	-1.48	0.84	0.74	D200
-116.745998	36.828158	-2.75	-0.81	0.99	0.75	P16X
-117.027592	37.274286	-2.48	-1.34	0.99	0.70	SARC
-116.889249	35.425156	-7.49	5.49	0.33	0.32	GOL2

continued on next page

Table B.2: *continued*

Longitude °E	Latitude °N	V_{east} mm/yr	V_{north} mm/yr	$Error_{east}$ mm/yr	$Error_{north}$ mm/yr	Station Name
-112.229625	41.015673	-3.31	0.31	1.00	0.81	NAIU
-112.121009	40.652592	-3.00	0.80	1.23	1.06	COON
-111.372716	40.514100	-1.84	1.66	1.46	0.87	HEBE
-111.928312	40.261421	-3.15	0.14	1.01	0.82	LMUT
-118.938780	39.513071	-4.43	3.89	0.87	0.81	B200
-119.244112	38.988116	-5.84	4.90	0.56	0.50	B300
-119.482475	39.552108	-7.20	2.38	0.85	0.75	EARN
-119.355455	40.416527	-6.89	1.45	0.75	0.66	GARL
-117.508934	39.685617	-3.94	1.91	1.60	1.31	NEWP
-120.944426	39.974554	-8.50	6.66	0.56	0.47	QUIN
-118.703180	39.995376	-6.23	2.05	1.09	0.94	RATT
-120.038837	39.790918	-8.43	4.77	0.67	0.59	SAGE
-120.225042	40.591679	-8.16	3.00	0.73	0.64	SHIN
-118.257503	40.403202	-6.70	0.36	0.73	0.64	TUNG
-118.802278	39.627113	-7.10	3.32	1.65	1.43	UPSA
-120.324940	39.317951	-9.22	4.05	1.25	1.12	UU83
-116.469283	36.837658	-3.44	-1.07	0.75	0.61	MILE
-116.261124	36.943377	-2.60	-0.94	0.94	0.72	SHOS
-115.979014	36.632513	-3.37	-2.97	1.01	0.85	MERC
-116.308237	36.745874	-2.93	-2.15	1.00	0.84	LITT
-116.468341	36.840354	-2.75	-1.92	0.99	0.84	REPO
-116.337792	36.644623	-2.51	-1.54	1.00	0.84	STRI
-116.450940	36.745336	-3.06	-1.81	1.00	0.84	BSST
-116.871699	36.917643	-3.03	-1.02	1.01	0.85	BLLL
-116.765524	36.746503	-3.69	-0.68	1.24	1.04	CHLO
-116.163181	36.690264	-2.93	-1.53	0.52	0.42	1PDI
-118.135659	36.023252	-9.65	8.85	0.48	0.40	3187
-117.675245	36.150394	-9.64	4.70	0.57	0.49	6813
-117.786760	36.537694	-7.62	4.85	0.59	0.51	CERR
-117.808888	35.982343	-1.83	12.75	0.41	0.39	COSO
-117.521942	36.050011	-6.80	6.71	0.62	0.58	ARGU

continued on next page

Table B.2: *continued*

Longitude °E	Latitude °N	V_{east} mm/yr	V_{north} mm/yr	$Error_{east}$ mm/yr	$Error_{north}$ mm/yr	Station Name
-117.085470	36.217878	-3.41	3.43	0.63	0.58	ROGE
-116.650076	36.316284	-3.68	0.45	0.57	0.54	RYAN
-116.099039	36.458815	-3.31	-0.64	0.58	0.54	JONY
-118.074091	35.878388	-9.23	10.59	0.98	0.87	BEPK
-118.474299	35.662271	-10.87	11.26	0.86	0.77	ISLK
-119.057903	36.359957	-8.72	10.44	0.79	0.72	LCOV
-118.283573	37.231991	-7.86	5.71	0.63	0.46	OVRO
-117.640972	36.306937	-5.90	4.18	0.64	0.52	P166
-117.582751	36.231732	-7.39	4.83	0.64	0.56	T19S